Understanding and Improving Perovskite Photovoltaic Devices with Carbon-based Back-electrodes

Dissertation

zur Erlangung des Doktorgrades der Technischen Fakulät der Albert-Ludwigs-Universität Freiburg im Breisgau



vorgelegt von

Dmitry Bogachuk

angefertigt am Fraunhofer Institut für Solare Energiesysteme (ISE)



Freiburg im Breisgau

2022

Dekan:
Prof. Dr. Roland Zengerle

Erstgutachter:
Prof. Dr. Stefan Glunz

Zweitgutachter:
Dr. Severin Vierrath

Vorsitzender der Prüfungskommission:
Prof. Dr. Oliver Ambacher

Beisitzer:
Prof. Dr. Seigo Ito

Datum der Prüfung:
06. Oktober 2022

Declaration

I hereby declare that I am the sole author and composer of my dissertation and that no other sources or learning aids, other than those listed have been used. Furthermore, I declare that I have acknowledged the work of others by providing detailed references of said work.

I hereby also declare, that my dissertation has not been prepared for another examination or assignment, either wholly or excerpts thereof.

_____

Dmitry Bogachuk

"For small creatures such as we,
*the vastness is bearable only through **love**."*

– Carl Sagan



Dedicated to my one and only – Fan



Abstract

Despite the rapid development of perovskite photovoltaics (PV), the device stability and large-area device manufacturing hinder this technology from entering the PV-market. Although perovskite devices with carbon electrodes have the potential to overcome these arduous challenges, their performance is currently far from reaching the radiative limits. This thesis discusses perovskite photovoltaic devices with **carbon-based electrodes**, novel methods to improve their performance, their stability and their potential for reduction of PV-associated emissions and waste streams.

Finding efficient ways to enhance power conversion efficiency (PCE) of a photovoltaic device necessitates a comprehensive **understanding** of the device physics and perovskite crystallization process. Hence, this dissertation starts with the investigation of the key properties of the carbon-based electrodes used in perovskite solar cells (PSCs) and the origins of energy losses in such devices. By utilizing a wide range of advanced characterization methods, the charge carrier generation, recombination, transport and extraction are investigated in-depth to quantify the associated losses. Moreover, controlling the perovskite photoabsorbing layer quality is paramount for any efficient PV device, which is why the liquefaction and crystallization kinetics of perovskite are thoroughly studied as well. Combining results from these meticulous works, a greater comprehension of the device operation and limitations is obtained, inspiring the development of new approaches to overcome them.

Based on these findings a novel nanoarchitectonic approach to engineer the pores in the solar cell architecture is proposed. The nanoarchitectured cell allows for a growth of larger perovskite crystals with a lower density of grain boundaries and a reduced non-radiative recombination rate, thus, **improving** the device performance to 15.7 %. Furthermore, alternation of the graphite crystals in the carbon-based electrode resulted in the reduction of sheet and interfacial resistances of these PSCs, minimizing the series resistance losses and enabling the device fill factor over 74 %.

Although perovskite PV devices stable enough to pass the international ageing tests have been demonstrated in literature, their degradation under **reverse bias conditions** remains to be one of the major concerns. Here, the exceptional stability of perovskite solar cells and modules with carbon-based electrode is shown, which, for the first time, withstand the "hot-spot" conditions of the IEC 61215:2016 test. The degradation in these devices originates from high tunneling currents at highly-negative voltages, rapidly oxidizing incorporated iodine and heating the device, thus, decomposing perovskite layer. Finally, to quantify the potential of perovskite devices with carbon-based electrodes to reduce PV-associated greenhouse gas emissions, a life-cycle-assessment of such modules was performed. This analysis revealed that the CO_2-eq. emissions can be significantly reduced if the glass substrate would be re-used, since it contributes to nearly 53 % of the module's global warming potential (GWP). Therefore, a novel thermally-assisted mechanochemical approach to remanufacture perovskite solar modules was developed, effectively reducing their GWP by up to 33 % and containing potential to have a lower CO_2-footprint than traditional

silicon-based PV. This demonstrates that perovskite PV devices with carbon-based electrodes can be not only efficient, stable and cost-effective, but also **sustainable**, thus, fulfilling all the criteria for a promising emerging PV technology.

Zusammenfassung

Trotz der rasanten Entwicklung der Perowskit-Photovoltaik (PV) erschwert die Stabilität dieser PV-Bauelemente und die Herstellung großflächiger Solarmodule den Eintritt dieser Technologie in den PV-Markt. Obwohl Perowskit-Solarzellen (PSZn) und -Module mit Kohlenstoffelektroden das Potenzial haben, diese schwierigen Herausforderungen zu überwinden, ist ihre Leistung weit von ihren physikalischen Grenzen entfernt. In dieser Arbeit werden Perowskit-Solarzellen mit kohlenstoffbasierten Elektroden, neuartige Methoden zur Verbesserung ihrer Leistung, ihre Stabilität und ihr Potenzial zur Verringerung der mit der Photovoltaik verbundenen Emissionen und Abfallströme erörtert.

Die Suche nach effizienten Methoden zur Verbesserung der Leistungsumwandlungseffizienz eines Photovoltaikgeräts erfordert ein umfassendes **Verständnis** der Solarzellenphysik und des Perowskit-Kristallisationsprozesses. Daher beginnt diese Dissertation mit der Untersuchung der Schlüsseleigenschaften der kohlenstoffbasierten Elektroden, die in PSZn verwendet werden, sowie der Ursachen von Energieverlusten in solchen Systemen. Durch den Einsatz einer breiten Palette fortschrittlicher Charakterisierungsmethoden werden die Ladungsträgererzeugung, die Rekombination, der Transport und die Extraktion eingehend untersucht, um die damit verbundenen Verluste zu quantifizieren. Darüber hinaus ist die Qualitätskontrolle der photoabsorbierenden Perowskit-Schicht für jede effiziente PSZ von entscheidender Bedeutung, weshalb auch die Verflüssigungs- und Kristallisationskinetik des Perowskits im Detail untersucht wird. Durch die Kombination der Ergebnisse dieser sorgfältigen Arbeiten erhält man ein besseres Verständnis der Funktionsweise und der Limitierungen der Zelle, was die Entwicklung neuer Ansätze zu deren Überwindung inspiriert.

Auf der Grundlage dieser Erkenntnisse wird eine neuartige Nanoarchitektur zur Gestaltung der Poren in der Solarzellenarchitektur vorgeschlagen. Die nanoarchitektonische Zelle ermöglicht das Wachstum größerer Perowskitkristalle mit einer geringeren Korngrenzendichte und einer reduzierten nicht-strahlenden Rekombinationsrate, wodurch der Wirkungsgrad der Zelle auf 15.7 % verbessert wird. Darüber hinaus führte die Veränderung der Graphitkristalle in der kohlenstoffbasierten Elektrode zu einer Verringerung der Schicht- und Grenzflächenwiderstände der Perowskit-Solarzellen, wodurch die Serienwiderstandsverluste minimiert wurden und der Füllfaktor der Solarzellen auf über 74 % anstieg.

Obwohl in der Literatur nachgewiesen wurde, dass Perowskit-Solarzellen und- Module stabil genug sind, um die internationalen Alterungstests zu bestehen, ist ihre Degradation unter Rückwärtsspannungsbedingungen nach wie vor eines der Hauptprobleme. Hier wird die außergewöhnliche Stabilität von Perowskit-Solarzellen und -Modulen mit kohlenstoffbasierten Elektroden gezeigt, die zum ersten Mal den "Hot-Spot"-Bedingungen des IEC 61215:2016-Tests standhalten. Die Degradation in Perowskit-Solarzellen entsteht durch hohe Tunnelströme bei hohen negativen Spannungen, die das inkorporierte Jod rapide oxidieren und die Solarzellen aufheizen,

wodurch die Perowskitschicht zersetzt wird. Um schlussendlich das Potenzial von Perowskit-Solarmodule mit kohlenstoffbasierten Elektroden zur Verringerung der mit der Photovoltaik verbundenen Treibhausgasemissionen zu quantifizieren, wurde eine Lebenszyklusanalyse für solche Module durchgeführt. Diese Analyse ergab, dass die CO_2-Äq.-Emissionen erheblich reduziert werden können, wenn das Glassubstrat wiederverwendet wird, da es zu fast 53 % des globalen Erwärmungspotenzials (GEP) des Moduls beiträgt. Daher wurde ein neuartiger thermisch unterstützter mechanisch-chemischer Ansatz für die Wiederaufbereitung von Perowskit-Solarmodulen entwickelt, der ihr GEP um bis zu 33 % reduziert und das Potenzial hat, einen geringeren CO_2-Fußabdruck als herkömmliche siliziumbasierte PV zu haben. Dies zeigt, dass Perowskit-PV-Bauelemente mit kohlenstoffbasierten Elektroden nicht nur effizient, stabil und kostengünstig, sondern auch nachhaltig sein können und somit alle Kriterien für eine vielversprechende neue PV-Technologie erfüllen.

Contents

Abstract i

Zusammenfassung v

Contents ix

Abbreviations xiii

1 Introduction 1

1.1 Motivation . . . 2
1.2 Fundamentals of photovoltaics . . . 4
1.2.1 Basic properties of semiconductors . . . 4
1.2.2 Photovoltaic effect . . . 13
1.2.3 Recombination processes . . . 17
1.2.4 Charge carrier separation . . . 27
1.2.5 Solar cell under illumination . . . 30
1.2.6 From cells to modules . . . 33
1.3 Perovskite photovoltaics . . . 36
1.3.1 Crystal structure of perovskite . . . 36
1.3.2 Unique properties of halide perovskite materials . . . 37
1.3.3 The genesis of halide perovskite photovoltaics . . . 39
1.3.4 Perovskite solar cells . . . 40
1.3.5 Processing techniques . . . 42
1.3.6 Crystallization . . . 45
1.3.7 Current challenges . . . 47
1.4 Aims and outline of dissertation . . . 51

2 Experimental methods **55**
2.1 Sample manufacturing . . . 56
2.2 Characterization techniques . . . 58
2.2.1 X-ray diffraction (XRD) . . . 58
2.2.2 Scanning electron microscopy (SEM) . . . 58
2.2.3 Energy dispersive X-ray spectroscopy (EDX) . . . 60
2.2.4 Atomic force microscopy . . . 61
2.2.5 Steady-state photoluminescence . . . 61
2.2.6 Transient photoluminescence . . . 63
2.2.7 Infrared thermography . . . 65
2.2.8 Raman shift spectroscopy . . . 65
2.2.9 UV-vis spectroscopy . . . 66
2.2.10 Four-point-probe . . . 66
2.2.11 Current-voltage measurements . . . 66
2.2.12 Light intensity-dependent measurements . . . 67
2.2.13 Spectral response and quantum efficiencies . . . 69
2.2.14 Electrochemical impedance spectroscopy . . . 70

3 Low-temperature carbon-based electrodes in perovskite solar cells **71**
3.1 Preamble . . . 72
3.2 Abstract . . . 73
3.3 Introduction . . . 73
3.4 Literature review . . . 75
3.5 Conclusion . . . 122
3.6 Critical discussion . . . 124

4 The nature of the methylamine–$MAPbI_3$ complex: fundamentals of gas-induced perovskite liquefaction and crystallization **127**
4.1 Preamble . . . 128
4.2 Abstract . . . 129
4.3 Introduction . . . 129
4.4 Experimental details . . . 131
4.5 Results and discussion . . . 132
4.6 Conclusions . . . 142
4.7 Critical discussion - research paper . . . 143
4.8 Critical discussion - general concept . . . 144

5 Perovskite solar cells with carbon-based electrodes – quantification of losses and strategies to overcome them **149**
5.1 Preamble . . . 150
5.2 Abstract . . . 151
5.3 Introduction . . . 151
5.4 Experimental details . . . 153
5.5 Results and discussion . . . 156

5.6 Conclusion . . . 171
5.7 Critical discussion . . . 172

6 Nanoarchitectonics in fully printed perovskite solar cells with carbon-based electrodes 175
6.1 Preamble . . . 176
6.2 Abstract . . . 177
6.3 Introduction . . . 177
6.4 Experimental details . . . 179
6.5 Results and discussion . . . 180
6.6 Conclusion . . . 185
6.7 Critical discussion . . . 186

7 Natural and synthetic graphites for electrodes in perovskite solar cells 189
7.1 Preamble . . . 190
7.2 Abstract . . . 191
7.3 Introduction . . . 191
7.4 Experimental details . . . 193
7.5 Results and discussion . . . 195
7.6 Conclusion . . . 204
7.7 Critical discussion . . . 205

8 Perovskite photovoltaic devices with carbon-based electrodes under reverse bias 207
8.1 Preamble . . . 208
8.2 Abstract . . . 209
8.3 Introduction . . . 209
8.4 Experimental details . . . 210
8.5 Results and discussion . . . 212
8.6 Conclusion . . . 224
8.7 Critical discussion . . . 225

9 Remanufacturing perovskite solar cells and modules – a holistic case study 227
9.1 Preamble . . . 228
9.2 Abstract . . . 229
9.3 Introduction . . . 229
9.4 Experimental details . . . 231
9.5 Results . . . 232
9.6 Discussion . . . 238
9.7 Conclusion . . . 241
9.8 Critical discussion . . . 242

10 Conclusion 243
10.1 Summary . . . 244

10.2 Perspective 247

11 Scientific contributions **249**
11.1 Publications 250
11.2 Oral contributions at international conferences 253

12 Acknowledgements **255**

Bibliography **259**

Abbreviations

5-AVA	5-ammonium valeric acid
ACN	Acetonitrile
AFM	Atomic force microscopy
AM	Air-mass (optical)
c-Si	Crystalline silicon
c-TiO_2	Compact titanium dioxide
CTL	Charge transport layer
CB	Conduction band
CBM	Conduction band minimum
CPSC	Perovskite solar cell with carbon-based electrode
CPSM	Perovskite solar module with carbon-based electrode
DMF	*N,N*-Dimethylformamide
DMSO	Dimethyl sulfoxide
DOS	Density of states
EBL	Electron-blocking layer
EDX	Energy dispersive X-ray spectroscopy
EIS	Electrochemical impedance spectroscopy
EQE	External quantum efficiency
ESL	Electron-selective layer
ETL	Electron-transport layer
FA	Formamidinium ($CH(NH_2)_2{}^+$)
FF	Fill factor
FTO	Fluorine-doped tin oxide
FWHM	Full width at half maximum
GB	Grain boundary
GBL	γ-butyrolactone
GWP	Global warming potential
H-CPSC	Perovskite solar cell with high-temperature carbon-based electrode (sometimes also referred to as HTCB-cells)
HBL	Hole-blocking layer
HOMO	Highest occupied molecular orbital
HSL	Hole-selective layer
HTCB	High-temperature carbon-based
HTL	Hole-transport layer
IEC	International electrotechnical commission
IR	Infra-red

IV	Current-voltage
JV	Current density-voltage
L-CPSC	Perovskite solar cell with low-temperature carbon-based electrode (sometimes also referred to as LTCB-cells)
LBIC	Light beam induced current
LCA	Life-cycle assessment
LTCB	Low-temperature carbon-based
LUMO	Lowest unoccupied molecular orbital
MA or MA^+	Methylammonium ($CH_3NH_3^+$)
MA^0	Methylamine (CH_3NH_2)
MPC	Methylamine-perovskite complex
MPP	Maximum power point
m-TiO_2	Mesoporous titanium dioxide
OC	Open circuit
PaPL	Perovskite as planar layer
PCE	Power conversion efficiency
PiPL	Perovskite in porous layer
PL	Photoluminescence
PLQY	Photoluminescence quantum yield
PS	Polystyrene
PSC	Perovskite solar cell
PSM	Perovskite solar modules
PV	Photovoltaic(s)
QFLS	Quasi-Fermi level splitting
R.H.	Relative humidity
SC	Short circuit
sc-XRD	Single-crystal X-ray diffraction
SEM	Scanning electron microscope
SRH	Shockley-Read-Hall
TCO	Transparent conductive oxide
TRPL	Time-resolved photoluminescence
UV	Ultraviolet
UV-vis	Ultraviolet-visible
VB	Valence band
VBM	Valence band maximum
XRD	X-ray diffraction

Chapter 1

Introduction

1

1.1 Motivation

Ever since the industrial revolution, humankind enjoyed the fruits borne by the raised average standard of living, which however also introduced numerous demands. The growth in consumption stimulated the industry sector to grow as well, further requiring exploitation of available resources. In comparison to previously utilized energy sources, such as organic matter (*e.g.* wood) and manual labor, the use of fossil fuels became a much more attractive alternative due to their high power densities and temporal availability. Over the last century along with the rapid technological development, an increase in global population accelerated the depletion of resources that our planet can provide. An overwhelming amount of evidence leaves no doubt (at least in the scientific community) that our planet's climate is changing due to anthropogenic activites, since the start of the industrial age. [1,2] Therefore, in order to avoid devastating consequences on our environment, humankind needs to find solutions to de-escalate the current climate situation and reduce our impact, while it is still possible. One way to reduce our negative effect on the global warming is the reduction of fossil fuel utilization and shift towards more environmentally-friendly energy sources.

Among the available electricity generation technologies, renewable energies, such as *photovoltaics* and *wind energy* are predicted to account for >60 % of the global electricity generation by 2050, if we aim towards the ambitious goal of keeping the global warming below 1.5°C. [3] Today, photovoltaics (PV) accounts for only 3.2 % of the global electricity generation with 707.5 GW cumulative installation, [4] which needs to grow to over 8.5 TW total generation capacity, thus, posing a tremendous challenge for the PV sector. [3] Fortunately, the learning curve[1] of photovoltaic energy generation in the last 40 years shows an encouraging trend of module price decrease by more than 23 % (as depicted in Figure 1.1a) with each doubling in total module production. [4, 6]. Therefore, today's PV electricity prices can already compete with that of fossil fuel-based technologies.

In order to maintain or even accelerate this steep learning rate one needs to consider candidates for the next-generation PV technologies, with an even lower module price or a higher power output. Due to a relatively simple manufacturing process, *thin-film* PV devices based on cadmium-telluride (CdTe), copper indium gallium selenide (CIGS) or similar materials were expected to become a much cheaper alternative to the conventional silicon-based technologies. However, over the last years the prices of silicon module constituents have decreased substantially, deminishing the cost-advantage of thin-film PV modules. Since such devices

[1] In production, typically, an increase in cumulative number of fabricated goods leads to a decrease in (unit) costs to fabricate this good. Such trend is commonly referred to as learning curve, represented by a relationship between the experience producing a product (which often translates into its price) and its production over the years, thus serving as an indicator of how rapidly the "new" knowledge of improvements in production is obtained (or learned). [5]

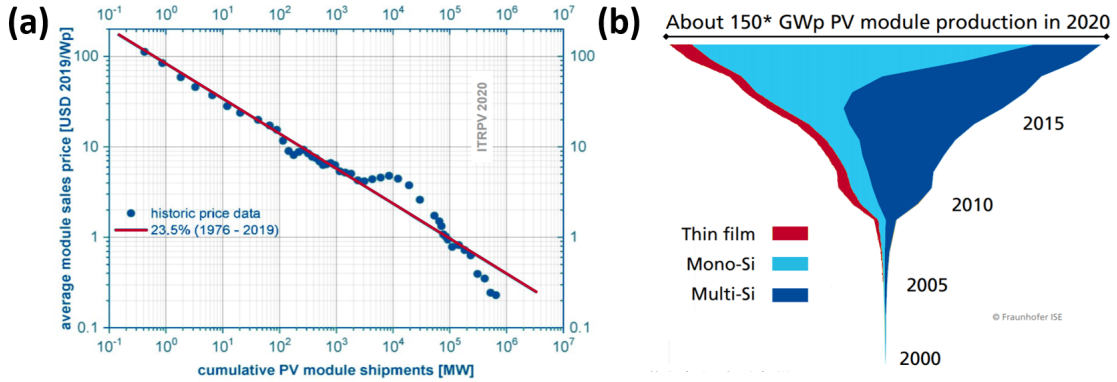


Figure 1.1: (a) Learning curve of PV sector between 1976 and 2019, showing rapid decrease in module price during the production growth. Adapted from [6] (b) Growth of module production and shares of thin-film and crystalline silicon PV technologies over the years. Adapted from [4]

typically also have a lower performance that the silicon-based devices, currently only about 5 % of all the PV modules produced annually are based on thin-films, and the rest are made using either monocrystalline or multicrystalline silicon (Figure 1.1b). [4] However, very recently, a new candidate for the next-generation PV technology came to spotlight due to its potential low production cost and favorable opto-electronic properties – a class of *perovskite* PV devices. Numerous researchers have been fascinated by the vast spectrum of tunable and unique features of perovskites, fuelling intensive research and leading to unprecedented development rate of perovskite photovoltaics. An increasing number of companies planning to produce perovskite PV modules emerge, while some of the largest global PV manufacturers are also considering utilization of perovskites in their modules.

Before introducing perovskite materials, let us firstly discuss the fundamentals of solid state semiconductor physics and the phenomenon of photovoltaic effect.

1.2 Fundamentals of photovoltaics

1.2.1 Basic properties of semiconductors

Since the key component of a photovoltaic device is the semiconductor, it is necessary to understand how such semiconducting material is composed and what gives it unique properties.

Like any solid-state material, semiconductors are formed by an arrangement of atoms, which consist of atomic cores and electrons surrounding them. In the case of isolated atoms, electrons will reside on *discrete* energy levels[2], forming so-called *atomic orbitals* – regions, described by the wave function[3] of a bound electron. However, when two or more atoms are brought together they can form certain bonds, causing their atomic orbitals to overlap and form *molecular orbitals* as shown in Figure 1.2. This process is known as *hybridization* commonly refers to the superposition of interacting electron wave functions, leading to various properties depending on the type of atomic orbitals (*e.g.* *s,p* orbitals) participating in hybridization. Due to the principle of superposition, the wave function overlap causes *constructive* and *destructive* interference, thus producing two separate molecular orbitals - *bonding* and *anti-bonding* orbitals, respectively.

Bonding molecular orbital has a lower discrete energy level than the atomic orbitals of each individual atom, therefore promoting bonding, while the anti-bonding orbital opposes it (therefore less stable) and has a higher energy level. Thus the number of orbitals is always conserved, since N combined atoms with N atomic orbitals will result in $N/2$ bonding and $N/2$ anti-bonding orbitals. However, the bonding orbital is always filled with electrons due to constructive interference of electron wave functions, unlike anti-bonding orbital which is not always filled. Figure 1.2b shows an exemplary case of formation of H_2, where only two electrons are present, resulting in filled bonding orbital, while anti-bonding orbital remains empty. However, in the case of He_2 formation reaction, two electrons will reside in bonding orbital and two in the anti-bonding orbital, making formation of He_2 thermodynamically not favorable.

Importantly, the *Pauli exclusion principle* states that fermions (*i.e.* particles with half-integer spin number, like electrons) cannot occupy the same quantum state in the same quantum system simultaneously. In the case of electrons, this

[2]The idea that a spatially confined particle can occupy only specific, discrete values of energy (known as energy levels) has been first introduced by Niels Bohr in 1913. However, the first evidence of energy quantization was observed already in 1800s from dark lines of the solar spectrum, which occur due to photon absorption by elements in solar atmosphere. These lines are known as *Fraunhofer lines*, named after their discoverer – german scientist Joseph von Fraunhofer, after whom a German Research Organization Fraunhofer Society is named.

[3]Wave function is a mathematical function describing probability of particle's quantum state, which is the key concept in quantum physics.

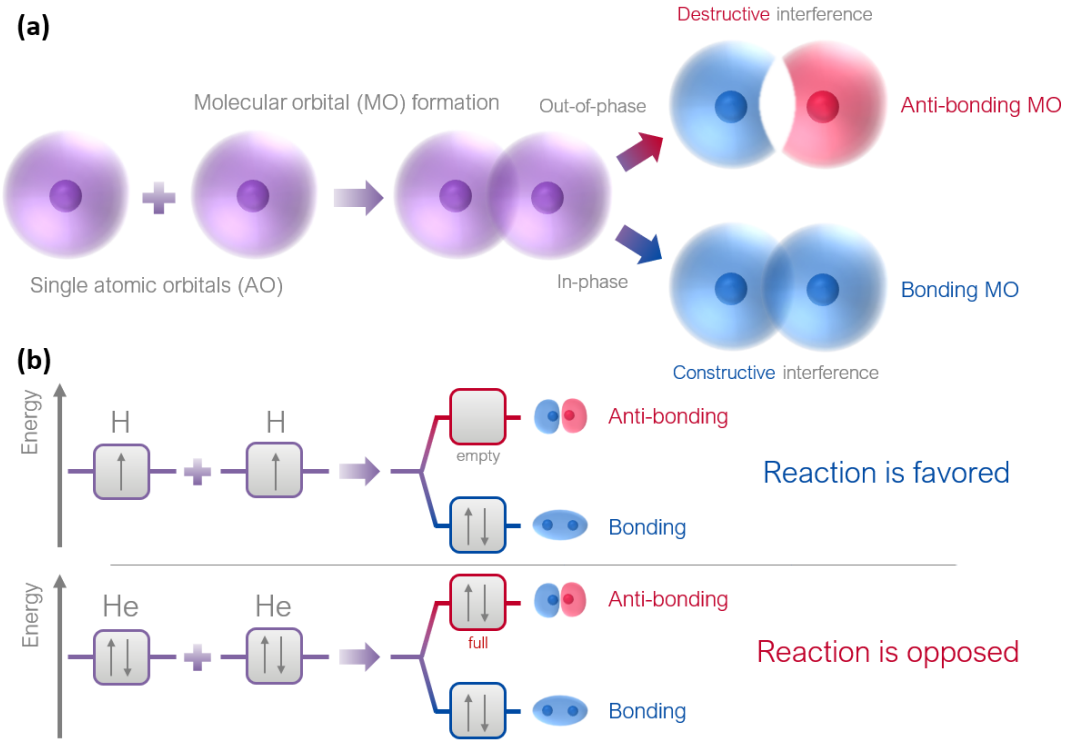


Figure 1.2: (a) Simplified illustration of molecular orbital (MO) formation and difference between bonding and anti-bonding orbitals, (b) Energy diagram depicting difference in energy of electron in atomic orbital vs its energy on bonding and anti-bonding orbital. Note that the He_2 is not thermodynamically favorable as it would contain electrons in the anti-bonding orbital which oppose the reaction, unlike H_2 formation reaction.

principle implies that electrons with overlapping wave functions cannot simultaneously possess same principle, magnetic, azimuthal and spin quantum numbers (n, l, m_l *and* m_s, respectively). Therefore, when electrons are in the same orbital (n, l, m_l numbers are same), they must have opposite spin-numbers: 1/2 and -1/2, designated by vertical arrows.

Given that the size of Si atom is around 0.2 nm, a macroscopic crystal of, for example, 2 mm^3 of pure silicon would already contain 10^{21} atoms, resulting in 10^{21} splitted energy levels. The difference between these levels becomes negligibly small ($<10^{-21}$ eV), meaning that energy levels cease to be discrete and can be considered as *continuous energy bands*.

Since each element of the periodic table contains a unique set of properties, the energy bands of compounds built from these elements also differ and in order to predict the material properties, quantum mechanical calculation have to be employed.

Schrödinger equation (Equation 1.1) and its variations introduced by Erwin Schrödinger in 1925 allowed scientists to predict the behavior of wave function in quantum systems and relate such properties of a particle as its position, energy, time and momentum. Its most general time-independent form is expressed as:

$$|\hat{H}|\Psi\rangle = |E|\Psi\rangle, \tag{1.1}$$

where the $|\hat{H}|\Psi\rangle$ is the Hamiltonian operator of the wave function state vector Ψ and E is the energy of the system. Hamiltonian mechanics is a reformulation of the Newtonian mechanics, which is especially useful in most of the formulations of quantum theory. Hamiltonian represents a sum of kinetic ($\hat{T}$) and potential ($\hat{V}$) energy operators:

$$\hat{H} = \hat{T} + \hat{V} = \frac{\hat{p}^2}{2m} + \hat{V} \tag{1.2}$$

, where $\hat{p}$ and m are the particle momentum operator and mass, respectively. For a single particle in one dimension, the momentum operator is expressed as:

$$\hat{p} = -i\hbar\frac{\partial}{\partial x} \tag{1.3}$$

, where i is an imaginary number and $\hbar$ is reduced Planck's constant. Therefore, in order to express $\hat{p}^2$ in 3-dimensional space, a Laplacian operator ∇^2 can be used. Rewriting Equation 1.2 as function of (Euclidean) space and time gives us:

$$\hat{H} = -\frac{\hbar^2}{2m}\nabla^2 + V(r,t) \tag{1.4}$$

Equation 1.4 can be applied to space and time wave function systems $\Psi(r,t)$ and allows us to find the solutions for the wave function $\psi(r,t)$ according to the Equation 1.1.

For solid-state materials composed of periodic crystal lattice it is particularly useful to consider not only the real-space *direct* lattice but also its Fourier transform[4] counter part - *reciprocal* lattice. Thus, a spatially dependent function can be transformed into a spatial frequency-dependent one, which is often used for the analysis of periodic lattices of materials. More importantly, the wave vector (called

[4]Besides the introduction of Fourier transform, Joseph Fourier is also known for the discovery of greenhouse effect in 1820s – physical phenomenon behind the global warming.

k-vector) of the electron wave function in a material is often used to describe the wave function in reciprocal space, known as *k-space* and has a unit of reciprocal length. Since crystal momentum **p** is proportional to the **k**-vector according to:

$$\mathbf{p} = \hbar\mathbf{k} \tag{1.5}$$

it is often more convenient to analyze the energetic landscape and properties of the material by looking at the electron energy plotted against momentum, commonly known as *E-k* plot or energy dispersion diagram.

To demonstrate how such *E-k* diagram can be plotted, let us consider a particle existing in one dimension with no potential energy. From de Broglie relation[5] of particle-wave duality we know that:

$$\lambda = \frac{h}{mv} = \frac{h}{p}, \tag{1.6}$$

where λ is the wavelength of the particle, v is its speed and p is the momentum. If we consider k as wavenumber ($k = \frac{2\pi}{\lambda}$), having a unit of reciprocal length (since λ is expressed in m) we can write:

$$p = \frac{h}{\lambda} = \frac{h}{2\pi}k = \hbar k \tag{1.7}$$

, which yields the same expression as Equation 1.5 but in one dimensional real space. Hence the kinetic energy of a particle in such a system can be expressed as:

$$E = \frac{1}{2}mv^2 = \frac{p^2}{2m} = \frac{\hbar^2}{2m}k^2 \tag{1.8}$$

Equation 1.8 can also be obtained by solving the Schrödinger equation using Hamiltonian operator in Equation 1.4 with $V = 0$, demonstrating that this relation between E and k then holds true not only for Euclidean real space but for any Hilbert space as well. From Equation 1.8 one can clearly see that plotting particle energy as function of k results in *parabolic* shape, which is also present in energy dispersion diagrams of real materials, as we will see later.

[5] In his PhD thesis in 1924 Louis de Broglie proposed that all matter has also wave-like properties – a revolutionary idea which was later confirmed experimentally and which earned him Nobel Prize in Physics few years later.

In order to apply Equation 1.1 to N atoms of a material, we firstly need to express it in **r,k** space using the Hamiltonian operator in Equation 1.4:

$$\Big[-\frac{\hbar^2}{2m}\nabla^2 + V(\mathbf{r})\Big]\psi(\mathbf{r},\mathbf{k}) = E(\mathbf{k})\psi(\mathbf{r},\mathbf{k}) \tag{1.9}$$

In a solid state material, which is composed of a periodic crystal lattice, the potential in direct lattice (real space) is also assumed to be periodic. In such case, *Bloch's theorem* can be applied, postulating that if potential $V(\mathbf{r})$ is periodic, the solutions for the wavefunction $\psi(r,k)$ of the Schrödinger equation exist in the form of plane wave, dictated by the periodic function u. The periodic function is related to the material structure and location of molecular orbitals in it. Therefore $\psi(r,k)$ in this case can be expressed as:

$$\psi(\mathbf{r},\mathbf{k}) = \mathrm{e}^{i\mathbf{k}\cdot\mathbf{r}}u(\mathbf{r},\mathbf{k}) \tag{1.10}$$

In order to extend the Bloch function to be used not only for one point in the lattice but by any other point as well, Equation 1.10 can take the following form:

$$\psi(\mathbf{r}+\mathbf{R},\mathbf{k}) = \mathrm{e}^{i\mathbf{k}\cdot(\mathbf{r}+\mathbf{R})}u((\mathbf{r}+\mathbf{R}),\mathbf{k}), \tag{1.11}$$

where $\mathbf{R} = n_x x + n_y y + n_z z$ having n_x, n_y and n_z as integer values and x, y and z as basis vectors in direct lattice. Thus, solving Equation 1.4 for wave function solution in Equation 1.11 allows us to construct an *E-k* plot of a material with known structure and see how electron energy in different molecular orbitals depends on its momentum.

As example, we can take a look at *E-k* plot of a semiconducting material gallium arsenide (GaAs) shown in Figure 1.3a. Note the presence of a lower continuous energy band and a higher continuous energy band, separated by a gap. Electrons in the lower band reside on the valence orbitals and therefore this energy band is called *valence band*. In the higher energy band, electrons are free to move along crystal lattice and therefore can conduct current, hence this band is called *conduction band*. Since both bands are closely related to molecular orbitals and number of occupied states in it, valence band is also often called *highest occupied molecular orbital* (HOMO) and conduction band – *lowest unoccupied molecular orbital* (LUMO). However, the bands designation has a physical meaning only when the number of energy levels is sufficiently large, unlike HOMO/LUMO designation, which can be applied even to a single molecule. The key property which defines a material as *semiconductor* is the presence of forbidden energy states between

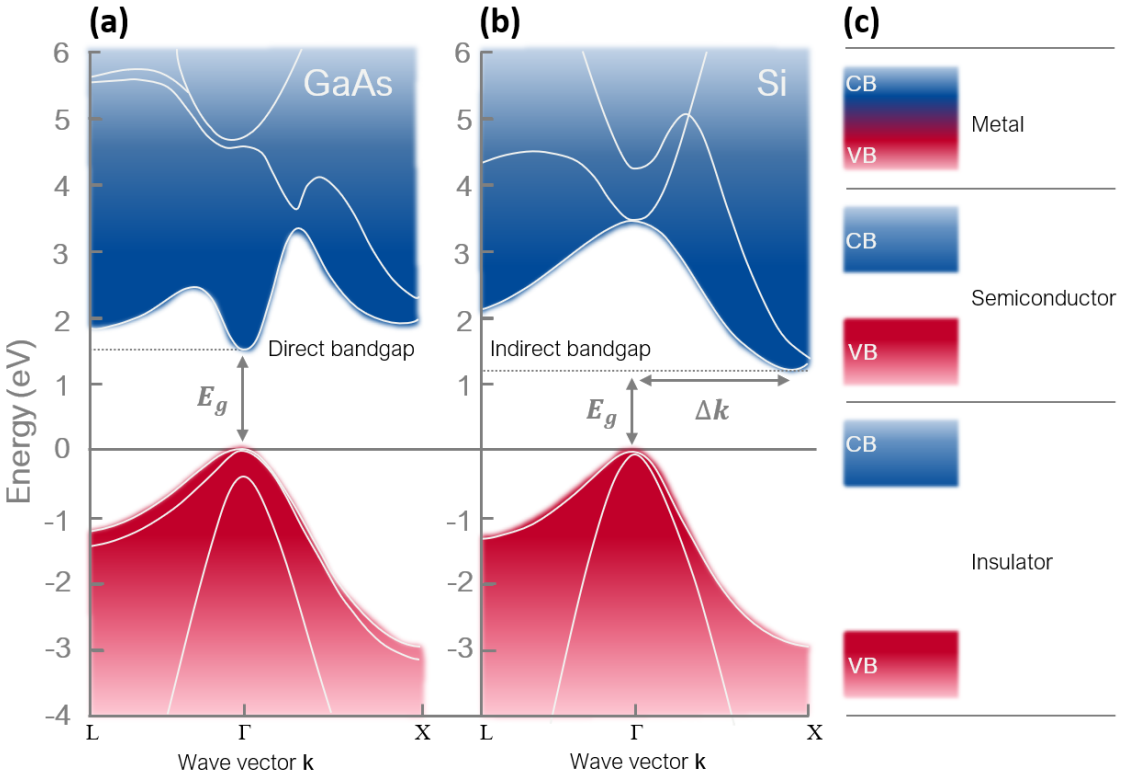


Figure 1.3: *E-k* plots of (a) GaAs and of (b) Si near the center of Brillouin zone (Γ-point). (c) Illustration of bandgap in metals (overlapping bands, *i.e.* no bandgap), semiconductors (moderate bandgap) and insulators (very large bandgap). Adapted from Ref. [7]

valence and conduction bands, which electrons cannot occupy in an ideal lattice. This gap is called *energy bandgap* (E_g).

As will be shown in subsection 1.2.2, what makes semiconducting materials useful in numerous applications is the ability of electrons to transition between the valence and conduction bands when certain criteria are met. In semiconductors like GaAs, the *conduction band minimum* (CBM) and *valence band maximum* (VBM) are located at the same k-point, meaning that in order to transition from VBM to CBM electrons only need an additional energy equivalent to E_g (or higher) and the momentum is conserved. However in the case of semiconductors like Silicon (Si), a difference in momentum between VBM and CBM exist (Figure 1.3b) decreasing the transition rate between these bands. This fundamental difference brings the differentiation between semiconductors with *direct bandgap*, like GaAs, and with an *indirect bandgap*, like Si.

Notably, the parabolic band shapes close to the VBM and CBM are often approximated by Equation 1.8 and can be used to find the *effective mass* (m^*) of electrons. The need to disentangle between an actual and effective mass of electron stems from

the fact that particle mass changes depending on its point in the first Brillouin zone[6], *i.e.* its k-value or momentum. Therefore, effective mass of an electron in a crystal lattice is usually expressed as a *tensor*:

$$m_e^* = m_{ij}^* = \left(\frac{1}{\hbar^2}\frac{\partial^2 E(k)}{\partial k_i \partial k_j}\right)^{-1} \tag{1.12}$$

Unlike semiconductors, *metals* have a distinct feature of overlapping conduction and valence bands, therefore allowing electron delocalization and their free movement across the lattice, which evidently results in superior electric and thermal conductivity of metallic materials. In contrast, when E_g of a material becomes large enough (normally >4 eV), high energies are required for transitioning between bands and electron transport, where such material can be considered an *insulator*. Figure 1.3c illustrates the simplistic view of the conduction and valence bands for metals, semiconductors and insulators.

As mentioned earlier, conduction and valence bands in a condensed matter represent a large continuum of energy states very similar in E- and k-values and therefore are typically not treated as discrete. In order to quantify the number of states, or even better, the *density of states*, we start by visualizing a sphere of available energy states in k-space. Since we assume a periodic crystal structure and potential, we can set a boundary condition for our electron wave function in k-space, which in Euler's representation would look as following:

$$e^{i(k_x x, k_y y, k_z z)} = 1, \tag{1.13}$$

meaning that the wave function described by Equation 1.10 has the same value at the beginning and at the end of its period. This condition allows us to set a 3D k-space, that can be described in integer numbers (n) multiplied by $2\pi/L$ (Figure 1.4a):

$$(k_x x, k_y y, k_z z) = (n_x \frac{2\pi}{L}, n_y \frac{2\pi}{L}, n_z \frac{2\pi}{L}) \tag{1.14}$$

Therefore, a unit cell volume in k-space can be considered as $V_{unit} = (2\pi/L)^3$. Now we can express the number of available states as:

$$N_s = 2\frac{V_{sphere}}{V_{unit}} = 2\frac{4\pi k^3}{3}\frac{L^3}{8\pi^3} = \frac{k^3 L^3}{3\pi^2} \tag{1.15}$$

[6] In general, a Brillouin zone is a unique primitive cell of a reciprocal lattice, representing a fundamental domain of the translational symmetry of crystal lattices. The "first" Brillouin zone is a smallest possible volume in k-space, limited by planes, which perpendicularly bisect vectors from the chosen point to the nearest equivalent point in reciprocal lattice. [7]

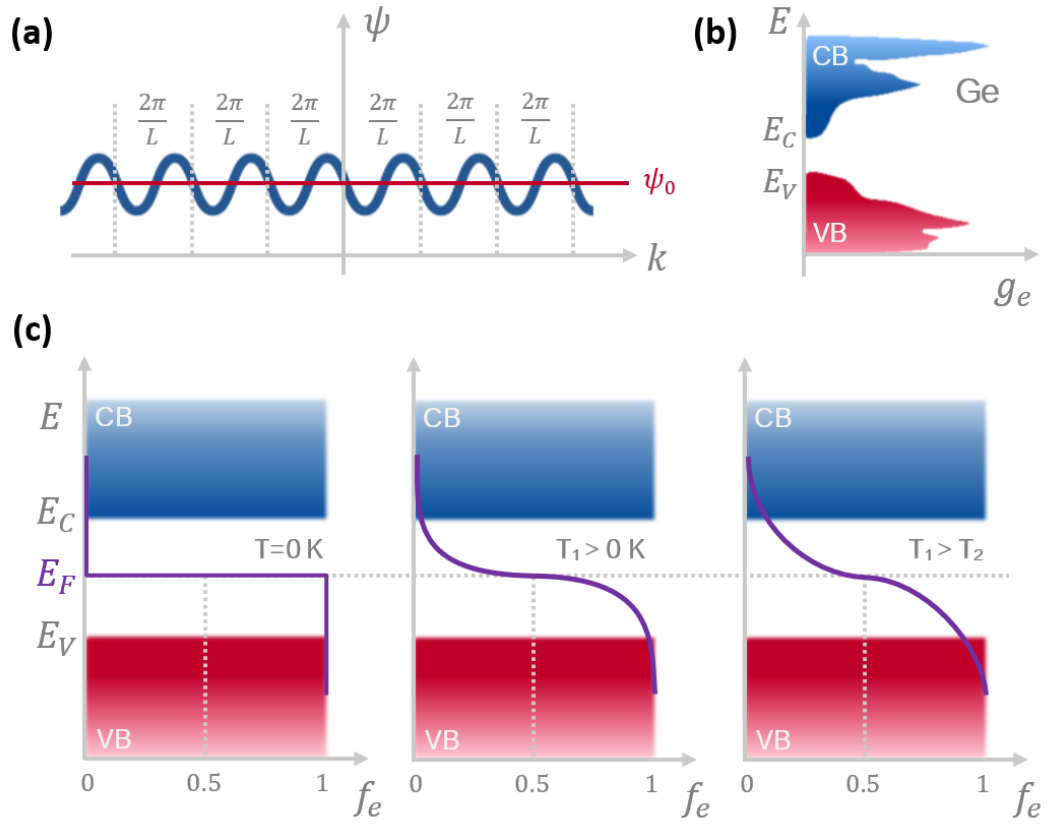


Figure 1.4: (a) Visual representation of periodic wave function, resembling periodicity of potential in crystal lattice, (b) density of states (DOS) in germanium (Ge) semiconductor. Adapted from Ref. [8] (c) Illustration of Fermi-Dirac probability distribution at different temperatures. Adapted from Ref. [9]

As we saw from the E-k plot, the VBM and CBM can be approximated by quadratic function in Equation 1.8 for parabolic dispersion function. In this case we can write k as:

$$k = \sqrt{\frac{2m^* E}{\hbar^2}} \tag{1.16}$$

Inserting Equation 1.16 into Equation 1.15 and considering $V = L^3$ as volume (in which states are located) yields number of states:

$$N_s = \frac{V}{3\pi^2}\left(\frac{2m^* E}{\hbar^2}\right)^{3/2} \tag{1.17}$$

Finally, dividing Equation 1.17 by volume and differentiating with respect to energy, gives us density of states (DOS):

$$g_0(E) = \frac{1}{V}\frac{\partial N_s}{\partial E} = \frac{1}{2\pi^2}\left(\frac{2m^*}{\hbar^2}\right)^{3/2} E^{1/2} \tag{1.18}$$

Equation 1.18 is valid for a free electron in a parabolic energy dispersion with a minimum energy of zero. In the case of semiconductor however, one must consider the energy of CBM (E_C) as minimum energy. Thus, for semiconductors the DOS is expressed as:

$$g_e(E) = \frac{1}{2\pi^2}\left(\frac{2m^*}{\hbar^2}\right)^{3/2} (E - E_C)^{1/2} \tag{1.19}$$

An example of DOS diagram can be seen in Figure 1.4b. By knowing the DOS available for electrons, one could also determine the electron densities in conduction and valence bands if the likelihood for electrons to occupy these energy states is known. To quantitatively estimate the probability of electrons occupying energy states ($f(E)$) between conduction and valence bands, Fermi-Dirac distribution can be utilized:

$$f_e(E) = \frac{1}{\exp\left(\dfrac{E_C - E_F}{kT}\right) + 1}, \tag{1.20}$$

where k is Boltzmann constant, T is temperature and E_F is the *Fermi energy level* of an electron. The derivation of Equation 1.20 is based on statistical description of non-interacting fermions using grand canonical ensemble. Since this ensemble assumes a number of particles placed in the reservoir with chemical potential μ, E_F in Equation 1.20 can also be considered as *chemical potential* and effectively represents an averaged energy of electrons, following Fermi-Dirac statistics. More precisely, E_F represents the energy state corresponding to an occupation probability of 50 %, *i.e.* $f(E_F) = 0.5$. As can be seen from Figure 1.4c, for the same semiconductor, Fermi-Dirac distribution function changes depending on its temperature, but not E_F. As temperature increases, the chances of spontaneous electron transition from valence to conduction band slightly increases. Finally, by knowing the DOS and occupation probability, one can obtain

$$n_e(E) = \int_{E_C}^{\infty} g_e(E) f_e(E) dE, \tag{1.21}$$

which described the density of free electrons in the conduction band.

1.2.2 Photovoltaic effect

After establishing such important properties of semiconductors as energy bands, density of states, Fermi level and electron density, the *photovoltaic effect* can be discussed in the following section.

Applying wave-particle dualism is not only possible for electrons as we saw earlier, but it is also applicable for *photons* – quanta of light waves. In one of his "Annus Mirabilis" papers[7] Albert Einstein proposed that Planck postulate can be adapted to relate the energy of each photon to its *frequency* (ν) by the following elegant expression:

$$E_{ph} = \hbar\omega = h\nu = \frac{hc}{\lambda}, \tag{1.22}$$

where $\omega = 2\pi\nu$ is the angular frequency, $h = 2\pi\hbar$ is *Planck constant* and c is the speed of light.

When light is incident on a material, it can either be *absorbed*, *transmitted* or *reflected*. Therefore, the approximation $A + T + R = 1$ often represents the possible outcomes for different photons incident on different materials, which effectively determine their visual appearance (*e.g.* color, transparency, gloss).

When non-reflected light is incident on a semiconductor, it will propagate through the material with a reduced intensity (I), due to absorption resulting in light attenuation. According to the Lambert-Beer law the light intensity attenuation decays exponentially (in the case of homogeneous absorption coefficient α along the material thickness) as:

$$I(z) = I_0 e^{-\alpha z}, \tag{1.23}$$

where I_0 is the light intensity on material's surface and z is distance. In order for a photon to be absorbed by a semiconductor, its energy E_{ph} has to be at least as high as the bandgap energy E_g. Therefore, according to Equation 1.23 essentially two properties of the semiconductor define whether a photon will be absorbed or transmitted through: its energy bandgap E_g and thickness.

In the case of absorption, the photon energy will be transferred to an electron in

[7] The year of 1905 is often marked as Einstein's "miracle year", when he published four breakthrough publications (*Annus Mirabilis papers*): on the subjects of Brownian motion, special relativity theory, mass-energy equivalence and the photoelectric effect. In 1921 he received the Nobel Prize in Physics for the latter discovery.

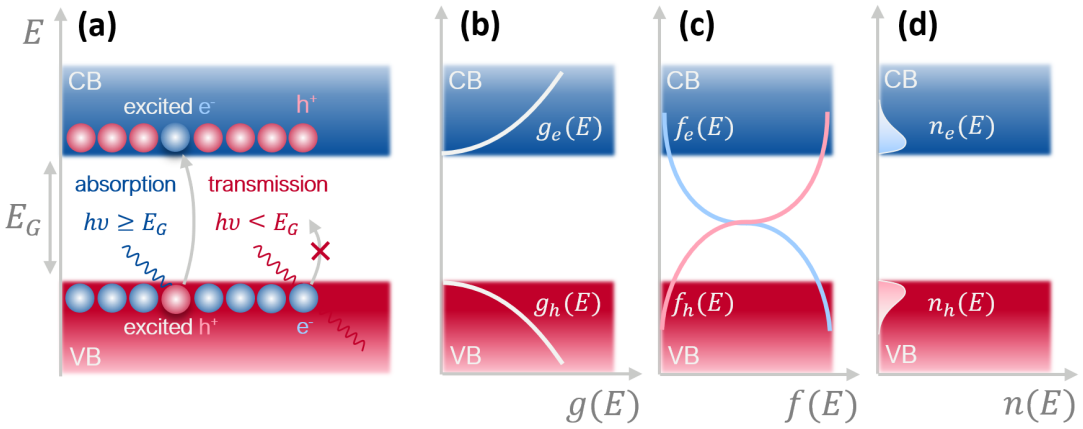


Figure 1.5: (a) Energy band diagram of a semiconductor depicting process of photon absorption, causing generation of excited electrons in conduction band and holes in valence band. Generation process is however only possible if the energy of the absorbed photon ($h\nu$) is at least as high as the semiconductor bandgap energy. If it is lower, the photon will not be absorbed but transmitted further. (b) Density of states, (c) Fermi-Dirac probability distribution and (c) electron and hole densities in conduction and valence bands, respectively.

the valence band, which will become *excited* and transition to the conduction band, since it can have an energy higher than the difference between conduction and valence bands ($E_{ph} > E_C - E_V$). This process is called charge carrier *generation* and it is the key process in solar energy generation systems, which convert solar energy into electricity via photovoltaic effect. That is why semiconductor devices converting solar energy into electricity are called photovoltaic (PV) devices and systems.

After an electron gets excited into the conduction band, it leaves a *hole* in the energy and momentum state, which it used to fill before excitation (Figure 1.5a). Consequently, it can become thermodynamically favorable for neighboring electrons to leave their state and fill this hole, which in turn creates a hole in the state it used to occupy. In such way, a hole can "move" across the crystal lattice, while being in valence band in a similar way as electrons can be transported while being in conduction band. Therefore, rather than considering the motion of all these valence electrons "hopping" from one bond to the next, it is common to treat hole as a quasi-particle moving in the opposite direction with its own effective mass, density of states, occupation probability *etc.* Notably, due to uncertainty principle, it is not possible to identify the exact location of a broken bond in the form of excited hole at every instant and, therefore, similarly to excited electrons, holes in valence band are considered to be *delocalized*.

When an *electron-hole pair* is generated upon photon absorption, it gives rise to new electron and hole densities in conduction and valence bands respectively.

Just like electrons, holes also have density of states $g_h(E)$ in valence band and occupation probability $f_h(E) = 1 - f_e(E)$.

In order to solve the Equation 1.21 analytically, one can use the so-called *Boltzmann Approximation*, which allows to omit the "+1" in the denominator of Equation 1.20, since the exponential dependency of $f(E)$ makes it negligibly small at large E ($E - E_F > 3kT$). Therefore, Equation 1.21 becomes:

$$\begin{aligned} n_e(E) &= \frac{1}{2\pi^2}\left(\frac{2m_e^*}{\hbar^2}\right)^{3/2}\int_{E_C}^{\infty}(E-E_C)^{1/2}e^{-\frac{E-E_F}{kT}}dE \\ &= 4\pi\left(\frac{2m_e^*}{h^2}\right)^{3/2}\int_{E_C}^{\infty}(E-E_C)^{1/2}e^{-\frac{E-E_F}{kT}}dE \\ &= 4\pi\left(\frac{2m_e^*}{h^2}\right)^{3/2}\frac{\pi^{1/2}}{2}(kT)^{3/2}e^{\frac{E_F-E_C}{kT}} \\ &= 2\left(\frac{2\pi m_e^* kT}{h^2}\right)^{3/2}e^{\frac{E_F-E_C}{kT}} \\ &= N_C e^{\frac{E_F-E_C}{kT}}, \end{aligned} \tag{1.24}$$

where N_C denotes the *effective density of states* of electrons in conduction band, which is solely determined by m_e^* and temperature of the material. Similarly to electron density in Equation 1.21 and Equation 1.24, we can derive hole density with DOS for free holes starting from VBM:

$$\begin{aligned} n_h(E) &= \int_{-\infty}^{E_V} g_h(E)f_h(E)dE = \int_{-\infty}^{E_V} g_h(E)(1-f_e(E))dE \\ &= 4\pi\left(\frac{2m_h^*}{h^2}\right)^{3/2}\int_{-\infty}^{E_V}(E-E_V)^{1/2}(1-e^{-\frac{E-E_F}{kT}})dE \\ &= 2\left(\frac{2\pi m_h^* kT}{h^2}\right)^{3/2}e^{\frac{E_V-E_F}{kT}} \\ &= N_V e^{\frac{E_V-E_F}{kT}} \end{aligned} \tag{1.25}$$

Figure 1.5(b, c) illustrates the DOS and Fermi-Dirac distribution of electrons and holes. Integrating under the overlapping functions of $g(E)$ and $f(E)$ according to Equation 1.24 and Equation 1.25 allows to calculate electron and hole densities as demonstrated in Figure 1.5d.

In principle we can differentiate between two different states of a system: *equilibrium* and *non-equilibrium*, which describe the relation between n_e, n_h and so-called *intrinsic* carrier concentration – n_i:

- **equilibrium** – $n_e n_h = n_i^2$

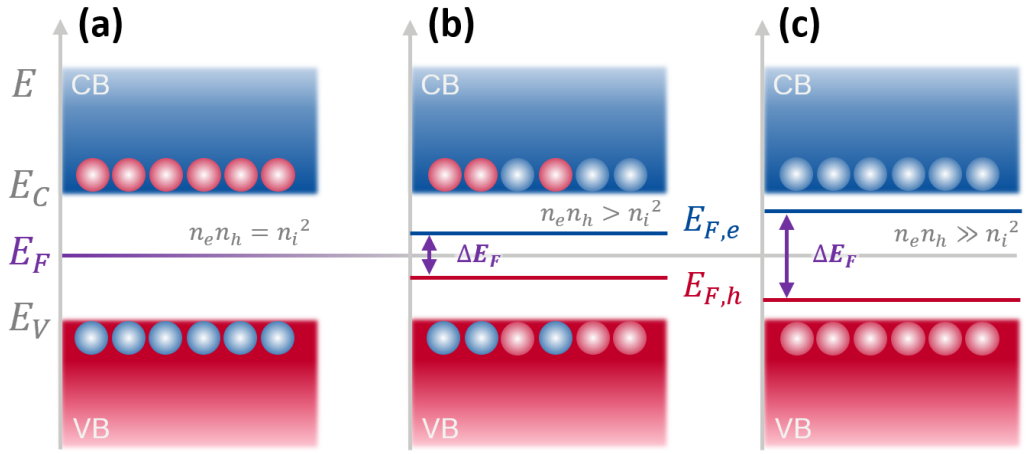


Figure 1.6: (a) Equilibrium state where only one Fermi level is present. (b) Non-equilibrium state where charge carriers got excited and shifted quasi-Fermi levels of electrons and hole closer to conduction and valence bands, respectively, thereby causing quasi-Fermi level splitting. (c) Highly perturbed system in non-equilibrium state with high densities of excited charge carriers and high quasi-Fermi level splitting.

- **non-equilibrium** – $n_e n_h > n_i^2$

Intrinsic charge carrier density is defined by the number of charge carriers of a pristine material (determined by its chemical structure), excited by the lattice vibrations and absorption of thermal energy. Therefore, n_i is zero at 0 K and temperature-dependent, typically increasing with higher temperature. For example, in intrinsic c-Si at 300 K, typically $10^{10}\,\mathrm{cm}^{-3}$ of broken bonds exist, resulting in $n_i = 10^{10}\,\mathrm{cm}^{-3}$.

In the case of equilibrium state, no external stimuli except surrounding temperature that affect charge carrier densities are present. In contrast, when such perturbations as illumination, applied electrical bias or mechanical stress are present, the system enters a non-equilibrium state, affecting n_e and n_h.

When electrons and holes get excited to conduction and valence bands, respectively, one cannot describe electrons and holes by only one Fermi energy level anymore, which necessitates an introduction of *quasi-Fermi levels* for electrons ($E_{F,e}$) and holes ($E_{F,h}$) in non-equilibrium conditions. The generation process shifts the electron quasi-Fermi level closer to the conduction band, due to higher number of electrons being present in it and hole quasi-Fermi level closer to the valence band (Figure 1.6). Based on the Equation 1.24 and Equation 1.25 we can write the following expression for a non-equilibrium condition:

$$n_e n_h = N_C N_V e^{\frac{E_V - E_C}{kT}} e^{\frac{E_{F,e} - E_{F,h}}{kT}} = n_i^2 e^{\frac{E_{F,e} - E_{F,h}}{kT}} \tag{1.26}$$

As will be shown later, properties of systems under non-equilibrium conditions can be described using:

$$\frac{n_e n_h}{n_i^2} = e^{\frac{E_{F,e}-E_{f,h}}{kT}} = e^{\frac{\Delta E_F}{kT}}, \tag{1.27}$$

where ΔE_F is called quasi-Fermi level splitting (QFLS), describing a potential difference between electrons and holes.

1.2.3 Recombination processes

Besides being generated (*i.e.* excited), charge carriers can also *recombine* – relax from the excited state to its ground state. In this process, a pair of excited electron and hole is eliminated by an electron "filling" an unoccupied energy state of lower value. In the following three different recombination mechanisms will be briefly discussed:

- Radiative recombination
- Auger recombination
- Shockley-Read-Hall (SRH) recombination

1.2.3.1 Radiative recombination

Radiative recombination[8] is a process where an electron at CBM recombines with a hole at VBM, accompanied by an emission of a photon with an energy equivalent to energy difference between both particles (Figure 1.7a), which is usually very close to E_g. In this case, the *recombination rate* R mostly depends on the charge carrier densities according to:

$$R_{rad} = B n_e n_h, \tag{1.28}$$

where B is a radiative recombination coefficient of a semiconductor.

In order to describe the photon emission coming from radiative recombination, one can start with *Planck's law of radiation*. In 1900 Max Planck formulated an empirical expression, which was later proven analytically, to describe the radiation of a

[8] In fact, radiative charge carrier recombination and generation are reciprocal processes: recombination is a process converting electrical energy into light, and generation is converting light into electrical energy. This phenomenon is known as optoelectronic *reciprocity relation* implying that, typically, a high-quality photovoltaic device can also be used as high-quality light-emitting device.

black body as energy current density per energy interval $d\hbar\omega$ in a solid angle interval $d\Omega$:

$$dj_{BB}(\hbar\omega) = \frac{d\Omega}{4\pi^3\hbar^3c^2}\frac{(\hbar\omega)^3}{e^{\frac{\hbar\omega}{kT}}-1}d\hbar\omega \tag{1.29}$$

The sun of our solar system can be considered an example of such black body, since its light emission comes primarily from its high temperature. Therefore, a good correlation between the extraterrestrial solar spectrum and a black body spectrum at 5,800 K ($\approx$ Sun's surface temperature), described by Equation 1.29 can be observed.

While Equation 1.29 holds true for black bodies, it cannot quantify the photon emission arising from the radiative recombination in semiconductors on its own. To describe it more accurately we need to also consider the absorption coefficient α of the semiconductor:

$$dj_{rad} = \alpha(\hbar\omega)dj_{ph} = \alpha(\hbar\omega)\frac{d\Omega}{4\pi^3\hbar^3c^2}\frac{(\hbar\omega)^2}{e^{\frac{\hbar\omega}{kT}}-1}d\hbar\omega, \tag{1.30}$$

where dj_{ph} is the energy current density transmitted by the emitted *photon current density*. This equation describes the radiative emission of a semiconductor in equilibrium state ($n_e = n_h = n_i$). As was shown in Equation 1.27. under non-equilibrium conditions such as charge carrier excitation, the generation rate changes according to:

$$G = G_0\frac{n_e n_h}{n_i^2} = G_0 e^{\frac{E_{F,e}-E_{F,h}}{kT}} = G_0 e^{\frac{\Delta E_F}{kT}}, \tag{1.31}$$

where

$$G_0 = \frac{\Omega}{4\pi^3\hbar^3c^2}\int_0^\infty \frac{\alpha(\hbar\omega)(\hbar\omega)^2}{e^{\frac{\hbar\omega}{kT}}-1}d\hbar\omega \tag{1.32}$$

This relationship between charge carrier densities and QFLS allows us to arrive at *Würfel's generalized Planck's law*, [8] describing non-thermal radiation of a semiconductor during radiative recombination:

$$dj_{rad}(\hbar\omega) = \frac{\alpha(\hbar\omega)\Omega}{4\pi^3\hbar^3c^2}\frac{(\hbar\omega)^2}{e^{\frac{\hbar\omega-\Delta E_F}{kT}}-1}d\hbar\omega = \frac{2\alpha(E)\Omega}{h^3c^2}\frac{E^2}{e^{\frac{E-\Delta E_F}{kT}}-1}dE \tag{1.33}$$

Thus, from Equation 1.33 it can be seen that the larger is the quasi-Fermi level splitting of a semiconductor, the larger the radiated (or emitted) photon current density j_{rad} will be.

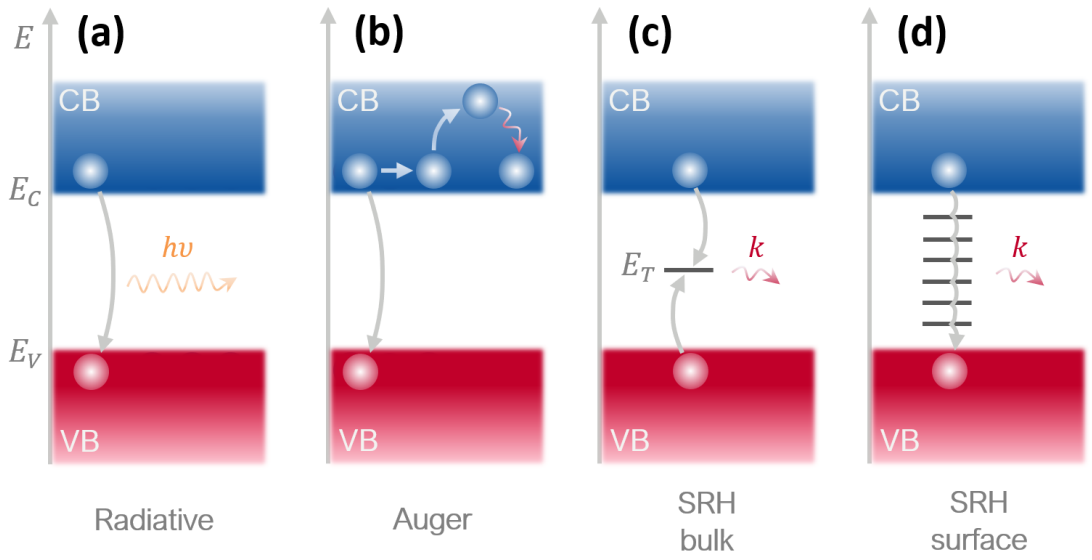


Figure 1.7: Illustrations of (a) radiative recombination (b) Auger (electron-electron-hole) recombination, (c) Shockley-Read-Hall (SRH) recombination and (d) Surface recombination

1.2.3.2 Auger recombination

Besides radiative recombination, several non-radiative recombination processes take place, such as *Auger recombination*. In this recombination mechanism, an excited electron recombines with a hole by giving the excess energy and momentum to a neighboring electron in the conduction band. Firstly, the neighboring electron is excited to higher energy states, but then quickly relaxes back to CBM by giving the excess energy to the lattice in the form of phonon(s)[9] (Figure 1.7b). A symmetrical process can also take place between holes in the valence band. Auger recombination rate is described by:

$$\mathrm{R}_{Aug} = R_{Aug,e} + R_{Aug,h} = C_e n_e^2 n_h + C_h n_e n_h^2, \tag{1.34}$$

where $R_{Aug,e}$ and $R_{Aug,h}$ are electron-electron-hole (EEH) and electron-hole-hole (EHH) recombination processes taking place in conduction and valence bands, respectively. C_e and C_e are the recombination constants for EEH and EHH Auger recombination processes. As can be deduced from Equation 1.34, Auger recombination mechanisms highly depend on the charge carrier densities and in case of highly-doped semiconductors, becomes the main source of recombination. [9]

[9]Phonon is quantized lattice vibrations in a crystal, which can provide additional momentum (k) to electrons and holes – particularly important for exciting electrons in indirect semiconductors such as silicon.

1.2.3.3 Shockley-Read-Hall (SRH) recombination

Another type of non-radiative recombination is *trap-assisted* or, also often called, *Shockley-Read-Hall* (SRH) recombination. When impurities and defects in periodic crystal lattice are present, they can induce additional *intragap* (located between VBM and CBM) energy states (E_T), which act as energy *traps*. As shown in Figure 1.7 in SRH process an electron and hole recombine via such trap energy state and excess of energy during the recombination is dissipated into lattice as heat. One can differentiate between SRH recombination happening in the bulk and at the surfaces of a crystal. The SRH recombination rate in the bulk strongly depends on the nature of impurity:

$$R_{SRH,b} = \upsilon_{th}^2 \sigma_e \sigma_h N_T \frac{n_e n_h - n_i^2}{\upsilon_{th}\sigma_e n_e + \upsilon_{th}\sigma_h n_h + \epsilon_e + \epsilon_h}, \tag{1.35}$$

where σ_e and σ_h represent *capture cross section* of electrons and holes, respectively by certain trap state, υ_{th} is the thermal velocity, ϵ_e and ϵ_h are the rates of electron and hole emission back from the trap state to the CBM and VBM, respectively. hence, the denominator represents 4 competing processes between charge carriers and the intragap state: electron and hole capture and their re-emission back from the trap state to the CBM or VBM. The emission rates highly depend on the difference between the intrinsic Fermi level E_{Fi} and the trap energy level:

$$\epsilon_e = \upsilon_{th}\sigma_e n_i e^{\frac{E_T - E_{Fi}}{kT}} \tag{1.36}$$

$$\epsilon_h = \upsilon_{th}\sigma_h n_i e^{\frac{E_{Fi} - E_T}{kT}} \tag{1.37}$$

Therefore, we can write Equation 1.35 in the following form:

$$\begin{aligned} R_{SRH,b} &= (n_e n_h - n_i^2)\upsilon_{th}^2 \frac{\sigma_e \sigma_h N_T}{\upsilon_{th}[\sigma_e(n_e + n_i e^{\frac{E_T - E_{Fi}}{kT}}) + \sigma_h(n_h + n_i e^{\frac{E_{Fi} - E_T}{kT}})]} \\ &= (n_e n_h - n_i^2)\upsilon_{th} \frac{N_T}{\sigma_h^{-1}(n_e + n_i e^{\frac{E_T - E_{Fi}}{kT}}) + \sigma_e^{-1}(n_h + n_i e^{\frac{E_{Fi} - E_T}{kT}})} \end{aligned} \tag{1.38}$$

From Equation 1.35 and Equation 1.38, it can be seen that a higher number of defects and their higher trapping cross-section results in higher SRH recombination. Therefore, typically, improvements of the purity of materials constituting a semiconductor, as well as better fabrication process control result in reduction of

defects in the material and therefore reduced SRH recombination. As an example, the grade of silicon crystal purity, used for manufacturing optoelectronic devices is normally >99.9999 %, meaning that only one out of a million atoms (at most) is not a silicon atom, *i.e.* is an undesired impurity. [9]

Crystal surfaces by definition are disruptions in crystal lattice, where an electron in the outer orbital is not coupled with an electron from (at least one) neighboring atom. Such kind of incomplete bond is called *dangling bond* and introduces intragap trap-states, resulting in SRH recombination *at the crystal surfaces*. Therefore, a continuous surface of a crystal would result in a large number of energy states close to each other in terms of energy (Figure 1.7d). Hence, the total surface recombination can be found via integration of SRH recombination at different possible trap states E_T between VBM and CBM:

$$R_{SRH,s} = \int_{E_V}^{E_C} R_{SRH,s}(E_T)dE \tag{1.39}$$

Inserting Equation 1.38 into Equation 1.39 we get [10]:

$$\begin{aligned} R_{SRH,s} &= (n_{e,s}n_{h,s} - n_i^2)\upsilon_{th} \\ &\times \int_{E_V}^{E_C} \frac{D_{it}(E_T)}{\sigma_h^{-1}(E_T)(n_{e,s} + n_i e^{\frac{E_T - E_{Fi}}{kT}}) + \sigma_e^{-1}(E_T)(n_{h,s} + n_i e^{\frac{E_{Fi} - E_T}{kT}})} dE_T \\ &= (n_e n_h - n_i^2)S \end{aligned} \tag{1.40}$$

, where D_{it} is the energy-dependent density of interface traps and $n_{e.s}$ and $n_{h,s}$ are the electron and hole densities at the surface, respectively. The quantity S is known as *surface recombination velocity*, since it describes how fast the charge carriers recombine through surface states with a unit of cm/s.

If the bulk semiconductor purity is very high, surface recombination can become the dominant source of non-radiative recombination. [9] Although for any kind of photovoltaic device it is important to reduce the surface recombination, it becomes especially critical in poly-crystalline materials with multiple *grain boundaries* and higher average crystal surface area. A common technique to reduce surface recombination is to introduce either an energetic barrier at the surface (*e.g.* via *highly doped layer*) or a *passivation* layer, which reduces the number of dangling bonds and surface energy states. [9]

1.2.3.4 Continuity equation and charge carrier lifetime

In order to describe the rate of change in charge carrier density over time, the so-called *continuity equation* can be used, which looks as following for the electron density:

$$\frac{\partial n_e}{\partial t} = \frac{1}{q}\nabla \cdot J_e + G_e - R_e \tag{1.41}$$

and for the hole density:

$$\frac{\partial n_h}{\partial t} = -\frac{1}{q}\nabla \cdot J_h + G_h - R_h, \tag{1.42}$$

where J_e and J_h denote electron and hole *current densities*, respectively, expressed as vectors. In principle, the continuity equation represents a fundamental description of possible outcomes of a particle, which can either be generated (excited), recombine or be transported along the lattice.

An important parameter describing how long the charge carriers remain excited before a certain recombination process takes place is *charge carrier lifetime*. First, let us consider a perturbed system with spatially homogeneous distribution of charges and electrostatic potential($\nabla = 0$). Then, the continuity equation becomes:

$$\frac{\partial n}{\partial t} = G - R \tag{1.43}$$

Unraveling the total recombination rate as a sum of Auger, radiative and SRH mechanisms we see that the change in charge carrier concentration is affected by these competing recombination processes:

$$\frac{\partial n}{\partial t} = G - R_{Aug} - R_{rad} - R_{SRH} \tag{1.44}$$

The density of charge carriers that are excited is often referred to as *excess carrier density* (Δn). In this case, we need to distinguish between the charge carrier concentrations under equilibrium condition – n_e^0 and n_h^0 from the total carrier concentrations: $n_e = n_e^0 + \Delta n_e$ and $n_h = n_h^0 + \Delta n_h$. In order to find lifetime of excited electrons in a system where density of holes remains nearly constant (*i.e.* $n_h \approx n_h^0$) we can write similarly to Equation 1.43:

$$\frac{\partial (n_e^0 + \Delta n_e)}{\partial t} = G_e^0 + \Delta G_e - (R_e^0 + \Delta R_e), \tag{1.45}$$

where G_e^0 and R_e^0 describe the generation and recombination rates under equilibrium. By definition of equilibrium state:

$$\frac{\partial n_e^0}{\partial t} = G_e^0 - R_e^0 = 0, \tag{1.46}$$

Based on Equation 1.46 and Equation 1.45 we can write:

$$\frac{\partial \Delta n_e}{\partial t} = \Delta G_e - \Delta R_e \tag{1.47}$$

Assuming that the generation process stops ($\Delta G_e = 0$) at $t = 0$, the change in excess electrons becomes:

$$\frac{\partial \Delta n_e}{\partial t} = -\Delta R_e = -(R_e - R_e^0), \tag{1.48}$$

which is solely determined by the recombination rate of the excess charge carriers. If only radiative recombination is present, we can use Equation 1.28 in Equation 1.48, which leads us to:

$$\frac{\partial \Delta n_e}{\partial t} = -(Bn_e n_h - Bn_e^0 n_h^0) = -B(n_e n_h - n_i^2) \tag{1.49}$$

since $n_e^0 n_h^0 = n_i^2$ by definition. Then we re-write $n_e n_h - n_i^2$ as a function of excess charge carrier densities:

$$\begin{aligned} n_e n_h - n_i^2 &= (n_e^0 + \Delta n_e)(n_h^0 + \Delta n_h) - n_i^2 \\ &= n_e^0 n_h^0 + \Delta n_e n_h^0 + n_e^0 \Delta n_h + \Delta n_e \Delta n_h - n_e^0 n_h^0 = \\ &= \Delta n_e n_h^0 + n_e^0 \Delta n_h + \Delta n_e \Delta n_h \end{aligned} \tag{1.50}$$

Since we consider that every absorbed photon excites one electron and one hole, *i.e.* $\Delta n_e = \Delta n_h$, Equation 1.50 becomes:

$$n_e n_h - n_i^2 = \Delta n_e n_h^0 + n_e^0 \Delta n_e + \Delta n_e^2 = \Delta n_e (n_h^0 + n_e^0) + \Delta n_e^2 \tag{1.51}$$

As was mentioned earlier, we assume a case in which concentration of holes remains nearly constant even in the presence of Δn, but the concentration of electrons does not. This condition can be satisfied when we consider a *doped semiconductor* (p-doped in this case) in which the change in *minority charge carriers* due to excitation (electrons in this case) is significantly higher than change in majority charge carriers.

Since in p-doped semiconductors $n_h^0 \gg n_e^0$, we can neglect the n_e^0 in Equation 1.51. Moreover, if we have a relatively low excitation, where $\Delta n_e \ll n_h^0$, the Δn_e^2 term also becomes negligible, meaning that Equation 1.51 becomes:

$$n_e n_h - n_i^2 = \Delta n_e n_h^0 \tag{1.52}$$

Inserting Equation 1.52 into Equation 1.49 brings us to:

$$\frac{\partial \Delta n_e}{\partial t} = -B \Delta n_e n_h^0 \tag{1.53}$$

And the solution for this differential equation is:

$$\Delta n_e(t) = \Delta n_e(0) e^{-B n_h^0 t} = \Delta n_e(0) e^{-t/\tau_{rad}} \tag{1.54}$$

As can be seen from Equation 1.54, excess of carrier density will *exponentially decay* over time, as well as the radiative recombination rate and consequently the emitted photon current density, described by Equation 1.33. More importantly the decay rate is determined by decay constant τ_{rad} (in this example it is equal to $1/Bn_h^0$), which represents the charge carrier lifetime – duration until the excited electrons recombine radiatively. This recombination lifetime can also be used to express the $\Delta R_{e,rad}$ via:

$$\Delta R_{e,rad} = B \Delta n_e n_h^0 = \frac{\Delta n_e}{\tau_{rad}} \tag{1.55}$$

Furthermore, the concept of lifetime can be extended to conveniently express recombination rates of other types of recombination as well, similarly to Equation 1.55:

- Auger recombination (Equation 1.34) in case of p-doped material:

$$\Delta R_{e,Aug} = R_{ehh} = C_h n_h^{0\,2} \Delta n_e = \frac{\Delta n_e}{\tau_{Aug}}, \tag{1.56}$$

  where τ_{Aug} is time until an electron recombines via Auger mechanism

- SRH recombination (Equation 1.35) in case of of p-doped material, where $\sigma_e = \sigma_h$:

$$\Delta R_{e,SRH} = \upsilon_{th,e} \sigma_e N_T \Delta n = \frac{\Delta n_e}{\tau_{SRH}} \tag{1.57}$$

  where τ_{SRH} is time until electron recombines via SRH mechanism

However in all the cases described by eqs. (1.55) to (1.57), the definition of the charge carrier lifetime was based on two important assumptions leading to the derivation of Equation 1.52:

- p-doped semiconductor – excitation only leads to a significant change in electrons, but not holes
- low excitation regime, which is also often referred to as *low-level injection*

For example, both conditions can be satisfied when describing $\Delta n_e(t)$ in p-doped c-Si illuminated with low light-intensity. Therefore, this lifetime definition is only meaningful for such specific cases, which might not hold true for other situations, especially when describing charge carrier lifetime of intrinsic semiconductors, or semiconductors under *high-level injection* conditions, when the change in both charge carrier densities is non-negligible.

If we consider a more realistic situation where not only radiative recombination is present but also the Auger and SRH mechanisms (and G is still zero), the change in excess electron concentration can be written in a more generalized way from Equation 1.44:

$$\frac{\partial \Delta n}{\partial t} = -\Delta R_{tot} = -\sum_i \Delta R_i = \frac{\Delta n}{\tau_{tot}}, \tag{1.58}$$

where the total charge carrier lifetime τ_{tot} can be found via:

$$\frac{1}{\tau_{tot}} = \sum_i \frac{1}{\tau_i} \tag{1.59}$$

Since we consider Auger, radiative and SRH recombination mechanisms, Equation 1.58 can be written as:

$$\frac{\partial \Delta n}{\partial t} = \Delta n \left(\frac{1}{\tau_{Aug}} + \frac{1}{\tau_{rad}} + \frac{1}{\tau_{SRH}} \right) \tag{1.60}$$

Note that since surface recombination is also effectively SRH recombination at semiconductor surfaces, it can be included into τ_{SRH} as:

$$\tau_{SRH} = \left(\frac{1}{\tau_{SRH}^{bulk}} + \frac{1}{\tau_{SRH}^{surface}} \right)^{-1} \tag{1.61}$$

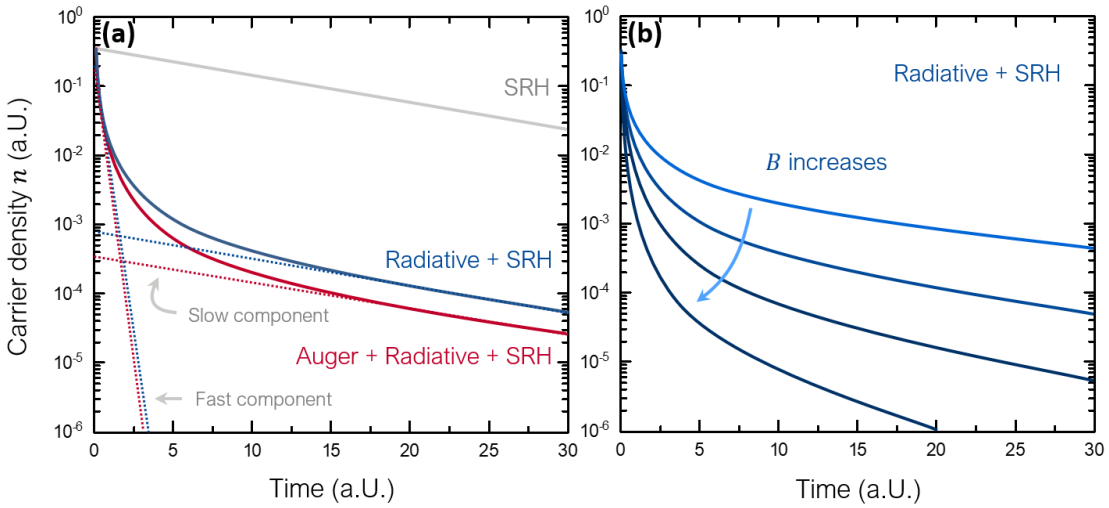


Figure 1.8: Exemplary plots of change in carrier density over time after excitation due to various recombination processes. (a) Change in decay regime from monoexponential to multiexponential due to addition of higher order recombination mechanisms (radiative and Auger recombination). (b) Demonstration of influence of radiative recombination coefficient B on the decay rate.

It is important to highlight, that τ_{SRH} is one of the key figures of merit for all kinds of semiconductors as it is directly linked to the defect-induced SRH recombination rate, which is strongly affected by the quality and purity of the material.

Although the solution to the differential Equation 1.60 would also be an exponential decay similarly to Equation 1.54, it cannot be described by only one time constant (equivalent to τ). For example, SRH recombination is the first-order recombination type and if it were the only recombination type present the decay would be *monoexponential*. However, since Auger and radiative recombination are higher order recombination types (*i.e.* they are more dependent on the charge carrier densities), the decay becomes *multiexponential*. In this case different recombination mechanisms dominate at different time-scales with Auger and radiative contributions determining the initial/fast decay (Figure 1.8b), while the SRH dictates the slow component of the decay. [11]

Besides charge carrier lifetime, the mean free path how far it can diffuse before it recombines also serves as a valuable information about semiconductor quality. This distance is known as *diffusion length* and can be quantified using the *diffusion coefficient* D (for electrons in this case):

$$L_e = \sqrt{D_e \tau_e} \tag{1.62}$$

Last but not least, since radiative recombination is considered as an "inevitable" charge carrier loss, which cannot be minimized, numerous efforts have been focused

on reducing the non-radiative recombination losses. Their minimization can be obtained by better semiconductor crystallization control, highly-pure environment during fabrication, passivation *etc.*. To quantify the proportion of non-radiative recombination losses to the total losses, a photoluminesce quantum yield ($PLQY$) often serves as a figure of such merit:

$$PLQY = \frac{j_{rad}}{j_{tot,rec}} = \frac{j_{rad}}{j_{rad} + j_{non-rad}} = 1 - \frac{j_{non-rad}}{j_{tot,rec}} \tag{1.63}$$

where j_{rad} is photocurrent of radiative recombination described by Equation 1.33 and $j_{non-rad}$ is the non-radiative recombination current.

1.2.4 Charge carrier separation

The operation of a photovoltaic device is based on extracting the generated charge carrier before they recombine. In order to do that, an electric field (ξ) must be applied to exert force on the charge carrier. If that happens, its motion is called *drift*, which can be expressed in the form of current (for electrons and holes):

$$J_{drift} = J_{e,drift} + J_{h,drift} = qn_e\mu_e\xi + qn_h\mu_h\xi = q\xi(n_e\mu_e + n_h\mu_h) \tag{1.64}$$

,where q is elementary charge and μ is *mobility*. In addition, a *diffusion* transport mechanism is also present, in which a particle (not only charge carriers) tends to move away from a region with high particle density towards a region with low particle density. Since the diffusion motion is proportional to gradient in local charge carrier concentration (according to Fick's law), the net diffusion current is expressed as:

$$J_{diff} = J_{e,diff} + J_{h,diff} = q(D_e\nabla n_e - D_h\nabla n_h), \tag{1.65}$$

where D_e and D_h are *diffusion coefficients* of electrons and holes, respectively. The total current densities of each charge carrier type is a sum of drift and diffusion current contributions and can be inserted in the continuity equation in Equation 1.41 and Equation 1.42 to find a change in carrier densities due to drift and diffusion transport.

While for a diffusion current one only needs a concentration gradient, for drift current an electric field needs to be created. To do that, two separated regions should be present in a device: n-region where $n_e \gg n_h$ and p-region (Figure 1.9a), where $n_e \ll n_h$ to form so-called *pn-junction*. Although according to Equation 1.24 and Equation 1.25, higher carrier densities result in a shift of Fermi levels, when p-

and n-regions are brought together, the Fermi level must be continuous throughout the junction under equilibrium condition. In order to satisfy this requirement, the conduction and valence bands between n- and p-regions bend, causing an electric field and thus enabling drift (Figure 1.9b), which is essential for the photovoltaic device operation.

Consequently, the difference in Fermi level within such device is accompanied by the difference in charge carrier *selectivity*, allowing electrons (but not holes) to move through the n-region and holes (but not electrons) through p-region. This can be deduced from expressing the diffusion current using the gradient in Fermi level instead of gradient in charge carrier concentration. By using Equation 1.65 and Equation 1.21, the diffusion current for electrons can be written as:

$$J_{e,diff} = qD_e\nabla n_e = qD_e n_e \frac{\nabla n_e}{n_e} = qD_e n_e \frac{\nabla\left(N_C e^{\frac{E_{F,e}-E_C}{kT}}\right)}{N_C e^{\frac{E_{F,e}-E_C}{kT}}} \tag{1.66}$$

Since N_C, k and T are constants, unlike $E_F - E_C$ derivating with respect to cartesian coordinates results in:

$$\begin{aligned} J_{e,diff} &= qD_e n_e \frac{\nabla\left(N_C e^{\frac{E_{f,e}-E_C}{kT}}\right)}{N_C e^{\frac{E_{f,e}-E_C}{kT}}} \\ &= \frac{qD_e n_e}{N_C e^{\frac{E_{F,e}-E_C}{kT}}} \frac{N_C e^{\frac{E_{F,e}-E_C}{kT}} \nabla(E_{F,e}-E_C)}{kT} = \frac{qD_e n_e}{kT}\nabla(E_{F,e}-E_C) \end{aligned} \tag{1.67}$$

The so-called Einstein relation allows to express charge carrier diffusion coefficient using its mobility:

$$D = \frac{\mu kT}{q} \tag{1.68}$$

Substituting Equation 1.68 in Equation 1.67 demonstrates that diffusion current for electrons can also be expressed in terms electron mobility and *conductivity* in p- or n-regions:

$$J_{e,diff} = \frac{q\mu_e n_e}{q}\nabla(E_{F,e}-E_C) = \frac{\sigma_e}{q}\nabla(E_{F,e}-E_C) \tag{1.69}$$

Similarly an expression for holes can be written as:

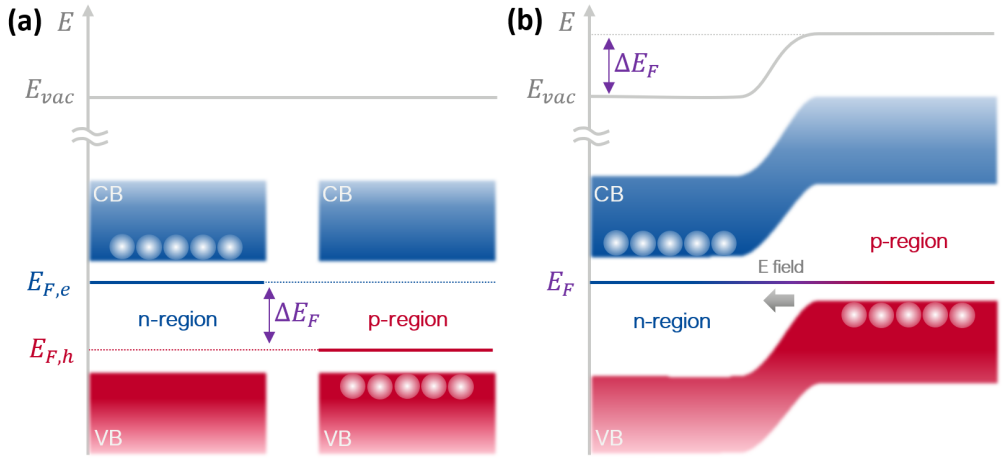


Figure 1.9: (a) Energy band diagrams of p- and n-doped semiconductors with shifted Fermi levels, which form (b) a pn-junction when brought together with a continuous Fermi level. Note that in this case, the energy bands get bent by a magnitude equivalent to difference between electron- and hole-Fermi levels, which also bend vacuum energy level E_{vac} and induce an electric field which enables drift.

$$J_{h,diff} = \frac{q\mu_h n_h}{q}\nabla(E_V - E_{F,h}) = \frac{\sigma_h}{q}\nabla(E_V - E_{F,h}) \tag{1.70}$$

In n-regions, the $\sigma_e \gg \sigma_h$ and in p-region, the $\sigma_e \ll \sigma_h$, creating phenomenon of charge carrier selectivity, favoring the transport of one charge carrier type, while prohibiting the transport of another.

In order to determine the dependency between the current flowing across the pn-junction and applied voltage, we can write continuity equation (Equation 1.42) in the steady-state condition ($\frac{\partial n}{\partial t} = 0$), allowing us to express the charge current density (using hole current for positive charge current) in terms of generation and recombination rates:

$$J_Q = -q\int \nabla J_h dx = -q\int (G_h - R_h)dx \tag{1.71}$$

For simplicity, we only consider 1D situation, with x defining position along the pn-junction. Next we assume boundary conditions, where $J_h = 0$ for $x < -L_h$ (in n-region) and $J_h = J_Q/e$ for $x > L_e$ (in p-region). These conditions can be applied to Equation 1.71. Since a voltage applied to a pn-junction changes its potential difference (and Fermi levels) between electrons and holes similarly to Equation 1.27, we can express recombination rate as function of applied voltage:

$$R_h(V_a) = R_h^0 \frac{n_e n_h}{n_i^2} = R_h^0 e^{\frac{qV_a}{kT}} \tag{1.72}$$

Assuming a situation when all the generated charge carriers can only recombine ($R_h = G_h$), provides an opportunity to write Equation 1.71 as:

$$\begin{aligned} J_Q(V_a) &= -q \int_{-L_h}^{L_e} (G_h - R_h) dx \\ &= -q \int_{-L_h}^{L_e} (G_h - G_h e^{\frac{qV_a}{kT}}) dx \\ &= -q \int_{-L_h}^{L_e} (G_h (1 - e^{\frac{qV_a}{kT}})) dx \end{aligned} \tag{1.73}$$

Integration of Equation 1.73 yields:

$$J_Q(V) = qG_h(L_e + L_h)\Big(e^{\frac{qV_a}{kT}} - 1\Big) = J_0\Big(e^{\frac{qV_a}{kT}} - 1\Big), \tag{1.74}$$

where the quantity J_0 is independent of applied voltage, but depends on the diffusion lengths of charge carriers (and hence semiconductor quality) described by Equation 1.62. J_0 is commonly known as *dark saturation current* and Equation 1.74 is called *Shockley equation*, which determines current density-voltage (JV) characteristics of an ideal pn-junction (whether it is a diode or a solar cell).

1.2.5 Solar cell under illumination

Placing such pn-junction under light causes excitation of charge carriers and splitting of the QFLs (due to non-equilibrium condition) and under an applied voltage also a motion of charge carriers due to drift and diffusion. The JV-characteristics of a photovoltaic device under incident light are also based on Shockley equation, but with an addition of current arising from the excited charge carriers. To derive it, we need to add generation of excess charge carriers ΔG to the initial generation rate in the dark G_h^0 in Equation 1.73:

$$\begin{aligned} J_Q(V_a) &= -q \int_{-L_h}^{L_e} (G_h^0 + \Delta G - R_h) dx \\ &= -q \int_{-L_h}^{L_e} (G_h^0 + \Delta G - G_h^0 e^{\frac{qV_a}{kT}}) dx \\ &= -q \int_{-L_h}^{L_e} (G_h^0 (1 - e^{\frac{qV_a}{kT}}) + \Delta G) dx \end{aligned} \tag{1.75}$$

leading to:

$$\begin{aligned} J_Q(V_a) &= qG_h^0(L_e + L_h)\left(e^{\frac{qV}{kT}} - 1\right) - q\int_{-L_h}^{L_e} \Delta G dx \\ &= J_0\left(e^{\frac{qV}{kT}} - 1\right) - J_{ph} \end{aligned}, \tag{1.76}$$

where J_{ph} is known as *photocurrent*. In this case the excited electrons contributing to photocurrent will get *extracted* by the n-regions and excited holes by p-region. Since n- and p-regions extract and transport charge carriers to the respective terminals/electrodes, they can also be referred to as *electron and hole transport layers* (ETL and HTL). Notably, as will be shown later, certain photovoltaic devices (like organic or perovskite solar cells) have a distinct intrinsic region between p- and n-regions, which is why such devices are commonly referred to as p-i-n junction, rather than pn-junction. [8] Nevertheless, the equations describing their working principle (shown earlier) remain same.

For reduction of resistive losses in photovoltaic devices, typically highly conductive electrodes (*e.g.* Ag, Cu) are applied to an ETL and an HTL in order to conduct the charge carriers to the respective terminals, thereby completing a *solar cell* structure (Figure 1.10a).

From the JV-characteristics of a solar cell (Figure 1.10a) described by Equation 1.76 we can see two distinct cases:

- $V_a = 0$, meaning that (in the ideal case) all the photogenerated charge carriers are **extracted** and solar cell is externally **short-circuited**. Inserting $V_a = 0$ in Equation 1.76 results in $J_Q = -J_{ph} = -J_{SC}$, which is then determined as *short-circuit current density*
- $J_Q(V_a) = 0$, meaning that (in ideal case) all the photogenerated charge carriers are **recombining** and solar cell is in **open-circuit**. The V_a at which no charges flow out of a cell is called *open-circuit voltage* V_{OC}, which can be found using Equation 1.76:

$$\frac{J_{ph}}{J_0} = e^{\frac{qV_{OC}}{kT}} - 1 \tag{1.77}$$

And then it is possible to rearrange Equation 1.77 to yield an expression for V_{OC} of an ideal solar cell:

$$V_{OC} = \frac{kT}{q} \ln\left(\frac{J_{ph}}{J_0} + 1\right) \tag{1.78}$$

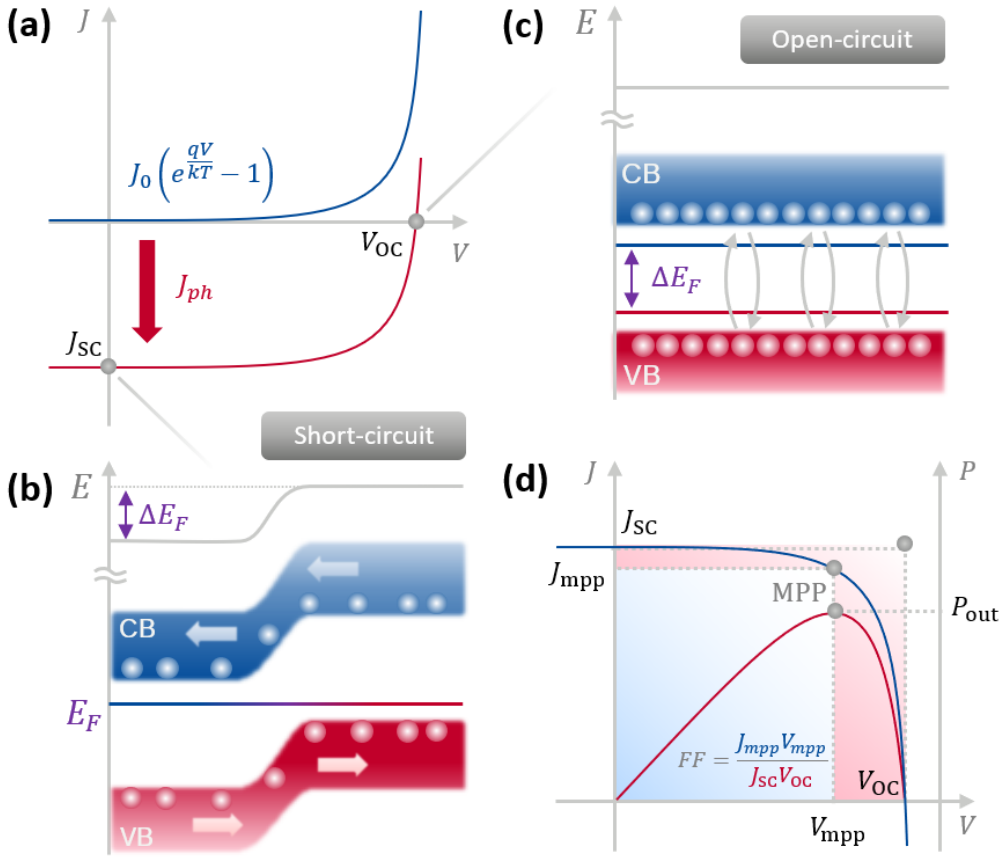


Figure 1.10: (a)JV-curve of an ideal solar cell following Shockley diode equation with and without incident illumination. Energy bands diagram of solar cell at (b) short-circuit condition and (c) open-circuit condition. (d) Illustration of the power-voltage (PV-) curve, maximum power point (MPP) and FF definition

The energy band diagrams of an ideal solar cell under short-circuit and open-circuit are presented in Figure 1.10b and c. Under short-circuit, the applied voltage is zero, meaning a continuous Fermi level across the junction even under light. In such case, strong electric field causes charge carrier separation, resulting in a large number of extracted carriers, *i.e.* high current density. Under open-circuit, the applied voltage is so that no charges are extracted, and QFLs are flat (for an ideal case), therefore, no electric field is present, resulting in zero current density.

Between these two extrema, the product of the current and voltage yields a generated *power* of photovoltaic device. By plotting the *power density* (P) as a function of applied voltage as demonstrated in Figure 1.10d, one can see that due to exponential behavior of the JV-curve (which is now shown with a positive J since we assume a generation process) there is a certain voltage at which the generated power is at maximum. Such point is called *maximum power point* (MPP) and it is used to determine such solar cell quality as *fill factor* (FF). Fill factor can be defined as:

$$FF = \frac{J_{mpp}V_{mpp}}{J_{SC}V_{OC}}, \tag{1.79}$$

where J_{mpp} and V_{mpp} are current density and voltage at maximum power point, respectively. The fill factor is strongly influenced by resistive losses, such as series resistance and *shunting* losses (internal short-circuiting of a solar cell due to direct contact between its p- and n-regions). Since FF is strongly linked to the MPP, it can also be used to describe the *power conversion efficiency* (PCE) of a PV device:

$$PCE = \frac{P_{out}}{P_{in}} = \frac{J_{mpp}V_{mpp}}{P_{in}} = \frac{J_{SC}V_{OC}FF}{P_{in}}, \tag{1.80}$$

where P_{in} defines the incident power density (W/m^2) on the PV device which can be found from solar irradiation spectrum. Outside the atmosphere of earth, the incident power density is $\approx$1361 W/m^2. However, the photon flux is attenuated due to scattering and absorption by the molecules (*e.g.* H_2O, O_2, CO_2 O_3) or particles in the atmosphere, therefore, light intensity on the Earth's surface is lower, which also depends on the time of day, as well as geographical location. Therefore, in order to standardize PV performance measurements, a set of *standard testing conditions* (STC) have been developed, which specify the solar spectrum[10], its intensity and the temperature at which solar cell measurement has to be carried out. Typically, solar cells are measured under the light intensity of 100 mW/cm^2 (or 1000 W/m^2), which is then used as P_{in} in Equation 1.80.

1.2.6 From cells to modules

Connecting several cells together, functioning as one large device forms a *PV module*. Like other electronic devices, solar cells can be assembled in series and in parallel to combine their power output. In series connection the current generated by a series of cells (called *string*) is the same as in the case of one cell, but their voltages add up. Symmetrically, when several cells are connected in parallel, their currents add up, but voltage is kept same (Figure 1.11a). However, if numerous cells are connected in parallel, high currents would result in increase of resistive losses in electrical cables. [9] Therefore, most of the PV modules consist of strings with series-interconnected cells.

[10]Since incident solar irradiation intensity depends on the sunlight path, for standartization, a quantity of *optical air mass* (AM) is often utilized to refer to a spectrum at certain condition. It is quantified by measuring sunlight's angle with zenith (θ) and using it for the expression AM=1/cos(θ). Thus, when the sun is at its zenith point ($\theta = 0°$), the AM is unity and such spectrum is called AM1. For standard testing conditions, a PV device is illuminated with AM1.5G spectrum, where letter "G" denotes *global irradiation*, taking into account direct and diffused light contributions.

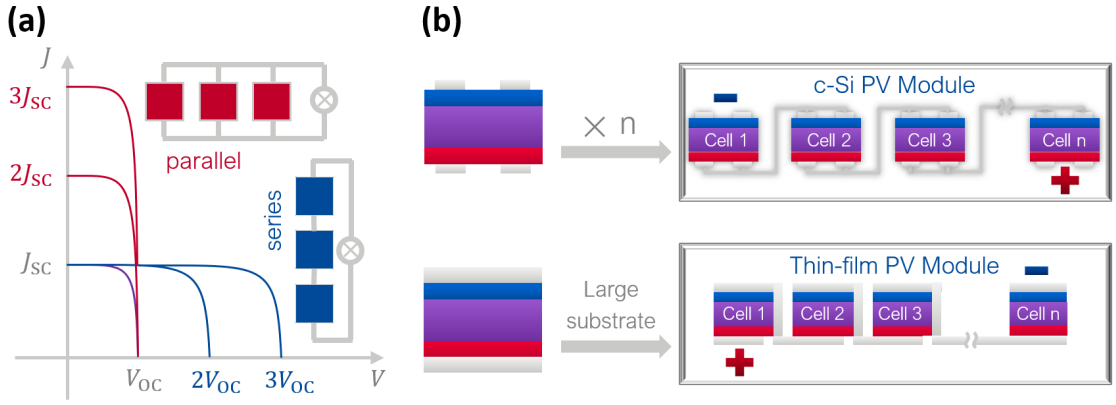


Figure 1.11: (a) Illustration of series- and parallel-interconnected solar cells and their cumulative *JV*-curves. (b) Brief illustration of wafer- and thin-film PV modules. A wafer-based (*e.g.* silicon) PV module is constituted by simple addition of n cells with interconnects in between, while a thin-film PV module is manufactured by depositing all the layers on the large area substrate and selectively removing the areas to create interconnects.

When transitioning from cells to modules, there are always additional losses introduced, which is why module PCE is often lower than that of cell PCE (even though the material quality is same). Such losses mostly occur due to the presence of *interconnects* – conductive materials, connecting terminals of two neighboring cells. Besides the addition of resistive losses, interconnects also represent an area on the PV module with no photogeneration, reducing the output power density. A quantity that characterizes the losses due to *dead area* (area of no power generation) is called *geometrical FF*. In addition, the current mismatch between cells also results in additional losses, since the current in series configuration is always limited by the cell generating least current. In the production process, some cells have more defects than others, contributing to heterogeneity in performance, which leads to current mismatch. However, some of the cell-to-module losses can be minimized in certain types of thin-film PV technologies, which were briefly mentioned in section 1.1.

In traditional Si PV modules, individual solar cells are manufactured first and then arranged together in series (or at least mostly series) configuration by interconnects (Figure 1.11b). In contrast, thin-film PV modules are typically fabricated by depositing continuous layers on a large substrate and then removing small portions of these layers to create space for interconnects between cells (typical line thickness is $< 0.5\,\text{mm}$). Afterwards, the deposition of the back-electrode partially fills the interconnect, forming a series connection with a front-electrode of the next cell, thus, connecting the separated cells in series (Figure 1.11b). Due to such narrow interconnects, thin-films PV modules typically have superior geometrical fill

factors, making such emerging PV technology appealing. One prominent example of such candidate for the "next generation PV systems" is *perovskite photovoltaics*, which will be discussed in the following section.

1.3 Perovskite photovoltaics

1.3.1 Crystal structure of perovskite

Originally derived from the archetypal mineral $CaTiO_3$, a class of compounds with a similar structure is known as *perovskite*[11] Typically such structure is generalized as ABX_3, where the A^+ is a large monovalent cation, the B^{2+} is a divalent cation and the X^- is monovalent anion. An ideal cubic ABX_3 structure consists of BX_6 octahedra in corner-sharing configuration with A-cations embedded within cuboctahedral framework (Figure 1.12a). [12] A so-called *Goldschmidt tolerance factor* (t_f),[12] which is solely determined by ionic radii (r) of perovskite constituents defines the phase stability and structural distortion of ABX_3 compound [13]:

$$t_f = \frac{r_A + r_X}{\sqrt{2}(r_B + r_X)} \tag{1.81}$$

Although numerous compounds are included into the perovskite class family, mainly the *metal-halide perovskites* attract particular attention due to their unique and favorable semiconducting properties. Thus, most of the perovskite PV devices are made using such perovskites, where A-cation can be an organic molecule or an inorganic ion, B-cation is a divalent transition metal and X is a halide. [12, 14] If the A-cation is too large or the B-cation is too small, the t_f becomes >1, forming a hexagonal perovskite. For the $0.8<t_f<1$, a 3D cubic metal halide perovskite structure is favored, while for $t_f<0.8$ an orthorhombic structure is formed. [13, 14]

Considering all the aforementioned conditions, a 3D metal halide perovskite structure can usually be formed using the following constituents:

- **A-cation**: $CH_3NH_3^+$ (MA: methylammonium), $CH_2(NH_2)_2^+$ (FA: formamidinium) or Cs^+
- **B-cation**: Pb^{2+} or Sn^{2+}
- **X-halide**: I^-, Br^- or Cl^-

Each combination of A, B, and X results in the formation of a stable or metastable 3D perovskite structure with a $0.8 < t_f < 1$ and favorable opto-electronic properties. [13, 15]

[11] In 1829, Gustavus (Gustav) Rose, Alexander von Humboldt and Christian Ehrenberg took part in a scientific expedition through the Russian empire, particularly in the mountain regions of Altai (rus. Алтай) and Ural (rus. Урал). Later in 1839 Gustav Rose discovered and described a new compound found in Ural mountains – calcium titanate, which he named "perovskite" after a russian mineralogist Lev Perovski (rus. Лев Перовский).

[12] This empirical factor for perovskites was first introduced in 1926 by norwegian mineralogist Victor Moritz Goldschmidt – one of the most prominent geochemists of 20th century, who also developed Goldschmidt geochemical classification of elements.

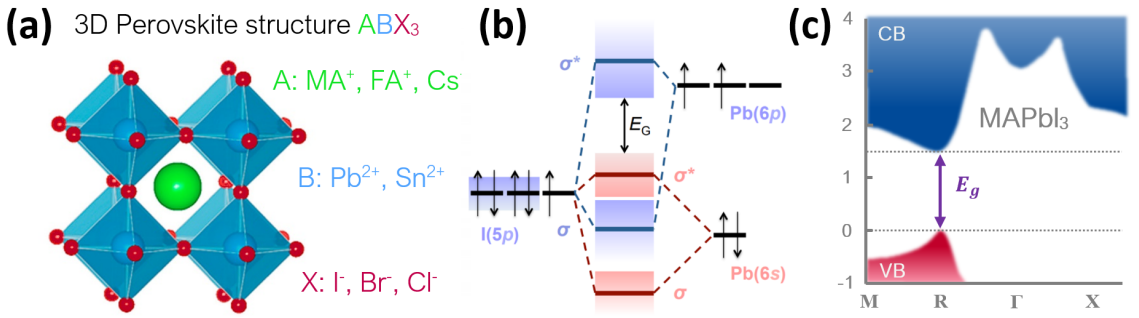


Figure 1.12: (a) Crystal structure of a 3D perovskites, commonly employed for PV applications. Adapted with permission from [13]. (b) Formation of bonding and anti-bonding molecular orbitals between Pb and I atoms, which form energy bandgap in lead-iodide perovskites. [16] (c) *E-k* plot of $MAPbI_3$ perovskite depicting VBM, CBM and energy bandgap. Adapted with permission from [17].

As was discussed in subsection 1.2.1, the crystal structure determines the relation between energy and momentum of charge carriers, including the VBM and CBM. Due to the presence of multiple elements in the ABX_3 stucture, a number of different molecular bonds are present, which create states within valence and conduction bands. As shown in Figure 1.12b, the VBM of perovskite is located at the anti-bonding orbital originating from a σ^*-bond between Pb($6s$) and I($5p$) atomic orbitals. [16] The anti-bonding nature of the valence band has been suggested as an explanation for unusual bandgap increase with higher temperature, due to lattice expansion and less wave function overlap. [18, 19] Interestingly, the CBM also comes from an anti-bonding orbital, but due to σ^*-bond between Pb($6p$) and I($5p$) orbitals. [16] Thus, a bandgap in halide perovskites is typically formed between two anti-bonding orbitals. Looking at the *E-k* plot of the archetypal $MAPbI_3$ in Figure 1.12c, one notes the direct bandgap of such material at the R-point of the first Brillouin zone, which is also the case for other halide perovskites used in PV applications. [17, 20]

1.3.2 Unique properties of halide perovskite materials

Several unique attributes of halide perovskites make them exceptionally promising for opto-electronic applications, particularly, their *defect tolerance*. A range of experimental and simulation studies show that halide perovskites are prone to formation of high trap densities ($N_T > 10^{15}$), owing to their low formation energy. [21–29] This property is often affiliated with liquid processing[13] of perovskite thin films which are

[13]Solution-based crystalline film formation is a much faster processing in comparison to seeded crystal growth, which is done to manufacture wafers for Si-PV. This key factor provides potential for low fabrication cost of perovskite-based PV devices.

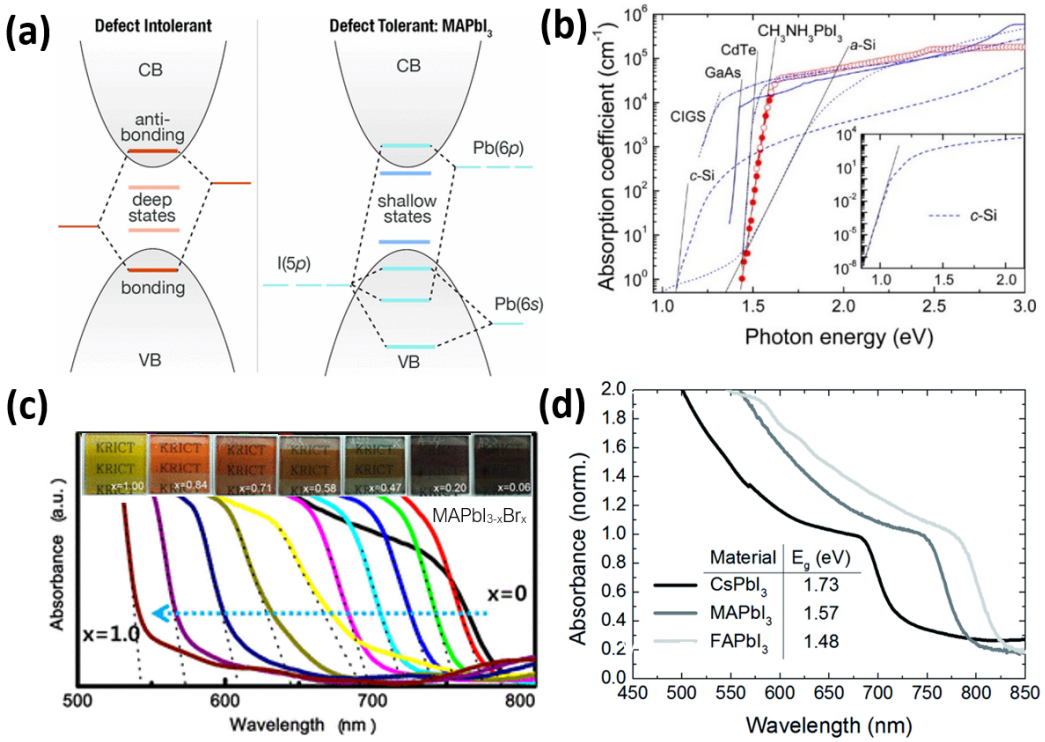


Figure 1.13: (a) Illustration of defect intolerant semiconductors with deep trap states and defect tolerant ones (like $MAPbI_3$) with shallow trap states. [40] (b) Absorption edges of different semiconductors used in PV field in comparison to that of $MAPbI_3$ perovskite. [41] (c) Absorption edges of mixed $MAPbI_{3-x}Br_x$, demonstrating the bandgap tunability. Inset photographs show the change in visual appearance of perovskite films with different halide proportions as a result of bandgap change. Adapted with permission from ref. [42]. (d) Absoprtion edges of pure $APbI_3$ perovskites. [43]

typically polycrystalline in nature. In addition, the purity of compounds for fabricating perovskite films is typically significantly lower than the purity grade of silicon, required for Si-PV, which also introduces numerous defects. [9,30] However, despite high N_T in perovskite films, a number of studies demonstrated that most of these defects are *shallow*, meaning that they are located in the vicinity of CBM or VBM (Figure 1.13a). [21, 22, 31–33] In such case the rate of charge carrier emissions ϵ_e and ϵ_h, which are driven mainly by the difference between the E_F and E_T become higher, thereby reducing the SRH recombination rate (Equation 1.35). Very long diffusion lengths [34–37] and high PLQYs [34, 36, 38, 39] have been reported in certain perovskite films, highlighting that even with moderate defect densities, halide perovskites still retain excellent opto-electronic qualities.

The light absorption coefficient and absoprtion edge are particularly important properties of a material used in PV applications. As was previously discussed, a direct bandgap increases the chance of charge carriers to become excited, which

is reflected in a sharper *absorption edge*. Figure 1.13b shows absorption edges for different semiconductors used in PV field, clearly demonstrating a difference in absorption between direct (CdTe, GaAs and $MAPbI_3$ perovskite) and indirect semiconductors (c-Si, a-Si). Such a sharp absorption edge and a high absorption coefficient of halide perovskites allows them to absorb a relatively large fraction of incident light, even if a crystal (or layer) is less than 1 µm thick. Concomitantly, it also means that halides perovskites can be efficient light-emitting devices by applying voltage to cause radiative recombination, with radiation described by Equation 1.33.

Another attractive feature of perovskites is their *bandgap tunability*. Replacing B or X elements results in different anti-bonding orbitals, directly shifting the VBM and CBM. [13, 42] Although the A-cation does not directly contribute to the change in bandgap, its hydrogen bonding and steric effects can cause structural distortion, which tilt the BX_6 octahedra, influencing the B-X-B angle and, thus, affecting the anti-bonding between B and X. [13, 44, 45] Hence, combinations of different A, B and X constituents results in different energy bandgaps (Figure 1.13c and d). [42, 43] Moreover, it is possible to obtain perovskites with properties, like E_g, intermediate in value between different pure perovskites (*e.g.* between $MAPbI_3$ and $MAPbBr_3$). Mixing all constituents with other suitable elements in a desirable ratio can yield stoichiometric *alloyed/mixed perovskites* with favorable intermediate characteristics (Figure 1.13c), *e.g.* $MAPbI_{0.5}Br_{2.5}$.

1.3.3 The genesis of halide perovskite photovoltaics

In 2009, Miyasaka *et al.* were the first to use metal-halides perovskites as light-harvesting materials in solar cells. [46] In their work, the authors utilized $MAPbBr_3$ and $MAPbI_3$ in a *dye-sensitized solar cell* (DSSC),[14] achieving an encouraging power conversion efficiency of 3.8 % (for $MAPbI_3$-cell). Following these first demonstrations of solar cells based on halide perovskites, a replacement of electrolyte with a solid-state hole-transporting layer [48] represented a major milestone in the establishment of a field separate from the dye-sensitized photovoltaics, which is now known as perovskite photovoltaics.

Such solid-state devices with numerous options of applicable charge transport layers with high mobilities and charge carrier selectivities provided further opportunities for scientists across the globe to explore and conduct research on perovskite materials and solar cells, ramping up the record device PCEs. [49] In 2022, the world record certified PCE of a single-junction perovskite solar cell has reached 25.7 %, which is already higher than most of other established PV technologies. [50] Such high device

[14] The first developed DSSC (also sometimes called *Grätzel cell*) was co-invented by Brian O'Regan and Michael Grätzel, who later together reported the first high-efficient DSSC in 1991 [47]. In 2010, Grätzel was awarded Millenium Technology Prize for the invention of DSSC.

efficiency combined with potentially low manufacturing costs facilitated the establishment of several companies and start-ups, planning to start the mass-production of large area perovskite PV devices in the next few years. [51] Given such wide spectrum of possible metal-halide perovskites and their impressive opto-electronic characteristics, it is not surprising to see that their application has quickly spread beyond photovoltaics to other fields, such as light-emitting diodes (LEDs), [52, 53] transistors, [54, 55] light-detectors, [56, 57] spintronics [58, 59] *etc.* Overall, due to their numerous favorable properties, perovskite semiconductors might become a major player in the electronics and PV industries of the next 10-20 years.

1.3.4 Perovskite solar cells

The general, working principle of a perovskite solar cell (PSC) follows mechanisms described in subsection 1.2.2, where the photogenerated electrons and holes are normally separated by an ETL and an HTL with suitable energy levels, respectively. These layers are introduced on the top and bottom of the perovskite absorber, which is normally assumed to be intrinsic (or slightly doped due to ion migration). In such cell, at least one of the layers (ETL or HTL) should permit incident light to pass through to reach the perovskite layer without causing additional undesired *parasitic absorption losses*. Conventionally, the side where the light comes from is denoted as the *front side*, where the charge transport layer (ETL or HTL) in the front as well as the *front electrode* should be as transparent as possible. Therefore, unlike in c-Si solar cells, where the front electrodes (also sometimes called *contacts*) are made of metals such as silver, the front electrodes in perovskite solar cells is usually some type of *transparent conductive oxide* (TCO), such as fluorine-doped tin oxide (FTO) or indium-doped tin oxide (ITO). Unless the PSC is designed to be semi-transparent or bifacial, the *back electrode* on the opposite side is typically made of a thin highly conductive metallic layer such as gold or silver.

One can distinguish between two fundamentally different configurations of PSCs, which vary in the position of the HTL and ETL. Since perovskite solar cells are typically very thin ($<20\mu$m), they are typically deposited on a *substrate* for reliable handling. The configuration, in which an ETL (*i.e.* n-region) is firstly deposited on a substrate is denoted as *n-i-p* (or *nip*) PSC (Figure 1.14a). Symmetrically, a configuration, in which an HTL (p-region) is firstly deposited on a substrate is known as *p-i-n* (or *pin*) as illustrated in Figure 1.14b. In either configuration, the excited electrons are extracted by an ETL due to applied electric field, while holes are extracted by HTL (Figure 1.14c). Most of the ETLs and HTLs, used in PSCs are only applicable in one configuration and not in the other, due to manufacturing constraints, which will be discussed later. In addition, certain highly efficient ETLs or HTLs absorb a significant portion of light, prohibiting their applications as charge transport layer on the front side.

In general, both: n-i-p and p-i-n cells with PCE $> 22\,\%$ have been demonstrated in

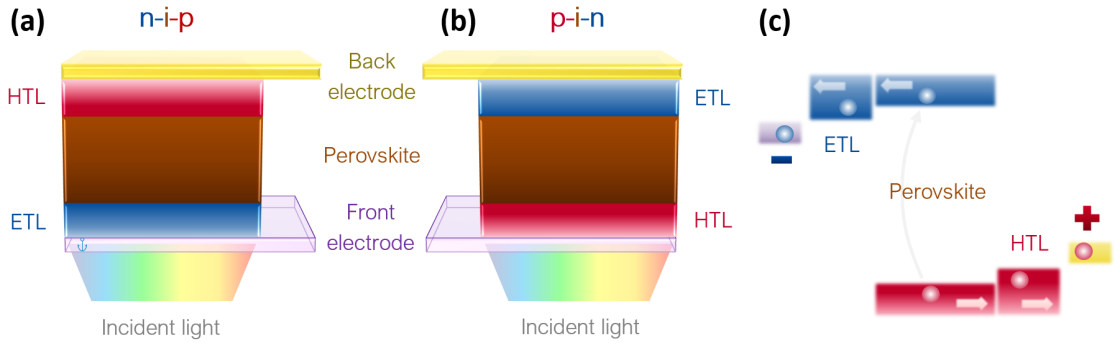


Figure 1.14: Generic perovskite solar cell structure in (a) n-i-p configuration and (b) p-i-n configuration. (c) Energy band diagram of an n-i-p cell, with excited electrons are being extracted from perovskite by an ETL and holes by HTL under positive applied voltage.

literature over the years, meaning that both concepts can be employed to fabricate high-efficient cells. [60] However, it is worth noting that certified world-record cells in the last years have been made using n-i-p structure, [49] while p-i-n have an advantage of slightly easier and quicker processing. [61]

Besides conventional p-i-n and n-i-p PSCs, which utilize metallic back-contacts, perovskite PV devices can also have electrodes from carbon-based materials. Such special type of device architecture, which will mainly be discussed in this dissertation is a class of perovskite PV devices with *carbon-based electrodes*, also denoted as CPSCs or CPSMs (for solar modules). Devices with such electrodes contain high potential to be more stable, cost-effective and sustainable, but their PCE is currently behind that of traditional PSCs. The properties, processing aspects and potential of CPSCs will be discussed in more details in chapter 3.

Notably, one of the most commonly-employed ETLs in PSCs is *mesoporous* titanium dioxide (m-TiO_2), due to its high electron mobility, low parasitic absorption and well-aligned energy levels. [62, 63] Its mesoporous architecture allows easier electron extraction from the perovskite absorber, resulting in slightly better performance than in the case of *planar* ETLs, like tin oxide (SnO_x) or zinc oxide (ZnO). [64] However, such mesoporosity of m-TiO_2 allows perovskite deposited on top to penetrate through and reach non-selective front electrode directly. Since TCO is typically a degenerate semiconductor with metal-like electrical properties it can induce additional non-radiative recombination at perovskite/TCO contact. To avoid this effect, another planar and *compact* layer is introduced between m-TiO_2 and TCO – compact titanium dioxide (c-TiO_2). Its function is to effectively block holes from reaching the front electrode, by creating a large energetic barrier (its VBM is much lower than the VBM of perovskite), which is why such c-TiO_2

is often called *hole-blocking layer* (HBL). [65] Moreover, introducing additional layers at the interface between perovskite and charge transport layers was found to be particularly useful, in order to suppress surface and interfacial non-radiative recombination losses and facilitate more efficient charge extraction. [66]

1.3.5 Processing techniques

Liquid-processing of high-quality perovskite layers provides potential opportunities for fast (and hence cost-effective) production of PV modules (*cf.* subsection 1.3.2). Perovskite and charge-transport layers are usually deposited from *solutions*, containing *precursors* needed to form the layer. In certain cases, the precursors are not dissolved but *dispersed* or exist in the form of colloids. After the solution, dispersion or a paste is deposited, it is typically *annealed* at temperatures sufficient to remove the solvent, coordinating agents, binders and other constituents, leaving only the desired material on the substrate.

1.3.5.1 Spin-coating

Among numerous different methods to deposit layers of PSCs, the most common one up to date is *spin-coating*. [67–69] In spin-coating, deposition process a solution dropped on a substrate is spread via centrifugal force, induced by rotating the substrate at certain speed (Figure 1.15a). Such deposition technique works excellent for small substrates (typically $< 10\,\mathrm{cm}^2$), resulting in homogeneous film coating and favorable surface morphology. An overwhelming majority of the current high-efficient PSCs with PCE $> 20\,\%$ are manufactured by spin-coating. [70] However, it has strong limitations when the substrate size increases, causing discontinuous morphology and poor homogeneity, which is why most of spin-coated high-efficient PSCs have a size of $< 1\,\mathrm{cm}^2$. [71,72] Clearly this issue makes spin-coating deposition effectively inapplicable for manufacturing large $\approx \mathrm{m}^2$ PV devices.

1.3.5.2 Meniscus coating

Besides spin-coating, several *meniscus-coating* techniques can be used to deposit layers of perovskite solar cells, as well as modules. In general definition, meniscus coating is based on spreading solution on a substrate via certain coating tool. [73] *Blade coating* is an example of a simple deposition route, in which solution is spread on a substrate via moving *doctor blade* as shown in (Figure 1.15b). The solution is applied at the gap (which can be finely controlled) between the substrate and the blade head. Once the blade starts to move across the substrate, it removes excess of solution leaving a wet film behind with a thickness controlled by (but not equivalent to) the adjusted gap height and speed of blade motion. In *slot-die coating* a solution is pushed through a moving thin slot of the coating head (Figure 1.15c), where the

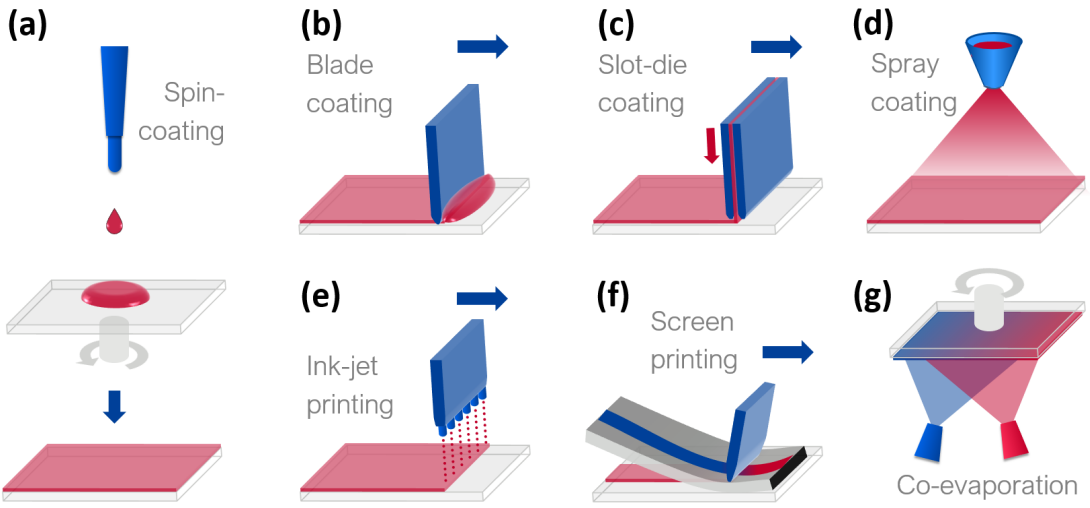


Figure 1.15: Layer deposition techniques commonly employed for perovskite PV device manufacturing: (a) spin-coating (b)blade coating, (c) slot-die coating (d) dip coating, (e) ink-jet printing, (f) screen printing and (g) co-evaporation

wet-film deposition is controlled by the speed and height of the slot-die head, as well as by capillary forces, acting on the liquid during its flow through the narrow slot. Another type of meniscus-coating is called *dip coating* and is performed by simply dipping the substrate into a solution bath and pulling it back out of the bath at specific speed, which leaves a wet film on its surface (Figure 1.15d). While the speed of blade coating and slot-die coating can be engineered for a more rapid mass production, the immersion process during dip coating is slower, making it not as promising for large are device fabrication. [73]

1.3.5.3 Spray coating

Spray coating technique is based on dispensing tiny droplets of solution through a nozzle onto a substrate. Typically, for the fabrication of PSCs, the aerosol droplets of solution are ejected from the nozzle by using a pneumatic atomizer with compressed air. Although, spray coating is rarely used to deposit perovskite films, it is often employed to deposit c-TiO_2 layer by spray *pyrolysis*. In this process, the solution containing titanium precursors is sprayed on a heated substrate, causing rapid assembly of TiO_2 crystals with compact morphology. However, deposition of other layers by spraying have also been demonstrated in the perovskite community.

1.3.5.4 Printing

Among different printing techniques, *ink-jet printing* allows highly precise and relatively quick deposition of different wet films. In ink-jet printing a number of minia-

ture nozzles is used to dispense an *ink* (normally in the form of solution or suspension) on a substrate (Figure 1.15e), which can be controlled by externally applied electrical signals, for example, via a piezoelectric element. [71] Typically, high density of nozzles, allows to reach remarkably high resolutions of the deposited layer, provided that the ink consistency is suitable. In such way, PV device patterning using ink-jet printing provides unique opportunities for several niche markets besides standard solar modules. Besides ink-jet printing, *screen printing* is also often employed for layer deposition within the PV sector. In screen printing, a layer is deposited on a substrate by pushing a *paste* through a *mesh* of threads (typically polyester or other synthetic material) in a *screen*, located above the substrate (Figure 1.15f). The pressure is applied using a *squeegee*, which slightly pushes and bends the screen down towards the substrate and, thus, the pattern of deposited paste is mostly determined by the mesh dimensions. However, the paste viscosity, substrate roughness and printing parameters also play a role in determining layer thickness and morphology. Although in silicon solar cells screen printing is only used to deposit electrodes, some PSCs, such as the ones with carbon-based electrodes, are mostly fabricated via screen-printing.

1.3.5.5 Vapor-phase deposition

Instead of solution being deposited on a substrate, one can evaporate or sublime perovskite precursors directly, and collect them on a rotating substrate above the evaporation source, as shown in Figure 1.15g. Such technique typically requires evaporation of multiple precursors in a vacuum chamber. It is generally called *co-evaporation* deposition or sometimes specified as dual-, triple-, or quadriple-source evaporation, according to the number of co-evaporated precursors. Besides simultaneous precursor evaporation, deposition can also be *sequential* to allow layer-by-layer deposition, as well as possible diffusion and, potentially, more controlled crystallization. [67] While the general principle is appealing due to the relative ease of operation and homogeneous deposition, the perovskite crystallization process from the vapor phase currently still lacks understanding and the resulting perovskite layer typically has small grains with unfavorable opto-electronic properties. [12] Therefore, currently, the PCEs of co-evaporated PSCs lag behind the ones deposited with solution-processed techniques. [67]

To partially alleviate this problem, a so-called *hybrid deposition* route was recently developed, in which firstly inorganic precursors (*e.g.* PbI_2, CsI) are evaporated on a substrate, followed by a wet-film deposition of the organic precursors (*e.g.* FABr, FAI), which rapidly react with the evaporated layer, converting it to perovskite. In this method, the deposition of inorganic precursors can be controlled with high precision, which form a homogeneous layer acting as a porous scaffold, which templates perovskite crystal growth upon addition of the organic precursors. However it should be noted that the necessity of high vacuum conditions for such

layer deposition results in (potentially) slower processing, which hinders potential for mass-production of such PSCs.

1.3.5.6 Other techniques

The versatility of halide perovskites allowed researchers to explore many other layer deposition routes as well, such as chemical vapor deposition (CVD), [67] pressure-assisted methods, [74, 75], spray-coating [76–78], melt deposition [79, 80] and more. However, it is worth mentioning that since most of the reported PSCs are produced via spin-coating, much less attention is given to the optimization of alternative deposition routes. Such trend, in turn, slows down their development, keeping these methods unfavorable for researchers and engineers to employ in order to achieve highly efficient devices.

1.3.6 Crystallization

The rapid development of perovskite PV was partially enabled by understanding the crystallization of halide perovskite films and its optimization. [49] For any of the aforementioned deposition techniques employed to manufacture perovskite films, a finely-tuned synthesis, deposition parameters and crystallization control are paramount for obtaining high-quality films with desirable opto-electronic properties. Therefore, it is essential to discuss the nucleation theory of growth mechanisms, applicable to model crystallization kinetics of perovskite materials in order to develop further routes towards highly efficient PV devices.

Normally, a LaMer growth model [81] serves as a good approximation of crystallization process based on the precipitation from the solution. Most of the techniques used for deposition of perovskite films are based on liquid processing. (*cf.* subsection 1.3.2) In this case, precursors containing elements needed for construction of perovskite crystal lattice are dissolved (or liquefied by other means), forming a *precursor solution*, which will be deposited on a substrate by methods demonstrated in subsection 1.3.5. Once the solution is deposited on a substrate, the solvent (or liquefying agent) evaporates at a certain rate, increasing the concentration of *monomers* (in the context of perovskite, its precursors existing as individual atoms, ions or molecules) as shown in Figure 1.16a. [12] This phase is known as *saturation* (since solution "saturates" with solute) or *pre-nucleation* and once a critical *supersaturation limit* is reached, the concentration of monomers becomes high enough, so that a formation of so-called *nuclei* becomes thermodynamically favorable. The nuclei represent the "seeds" of crystals - tiny particles only few unit cells in size. Process of nucleus formation is called *nucleation* and it plays critical role in the formation of a uniform high-quality film. After and during nucleation, the nuclei start to grow in size by the diffusion of monomers and their attachment to nuclei surface. This process is known as (crystal) *growth*, which proceeds until

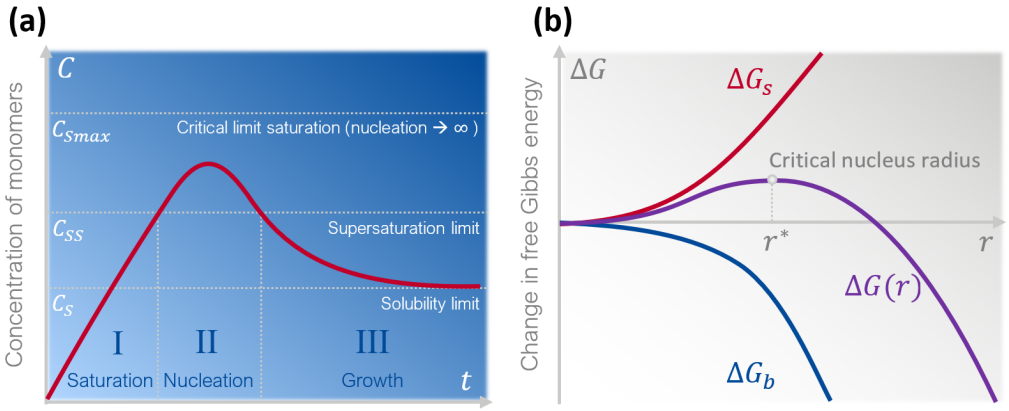


Figure 1.16: (a) LaMer precipitation model with homogeneous nucleation, displaying three stages of crystallization: saturation, nucleation and growth, which can be distinguished from the evolution of monomer concentration over time. (b) Classic nucleation theory, depicting change in free Gibbs Energy (ΔG) as function of radius of nucleus, including an interplay between the surface and bulk/volume contributions.

the molecules of solvent (or liquefying agent) are depleted. [12, 68] Based on this model, the LaMer diagram depicting 3 stages of crystallization as function of concentration of monomers (C) over time is constructed (Figure 1.16).

Looking closer at the nucleation stage, one notices that its on-set starts when the monomer concentration reaches the supersaturation limit (C_{ss}). This limit is determined by the *change in free Gibbs energy* ΔG of a nuclei, which has two contributions: surface free energy ΔG_s and bulk free energy ΔG_b. ΔG_s represents a change in energetics due to creation of new area unit on a nuclei surface, where it interacts with solvent molecule. ΔG_b is associated with energy change during conversion of dissolved precursors into nuclei. Due to the surface tension, the surface term is assumed to be positive, opposing the nuclei formation, whereas the bulk term is negative, thermodynamically favoring nucleation due to increase in monomer concentration. If we consider a homogeneous nucleation of a spherical particle, its total change in free Gibbs energy as a function of particle radius r can be expressed as:

$$\Delta G = \Delta G_s - \Delta G_b = 4\pi r^2 \gamma_{CL} - \frac{4\pi r^3}{3V_m} kT \ln S, \tag{1.82}$$

where γ_{CL} is the surface energy between the crystalline nuclei surface and solvent molecules, V_m is the molar volume of the nucleus and S is the supersaturation degree, defined as $S = C/C_{ss}$.

Plotting the ΔG and its components as a function of nucleus radius during homogeneous nucleation (Figure 1.16b) reveals that initially the total ΔG is positive, which hinders (or even opposes) nucleation due to the high surface area (and thus surface contribution) of small particles. However, if its radius reaches a critical value $r*$ (critical radius), ΔG starts to decrease thermodynamically favoring nucleation due to higher bulk contribution. Hence, C_{ss} can be found by analysis of surface energetics and solvent-solute interactions, which can provide additional insights into nucleation and crystallization control.

It must be noted that the classic nucleation theory discussed above serves strictly as a qualitative model in the case of *homogeneous* nucleation – when the nucleation occurs without preferential nucleation sites, where nuclei formation might have lower or higher ΔG. In reality, all the nucleation processes are *heterogeneous*, and in the case of perovskite films, the substrate on which the film is grown is usually assumed to provide favorable nucleation sites. One of the milestones, which pushed development of halide perovskite materials further is the development of advanced crystallization strategies. A remarkable example of such approach is the introduction of *anti-solvent* – a non-polar solvent, which is miscible with the solvent of precursor solution and simultaneously does not dissolve perovskite precursors. [82] Dropping such anti-solvent on a spinning wet film with precursor solution allows to rapidly remove the solvent causing instantaneous supersaturation with high nucleation density, which consequently leads to fabrication of uniform films with smooth morphology and large perovskite grains. [68] Despite the complexity and finesse required by anti-solvent engineering method, it is currently the most commonly used technique to manufacture high-efficient PSCs. [83]

Notably, very recently Chen *et al.* have demonstrated experimental evidence showing that perovskite films tend to nucleate at the film surface due to rapid localized solvent removal, and thus supersaturation. [84] This implies that perovskite crystallization progresses downward from the film upper surface towards to the interface between film and the substrate, and not upward (as often assumed). However, different solvent and crystallization methods result in different nucleation and crystal growth, which is why crystallization kinetics is vital to understand and optimize regardless of the chosen fabrication approach.

1.3.7 Current challenges

Although, halide perovskite materials provide tremendous potential for its commercialization and deployment by the semiconductor industry, several crucial challenges remain unsolved, which will be briefly discussed below.

1.3.7.1 Degradation

The first one is the intrinsic and extrinsic *instability of halide perovskites*. Due to the low energetic barrier of crystallization, many types of perovskites can be readily formed at low temperatures, but also can *degrade* relatively easily due to their soft ionic nature. [69] As was shown in a number of reports, several commonly used perovskite compositions have a thermodynamically favorable tendency to undergo phase-transition towards photo-inactive phases or to decompose at temperatures which can be encountered during PV module operation. [85, 86] Thus, the commercialization of halide perovskite in the PV sector, where solar modules are expected have stable performance for over 20 years, is seriously threatened by these stability issues.

1.3.7.2 Ion migration

A closely-related problem, which is also stemming from the ionic nature of halide perovskites is *ion migration*. Ions constituting the lattice structure of halide perovskites tend to migrate through the lattice under the influence of temperature, electric field (which happens under PV operational conditions) and other external stimuli. [69] Typically such ion migration occurs via lattice defects, which are numerous in halide perovskites, as was mentioned earlier. Owing to the lowest activation energy, halide vacancies are considered to be the most common source of ionic defects, which tend to migrate and accumulate at the interfaces between perovskite and charge transport layer. [69, 85, 87, 88] Such charge-accumulation affects a range of properties, such as charge carrier extraction (or injection), interfacial transport, trap densities and charge carrier lifetime, consequently affecting the device performance in a complex way (Figure 1.17a). [89]

Consequently, this dynamic ionic behavior also causes a pronounced *hysteresis* in JV-curve of PSCs, where ions accumulation at the interfaces depends on the applied electrical bias and influences the charge extraction and transport. This in turn results in significant difference between *forward-scanned* JV-curve (constructed by conducting a voltage sweep from $V_a = 0$ to $V_a = V_{OC}$) and *reverse-scanned* JV-curve (from $V_a = V_{OC}$ to $V_a = 0$). Over the years, numerous researchers highlighted that PSC performance can be deceptive when a JV-scan in only one direction is reported and can lead to an overestimation of the PSC "true" power output and, thus, PCE.

1.3.7.3 Up-scaling

Up-scaling any PV technology from cells to modules inevitably results in additional losses (*cf.* Figure 1.11). However, in comparison to c-Si, CdTe or organic PV technolgies, halide perovskites display particularly large cell-to-module loss

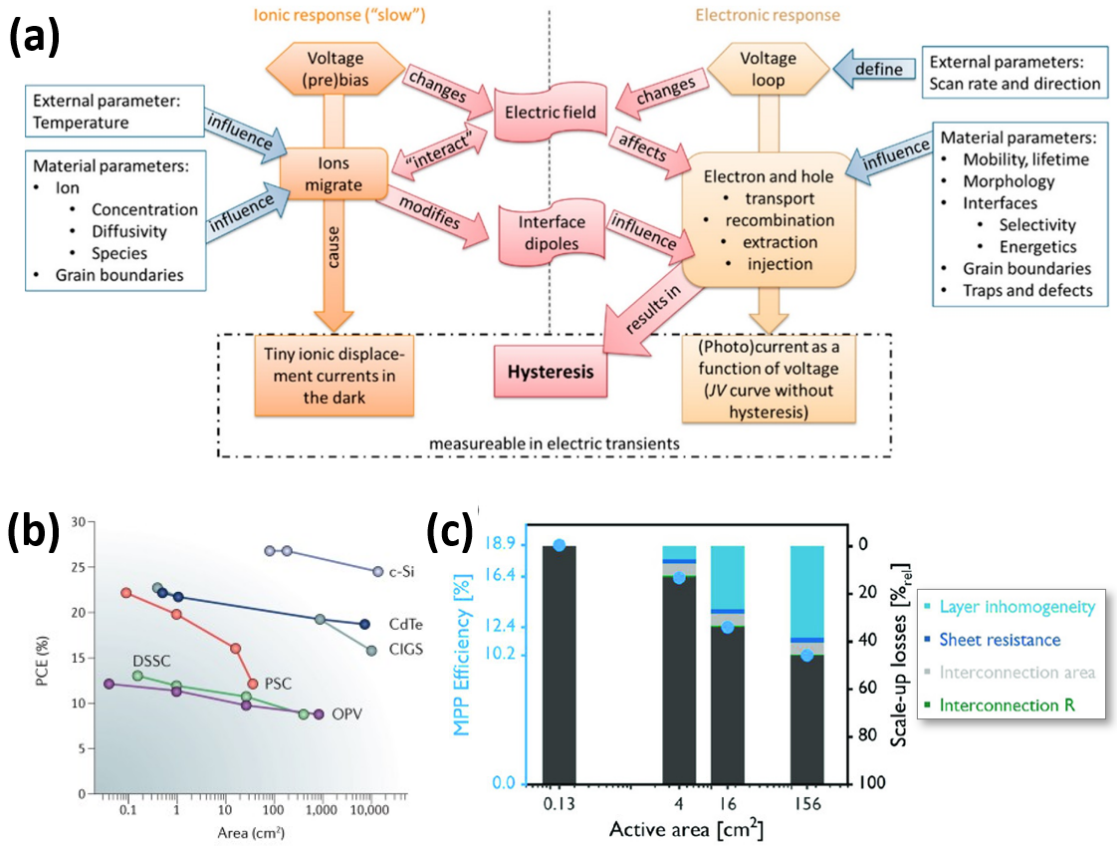


Figure 1.17: (a) Complex relation between halide perovskite properties, ion migration, electronic response, hysteresis and *JV*-curve. Reproduced with permission from [89] (b) Change in the PCE of PV device due to up-scaling (enlargement of active area). Reproduced with permission from [71] (c) Quantification of up-scaling losses in perovskite PV device. Reproduced with permission from [90]

(Figure 1.17b). [71, 90] It is partially related to the aforementioned fact that most PSCs are produced via spin-coating and not other processing techniques compatible with *large area deposition*. As shown in the exemplary case in Figure 1.17c, the current state-of-the-art large area deposition, such as blade-coating, slot-die coating or ink-jet printing still cannot compete with the superior level of homogeneity and crystallization control obtained in spin-coated films. Therefore, there is a relatively large difference between the current certified world-record PCEs of perovskite PV modules and cells: 18.1 % for 802 cm^2 module manufactured by Panasonic [91] and 25.7 % PCE for PSC with <0.1 cm^2 active area. [50]

1.3.7.4 Presence of lead

Another challenge that perovskite PV is facing before entering the market is the *lead toxicity* and its social perception. Several studies demonstrated that since perovskite

layer itself is very thin, the amount of lead in a $\approx 1\,m^2$ perovskite module is even less than that of a traditional c-Si module, which contains lead traces in its silver contacts. In addition, self-encapsulation strategies have been reported to prevent lead leakage in case of module damage or delamination, which provide additional "safety cushion" to perovskite PV modules.

1.4 Aims and outline of dissertation

One of the promising approaches to tackle some of the aforementioned challenges is to utilize carbon-based contacts in perovskite PV devices. These carbon-based electrodes have a strong potential to retard degradation and PSCs with such contacts can be readily fabricated with up-scalable techniques for large area deposition mentioned in subsection 1.3.5. However, the PCE of such devices is currently lower than that of the standard PSCs with metallic contacts.

This dissertation is focused on understanding fundamental loss mechanisms of perovskite solar cells with carbon-based electrodes (CPSCs) and developing ways to reduce them, in order to boost their power conversion efficiency. Specifically, it present a series of studies to tackle the following previously unresolved and challenging questions:

- What are the key properties of carbon-based electrodes and how do they compare with metal-based electrodes?
- What are the mechanisms driving the perovskite liquefaction and crystallization and how can they be controlled?
- Which effect does the electrode curing temperature has on the solar cell performance?
- How can the non-radiative recombination losses be reduced in perovskite solar cells with carbon-based electrodes?
- How can the series resistance losses be reduced in perovskite solar cells with carbon-based electrodes?
- How stable are such perovskite PV devices, particularly, under reverse bias conditions?
- How do such devices compare with the state-of-the-art PV in terms of sustainability and environmental impact?

Firstly, **chapter 3** provides the reader with a profound literature review and discussion on the existing PSCs with carbon-based electrodes, their advantages and issues, hindering further development (Figure 1.18). Next, **chapter 4** introduces a novel liquefaction and re-crystallization method of halide perovskites using methylamine gas and its derivatives. At the start of the presented work, synthesis of liquefied perovskite using methylamine was considered a highly promising route towards rapid, controllable and up-scalable perovskite layer deposition. Therefore, an in-depth investigation of the perovskite-methylamine interaction during liquefaction and re-crystallization shown in chapter 4 has been carried out in order to understand it and find effective methods to control this reaction.

After that, **chapter 5** presents a study of CPSCs with two archetypal, but

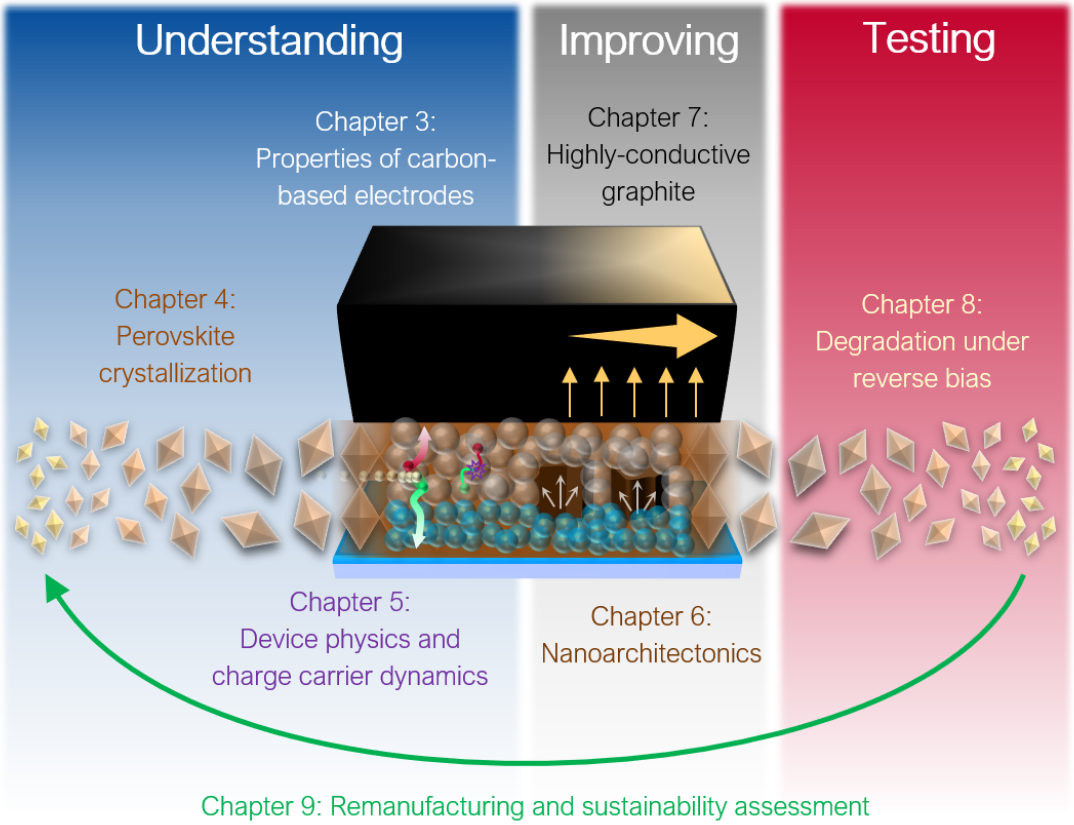


Figure 1.18: Illustration of interconnection between different chapters of this thesis, outlining that by understanding properties of carbon-based electrodes (chapter 3), perovskite crystallization (chapter 4) and charge carrier dynamics (chapter 5) new strategies for device improvement have been proposed and successfully implemented (chapters 6 and 7). Such PV devices exhibit an impressive resilience to reverse bias-induced degradation (chapter 8) and offer unique opportunities for recycling (chapter 9), making them highly promising for a sustainable energy generation systems.

fundamentally different architectures – with low- and high-temperature treated carbon electrodes. The deposition temperature of carbon electrode significantly influences cell structure, processing and also performance losses. The loss mechanisms in these systems were systematically compared via multi-modal characterization, allowing to propose effective strategies for developing both cell types further.

In chapter 5 it was identified that high non-radiative recombination losses in CPSCs with high-temperature cured electrodes originate from a large number of grain boundaries. This finding led to the development of an approach to tackle this issue by modifying the device structure, as described in **chapter 6**. Such strategy allowed to form well-ordered cavities in the cell architecture for templating growth of large perovskite crystals with favorable opto-electronic properties.

Furthermore, based on the gained insights from chapter 5, the problem of series resistance losses in CPSCs has been identified. This stimulated further investigation, described in **chapter 7**, resulting in the development of highly conductive carbon-based electrodes with low defect densities and resistance losses.

After the performance improvements described in chapter 6 and chapter 7 have been demonstrated, the stability of CPSCs has been addressed. Specifically, a hitherto unresolved problem of perovskite instability under reverse-bias has been investigated. The study in **chapter 8** demonstrates how perovskite solar cells and modules can withstand surprisingly high negative voltages, proving their resilience against reverse-bias and hot-spot degradation. Moreover such devices could pass the international accelerated ageing test of hot-spot endurance, which is the first report of such kind according to the author's knowledge.

Last, but not least, a new method for a technologically-simple and cost-effective remanufacturing process of perovskite solar cells and modules with carbon electrodes after their lifetime has been developed. The conducted life-cycle analysis of such devices discussed in **chapter 9** allowed to quantitatively estimate their reduction of environmental footprint due to the presented novel remanufacturing approach. This further underlines that perovskite PV devices can be not only stable and efficient, as demonstrated in earlier works, but have a potential to reduce greenhouse gas emissions from PV manufacturing.

This thesis is based on five published peer-reviewed articles in scientific journals (chapters 3 to 5, 7 and 8) and two not peer-reviewed studies (chapters 6 and 9).

Chapter 2

Experimental methods

2.1 Sample manufacturing

Most of the results presented in this dissertation are based on the experimental findings, obtained from characterizing a wide spectrum of samples. Therefore, it was necessary to employ various types of manufacturing techniques outlined below.

Fabrication of planar perovskite films for analysis of their structural, morphological or opto-electronic properties was carried out using spin-coating (*cf.* subsubsection 1.3.5.1). Different solutions typically required optimization of deposition parameters until a satisfactory layer was obtained. This was utilized in publications discussed in chapter 4 and chapter 5.

However, most of the samples were manufactured by screen-printing corresponding pastes (*cf.* subsubsection 1.3.5.4) with inorganic nanoparticles (*e.g.* TiO_2, ZrO_2) or carbon-based materials (*e.g.* carbon-black, graphite) mixed with organic solvents and binders. In most cases, these commercially-available pastes were screen-printed using a polymer-based screens with various mesh sizes. However, for deposition of c-TiO_2 layer spray pyrolysis was employed throughout the work (*cf.* subsubsection 1.3.5.3).

In certain experiments, the carbon-based electrode was deposited by blade-coating (*cf.* subsubsection 1.3.5.2), as it was necessary to manufacture samples with carbon electrodes treated at high (≈400°C) and low temperatures (<150°C). The comparison of PSCs with both types of electrodes is discussed in chapter 5.

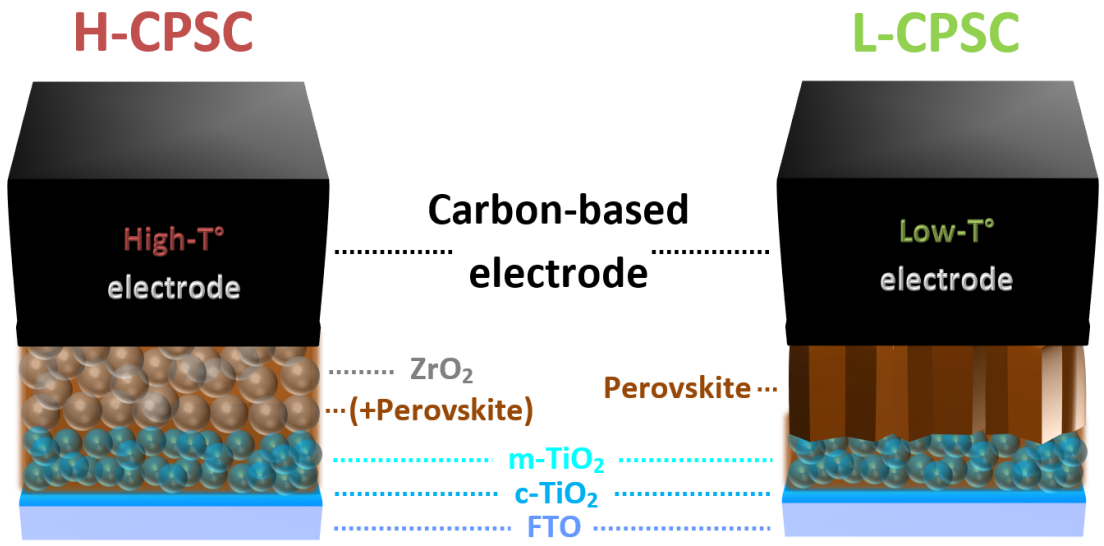


Figure 2.1: Structure of perovskite solar cells with carbon-based electrodes sintered at high temperatures (left) and low temperatures (right).

The work presented in chapter 6 contains a novel process of ink-jet printing a suspension of polystyrene beads. The suspension composition and its ink-jet printing (*cf.* subsubsection 1.3.5.4) process have been rigorously optimized by the author until a layer of deposited polystyrene beads had a desired morphology, thickness and homogeneity.

All the photovoltaic devices presented in these works utilized an HTL-free structure with carbon-based electrodes. The device architecture was similar to an n-i-p structure (*cf.* subsection 1.3.4), having FTO as front electrode, c-TiO_2 ($\approx$ 20 nm) as HBL and m-TiO_2 ($\approx$ 400 nm) as ETL, with perovskite either deposited as planar film or embedded into a ZrO_2 scaffold ($\approx$ 1 µm) and having a carbon electrode ($\approx$ 10-15 µm) on top (Figure 2.1). In the case of devices with high-temperature electrodes, perovskite photoabsorber ($MAPbI_3$-based) was formed by infiltrating the mesoporous cell stack with precursor solution, followed by annealing process to remove the solvent and to crystallize perovskite (*cf.* subsection 1.3.6). The infiltration as done either by pipetting the solution on top of carbon electrode or by filling it with an ink-jet printer. For manufacturing solar cells with low-temperature carbon electrodes discussed in chapter 5, a layer-by-layer deposition was employed, where ETL and perovskite layers were spin-coated.

A more detailed description of manufacturing procedure utilized in each individual study can be found in the supporting information of the corresponding work.

2.2 Characterization techniques

Understanding the fundamental physical processes occurring in the fabricated samples necessitated a certain number of characterization tools to observe them. Hence, this work contains a wide spectrum of characterization methods, that have been employed.

2.2.1 X-ray diffraction (XRD)

When electromagnetic radiation is incident onto a matter, it can cause *scattering*, due to interaction between electrons (of the material) and the incident radiation. The X-ray diffraction characterization technique takes advantage of the elastic scattering, which forms constructive interference under certain conditions, resulting in *diffraction patterns*. These conditions are determined by the so-called Bragg's law, linking the incident angle (θ), X-ray wavelength and lattice constant (d):

$$n\lambda = 2d\sin\theta, \tag{2.1}$$

where n is an integer number (Figure 2.2a). Alternation of the incident angle will form different diffraction patterns which depend on the scattering along certain planes. Thus, electron density and consequently structure of a material can be constructed and indexed by measuring X-ray diffraction at different incident angles.

In this work, two types of XRD-modes were used: (1) XRD on thin films and (2) single-crystal XRD. Thin-film XRD was conducted using Bragg-Brentano optical setup allowing to resolve XRD with angle variation only along one plane, thus, leading to one-dimensional XRD patterns. Such technique was utilized in studies described in chapters 4, 5, 7 and 8. On the other hand, single-crystal diffractometers typically use goniometers (instrument to precisely position a sample at certain angle) with 3 or more circles along different planes, which allow to resolve diffraction patterns arising from incident angles in multiple planes. Such technique provides an opportunity to fully reconstruct the sample structure with deep crystallographic information and was employed in chapter 4 for a more detailed analysis.

2.2.2 Scanning electron microscopy (SEM)

Scanning electron microscopy (SEM) is a powerful characterization method, which can produce a sample image with high resolution (down to the nm range) by scanning its surface with a focused electron beam. Depending on the type of interaction between the incident electrons and the sample, different types of electrons will be

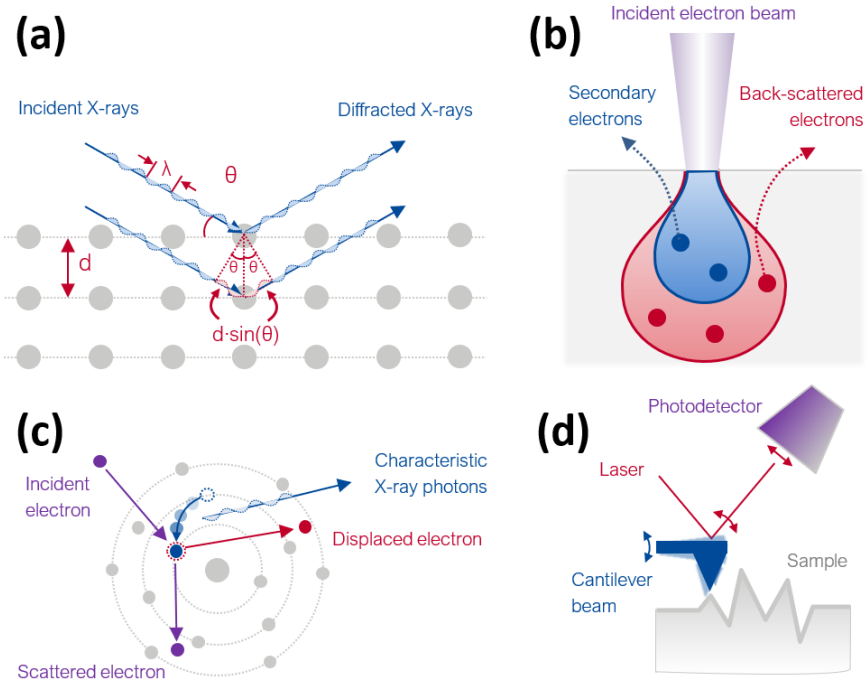


Figure 2.2: (a) Illustration of diffraction of X-rays incident on a sample and key parameters in the Bragg's law, defining conditions for diffraction effect to take place (Equation 2.1). (b) Schematics of the secondary and back-scattered electrons generated by the incident (also known as primary) electron beam, during scanning electron microscopy measurement. (c) Illustration of X-ray photon generation process as a result of electron displacement form atomic core levels during energy dispersive x-ray spectroscopy. In this process, the electron from a higher orbital fills the hole left from the displaced electron by transitioning to a lower orbital and emitting the excess of energy as element-specific X-ray photons. (d) Simplified representation of atomic force microscopy, wherein a cantilever beam with a sharp tip, contacting the surface is scanned through the sample, while the cantilever deflection is measured by detecting changes in laser light reflected from it.

ejected from the sample surface. Capturing these ejected electrons and correlating them with the location of the incident beam allows to produce an electron microscopy image. Three types of electrons can arise from the interaction between the incident electron beam and the sample: (1) secondary electrons (2) back-scattered electrons and (3) Auger electrons.

Secondary electrons arise from ionizing the sample surface with the incident electrons having energies exceeding ionization potential (Figure 2.2b). Depending on the accelerating voltage of the incident beam, the depth of penetration (and thus interaction with the sample) will be different. However, normally only very

localized secondary electrons at the very surface can escape the sample and be captured by the detector, allowing the images based on such electrons to reach high resolutions. Most of the SEM images shown in this work were obtained by a secondary electron (more precisely, Everhart-Thornley) detector.

Back-scattered electrons are electrons ejected form the sample as a result of elastic scattering of electrons back towards the incident beam direction (Figure 2.2b). Typically, images based on back-scattered electrons need to have high energy, which also requires higher accelerating voltages. Since elastic scattering highly depends on the atomic number of the interacting atom, heavier elements will back-scatter electrons with higher intensity, resulting in brighter images. This feature allows to spatially map the elements (when the sample composition is known) by image contrast. The process of Auger electrons ejection is similar to the Auger recombination mechanism described in subsubsection 1.2.3.2 – when an electron relaxes to a lower energy state, it transfers the energy difference between the initial and the final states to one of the neighboring electrons. In the case of Auger electrons, however, the transferred energy might exceed the ionization potential of a (weakly-bound) electron on the outermost orbital, leading to its ejection. Since it is closely related to the energy difference between different energy states, Auger electrons are element-unique and are useful for spectroscopy-based analysis.

Although SEM images can provide some small fraction of information about the sample in the direction of the beam (*i.e.* along sample "depth"), it primarily probes the sample surface and yields a 2D image. However, in order to obtain information about the sample at certain depth, one can combine 2D SEM images taken each time after the surface has been polished with a focused ion-beam (FIB). The local sample ablation using FIB is performed by bombarding a sample with heavy ions (typically Ga^+), effectively sputtering material off the sample surface. If the FIB-gun is placed at a sufficient angle with the electron beam, such FIB-polishing allows to remove a layer of predetermined depth from the sample surface, take a SEM image, remove another layer using FIB, take the next SEM image *etc.*, thus taking a series of 2D images along the sample depth. Such technique is known as 3D FIB-nanotomography, and will be demonstrated in chapter 6.

2.2.3 Energy dispersive X-ray spectroscopy (EDX)

Another characterization technique that is well-coupled with SEM is energy dispersive X-ray spectroscopy (EDX or EDS). When an electron beam is incident on a sample (as in the case of SEM measurement), some of the electrons from the inner orbitals can be removed from the energy states, leaving a hole (Figure 2.2c). Since it becomes energetically favorable for an electron on the higher energy level to

fill this available state, it will emit the excess of energy during its transition as an X-ray photon. These emitted X-ray photons are directly linked to the energy difference between different atomic orbitals and, thus, element-specific. By measuring the energy of the emitted X-rays it is thus possible to obtain information about the sample elemental composition. Moreover, combining with the microscopy images with the locally-detected X-rays, one can spatially map the elemental composition and precisely identify different entities present in the sample image.

2.2.4 Atomic force microscopy

Unlike SEM, atomic force microscopy (AFM) is not an electron microscopy technique and is based on a direct "physical" interaction between a probe (called cantilever beam) tip and the sample surface. One of the most common results obtained by the AFM measurement is the topographical and morphological characterization of a sample to quantify such properties as surface roughness and homogeneity.

During AFM measurements, the tip of the cantilever beam is scanned along the sample surface, which can either (1) continuously remain in direct contact with the sample (referred to as contact mode), (2) regularly oscillate at frequency close to its resonance frequency (called tapping mode) or (3) even not be in contact with the sample (non-contact mode) and change its oscillating frequency based on the difference in long-range forces (*e.g.* van der Waals forces). In any mode, the tip location will change (in direction perpendicular to the sample surface) as it scans through the sample due to its interaction with the surface and its morphological features. Thus, the changes in "height" of the tip at different locations on the sample surface represent its morphology. To detect these changes in tip height, a laser is incident on the cantilever, which is reflected from its surface onto a photodiode. In such way, the changes in tip position deflect the cantilever, causing the laser light to reflect at different angles onto the photodiode, providing spatial information of the surface height in digital form (Figure 2.2d). AFM was briefly used in chapter 5 to study the differences in surface morphology of planar perovskite films with perovskite embedded in mesoporous ZrO_2.

2.2.5 Steady-state photoluminescence

The emission of a semiconductor due to radiative recombination of charge carriers (*cf.* subsubsection 1.2.3.1) is a measurable quantity, which can provide particularly useful information about the material opto-electronic properties. The radiative recombination can be measured via *photoluminescence* - a process when the photoexcited charge carriers recombine radiatively (Figure 2.3a) emitting photons. - Although in this work several different methods were utilized to characterize photoluminescence (PL) of manufactured samples, this section discusses the PL

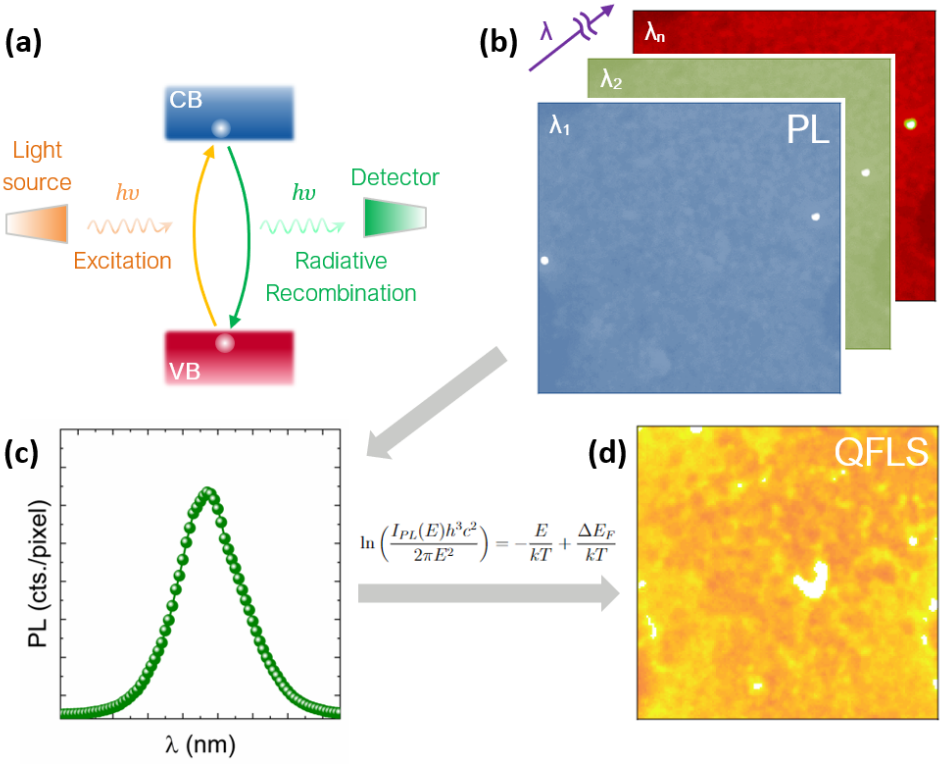


Figure 2.3: (a) Basic working principle of photoluminescence-based measurement: charge carriers, excited by incident light recombine radiatively, emitting a photon which is detected. Typically this measurement is conducted in a spatially-resolved mode (PL mapping) or spectrally-resolved mode. (b) maps of PL emission of photons with specific wavelengths (λ_1,λ_2...λ_n), the combination of which can produce a (c) PL spectrum of each pixel on the map. If the measurement was conducted using an absolute photon-counting setup, Würfel's generalized Planck law can be applied to construct a (d) map of quasi-Fermi level splitting. Adapted and reprinted with permission from [92].

measurement conducted only under steady-state.

To qualitatively estimate the spatial variation in PL (Figure 2.3b), a microscope with a camera and an LED as excitation light source were used. Such PL microscope can clearly identify regions with highly-radiative perovskite and compare them with the regions with either no solid-state perovskite (as shown in chapter 4) or with perovskite, which has numerous defects causing excessive non-radiative recombination subsubsection 1.2.3.3 and, thus, lack of PL signal (chapters 5 and 6).

PL intensity can also be measured as a function of wavelength, allowing to plot a PL spectrum (Figure 2.3c). Typically, the photons originating from the radiative recombination have energy equivalent to material bandgap energy, thus the PL

spectra normally have a Gaussian shape with a peak at the bandgap energy. Notably, when more than one perovskite phase is present, additional PL peaks can arise. Such PL spectrum measurements are shown in chapter 7.

A more quantitative analysis of photoluminescence can be conducted by the so-called absolute PL measurement, or PLQY measurement (*cf.* Equation 1.63). In this work it is based on "direct approach", which utilizes an integrating sphere coated with highly-reflective coating to capture all the light emitted from the sample and direct it towards the detector and relate it to the emitted photon flux. Such methods allows to quantitatively compare the radiative efficiency of perovskite samples and the extent of non-radiative recombination in them, which will be briefly discussed in chapter 5. By obtaining absolute PL spectra, it is also possible to determine the QFLS of a sample from Equation 1.33. A commonly used approach is to assume that the absorbance above bandgap energy is unity, allowing to rewrite Würfel's generalized Planck law using PL emission intensity I_{PL}:

$$\ln\left(\frac{I_{PL}(E)h^3c^2}{2\pi E^2}\right) = -\frac{E}{kT} + \frac{\Delta E_F}{kT} \tag{2.2}$$

Plotting the left-hand part of Equation 2.2 as the y-axis, allows to extract two parameters from the high-energy wing of the PL spectrum: (1) temperature of the measured semiconductor by fitting its slope to $-\frac{1}{kT}$ and (2) the QFLS (ΔE_F) of the material by finding y-intercept (at $E = 0\,\text{eV}$) of the fit. [66, 93]

A technique that essentially combines all of the above mentioned methods: the absolute PL, spatial PL and spectrally-resolved PL was also implemented in this work [92] – absolute hyperspectral PL mapping. [66, 94] Similarly to the spatial PL it utilizes a (in this case, however, confocal) microscope, which excites the region of interest with a laser beam, but the camera obtains a series of spectrally-resolved images of the same region with a short step size ($\approx 2\,\text{nm}$). Thus, it is possible to collect not only absolute PL maps, but also PL spectra for each pixel of the image. And since each of these spectra are considered to be absolute PL measurement, a map of QFLS can be obtained by using method described above (Figure 2.3d). A similar approach to map the spatial distribution of QFLS was utilized in the study described in chapter 5.

2.2.6 Transient photoluminescence

Unlike steady-state approaches mentioned above, transient PL techniques measure a semiconductor's response to a change in (non-steady) state. One of the most common characterization methods in perovskite scientific community is to evaluate charge carrier lifetime (*cf.* subsubsection 1.2.3.4) by measuring its time-resolved PL (TRPL) response, or, more precisely, its decay, after optical excitation. In TRPL

measurement, a sample is illuminated with a specified intensity long enough to reach a steady-state, having a constant recombination rate and, hence, constant PL. Since, typically <1μs of constant illumination is enough to reach a steady-state, a low-frequency pulsed light source can also be used. Then the excitation stops, resulting in an exponential decay in excited charge carriers (Figure 1.8) and, hence, their radiative recombination rate, which is measured by the emitted photon flux. By fitting the measured TRPL to the exponential decay function in Figure 1.8, one can estimate the SRH lifetime of the minority charge carrier under low-injection conditions. Although this assumption holds true for quantifying lifetime of photoexcited electrons in, for example, p-doped Si, it is not directly applicable to such complex system as undoped perovskite layers. Hence, the PL decay is governed by Equation 1.60, which can be re-written as [95]:

$$\frac{\partial \Delta n(t)}{\partial t} = -B\Delta n_e(t)\Delta n_h(t) - \frac{\Delta n(t)}{\tau_{SRH}}, \tag{2.3}$$

showing that the radiative recombination is a second-order recombination mechanism, whereas the trap-assisted SRH recombination is only a first-order process. Equation 2.3 describes the excess charge carrier depopulation (and hence the transient PL) after the excitation stops ($\Delta G = 0$) and does not include the third-order Auger recombination since it can be ignored for intrinsic semiconductors such as perovskite, unless the charge carrier densities approach $\approx 10^{17}$. [95]

A common practice in the perovskite community is to fit the measured TRPL decay to a bi-exponential decay function and to consider the second (longer) time constant as the carrier lifetime. While it might coincide with the actual charge carrier lifetime in certain cases, in the author's opinion, there is no physical reasoning why the decay should be fitted to a bi-exponential decay function. Moreover, the meaning of the first (shorter) time constant of such bi-exponential fit is still under debate in the community, bringing even more ambiguity into this bi-exponential fit method. Recently an alternative method was proposed by Krückemeier *et al.* to consider a carrier-density-dependent decay time as a function of time (after excitation) instead of the equivocal decay constants for a more objective interpretation of the TRPL measurements. [11] Hence, the PL decay of a perovskite film can only serve as qualitative measure to compare the lifetime of charge carriers between different samples and a number of considerations must be kept in mind before attempts to interpret the quantified charge carrier lifetime from such measurement.

The TRPL measurements utilized in this work (chapters 4 to 7) can be generally described in three steps:

1. **Excitation** – light produced by a picosecond laser (for short pulses) or a continuous wave (CW) laser with a possibility to be switched off on the ps-ns scale

2. **Detection** – the photons emitted from the sample are detected by a sensitive photodetector with high dynamic range
3. **Recording** – the signal from a photodector is recorded with the help of a fast oscilloscope or a single-photon counting system for a better temporal resolution

2.2.7 Infrared thermography

The radiation emitted by a body with temperature >0K can be approximated by the Plancks's radiation law (*cf.* Equation 1.29), which highly depends on the body's temperature. While the bodies with high temperatures, such as the Sun, have a strong emission in the visible region, the bodies with lower temperature emit mainly in the infra-red (IR) region (0.75-15 µm). If an object has a temperature higher than the surrounding, the thermal radiation can be detected with the help of, for example, an IR-camera. However, if the surrounding is not at 0 K, it would also emit thermal radiation, which is why a lock-in approach is typically utilized to separate between the emission from the surrounding and a specific body.

From an intensity and spectrum of thermal radiation, it is possible to calculate the object's temperature, if the object's emissivity is known. However, even if it is not known, the IR thermograms can provide a useful image of spatial temperature distribution in the sample. Such IR thermography was implemented in chapter 8, where photovoltaic devices were locally heated by placing them under reverse bias.

2.2.8 Raman shift spectroscopy

Raman shift spectroscopy is an optical contactless measurement method to characterize molecular vibrations and interatomic bonds present in a material or substance. This measurement technique is based on scattering of a monochromatic light incident on a sample, which contains not only photons with the same wavelength as the incident ones (elastic Rayleigh scattering), but also photons with a slightly shifted wavelength (inelastic Raman scattering). This difference in the photon wavelength (or wavenumber) with respect to the incident light wavelength is called Stokes shift and is related to the polarizability of the molecules in the sample.

When a molecule, is placed in an external field of electromagnetic radiation, a dipole moment will be induced in this molecule, changing its rovibronic (rotational, vibrational, electronic) state. Therefore, the difference between the rovibronic states of molecule before the incident photon and after its scattering essentially depends on the molecule's polarizability (with respect to nuclear displacement at the initial rovibronic state). Consequently, to observe Raman

scattering in certain molecules, or more specifically, in some of their bonds, the molecules need to be polarizable to induce a change in their rovibronic state and the scattering intensity is proportional to the change in polarizability.

In Raman shift spectroscopy, a sample is illuminated with a laser beam, causing scattered light, that is filtered and directed to a spectrometer to analyze Stokes shifts at different wavelengths. Such Raman shift spectra were obtained for a study on perovskite liquefaction and crystallization, shown in chapter 4.

2.2.9 UV-vis spectroscopy

Measurements of transmission and reflection of a sample in the ultraviolet-visible part of the spectrum can be performed by so-called UV-vis spectroscopy. Its underlying principle is based on passing light through a monochromator and measurinig changes in its intensity after being transmitted through or reflected from a sample. Both measurement modes – transmission and reflection – require slightly different setups: in the measurements of transmission the detector is placed behind the sample, while for reflection mode a detector must be placed inside the integrating sphere which traps all of the reflected light. The sample reflection and transmission spectra are normally obtained from the difference between the measured light intensity with and without the sample. Under the assumption that light can be either reflected, transmitted or absorbed, the sample light absorbance can be calculated. These optical measurements were performed in chapters 5, 6 and 8.

2.2.10 Four-point-probe

To accurately measure ohmic resistance, a four-point-probe measurement can be utilized. It consists of four pins placed in a linear arrangement, with equal (or at least precisely known) margins between them. During the measurement a current is applied between the two outer pins (often referred to as force connections), while the voltage drop between the two inner pins (often referred to as sense connection) is measured. Such configuration allows to account for an additional series resistance in the pins where the voltage drop is measured, thus, making such 4-point-probe measurement highly accurate. This technique was employed to measure sheet resistance of electrodes in chapters 5, 7 and 8

2.2.11 Current-voltage measurements

The current-voltage, or more specifically, current density-voltage curve is an essential measurement for researchers in photovoltaic field, since it is needed to estimate the PCE of a PV device. This curve is obtained by placing a solar cell under forward bias, varying the potential and measuring the resulting current until all the desired

points of the curve are obtained. The JV-curve of a PV device can be measured in either reverse-scan (decreasing applied voltage during the measurement) or forward-scan (increasing applied voltage during the measurement). Measurement of current, application of voltage, as well as the voltage scan are performed by a source-meter (connected to a PV device), which can also control the scan speed (in V/s), step size, the starting and the final voltage values.

To obtain a PCE value, a JV-curve is measured when a photovoltaic device is placed under a standard illumination of AM1.5G with intensity of $100\,\mathrm{mW/cm^2}$ (*cf.* subsection 1.2.5). However, JV-measurements can also be performed at higher or lower intensities (as will be shown below), or even in the dark. JV-measurements have been performed in each work of this thesis, except chapter 3.

As was mentioned earlier (*cf.* subsubsection 1.3.7.2), perovskite PV devices often suffer from a pronounced hysteresis between both scans, resulting in a significant uncertainty about the "true" JV-characteristics. To avoid wrong estimation of PCE, a so-called stabilized PCE measurement can be performed by keeping a PV device under a constant voltage close to the MPP obtained from either JV-scan and measuring the output current at such V_{mpp}. Such measurement resembles the operation of a PV module in practical conditions at a MPP, which is usually achieved by an MPP-tracker. Thus, such measurement serves as a more objective merit of power conversion efficiency at a (quasi-) steady state. The measurement of stabilized PCE was performed in chapter 8.

2.2.12 Light intensity-dependent measurements

Since $J(V)$ highly depends on the J_{ph} according to Shockley equation in Equation 1.76, a variation in light-intensity significantly alters the measured JV-curve. While J_{ph} and J_{SC} depend linearly on the illumination intensity, V_{OC} has a logarithmic dependency according to Equation 1.78. In order to express V_{OC} of a non-ideal diode (or a solar cell) with non-radiative recombination present, Equation 1.78 can be slightly modified to add so-called *ideality factor* n:

$$V_{OC} = \frac{nkT}{q} \ln\left(\frac{J_{ph}}{J_0} + 1\right) \tag{2.4}$$

The ideality factor is a dimensionless quantity and theoretically can be equal to any value between 1 and 2. Conventionally, $n = 1$ assumes that all the recombination mechanisms are radiative, whereas $n = 2$ means that all the recombination in the diode is non-radiative. Hence, it can be particularly useful to measure the V_{OC} as a function of light intensity, which will have a slope equivalent to $\frac{nkT}{q}$, from which n can be extracted, providing information on the dominant recombination mechanism.

Let us assume that V_{OC} of an ideal diode ($n = 1$) is measured at two different intensities, which differ exactly by one order of magnitude, *i.e.* we have two different photocurrents: $J_{ph,1}$ and $J_{ph,2}$, where $J_{ph,2} = 10J_{ph,1}$. Then, similarly to Equation 1.77 one can write:

$$\frac{J_{ph,2}}{J_0} = \frac{10J_{ph,1}}{J_0} = \frac{10}{J_0}J_0\left(e^{\frac{qV_{OC,1}}{kT}} - 1\right) = e^{\frac{qV_{OC,2}}{kT}} - 1, \tag{2.5}$$

which then leads to:

$$\left(e^{\frac{qV_{OC,2}}{kT}} - 1\right)\left(e^{\frac{qV_{OC,1}}{kT}} - 1\right)^{-1} = 10 \tag{2.6}$$

Taking natural logarithms on both sides results in:

$$\frac{qV_{OC,2}}{kT} - 1 - \left(\frac{qV_{OC,2}}{kT} - 1\right) = \frac{q}{kT}(V_{OC,2} - V_{OC,1}) = \ln(10) \tag{2.7}$$

Therefore the a ten-fold increase in illumination incident on an ideal diode would result in a V_{OC} increase of:

$$\Delta V_{OC} = V_{OC,2} - V_{OC,1} = \frac{kT}{q}\ln(10) \approx 59.6\,mV \tag{2.8}$$

If the increase in V_{OC} per decade is higher than this value (Figure 2.4a), it is presumed to be due to "non-ideality" of the diode, implying that non-radiative recombination is present which increases the slope. However it should be noted that n can not serve as an accurate quantification of non-radiative recombination and can only serve for qualitative comparison between different PV devices.

When V_{OC} is measured at different light intensities, no current is extracted and, thus, no series resistance losses are present. J_{SC} is influenced by series resistance only when it becomes high enough to induce a slope at $V = 0$. So measurements of V_{OC}-J_{SC} pairs at different light intensites produce a so-called pseudo-JV-curve (pJV) – a JV-curve of a solar cell without series resistance losses. The pseudo-current density as a function of light-intensity I is calculated as:

$$pJ(I) = J_{SC}^{1\,Sun} - J_{SC}(I) \tag{2.9}$$

Plotting the pJV-curve (Figure 2.4b) allows to calculate the pFF and pPCE as well, in order to provide potential of a solar cell, if series resistance was minimized. Such analysis of light-intensity dependent behavior was implemented in chapter 5.

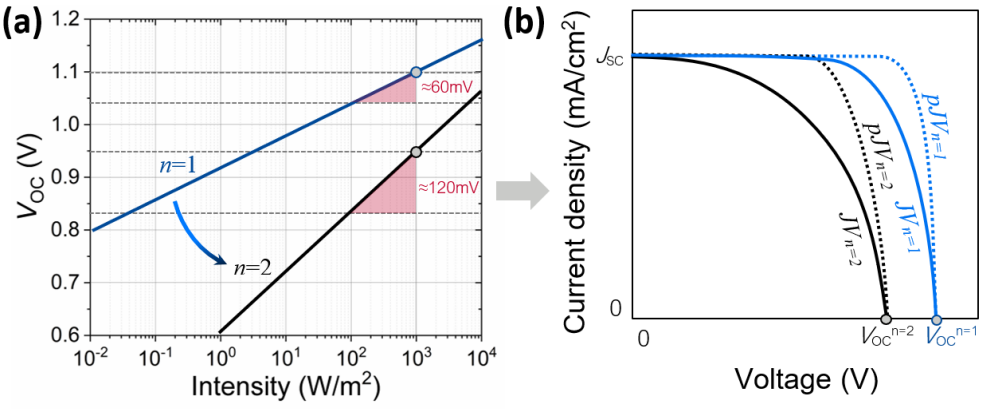


Figure 2.4: Exemplary plots of (a) V_{OC} measured at different light intensities of 2 solar cells, from which ideality factors of 1 and 2 can found (from the slope) and (b) pseudo JV-curves (pJV) of these solar cells plotted based on the measurement in (a). In this example, the J_{SC} of both cells was assumed ot be the same for simplicity. Note the difference between the JV- (solid) and pJV-curves (dashed) of each cell, which occurs due to charge transport losses (*i.e.* loss in FF).

2.2.13 Spectral response and quantum efficiencies

A useful figure of merit that describes how the photogeneration current of a solar cell depends on the incident light wavelength is commonly known as *spectral response* (SR). It can be found by dividing the current, which is measured when a short-circuited solar cell is placed under monochromatic light, by the power of the incident light. A similar property – *external quantum efficiency* (EQE) – describes the ability of a solar cell to convert photons into free charge carriers, which were collected by the respective electrodes. The difference between SR and EQE is that SR is expressed in A/W, while EQE is a dimensionless quantity, relating the number of collected charge carriers to the number of incident photons. The SR and EQE are linked via the following expression:

$$SR = \frac{q\lambda}{hc} EQE \tag{2.10}$$

If the EQE (or SR) is known, one can also calculate the photogeneration current J_{ph}. Since EQE effectively describes the incident photon-to-electron conversion efficiency (also sometimes referred to as IPCE), the photocurrent J_{ph} can be obtained from the cell's EQE and the known incident spectral *photon flux* $\Phi_{ph,\lambda}$:

$$J_{ph} = -q \int EQE(\lambda)\Phi_{ph,\lambda}(\lambda)d\lambda \tag{2.11}$$

Since SR and EQE only consider the collected charge carriers as output, they do not provide information on the wavelength-dependent optical losses, such as transmission and reflection. Such complementary information can be obtained by measuring

the absorption of a solar cell, using UV-vis spectroscopy (*cf.* subsection 2.2.9), in order to find *internal quantum efficiency* (IQE):

$$IQE = \frac{EQE}{A} = \frac{EQE}{1 - R - T} \tag{2.12}$$

Thus, SR, EQE, and IQE are characteristics of a PV device, describing its spectral utilization. These techniques have been used in the work discussed in chapter 5.

2.2.14 Electrochemical impedance spectroscopy

A powerful characterization tool, which monitors electrical and electrochemical processes of the sample *in-operando* is electrochemical impedance spectroscopy (EIS). Such measurement is performed by applying an alternating current (AC) to a sample and measuring its frequency-dependent response, which is then fitted to equivalent circuit(s), that could describe such behavior. The selection of the equivalent circuit should be physically meaningful and be linked to the key electrochemical processes stimulated by AC at different frequencies. Hence, prior knowledge of the sample operation and working principle is crucial for a purposeful EIS measurement.

The sample's response to an AC perturbation allows to disentangle between various processes happening simultaneously but at different time-scales. By fitting the response to the chosen equivalent circuit, properties of each component of a circuit (*e.g.* resistance, capacitance) can be attributed to the physical processes happening in the sample, providing valuable information on, for example, charge transfer or reaction rates.

While EIS has been actively employed by the scientists involved in electrochemical applications, a number of researchers have also employed it to study PSCs. However, as recently highlighted by von Hauff and Klotz, literature research shows that currently an unequivocal assignment of PSC's response to a specific equivalent circuit proves difficult. [96] The main problem with fitting of EIS of PSCs to a specific equivalent circuit is a large number of dynamic processes happening on the same or similar time-scales, which contribute to complex interplay between them, as was shown in Figure 1.17. Moreover, degradation of PSCs during EIS measurements add another level of complexity of EIS interpretation, leading to even more ambiguous results. Hence, although the author utilized such characterization method in chapters 5 and 7, EIS measurement of PSCs is better suited to provide qualitative comparison between different samples, rather than to extract quantified parameters obtained from the equivalent circuit fits.

Chapter 3

Low-temperature carbon-based electrodes in perovskite solar cells

3.1 Preamble

Since the herein presented thesis revolves around the carbon-based electrodes in perovskite PV devices, it is essential to discuss the motivation behind using such electrodes, recent developments and future prospects. Although the review publication discussed in this chapter is primarily focused on the low-temperature carbon-based electrodes in perovskite solar cells,[†] it provides a comprehensive overview on the current stability issues of perovskite PV (*cf.* subsection 1.3.7), types of carbon-based electrodes, PSC fabrication with such electrodes, state-of-the-art devices and their evolution over the years. Thus, the purpose of chapter 3 is to introduce the reader to to PSCs with carbon-based electrodes (referred to as CPSCs throughout this thesis) and their advantages to devices with conventional metallic electrodes as well as their current challenges.

[†]This chapter (except for the critical discussion in section 3.6) has been published as review publication in the peer-reviewed scientific journal "Energy and Environmental Science" (impact factor 2022: 38.5):

Bogachuk, D., Zouhair, S., Wojciechowski, K., Yang, B., Babu, V., Wagner, L., Xu, B., Lim, J. Mastroianni, S., Pettersson, H., Hagfeldt, A. Hinsch, A. (2020). Low-temperature carbon-based electrodes in perovskite solar cells. *Energy Environ. Sci.*, 13(11), 3880-3916.

The individual contributions were as follows:

- **D.B.**: conceptualization, preparation of each chapter, summary of the findings and writing the perspective, figure preparation, handling of citations, coordination of co-author contributions
- **S.Z.**: conductivity improvement methods, charge selectivity improvement strategies, methods to improve the perovskite/carbon interface
- **B.Y.**: stability of conventional PSCs and carbon-based PSCs, differences between the low- and high-temperature carbon-based devices, advantages of low-temperature carbon-based electrodes
- **K.W.,V.B.**: advantages of low-temperature carbon-based electrodes, carbon layer deposition methods, charge selectivity improvement strategies, methods to improve the perovskite/carbon interface
- **L.W.**: environmental and cost analysis of conventional PSCs, conductivity improvement methods, charge selectivity improvement strategies, assistance with manuscript preparation
- **B.X.,H.P.**: summary of low-temperature carbon paste formulations
- **J.L.**: literature research on the cost analysis of PSCs
- **S.M.**: analysis the environmental concerns of conventional PSCs
- **A.Ha.**: summary of the findings and contributing to the perspective
- **A.Hi.**: contributed to the description of charge selectivity improvement strategies, summary of the findings and contributing to the perspective
- **All authors**: contributed to the study with valuable discussions and reviewed the manuscript

3.2 Abstract

Carbon-based electrodes have been widely applied in perovskite solar cells (PSCs) because of their chemical inertness and compatibility with up-scalable techniques, signifying their solid potential for mass-production. The material scarcity and complexity of metal ore extraction further highlights that conventionally used noble metal electrodes cannot represent a sustainable option for back-contact in PSCs, while cells with carbon-based electrodes represent an excellent solution to these problems. However, their power conversion efficiencies (PCEs) still lag behind the traditionally processed cells with metal electrodes, resulting in a considerable efficiency gap. To overcome this issue, we propose the use of low-temperature carbon-based (LTCB) electrodes, which offer several key advantages in comparison to mesoscopic high-temperature treated ones: 1) larger choice of selective layers, 2) applicability to all perovskite crystallization methods, 3) compatibility with flexible substrates and 4) faster deposition process. In this review we analyze numerous techniques to formulate the LTCB-paste and ways to deposit it on the cell stack which have been developed in order to improve the interfacial contact and electrode conductivity. Besides describing the current state-of-the-art perovskite solar cells with LTCB-electrode, the most promising strategies to enhance the PCE of such photovoltaic (PV) devices are discussed. Overall, we emphasize that PSCs with LTCB-electrode combine high device stability, low manufacturing costs and low environmental impact, while having options for pushing the efficiency of carbon-based PSCs closer to the record-breaking cells, all of which are vital in order to fulfill the true potential of perovskite PV.

3.3 Introduction

Ever since the potential of perovskite materials in solar cell applications was discovered in 2009, [46] the photovoltaic (PV) community is still nowadays being impressed by their exceptional light-absorbing and opto-electronic properties. One of the appealing points of this type of photovoltaic devices is the versatility of the semiconductor crystal structure. [43, 97, 98] This phenomenal tunability of various fundamental properties fuels the intensive research activities across the globe and makes them attractive to researchers not only in field of PV, but also in the disciplines of light-emitting-diodes (LEDs), [99–102] photodetectors, [103–106] sensors [107–110] and electrochemical cells. [111–113] In PV applications, once the device efficiencies became comparable to the well-established technologies such mono- or poly-crystalline silicon, the aspect of performance stability became the center of attention for scientists working on perovskite PV. [72, 114–117]

Considering the nature of metal-halide perovskite, it has been noticed that one of its most-appealing points – low energetic barrier for crystal formation – is also one of its biggest drawbacks. [118] This peculiar material characteristic

allows for quick liquid processing during cell production, while simultaneously possessing "soft ionic crystal" properties prone to multiple defects and degradation mechanisms due to weak metal-halide bond. [118–121] Over the years, researchers have developed countless techniques to solve the instability problem of perovskite solar cells (PSCs). However, it is still a challenge to combine high-efficient light absorption and charge extraction with stable performance in one perovskite device.

Generally, most of the cells are fabricated on a transparent substrate, coated with conductive oxide (*e.g.* FTO, ITO) which functions as a front electrode. The charge selectivity in perovskite cells is obtained by placing a photoabsorber between hole and electron-selective contacts. The cell configuration, where on the transparent front contact an electron selective layer (ESL), perovskite and a hole-selective layer (HSL) are sequentially deposited, is commonly referred to as n-i-p structure. The cell stack is completed by a counter- or back-electrode. Both electrodes allow an effective lateral charge conduction, while the charge selective layers extract photogenerated electrons and holes from perovskite and further conduct them to the electrode. The cell structure can also be inverted, resulting in the p-i-n configuration. Some p- and n-layers can only be interchangeably employed, and the question which device structure offers best power conversion efficiencies (PCEs) and performance stability is still under debate. Carbon-based

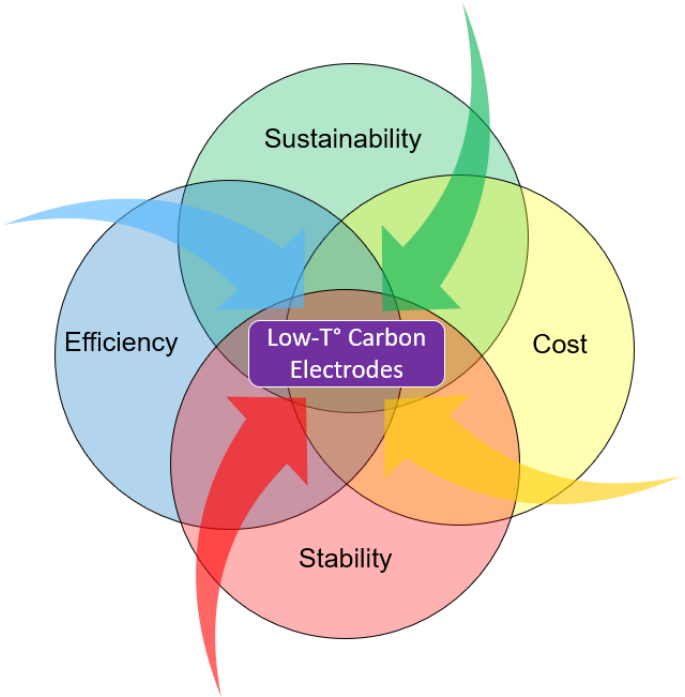


Figure 3.1: Illustration of main characteristics, that are required for perovskite to become the next generation PV technology, where we identify low-T° carbon as the key element to reach that goal.

perovskite solar cells (CPSCs) are a cell concept that has been introduced to sort the issues of instability, manufacturing complexity and high costs faced by record-breaking metal/HSL-based PSCs. [122] The hydrophobic nature of carbon promotes lower in-take of moisture into the cell, making it possible to improve the cell lifetime. [123, 124] Additionally, carbon electrodes have proved their ability to extract photogenerated holes by themselves allowing researchers to manufacture PSCs without the need of using expensive and unstable HSLs, promoting the concept of HSL-free monolithic perovskite solar cells. [125] Conventional carbon-based PSCs use carbon black and graphite as counter electrodes, that require high processing temperatures to burn out the organic binder. [126, 127] This review aims to explore the recent promising progresses of low temperature carbon-based PSCs, along with their unique potential to meet the optimal point for game-changing and disruptive PV: low cost, high stability, high efficiency and sustainability (Figure 3.1).

Here, we shortly highlight main challenges of traditional perovskite PV, namely the device stability, high manufacturing costs, up-scaling and environmental impact, followed by the discussion how carbon-based cells can overcome these drawbacks. Different concepts of CPSCs are described as well as the key advantages of low-temperature processed CPSCs over the high-temperature processed ones. Later, we discuss the recent developments in low-temperature carbon-paste formulations and methods of depositing such layer on a cell. Finally, we propose a number of strategies to close the efficiency gap between the traditional PSCs and low-temperature carbon-based ones.

Motivation behind perovskite solar cells with carbon-based electrode

Stability issue in perovskite solar cells

It is well-known that perovskite solar cells are more susceptible to degradation than mature PV technologies such as amorphous/crystalline Si and thin film technologies (*e.g.* CdTe, CIGS). [128, 129] Many systematic investigations and review publications have shown that the degradation of perovskite is an extremely complex problem including issues related to moisture, oxygen, UV light, heat and electrical bias. [130–134] Moreover, this makes also the assessment of PSC stability complicated as it highly depends on the measurement conditions. To resolve this ambiguity, scientists in the perovskite community have recently proposed a number of standardized procedures for studying the stability of perovskite PV device based on ISOS protocols. [135] In this review we would like to focus the reader's attention on the intrinsic stability of back contacts and organic hole-selective layers that are implemented in PSCs (Figure 3.2). Therefore, the main degradation mechanisms related to the ambient environment, containing oxygen and moisture, are accentuated in

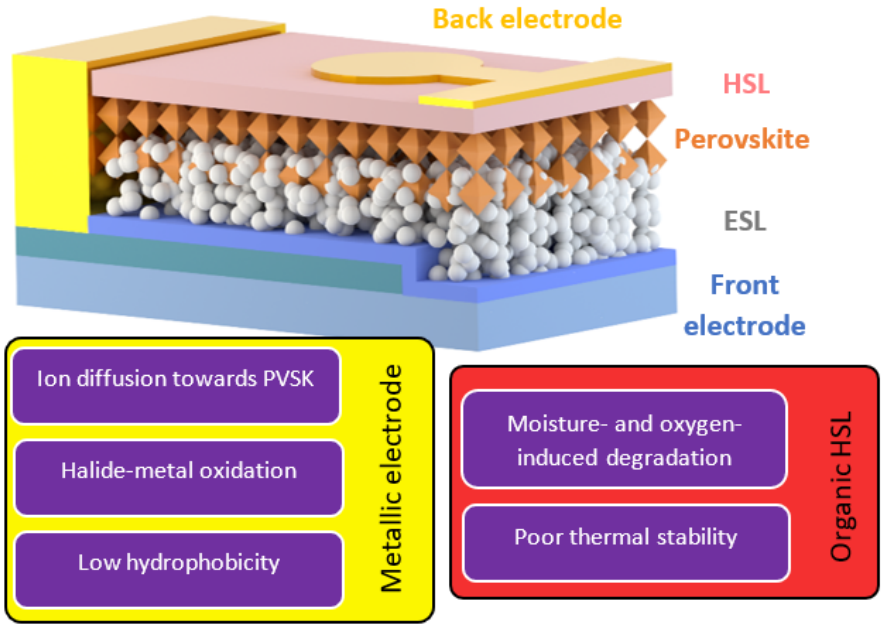


Figure 3.2: Basic mesoporous n-i-p perovskite cell configuration and the main drawbacks of metallic electrodes and organic HSLs, affecting the performance stability of such cell. HSL and ESL denote hole- and electron-selective layers, respectively.

this chapter.

Moisture-induced degradation of perovskite

It has been found in numerous studies that perovskites with CH_3NH_3I readily decomposes in humid conditions into CH_3NH_2 and HI gases, resulting in the formation of PbI_2 in unsealed cells. [87, 118, 136–138] Highly polar water molecules can directly affect the hydrogen bonds between the organic A-cation and inorganic X-anions in the ABX_3 perovskite structure, [139] resulting in the loss of CH_3NH_3I via sublimation. [136] However, it has also been demonstrated that perovskite is more likely to firstly form monohydrate $CH_3NH_3PbI_3{\cdot}H_2O$ and dihydrate $(CH_3NH_3)_4PbI_6{\cdot}2H_2O$ complexes in the presence of water, which also leads to the formation of PbI_2. [118, 140–142]

Replacing CH_3NH_3 cation with a commonly used formamidinium – $HC(NH_2)_2$ cation does not yield an improvement in moisture stability, as the latter can also decompose into ammonia and sym-tryazine in the presence of water. [143,144] The *ab-initio* molecular dynamics simulations show that $CsPbI_3$ has a higher interaction with water molecules and thanks to the low lattice distortion, the moisture-induced degradation is suppressed in such material, in comparison to that of the $CH_3NH_3PbI_3$. [145] Partial substitution of cation with Cs was found to improve the moisture-tolerance

of perovskites, [123, 144] however at the cost of less optimal bandgap and light-absorption properties. [137, 146] While, on the other hand, barriers at the interface with perovskite can efficiently improve the quality of the perovskite film, reduce the interface recombination, enhance the surface hydrophobicity and therefore protect the perovskite from moisture. [145, 147–153] For example, additional two-dimensional (2D) A_2PbI_4 perovskite layers using pentafluorophenylethylammonium (FEA) have been introduced on top of the 3D bulk perovskite film, enabling a power conversion efficiency of over 22 % and superb stability of retaining 90 % of initial PCE during operation condition for 1000 hours in humid air under one sun illumination without encapsulation. [147] An additional thin layer of lead oxysalt with wide-bandgap has been proved to be an excellent interlayer to passivate the perovskite surface with reduced defect density. More importantly, this barrier layer effectively protects the underneath perovskite layer with enhanced water resistance, and therefore, leading to an excellent stability of the device of 96.8 % from initial PCE after operation at maximum power point under illumination for 1200 hours at 65°C. [154] Introduction of an inorganic WO_3 interlayer between perovskite and HSL has been demonstrated, which helped to increase PSC moisture stability, maintaining 60 % of initial PCE for over 160 h under humidity over 80 %. [153]

Intrinsic and moisture stability of organic HSLs

The PSC structure which is commonly shown in literature includes a metal-based electrode and an organic HSL such as 2,2',7,7'-tetrakis (*N,N*-di-methoxyphenylamine)-9,9'-spirobifluorene (spiro-OMeTAD), poly(3,4-ethylene dioxythiophene): poly(4-styrenesulfonate) (PEDOT:PSS) or polytriarylamine derivatives (PTAA). [139, 155, 156] Most of them are very sensitive to the presence of water in ambient atmosphere. In order to facilitate an efficient charge transport, spiro-OMeTAD (which has low intrinsic hole mobility) requires it to be doped with an additive such as bis(trifluoromethane)sulfonimide lithium salt (LiTFSI), which is hydrophilic and therefore serves as a source of rapid degradation in the presence of moisture. [139, 157, 158] In addition to LiTFSI, spiro-OMeTAD can be doped with *tert*-butyl pyridine (*t*BP) to increase the photovoltaic performance, but it can also degrade perovskite, as pyridine molecules can diffuse to perovskite layer and form PbI_2-pyridine complex. [159, 160] Qi *et al.* have found how the often occurring pin-holes (Figure 3.3a) in spiro-OMeTAD layer can facilitate a rapid ingress of moisture into the perovskite layer (Figure 3.3b). [161, 162] However, by replacing the commonly used dopant LiTFSI with $Zn(TFSI)_2$,(which were additionally doped with *t*BP) a significant improvement in both photovoltaic performance and long-term stability has been reported, [163] owing to one order of magnitude enhancement in hole mobility and a facilitated oxidation process of spiro-OMeTAD by complexation between the zinc cation and *t*BP even in the absence of oxygen and light, which is completely different from the conventional mechanism of LiTFSI. [164] Nevertheless, the use of dopants is normally problematic due to undesired ion migration and oxidation procedure, inducing stability

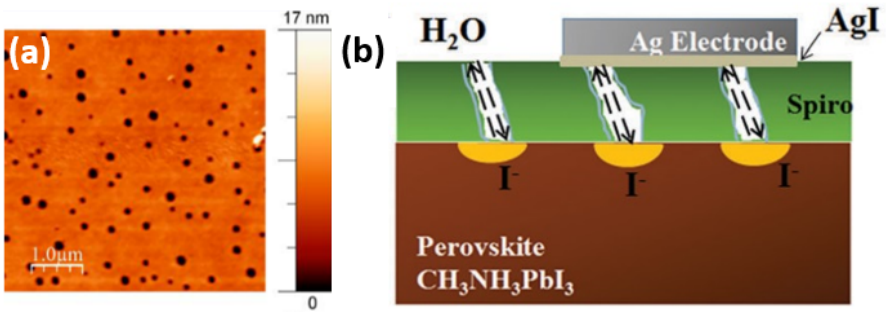


Figure 3.3: (a) AFM images of the spiro-OMeTAD layer surface with multiple pinholes of 135 nm average diameter. (b) Schematic drawing of the perovskite degradation and halide diffusion in the presence of pin-holes in spiro-OMeTAD. Adapted and reproduced with permission from references [161] and [162].

issues. [165] Therefore, dopant-free HSL becomes a more promising material for stabilizing PSCs. [166–169] Fabrication of di(1-benzothieno)[3,2-b:2',3'-d]pyrrole (DBTP) derivatives with arylamine wings such as *m*DPA-DBTP have proven to be an effective route to synthesize dopant-free HSLs with exceptional hole-transport properties, arising from the good molecular backbone planarity, enhanced $\pi - \pi$ stacking and well-aligned valence band maximum. [170] The devices with *m*DPA-DBTP exhibited PCE of 18.09 %, which remained 81 % of its original PCE after 33 days under air-storage, whereas in comparison, the PSC devices with doped spiro-OMeTAD have completely degraded (PCE $<$ 1 %) under the same storage conditions. In addition, two copper phthalocyanine (CuPc) derivatives, CuPc-Bu (containing butyl groups) and CuPc-OBu (containing butoxy groups), have also been developed for dopant-free HSLs in PSCs, which achieved PCE of 14.3 % and 17.6 %, respectively. [171] PSCs with CuPc-Obu HSL exhibited remarkably improved ambient stability under storage in an environment with 85 % relative humidity without encapsulation, owing to the high moisture resistivity of the CuPc-Obu. Moreover, highly efficient polymeric HTM has also been demonstrated by incorporating the diethylene glycol (DEG) groups, which could be used to fabricate highly-efficient PSCs with a certified PCE of 20.10 %. The champion device also presents an impressive long-term stability, by retaining 92.25 % of the initial PCE after storage in ambient air for 30 days. [167] A popular choice of HSL in p-i-n cells, PEDOT:PSS, can react with moisture and oxygen in ambient, [137, 155, 156, 172, 173] Despite the advantages offered by these HSLs, it becomes clear that these layers have to be protected by a hydrophobic layer (such as carbon-based electrode), in order to suppress water ingress into the perovskite absorber.

Some studies have attempted to develop efficient HSL-free PSCs to overcome this issue. Etgar *et al.* reported an HSL-free concept for perovskite solar cells with a $CH_3NH_3PbI_3/TiO_2$ heterojunction cell yielding a PCE of 5.5 %. [174] The idea

consisted of having a thick perovskite layer on top of the mesoporous TiO_2 acting both as a photoabsorber and selective layer.

On the other hand, inorganic HSLs such as NiO_x and CuI can offer much better chemical stability and carrier mobility than the organic ones. [123, 156, 176] You *et al.* have demonstrated how PSCs with PEDOT:PSS completely deteriorate over course of 5 days in ambient environment (25°C with 30-50 % humidity), while the ones with NiO_x as HSL maintained their initial PCE for almost 60 days. [156] [64] Although in most cases NiO_x serves as a p-contact in p-i-n cells, there are also several reports displaying the capability of NiO_x to be integrated on top of perovskite. A low-temperature processing of NiO_x was reported by Liu *et al.*, where the metal oxide nanoparticles were capped with stearate ligand and dispersed in a non-polar solvent chlorobenzene. [177] However, the p-i-n devices with such NiO_x layer have shown better PCE than the n-i-p devices due to remaining ligands at the perovskite/HSL interface, hindering the hole-extraction. Cao *et al.* have demonstrated another low-temperature method to deposit NiO_x on top of perovskite, which provided higher thermal stability of the PSC, in comparison to cells with spiro-OMeTAD and copper thiocyanate (CuSCN). [178] Thermally-induced degradation in samples with spiro-OMeTAD was attributed to formation of morphological defects at the perovskite/HSL interface, whereas the reaction between perovskite and CuSCN at elevated temperatures was found to jeopardize the cell stability. Zhang *et al.* have proposed to use $CuGaO_2$ as an efficient and stable HSL, which can be deposited on top of perovskite, resulting in a better device PCE and stability than that of devices with spiro-OMeTAD (Figure 3.4). [175] The suppressed interfacial recombination and lower dark saturation current (J_0) were determined to be the origins

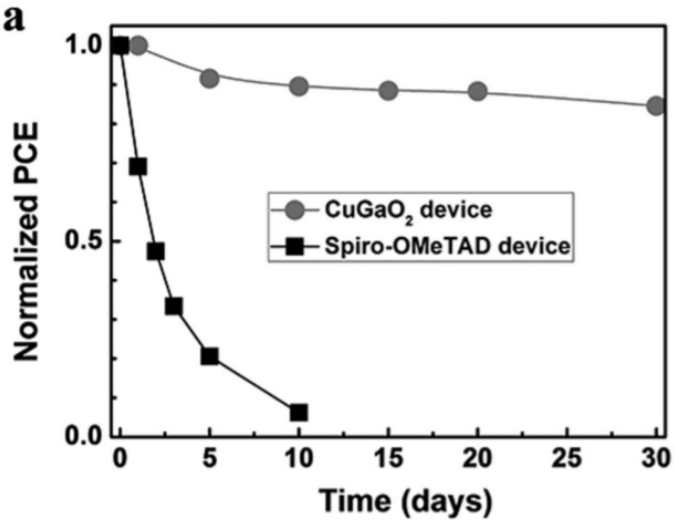


Figure 3.4: Normalized PCE of PSCs with $CuGaO_2$ and spiro-OMeTAD as HSLs measured under ambient environment (RH=30-55 %, T=25°C). Adapted and reproduced with permissions from reference [175].

of the PCE improvement, whereas the stability enhancement was attributed to less hydrophilic properties of the $CuGaO_2$.

The reported findings in literature show that, as anticipated, some inorganic HSLs exhibit higher stability than the organic ones, because of their lower affinity for water and higher structural robustness in ambient environment. [137] Moreover, inorganic materials typically exhibit higher thermal stability [123] as well as ability to retard sublimation of volatile perovskite components (*e.g.* HI and CH_3NH_2) and layer decomposition. [180] This is an important note, as in n-i-p cells the HSLs should protect the moisture- and oxygen-sensitive perovskite photoabsorber and not accelerate its deterioration.

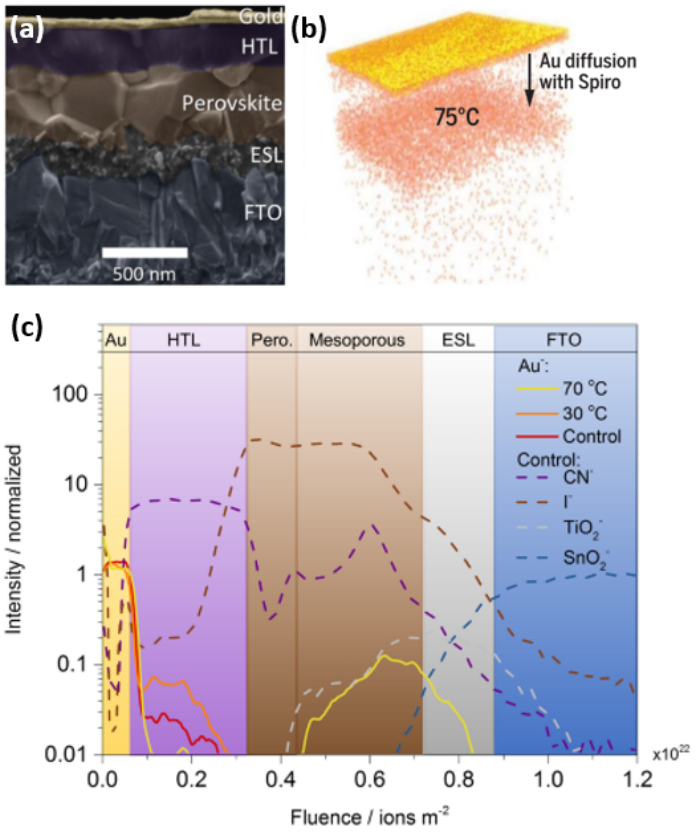


Figure 3.5: (a) Solar cell stack with m-TiO_2 (ESL), perovskite, spiro-OMeTAD (HTL) and gold cathode. (b) Reconstructed 3D map of gold diffusion towards perovskite, accelerated by higher temperatures (c) Time-of-flight SIMS profile of the aged cell-stack. Adapted and reproduced with permission from references [72] and [179].

Intrinsic and moisture stability of metal-based electrodes

Metal-based layers such as gold (Au), silver (Ag) and copper (Cu) are generally favored as a back-electrode in perovskite solar cells, due to their high conductivity. Unfortunately, they are often a source of degradation phenomena in PSCs, decreasing the cell stability. It was found that ions from Au layer can diffuse through the HSL producing shunts and deep trap states (Figure 3.5). [179, 181] This ion diffusion can be alleviated to a limited extent by inclusion of chromium (Cr) or Cr_2O_3 buffer layer between HSL and Au contact. [179, 182] In addition to ion migration, Au electrodes show capability of moisture trapping and hindering the release of H_2O molecules from perovskite. [138, 183]

Multiple studies have shown that PSCs with silver contact degrade due to tendency of Ag^+ ions to diffuse towards perovskite and due to formation of silver halides, arising from oxidation reaction with migrated I^- ions or with volatile perovskite degradation products (*e.g.* HI) as depicted in Figure 3.6. [181, 184–187] Cu electrode can be easily oxidized in the presence of air and moisture, leading to increased series resistance losses in PSCs. [123] Also, its oxidation products can react with perovskite decomposition products such as HI, which further deteriorates perovskite. [188] Notably, over the last years, more materials such as reduced graphene oxide, [189] bismuth [190] and transparent conductive oxides [186] have been implemented as barrier layers to reduce the metal-electrode induced degradation. Nevertheless, the fundamental mechanisms inducing water- and metal-induced degradation remain and even in the presence of interfacial modifications, there remains a risk that future barrier development will not enable long term stabilities in the order of decades, as currently warranted for silicon PV modules. This suggest that, regarding the current research status, metal-electrode based PSC might not be able to achieve long-term device stabilities. [191] Indeed, to the best of our knowledge, today the longest demonstrated operational stability of metal-based PSCs is 5,000 h (illuminated with intensity of 13 mW cm^{-2}, which is almost 1/8 of the Sun irradiation intensity, under relative humidity of 70 %), which is still too low for passing international PV standards of long-term stability. [117, 139, 192]

Encapsulation of PSCs

Considering that often PSC stability measurements are carried out in inert atmosphere to avoid degradation from moisture and air, [193] the ability to reach the IEC61215:2016 standard is still not on the horizon for unencapsulated cells with metal-based electrodes. This fundamental obstacle of long-term stability must be addressed and changing the electrode material is one way to bring perovskite PV closer towards its commercialization. Moreover, the stability tests should be carried out at similar, standardized conditions in order to unify the stability assessment between various reports and develop a deeper understanding of the degradation pathways in photovoltaic devices. [135]

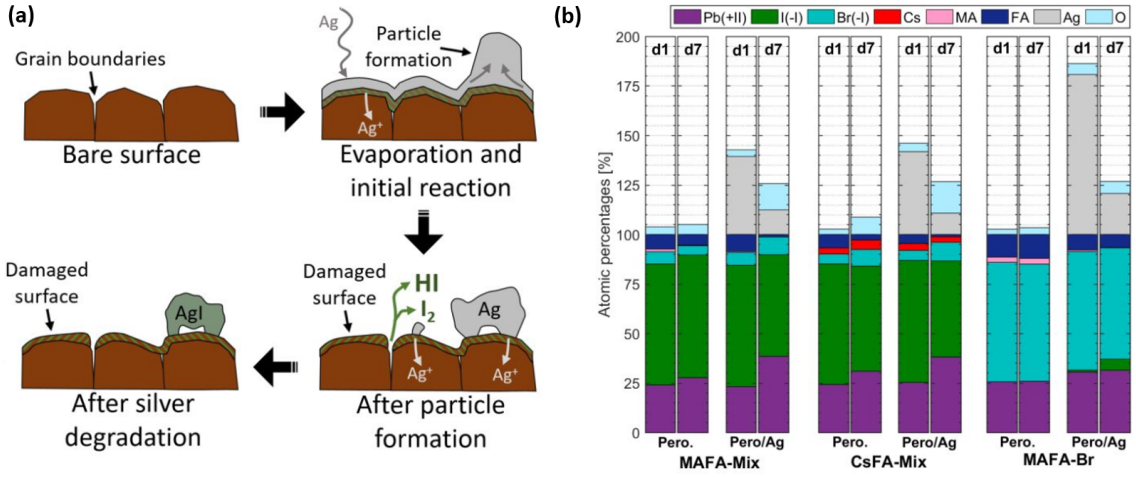


Figure 3.6: (a) Model of the silver degradation in the presence of mobile volatile species (*e.g.* HI, I_2) and I^- and Ag^+ ions in perovskite. (b) The relative elemental percentage of each species at the surface, determined from core level XPS analysis of the pure perovskite (noted as Pero.) and when the Ag is deposited on top (Pero/Ag) for different perovskite cation compositions on day 1 (d1) and day 7 (d7). Adapted and reproduced with permission from reference [184].

It needs to be mentioned that despite strong stability disadvantages of organic HSLs and metallic contacts there has been a tremendous progress in developing encapsulation techniques to bring the decomposition reactions to equilibrium and prevent the PCE deterioration of such devices. Glass-glass encapsulation as well as the use of edge-seal technology have been proposed, although low perovskite decomposition temperature presents a challenge for selecting a benign sealant. The authors demonstrated how such encapsulation provides a sufficient protection against ambient environment and improves cell stability, namely, the fabricated encapsulated PSCs could withstand damp heat, dry heat and thermal cycling tests. [194] Recently Shi et al. reported how encapsulation with polyisobutylene provided an effective moisture barrier, surpassing over 1800 h of damp-heat test and over 70 humidity-freeze test cycles, meeting the requirements set by IEC61215:2016 standard. [195]

Although, undoubtedly, encapsulation helps to reduce the moisture ingress into the photovoltaic device, the stability of photoabsorber, selective layers and cathode materials still needs to be considered and effective strategies to passivate perovskite and mitigate decomposition reactions need to be developed besides encapsulation. For example, Liu *et al.* have demonstrated implementation of interfacial engineering in perovskite solar modules, which provided a moderate operational stability. Although the encapsulated device retained 86 % of the initial

PCE after 2000 h of operation under AM1.5G illumination, [196] the authors noted that the modules without encapsulation had a similar operational stability, highlighting that encapsulation can only partially prevent the deterioration of the perovskite photovoltaic device and the main stability improvements should be achieved via PSC architecture modification, for example by replacing metallic electrodes with the carbon-based ones.

Stability improvements using hydrophobic carbon-based electrodes

At the moment, a carbon-based hydrophobic electrode is the only counter electrode material that does not have any intrinsic and moisture-induced degradation. It is chemically stable with halides, [123, 184] shows highly hydrophobic properties [124, 127, 197–199] and exhibits a very high thermal stability, [200–202] which provides a strong protection from the environment to the sensitive layers underneath.

Deposition of the carbon-based contact on top of the monolithic cell stack is one of the most promising routes to prolong the lifetime of perovskite PV device. In this case, carbon-based electrodes are typically >5 µm thick, meaning that the over-excess of perovskite can be applied in its porous structure, which makes it more tolerant against the decomposition in the photo-absorber. In 2014, Mei *et al.* employed a mixed-dimensional perovskite of $(5\text{-AVA})_x(MA)_{1-x}PbI_3$ into mesoscopic carbon-based HSL-free perovskite solar cells, resulting in a stable certified PCE of 12.8 % (>1,000 h) under ambient air and full sunlight without encapsulation. [125] Notably, Grancini *et al.*, in collaboration with the company Solaronix, reported an outstanding 10,000 h stability (Figure 3.7a) with the same device structure, whereas the PCE of the n-i-p cell (with the same photoabsorber layer) with spiro-OMeTAD layer and Au electrode, has decreased by almost 40 % relatively to the initial value after only 300 h of continuous 1 Sun illumination. [203] Zhou *et al.* have shown how a low-temperature processed carbon layer is able to repel water better than Au and Ag metal electrodes, resulting in a better overall performance stability without encapsulation. [198] Ye *et al.* have shown how a planar cell with Zn-doped SnO_2 as ESL, CuPc as HSL and a carbon electrode gave a stable PCE close to 18 % for 1,200 h without encapsulation. [204] Zhang *et al.* have demonstrated a cell with 19.2 % PCE with 1,000 h stability, where a carbon-based electrode was deposited on top of HSL by press-transferring a self-adhesive carbon film. [205]

In addition, Li *et al.* have conducted for the first-time extensive stability tests under outdoor conditions with elevated temperatures (Figure 3.7b) and long-term light soaking as well as thermal stress at 80-85°C during 3 months on the carbon-based HSL-free perovskite solar cells. [200] Remarkably, the device performance does not present significant degradation under those stability test conditions, providing a promising pathway towards stable perovskite solar cells with carbon contact. Emami *et al.* have implemented a laser-sealed glass-frit encapsulation on the CPSCs which allowed for the cells to withstand damp-heat and

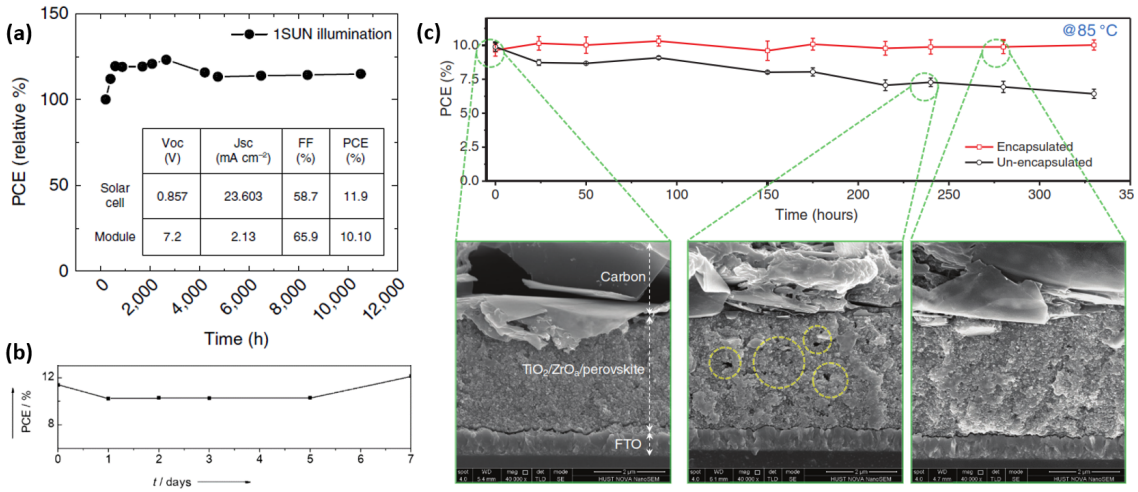


Figure 3.7: (a) Long-term stability measurement of carbon-based perovskite solar cells and 10x10 cm^2 module with IV-parameters shown in the inset. (b) Outdoor stability tests of HSL-free CPSC in Jeddah, Saudi Arabia. (c) Thermal stability measurement of encapsulated and non-encapsulated 10x10 cm^2 modules with SEM images right after the encapsulation and after thermal stress. Adapted and reproduced with permission from references [200, 203, 209].

thermal cycling tests (although they were carried out for less than 1,000 h). [206] Wu *et al.* have also conducted damp-heat tests on the non-encapsulated CPSCs, where the authors observed that such cells are able to retain 77 % of the initial PCE after such an intensive test. [207] Furthermore, due to the ease of carbon-based electrode deposition, large sized modules of 70 cm^2 have been fabricated, showing an extraordinary stable performance of perovskite modules even in humid environments. [208] More recently, by encapsulating carbon-based HSL-free printable PSC submodules (substrate area 100 cm^2) with polyurethane (PU) at a mild temperature of 80°C, the thermal stability of the cell was dramatically enhanced. [209] The submodules can still maintain over 97 % of its initial PCE after over 2,000 h under outdoor conditions (Figure 3.7c), which provides potential for commercial viability of the carbon-based perovskite solar cells with excellent stability under proper encapsulation. As clearly shown in these reports, in comparison to devices with metallic electrodes, carbon-based cells show very stable operation, providing strong arguments for it to be used as a stable back contact in perovskite solar cells and modules. We have mentioned some of the reported stability tests in literature on CPSCs and conventional PSCs in Table 3.1 for comparison. From these results, it can be observed that most of the reported CPSCs remain stable under ambient environment without encapsulation for over 1,000 h, whereas the conventional devices with metallic electrodes remain stable in most cases only when they are encapsulated or measured under inert gas atmosphere. However, to the best of our knowledge, so far there has been no systematic study performed comparing

the cell stack with a carbon-based back-contact versus a metallic one in terms of stability (thermal, humidity, oxygen etc.) in the exact same conditions. We would like to invite researchers in the perovskite community to address this issue and quantitatively compare the precise effect of applying carbon-based electrode instead of the metallic ones on the stability of PSCs.

Low-cost

Perovskite PV has a chance to be a disruptive technology, promising low fabrication costs and therefore final product price. However, several studies revealed that material and processing costs of metal electrodes like gold and HSLs (*e.g.* spiro-OMeTAD and P3HT) as currently employed in many laboratory-scale devices together with the TCO account for the highest costs in the total module price. To decrease the cost further, this mandates to either reduce the usage of these materials or to replace them with cheaper alternatives.

According to a report by Chang *et al.*, in devices with evaporated Au-electrode, more than 90 % of the total device costs are attributed to material costs, 76.6 % of which come from gold, contributing to 74.7 % of the total fabrication costs (including materials, evaporation process etc.). [211] The authors estimated the cost of module of FTO/c-TiO_2/m-TiO_2/Perovskite/P3HT/Au to be around 330 \$US/m^2, which was significantly more expensive than the CdTe (86 \$/m^2) and c-Si (136 \$/m^2) modules at that time (in 2017). In addition, the study suggested that replacing Au with Ag would decrease the price to a comparable value of 102 \$/m^2 or can even be reduced to 90 \$/m^2 if one avoids using sacrificial metal mask during spray deposition of c-TiO_2 and uses laser patterning instead.

The cost of roll-to-roll manufactured flexible perovskite PV devices has also been investigated by Chang *et al.* in a later report. They found that using screen-printing for back contact metallization strongly reduces the capital costs of the final module, in comparison to metal evaporation deposition. [212] Considering that with higher web-speeds the manufacturing costs decrease, the material costs become more and more dominant in the total module fabrication costs. Therefore, cheaper HSLs and back-contacts such as carbon-graphite are vital for the further reduction of module price in industrially relevant high/throughput fabrication methods.

Song *et al.* have investigated the material and manufacturing costs of industrially fabricated modules with inorganic selective layers and Al back electrode in a p-i-n configuration. [213] Notably, the authors found that depositing such inexpensive materials by industry-scale deposition techniques (screen-printing and sputtering) leads to a very low material costs of the functional layers of a PV device (ESL, perovskite, HSL), accounting for only 1.1 % of the total material cost of a module. Interestingly, when the employed functional layers are so low-priced, 93.5 %

Table 3.1: Reported stability tests on PSCs with metallic, HTCB- and LTCB-electrodes. Side note: the references are written in accordance with the original work. [210]

	Device structure Perovskite	Champion cell PCE (%)	Ageing conditions	Relative PCE retained after ageing (%)	Duration	Ref.
PSCs with metallic electrodes	ITO/NiO_x/PVSK/LiF/C_{60}/SnO_2/ Ag $FA_{0.83}Cs_{0.17}PbI_{2.49}Br_{0.51}$	~14	Encapsulated, Damp-heat test (85°C, RH=85%)	~99	1,000 h	103
		~14	Encapsulated, Dry-heat test (85°C, RH=25%)	~97	1,000 h	
		~14	Encapsulated, Thermal cycles (-40 to 85°C)	~103	200 cycles	
		~11	Non-encapsulated, N_2 atmosphere, 85°C	~80	1,000 h	
		~12	Encapsulated, N_2 atmosphere, 85°C	97	1,000 h	
	ITO/SnO_2/PVSK/PTAA/NiO_x/Au/ PEN $Cs_{0.1}(MA_{0.17}FA_{0.83})_{0.9}PbI_{0.83}Br_{0.17}$	14.6	Laminated, 25°C, Continuous MPP-tracking	~100	93 h	172
	FTO/NiO_x/PVSK/PCBM/BCP/Cr/ Cr_2O_3/Au $(FA_{0.83}MA_{0.17})_{0.95}Cs_{0.05}Pb(I_{0.9}Br_{0.1})_3$ with $BMIMBF_4$	19	Non-encapsulated, RH=40-50%, 60-65°C	86	100	
			Encapsulated, 70-75°C	95	1,885 h	
	ITO/NiO_x/PVSK/PCBM/BCP/AZO/ Ag/Al_2O_3 $Cs_{0.05}MA_{0.95}PbI_3$	18.45	Non-encapsulated, 1 Sun illumination with UV filter, 85°C	86.7	500 h	88
	m-TiO_2/PVSK/CuSCN/rGO/Au $(FA_{1-x}MA_x)_{0.95}Cs_{0.05}PbI_{3-x}Br_x$	20	1 Sun illumination with UV filter, N_2 atmosphere, 60°C	95	1,000 h	98
	m-TiO_2/PVSK/spiro-OMeTAD/Au $(5AVA)_{1-x}MA_xPbI_3$	14.6	1 sun illumination, under Ar atmosphere	60	300 h	112
High-temperature route	m-TiO_2/ZrO_2/C $(5AVA)_{1-x}MA_xPbI_3$	11.4	Encapsulated, at 80–85 °C, dark	92.5	3 months	109
			Encapsulated, outdoor illumination, non-continuous measurement	~105.2	7 days	
	m-TiO_2/ZrO_2/C $(5AVA)_{1-x}MA_xPbI_3$	12.7	Encapsulated, Indoor, 1 sun illumination with UV filter	~115	10,000 h	112
	m-TiO_2/ZrO_2/C $(5AVA)_{1-x}MA_xPbI_3$	10.74	Non-encapsulated, indoor, 1 sun illumination	>95	2,000 h	117
	m-TiO_2/ZrO_2/C $(5AVA)_{1-x}MA_xPbI_3$	12.8	Indoor, 1 Sun illumination	~100	1,008 h	32
	m-TiO_2/ZrO_2/NiO/C $MAPbI_3$	14.9	Non-encapsulated, dark	>93	1,000 h	136
			Non-encapsulated, dark at 60 °C	79.7	1,000 h	
	m-TiO_2/ZrO_2/C $MAPbI_3$ (MA^0-liquefied)	15.9	Non-encapsulated, RH = 55-75%, dark	~100	3,500 h	173
	m-TiO_2/Al_2O_3/NiO/C $Cs_{0.05}(FA_{0.4}MA_{0.6})_{0.95}PbI_{2.8}Br_{0.2}$	17.02	Encapsulated, at 85 °C, dark	91	1,000 h	137
	m-TiO_2/ZrO_2/C $(5AVA)_{0.05}MA_{0.95}PbI_3$	~11	Encapsulated, Damp-heat test (85°C, RH=85%)	100.9	50 h	115
		~11	Encapsulated, Thermal cycles (-40 to 85°C)	97.7	70 cycles	
		~11	Encapsulated, RH=80%, dark	~110	500 h	
Low-temperature route	m-TiO_2/PVSK/CuPc/C $MAPbI_3$	16.1	Non-encapsulated, dark	91.5	600 h	142
	SnO_2@TiO_2/PVSK/P3HT-graphene/C $FA_{0.3}MA_{0.7}PbI_3$	18.1	Non-encapsulated, RH = 50%, dark	97	1,680 h	146
			Encapsulated, 1 sun illumination without UV and IR, indoor	89	600 h	
	Ni:TiO_2/PVSK/CuPc/C $Cs_{0.05}(FA_{1-x}MA_x)_{0.95}PbI_{3-x}Br_x$	17.46	Non-encapsulated, RH = 30-40%, dark	97	1,200 h	157
	m-TiO_2/PVSK/spiro-OMeTAD/C $FA_{1-x}MA_xPbI_{3-x}Br_x$	19.2	Non-encapsulated, RH = 30%, dark	95	1,000 h	114
	Zn:SnO_2/PVSK/CuPc/C $Cs_{0.05}(FA_{1-x}MA_x)_{0.95}PbI_{3-x}Br_x$	17.8	Non-encapsulated, RH = 20%, dark	100	1,200 h	113
	m-TiO_2/PVSK/TPDI/C $MAPbI_3$	15.5	Non-encapsulated, outdoor illumination	82.6	30 days	140
	SnO_2/PVSK/spiro-OMeTAD/C/ Graphite paper $Cs_{0.05}(FA_{0.85}MA_{0.15})_{0.95}PbI_{2.55}Br_{0.45}$	18.56	Non-encapsulated, dark	>90	1,500 h	174
	FTO/m-TiO2/PVSK/PEO/C $FA_{0.8}Cs_{0.2}PbI_{2.64}Br_{0.36}$	14.9	Non-encapsulation, Damp-heat test (85°C, RH=85%)	77	192 h	116

of the total material costs come from the balance of system/module, which includes glass substrates, interconnection busbars, sealant, lamination film, edge-sealing frame, a junction-box and wiring. These results show that using up-scalable deposition techniques for fabricating back-electrodes results in reasonable module prices (unlike evaporation of noble metals), which serves as a further motivation towards printable PSCs with carbon-based contacts, due to higher long-term stability than the metal-based ones.

All of the studies mentioned above have been conducted via a bottom-up cost calculation approach, which considers the cost and its uncertainty at each manufacturing step. [213] In summary, we postulate that in order to reach perovskite module prices lower than that of c-Si or thin-film technologies, one needs to implement low-cost materials, which can be easily applied on an industrial scale. An example of such module cost reduction can be a replacement of metal electrode with carbon-based contact in a perovskite PV device stack.

Up-scaling

An increasing number of companies, such as Microquanta Semiconductor, Saule Technologies and Toshiba, have recently started to develop large-scale single-junction perovskite PV modules. [51] However, for the large-scale applications it is still challenging to accurately control layer deposition to form homogeneous pin-hole-free films. [114] Most of the record-breaking perovskite solar cells or modules utilize metal evaporation step in the device fabrication process, which requires high vacuum conditions, making it difficult and costly to upscale, in addition to the high CO_2 footprint of such modules. Carbon pastes can be solution-processed with a variety of fast, large area-compatible, and low-cost deposition techniques. Moreover, low-temperature pastes can be processed on top of perovskite photovoltaic stack, which makes these materials one of the most up-scalable back contact electrode option for perovskite technology.

Over the last few years multiple large-area perovskite PV modules utilizing carbon electrodes were reported. In 2016, Priyadarshi *et al.* reported carbon-based PV modules yielding 10.74 % PCE (70 cm^2 active area) and good ambient stability (less than 5 % drop over more than 2,000 h). [208] Subsequently, Grancini *et al.* demonstrated 11.2 % PCE for the perovskite module of the same architecture (47.6 cm^2 active area out of 100 cm^2 module area). [203] Already in 2016, the swiss-based company Solaronix has demonstrated an HSL-free 500 cm^2 carbon-based perovskite module with a PCE of 12 %, produced by drop-casting method. [51] Recently, Xu *et al.* reported a modules with an area of 60.08 cm^2, having PCE of 12.87 %, infiltrated with perovskite solution using slot-die coating. [214] The group of Hongwei Han from Huazhong University of Science and Technology showed large-area perovskite solar panels of 7 m^2, which were fully fabricated with printing techniques. [209] Weihua Solar, a Chinese perovskite PV manufacturer,

demonstrated a power station made out of 32 carbon-based, perovskite panels of 45x65 cm^2 area. [215] Cai *et al.* printed carbon back contact on top of a perovskite layer, delivering 10.6 % PCE for the HSL-free architecture (FTO/ZnO/$MAPbI_3$ perovskite/Carbon), with an active area of 17.6 cm^2 (module area: 5x5 cm^2). [215]

These examples highlight significant progress in the scalable manufacturing of carbon-based perovskite PV modules, and big potential for the large-scale industrial deployment.

Sustainability: CO_2-footprint and resource consumption

The motivation behind the development of every renewable energy generation has been mainly attributed to decreasing green-house-gas emissions (*e.g.* CO_2, CH_4) and preventing the depletion of fossil energy sources. Therefore, even though the CO_2-footprint of the photovoltaics is much lower than that of fossil fuel energy generation, based on global PV installation projections until 2050, the total CO_2-emissions from Si PV manufacturing could have a substantial share on global greenhouse gas emissions. [216] Such projection displays how crucial it is to continuously develop the PV sector, aiming for technologies with lower CO_2 footprint.

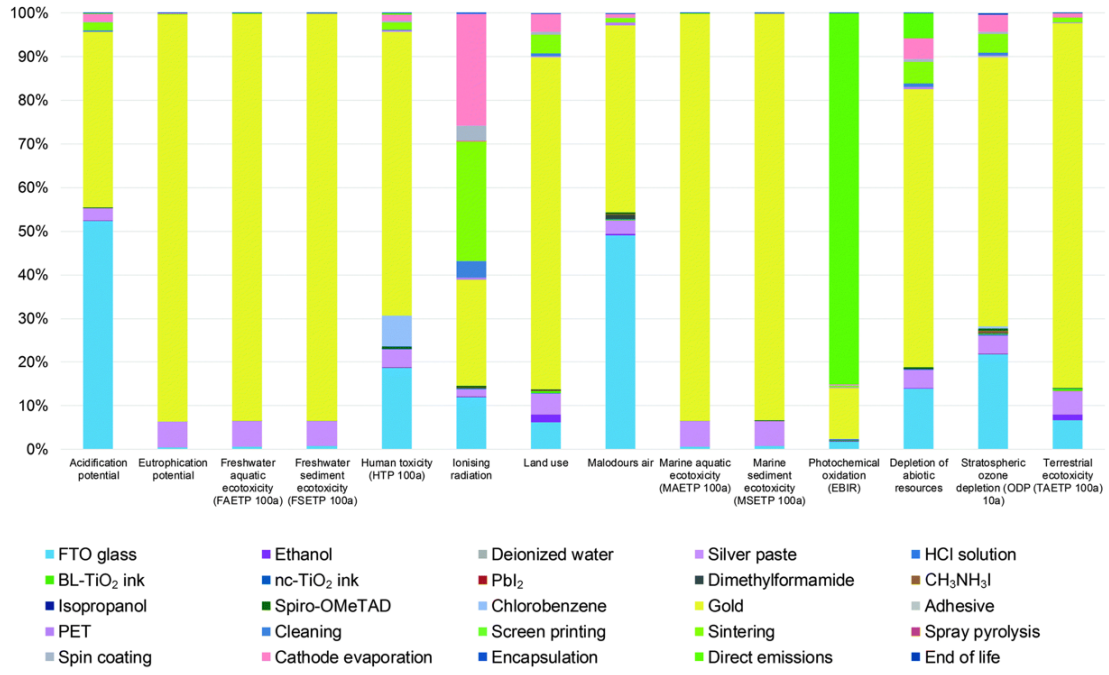


Figure 3.8: Environmental profile of 1 m^2 FTO/c-TiO_2/m-TiO_2/$MAPbI_3$/Spiro-OMeTAD/Au perovskite PV device. Adapted and reproduced with permissions from reference [217].

Soon after perovskite PV emerged as a booming research field, there have been several extensive life-cycle assessments of perovskite solar cells. [217–219] The authors found that among the manufacturing processes of each cell layer, the primary energy consumption of cathode evaporation is the highest and Au has the highest embedded energy – an energy required to extract this material from the ore. More importantly, gold cathode has the highest impact on the environmental profile of the cell (Figure 3.8) and its replacement would greatly reduce the environmental harm during the PSC manufacturing process. Notably, a recent study conducted by our group revealed that CO_2 footprint of some high-temperature carbon-based perovskite modules can be as low as 4.7 % of that of c-Si PV modules. [216] In addition to the scarcity of noble metals, it is strongly suggested that, to minimize the environmental impact of perovskite PV, another type of cathode material that can be deposited with less energy consumption needs to be developed, such as carbon-based electrode.

For a truly sustainable global society, a circular economy needs to be implemented where resources are not lost, but recycled or based on renewable sources. Metals are a group of materials well-suited for recycling. However, their recycling efficiencies are governed by second law of thermodynamics, [220, 221] where the created entropy across the chains of circular economy dictates the inevitable energy losses. Especially for highly technological electronic devices, this implies that fine distributions of different materials such as a hundred nanometers thin metal back electrode of a perovskite solar module inevitably leads to dissipation and thus loss of at least a part of these metals from the circular economy. Graphite, although today mainly extracted from fossil resources, can already be produced from renewable, plant-based resources such as coconut shells and aloe vera. [222]

One step forward to design a less-unsustainable energy technology is consequently the replacement of the metal back electrode by stable, organic matter-based materials like graphite.

High-temperature carbon vs. low-temperature carbon

Carbon electrodes in perovskite solar cells can be prepared through two main routes: high- and low-temperature curing (Figure 3.9). A typical high-temperature carbon-based (HTCB) cell is fabricated by depositing mesoscopic selective and electrode layers, which are usually printable (*e.g.* by screen-printing) and require high-temperature pyrolysis of the organic binders and solvents in them. Therefore, a processing temperature of 400-500°C during layer deposition is needed, [223] meaning that perovskite precursor solution can be only added afterwards. On the other hand, in low-temperature carbon-based (LTCB) cells, the electrode layer is fabricated at temperatures below the irreversible perovskite degradation, allowing for the deposition of perovskite before the back-electrode.

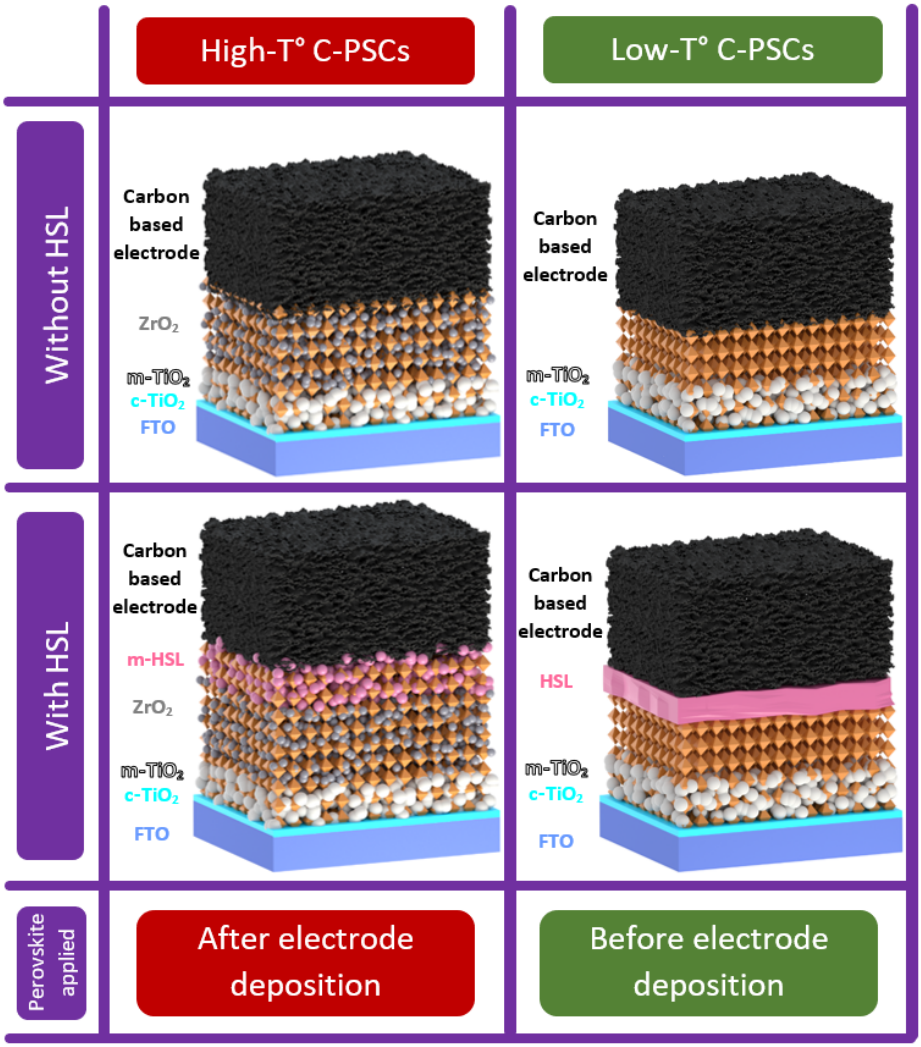


Figure 3.9: Schematics of perovskite solar cells with high- and low-temperature carbon-based electrodes with and without HSL.

Both strategies can be implemented with or without HSL. However, as will be noted later in this work, the LTCB-cells allow for an easier integration of HSL than the high-temperature treated ones.

Cell structures

High temperature carbon-based electrodes

Since the perovskite precursor solution is added after all the cell layers are fabricated, most of them need to be highly porous and no planar configurations can be implemented.

The overall structure of a typical HTCB-cell without a hole-selective layer consists of a front FTO/Glass substrate, a mesoporous inorganic electron-selective layer, an insulating layer and a mesoporous HTCB-electrode. In order to improve the efficiency by avoiding non-radiative recombination at the front-electrode, a compact hole-blocking layer (*e.g.* c-TiO_2) has proven to be essential for reaching high PCEs. Emerging from the dye-sensitized solar cells, anatase mesoporous TiO_2 layer has been the widely used as electron-selective layer not only in the traditional mesoscopic n-i-p cells, [123, 224] but also in HTCB-cells. The insulating layer was found to be crucial, in order to avoid ohmic shunts via contact between the counter electrode and front electrode or ESL. Metal oxides with suitable valence and conduction bands are commonly employed as ESLs and insulating layers in HTCB-cells. Porous dielectric oxide layers of ZrO_2 and Al_2O_3 have been mainly used as insulators, due to their ability to avoid direct shunts and inability to extract charge carriers. [124, 126] Sputtered layers of Al_2O_3 as thin as 10 nm, which can also electrically isolate electrons in conduction band of m-TiO_2 from reaching the back-contact and respective the electrodes against pin-holes to the TCO layer have been demonstrated by us earlier. [225] The latter advantage is particularly useful for the large-area device fabrication, to avoid the shunted regions in the modules. Because of the nature of sputtering process, the inner surface (*i.e.* inside the pores) of the m-TiO_2 is not covered and therefore accessible for electrons extracted from the perovskite.

After the insulator layer is fabricated, the mesoporous cell stack is completed by depositing HTCB-layer and drop-casting the perovskite solution. The concept of fully-printable triple-layer carbon-based (TiO_2/ZrO_2/Carbon) perovskite solar cell (Figure 3.9) has gained wide attention after Mei *et al.* displayed an exceptional stability and strong upscaling potential of such devices. [125] Since then, the development of such HTCB cells has been rapid, resulting in extensive list of reports demonstrating large area devices with moderate efficiencies. In 2018 a company WonderSolar has launched a 110 m^2 PV system based on the triple-layer architecture. [114] Also a double-mesoscopic layer structure was proposed by replacing the thick porous spacer layer with sputtered ultra-thin pseudo-porous Al_2O_3 layer. [225] However, the absence of hole-selective contacts in such PV devices results in excessive surface recombination at the counter electrode and limits the open-circuit voltage of the device. [223] To overcome this issue in HTCB-cells, Xu *et al.* proposed to use a mesoporous NiO_x layer as hole-selective material. [227]

The HTCB-cells with TiO_2/NiO_x/Carbon layers have been found to have a slightly higher PCE than that of the standard triple-layer configuration, but the strong recombination at the TiO_2/NiO_x interface poses a problem for reaching high efficiencies in such devices. [227] In fact, the highest reported PCE of 17.02 % (non-certified) for the HTCB-cell to date was achieved by Liu *et al.* via integration of mixed absorber $Cs_{0.05}(FA_{0.4}MA_{0.6})_{0.95}Pb_{2.8}Br_{0.2}$ into TiO_2/Al_2O_3/NiO_x/Carbon structure (mesoscopic cell with HSL, as well as *JV*- and EQE measurements are

shown in Figure 3.10). [226] Although, the V_{OC} in these cases was still below 1.01 V, highlighting that the implementation of NiO_x (as a mesoporous or thin layer) into the CPSCs is still an ongoing research topic. Apparently, there is still large room to further improve of the efficiencies of these devices, however, it is limited by the compatibility of HSLs with the sintering process of such mesoscopic structures under high temperatures.

Low temperature carbon-based electrodes

The most common architecture of cells with LTCB-electrode consist of the n-i-p structure, where n-region is usually m-TiO_2 [124] or SnO_x [204] and FTO is implemented as a front-electrode. PSCs with carbon-based back electrode cured at low temperatures can consist of the same functional layers as the traditionally (layer-by-layer deposited) processed cells, where LTCB-layer is used to directly replace the metal-based back electrode. Here, the carbon-electrode can be cured at temperatures lower than hybrid perovskite decomposition temperatures. Thus, it allows for an easier integration of perovskite into the layer stack without the need of infiltrating the precursor solution through a carbon-based electrode and a spacer layer (*e.g.* ZrO_2, Al_2O_3) between the back electrode and ESL, unlike in

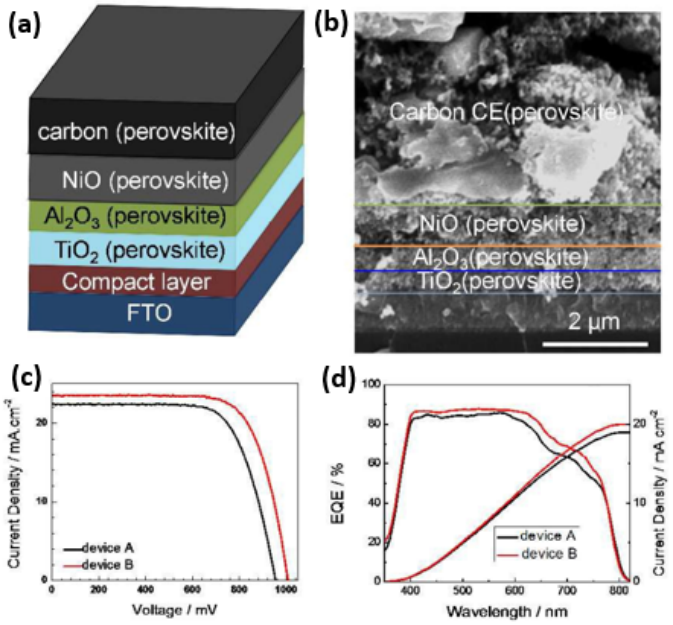


Figure 3.10: (a) Schematic cell architecture of the HTCB-cell with highest PCE reported to date. (b) Cross-section SEM image of the device. (c) *IV*-curves of the devices with such architecture, including different absorbers: device A - $FA_{0.4}MA_{0.6}PbI_{2.8}Br_{0.2}$, device B - $Cs_{0.05}(FA_{0.4}MA_{0.6})_{0.95}PbI_{2.8}Br_{0.2}$. (d) External quantum efficiency and integrated current density of devices A and B. Adapted and reproduced with permission from reference [226].

HTCB-cells. Such properties allow to produce not only mesoscopic LTCB-cells, but also planar ones. [204] Generally, we can distinguish between two types of such PSC architectures that are reported to date: with and without HSLs.

After the deposition of hole-blocking layer and ESL, the perovskite photoabsorber layer is deposited straight away. [124] In contrast to high-temperature processed cells, here perovskite can have large crystals, that are not constrained by the pore size as in triple-layer porous structure. Also, it provides a wide range of opportunities for solvent engineering and crystallization control techniques that are often challenging in the cells with HTCB-electrode. [124] When the perovskite layer is crystallized, carbon layer completes the HSL-free cell architecture, followed by mild annealing (in most cases <120°C).

In the cells where the hole-selective layer is present it can be added either as a dense film between perovskite and carbon (before electrode deposition) or it can be added directly to the LTCB-paste prior to paste manufacturing process. [228] In the latter case, the HSL is formed directly at the perovskite/carbon interface upon curing process of the electrode.

Key advantages of the low-temperature processed electrodes

The low-temperature CPSC concept has several important advantages depicted in Figure 3.11 in comparison to the high-temperature one, such as ability to *easily integrate a planar hole-(or electron-) selective layer*, *a higher control over the perovskite crystallization*, compatibility with *flexible substrate* and *higher processing speed*, without requiring high-temperature sintering.

Easier integration of HSLs

The LTCB-cells with a hole-selective layer represent a promising route towards higher efficiencies for CPSCs due to a potentially improved hole-extraction rate and lower non-radiative recombination at the perovskite/carbon interface, which should be prevented by hindering electrons from reaching the carbon surface. Therefore, the main requirements for every HSLs is to block the electrons from reaching this contact and to allow a fast hole-transport.

In state-of-the-art PSCs, the organic HSLs with suitable valence bands are implemented, although, the drawback of this strategy is the layer stability. As mentioned before, there are few choices of materials which do not have a hygroscopic nature, do not degrade perovskite and meet the demands of high hole mobility and suitable valence band. Nevertheless, a lot of research in the past years was focused on improving the cell efficiency by introduction of HSLs described below.

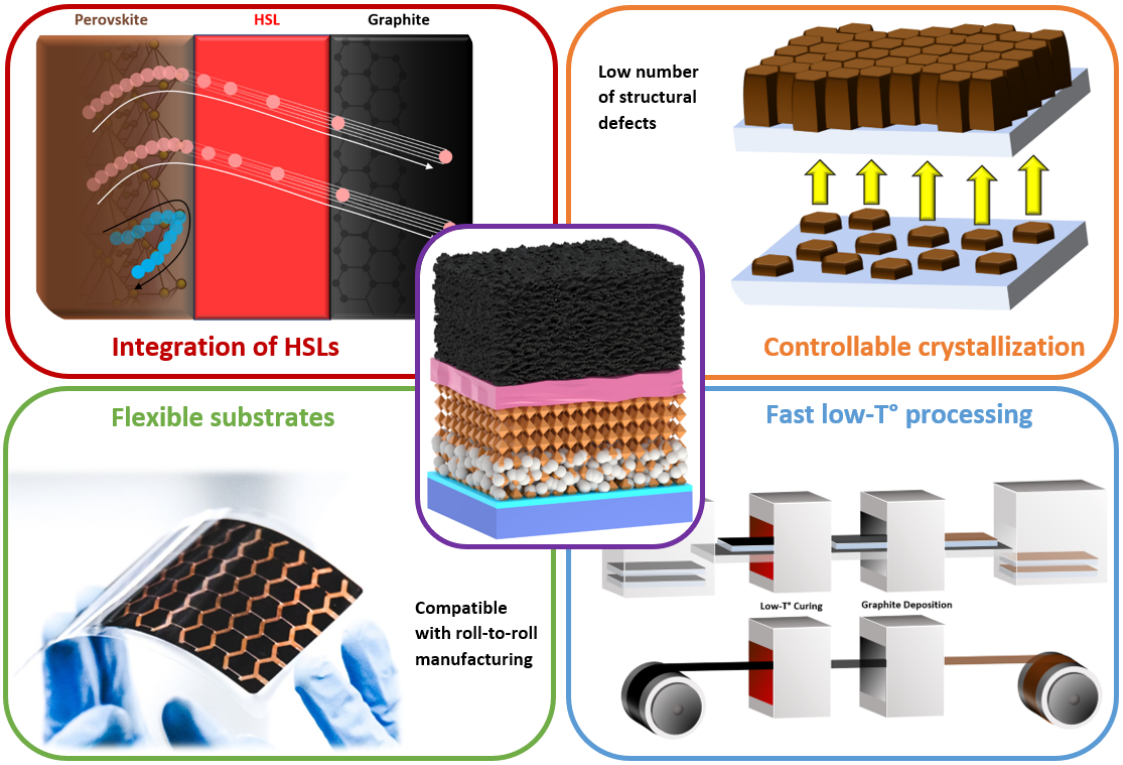


Figure 3.11: Key advantages of the low-temperature carbon-based concept: 1) ability to integrate various planar HSLs (or ESL in p-i-n configuration) into the cell stack, 2) better control over the crystallization in planar perovskite films, 3) processability of carbon-based module on flexible polymeric substrates (reproduced with permission. Copyright 2020, Saule Technologies), 4) faster processing at lower temperatures due to faster solvent evaporation and binder removal

According to a recent report from Ren *et al.*, a layer of fluorinated small molecules based on difluorobenzene, benzo[1,2- b:4,5-b']dithiophene (BDT) and 4,4-dimethoxydiphenylamine (DPA) – BDT2FMeDPA can be used as a dopant-free hydrophobic HSL. In particular, the authors have deposited this novel HSL in between perovskite and LTCB-electrode achieving PCE of 14.5 %, keeping 90 % of the initial value after 30 days. [229] As an alternative HSL with improved thermal stability, hole mobility, valence band alignment and cost-effectiveness, a 5,10,15-triphenyl-5H-diindolo[3,2-a:3',2'c]carbazole (TBDI) was proposed. [230] Implementation of this layer resulted in reduction of perovskite/carbon interface energy barrier, comparable PCE with cells containing spiro-OMeTAD and a much higher stability. Deposition of PEDOT:PSS in cells with LTCB-electrode appears to improve this contact, thereby decreasing the hysteresis. [231]

Integration of copper phthalocyanine (CuPc) nanorods as HSL in the LTCB-cell (Figure 3.12a) yielded a similar hole-extraction ability to spiro-OMeTAD and

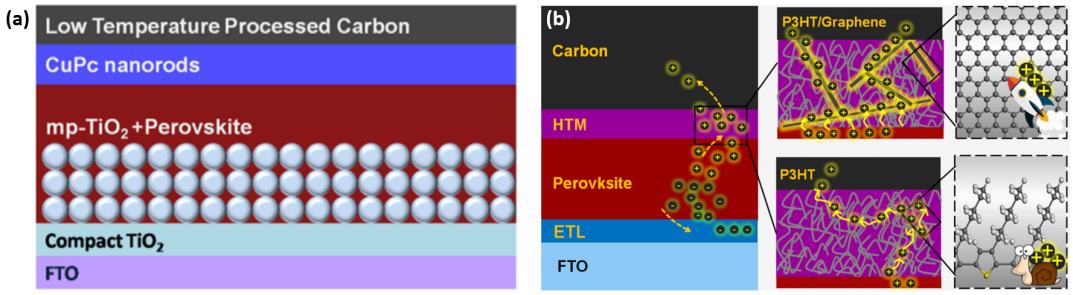


Figure 3.12: (a) Schematic structure of the LTCB-cell with CuPc nanorods as HSL. (b) Schematic structure of the LTCB-cell with P3HT as HSL(HTM), illustrating how incorporation of graphene results in higher hole mobility and better charge transport. Adapted and reproduced with permission from references [232, 236].

decreased charge carrier recombination at the back electrode, resulting in an impressive PCE of 16.1 %. [232] A commonly used electron-donor layer in organic PV – poly(3-hexyl thiophene) (P3HT), has also been employed as an HSL, not only in standard PSCs, but also in LTCB-cells. [233–235] By adding graphene to the pristine P3HT (Figure 3.12b), Chu *et al.* were able to enhance the hole mobility of the HSL by almost two orders of magnitude. [236] With the help of this composite P3HT/Graphene layer, the authors reported an outstanding certified efficiency of LTCB-cell, which is the highest at the moment for CPSCs – 17.8 %. Another inorganic HSL that has been often exploited in perovskite and dye-sensitized solar cells, CuSCN, has been implemented by Baranwal *et al.* to enhance the FF and slightly improve the V_{OC} of LTCB-cells. [201] However, it was found that over long time, degradation at CuSCN/perovskite interface occurs, mediated by the loss of SCN group, leading to an interdiffusion between perovskite and HSL. A similar result on poor long-term stability of pristine CuSCN/perovskite interface was also noted by Arora *et al.* [189]

Several studies have highlighted the enhanced hole-extraction and reduced recombination at the back electrode of HTCB-cells by addition of mesoporous NiOx into the cell stack. [226, 227, 237, 238] Peiris *et al.* have demonstrated how LTCB-electrode can be applied on top of a fully-printed m-TiO_2/ZrO_2/NiOx stack with minimized perovskite capping layer via N_2 blow drying. [239] Although, planar NiOx, which are often used in p-i-n and n-i-p PSCs with metal electrode can also be implemented in LTCB-cells, there were no reports of such cell configuration, according to our knowledge.

Higher control over perovskite crystallization

In HSL-free carbon-based PSCs, perovskite not only acts as light absorber to generate electron and hole pairs under illumination, but it is also responsible for hole-

transport to the cathode. Therefore, the quality of the perovskite layer is critical in order to achieve efficient charge transportation and reduced recombination for highly efficient perovskite solar cell devices. However, an important difference between perovskite crystallization kinetics in HTCB-cells with highly porous layers and LTCB-cells are the interface-energetics and crystallization constraints. Since porous layers provide multiple nucleation sites, the crystallization is highly heterogeneous. In addition, the pores confine the crystals during the perovskite formation, resulting in additional pressure exerted on a crystal which normally does not occur in planar cells. [12] Moreover, the evaporation of solvent, driving the crystallization, also occurs at different rates in HTCB- and LTCB-cells due to different diffusion paths. Considering that multiple advanced crystallization control mechanisms were developed for traditional cells with metal-based electrode, the same methods can be easily implemented for planar cells with LTCB-electrode, but not for HTCB-cells.

An example of carefully controlled crystallization in LTCB-cells was given by Chen *et al.*, who obtained an outstanding result of 14.38 % PCE with a V_{OC} above 1 V on 0.07 cm^2 active area and 10 % PCE on 1 cm^2 devices. [240] The high-quality perovskite film was obtained via 2-step approach, where the solvent of MAI in the second step was changed from isopropanol (IPA) to a mixed solvent of IPA/Cyclohexane (CYHEX) (Figure 3.13). This mixed-solvent strategy has been proved not only to accelerate the conversion of PbI_2 to $MAPbI_3$, but also to effectively suppress the Ostwald ripening process, which eventually provided a pure high-quality perovskite layer with a uniform surface and compact capping layer structure. [240] The similar method of solvent engineering was realized later by the same group to deposit a more thermally stable $MAPbBr_3$ perovskite through the addition of non-polar CY-

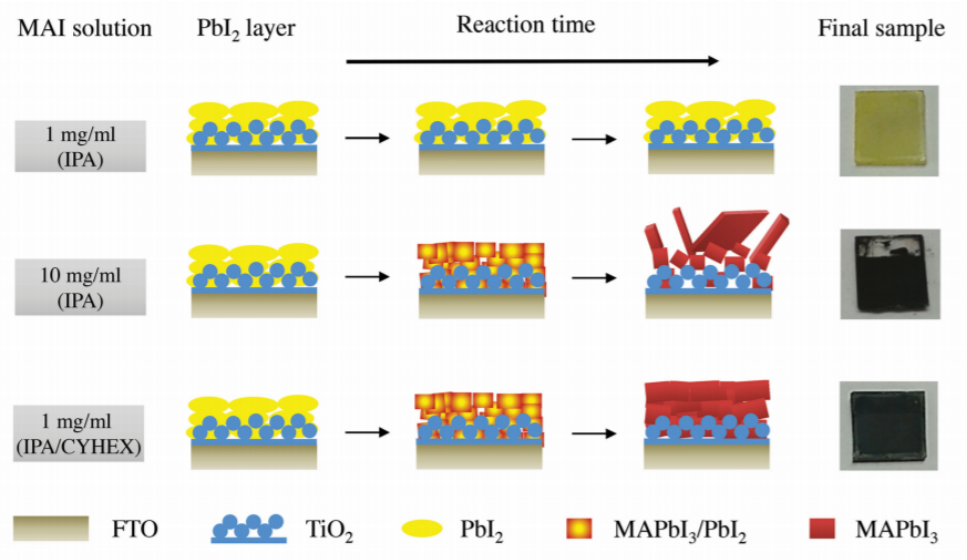


Figure 3.13: Illustration of crystallization dynamics where MAI in IPA and augmented IPA/CYHEX mixed solvents are added to the PbI_2 layer. Adapted and reproduced with permission from reference [240].

HEX into the second step solvent of IPA, leading to a LTCB-cell with a PCE of 8.09 %. [241] In addition, the perovskite composition with a mixed cation of methylammonium (MA) and formamidinium (FA) has been explored by Bai *et al.* in order to enhance the light harvesting capability. The synthesized cubic: column composite structure of $(FA)_x(MA)_{1-x}PbI_3$ has demonstrated to broaden the light harvesting area and reducing probability of the electron recombination. [242]

Furthermore, in 2016, Chang *et al.* have implemented a colloidal engineering approach, where the authors control the crystallization via formation of PbI_2(DMSO)-adducts dispersed in DMF (Figure 3.14). [243] The resulting film shows an impressive perovskite layer homogeneity, leading to a better interfacial contact at perovskite/carbon interface. The renowned anti-solvent engineering techniques, which are widely used nowadays to prepare high-quality dense perovskite crystals, [12] have also been realized in LTCB-cells, by adding chlorobenzene during the precursor deposition process. [244] Zhou *et al.* have demonstrated how the incorporation of amino-group functionalized ionic liquid to the precursor solution, yields highly crystalline perovskite with large grains and hydrophobic surface, promoting even higher stability in HSL-free LTCB-cells. [245] As can be seen from multiple reports on the topic, the mixed-cation, mixed halide hybrid perovskite films with high crystallinity can be easily manufactured in LTCB-cells, [204, 205, 236, 246] since the processing conditions are identical to conventional cells with metallic electrodes, which provides a strong foundation for CPSCs reaching high PCEs. CPSCs with inorganic $CsPbBr_3$ perovskite, having an LTCB-electrode were reported as well, which had an outstanding stability in humid environment (90-95 % R.H.) for over 3 months, in addition to stable performance even under harsh temperature conditions (100°C to -22°C). [247] By introducing small amounts of Sn into the perovskite structure, Liang

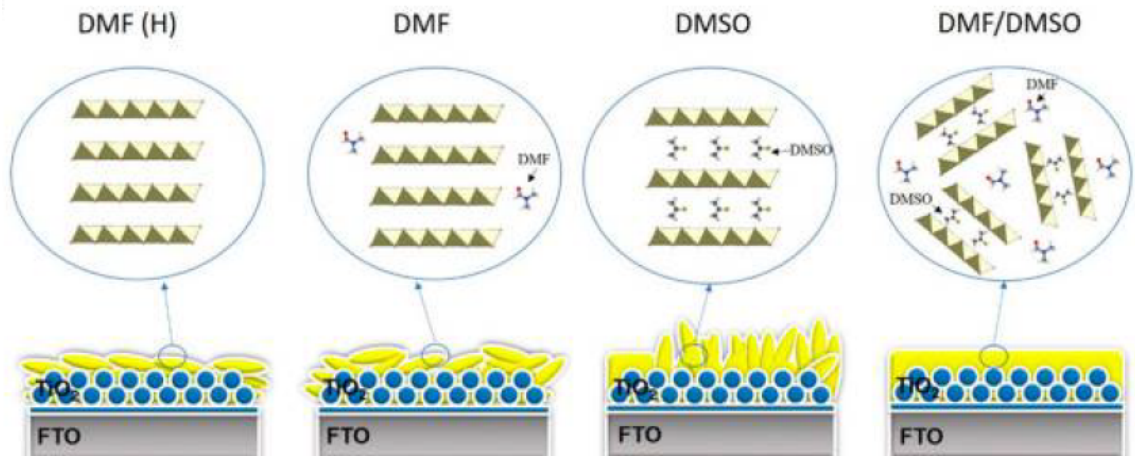


Figure 3.14: Illustration of role of DMF and DMSO solvents in the crystallization and how PbI_2(DMSO) adducts dispersed in DMF, yield the superior film morphology. Adapted and reproduced with permissions from reference [243].

et al. fabricated mixed $CsPb_{0.9}Sn_{0.1}IBr_2$ all-inorganic perovskite solar cell, covered with LTCB-electrode, which exhibited an impressive PCE of 11.33 %. [248] LTCB-cells with Mn-doped all-inorganic perovskite absorber have also been reported, displaying a moderate stability, thanks to the inorganic nature of perovskite and stable LTCB-electrodes. [249] In addition to all these crystallization-controlling techniques, which were already applied in LTCB-cells, many more effective methods coming from traditional PSCs with metal electrodes can be implemented. We also note that passivation and interface engineering that plays crucial role in enhancing the PCE and stability can also be easily realized in cells with LTCB-electrodes, as was recently demonstrated by Di Carlo *et al.* [250]

Compatible with flexible substrates

In most of the perovskite solar cells produced today, glass is used as a cell substrate, which is coated with conducting oxide layer. However, they can also be manufactured on flexible polymeric substrates, which provide several benefits, such as light device weight, while maintaining comparable power output, high mechanical flexibility, compatibility with roll-to-roll processing and low-cost manufacturing. Unfortunately, thermal stability of such substrates remains one major concern for the fabrication at higher temperatures. Ordinary plastic substrates, especially the transparent ones like polyethylene terephthalate (PET), polyimide (Kapton^{TM}), polyethylene naphthalate (PEN) can only withstand temperatures up to 200°C. [251] This drawback highlights that carbon-based electrodes in such flexible PSCs can only be deposited using low-temperature carbon pastes, giving it unique advantage over HTCB-cells.

Using this advantage of low-temperature processing, Zhou *et al.* have applied this layer on a flexible substrate showing a potential of producing flexible PSCs with a hydrophobic carbon-based electrode. [198] In manufacturing flexible PSCs, mechanical integrity after multiple bending cycles is an important consideration. Wang *et al.* have tested the durability of their LTCB-cell and showed that it could keep 70 % of its initial PCE even after 1,000 bending cycles (Figure 3.15). [231]

To date, there are few published works of carbon-based PSC on flexible substrates. Chu *et al.* fabricated LTCB-cell (n-i-p configuration) with graphene-doped P3HT as the HTL. [236] The devices on PEN foil delivered an efficiency of 12.4 % with only 3 % drop after storage in ambient conditions (humidity: ca. 50 %) for 1,680 h. Recently, Babu *et al.* demonstrated carbon-based flexible perovskite solar cells in p-i-n configuration on PET foil. [252] The devices with an active area of 1 cm^2 delivered an efficiency of 15.18 % and excellent operational (MPPT) and thermal (85°C) stability over 1,000 h of ageing. In one of the studies by integrating copper phthalocyanine (CuPc) as an interface modifier and dopant, He *et al.* demonstrated a LTCB module with an active area of 22.4 cm^2. The module retained 75 % of its initial PCE of 6 % after 2000 bending cycles. [228]

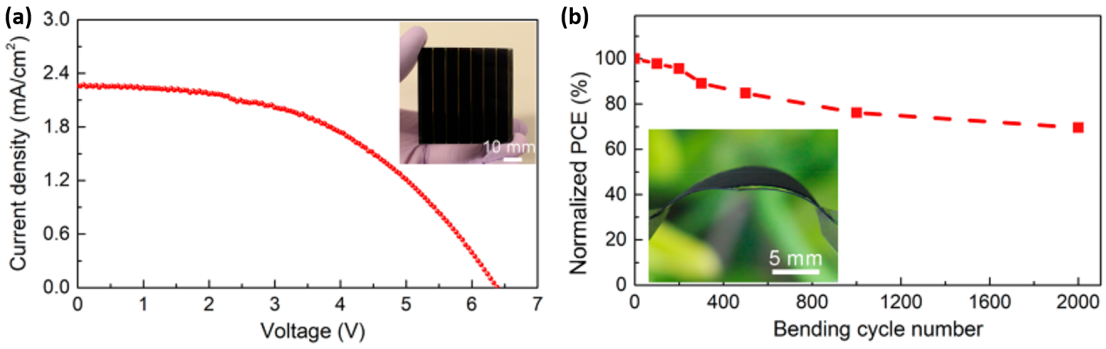


Figure 3.15: (a) *JV*-curve of the as-prepared flexible 5x5 cm^2 LTCB-minimodule. (b) PCE change of the LTCB-minimodule after multiple bending cycles (photograph of the minimodule in bent state is shown in the inset). Adapted and reproduced with permissions from reference [228].

One of the key problems of flexible PSCs is the use of expensive conductive metal oxides, such as ITO, which significantly hinders the full commercialization potential. In other thin-film technologies, the front-contact materials such as Al-doped zinc oxide (AZO) and thin transparent Ag are not chemically compatible with perovskite in the long-term. Therefore, we suggest that cheaper and long-term stable alternatives (*e.g.* using titanium foil [253] or "wrap-through" concept [254]) for transparent front-contact are essential for the development of flexible PSCs.

Fast processing

Sintering high-temperature carbon-paste normally adds a considerable additional time during cell/module processing, although it could be alleviated by such techniques as heating up the glass substrates via near-infrared processing. [255] Regardless of the sintering method, the low-temperature carbon paste is annealed at much lower temperatures, which reduces the energy consumption and processing speed, positively affecting the potential for upscalability in terms of higher throughput. [201] Dou *et al.* have demonstrated 19.6 % efficient flexible PSCs manufactured by roll-to-roll fabrication, which significantly reduces the processing time, allowing for web-speeds up to 3 m/min. [256] The combination of such high efficiency and high-throughput fabrication process is crucial for having lower PV module costs and levelized cost of electricity. Notably the authors implemented a rapid methylamine-induced liquefaction and re-crystallization process to manufacture perovskite photoabsorber in record short times (< 2 min). As recently demonstrated by Bogachuk *et al.* in this process, methylamine (MA^0) molecules bind with Pb^{2+} and MA^+ forming $PbI_xMA^0{}_{6-x}$ liquefied complex and MA^+-MA^0 dimers, which rapidly rearrange back to $CH_3NH_3PbI_3$ due to high volatility of MA^0. [257] Even higher speeds of 3-

5 m/min on 30 cm wide flexible webs have been reported by Galagan *et al.* by using slot-die coating deposition. [258] Although these publications on roll-to-roll manufacturing have displayed strong up-scalability potential of such PV device, both back-contacts were deposited by evaporation of a noble metal and replacing it with an efficient low-temperature carbon contact would yield an ultimate combination of low-cost, more stable, moderately efficient and more environment-friendly perovskite PV modules.

Low-temperature offers to close the gap between CPSCs and traditional cells

To date, the highest reported open-circuit voltages in HTCB cells are around 1 V, [225, 226, 259, 260] despite tremendous efforts to boost this value closer to the cells with HSL and metallic electrode. On the contrary, the versatility of implementation of LTCB-layer is the most attractive advantage of this approach, as the layer can be simply used to replace the costly metal-based electrodes on top of HSL to improve cell stability at low cost.

As mentioned earlier, the multiple crystallization control and passivation techniques, which were implemented in traditional PSCs, can also be applied here, which can allow growth of high-quality crystals with less grain boundaries as well as less structural and electronic disorder. In addition, implementing selective layers in LTCB-cells with high carrier-mobilities and favorable band alignment will provide much higher PCEs than the standard HTCB-cells can offer. One can notice from Table 1 and Figure 3.16 that since 2018 LTCB-cells went beyond 17 % PCE (with 17.8 % certified PCE), bridging closer to the record-breaking cells with metallic electrodes. Therefore, replacing metal electrodes with more moisture-resistant and chemically stable low-temperature carbon-based electrodes is the most promising route to mitigate the efficiency gap between standard perovskite cells and carbon-based ones.

Low-temperature carbon paste composition

The composition of the carbon paste plays an important role in the device performance and stability of the carbon-based perovskite soar cells. Typically, the composition of carbon paste includes carbon-based materials, organic solvents or/and organic binders in different ratios, which could be deposited by solution processable methods, such as doctor-blading and screen printing. [223] Carbon black, graphite, graphene and carbon nanotubes are commonly used materials for carbon paste. Wei *et al.* have shown that carbon-based electrode composed of pure carbon black particles deposited by "candle soot" method can be employed as the counter electrode for PSCs yielding an impressive PCE of 11.02 %. [261] In order to further improve

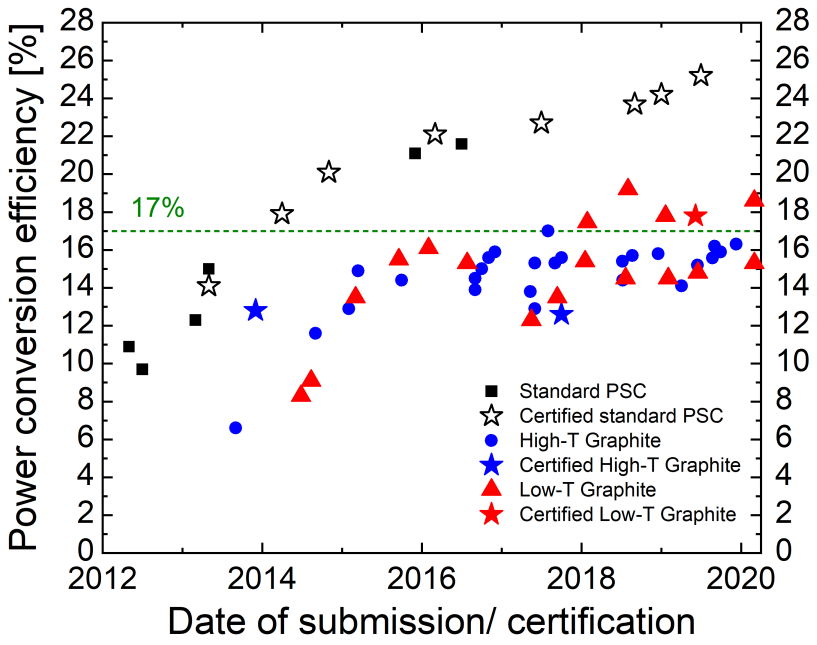


Figure 3.16: Development of reported PCEs of perovskite solar cells over the last years.

the conductivity of the carbon electrode, in further works graphite was introduced to the carbon paste to reduce the resistive losses. High conductivity of graphite is associated with high number of delocalized electrons, meaning that increasing the graphite content in the layer decreases its sheet resistivity. [262] Ku *et al.* have shown how the graphite shape (*e.g.* spheroidal, flaky) affects the photovoltaic properties of the solar cell devices. [122]

To make the resulting electrode more porous, normally carbon black particles are added to the carbon paste, which create space between flakes. [126] The main roles of carbon black particles are to adjust the paste processability and facilitate an efficient interconnection between graphite flakes [263] as well as between perovskite layer and graphite flakes. [264] In order to form a continuous electrode layer, an organic binder such as ethyl cellulose is normally used. [262] Since such binder has to be removed before the introduction of perovskite solution into the cell layers, the carbon-based layer has to be sintered at temperature over 400°C. This introduces a serious obstacle for traditional layer-by-layer deposition method that is predominant in the perovskite community. Therefore, in high temperature carbon-based cells, the perovskite solution is drop-casted on the monolithic cell stack after all the functional layers are manufactured and sintered. This highlights that the porosity of carbon-based electrode (enhanced by carbon black particles) is essential for allowing the complete cell infiltration with solution. Once the cell is impregnated with it, the

annealing removes the solvent, causing the crystallization of perovskite inside the cell stack.

Since low-temperature carbon-based layer, *a priori* does not need to be annealed at high temperatures to remove the binder, it can be deposited on top of perovskite or charge-selective layer directly. The paste in this case can be composed of carbon powder, a moderate solvent and curing resin or a binder that can be annealed at temperatures less than the decomposition temperatures of HSL and perovskite. Zhou *et al.* demonstrated how a simple dispersion of dried carbon powder (obtained from commercial paste) with a small portion of ZrO_2 particles can be dispersed in chlorobenzene to produce a LTCB ink. [198] A similar approach was later implemented by Gholipour *et al.* except for the absence of ZrO_2 particles. [202] Liu *et al.* have produced a LTCB paste using carbon powder, polyvinyl acetate (PVAc) as a binder with a small portion of hydroxypropyl cellulose to adjust the viscosity of carbon paste, which were dispersed in ethyl acetate. [265] Dileep *et al.* implemented carboxy-methylcellulose, which could be used as a low-temperature curable binder. [262] Adding a carbon powder, they were able to get a paste curable at room temperature. Recently, Han's group has successfully developed a LTCB paste, with the help of titanium (IV) isopropoxide and acetic acid acting as low-temperature binder dispersed in terpineol. [266] The peculiar interaction between

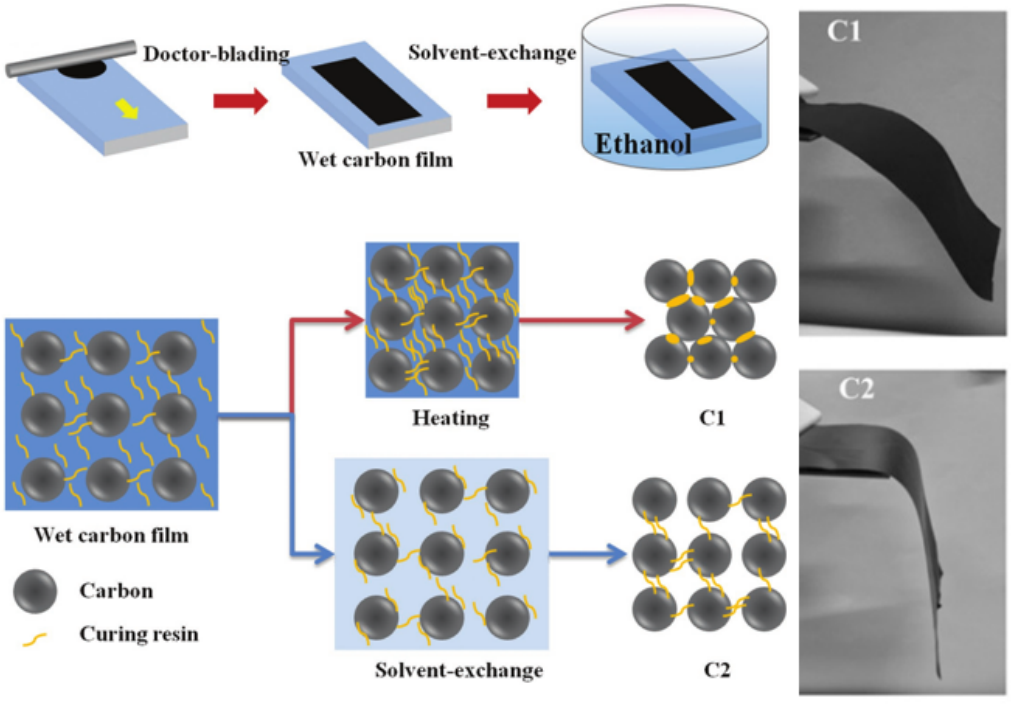


Figure 3.17: Schematic diagram of room-temperature solvent-exchange (C2) LTCB-electrode preparation vs. standard low-temperature annealing method (C1). Photographs of the differences in mechanical flexibility between both preparation methods. Adapted and reproduced with permissions from reference [205].

the binders was attributed to the separation of acetate group from acetic acid and formation of ligands with Ti^{4+} in bidendate and bridging binding modes. The resultant polymeric Ti-O-Ti species encapsulate the graphite and slightly permeate carbon-black particles, producing a strong inter-particle connection, responsible for the layer robustness and conductivity. The resulting LTCB-layer showed an exceptionally low sheet resistance, even lower than that of a HTCB-layer. The same group later demonstrated how such paste can form cracks on top of perovskite layer after deposition, unless an anti-solvent like chlorobenzene is dripped upon the cell. [231] Later the cell can be annealed at 100°C for 20 min to completely evaporate chlorobenzene.

Zhang *et al.* have implemented a solvent-exchange process, shown in Figure 3.17, where ethanol was added to the paste in order to suppress excessive curing to avoid densification of carbon-film. [205] However, since ethanol can partially dissolve perovskite (but not PbI_2), the carbon layer had to be transferred on top of the cell layers by a press-transfer technique using another substrate. A notable perovskite-friendly approach has been proposed by Chu *et al.*, where the authors produced their LTCB-paste based on propylene glycol monomethyl ether acetate (PGMEA) and polyacrylic resin binder and directly applied it on perovskite layer. [260]

This myriad of different LTCB-paste compositions shows that there are a lot of alternative routes to produce highly quality and conductive pastes through composition engineering, giving a large space for researchers in perovskite community to explore.

Deposition methods of low-temperature carbon-based electrodes

The reported deposition techniques of low-temperature carbon-based electrodes, based on liquid processing include: *blade coating, press transfer and screen printing*. Despite high potential of slot-die coating for large area films, there were no perovskite solar devices with slot-die coated LTCB-electrode reported, according to our knowledge. Also, since in the past years most of record-breaking cells were produced using spin-coating and metal evaporation, less attention was given to the aforementioned up-scalable methods. Naturally, this influenced the rate of development of these strategies, which currently lag behind the conventional ones. Although there has been slightly more reports on HTCB-cells and modules, due to strong advantages of LTCB-concept discussed earlier (to reach efficiencies comparable to the ones with metal electrodes), we strongly encourage scientists and engineers in the perovskite community to explore this option.

Blade-coating

Blade-coating (or doctor-blading) is an up-scalable layer deposition technique where solution/paste is dropped on a substrate and then spread by sweeping a blade across the substrate at a fixed height. The resulting thin layer can have comparable heights (controllable by blade height and speed) to spin-coating, allowing for swift solvent evaporation and uniform, dense film deposition. This promising technique has a potential to be implemented for LTCB-manufacturing in ambient environment on a large scale and it is also compatible with roll-to-roll manufacturing.

In the first reports on LTCB-electrode in PSCs, the authors used blade coating to deposit carbon and achieved PCEs of 8-9 %. [198, 230] Over the years, many of the LTCB-electrodes demonstrated in literature are manufactured this way and remarkable power conversion efficiency over 19 % (Table 2) have been achieved in PSCs.

Table 3.2: Summary of PCEs of CPSCs with a low-temperature carbon-based electrodes described in recent reports, with corresponding electrode deposition methods.

Carbon deposition method	Device structure (Perovskite)	PCE (%)	Year	Ref.
Blade-coating	m-TiO_2/PVSK/C ($MAPbI_3$)	9	2015	107
Blade-coating	m-TiO_2/PVSK/TPDI/C ($MAPbI_3$)	15.5	2015	140
Blade-coating	m-TiO_2/PVSK/CuPc/C ($MAPbI_3$)	16.1	2015	142
Blade-coating	m-TiO_2/PVSK/C ($MAPbI_3$)	12.3	2017	181
Blade coating	m-TiO_2/PVSK/C ($MAPbI_3$)	13.5	2018	171
Blade-coating	m-TiO_2.SnO_2/PVSK/CuPc/C ($Cs_{0.05}(MA_{0.17}FA_{0.83})_{0.95}Pb(I_{0.83}Br_{0.17})_3$)	15.4	2018	186
Blade-coating	m-TiO_2/PVSK/BDT2FMeDPA/C ($(FAPbI_3)_{0.85}(MAPbBr_3)_{0.15}$)	14.5	2018	139
Blade-coating	Ni:TiO_2/PVSK/CuPc/C ($Cs_{0.05}(FA_{1-x}MA_x)_{0.95}PbI_{3-x}Br_x$)	17.46	2018	157
Blade-coating	m-TiO_2/PVSK/CuPc/C ($MAPbI_3$)	14.8	2019	138
Blade-coating	Zn:SnO2/PVSK/CuPc/C ($Cs_{0.05}(FA_{1-x}MA_x)_{0.95}PbI_{3-x}Br_x$)	17.8	2019	113
Press-transfer	m-TiO_2/PVSK/spiro-OMeTAD/C ($FA_{1-x}MA_xPbI_{3-x}Br_x$)	19.2	2017	114
Press-transfer	SnO_2/PVSK/spiro-OMeTAD/C/Graphite paper ($Cs_{0.05}(FA_{0.85}MA_{0.15})_{0.95}PbI_{2.55}Br_{0.45}$)	18.6	2019	174
Hot-press	m-TiO_2/PVSK/spiro-OMeTAD/C ($Cs_{0.05}(FA_{1-x}MA_x)_{0.95}PbI_{3-x}Br_x$)	15.3	2016	111
Hot-press	SnO_2/PVSK/CuSCN/C ($Cs_{1-x}(FA_{0.83}MA_{0.17})x\ PbI_{2.53}Br_{0.47}$)	15.3	2020	182
Screen-printing	m-TiO_2/PVSK/C ($MAPbBr_3$)	8.1	2016	152
Screen-printing	m-TiO_2/PVSK/C ($MAPbI_3$)	14.4	2016	151
Screen-printing	m-TiO_2/PVSK/PEDOT:PSS/C ($Cs_{0.05}(FA_{0.83}MA_{0.17})_{0.95}Pb(I_{0.83}Br_{0.17})_3$)	14.5	2019	141
Screen-printing	SnO_2/MOH/PVSK/C ($CsPbIBr_2$)	11.8	2019	187
Ink-jet printing	m-TiO_2/PVSK/C ($MAPbI_3$)	11.6	2014	184
Spraying	SnO_2/PVSK/spiro-OMeTAD/C-carbon black ($Cs_{0.05}(FA_{1-x}MA_x)_{0.95}PbI_{3-x}Br_x$)	14.1	2019	185
	SnO_2/PVSK/spiro-OMeTAD/C-graphite ($Cs_{0.05}(FA_{1-x}MA_x)_{0.95}PbI_{3-x}Br_x$)	9.9		
	SnO_2/PVSK/spiro-OMeTAD/C-graphene ($Cs_{0.05}(FA_{1-x}MA_x)_{0.95}PbI_{3-x}Br_x$)	18.7		

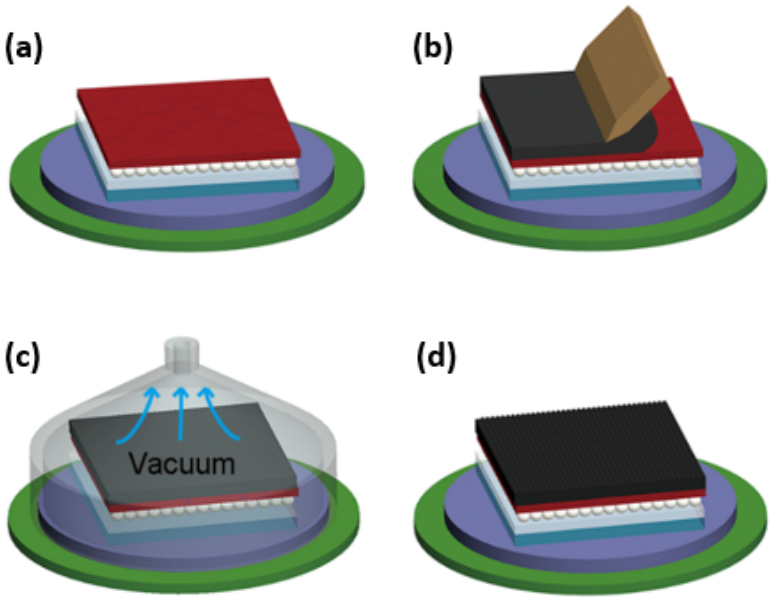


Figure 3.18: Schematic diagram of fabrication process of LTCB-electrode using blade coating and subsequent drying, which can be vacuum-assisted. Adapted and reproduced with permissions from reference [267].

Chu *et al.* have implemented a "fast drying" process (Figure 3.18) to show that a blade-coated carbon paste can be dried by mild annealing at 100°C and exposure to vacuum for a short amount of time. [267] Since the paste is directly applied on the cell layer, it should not contain solvents that can dissolve the layers underneath. The speed and pressure applied on top of the blade play critical role in deposition of homogeneous LTCB-layers with a tight connection to the layers beneath it.

Press-transfer

Due to the often-occurring issue of poor contact between perovskite or HSL to carbon electrode, the cells often have high series resistance at the carbon/perovskite or carbon/HSL interfaces. A press-transfer technique has been praised by being able to partially minimize this problem. Additionally, this technique is well-compatible with fast roll-to-roll production. The first step of this method is deposition of LTCB-layer on a substrate (*e.g.* by blade-coating) followed by subsequent solvent removal. Then, the substrate with carbon-based layer is pressed against the remaining cell layers leading to an improved adhesion and interfacial contact.

As of today, some of the highest efficient PSCs with carbon-based electrode (not only among low-temperature processed ones) have been realized via the press-transfer approach. Zhang *et al.* proposed an impressive approach – to reduce

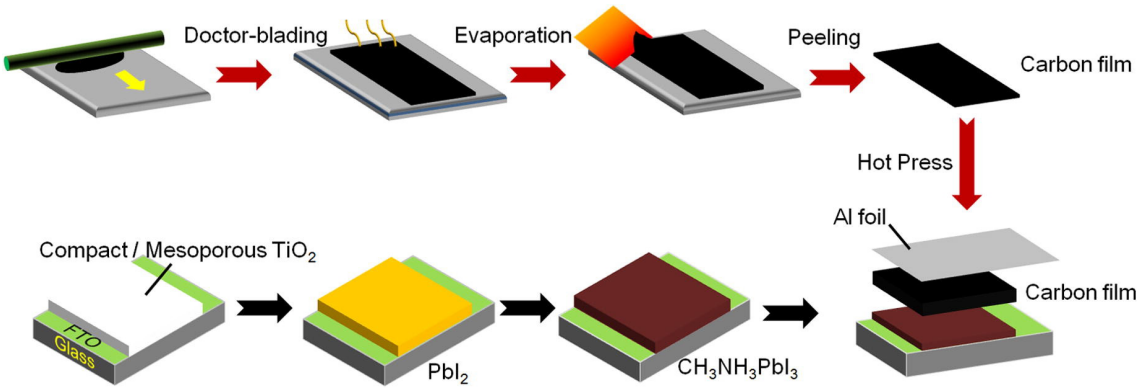


Figure 3.19: Schematic diagram of the LTCB-cell assembly process using hot-press approach. Adapted and reproduced with permission from reference [263].

the number of agglomerated carbon blocks during film curing by a solvent-exchange process instead of a common annealing. After removing a solvent in the paste, the LTCB-layer was deposited on top of the cell stack by press-transfer method. The combination of high film compressibility (thanks to avoidance of carbon-agglomerations) and pressing technique (which improves the interface between carbon and layer underneath) resulted in achieving a record PCE of 19.2 %. [205] Later, the same group has modified their novel deposition method by using a highly conductive transferring substrates in order to successfully implement it on a large area (1 cm^2) device, reaching PCE above 17 %. [268]

The so-called "hot-press" approach (in the context of PSC manufacturing) is a press transfer method carried out at elevated temperatures (Figure 3.19). Interestingly, Yang *et al.* have found how applying higher temperatures during the press-transfer method improves J_{SC}, FF and V_{OC}. [269] Meng *et al.* have demonstrated a cell with coal-based low-temperature processed electrode fabricated by hot-press approach, as an example of an ultralow-cost perovskite solar cell. [270] Using such technique Wei *et al.* reached an impressive 13.5 % PCE on HSL-free cell with a performance drop of only 5 % after 20 days under ambient conditions. [263]

Screen-printing

Same as in the case of most of PSCs with high-temperature carbon-based reported in literature, LTCB-electrode can also be deposited by screen printing. This printing method is based on moving a blade across the screen to fill a fine aperture mesh with a paste and then a squeegee applies a pressure on the screen, while moving backwards. In such way, the pressure applied by the squeegee pushes the ink through the aperture area, which touches the substrate only in the locations corresponding to the aperture area, while rest ink is blocked by stencils. Consequently, the resulting

print area is fully defined by the screen aperture area, whereas its thickness depends on mesh properties and printing parameters. A big advantage of screen-printing technique, in comparison, for instance, to blade-coating, is the ability of precise layer patterning (without the use of masks), at an accuracy which is defined by the screen fineness. Notably, it can also be applicable to roll-to-roll manufacturing.

Other deposition methods

Ink-jet printing technique was demonstrated as a deposition method for fabricating low temperature nanocarbon electrode in HSL-free mesoscopic PSCs. The carbon ink was formulated with the addition of CH_3NH_3I, which allowed *in-situ* transfor-

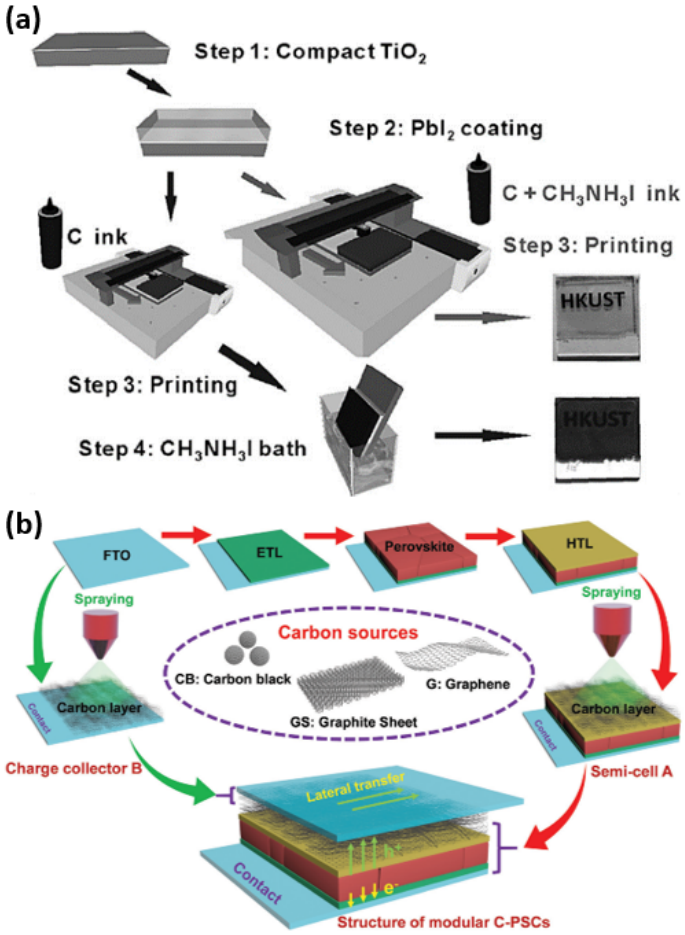


Figure 3.20: (a) Schematic demonstration of the process flow for fabricating perovskite solar cells with ink-jet printed carbon electrode (two alternative routes are shown). (b) Overview of the fabrication process of the LTCB-cells with sprayed carbon electrode. Adapted and reproduced with permissions from references [271, 272].

mation of PbI_2 layer into $CH_3NH_3PbI_3$ perovskite (Figure 3.20a). [271] With this strategy, improved characteristics of perovskite/carbon interface were obtained, reaching 11.60 % efficiency. Furthermore, ink-jet technique allowed to produce precisely controlled patterns of carbon electrode.

In the work of Zhang *et al.*, three commercialized carbon sources (graphene, carbon black, graphite sheet) have been tested as back electrodes in an innovative modular PSC design, where the carbon materials were sprayed upon HTM (Figure 3.20b). [272] Remarkably, the sheet resistance and thickness were dramatically reduced by covering the cell with an additional carbon-coated FTO glass with applied pressure. Among different carbon sources, graphene provided the best performance for a carbon-based PSC with an impressive PCE of 18.65 %. The device performance could maintain 90 % of its initial PCE after ageing at 85°C for 1000 h without encapsulation. Notably, the optimized graphene-based PSCs exhibited excellent structural flexibility with negligible degradation in PCE with multiple re-assembling (detaching the substrate with a half-cell and re-attaching it back) for more than 500 cycles, providing a promise strategy for facile repair and maintenance of PSC through modular interconnections.

Strategies to reach high efficiencies using low-temperature carbon electrode

As demonstrated earlier, the cells with low-temperature carbon-based electrode have already shown superior PCEs to the ones produced by high-temperature method. However, to our knowledge, they still have not surpassed PCE of 20 %. Despite the physical limitations of LTCB-materials for PSCs, we are confident that there are still multiple ways to improve them and bring the power-conversion efficiencies of CPSCs closer to the ones with metal-electrodes. In Figure 3.21 we highlight that the main properties, which need to be optimized in order to close this efficiency gap are *conductivity, charge selectivity and perovskite/carbon contact.*

Increase of conductivity

By definition, metals are materials where the Fermi level of electrons lies within the conduction band of this material. This leaves electrons free to travel through the lattice. Due to highly periodic lattice in noble metals, the mobility of free charge carriers is generally higher than in semiconductors and most of the carbon-based materials.

Graphite particles (which are present in most of the carbon-based electrodes) consist of stacked graphene sheets. [275, 276] It has a hexagonally close packed crystal structure and is a 2D layer of periodically arranged carbon atoms interconnected

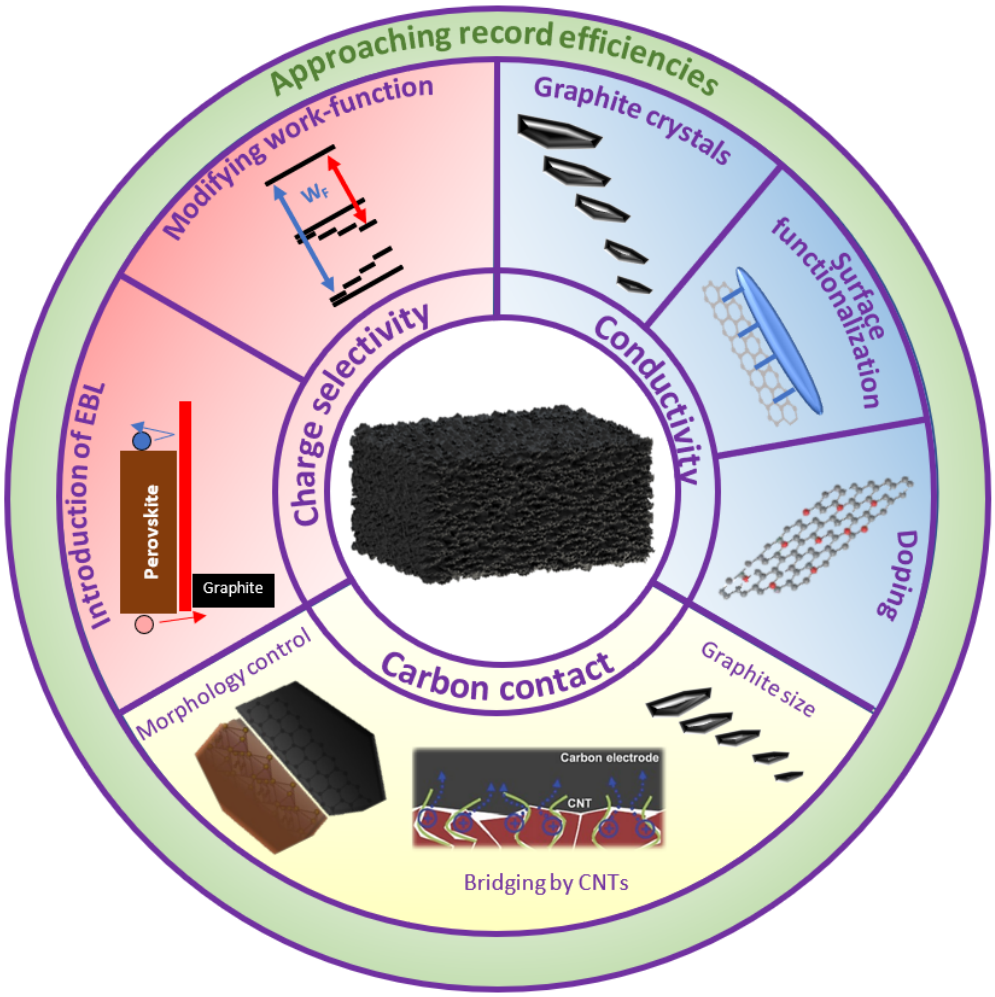


Figure 3.21: Proposed approaches to improve PCE of low-temperature carbon-based cells. Partially adapted and reproduced with permissions from references [273, 274].

by covalent bonds. [277] These graphene sheets can be AB stacked upon each other by weak van der Waals forces to form graphite or can be wrapped into a tube shape, which would form a carbon nanotube (CNT). Graphene is formed by sp^2 hybridization of carbon with neighboring three carbon atoms, while the fourth valence electron ($2p_z$) is delocalized and forms a π-orbital. [276] These delocalized π-electrons have ultra-high mobility along the sheet and are responsible for such low resistivity of graphene, which is even lower than silver. Since graphite consists of stacked graphene sheets it has high conductivity in the direction along the carbon-sheets, but worse conductivity between the sheets, leading to anisotropic electrical nature of graphite. [276] Since carbon-based electrodes in PSCs consist not only of multiple graphite flakes, but also carbon black particles, the layer conductivity is severely decreased. Nevertheless, there were several effective strategies suggested

to enhance this property by *doping, altering graphite size* and *functionalization the carbon surface*.

Increase of conductivity by doping

One of the proposed methods to improve the conductivity of carbon-based layer is to dope the graphite with boron atoms. Duan *et al.* added boron carbide to coke powder prior to the carbonization process (Figure 3.22). After the graphitization, it was mixed together with carbon black in terpineol solution. Introduction of boron atoms was found to decrease the interlayer distance along (002) plane, leading to improved graphitization degree, crystallinity and conductivity (Figure 3.23a). [274] Doping techniques that improve the conductivity of graphene might also be applicable for doping graphite flakes (as in the case of B-doping). Another reports show that sheet resistance can be tuned to $8.41\,\Omega/\mathrm{cm}^2$ and $7.98\,\Omega/\mathrm{cm}^2$ for the B-doped and P-doped carbon layers, respectively, compared to $14.75\,\Omega/\mathrm{cm}^2$ of pure carbon. This improvement subsequently led to an increase in the overall performance of the PSCs, allowing for the PCE to almost double, comparing to the ones obtained with a pure carbon electrode. [278] However, relatively few works in the perovskite research field have been focused on graphite-doping and more on doping of graphene-based electrodes and CNTs.

One of the first studies investigating the increase of CNT conductivity by boron doping on the electrical behavior of CNTs was conducted by Liu *et al.* [279] Moreover, Zheng *et al.* have achieved noticeably higher PCEs through the incorporation of boron doped multi-walled carbon nanotubes (MWCNTs) in their perovskite structure as back contact electrodes. [280] The authors demonstrated that boron doping MWCNTs through thermal annealing allows to increase their work function, carrier concentration and conductivity, enhancing their hole extraction and transport properties and therefore the performance of the PSC, with a PCE improvement from around 10.7 % with undoped MWCNTs to approximately 14.6 % with B-doped MWCNTs with a relatively insignificant hysteresis and an efficiency of over 15.2 % with an added aluminum oxide (Al_2O_3) as an insulating layer.

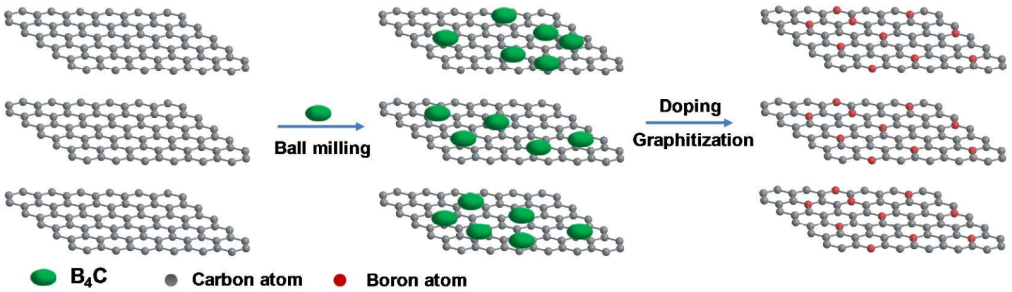


Figure 3.22: Schematic of boron-doped graphite preparation process. Reproduced with permissions from reference [274].

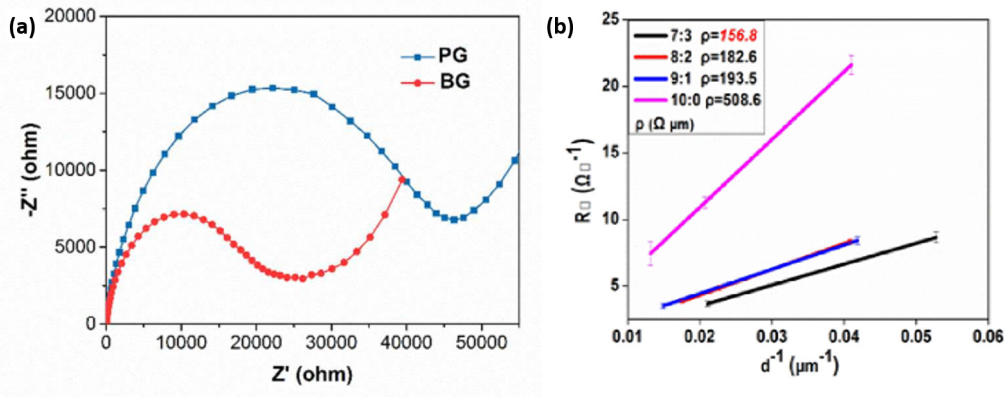


Figure 3.23: (a) Nyquist plots of the PSCs with boron-doped (BG) and boron-free (PG) carbon-based electrodes. (b) Square resistance measurements of LTCB-electrodes with varied graphite to carbon-black ratio (G:CB). Adapted and reproduced with permissions from references [267, 274].

The impact of vapor assisted trifluoromethanesulfonic acid (TFMS) *ex-situ* doping was investigated by Lee *et al.* Such doping was performed through exposing self-standing CNT sheets to TFMS vapor. [281] The authors found that it effectively improved conductivity of CNTs and their performance in PSCs, reaching an outstanding PCE of 17.6 %, with 72 % fill factor. The TFMS-doped CNT-based devices have also shown a better stability compared to undoped devices.

We expect that methods of CNT doping presented above can also be applied to the carbon-based electrodes, in order to decrease the series resistance losses and enhance power conversion efficiency of the PV device.

Increase of conductivity by adjusting graphite size and its portion in the paste

Most of the graphite materials consist of aggregates of smaller graphite crystallites forming a polycrystalline structure. The crystallite size (perpendicular to the basal plane) can vary from few to hundreds of nanometers, depending on the graphite type, which are determined by the carbon precursors and fabrication methods. [282, 283] Larger crystallites, their improved alignment and lower number of structural defects (*e.g.* vacancies, stacking faults, dislocation and disinclinations) will have strong impact on the layer conductivity [276, 283] (as in the case of pyrolytic graphite) and can reduce the series resistance losses in CPSCs.

The graphite particle size has found to play a role in the conductivity of layer, where lower square resistance can be achieved with larger flakes. [284] The size distribution as well as contact area between graphite flakes directly affect the interparticle resistance and represent a critical parameter to consider during

manufacturing process of the carbon-based paste. [266] Notably, the ratio of graphite to carbon-black particles is another factor that requires fine-tuning to reach the highest conductivity of the carbon-based layer. Despite the fact that graphite is more conductive than carbon-black, the latter particles serve as a crucial inter-particle medium for graphite and a significant portion of it is required to obtain highly conductive carbon-based electrodes. [266] Based on the studies from Jones *et al.* [285] and Jiang *et al.* [266] the optimal ratio of graphite to carbon-black was found to be (7:3) as shown in Figure 3.23b, however, reports with various ratios have been shown in literature, [286] which is probably related to the disparity between used graphite and carbon-black powders.

Increase of conductivity by surface functionalization

Surface chemistry can also alter the conducting properties via functional groups at the layer surface, which can cause electron localization, introduction/removal of electron traps and changes in conduction activation energy. Polovina *et al.* have investigated how oxidation of activated carbon cloth by air, nitric acid, hydrogen peroxide and iron-nitrate-crystallohydrates can directly affect the series resistance of carbon-based material. [287] By adding highly conductive antimony-doped tin oxide nanoparticles (ATO) to the carbon precursor prior to carbonization, a carbon/ATO-decorated graphite was demonstrated with exceptionally low sheet resistance. [288] Oxidizing graphite with $(NH_4)_2S_2O_8$ was also found to improve the electrode conductivity. [289] In literature, CNTs functionalized with PEI have displayed an improvement in electrical conductivity and thus enhancement of solar cell PCE. [290] In organic photovoltaics the addition of surface functionalized carbon nanotubes and graphene nanocomposites to the electrodes have proven to improve their performance. [291]

We suggest that further exploration of doping techniques, careful control of graphite particle size and surface functionalization of the carbon-based layer can result in the development of effective strategies to improve the layer conductivity and enhance the FF of cells with low-temperature carbon-based contact.

Improve charge selectivity

As mentioned earlier, the issue of poor hole selectivity in HSL-free perovskite solar cells with a carbon-based electrode has to be solved in order to bridge closer to the high-efficient cells above 20 %. Lack of potential barrier for electrons at the perovskite/carbon interface allows electrons to recombine non-radiatively back contact with holes, resulting in a significant drop of V_{OC}. Therefore, an excellent charge extraction and hole conductivity of the low temperature carbon counter electrode is fundamental to improve device PCE. Many attempts have been made to resolve

this issue either by introduction of an HSL into the cell stack (by adding it to the carbon paste or by depositing a planar layer) or by *increasing the work function of carbon-based electrode*. In addition, *introduction of an electron-blocking layer* on the LTCB-surface can also resolve the issue of electron-hole recombination at the back contact. The main advantage of low-temperature carbon-based electrode is its compatibility with any given structure and versatility of implementation, which makes it an ideal candidate to reach comparable PCEs with record-breaking cells with metal-based electrodes, while maintaining superior stability.

Modifying the work function of carbon-based electrode

Besides the insertion of a hole-selective layer, the LTCB-electrode layer itself could be modified to energetically favor the hole extraction. One can shift the work function of the carbon electrode by modifying its formulation. This method is fundamentally different to integration of HSL, since it changes the electron energy band structure of carbon-based electrode. Additionally, it becomes not prone to degradation mechanisms induced by HSL, while having efficient hole extraction. In fact, simulations by Minemoto and Murata have shown that if the electrode work function is similar to valence band of perovskite, the built-in voltage can be equally high with or without HSL material. [292, 293]

In addition to improving the conductivity, doping (*e.g.* by boron) was found to alter the work-function of the carbon-based layer (Figure 3.24a). [274] Chen *et al.* fabricated a PSC involving boron (B) and phosphorus (P) co-doped carbon electrode through coating the B-atoms onto a hydrothermally P-doped carbon layer. The B/P-doped carbon layer showed an improved work function and electrical conductivity compared to the pristine pure carbon sample. [278] By adding a surface modifying layer to an electrode, it is also possible to alter its surface dipole, which has a direct influence on the material work-function. [294] Another carbon-layer modification by p-doping was demonstrated by Kim *et al.*, where the authors exposed a complete HSL-free cell to C_4F_8 plasma treatment as a post-processing step. They found that such fluorine-based treatment was able to form various C-F_x groups, which in turn increase the work-function of the electrode (Figure 3.24b). [295] Tian *et al.* have proposed a method to increase the work function of carbon-based electrode by augmenting the oxygen content in it (Figure 3.24c-d). [296] The authors attributed the increase in work function to introduction of sp^3 hybridization into the sp^2 conjugated hexagonal lattice during formation of graphite, resulting in an increase of interplanar distance along (002) plane. A similar difference in work-function between pure graphene (4.6 eV) and graphene oxide (4.9 eV) was demonstrated earlier in organic PV cells, making it a promising HTM. [297] Since oxygen is more electronegative than carbon, a creation of surface dipole has been proposed as the underlying reason behind the shift in work-function of graphene oxide. TFMS acid doping of counter electrode CNTs has proved to improve their conductivity as well as tune their work function, from

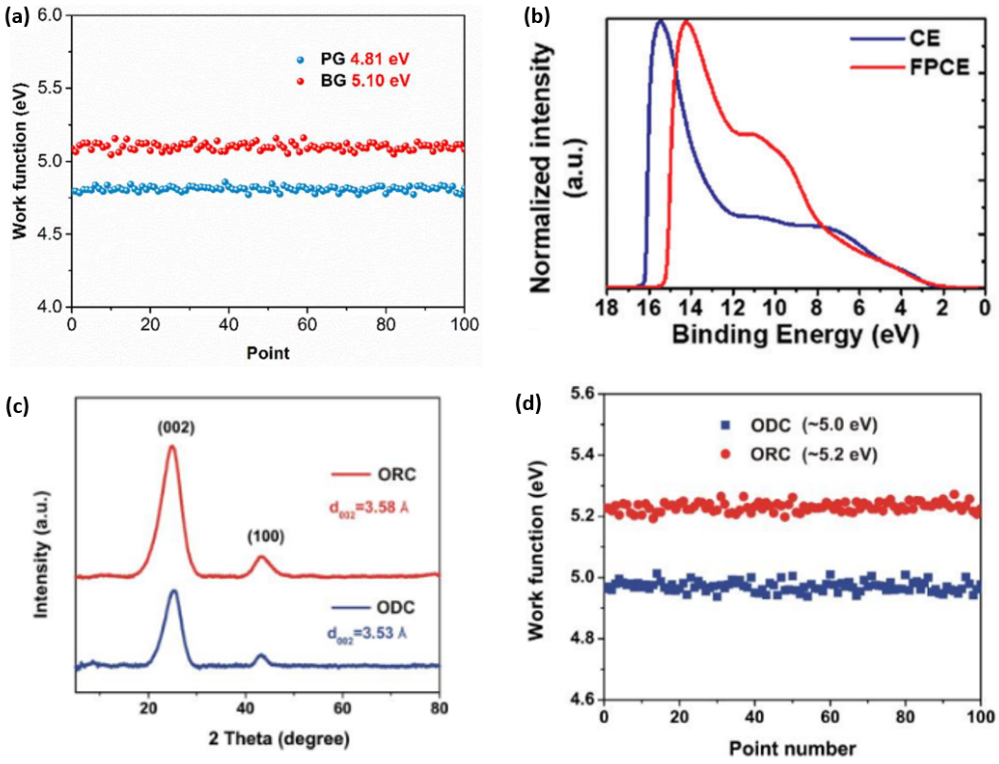


Figure 3.24: (a) Work function curves of the boron-free (PG) and boron-doped (BG) carbon-based electrodes. (b) UPS spectra of standard (CE) and fluorine-plasma treated (FPCE) carbon electrodes, highlighting the higher secondary electron cut-off region and work-function in the fluorine-plasma doped electrode. (c) XRD-patterns and (d) work-function curves of oxygen-deficient (ODC) and oxygen-rich (ORC) carbon electrodes. Adapted and reprinted with permissions from references [274, 295, 296].

4.75 eV to 4.96 eV, subsequently enhancing the energy alignment of the cell and V_{OC}. [281]

Li *et al.* have shown that a device with a carbon/graphite/single-walled carbon nanotubes (SWCNTs) counter electrode mixture (Figure 3.25) yielded an improved efficiency of 14.7 % compared to devices employing pristine carbon CE. [298] This was attributed to the higher work function of 4.7 eV measured for carbon/SWCNT layers as well as to the longer interfacial charge recombination lifetime at the perovskite/SWCNT-carbon electrode interface.

Another strategy to modify the work function of carbon electrode was demonstrated with a p-type material of high hole mobility blended into the carbon formulation. He *et al.* used copper phtalocyanine (CuPc) addition to change carbon bulk properties (Figure 3.26a). [228] The work function measured by ultraviolet photoelectron spectroscopy increased from 4.03 eV for the unmodified carbon to 4.22 eV for the

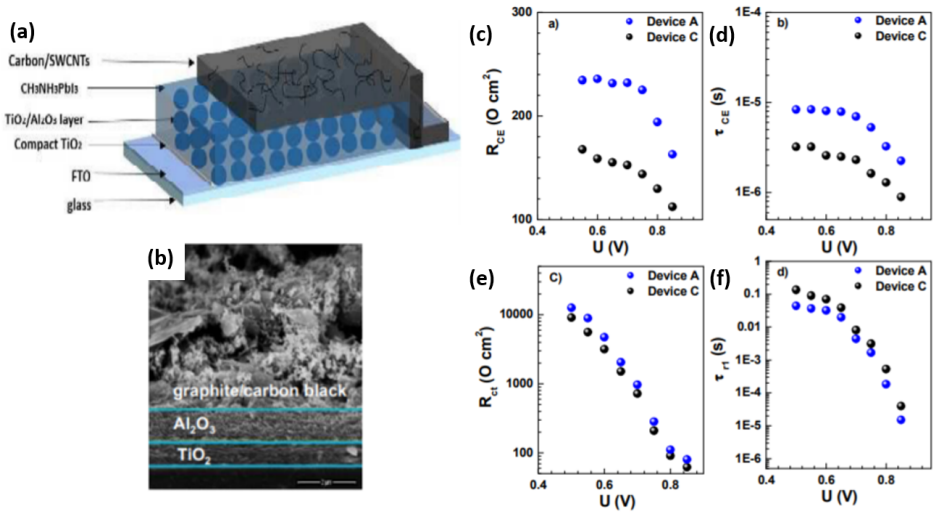


Figure 3.25: (a) Schematic device architecture with SWCNTs integrated into the carbon-based counter electrode. (b) SEM image of the fabricated device. (c) Charge transfer resistance, (d) charge lifetime at the carbon-based counter electrode (CE), (e) interfacial recombination resistance, (f) charge lifetime at the interface between perovskite and carbon-based electrode as a function of applied bias. Adapted and reprinted with permission from reference [298].

paste blended with 1 wt.% of CuPc (Figure 3.26b). Upward shift of the electrode work function resulted in a better hole extraction and overall PCE improvement, from 11.4 % to 14.8 %. The cells were fabricated in an HSL-free perovskite solar cell architecture (structure: FTO/TiO_2/$MAPbI_3$/carbon). Additionally, the authors compared the performance of CuPc-modified carbon devices with the ones where CuPc interlayer was thermally evaporated between perovskite and bare carbon layer. The modification of carbon bulk properties yielded better results than the insertion of CuPc as the HSL.

Hu *et al.* observed that incorporating small amounts of CuS into their LTCB-layer leads to improved hole extraction and reduced recombination at the back electrode. [299] Similar effects were reported for different metal oxides embedded into the high temperature carbon paste. Tungsten oxide (WO_x) nanoparticles were utilized to facilitate a more effective hole collection, which resulted in improved J_{SC}. [300] Jiang *et al.* conducted an extensive research on the metal-oxide modifiers (Co_2O_3, CuO, MoO_3 and NiO) of carbon-based electrode, which increased its work function and improved hole selectivity at the perovskite/carbon interface. [301] Since these metal oxide additives are applicable for the HTCB-pastes, they can also be embedded into the LTCB-formulations.

Most of the reported perovskite solar cells with a carbon-based back contact electrode are fabricated in a "normal" configuration, which means that holes are

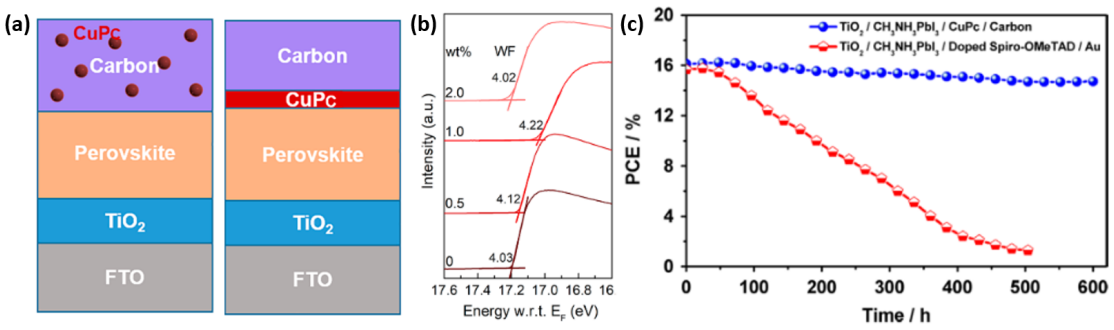


Figure 3.26: (a) Schematics of integrated copper phthalocyanines (CuPc) HSL into the cells stack by embedding it into the carbon paste and by introducing it as a planar interlayer. (b) UPS measurements of different contents of CuPc in the carbon-paste displaying ability to tune the work-function of LTCB-electrode by varying CuPc thickness. (c) Stability tests of perovskite solar cells using CuPc and LTCB-electrode vs. spiro-OMeTAD and Au-cathode. Adapted and reproduced with permissions from references [228, 232].

collected at the carbon layer. The strategy of work function modification could be also extended to the upward shift (lowering work function). This could provide energetic alignment more favorable for electron extraction, and realization of "inverted" perovskite solar cell configurations.

A study conducted by Zhou *et al.* demonstrates that polyethylenimine (PEI) surface modified super-aligned cross stacked CNTs employed as counter electrodes for inverted planar PSCs allow for a better energy level alignment throughout the cell, consequently enhancing the photovoltaic performance of the cell. [290] These improvements were attributed to the impact of the PEI surface modification on the work function of the CNTs which lead to reducing electron accumulation and suppressing interfacial charge recombination.

Introduce electron-blocking layer

Poor contact between two foreign crystal lattices results in more occurring dangling bonds, causing inter-gap energy states at the perovskite surface which serve as recombination centers, lowering quasi-Fermi level. Minimizing the surface recombination at this interface would decrease the need of high electrode work-function and, therefore needs to be pursued as promising strategy to enhance HSL-free PSCs with carbon-based electrode.

One way to reduce the non-radiative recombination in HSL-free cells is to introduce an electron-blocking layer at the carbon electrode surface. A blocking layer

has a slightly different function from charge-selective layer, although they often possess similar physical properties. The main requirement of a charge-blocking layer is not to extract and conduct charges to the respective electrode, but to only effectively block the charge carriers from reaching electrode of the opposite charge, which would otherwise result in higher recombination (*e.g.* hole-blocking c-TiO_2 layer). Therefore, a thin, compact, electron-blocking layer would be enough to significantly reduce surface non-radiative recombination enhancing the V_{OC} of the device.

In a recent work by Liu *et al.*, MABr was deposited on top of $MAPbI_3$ absorber with excess of PbI_2, which predominantly located at the layer surface. [302] The excess of PbI_2 reacting with MABr can form $MAPbI_{3-x}Br_x$ perovskite on top of $MAPbI_3$, resulting in stacking structure. The authors found that due to the upshift of Pb $4f_{7/2}$ and I $3d_{5/2}$ core levels by 0.31 eV, the valence band maximum and conduction bands were both be upshifted in the $MAPbI_{3-x}Br_x$ layer (located at the $MAPbI_3$/graphite interface) by 0.23 eV and 0.25 eV, respectively (Figure 3.27). This intermediate layer facilitates an easier extraction of holes, but more importantly, it forms an energy barrier for excited electrons diffusing towards carbon-based electrode.

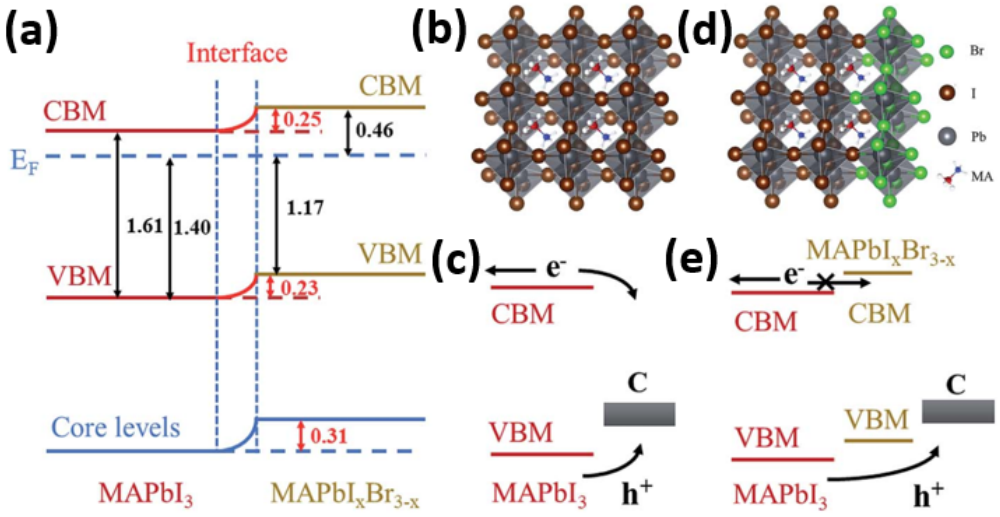


Figure 3.27: (a) Energy level diagram of the stacked $MAPbI_3$/$MAPbI_xBr_{3-x}$ perovskite interface. (b) Crystal structure and (c) charge transfer diagram at the $MAPbI_3$/carbon electrode interface. (d) Crystal structure and (e) charge transfer diagram of the stacked $MAPbI_3$. Adapted and reprinted with permission from reference [302].

Improve contact to perovskite

One of the strong suits of evaporated metal-electrode is homogeneous and dense layer deposition, which facilitates an efficient contact to underlying charge selective layer. However, often the perovskite/carbon interface suffers from low number of interfacial contact sites and poor adhesion, which seriously limit hole extraction and transport in the PV device. [124] Moreover, we believe that the introduction of barriers under the carbon-based electrode, that have been mentioned earlier will facilitate an even longer operational stability of the CPSCs, in comparison to that of devices with metallic contacts.

Liu *et al.* found that the interfacial charge transfer between perovskite and LTCB-layer is highly influenced by the size of graphite particles. [265] Besides conductivity, the graphite size also has influence on the perovskite/carbon contact area, which can be increased by decreasing the particle size (Figure 3.28). [264] Thus, finding a careful balance between a high conductivity and an efficient hole-extraction would be optimal for reaching high PCEs with carbon-based electrodes. A poor contact between perovskite and carbon-based electrode can also lead to larger anion migration towards the interface, which will increase hysteresis. [231] Addition of NiO-modifier also promoted a more intimate contact at this interface and enhanced charge transfer rate. [301]

It is clear, that solvents in the LTCB-pastes play critical role in determining the properties of the final electrode and should be compatible with perovskite and layers underneath the LTCB-layer to form a smooth, intimate interface. [303] In contrast, there were reports that solvents present in the LTCB-paste, which are not fully compatible with the perovskite layer, [303] can lead to significant damage of the perovskite morphology and worsen the interface characteristics. In some cases, LTCB-paste can contain polar solvents (*e.g.* ethyl carbitol acetate or alcohols)

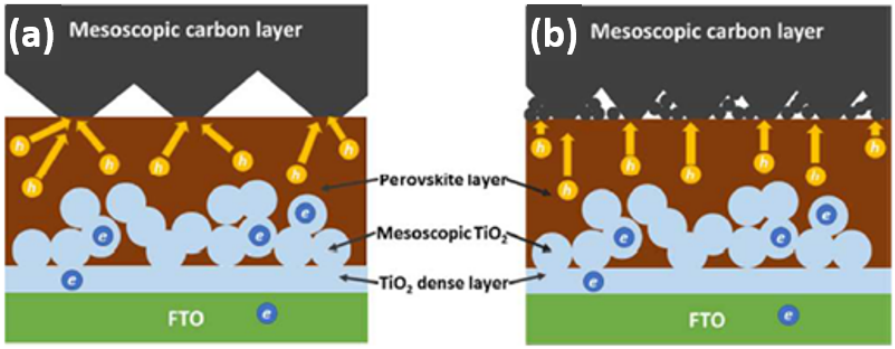


Figure 3.28: Scheme of charge transfer in HTM-free $CH_3NH_3PbI_3/TiO_2$ heterojunction solar cells with carbon electrode, consisting of (a) large and (b) small graphite flakes. Adapted and reprinted with permission from reference [264].

that can dissolve the layers underneath, including perovskite since the paste is directly applied on top of the cell layers. Hence, we advocate for LTCB-pastes with "harmless" solvents preserve dense and uniform morphology, resulting in lower interfacial resistance and higher stability. [260]

Similarly, Chen *et al.* in the work mentioned above, improved the electronic contact at the perovskite/carbon interface by growing smoother perovskite films of higher surface quality. Obtained 14.38 % PCE was a record value for HSL-free carbon-based PSC at that time.

Notably, carbon nanotubes manifest impressive electrical conductivity properties making them an excellent candidate for improving the hole conductivity of the carbon electrode and decreasing interfacial recombination resistance at the carbon/perovskite interface. In addition, many studies on CPSCs have aimed to improve the electrical conductivity as well as enhance the charge selectivity at the perovskite/carbon interface through the incorporation of different additives, the most promising among which are carbon nanotubes. The incorporation of CNTs in perovskite solar cells have demonstrated a noticeable improvement in device performance. [304]

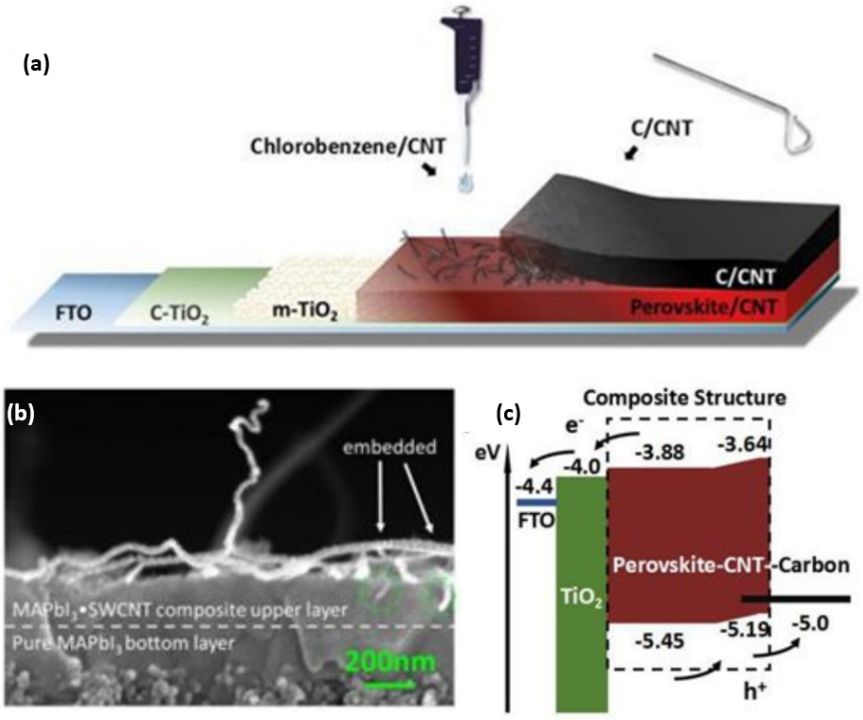


Figure 3.29: (a) LTCB-device architecture with CNTs incorporated into perovskite and electrode. (b) Cross-sectional SEM image and (c) energy band diagram of such device. Adapted and reprinted with permission from reference [273].

For example, Wang *et al.* have opted for a "bridging method", where they incorporated CNTs into both: the perovskite and carbon electrode (Figure 3.29), for the purpose of forming a better interface quality via CNT-bridges between these layers. [273] The cells showed an efficiency of over 15.7 %, with a FF of around 70 %.

An alternative strategy is to incorporate CNTs between the perovskite and carbon electrode layers. Ryu *et al.* introduced a MWCNTs chlorobenzene dispersion into the complete LTCB-cells by a dripping method. [305] The MWCNTs, penetrating both the perovskite absorber and carbon electrode, created a pathway that allowed for a more optimal carrier harvesting and transport properties, achieving a PCE of 13.57 %.

Yet another approach for improved hole selectivity and reduced recombination could be obtained with the perovskite surface modification at the perovskite/carbon interface. Hou *et al.* applied guanidinium chloride into $MAPbI_3$ perovskite precursor solution. [306] The additive passivated trap states in the perovskite layer and reduced recombination rate at the perovskite/carbon interface (mesoscopic architecture, TiO_2/ZrO_2/carbon, infiltrated with perovskite solution). It led to V_{OC} enhancement, from 0.88 V to 1.02 V. Rong *et al.* used ammonium chloride (NH_4Cl) additive in the precursor solution, which also improved optoelectronic quality of $MAPbI_3$ films. [307] Impressive efficiency of 15.6 % was reported for the same mesoscopic, triple-layer scaffold architecture (TiO_2/ZrO_2/carbon).

Liu *et al.* applied cesium acetate (CsAc) treatment after the carbon deposition. [308] They suggested that the acetate salt could penetrate to the buried perovskite surface, modifying its composition, which grants a higher hole selectivity. The CsAc treatment improved the average PCE of HSL-free devices, from 12.6 % to 15.3 %, with a V_{OC} value reaching 1.1 V. Another defect post-healing method was shown with dip-coating pre-fabricated carbon-based mesoscopic PSCs in trioctylphosphine oxide (TOPO) solution. [309] TOPO ligands act as Lewis base, selectively adsorbing onto halide-deficient defects sites at the perovskite surface, reducing non-radiative recombination at the interface with carbon electrode (Figure 3.30). PCE improved after the treatment from 11 % to 12.8 %, primarily due to V_{OC} increase. In another example, Liu at al. applied polydimethylsiloxane (PDMS) encapsulant on carbon-based, HSL-free mesoscopic $MAPbI_3/TiO_2$ heterojunction solar cells. [310] It was demonstrated that PDMS, during its solidification, fills the gaps in the mesoporous carbon film, which significantly improves the perovskite/carbon interface characteristics. The authors demonstrated that charge extraction efficacy was improved and recombination rate got reduced, which resulted in a 54 % enhancement of photovoltaic performance, reaching 10.8 % PCE.

Similarly, different strategies for improving electronic contact and charge selectivity

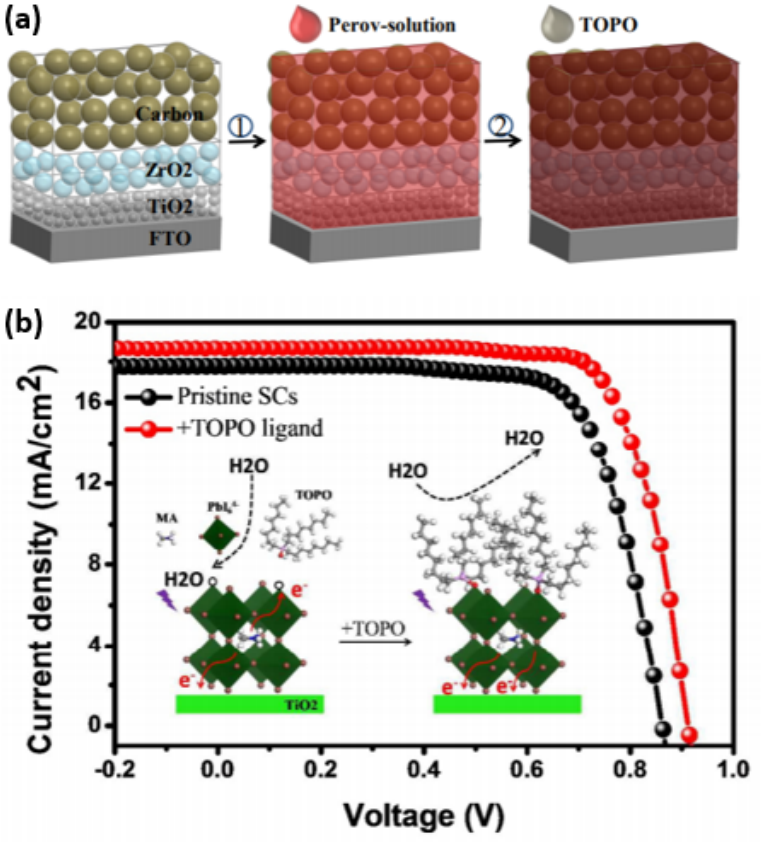


Figure 3.30: (a) Schematic illustration of a mesoscopic perovskite solar cell fabrication process with a TOPO passivation step; (b) JV curves of a TOPO-passivated device and a reference cell, combined with a schematic drawing of the TOPO interaction with perovskite defects. Adapted and reprinted with permission from [309].

at the interface with the carbon electrode were also demonstrated for the inverted perovskite solar cell architecture (p-i-n configuration). Luo *et al.* reported devices utilizing back contact electrode based on transfer-printed carbon nanotubes. [311] In order to improve the efficacy of electron extraction from the perovskite layer, the authors applied SnO_2-coated cross-stacked carbon nanotubes (SnO_2@CSCNT). The SnO_2 coating improved the PCE from 10.7 % to 14.3 %, with significantly reduced hysteresis. Furthermore, flexible PSCs applying SnO_2-modified CNT electrode were demonstrated, reaching 10.5 % efficiency.

Recently, Babu *et al.* demonstrated Cr buffer layer inserted between electron transport layer and carbon electrode as a way to obtain ohmic contact at that interface and efficient charge collection in p-i-n devices. [252] They reported 15.18 % PCE for flexible perovskite solar cell (Figure 3.31) with a large active area of 1 cm^2. Furthermore, Cr interlayer was also applied in n-i-p configuration, inserted between hole transport layer and carbon electrode. It resulted in an improvement

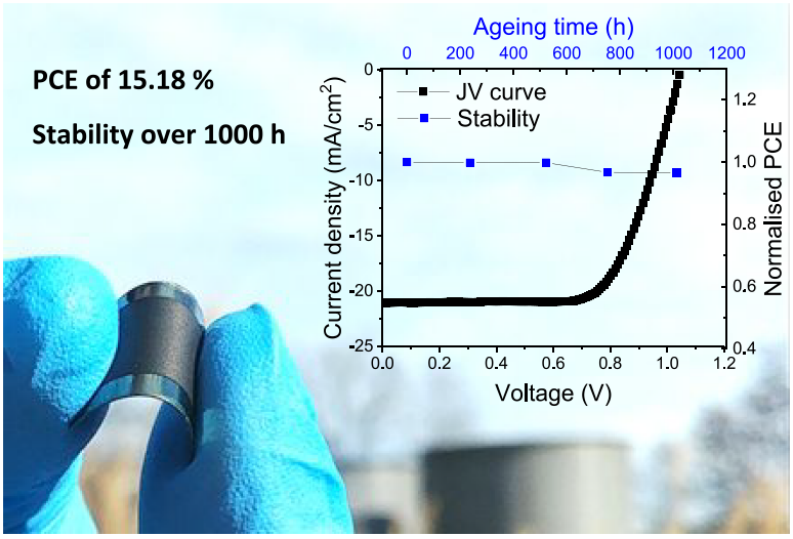


Figure 3.31: *JV*-curve and performance evolution during aging test of a flexible inverted PSC with a carbon back contact electrode. Adapted and reprinted with permission from reference [252].

in fill factor, assigned to improved electronic contact, yielding 12.06 % PCE (flexible PSC, 1 cm^2 active area).

3.5 Conclusion

Summary

Most of the state-of-the-art perovskite solar cells use metal electrodes as a back contact, attempting to bridge cell efficiencies closer to the radiative limits. However, in this review we point out that poor stability of these metallic layers, limited up-scalability potential, high costs and negative environmental impact hinder further development of perovskite PV in the direction of commercialization. Therefore, carbon-based electrodes have been proposed to alleviate these issues and to fulfill the potential of perovskite to become the next generation PV technology. Comparing between high-temperature and low-temperature cured carbon-based layers, the latter ones come along with multiple processing advantages: 1) easier integration of hole-selective layers, owing to the electrode low curing temperature, which is compatible with perovskites and HSLs, 2) possibility to implement advanced crystallization and passivation techniques (in comparison to poorly controlled crystallization after the solution infiltration in CPSCs with high-temperature cured electrodes), 3) applicability to flexible substrates and roll-to-toll manufacturing and 4) shorter processing time. Based on the multiple reports showing PCEs above 17 % (with 17.8 % certified value), we postulate that low-temperature carbon

electrodes can be used to produce high-efficient PSCs, while simultaneously being a more chemically stable, up-scalable, cost-efficient and sustainable alternative to conventional metal contacts.

We summarize different paste formulations present in literature, displaying the effect of various additives, solvents, binders and carbon powder compositions (*e.g.* carbon-black to graphite ratios) on the final film properties. Literature on carbon-based electrodes suggests that they can be deposited by blade-coating, press-transfer, screen-printing methods and even ink-jet printing or spray coating all of which are up-scalable techniques and can be implemented to fabricate large area modules.

Furthermore, we propose effective strategies that have been reported for low-temperature carbon-based electrodes, to improve the layer conductivity, charge selectivity and contact between carbon and the layer underneath: 1)A higher conductivity can be reached by modification of graphite crystals and its portion in the paste, surface functionalization and foreign atom doping. 2) Enhancing charge selectivity is suggested to be improved by modification of the work-function and integration of electron-blocking layers at the perovskite/carbon interface. 3) Finally, a better contact at the carbon surface can be obtained by producing smooth pin-hole free films, introducing carbon-nanotubes to facilitate better interfacial charge transfer and tuning the graphite size.

Perspective

In order to overcome the voltage loss of still 200 mV compared to highest-efficient cells, two conditions have to be fulfilled: non-radiative surface recombination at the back-contact has to be reduced and the valence (for n-i-p cells) or conduction (for p-i-n cells) band of the back-contact have to be match the energy levels of the perovskite absorber, which can be achieved by tuning the carbon-based electrode or by adding a selective layer in between. In this review, different strategies have been proposed: to introduce a HSL as an electron-blocking and hole-conducting layer between perovskite and carbon-based electrode or to modify the work-function of carbon electrode itself.

To increase the photo-current and fill factor of the CPSCs, the efficient extraction of holes from the perovskite to graphite is required, highlighting the necessity to find a method to reach this goal. The low-temperature cured carbon-based layers display clear advantages of higher flexibility in implementing the strategies mentioned above, originating from the capability of LTCB-layer to be applied before or after the perovskite deposition. In particular, this allows for new options for functionalizing the interface at the perovskite/carbon contact. It is not surprising that in the last years PSCs with low-temperature cured electrodes

have already reached higher efficiencies than the ones with high-temperature treated contacts.

Overall, we emphasize that the vast knowledge acquired by the perovskite community on methods to fabricate high-efficient solar cells so far can be readily transferred to low-temperature carbon-based perovskite solar cells, which represents a strong potential to bring perovskite technology closer to the PV market.

3.6 Critical discussion

From this extensive overview on the recent developments and prominent features of low-temperature carbon-based electrodes, it is clear that the PSCs with such contacts contain high potential to reach record PCEs. Concomitantly, these electrodes effectively retard device degradation, thus providing an opportunity to produce highly stable and efficient PSCs. However, several key challenges of CPSCs with low-temperature electrode need to be highlighted:

- From a number of experiments throughout this thesis, it was found that solvents within such low-temperature carbon paste are typically incompatible with many of the currently-employed HTLs and ETLs between carbon and perovskite. In the author's opinion, it is to some extent related to the fact that the most efficient CPSCs with low-temperature carbon electrodes are produced via press-transfer approach, where integration of transport layers with high charge carrier mobilities (*e.g.* doped spiro-OMeTAD) is possible due to removal of initial solvents in the carbon paste. Although this issue has not been discussed in publications, according to the author's assessment, it is a critical hindrance in the development of high-efficient CPSCs with such electrodes. Therefore, the author encourages the perovskite community to investigate the issues related to interaction between the carbon-paste solvents and the charge transport layers underneath.
- Although the press-transfer and hot-press techniques can alleviate the challenge described above, (in the author's opinion) it is debatable if a homogeneous and good physical contact between carbon and the layer underneath can be obtained. Depositing a carbon wet film directly on the cell stack seems to have a much stronger adhesion, providing a more intimate contact (Figure 3.32a) with all the unraveling favorable characteristics such as low interfacial resistance, excellent charge extraction *etc.* Moreover, such contact is expected to also positively affect the device stability. Cells with pressed carbon electrode often exhibit a pronounced gap between the carbon layer and the underlying layer (Figure 3.32b). Therefore, the future research is likely to show whether PV cells and modules with electrodes deposited via such approach are promising.

- While the record PCEs of CPSCs with low-temperature carbon electrodes are higher than that of cells with high-temperature electrodes, no reports demonstrate adequate accelerated ageing tests, comparable to the requirements of the IEC 61215 standard. In contrast, numerous reports have shown that CPSCs with high-temperature electrodes tend to be exceptionally stable under several of these tests (*cf.* chapter 8), suggesting that although their PCE may be lower, their operational stability is still significantly higher than their low-temperature counterparts. Furthermore, the processing temperature of the electrode not only dictates the cell structure, but also whether perovskite crystals would be (partially) filling the mesoporous carbon electrode. Since the high-temperature carbon electrodes are filled with perovskite, it inhibits the diffusion of molecules from the ambient towards perovskite photoabsorber, thus, acting as a sacrificial layer. Due to layer-by-layer processing, CPSCs with low-temperature electrodes do not possess such feature, which might explain their shorter operational lifetime. Although, this is a critical question in understanding the degradation mechanisms of CPSCs, unfortunately, according to the author's knowledge, this hypothesis has not been confirmed with experimental evidence.
- In principle, L-CPSCs are manufactured by up-scalable deposition techniques, making them promising from the industrialization perspective. Nevertheless, according to the author's knowledge there are currently only few reports of perovskite PV modules with LTCB-electrodes, in contrast to multiple reports on modules with HTCB-electrodes. Hence, despite high PCE potential, more PV modules with LTCB-electrodes need to be demonstrated, in order to be able to claim that L-CPSCs are truly up-scalable.

Notably, in this review publication, the author claimed the possibility of large perovskite crystal growth as one of the possible reasons for the higher efficiency of L-CPSCs in comparison to their high-temperature analogues. Even though from a solid-state physics perspective it is true, at the moment of publication of this review, no experimental evidence of this hypothesis was shown in literature. This critical question motivated the author to conduct a study on comparing CPSCs with nearly identical cell structures, with the exception of perovskite photoabsorbing layer: in H-CPSCs it was embedded in ZrO_2, while in L-CPSCs it was deposited as planar film. Therefore, the hypothesis proposed in this chapter was later (experimentally) proven to be correct in the work, described in chapter 5.

Moreover, the author of this contributed to a recently published article on the effectiveness of an electron-blocking layer in L-CPSCs, which suppressed non-radiative recombination at the back contact and boosted the performance from 15.7 % to 18.5 %. [312] The electron-blocking feature was obtained by utilizing a 2D perovskite with shifted CBM, allowing the extraction of holes but blocking electrons from reaching carbon electrode.

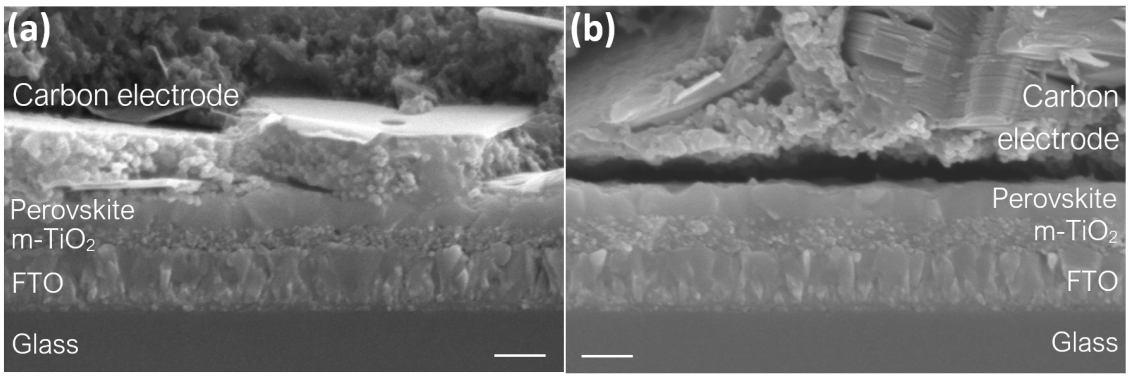


Figure 3.32: SEM images of L-CPSC cross-section with carbon electrode deposited by: (a) blade-coating directly on top of a cell stack and (b) deposited via press-transfer technique, which often results in insufficient physical contact between carbon layer and the perovskite underneath. Scale bar – 500 nm.

After the review discussed in this chapter was published, the PCE of L-CPSCs kept rising and just recently went beyond 20 %, [313, 314] achieving a major milestone in the development of PSCs with carbon-based electrodes.

Chapter 4

The nature of the methylamine–$MAPbI_3$ complex: fundamentals of gas-induced perovskite liquefaction and crystallization

4.1 Preamble

After analysing scientific literature on CPSCs, their current challenges and prospects in chapter 3, experimental work was conducted, in order to understand characteristics of CPSCs and to develop strategies for enhancing their performance. Since the perovskite photoabsorber is the very cornerstone of the PSC operation, the following chapters 4 to 6 will describe the work of this thesis, primarily related to the perovskite layer properties.

At the beginning of this thesis, it was author's belief that perovskite liquefaction and re-crystallization method using methylamine gas has several potential advantages in comparison to the processing from the conventional polar, high-boiling point solvents, that are normally used for PSC processing. Although this method has been demonstrated before and employed to make high-efficient PSCs, the underlying mechanisms behind the reaction between such halide perovskites and methylamine gas have not been described to a full extent. This stimulated the author to investigate this fascinating reaction in order to find means to control it and correlate the characteristics of this reaction with the opto-electronic properties of the crystallized perovskite photoabsorber. Hence, the work on revealing the nature of methylamine-perovskite complex formation, perovskite liquefaction and recrystallization[‡] has been carried out, which is presented in the following.

[‡]This chapter (except for the critical discussion in section 4.7 and section 4.8) has been published as peer-reviewed research paper in the scientific journal "Journal of Materials Chemistry A" (impact factor 2022: 12.7):

Bogachuk, D., Wagner, L., Mastroianni, S., Daub, M., H., Hillebrecht, A. Hinsch, A. (2020). The nature of the methylamine–$MAPbI_3$ complex: fundamentals of gas-induced perovskite liquefaction and crystallization. *J. Mater. Chem. A*, 8(19), 9788-9796.

The individual contributions were as follows:

- **D.B.**: conceptualization of the study, design of the experiments, device manufacturing, perovskite precursor solution synthesis, photoluminescence measurement, development of FTO-hotplate setup, analysis of data, results interpretation, manuscript and figure preparation, coordination of co-author contributions
- **L.W.**: discussion of the results, assistance with the results interpretation and manuscript preparation
- **S.M.**: mentored the study, discussion of the results, assistance with manuscript preparation
- **M.D.**: sc-XRD and Raman measurements, analysis of XRD data, formulation of chemical reaction, assistance with manuscript preparation
- **H.H.**: interpretation of results from sc-XRD
- **A.H.**: discussion of the results, assistance with manuscript preparation
- **All authors**: reviewed the manuscript

4.2 Abstract

The liquefaction and recrystallization of $CH_3NH_3PbI_3$ perovskite with methylamine - MA^0 / CH_3NH_2 gas in solar cells have been intensively studied in the past years, yet the exact mechanisms remained hypothesized and unclear due to lack of experimental evidence. The investigation presented in this work connects the interatomic bonding in the methylamine-$MAPbI_3$ complex during liquefaction and recrystallization with the crystal morphology and the lifetime of photo-generated carriers in planar and mesoporous layer structures. Raman shift analysis and XRD structural investigation have been performed, showing that MA^0 gas forms a complex with $MAPbI_3$ via chemisorption of gas molecules to the perovskite crystal surface by replacing I^- atoms in the PbI_6 octahedra and via coordination of MA^+. Through real-time photoluminescence, the changes in bonding during the liquid-solid transition are related to the radiative charge carrier recombination during the liquefaction and recrystallization. We found that the amount of MA^0 gas reacting with perovskite determines the crystal morphology, pore-filling and, most importantly, the charge carrier lifetime.

4.3 Introduction

In the last decade, perovskite photovoltaics (PV) has been investigated by a tremendous number of scientists and researchers, reaching outstanding power conversion efficiencies (PCEs) which in the laboratory have already exceeded the record efficiencies of such mature technology as polycrystalline Silicon, Cadmium Telluride (CdTe) and Copper Indium Gallium Selenide (CIGS). [50]

Such rapid development was realized by continuous improvements of the molecular structure, film morphology and physical properties of perovskite crystals. One successful method to achieve this goal was proposed in 2015 by Zhou *et al.*, where a peculiar phenomenon was described in which methylammonium lead iodide ($MAPbI_3$) has be liquefied upon exposure to methylamine (CH_3NH_2/MA^0) gas. [315] This liquefaction process is reversible and upon removal of the MA^0-gas, crystalline $MAPbI_3$ is formed again. The chemical reaction has been suggested in literature as following:

$$CH_3NH_3PbI_3\,(s) + xCH_3NH_2(g) \rightleftarrows CH_3NH_3PbI_3{\cdot}xCH_3NH_2\,(l) \tag{4.1}$$

This process has often been used as a post-treatment step to improve film morphology and crystal quality. [316–319] Enhancements of photovoltaic properties of solar cells using methylamine gas were repeatedly reported due to an improved film quality, charge carrier lifetime, perovskite film homogeneity and more favorable

crystallinity. [318, 320–324] bridging to an efficiency of above 20 %. [325, 326] On the technological side, Noel *et al.* have proposed to dissolve perovskite precursor in a mixed solvent of acetonitrile (ACN) and MA^0 to produce a solution which can be used for manufacturing high-efficient perovskite solar cells with PCE of 18 %. [327] In this process the solvating capability of ACN was increased by methylamine bubbling, leading to formation of a clear perovskite solution. In 2018, we have developed a drop-casting method where a similar approach can be used for infiltration of the porous scaffold of carbon-based printable, low-cost, hole conductor-free perovskite solar cells (CPSCs). The champion device had a V_{oc} of over 1 V and a stabilized efficiency of 12.6 % certified by Fraunhofer ISE CalLab. [259] Consequentially, manufacturing the photo-absorber layer of a PV device using methylamine-perovskite interaction establishing itself as a promising, cost-effective approach, that can be implemented on a large scale module production. [328–330]

The question what stands behind the observed mechanism of perovskite liquefaction was already raised in previous reports. Zhou *et al.* supposed that the lone-electron pair in the nitrogen (N) atom of methylamine gas interacts with PbI_6 octahedra, which leads to a liquefied state. [315] It has also been noted that the "molten state" can be achieved by exposing the precursor salt PbI_2 to methylamine or other amines which suggests that the reaction is driven by interaction between the alkylamines and Pb(II). [74, 320, 321, 331, 332] The interaction between $MAPbI_3$ and MA^0 gas was also described as a moderate ligand coordination of the lead atoms changing the lead halide framework. [321] Simultaneously, Rand *et al.* have reported that the proton transfer from PbI_2 to alkylamines results in the formation of Pb-amide bonds, responsible for the perovskite liquefaction. [332] Also the formation of colloids has been attributed to the presence of a xMA^0-$MAPbI_3$ complex which is strengthened by witnessing Tyndall effect in this complex. [321, 333] However, despite the substantial research in the field of MA^0 gas treatment of $CH_3NH_3PbI_3$ perovskites [74, 315–323, 326, 327, 333, 334] the exact mechanism of the Methylamine-Perovskite Complex formation (which will be referred to as MPC further in this work) and the chemical bonding in the liquefied state remain unclear due to lack of experimental evidence. In particular the following underlying questions of this method remain pending: (1) how does the stoichiometry of the MPC formation reaction affects the crystal parameters, (2) what dictates the crystallization dynamics during up-take and removal of the MA^0-gas and (3) what happens to the $MAPbI_3$ lattice when it is exposed to MA^0 gas molecules. We accentuate that the answers to those questions in this work contain vital importance not only for the fundamental chemistry scientists but also for numerous researchers in the perovskite community, which aim to reach high device efficiencies.

In this work, we were able to isolate single crystals and to determine the crystal structures of intermediates from the reaction of MA^0 with $MAPbI_3$. These empirical results clearly present how MA^0 can coordinate Pb^{2+} and MA^+

(CH_3NH_3) leading to the formation of crystalline materials, which are stable only in the presence of MA^0-rich environment. We combine the knowledge of crystalline intermediates to elucidate how does methylamine interact with $MAPbI_3$ perovskite, what are the possible reaction pathways and in particular how the properties of MPC affect the opto-electronic properties of the crystallized perovskite.

We demonstrate by Raman spectroscopy that, upon introduction of methylamine, the lead-halide framework changes through partial replacement of I^- with MA^0 during its coordination of Pb^{2+} and MA^+. We also show the bonding environment in the molten state and how it correlates with the opto-electronic properties of the recrystallized films. Through real-time photoluminescence (PL) microscopic measurement during crystallization we reveal the underlying mechanisms happening inside a porous layer (ZrO_2/Graphite which are normally a part of CPSCs) during the conversion of MPC to crystalline $MAPbI_3$. In addition, we investigate the effect of methylamine/perovskite ratio in the solution on the crystallized absorber layer. Our extensive analysis sheds light onto the chemistry of the MPC, its crystallization kinetics and the mechanisms to control the fundamental properties of perovskite absorber, which define solar cell efficiencies.

4.4 Experimental details

Precursor Solution Preparation

The PbI_2/MAI (1:1) - DMF Complex (purchased from TCI, 99.99 % trace metals basis) was heated at 100°C under nitrogen atmosphere and thus a nearly pure $MAPbI_3$ perovskite powder was obtained. The liquefied perovskite using MA^0 gas (>=99 %, purchased from Linde) of certain amount has been further diluted using acetonitrile with a ratio of 1 mg $MAPbI_3$ to 1 µL of ACN (purchased from Carl Roth >99 %).

Sample preparation

The glass plates with Fluorine-doped Tin oxide on top were treated in an ultrasonic bath containing 3 % Deconex OP153 at 60°C followed by rinsing with DI water. An ultrasonic treatment at 60°C for 1 min in DI water was further operated to ensure removal of any detergent residual. Glass plates were then blown dry using nitrogen. ZrO_2 (Zr-nanoxide paste obtained from Solaronix SA) of 2 µm thickness was screen printed on top of glass and sintered at 500°C for 30 min, after which the graphite-based counter electrode of 12 µm thickness was screen printed, followed by sintering at 400°C for 30 min. Samples filled with perovskite in ZrO_2 and graphite layers were kept under MA^0 environment for 30 minutes to facilitate

a better pore impregnation, after which the samples were annealed at 80°C for 30 minutes. Perovskite films were spin-coated on glass substrates, pre-treated with plasma and annealed at 80°C for 30 minutes.

For the complete perovskite solar cell devices (shown in SI) with carbon-based electrode, a compact TiO_2 layer of 25-30 nm thickness was deposited by spray pyrolysis using a solution comprising 0.05 M of titanium disisopropoxy (bis) acetyl acetone (Sigma Aldrich) diluted with ethanol (>= 99.5 % from Carl Roth). Mesoporous layers of TiO_2 (paste prepared via mixing Dyesol DSL-18NRT with terpineol in 1:0.75 weight ratio) and ZrO_2 of 500 nm and 1 µm thicknesses respectively were screen printed and sintered at 500°C. Afterwards the graphite-based layer (Elocarb B/SP paste purchased from Solaronix SA) was screen printed and subsequently sintered as described above. The positive and negative electrodes were applied by ultrasonic soldering on the FTO. The applied silver paste on the electrodes completes the architecture of the cell. The device active area was 0.4 cm^2.

Characterization

Raman spectra were measured on a Bruker Vertex 70 with a Bruker RAM II module (Nd:YAG laser (λ = 1064 nm) in a range of 50-4000 cm^{-1}. X-ray diffraction (XRD) patterns of films were collected with a Bruker D8 diffractometer (CuKα = 0.1540598 nm) equipped with a LynxEye detector. The PL images were obtained by OLYMPUS BX50 stereomicroscope and sCMOS camera ("Zyla 5.5 sCMOS" by Andor) with a long-pass filter while the partial illumination of the sample was provided by a 623 nm red light-emitting diode (Thorlabs, SOLIS-623C). Due to the presence of long-pass we can exclude that the recorded signal originates from radiative recombination of free charge carriers and not from the reflectance of the excitation source. Time-resolved PL measurement were conducted using externally triggered CW laser (Coherent Orbis) of 660 nm wavelength with 100 mW power, with a fall and rise time (10 % and 90 %) below 2 ns. The laser was triggered to produce rectangular-shaped signals at 7 Hz frequency. The current-density and voltage curves of the devices were measured with a source meter (Keithley 2400) at a scan rate of 50 mV/s using a solar simulator providing a 100 mW/cm^2 illumination intensity(of AM1.5G).

4.5 Results and discussion

Synthesis and characterization of Intermediates MA^0 /MA^+ / PbI_2

Following the conditions in the course of the liquefaction transformation process, single crystals of several intermediates were isolated and characterized.

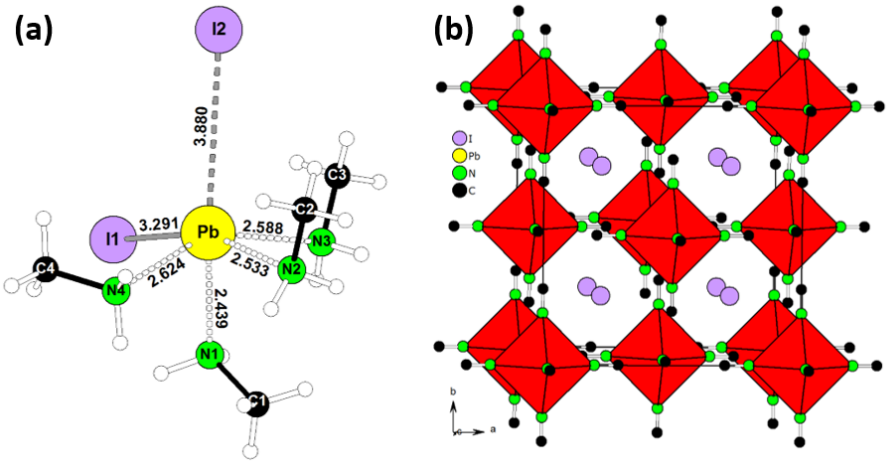


Figure 4.1: Visual representation of neutral complex $PbI_2(CH_3NH_2)_4$ with corresponding bonds lengths. (a) Crystal structure of $[Pb(CH_3NH_2)_6]I_2$ idealised as cubic K_2PtCl_6 type (b) as derived from the single crystal XRD measurement Reprinted with permission from [257]

Passing a stream of MA^0 / CH_3NH_2 gas over powdered PbI_2 yielded a highly viscous liquid from which pale-yellow platelets were crystallized. The crystal structure determination (Table S1) revealed a neutral complex of Pb(II) with the composition $(CH_3NH_2)_4PbI_2$. A simplified description classifies $(CH_3NH_2)_4PbI_2$ as a neutral octahedral complex with two iodine anions in a cis-position (Figure 4.1a, details Table S1). CH_3NH_2 acts as a classical donor ligand to Pb^{2+}.

Passing a strong stream of methylamine evaporated from the cold trap over $MAPbI_3$ was readily liquefied and colorless crystals were precipitated from the $MAPbI_3xMA^0$. They were stable at room temperature if the sample was kept in a closed vessel with pure methylamine as equilibrium gas phase. For the measurement the crystals were directly transferred from the mother liquid into the cold N_2-stream of the sc-XRD (at 100 K). Further examination revealed a multiply twinned crystal where the idealized structure is based on a face-centered cubic unit cell. The refinement (Table S1) yielded a structure model close to the well-known K_2PtCl_6 type with octahedral $[Pb(CH_3NH_2)_6]^{2+}$ complexes and isolated I anions. (Figure 4.1b, details Table S1). This K_2PtCl_6-related structure is a very common motif for hexammine complexes of divalent transition metal halides $[M(II)(NH_3)_6]X_2$. (M = V, Cr, Mn, Fe, Co, Ni; X = Cl, Br, I). [335]

In some cases, small colorless needles were formed as by-product which can't be recovered as $MAPbI_3$ in the course of the re-crystallization process. The small needles were characterized by sc-XRD as Pb(OH)I. [336, 337] Additionally, pale-yellow platelets were separated from the bulk material, which were characterized as $(CH_3NH_3)_5(CH_3NH_2)_2Pb_2I_9$. This compound contains $[Pb_2I_9]^5$ units consisting of two face-sharing octahedra and MA^0/MA^+ dimers $[CH_3NH_3\text{-}NH_2CH_3]^+$ bridged

by a hydrogen bond (Figure S1, details Table S1). The formation is explained by moisture according the following reaction:

$$4\,MAPbI_3 + 4\,CH_3NH_2 + 2\,H_2O \rightarrow (CH_3NH_3)_5(CH_3NH_2)_2Pb_2I_9 + 2\,Pb(OH)I + MAI \quad (4.2)$$

Composition of MA^0-$MAPbI_3$ complexes in solution of liquefied $MAPbI_3$ and evolution/precipitation of perovskite.

From the above-mentioned findings, it is strongly suggested that the liquefaction of $MAPbI_3$ in the presence of MA^0 is driven by its coordination of Pb^{2+} and MA^+. To gain new insights into the interaction between MA^0 and $CH_3NH_3PbI_3$, an MPC solution (diluted in ACN) with high excess of MA^0 was produced in a closed vial. The Raman spectrum was then measured as the vial was opened in ambient conditions at room temperature and MA^0 gradually left the liquid over a course of 125 minutes throughout which the pale-yellow liquid gradually turned to saturated clear yellow and, consequently with additional annealing, turned dark, resembling crystalline $MAPbI_3$. In the liquified state (Figure 4.2, purple) at high MA^0 pressure, the most intense peak is at 78 cm^{-1}, followed by a peak at 94 cm^{-1}. Upon opening of the vial, an intermediate state is introduced which has a dominant peak at 104 cm^{-1} and a smaller peak at 82 cm^{-1}. Finally, upon additional annealing the bands at 94 cm^{-1} and 82 cm^{-1} arise. Furthermore, the bands at 155 cm^{-1} and 290 cm^{-1} are only present in the MPC and both of them disappear during crystallization, while the new bands at 120 cm^{-1} and 242 cm^{-1} occur.

In the context of $MAPbI_3$ Raman shift spectrum, the region between 70 and 120 cm^{-1} is usually attributed to Pb-I framework interactions, such as symmetric and asymmetric Pb-I bond stretching. [338–341] As soon as the vial with the MPC is opened, MA^0 molecules start to leave and both peaks shift, indicating a structural reorganization of the Pb-I framework (*i.e.* a change in Pb-I valence vibrations) during the transition between the liquid and solid phases. The Raman shifts in wavenumber region of 150-3000 cm^{-1} is commonly attributed to numerous vibrational modes of organic cations such CH_3 bending, C-N stretching, N-H stretching and others [339,342] (complete Raman shift spectra are presented in Figure S2 in the SI). Notably, we highlight the presence of a band at 290 cm^{-1} existing only in the liquid state under high pressure, which we affiliate with a rotational mode of MA^+. In a recent report from Park *et al.* a similar band at 288 cm^{-1} was found to be responsible for a rotational mode of MA^+ cation, which is normally inactive, but can be seen here either due to the fact that in the MPC the local symmetry of PbI_3 framework is lower or because MA^+ form MAI-MA^0_x during the MPC formation as will be shown later. [340]

As seen from Figure 4.2, the band at 290 cm^{-1} gradually reduces during the crystallization, while the band at 120 cm^{-1} rises, which can be attributed to MA^+

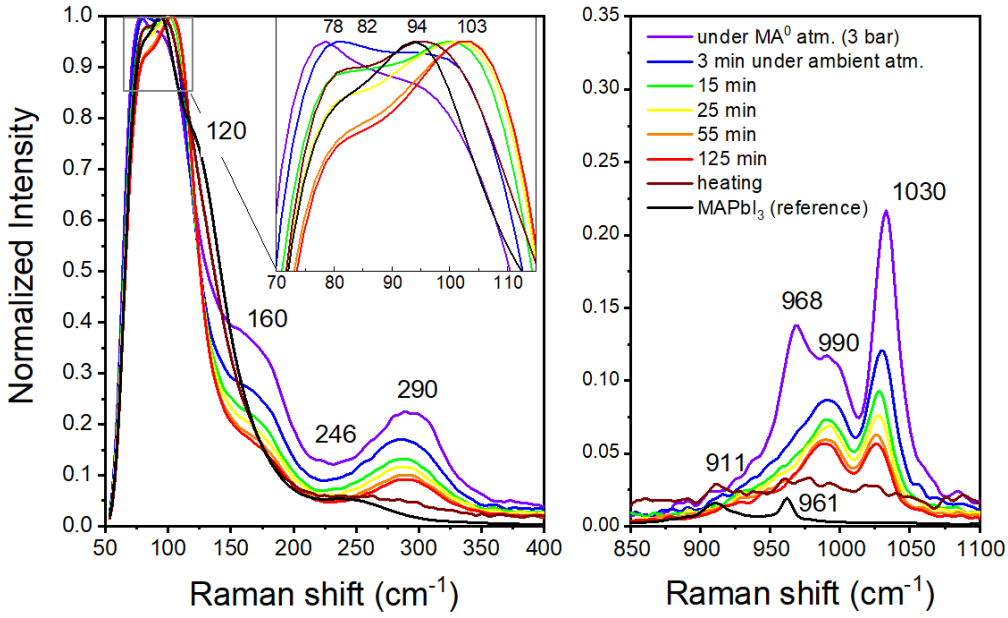


Figure 4.2: Raman spectra of a liquefied $MAPbI_3xMA^0$ complex (MPC) during liquid–solid conversion as the MA^0 leaves the complex. Note the shifts in the 70-115 cm^{-1} region (inset) corresponding to Pb-I symmetric and asymmetric stretching vibrations, suggesting that the PbI_6 octahedra undergo changes.

libration mode. [339] In addition, the bands at 1030 cm^{-1} and 990 cm^{-1} which nearly ideally correspond to the CH_3-NH_3 rocking and C-N stretching vibrations respectively for a free MA^+ in vacuum, vanish during crystallization. [342]

Simultaneously, the bands assigned to the same vibrational modes in $MAPbI_3$ appear at 911 cm^{-1} and 961 cm^{-1} for CH_3-NH_3 rocking and C-N stretching, respectively. Such band shifts suggest the reduction of free MA^+ cations and the increase of the Pb-I framework symmetry due to insertion of MA^+ yields recrystallized $MAPbI_3$. In the presence of humidity, H_2O and CH_3NH_2 are reacting in an acid base reaction to produce MA^+ cations and OH^- anions. In this case degassing results in the formation of crystalline $(CH_3NH_3)_3(CH_3NH_3\text{-}NH_2CH_3)_2Pb_2I_9$ and colorless rod-shaped crystals of Pb(OH)I. $(CH_3NH_3)_3(CH_3NH_3\text{-}NH_2CH_3)_2Pb_2I_9$ is build up by isolated $[Pb_2I_9]^{5-}$ dimers of face sharing PbI_6-octahedra. (Figure 4.3) Charge balance is achieved by MA^+ as well as the dimeric $(MA\text{-}MA^0)^+$ cations. Further degassing yields also $MAPbI_3$, but Pb(OH)I stays as a by-product, which emphasizes that humidity should be avoided during the recrystallization of $MAPbI_3$ with MA^0. Thus, the $MAPbI_3$ liquefaction may be driven by two effects, MA^0 bonding to Pb^{2+} atom via lone electron pair as well as by the formation of MA^0-MA^+ dimers. Very recently (this manuscript had already been submitted at that time), another publication on the liquefaction of $MAPbI_3$ using methylamine gas was published. [343] In accordance with our own work, they also found the existence

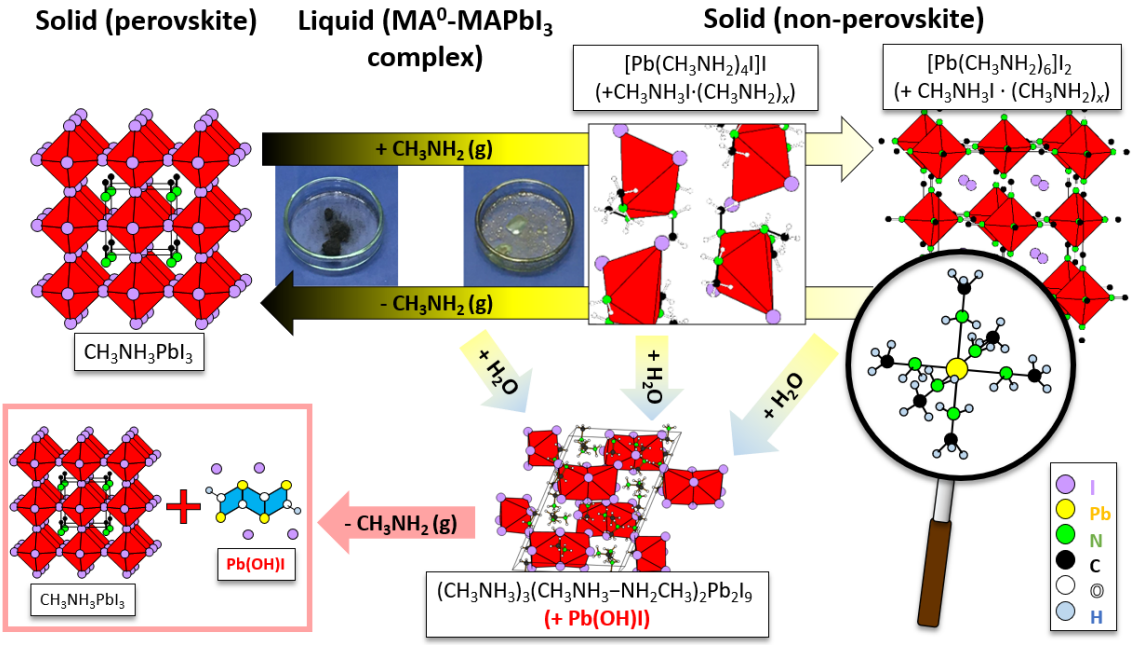


Figure 4.3: Structural changes during the liquefaction of $MAPbI_3$ upon the introduction of MA0 and formation of the neutral complex $[PbMA_4^0I]I$ $(+MAI{\cdot}MA_x^0)$ in which Pb^{2+} is coordinated by MA^0 molecules. The MA^0 amount increase into the complex leads to the increase of coordinated MA0 and to the formation of crystalline $PbMA_6^0I_2$ $(+MAI{\cdot}MA_x^0)$. Note that in the presence of humidity a crystalline $(CH_3NH_3)_3(CH_3NH_3\text{-}NH_2\text{-}CH_3)_2Pb_2I_9$ and Pb(OH)I are produced. Upon further degassing Pb(OH)I stays as an unwanted by-product. These measurements are derived from detailed XRD pattern analysis and visualized via embedded software.

of methylammonium-methylamine dimers. The dimers can be regarded as large cations with low charge density, reducing the lattice energy of the corresponding salt, which yields a situation comparable to ionic liquids.

Real-Time Crystallization Dynamics Observed by Photoluminescence

We investigated the crystallization dynamics using real-time photoluminescence microscopy. Such characterization tool allows us to link the emission of photons from radiative recombination with the surface chemistry of the crystallizing layer to understand the behavior of nucleation and absorber layer formation inside the mesoporous scaffold. [344] A layer of graphite (12 µm) on top of thick ZrO_2 layer (2 µm) on a glass substrate was filled with perovskite solution (MPC with ACN) and subsequently annealed at 70°C to crystallize the perovskite. Then, the substrate was placed in a transparent gas chamber (as depicted in Figure S4), to which MA^0 gas is later supplied, inducing the perovskite liquefaction. After reaching the liquefied state, a small outlet was opened in the box allowing MA^0 gas to leave

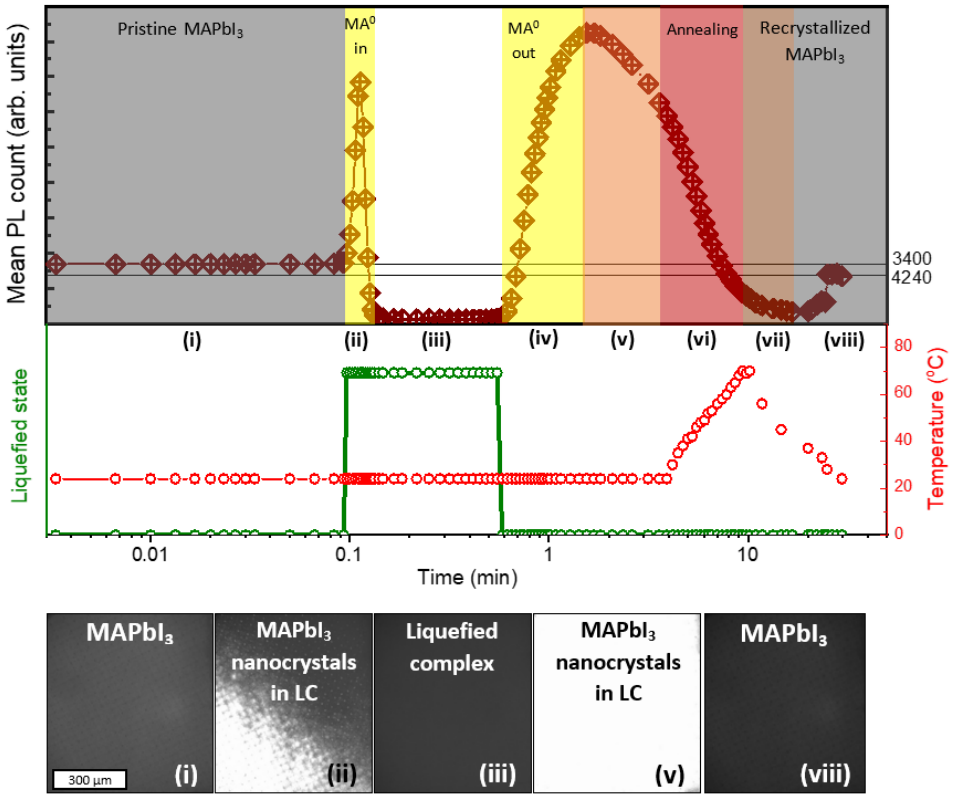


Figure 4.4: Investigation of liquid–solid evolution of MPC in mesoporous layers. The photoluminescence is monitored in real-time on the glass/ZrO_2/graphite device. When the MA^0 is supplied through an inlet, the layer turns pale-yellow, causing a drop in the PL signal due to the collapse of the ABX_3 structure. Once, the inlet is opened, the MA0 leaves the MPC, reforming perovskite and causing a rise in PL. When the sample is heated up to ≈70°C, it induces a more rapid leave of MA^0 and the subsequent crystallization. The full PL microscopy measurement can be found in Video S1 in ESI

and upon rise in temperature induced by a transparent hotplate, the methylamine molecules start to evaporate even more rapidly inducing a crystallization within the mesoporous layers. A more detailed description of the setup and the procedure is shown in Figures S4 and S5. We ascribe several processes to the different stages observed during the liquid-solid conversion of the perovskite crystals. The real-time PL measurement starts with solid perovskite without MA^0 (denoted as stage i in Figure 4.4). Upon introduction of MA^0 to the system, in a first instance the PL sharply rises, reaching a PL intensity 4 times higher than initially and subsequently drops to PL counts close to zero (stage ii) since the perovskite now is in a liquefied form (stage iii). When the MA^0 is removed again, the nucleation takes place, and a rise in the PL signal (stage iv) is observed, followed by a slow decay (stage v) during which the annealing takes place (stage vi). After that in the final stages (vii and viii) the PL signal slightly rises and stabilizes at a value close to the initial one.

The real-time PL microscopy measurement is provided in detail in Video S1 in SI.

We manifest that the MA^0 gas forms the MPC with $MAPbI_3$ via chemisorption of gas molecules to the perovskite crystal lattice by replacing I^- atoms, thus coordinating Pb^{2+} as well as MA^+. Therefore, when MA^0 is introduced to a perovskite bulk, it diffuses through the grain boundaries and is adsorbed by the crystal surface resulting in the formation of separated nano-crystals. This phenomenon is accompanied by the sharp rise in PL (as seen in stage ii Figure 4.4), which arises from the reduced number of available bulk recombination centers per perovskite crystal. In literature, high PL in nano-sized perovskite crystals and quantum dots has been observed too. [345–347] Then the PL signal drops to nearly zero and the absorber layer color becomes transparent-yellow, highlighting that the ABX_3 crystal structure is collapsed leading to the inability of the perovskite to have a periodic wave function. Upon the removal of MA^0 from the MPC during the crystallization process, the $(PbI_xMA^0{}_{6-x})^{2-x}$ octahedra first start to form into clusters, as the number of free MA^+ decreases (seen from the decrease of Raman shift band at 290 cm^{-1}), and the number of MA^+ embedded into the ABX_3 structure increases (seen from the increase of band at 120 cm^{-1}). We note that $(PbI_xMA^0{}_{6-x})^{2-x}$ are charged species where the total charge of a cluster is

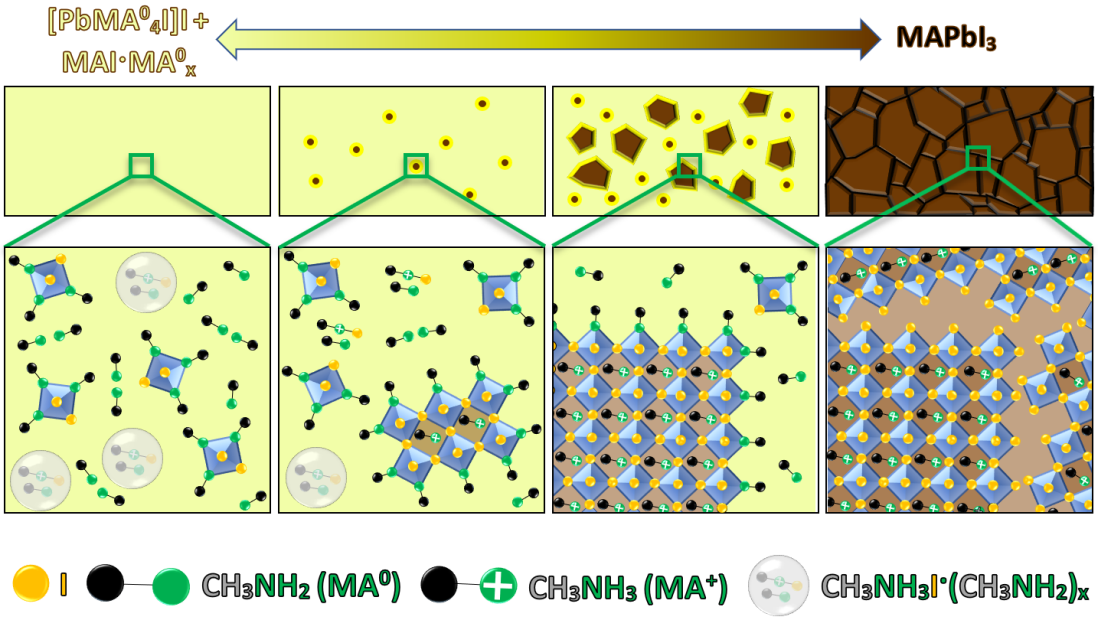


Figure 4.5: Schematic illustration of $MAPbI_3$ perovskite recrystallization during desorption of MA^0 from the methylamine–perovskite complex or crystalline $[PbMA^0_4I]I + MAI{\cdot}MA^0_x$. The double-sided arrow highlights that the reaction and mechanisms are reversible. The upper row depicts the crystal morphology change, while the bottom row illustrates the interaction of PbI_6 octahedra with MA^0 and the by-products in the solution such as $MAI\text{-}MA^0_x$ and MA^+MA^0.

determined by the number of residing I^- atoms. These clusters act then as nuclei in the beginning of the crystallization process. The supposed process is sketched in Figure 4.5.

Revealingly, the adsorption and desorption of MA^0 both tend to increase the PL signal, since the non-radiative recombination mechanisms in bulk are suppressed. Between stages iv and v, when the PL signal reaches its maximum (t=1.55 min) the bulk recombination starts to dominate because of crystal growth whereas surface passivation by MA^0 starts to fade away, decreasing the overall PL. During the recrystallization for ~20 min, stabilization is reached as is indicated by constant slightly higher PL. During the stabilization, improvement of perovskite quality through the change of grain structure and removal of residual MA^0 caused by annealing, has been reported before. [327] A similar overall trend, where the PL starts to rise, then drops and rises slightly again during annealing until stabilization has been observed also before for the 2-step solution processing, where PbI_2 instead of MA^0 passivates the grain boundaries [327, 348] until its complete conversion to the $CH_3NH_3PbI_3$, after which the PL decreases. [344,349]

Influence of MA^0 concentration in the MPC solution on the fully-crystallized photoabsorbers

Accurate estimation of the reaction products during liquefaction is challenging, therefore we quantitatively compare the effect of various given amounts of MA^0 in the solution by reacting it with the known quantity of $CH_3NH_3PbI_3$.

We prepared three different solutions using x (ratio of moles of MA^0 per moles of perovskite) of 19.2, 14.4 and 11.5. The estimation of x is shown in the SI. The lowest value (x=11.5) already allows the complete melting of the perovskite, whilst x>20 lead to formation of white precipitates in the solution.

Perovskite films were deposited on glass substrates by spin-coating the MPC (diluted with ACN) of different ratios x of MA^0 in it. The obtained XRD patterns of each sample are shown in Figure 4.6d, where the (110) and (220) diffraction peaks increase with higher concentration of MA^0 in the complex, while most of other reflections decrease. Such trend highlights how the concentration of methylamine can directly affect the preferential orientation of the crystal lattice. Looking at the most pronounced diffraction signal of (110) plane, an increase in full-width at half maximum (FWHM) from 0.095° over 0.119° to 0.165° can be observed as the amount of MA^0 in the MPC rises. The change in FWHM indicates that by varying the MA^0 ratio in the MPC, the perovskite grain size can be tuned (*i.e.* large grain sizes are grown using high amounts of MA^0), which can also clearly be seen in SEM top-view images in Figure 4.6a-c and crystal area distributions (Figure S7), obtained by analysing these images via ImageJ.

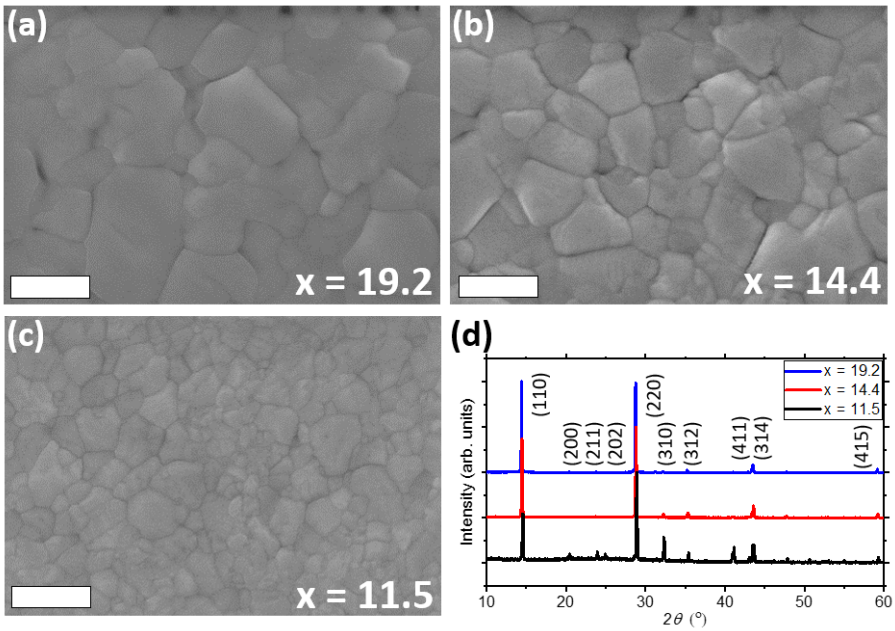


Figure 4.6: SEM images of $MAPbI_3$ crystallized from various amounts of MA^0 in the liquefied $xMA^0 \cdot MAPbI_3$ complex (a–c), where the crystal size increases with higher MA^0 concentration, which can also be seen from an decrease in FWHM of (110) and (220) diffraction peaks at highly concentrated (with MA^0) samples. The presented XRD patterns of three samples show how strongly MA^0 coordinates the recrystallization of $MAPbI_3$ along (110) and (220) planes (d). Scale bar – 300 nm.

It has been numerously reported that the change of stoichiometry in the precursor perovskite solution leads to different crystallization dynamics, which can lead to variation in such fundamental material properties as crystal size, charge carrier transport and contact at the interface between perovskite and charge extracting layer. [350–353] A similar dependency on the solution composition is seen in the MPC, where, as a result of the MA^0/perovskite ratio, crystals with different domain size have been grown which coincides with the observations by Chen et al. [316] The differences in FWHM in the XRD measurements correlate with the observations by SEM. We attribute such behavior to a stronger chemical coordination of Pb^{2+} and MA^+ with the higher MA^0 concentration, which causes a more preferential orientation of the crystal lattice along <hk0> planes such as (110) and (220), [321,354] resulting in the growth of larger crystals. It is worth mentioning that the commonly observed peak at $2\theta = 12.7°$ which is usually observed when PbI_2 is formed [338, 348, 355, 356] was absent in all the samples. However, this residual PbI_2 could be screened by the formation PbI_2-alkylamide impurities, resulting in the reduced carrier lifetime of the crystallized absorber. The peaks at $2\theta = 9.84,° 19.74°$ and $29.79°$ which are attributed to MAI reflections [338, 357] are also not present, concluding that upon crystallization the MPC forms a pure, stoichiometric $MAPbI_3$ photoabsorber from an additive-free "perovskite melt".

The finding that the morphology of the final crystal layers changes as a function of the x (MA^0/Perovskite) ratio suggests that the crystallization kinetics could also be different within the mesoporous layers of the CPSCs. While perovskite crystals using MPC can even reach sizes of >1 µm on planar substrate, [354] the crystal growth inside the porous layers of CPSCs is clearly different, as the majority of pores have diameters of less than 20 nm. Therefore, crystallization is confined by the pore size, which means that the interface plays a big role in the nucleation process as it provides multiple nucleation sites. [12] To gain a better understanding of the effect of ratio x in the solution on the crystallized absorber layer in porous isolating ZrO_2 scaffold, we use steady-state and time-resolved photoluminescence (TRPL) intensity measurements. A series of perovskite-filled mesoporous layers with different x variations were characterized. As seen from Figure S8, the steady-state PL intensity image of layers crystallized from a low-concentrated solution show strong PL signal. With higher concentration of MA^0 the average number of PL counts decreases, while the overall homogeneity of the PL signal increases as a result of better infiltration in the mesoporous layers. We quantify the homogeneity (h) of the PL image by comparing the histogram of the PL intensity shown in Fig. S9.

Due to a higher concentration of MA^0 in the solution, the liquefied complex becomes less viscous enabling an easier infiltration through the pores. Zhou *et al.* suggested that the excess of MA^0 in the MPC "trims" the clusters, leading to a decrease in cluster size and lower viscosity. [358]

A TRPL was employed to derive the carrier lifetime (τ). Generally, as it has been demonstrated in numerous works, the PL-decay is affiliated with the transient behavior of radiative and non-radiative recombination of charge carriers in a semiconductor. [322, 327, 359–361] In the absence of a quencher (as in this case), the longer the PL-decay, the longer the excited diffusing carriers are present in the perovskite, and therefore the longer carrier lifetime and diffusion length, both of which are vital characteristics of any PV device.

We quantify the charge carrier lifetime by fitting the PL-decay to a bi-exponential function, accounting for Schockley-Read-Hall recombination processes at surfaces and in the bulk. The TRPL results in Figure S10 show that the decay is much slower (longer carrier lifetime) in the photoabsorbers fabricated with MPC using low ratio of $MA^0/MAPbI_3$ in it (273.65 ns and 140.67 ns for x = 8.6 and 11.1, respectively). Contrarily, for the higher ratio of MA^0 the PL-decay is significantly faster: 20.9 ns for x = 14.8 and 22.56 ns for x=18.2. As seen from Table 4.1, large amounts of MA^0 (x>12) yield an absorber with lower carrier lifetime having lower averaged PL, indicating that despite strong advantages from crystallographic perspective (as seen from XRD patterns) such ratios of MA^0 are not desired due to poor opto-electronic properties of the layers. Conings *et al.* have also found that the recrystallized layer after the MA^0 treatment helps the infiltration through the

Table 4.1: The mean PL counts, calculated homogeneity and trap-assisted decay lifetime τ obtained from PL images of absorber layers crystallized from solutions with various x inside mesoporous ZrO_2 layers (a-d)

xMA^0	x = 8.6	x = 11.1	x = 14.8	x = 18.2
PL (cts.)	$6.6{\cdot}10^3$	$4{\cdot}10^3$	$3.8{\cdot}10^3$	$3.8{\cdot}10^3$
homogeneity	$2.6{\cdot}10^{-4}$	$3.3{\cdot}10^{-4}$	$7.4{\cdot}10^{-4}$	$8{\cdot}10^{-4}$
τ **(ns)**	273.65	140.67	20.9	22.56

pores, but, on the other side, leading to an inferior electronic quality. [323] Since no quenching layers are involved, the observed reduction in carrier lifetime is likely related to a more efficient bulk/surface non-radiative recombination processes. This means that there are either more of faster recombination channels, most likely in the form of trap-assisted recombination. Since only the stoichiometry of the MPC changes without introduction of any other additive, the trap capture cross-section (*i.e.* quenching efficiency of each trap) should remain unchained. We therefore suggest that at high x, high number of trap energy states inside the bandgap outweigh the advantages of smoother film and better infiltration and start to play major role in defining the electronic properties of the absorber. Such a dependency of τ on x emphasizes the importance of a careful control of xMA^0 (in Reaction 4.1) which should be within a certain processing window when producing solutions for perovskite PV devices.

4.6 Conclusions

In this work, the nature of methylamine-$MAPbI_3$ complex formation and its re-crystallization during the degassing in perovskite solar cells is presented. We show through XRD single crystal measurements, that MA^0 simultaneously forms neutral complexes with both Pb^{2+} and MAI leading to the collapse of the perovskite crystal structure. In the excess ($\gg$1 atm.) of MA^0 this reaction induces the formation and precipitation of non-perovskite solid crystals of $[Pb(CH_3NH_2)_4I]I$ and $[Pb(CH_3NH_2)_6]I_2$. We highlight that the presence of H_2O leads to the irreversible formation of Pb(OH)I, which act as impurities in the photoabsorbing layer. Therefore, the formation of pure methylamine-perovskite complex needs to be carried out under normal atmospheric pressure of the MA^0, and in the absence of water.

During the degassing of MA^0 from the complex, the iodide bonds with Pb^{2+}, forming PbI_6 octahedra, while MA^+ cations get embedded in the A-site of the original pseudo-cubic ABX_3 structure. Real-time photoluminescence (PL) microscopy

as a measure of the crystal quality visualizes the interaction of MA^0 gas with perovskite crystals. We postulate that the liquefaction starts from diffusion of MA^0 gas molecules through grain boundaries, leading to a break-up of bulk crystals and therefore reducing bulk recombination. This process is then followed by a complete collapse of the perovskite structure, as the PL signal approaches zero. When the MA^0 gas is desorbed afterwards in inert atmosphere, in accordance with the PL recovery a reversible process takes place, where the isolated non-bulk crystals of $MAPbI_3$ start to re-emerge from a liquefied state till the crystal coalescence is complete.

Furthermore, we find that the amount of MA^0 in the complex plays a vital role in the control of crystal size and trap-assisted charge carrier lifetime. In planar films with high MA^0 concentration, the MA^0-$MAPbI_3$ complex leads to growth of larger crystals, while the low concentration leads to smaller crystals. In perovskite-filled mesoporous layers time-resolved PL decay shows that high amount of MA^0 in the complex causes an increase in trap-assisted monomolecular charge carrier recombination suggesting the formation of numerous trap energy states.

With this work we show that the understanding of liquefaction processes and crystallization kinetics is paramount for the further development of perovskite photovoltaics.

4.7 Critical discussion - research paper

In the presented research, the interaction between perovskite and methylamine was studied in detail, which provided new insights into how MA^+-based perovskites and their precursors are liquefied in the presence of MA^0. In addition, the driving mechanisms causing perovskite crystallization as well as methods to control it were identified by combined crystallographic and opto-electronic characterization techniques. However, the author would like to underline several suggestions, which could have improved the significance of this research paper further:

- The assignment of Raman shift bands to vibrations of specific bonds in this work relies entirely on similar reports in literature. However, it could have been more accurate if it were supported by density functional theory (DFT) simulation of the proposed complexes and dimers. In such case, the Raman shifts could also be simulated, which would allow precise assignment of the measured bands to the specific (modelled) vibrations.
- It is interesting to note that an increase in MA^0 concentration in the MA^0-$MAPbI_3$ complex deposited on a planar substrate affects the crystal size of the resulting perovskite layer, but it does not describe its effect on the opto-electronic quality of such planar films. In contrast, the effect of MA^0 concen-

tration on the non-radiative recombination of the photoabsorber embedded in mesoporous layers is discussed well. A similar opto-electronic characterization of planar films produced from different concentrations of methylamine would be beneficial.

- It is easy to confuse the x mentioned in the text, which means the calculated amount of MA^0 that is introduced to the system with the x in the $MAPbI_3 \cdot xMA^0$ complex. According to several reports, [74, 325, 362, 363] the latter x was found to be around 2.5-3 based on different characterization techniques. Therefore, most of the methylamine gas introduced to the precursors (in this work) is lost to ambient due to improper sealing. Furthermore, it would be much more informative to quantify the actual x in the $MAPbI_3 \cdot xMA^0$ complex by gas adsorption or similar techniques.

While the MA^0-based perovskite solution can be applied to manufacture perovskite solar cells and modules, the author would suggest to take a step back and assess this method more critically. In particular, it is important to discuss the current challenges of such perovskite crystallization method and further prospects, before considering to use it in later work.

4.8 Critical discussion - general concept

The herein discussed approach to liquefy and recrystallize perovskite is fundamentally different from the traditional process of dissolving perovskite precursors, followed by solvent removal, nucleation and growth (*cf.* subsection 1.3.6). Normally, the precursors are dissolved in a polar, aprotic solvent with a (relatively) high boiling point, like *N,N*-Dimethylformamide (DMF), Dimethyl sulfoxide (DMSO), γ-butyrolactone (GBL) or *N*-Methyl-2-Pyrrolidone (NMP). Their high boiling point and low vapor pressure causes a slow rate of solvent removal and thus slow rate of supersaturation, which frequently leads to a growth of large, but isolated randomly-oriented crystals (often in a dendritic shape), resulting in a discontinuous layer morphology. Hence, typically, to achieve satisfactory perovskite films, additional treatments for advance crystallization control are required to rapidly remove the solvent and cause fast supersaturation (*cf.* subsection 1.3.6).

When certain perovskites or their precursors come in contact with methylamine (or other amines) – CH_3NH_2 (or MA^0), the precursors liquefy due to their coordination by MA^0 as discussed in the present work. Thus, methylamine can be considered as a volatile and low-boiling "solvent" (boiling point $\approx$ -6°C), which can also be quickly removed from the solution, causing rapid supersaturation without the need of sophisticated crystallization approaches. Due to this advantage, perovskite films produced by such MA^0-liquefaction are well-known to be smooth with excellent homogeneity. [315, 320, 321, 327, 329, 362] Notably, numerous reports in literature employ this method not to synthesize a solution, which is deposited on

a substrate, but only as a post-treatment step to "heal" the initial rough perovskite layer (Figure 4.7a). [315, 319, 324, 362, 364, 365] In addition, fast solvent removal has a strong potential to increase processing speed and, thus, decrease production costs. [366, 367] However, ever since the discovery of this liquefaction effect in 2015 by Zhou *et al.*, [315] until the presented work [257] was conducted, the exact chemical interaction and liquefaction mechanisms were only hypothesized and not proven experimentally. Later studies shown in literature after this publication have confirmed the findings of this work, particularly the formation of a strong coordination bond between Pb^{2+} and N atom of MA^0, as well as presence of MA^+-MA^0 dimers during the perovskite liquefaction. [343, 368–370]

Although this MA^0-liquefaction approach has several advantages described above, over the course of this thesis, the author discovered several critical challenges, that hinder further development of such perovskite crystallization method, particularly in the context of CPSCs:

- In the chapter 3, it was mentioned that H-CPSCs have to be infiltrated with a perovskite solution, since it is introduced only after thick porous carbon-based electrode is deposited. Consequently, solution with lower viscosity are more likely to homogeneously spread within the mesoporous scaffold of a H-CPSC, which is needed for manufacturing efficient PV devices reproducibly. In the context of MA^0-based approach, this can be achieved by introducing higher amounts of methylamine, which causes reduction of solvent viscosity and faclitates effective filling of the cell (Figure 4.7b). On the other hand, perovskite photoabsorber with the highest charge carrier lifetime and PL intensity is obtained when the concentration of MA^0 is lowest, and, therefore, the solution viscosity is highest. This issue is thought to be the origin behind high but inhomogeneous PL over the device active area (*cf.* Table 4.1 of this publication). Diluting the solution with other agents, like acetonitrile used in this work to decrease viscosity can improve the infiltration efficacy but will cause a reduction of photoabsorbing material density, since the perovskite molar concentration would be decreased. Therefore, using such MA^0-based solution is challenging for reproducible fabrication of H-CPSCs, but not for L-CPSCs.
- The methylamine concentration also plays a crucial role not only in determining the viscosity of a solution but also in opto-electronic quality and therefore needs to be carefully controlled to produce high-efficient PV devices. Furthermore, the MA^0 evaporation rate essentially determines the saturation rate and, therefore, its control allows to alter the crystal growth. To carefully fine-tune the concentration of MA^0 and its evaporation, typically closed environment chambers are used in which the in- and out-flow of gas can be precisely controlled (Figure 4.7c). [321, 362] Although such approaches were demonstrated in literature to fabricate small-scale PV devices, [319, 325, 362, 364, 365] it can be expected that this additional processing complexity negatively affects the up-scalability of this approach, which would diminish its rapid processing po-

tential.

- For the cases, when the MA^0-based solution is directly spread on a substrate, practical issues arise, stemming from the rapid evaporation rate of MA^0. If the perovskite solution deposition process is not continuous at some point, solution might crystallize at the advancing meniscus, in the nozzle, in the print-head or other components of the deposition device, causing "clogging". In the author's opinion, it is a critical issue to keep in mind, when such solvent system is considered for large device manufacturing.

As described in this work, the $MAPbI_3$-MA^0 complex is formed due to (1) interaction between Pb(II) and lone electron-pair of N atom in the amine group, as well as due to (2) formation of MA^0-MA^+ dimers. Since the latter mechanism is based on hydrogen bonding, MA^0 is not always able to fully liquefy perovskite with different A-cations. Cs^+ salts, like CsI or CsBr build a strong ionic bond close to 4 eV/molecule, making their reaction with MA^0 energetically unfavorable. But remarkably, with an addition of excess MAX salts to the stoichiometric inorganic compositions it is still possible to produce Cs-based perovskites via

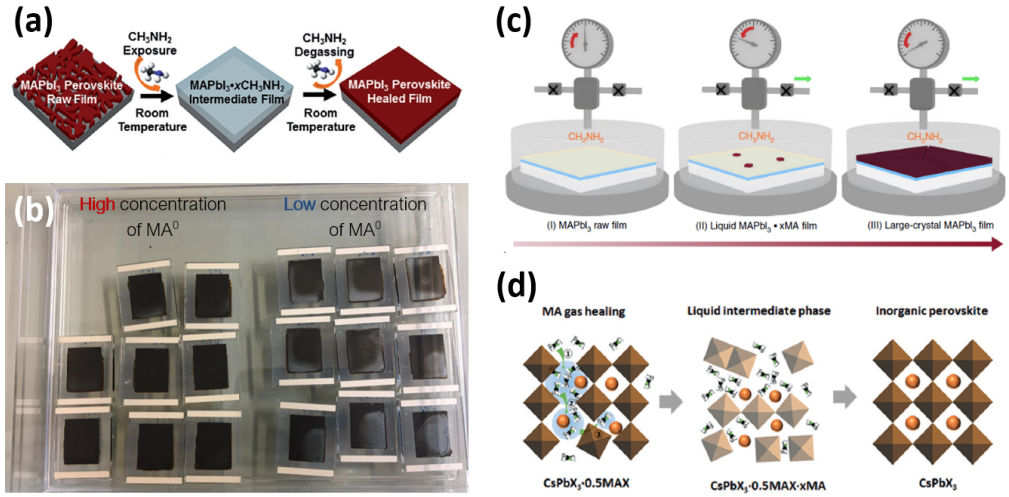


Figure 4.7: (a) Illustration of perovskite film "healing" process using methylamine gas as morphology-improving post-treatment. Reprinted with permission from [315]. (b) Photographs of H-CPSCs (manufactured during this thesis) infiltrated under two different conditions: (1) high concentration – filling cells in a closed environment, where atmosphere was saturated with MA^0 gas and (2) low concentration – filling cells were filled in an opened environment. As a result, without controlling the evaporation rate of MA^0, its concentration rapidly drops during the filling, causing insufficient infiltration of H-CPSC and formation of perovskite on top of the carbon electrode. (c) Illustration of setup to control MA^0 partial pressure (and hence its concentration). Reprinted with permission from [362] (d) Visualization of healing inorganic perovskite $CsPbX_3$ with MA^0 gas by adding excess MAX salt(s). Reprinted with permission from [364].

MA^0-approach, whereby localized absorption of MA^0 molecules at MA^+ sites collapses the Cs-based perovskite structure, which can be recrystallized back by degassing MA^0 (Figure 4.7d).

More intricate is the interaction between MA^0 and the FA-based perovskite materials. Several reports have demonstrated that perovskite films containing FA tend to crystallize directly into a photoinactive δ-phase $FAPbI_3$. [317,371] Although, small amounts of such δ-$FAPbI_3$ can have a favorable defect-passivating effects, fabrication of FA-rich perovskite films using MA^0 is problematic. [256, 325] This critical issue significantly limits the opportunities of MA^0 to be used for producing high-efficient and stable perovskite opto-electronic devices. Consequently, today most of the PSCs produced via MA^0-approach have the archetypal $MAPbI_3$ composition, which is widely considered to be unstable. Due to the issues mentioned above, the author of this work (despite investigating the MA^0-crystallization approach in detail) has pursued other methods to synthesize perovskite solution and control its crystallization. More specifically, perovskite solutions for fabricating devices discussed in chapters 5 to 9 were prepared by dissolving MAI, PbI_2 and small amounts of 5-ammonium valeric acid iodide (5-AVAI) in GBL (unless otherwise specified).

However, very recently an alternative volatile low-boiling point solvent/gas has been proposed to alleviate the issue with crystallizing FA-based perovskites. Pang and co-workers have discovered that when FAX salts are exposed to MA^0, the nucleophilic lone electron-pair of N (in MA^0) attacks the electrophilic groups of an imine bond in FAX. [363] This triggers an addition-elimination reaction, replacing an amino group (-NH_2) in FAI with a CH_2NH from MA^0 and, thus, removing ammonia (NH_3). As a result *N*-methylformamidinium iodide (MFAI) is formed, which can again react with MA^0 by the same addition-elimination process of -NH_2^+ group to form *N,N'*-dimethylformamidinium iodide (DMFAI), as shown in Figure 4.8a. Unlike the ion exchange reactions between MA^0, FAI, MFAI and DMFAI taking place simultaneously, these addition-elimination reactions are irreversible. Consequently, cations like MFA^+ and $DMFA^+$ are too large for their incorporation into a cubic 3D perovskite structure, explaining the inability of FA-based perovskites to recrystallize to the α-phase after their exposure to MA^0 gas. Based on this phenomenon, the authors of this work proposed to use ammonia as liquefying agent of FA-rich perovskite (Figure 4.8b) instead of aliphatic alkylamines like MA^0. Introduction of NH_3 to a $FAPbI_3$ film forms a $FAPbI_3{\cdot}xNH_3$ complex, which is however solid at room temperature, due to insufficient intake of ammonia by the perovskite. Therefore, the authors have exposed a FA-rich films to a NH_3 gas at -15°C allowing the x in the complex to reach values close to 12 (Figure 4.8c), at which point a colorless liquid film was formed. Once the film was removed from the NH_3 environment and heated on a hotplate, an α-phase FA-based perovskite film crystallized.

This phenomenal discovery highlighted that FA-containing perovskites (which

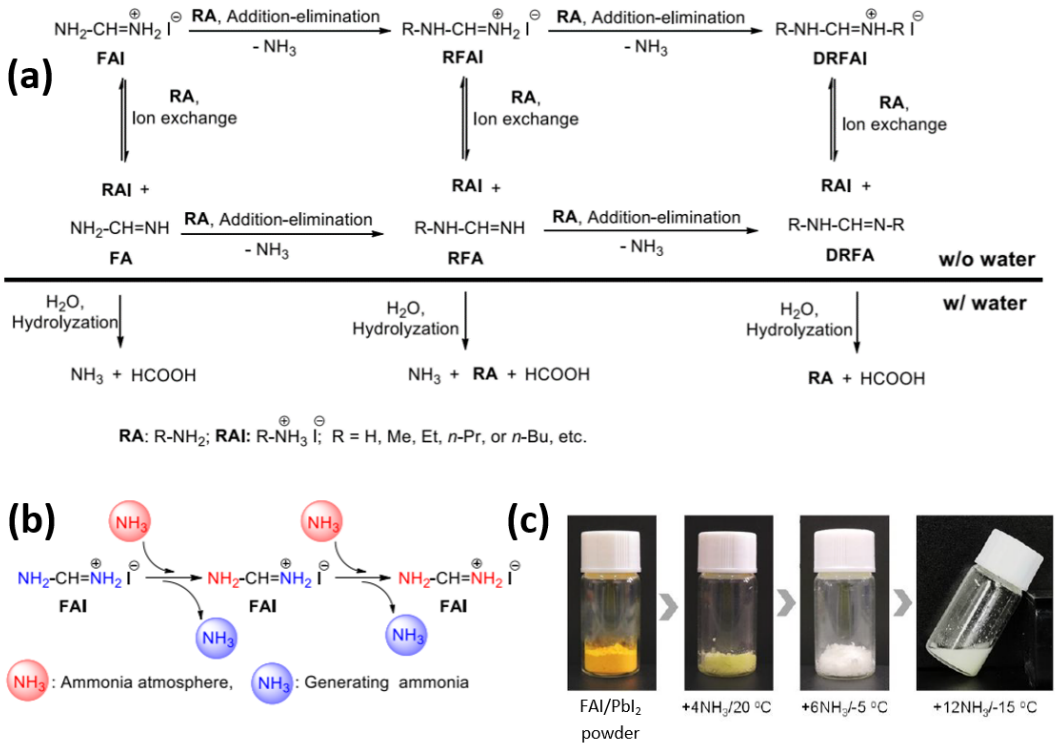


Figure 4.8: (a) Chemical reactions between amines (**RA**), FAI and cations with NH_3 group in the presence of methylamine, showing that two types of reactions are possible: (1) ion exchange, which is reversible and (2) addition-elimination, which is irreversible and is the reason behind inability of FA-based perovskites to recrystallize back into 3D cubic α-phase due to loss of ammonia. In addition, another reaction is possible – (3) hydrolization, if water is present. (b) Proposed chemical reaction behind liquefaction of FA-based perovskites using ammonia. (c) Photographs of FAI/PbI_2 powders reacted under NH_3 atmosphere at different temperatures. Adapted and reprinted with permission from [363].

are now widely used for the high-efficiency PSCs) cannot be produced via MA^0-mediated liquefaction-recrystallization approach and NH_3-based treatments need be implemented in this case.

Chapter 5

Perovskite solar cells with carbon-based electrodes – quantification of losses and strategies to overcome them

5.1 Preamble

Although from the review study described in chapter 3 the CPSCs with low-temperature carbon-based electrodes seem more promising in terms of reaching higher PCEs, there has been no experimental study demonstrated proving this hypothesis. Moreover, one critical question regarding perovskite photoabsorber in CPSCs have never been answered: what are the differences between perovskite embedded in the ZrO_2 scaffold (in cells with high-temperature carbon-electrodes) and planar perovskite film (in cells with low-temperature carbon electrodes)? In addition, due to significant differences in device architecture, the dominant power loss mechanisms and, consequently, methods for further device improvement can vary. Therefore, the author of this dissertation initiated an extensive study of quantification of losses in PSCs with carbon-based electrodes (including both: low- and high-temperature electrodes) and development of strategies to overcome them,[‖] which will be presented in the following.

[‖] This chapter (except for the critical discussion in section 5.7) has been published as peer-reviewed research paper in the scientific journal "Advanced Energy Materials" (impact factor 2022: 29.4):

Bogachuk, D., Yang, B., Suo, J., Martineau, D., Verma, A., Narbey, S., Anaya, M., Frohna, K., Doherty, T., Müller, D., Herterich, J.P., Zouhair, S., Hagfeldt, A., Stranks, S.D., Würfel, U., Hinsch, A., Wagner, L. (2022) Perovskite Solar Cells with Carbon-Based Electrodes-Quantification of Losses and Strategies to Overcome Them. *Adv. Energy Mater.*, 12(10), p.2103128.

The individual contributions were as follows:

- **D.B.**: conceptualization of the study, design of the experiments, spatially-photoluminescence measurement, development of numerical simulation, measurements of light-intensity dependent behavior of fabricated devices, JV-, EIS, UV-Vis measurements of all manufactured solar cells, analysis of data, results interpretation, manuscript and figure preparation, coordination of co-author contributions
- **B.Y.,J.S.**: manufacturing perovskite films, partial and complete solar cells with low-temperature carbon electrodes, TRPL and XRD measurements
- **D.Ma.,S.N.**: manufacturing complete solar cells with high-temperature carbon electrodes
- **A.V.**: manufacturing samples of perovskite embedded in ZrO_2 on glass, partial solar cells
- **M.A.,T.D.**: performing spatially-resolved absolute hyperspectral PL measurement
- **K.F.**: extraction of PL- and QFLS-maps using a Python-based script, assistance with manuscript writing
- **D.Mü.**: measurements of light-intensity dependent behavior of fabricated devices
- **J.P.H.**: performing and analyzing LBIC measurements
- **S.Z.**: performing EIS measurements, assistance with manuscript writing
- **A.Ha.,A.Hi.**: providing valuable comments
- **S.D.S.,U.W.**: providing important conceptual ideas and valuable comments to the manuscript
- **L.W.**: supervision of the work, providing important conceptual ideas and assistance with manuscript preparation
- **All authors**: reviewed the manuscript

5.2 Abstract

Carbon-based electrodes represent a promising approach to improve stability and up-scalability of perovskite photovoltaics. The temperature at which these contacts are processed defines the absorber grain size of the perovskite solar cell: in cells with low-temperature carbon-based electrodes (L-CPSCs), layer-by-layer deposition is possible, allowing perovskite crystals to be large (>100 nm), while in cells with high-temperature carbon-based contacts (H-CPSCs), crystals are constrained to 10-20 nm size. To enhance the power conversion efficiency of these devices, the main loss mechanisms were identified for both systems. Measurements of charge carrier lifetime, quasi-Fermi level splitting (QFLS) and light-intensity-dependent behavior, supported by numerical simulations, clearly demonstrate that H-CPSCs strongly suffer from non-radiative losses in the perovskite absorber, primarily due to numerous grain boundaries. In contrast, large crystals of L-CPSCs provide long carrier lifetime (1.8 µs) and exceptionally high QFLS of 1.21 eV for an absorber bandgap of 1.6 eV. These favorable characteristics explain the remarkable open-circuit voltage (V_{OC}) of over 1.1 V in hole-selective layer-free L-CPSCs. However, the low photon absorption and poor charge transport in these cells limit their potential. Finally, effective strategies are provided to reduce non-radiative losses in H-CPSCs, transport losses in L-CPSCs and to improve photon management in both cell types.

5.3 Introduction

Following remarkably rapid development of power conversion efficiencies (PCEs) of perovskite solar cells (PSCs) in the past years, [49, 114] the stability of perovskite-based photovoltaic (PV) devices became the center of attention for numerous researchers across the globe. [72, 123] While, numerous various techniques to solve this issue (*e.g.* passivation, [372, 373] additive engineering, [374, 375] barrier layer [186,376] have been proposed so far, the most stable PSCs were achieved by the incorporation of a carbon-based back-contact. [203, 377, 378] Its highly hydrophobic properties, chemical inertness and large thickness provide a strong protection of the sensitive layers underneath it from the ambient environment. [210] However, PCEs of PSCs with such carbon-based electrodes (CPSCs) are still behind the ones demonstrated in "conventional" perovskite solar cells with metal-based contacts, which is partially attributed to the lower conductivity of the graphite-based material, its contact to the layer underneath, higher parasitic absorption coupled with rather poor reflection and not well-aligned electrode work-function. [210]

In 2013, Ku *et al.* have been the first to propose the concept of a CPSC, where the carbon-based contact would need a high-temperature treatment (400°C) for removal of organic solvents and binders. [122] As hybrid lead-halide perovskites degrade at temperatures above 150°C, [357] this implies that the perovskite cannot be introduced into the cell stack before this electrode is deposited. Therefore,

each layer of the device stack needs to be mesoporous to allow the perovskite to be added at the last processing step. These PSCs with a carbon-based electrode cured at high temperatures (H-CPSCs) are particularly attractive for perovskite PV commercialization, since the entire cell stack can be deposited on a large scale using industrially relevant manufacturing techniques. [124, 209, 216] Recently we have shown that utilization of perovskite solar modules with such carbon-based electrodes can effectively reduce the CO_2-footprint of the PV module down to 3.35 g CO_2-eq./kWh, which is less than 5 % of the CO_2-footprint of the conventional silicon-based module. [216] Such strong reduction of the green-house emissions during PV module manufacturing would be tremendously helpful in reducing negative anthropogenic impact on environment, especially if we aim towards terawatt-scale PV systems in the near future.

Shortly after the development of H-CPSCs, an alternative approach was proposed, based on the development of a carbon paste which contains solvents and binders that can be removed at lower temperatures allowing for the electrode deposition after the perovskite is introduced. [198, 379] These PSCs with a low-temperature cured carbon-based contact (L-CPSCs) have several advantages regarding the degrees of freedom during device preparation (*e.g.* layer-by-layer deposition, wide range of applicable charge transport layers, compatibility with flexible substrates). [210] For comparison, the current PCE record of L-CPSCs is > 20 %, [314] which is still slightly above the recently obtained record of 18.1 % PCE in H-CPSCs (whereby it is noteworthy that the latter did not have a hole-selective layer). [380]

Although CPSCs become more and more attractive in terms of stability, upscalability and low CO_2-footprint, [210, 216] so far, a quantitative comparison between the H-CPSCs and L-CPSCs has not been reported. Identifying why cell properties differ and ideally combining the advantages of both types is of paramount importance for developing high-efficient and stable perovskite PV devices with carbon-based electrodes. Here, we scrutinize the fundamental differences between these two types of CPSCs, starting from analyzing the key difference in the perovskite layer, namely the number of grain boundaries in the photoabsorber. Firstly, we use numerical simulations to study the influence of the number of grain boundaries on CPSC performance losses, which shows that the quasi-Fermi level splitting (QFLS) is reduced in cells with smaller grains. This agrees with our experimental evidence demonstrating that even for an identical perovskite composition the QFLS is indeed lower in H-CPSCs than in L-CPSCs. Moreover, the charge carrier lifetime in perovskite with large grains (as utilized in L-CPSCs) is higher by over one order of magnitude than in perovskite with smaller grains (similarly to H-CPSCs) suggesting a lower non-radiative recombination rate and resulting in a strong difference of almost 120 mV in the final open-circuit voltage (V_{OC}) of these devices. Furthermore, we analyze the origins of the fill factor (FF) losses, constituted by non-radiative recombination and transport losses.

Disentangling between different individual contributions to the transport losses we are able to identify promising methods to improve carrier extraction and transport. Finally, we combine all the presented evidence to outline a roadmap for the most promising routes to achieve high PCEs in CPSCs. This work paves way for scientists in the perovskite community to accelerate the development of advanced, efficient, stable, low-cost and sustainable perovskite PV devices with carbon-based electrodes, which contain enormous potential for industrialization and bringing humanity closer towards climate change goals.

5.4 Experimental details

Fabrication of samples

Perovskite as a planar layer (PaPL) and perovskite in porous layer (PiPL)

Perovskite as planar layer (as in L-CPSCs)
Glass substrates were sonicated in 2 % Hellmanex water solution for 30 min, acetone for 15 min and ethanol for 15 min, respectively. Then, all substrates were further cleaned by UV-Ozone for 15 min. The perovskite precursor solution was prepared by dissolving a mixture of methylammonium iodide (1.25 mmol, Dyenamo), lead iodide (1.29 mmol, Alfa Co. Ltd.), 5-AVAI (0.075 mmol, TCI) in 1 mL mixture of DMF and DMSO (DMF:DMSO=9:1 v/v, Acros). The perovskite solution was spin-coated through two-step program (1000 rpm for 10 s and 4000 rpm for 20 s) with pouring chlorobenzene as an anti-solvent 15 s before the end of the second step. Then the substrates were annealed at 100°C for 40 min in dry air.

Perovskite in porous layer (as in H-CPSCs)
The methylammonium lead iodide perovskite precursor solution containing 5-ammonium valeric acid additive (5-AVAI) was provided by Solaronix SA. This solution was deposited selectively on the area of interest by inkjet with a 10 pL droplet volume and a spatial resolution tuned to match the desired quantity. The optimal resolution was determined to be 350x350 dpi. The freshly printed samples were subsequently annealed for 10 min on a hot-plate set to 50°C, thus forming the perovskite crystals in the porous electrode structure.

Perovskite solar cells with low-temperature treated carbon-based electrodes (L-CPSCs)

Fluorine doped tin oxide (FTO) substrates (NSG-10) were chemically etched by zinc powder and 4 M HCl solution and cleaned in the same manner as described for the glass substrates. Then, a compact TiO_2 layer was deposited on cleaned FTO

substrates via spray pyrolysis deposition from a precursor solution of titanium diisopropoxide bis(acetylacetonate) (Sigma-Aldrich) in anhydrous ethanol (Acros), with oxygen as carrier gas. Substrates were heated at 450°C and kept at this temperature for 15 min before and 30 min after the spray of the precursor solution, then left to cool down to room temperature. Mesoporous TiO_2 layer was spin-coated at 4000 rpm for 20 s, with the acceleration rate of 2000 rpm/s, using a 30 nm TiO_2 paste (Dyesol 30 NR-D) diluted in ethanol with 1:6 volume ratio. After the spin-coating, the substrates were dried at 80°C for 10 min and then sintered at 450°C for 30 min under dry air flow. Perovskite layer was prepared in the same manner as described for the glass substrates. The carbon paste (Dyenamo) was deposited on the perovskite film by doctor-blading and dried at 100°C for 15 min. This procedure was carried out in ambient atmosphere.

Perovskite solar cells with high-temperature treated carbon-based electrodes (H-CPSCs)

Devices were fabricated on 10x10 cm^2 plates of FTO-coated glass (TCO22-7/LI, sheet resistance – 7 Ω/sq.). First, a laser pattern defined cathode and anode areas with an automated fiber laser. After that, the substrate was subjected to sequential cleaning steps in 1 % aqueous solution of Hellmanex (Sigma-Aldrich), acetone (Carl-Roth), and isopropanol (Sigma-Aldrich) respectively (20 min each) in an ultrasonic bath and subsequently dried in air. The thin compact titania layer (c-TiO_2) was grown by spray-pyrolysis on a hot-plate set to 450°C, using a glass mask to protect the contact areas. A volume of 20 mL of titanium diisopropoxide bis (acetylacetonate) (Sigma-Aldrich) diluted in absolute ethanol (Alcosuisse) (1:160) was sprayed with oxygen as a carrier gas, and warming was prolonged for 30 min before allowing the sample to cool down. An array of 18 electrodes was subsequently defined by screen-printing silver contacts (silver paste Elcosil SG/SP), m-TiO_2 (titania paste Ti Nanoxide T165/SP), ZrO_2 (zirconia paste Zr Nanoxide ZT/SP) and carbon layers (carbon-graphite paste Elcocarb B/SP) using a 100-40, 165-30, 90-48, and 43-80 mesh stencil, respectively (the number of strands is per cm). After printing the wet film, each screen-printed layer was allowed to dwell for 10 min before drying at 120°C for 10 min, followed by a firing step at 500°C (or 400°C for carbon) for 30 min, after a 30 min ramp.

This solution was deposited selectively on the area of interest by inkjet similarly to the manufacturing procedure of filling perovskite in ZrO_2 layer (PiPL), mentioned above. The only difference was the optimal resolution, which was determined to be 1200x1200 dpi. The freshly printed samples were subsequently annealed for 10 min on a hot-plate set to 50°C, thus forming the perovskite crystals in the porous electrode structure. The resulting devices were submitted to heat and damp treatment at 40°C and 75 %R.H. for 150 h. according to the previously reported method by Hashmi et al. [381]

Characterization

Morphological and structural properties

The X-ray diffraction patterns were recorded with PANalytical Empyrean system with a PIXcel-1D detector, Bragg-Brentano beam optics and parallel beam optics. Light source is from copper Kα beam filtered with nickel β filter. Diffraction spectra were characterized between 2θ of 3° and 50° at a scan rate of 1° per minute with the step width of 0.02°. Scanning Electron Microscopy (SEM) images were obtained with a Zeiss Auriga 60 electron microscope. The current-density and voltage curves of fabricated devices were measured with a source meter (Keithley 2400) at a scan rate of 20 mV/s using a class A solar simulator providing 100 mW/cm2, AM1.5G illumination. The layer surface morphology and roughness were investigated by an atomic force microscope (Bruker Dimension Edge AFM) in a tapping mode. The scanned surface area was 5x5 m^2 with 512 data points per line.

Opto-electronic Characterization

Time-resolved photoluminescence (TRPL) was measured by using a picosecond pulse diode laser (EPL-405) with an excitation wavelength of 405 nm, pulse width of 49 ps. The current-density and voltage curves of solar cells were measured with a source meter (Keithley 2400) at a scan rate of 20 mV/s using a class A solar simulator providing 100 mW/cm^2, AM1.5G illumination. The devices were covered with a black metal mask with an active area of 0.16 cm^2.

The light-intensity dependent V_{OC} and J_{SC} measurements were carried out using a pulsed green LED (λ=525 nm, 1 A, custom fast switching driver). The intensity was controlled by several reflective neutral density filters from Schott (OD0 - OD7). The V_{OC} was measured via a custom build buffer amplifier with R_{in} >10 GΩ to ensure negligible external current flow. The J_{SC} was measured using a trans-impedance amplifier from Femto (DLPCA-200). J_{SC} measurements were used to calibrate the system to the AM1.5G measurements from the solar simulator. The signals were recorded with a digital oscilloscope from PicoScope (5000 series). The Electrochemical Impedance Spectroscopy (EIS) was carried out using a Ivium CompactStat in the frequency range of 100 mHz to 1 MHz at negative voltage bias of -0.6 V and under illumination. The fitting of the EIS-response to the equivalent circuit was conducted via IviumSoft program.

Quasi-Fermi level splitting (QFLS) values were extracted from absolute calibrated, hyperspectral photoluminescence (PL) maps. The maps were acquired using a calibrated IMATM Vis system from Photon Etc. through a Nikon 20x objective. The samples were excited using a 405 nm continuous wave laser at an intensity of $\approx$ 60 mW cm^{-2}, approximately one sun illumination intensity for this perovskite bandgap and a 405 nm wavelength excitation. A commercially available

confocal Raman scanning microscope (Witec) is used to focus a laser beam onto the sample (laser spot FWHM ≈ 5 µm). With a low noise current amplifier the current output of the cell can be measured at each scanning position every 40 µm). The laser used for excitation is a 635 nm diode laser (Laserpower = 1.1 µW). Absolute PL spectrum measurements were carried using an FLS 1000 custom, Edinburgh Instruments with an integrating sphere containing single-photon counting device. The excitation in this case was provided by a 520 nm laser. For the evaluation of PL quenching and charge-carrier extraction, spatially-resolved PL images were obtained by an OLYMPUS BX50 stereomicroscope and a sCMOS camera ("Zyla 5.5 sCMOS" by Andor) with a long-pass filter while the partial illumination of the sample was provided by a 623 nm red light-emitting diode (Thorlabs, SOLIS-623C). Its intensity is adjusted to a value such that I_{SC} of the measured cell matches I_{SC} measured on the mismatch corrected solar simulator ensuring the PL measurement to be conducted in an excitation regime close to one sun illumination.

Simulation

Simulation parameters and further details are discussed in the following supplementary tables S1 and S2. SCAPS is an open-source 1D drift-diffusion simulation tool, that can be obtained from https://users.elis.ugent.be/ELISgroups/solar/projects/scaps upon the request from the developers Marc Burgelman *et al.*

5.5 Results and discussion

Two Types of Perovskite Solar Cells with Carbon-based contacts (CPSCs)

Although H-CPSCs and L-CPSCs both belong to the group of PSCs with carbon-based electrodes, they display significant differences in the device architecture and their opto-electronic characteristics. L-CPSCs are made using layer-by-layer deposition, allowing to precisely control the perovskite layer thickness and grain size, whereas the H-CPSCs are manufactured by the deposition of all the mesoporous layers first, which are later infiltrated by the perovskite solution. Since the pore size in the mesoporous titanium oxide (m-TiO_2) and zirconium oxide (ZrO_2) layers of H-CPSCs are typically in the range of 10-20 nm, the perovskite crystals are most probably constrained to this size (Figure 5.1a), inducing numerous grain boundaries (GBs) along the entire solar cell stack, presumably causing non-radiative recombination and hindering carrier transport. In contrast, in L-CPSCs the perovskite crystals can reach sizes of hundreds of nanometers, (potentially) providing a single grain along the entire layer thickness, which is likely to be beneficial for the solar cell performance (Figure 5.1b). Thus, one of the most fundamental differences in

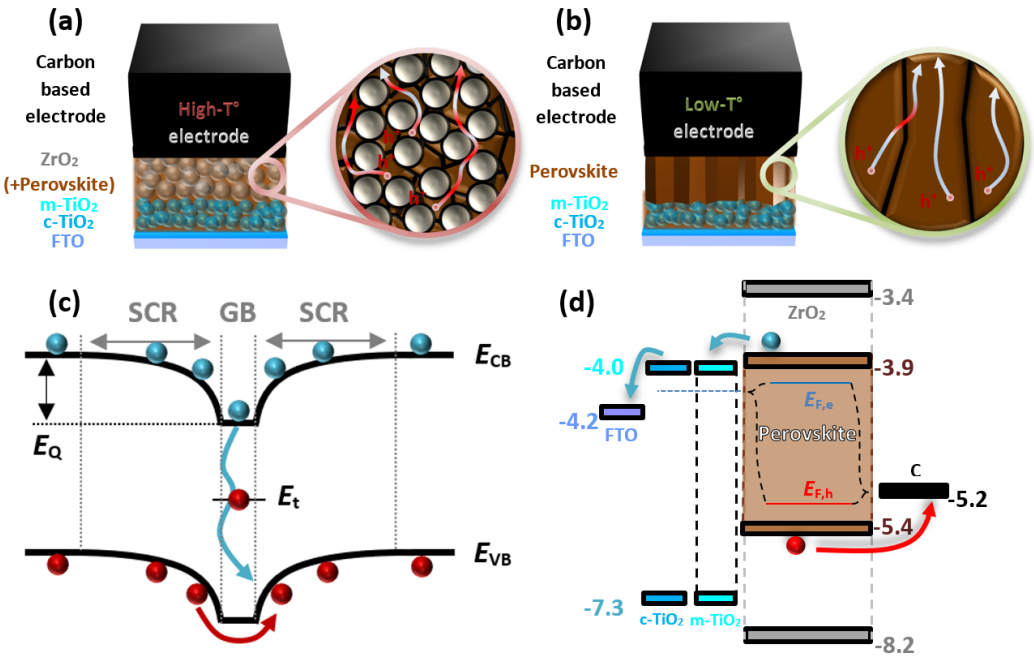


Figure 5.1: (a,b) Illustration of two types of perovskite solar cells with carbon-based back-electrodes (CPSCs), showing cell stacks and charge carrier transport, which in the case of CPSCs with electrodes treated at high-temperature (H-CPSCs) is hindered by multiple grain boundaries in the perovskite layer due to constrained pore size of the ZrO_2 layer. (c) Energy band diagram of the region with charged grain boundary (GB) having a band offset of E_Q, inducing a space-charge region (SCR) which extends toward the bulk of the grains, providing non-radiative recombination pathways and hindering the transport of holes, by creating a potential barrier. (d) Energy band diagram of CPSCs, where the electrons (blue) are extracted by m-TiO_2 and further conducted to the front electrode, whereas holes (red) are extracted by carbon-based back-electrode.

the absorber layer between both cell types is the number of GBs and the transport distance.

Numerical simulation of neat perovskite and CPSCs with different grain boundary densities

In order to evaluate the effect of GBs on the solar cell performance, we firstly simulate perovskite layer and CPSCs according to the standard representation of GB in silicon-based material, where creation of vacancies as well as bent, strained or broken bonds is typically observed, all of which increases the defect density at the GBs in case the defects are not passivated. [9, 382, 383] In this case, the charge carriers trapped at these defects build up a charge Q_{GB}, which is compensated by accumulating the opposite type of free charge carriers from

the bulk at the GB due to Coulombic forces. [384] This leads to the creation of a space-charge region (SCR) and hence an electric field at the GB, bending the energy bands, similarly to semiconductor-metal-semiconductor contacts (Figure 5.1c). [382]

According to several reports investigating the nature of grain boundaries in perovskites, the band bending at GBs in perovskite is normally downwards, [384, 385] likely to be due to charged iodide vacancies (V_I^+), implying positively charged GBs. [383] Consequently, on one hand the holes have to overcome a potential barrier at the GB, perturbing the carrier flow and negatively affecting the mobility and overall resistivity, while on the other hand, more electrons will recombine non-radiatively via the defect energy level E_t. Although in this work we implement the aforementioned GB representation in our simulation, we also note that different processing conditions can significantly affect structural properties of GB in perovskite films, even though its composition is the same. [386] Hence, the GB simulation in different halide perovskite films or layers has to be carried with great caution, as there is no generalized model developed at the moment, according to our knowledge. [387]

We first evaluate the impact of the GBs on the quasi-Fermi level splitting (QFLS) in neat perovskite absorber (400 nm thick) by using a SCAPS numerical simulation tool, utilizing drift-diffusion model (simulation parameters are described in Table S1). Although it is a 1D model (meaning that it does not allow for lateral variations in properties) the vertical grain stacking is more detrimental for the carrier transport, which could be simulated in SCAPS. Each grain boundary was simulated based on the energetic band diagram in Figure 5.1c which transverses across the perovskite layer thickness. Here only one type of GB was considered with properties (*e.g.* E_t, Q_{GB}) adjusted to match the experimental values determined in literature for similar type of perovskite. [388, 389] Figure 5.2a depicts how the high number of grain boundaries (*i.e.* smaller grain size) lowers the QFLS of the perovskite photoabsorber. In this model, a crystalline $MAPbI_3$ (MA – $CH_3NH_3^+$) absorber layer with an (ideal) single grain along the layer thickness has a QFLS of 1.33 eV (which is the radiative limit for perovskite absorber with energy bandgap of 1.6 eV [22, 390, 391]. Introducing one GB along the layer thickness (leading to the grain size of 200 nm) with a trap density N_t=10^{16} cm^{-3} (Figure 5.2a) reduces the splitting already by 100 meV. For comparison, several reports have demonstrated that the typical defect densities in perovskite films (most of which are shallow traps) are in the range of 10^{17}-10^{19} cm^{-3} [120, 388, 392], with deep trap densities in the order of 10^{15}-10^{16} cm^{-3}, which dominate the non-radiative recombination. [393] Notably, even if one considers a very optimistic case of non-radiative recombination exclusively at the GBs with a very low N_t=10^{14} cm^{-3}, a PSC with a grain size of 25 nm, which is similar to the crystal size found in H-CPSCs, [394] would still have a reduction of QFLS by ~63 meV.

To further demonstrate the negative effect of GBs on the final solar cell perfor-

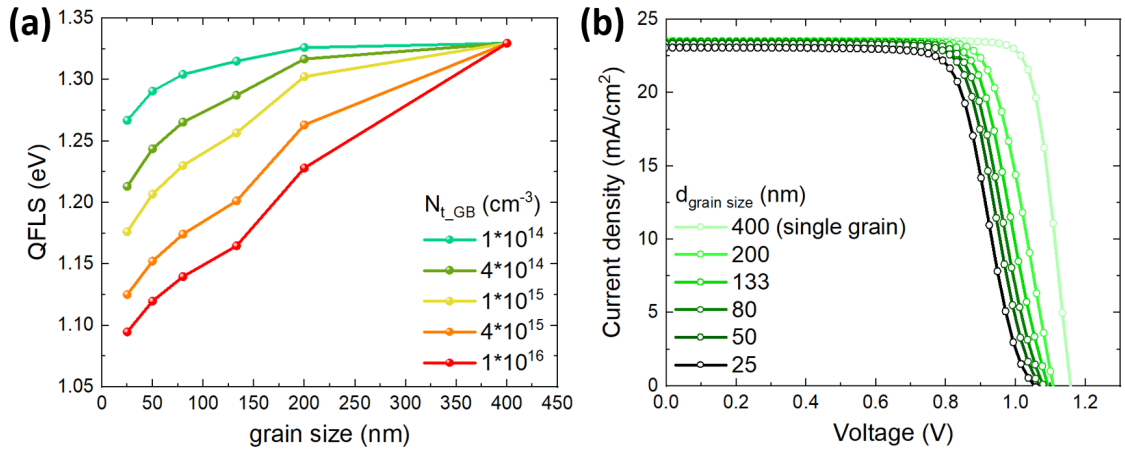


Figure 5.2: (a) QFLS in simulated neat perovskite films with different numbers of grain boundaries (b) JV-curves of the simulated CPSCs with different numbers of grain boundaries. The cell parameters can be found in Figure 5.1d and Table S1.

mance, we simulate the hole-transport-layer (HTL)-free PSC with a carbon-based back-contact, according to the energy band diagram shown in Figure 5.1d (more detailed simulation parameters can be found in Table S2). In order to focus only on the contribution of grain boundaries on the performance loss, in this simulation we only consider non-radiative recombination at the GBs and ignore interfacial recombination at charge extraction layers. In Figure 5.2b the JV-curves of the simulated cells are depicted where the FF and the V_{OC} are significantly affected by grain-boundaries, whereas the short-circuit current density (J_{SC}) is affected only slightly.

The non-radiative recombination can affect not only the QFLS, and consequently the V_{OC}, but also the FF, especially with a considerable amount of recombination happening at the interfaces. [395] In order to demonstrate the effect of GBs on non-radiative recombination we firstly look at the V_{OC}, which in the case of radiative limit can be defined as [390, 396]:

$$V_{OC,rad} = \frac{k_B T}{q} \ln\left(\frac{J_G}{J_{0,rad}} + 1\right), \tag{5.1}$$

where k_{B} is Boltzmann constant, T is temperature, q – elementary charge, J_{G} – photogeneration current and $J_{0,\mathrm{rad}}$ – radiative thermal equilibrium recombination current density in the dark (which in the absence of non-radiative recombination is equal to the dark saturation current J_0). J_{G} and $J_{0,\mathrm{rad}}$ can be found by multiplying q with an integrated product of external quantum efficiency (EQE_{PV}) and incident photon flux, namely of AM1.5G for J_{G} and of black body ($\mathrm{T_{BB}}$=300 K) for $J_{0,\mathrm{rad}}$, respectively (detailed derivation is shown in Supplementary Note 1).

The EQE_{PV} onset and the emitted photon flux in the dark Φ_{em} of the simulated CPSCs with different grain sizes are presented in Fig. S1. As one can see, the EQE_{PV} is affected by the grain size especially in the region close to the bandgap energy, reducing both: $J_{0,rad}$ and J_G. The calculated values are presented in Table S3. Based on the difference between the obtained $V_{OC,rad}$ and the final V_{OC} of the simulated CPSCs we can estimate the $V_{OC,loss}$ that is lost due to contribution of non-radiative recombination, which increases with higher number of grain boundaries (Table S3).

The calculated external Photoluminescence Quantum Yield (PLQY) is shown in Table S3, which is the lowest for samples with most GBs along the cell thickness and is the highest in the CPSCs without any GBs, where the PLQY approaches 2.5 %. Moreover, the total dark saturation current J_0 is lowest in simulated CPSCs without GBs and is the highest in cells with a perovskite grain size of 25 nm, due to large contribution of recombination-active traps at the GBs. The simulation results demonstrate, that reducing the grain-boundaries in CPSCs should significantly help to reduce non-radiative recombination in the cell, slightly improve the light-absorption near the band edge and thus boost its V_{OC} (as the higher V_{OC} is a consequence of reduced non-radiative recombination) and overall PCE. Now we move from the numerical simulation of CPSCs with GBs to the actual manufactured devices.

Properties of perovskite layer in CPSCs

Morphological and crystallographic differences

In order to compare non-radiative losses of perovskite layers in both L-CPSCs and H-CPSCs, we firstly analyze the properties of a pristine absorber layer. For this, the perovskite has to be deposited on a dielectric substrate that does not allow for charge carrier extraction, such as glass. The ZrO_2 layer, in which the absorber layer in H-CPSCs is normally embedded into, is also dielectric as it has a conduction band minimum at around -3.4 eV and a valence band maximum at around -8.2 eV (Figure 5.1b), [125,397] meaning that it can neither extract electrons nor holes from the perovskite. Therefore, to mimic the perovskite absorber behavior in H-CPSCs, we deposited perovskite in a ZrO_2 porous layer (of same thickness as in complete solar cells) on glass substrates. To ensure that perovskite completely fills the pores of a ZrO_2 layer without having any capping layer on top, here we employ ink-jet pipetting to precisely control the filling conditions, producing samples that we further refer to as perovskite in porous layer (PiPL). The perovskite as planar layer (PaPL) was spin-coated on glass to produce a 350 nm film which is normally used to manufacture complete L-CPSCs. For the entire study, we utilize $5AVA_{1-x}MA_xPbI_3$ perovskite (5AVA-aminovaleric acid, MA-methylammonium and $0<x<1$), which

has been a popular choice of perovskite in H-CPSCs over the last years, due to high moisture retention properties, favorable anchoring of the carboxylic acid group to the TiO_2 during crystallization and improved infiltration through the porous scaffold. [125, 203, 398]

Fig. S2a shows the cross-sectional view of the PiPL displaying the absence of any capping layer above ZrO_2, while simultaneously filling the porous layer homogeneously across its entire thickness. Looking at the AFM images (Fig. S3) of both layers we note that the PaPL has a smooth surface morphology with a 12.9 nm average surface roughness in comparison to a larger value of 19.5 nm in the case of PiPL. The X-ray diffraction measurements in Fig. S4 show much more pronounced peaks corresponding mostly to $MAPbI_3$ (since the amount of 2D $5AVAPbI_4$ perovskite is rather small) perovskite in PaPL than in PiPL due to higher degree of crystallinity. However, the diffraction angle of core reflection planes (*e.g.* (110) and (220)) remain the same in PaPL and PiPL, confirming that perovskite crystal structure and lattice dimensions are nearly identical in both configurations, planar and mesoscopic.

Non-radiative losses in perovskite absorber due to grain boundaries

To quantify the charge carrier lifetime in PiPL and PaPL we firstly carried out time-resolved photoluminescence (TRPL) measurements (Figure 5.3b). From the transient photoluminescence response in the high-level injection regime the lifetime for PiPL was found to be much lower than that of the PaPL: 72.9 ns in comparison to that of nearly 1.8 µs in planar films. This astonishing difference in carrier lifetime, despite identical perovskite (elemental) composition, demonstrates the presence of excessive non-radiative recombination in PiPL, most likely due to numerous GBs as discussed earlier. This will have detrimental effects on the IV-parameters of the H-CPSCs, especially V_{OC}. Although V_{OC} is not affected by diffusion length (which is coupled to carrier lifetime by definition) in first order, it is strongly influenced by the lifetime and therefore the potential of H-CPSCs to reach high PCEs becomes limited.

Although it has been often demonstrated that grain-size engineering in perovskite films is a promising method to reduce the non-radiative recombination at GBs, [362, 388, 399–401] more studies suggest that the exact nature of GBs and their effect on PSC performance is still ambiguous. [384] The intuitive affiliation of GBs with differences in morphological properties of perovskite films (as can be seen from, for example, scanning electron microscopy SEM images) does not account for sub-grain crystallographic heterogeneity within the same morphological domain. [402–404] highlighting that for the exact identification of a GB in halide perovskite, diffraction-based techniques are required. [387, 405] In this work, however, we use the term grain boundary to describe "morphological grains

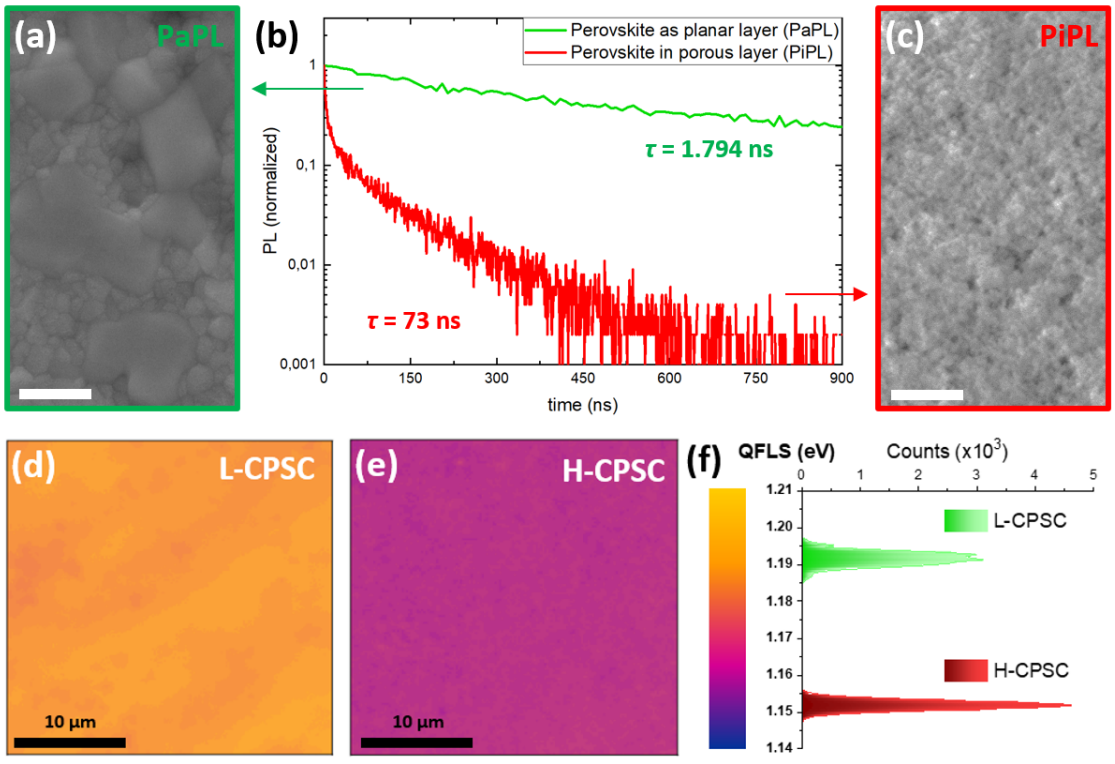


Figure 5.3: Top-view SEM image of (a) perovskite as planar layer (PaPL) and (c) perovskite in porous layer (PiPL). (b) Time-resolved photoluminescence (TRPL) measurement of perovskite produced as a planar layer (as it is done in L-CPSCs) and perovskite embedded in nanoporous ZrO_2 (as it is done in H-CPSCs). Scale bar – 300 nm. QFLS maps of (d) PSC with a low-temperature cured carbon electrode (L-CPSC) and (e) with high-temperature cured carbon-electrodes (H-CPSC). (f) The color scale and pixel distributions for each sample.

boundaries", observed from SEM measurements. Although, these morphological grain boundaries do not define the dimensions of a continuous uninterrupted perovskite lattice, an experimental evidence shown in literature suggests that larger morphological grains visible from SEM also result in larger grains with the same orientation. [404] The top-view SEM images (Figure 5.3a and Figure 5.3c) confirm that PaPL indeed includes large-sized perovskite crystals (with some small crystals in between as well).

Next, we utilize hyperspectral absolute PL imaging on PiPL and PaPL to evaluate the local non-radiative recombination of neat perovskite layers (Fig. S5a,b) and complete cells in both configurations: L-CPSCs and H-CPSCs (Fig. S7). The obtained PL maps, clearly demonstrate that samples with large perovskite crystals (PaPL and L-CPSC) exhibit higher photoluminescence intensity, highlighting the reduced non-radiative recombination in these samples and suggesting a lower

number of defects. Notably, we observe a slight difference in the PL peak position, where the samples with larger crystals are red-shifted by ~3 nm, relative to the spectral peak position of the sample with small crystals (Fig. S7c). We attribute this to a change in Pb-I bond strain and its effect on the material bandgap, when perovskite grains differ in size, as was demonstrated in earlier works. [353, 406–409]

To confirm our hypothesis that the perovskite/ZrO_2 interface does not introduce an additional loss channel for non-radiative recombination, we carried out absolute photoluminescence measurements (detecting all photons, arising from the radiative recombination in the semiconductor) on PaPL samples deposited on top of glass, ZrO_2 and m-TiO_2 (Fig. S6). The PL intensity is similar in samples deposited on glass and ZrO_2, suggesting that ZrO_2 does not cause a reduction in PL (and therefore charge-carrier densities). For comparison, m-TiO_2/PaPL sample has a significantly reduced PL intensity due to additional quenching of charge-carriers. Thus, we confirm that the perovskite/ZrO_2 interface does not introduce a noticeable non-radiative recombination mechanism and the reduction in PL, QFLS and carrier lifetime in H-CPSCs is ascribed to numerous grain boundaries of perovskite embedded into the nano-porous ZrO_2 and not to perovskite/ZrO_2 interface.

Such absolute steady-state PL measurement also allows for precise quantification methods to experimentally determine the QFLS in solar cells. [94, 410] Assuming that for the photons with energies higher than the PL maximum, the material absorptivity approaches unity, Würfel's generalized Planck law can be used to extract the QFLS from the high-energy slope of the PL spectrum (more details in Supplementary Note 4). [66, 93] Using the PL maps in Figs. S5a and S5b, we construct the QFLS maps of L-CPSCs and H-CPSCs shown in Fig. S5d and S5e.

It was already demonstrated in the photovoltaic community that the QFLS in perovskite solar cells is strongly reduced by the interfaces between absorber and a charge-selective layer. [62, 66, 395] By comparing the QFLS of the neat perovskite with large crystals (PaPL) shown in Fig. S5d with the QFLS of L-CPSC shown in Figure 5.3d, one can observe that the introduction of charge selective layers reduces the QFLS by less than 20 meV, highlighting that the interfacial non-radiative recombination in this cell type is not only low, but comparable (or in some cases even better) with the state-of-the-art p-i-n and n-i-p stacks. [62, 395] In contrast, the QFLS of the H-CPSC is reduced by 40 meV to 1.15 eV. We note that the difference in QFLS of the H-CPSCs and L-CPSCs correlates with the commonly observed large difference in V_{OC} between the H-CPSCs and the L-CPSCs (a comparison of the reported V_{OC}s for H- and L-CPSCs can be found in Fig. S8).

Analysis of manufactured CPSCs with low- and high-temperature carbon-based electrodes

Non-radiative losses in CPSCs

Next, we manufactured H- and L-CPSCs using the same charge-transport layers and the same perovskite composition, to focus only on the absorber layer and to scrutinize an objective comparison between these two structures. We note that the optimal layer thicknesses for each structure are different, and in order to compare only the effect of the absorber layer on the device performance, all the layers in the stack have been optimized to reach highest efficiency in both device configurations. Cross-sectional SEM images (Fig. S9) show that the m-TiO_2 layer had thicknesses of around 150 nm and 500 nm in L-CPSCs and H-CPSCs, respectively. The perovskite layer in L-CPSCs had a thickness of around 350 nm, while in the case of H-CPSC it is embedded into a 1µm thick ZrO_2 layer. Although L-CPSCs have thinner layer thickness which implies a less charge carrier generation, as will be shown below, still the V_{OC} and QFLS are higher. This indicates lower non-radiative recombination and hence a higher number of photoexcited carriers. Both types of cells had an approximately 10-12 µm thick carbon layer completing the cell stack.

The JV-parameters of the manufactured devices with mesoscopic and planar configurations are shown in Figure 5.4a-d. The average V_{OC} of the H-CPSCs is around 920 mV, while some of the L-CPSCs have a V_{OC} above 1.1 V, which agrees with our previously shown long carrier lifetime, high photoluminescence intensity and high QFLS in neat perovskite films of the L-CPSCs. This enormous difference in V_{OC} between the samples despite the same perovskite absorber and contact layers, also suggests that the photoluminescence yield in L-CPSCs is higher than in H-CPSCs by almost three orders of magnitude ($\frac{k_B T}{q} \ln(10^3) \approx 180\,mV$) (assuming T=300 K). We note that according to our knowledge there has not been any report yet on an HTL-free CPSC with a V_{OC} above 1.1 V, utilizing perovskite with such energy bandgap of 1.6 eV (Fig. S8). In Fig. S10 we show the V_{OC} and carrier lifetimes reported in literature, highlighting that these properties of our L-CPSCs are comparable even with the state-of-the-art PSCs, containing an HTL and metallic electrode. Remarkably, the V_{OC} values of 1.1 V align well with the V_{OC} predicted by our simulations of CPSCs with low number of grain boundaries (Table S3). Namely CPSCs with only 1 or 2 grain boundaries along the absorber thickness have the V_{OC} close to 1.1 V, indicating the validity of our simulation.

Based on the obtained current densities J_G and $J_{0,rad}$ (from EQE_{PV}) we calculate $V_{OC,rad}$ and $V_{OC,loss}$, which are presented in Table 5.1. Clearly, L-CPSCs exhibit lower $V_{OC,loss}$ than the H-CPSCs due to lower non-radiative recombination at the grain-boundaries.

The structural disorder of the absorber causes an exponential tail in the ab-

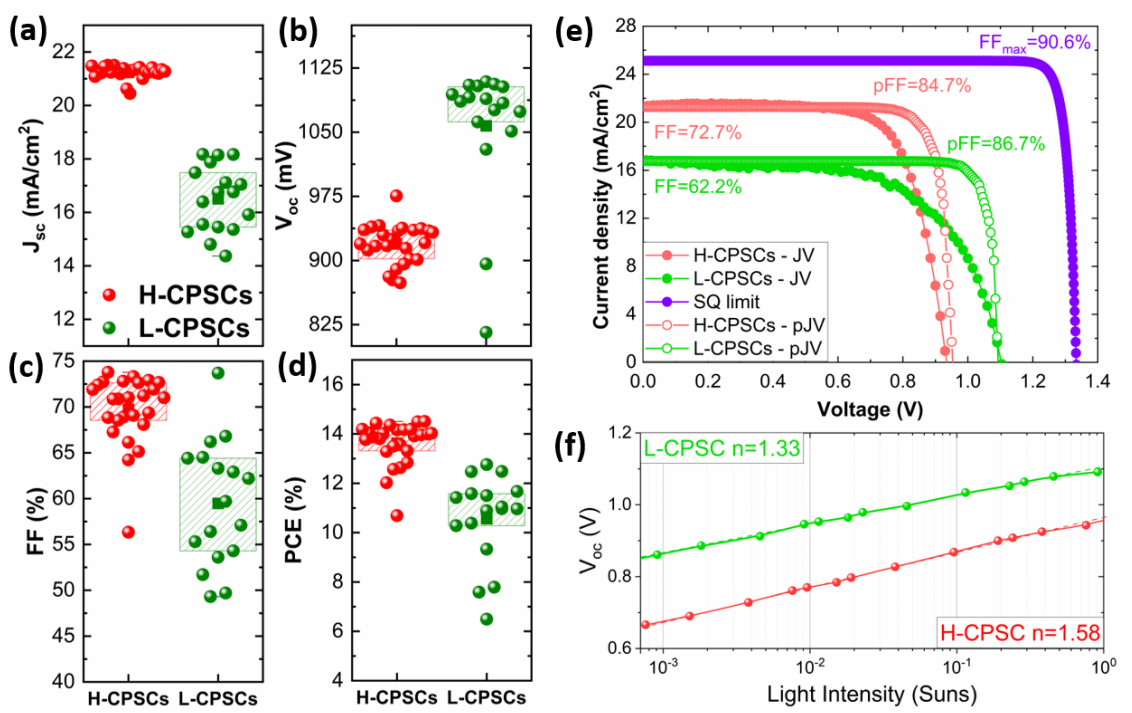


Figure 5.4: (a-d) JV-parameters of the manufactured H-CPSCs and L-CPSCs, (e) JV-curve of champion devices and pseudo-JV-curves obtained from V_{OC}-vs-Light intensity measurement. Ideal JV-curve of a solar cell with the utilized bandgap (purple), which is limited by radiative recombination (obtained from the Shockley-Queisser limit) is shown for comparison. (f) V_{OC}-vs-Light intensity measurement and the ideality factor n for L-CPSC and H-CPSC

sorption coefficient close to the absorption edge due to multiple sub-bandgap states. The slope of the exponential part, which depends on the degree of structural disorder is also described by Urbach energy (E_U). [396] Based on the EQE_{PV}, the Urbach energy for H-CPSCs and L-CPSCs was determined to be 25.8 meV and 18 meV (Fig. S11), respectively, which once again supports the hypothesis that the perovskite crystals grown inside mesoporous ZrO_2 exhibit lower opto-electronic quality than in case of planar large crystals. In fact, Choi *et al.* have also demonstrated that in the mesoporous layers ~70 % of the embedded perovskite consist of highly disordered phase which has significant consequences on the opto-electronic properties. [411]

Non-radiative recombination affects not only the V_{OC} losses but also the FF due to losses during carrier transport (including resistive losses at the GB interfaces). By measuring the dependency of V_{OC} on the incident light intensity, a so-called pseudo JV-curve can be obtained, in order to disentangle between non-radiative and transport losses of the FF, where the latter are caused by resistance of the cell

Table 5.1: Opto-electronic parameters of manufactured H-CPSCs and L-CPSCs as determined by EQE, V_{oc} and absolute PL measurements

	H-CPSC	**L-CPSC**
$\boldsymbol{J_{0,rad}}$ **(mA/cm²)**	$3.2 \cdot 10^{-21}$	$8.1 \cdot 10^{-22}$
$\boldsymbol{V_{OC,rad}}$ **(V)**	1.302	1.33
$\boldsymbol{V_{OC,cell}}$ **(V)**	0.913	1.109
$\boldsymbol{V_{OC,loss}}$ **(mV)**	389	221
QFLS (eV)	1.15	1.192

layers and interfaces between them. [395, 412] Here we employ the same strategy to elucidate the effect of non-radiative and transport losses on the FF of CPSCs in both configurations. Figure 5.4e shows the ideal JV-curve of a solar cell with the utilized bandgap, which is limited by radiative recombination (obtained from the Shockley-Queisser limit), as well as the obtained pseudo-JV for the L-CPSCs and H-CPSCs. The pseudo-FF (pFF) were found to be 86.7 % and 84.7 % for the L-CPSC and H-CPSC, respectively. Clearly, the higher QFLS and lower non-radiative recombination in the perovskite absorber with larger crystals positively affects not only the V_{OC} as was shown earlier but also the FF, providing potential for such "planar" cells to reach higher efficiencies. Nevertheless, the actual FF of the L-CPSCs, obtained from the JV-measurement is lower, suggesting that the transport losses play the dominant role in the reduction of the FF. We also note that the ideality factor n, describing the dominant recombination mechanism in the cell, [22] is rather low in $MAPbI_3$-based L-CPSCs – only 1.33, in comparison to 1.58 in H-CPSCs (Figure 5.4f). This further supports our arguments that non-radiative recombination in L-CPSCs is reduced due to lower number of GBs and carrier trap densities. However, the L-CPSCs seems to suffer more than H-CPSCs from the transport losses.

Charge extraction and transport losses in CPSCs

To look more in depth at the transport losses, we extract the series resistance (R_s) of both cell types from the slope of the JV-curve at V_{OC}. The R_s for H-CPSCs and L-CPSCs were determined to be 6.8 Ωcm² and 14.3 Ωcm², respectively. Based on the geometry of the cell and the transport distance for electrons and holes in the respective electrodes, the total electrode resistance was found to be similar in both cell types: 1.76 Ωcm² for L-CPSCs and 1.25 Ωcm² for H-CPSCs (more detailed discussion of the electrode contribution to the total series resistance is provided in Supplementary Note 5).

Using Electrochemical Impedance Spectroscopy (EIS), we were able to disentangle between the contribution of pure ohmic and charge transport losses. From Nyquist plots presented in Fig. S12, two semicircles appear, which correspond to the capacitor-like behavior of several interfaces of the stack. We attribute the high-frequency semi-circle to the charge transport resistance primarily at carbon/perovskite interface, [197, 227, 260, 300] from which real part of the impedance can be extracted. In H-CPSCs the perovskite/carbon interface has an interfacial resistance of $3.04\,\Omega\text{cm}^2$, whereas in L-CPSCs it was determined to be approximately $11.4\,\Omega\text{cm}^2$ (obtained from fitting the Nyquist plot to the equivalent circuit in Fig. S12). This finding suggests that the interfacial resistance at the perovskite/carbon contact represents the main transport limitation of the L-CPSCs. To confirm this hypothesis, we needed to distinguish between the reduction of FF due to carbon electrode sheet resistance and perovskite/carbon interfacial resistance. Hence, to confirm this hypothesis, the carbon layer was removed from an H-CPSC device and a low-temperature carbon electrode was deposited instead. Thus, an L-CPSC electrode on an PiPL absorber layer has been produced. This allows to compare the performance differences affiliated with the carbon electrode itself and the perovskite/carbon interface while the differences related to the perovskite absorber in both architectures need not to be considered. From the JV-curves before and after carbon electrode replacement in Fig. S13, we observe that the FF drops from nearly 70 % to 58.8 %, respectively which agrees with the mean values of H-CPSCs and L-CPSCs (Figure 5.4c). We attribute this reduction in FF to higher interfacial resistance at perovskite/carbon interface. An effect of sheet resistances can be excluded, since the sheet resistance of low-temperature carbon electrode is even lower than that of high-temperature type.

During perovskite crystallization in mesoscopic layers of H-CPSCs, pores provide multiple nucleation sites, leading to a rather heterogeneous nucleation and growth. Although such crystallization causes multiple defect-induced energy states in the neat perovskite (as demonstrated earlier), it also means that some crystals grow directly on the surface of the carbon-based electrode, which could explain the exceptionally low interfacial resistance of such cells demonstrated earlier. We also note that the second semicircle in the Nyquist plot, which is attributed to the recombination resistance (and therefore should be high) is 50 times larger in L-CPSCs than in H-CPSCs, supporting the previously shown non-radiative recombination analysis.

Another strong limitation of our L-CPSCs is the J_{SC}, which can be related to lower photon absorption, worse charge carrier extraction or a combination of both. To compare the homogeneity of current extraction across the active area we measure the spatially resolved light-beam induced current (LBIC) under short-circuit condition. The LBIC map in Figure 5.5a and Figure 5.5b shows that the photogenerated current is produced homogeneously in the entire cell, although its value is higher in the H-CPSCs than in L-CPSC, which also correlates with the JV-measurements.

In order to qualitatively resolve the differences in charge carrier extraction we perform spatially resolved PL measurements under open- and short-circuit conditions. The underlying principle of this novel characterization method is the following: under open-circuit the recombination rate is equal to the generation rate, hence, the excited charge carriers will recombine radiatively and non-radiatively, implying that in an ideal solar cell without non-radiative recombination the PL is homogeneous across the entire active area and as high as possible (limited by the maximum number of photoexcited carriers). However, under short-circuit the charge carriers are able to be extracted by the respective selective contacts and forwarded further to the external load, instead of recombining. Thus, it is favorable to see a low PL signal under short-circuit condition and the difference between the PL of the cell under open- and short-circuit can be used as a qualitative measure to evaluate the charge extraction of the cell. [413] Figure 5.5c-f depict that the PL of H-CPSC is almost one order of magnitude lower than that of L-CPSC (due to excessive non-radiative recombination as was shown above). Switching from open circuit to short-circuit quenches the PL, suggesting that the charge extraction in both cell types is similar.

The external quantum efficiency (EQE) in Fig. S14 demonstrates that the L-CPSCs suffer from a lower light absorption, particularly in the long-wavelength

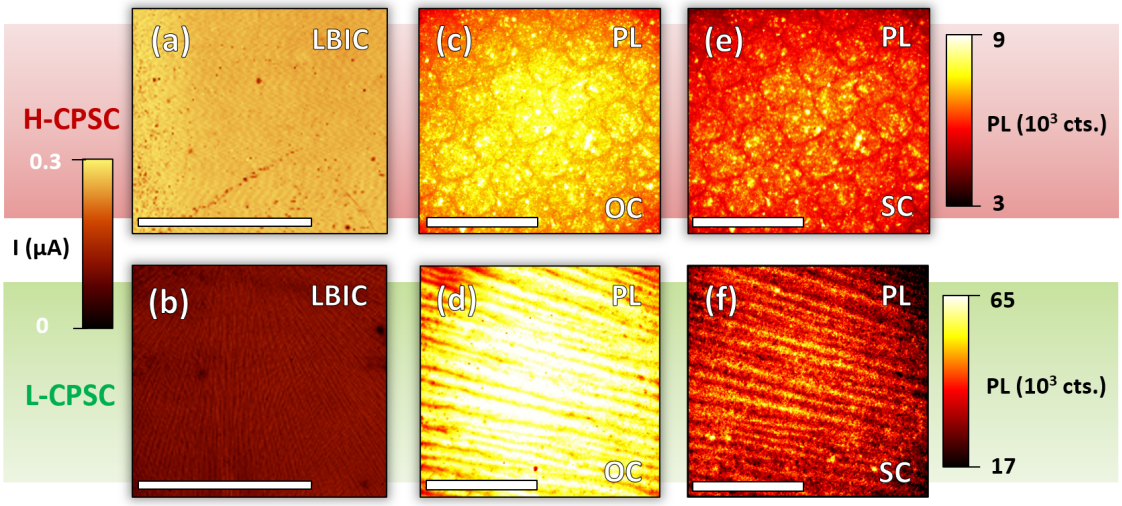


Figure 5.5: (a-b) Light-beam induced current (LBIC) measurements of an H-CPSC and an L-CPSC. Scale bar – 4 mm. (c-f) PL images of a H-CPSC and L-CPSC under open-circuit (c,d) and short-circuit (e,f), highlighting a difference in PL between these two states due to efficient charge extraction in both cell types. Scale bar – 0,4 mm. Note that the number of PL counts in L-CPSCs is higher than in H-CPSCs by almost one order of magnitude.

region compared to H-CPSCs. The reduced absorption spectrum of PaPL in comparison to PiPL (due to lower layer thickness) was confirmed via UV-Vis reflectance and transmission spectra measurement in Fig. S15. This provides a plausible explanation why the J_{SC} values of L-CPSCs are lower than that of H-CPSCs.

Outlining promising strategies to improve the PCE of CPSCs

We particularly highlight that the cell layers and perovskite composition were chosen to have as similar properties as possible, and to allow an objective comparison between the two types of stacks (rather than between two types of perovskite compositions or charge-extracting layers). Hence the conclusions drawn from this study can be applicable as well for the cases when other stacks are utilized.

Combining measurement results from the series resistance losses in both cell structures (Supplementary Note 6), it becomes clear that the FF in H-CPSCs is limited by the non-radiative losses, induced by numerous grain-boundaries, whereas the FF of L-CPSC strongly suffers from the interfacial resistance at perovskite/carbon contact (Figure 5.6a). The losses in the electrodes can be reduced further by selecting a more conductive TCO front contact and the conductivity of the carbon-based contact can be improved by altering the graphite crystal type, [414] surface functionalization and dopants. [210] Other ohmic FF losses, except for the electrodes are negligible, while additional FF losses, could possibly be alleviated by improving perovskite/TiO_2 contact and reducing its interfacial resistance.

Figure 5.6b and c depict the main free power losses in both cell structures, serving as a guideline for the main strategies to improve the PCE of both types of CPSCs:

1. Non-radiative losses in H-CPSCs strongly limit the potential of such cells to reach higher efficiencies, especially the V_{OC}. To date, the highest photovoltages in H-CPSC with $MAPbI_3$ absorbers are only slightly above 1.0 V. [259] Considering that one of the key limitations of V_{OC} is due to numerous GBs, pore-size engineering seems to be a promising strategy to allow for growth of large perovskite crystals in a "microporous" scaffold (as opposed to nanoporous scaffold in H-CPSCs). Up to now, only few reports have focused on optimizing the pore size of mesoscopic layers to improve the photovoltaic performance of the PSCs [415, 416] and this strategy needs to be further explored. Naturally, methods to passivate the GBs and reduce trap densities there also represent a promising approach to reduce the V_{OC} gap with the radiative limit. We note that there are examples in literature of boosting the V_{OC} by introduction of a porous HTL, compatible with high-temperatures, namely NiO_x. [226, 227] Additionally, according to our numerical simulation the V_{OC} could be boosted by

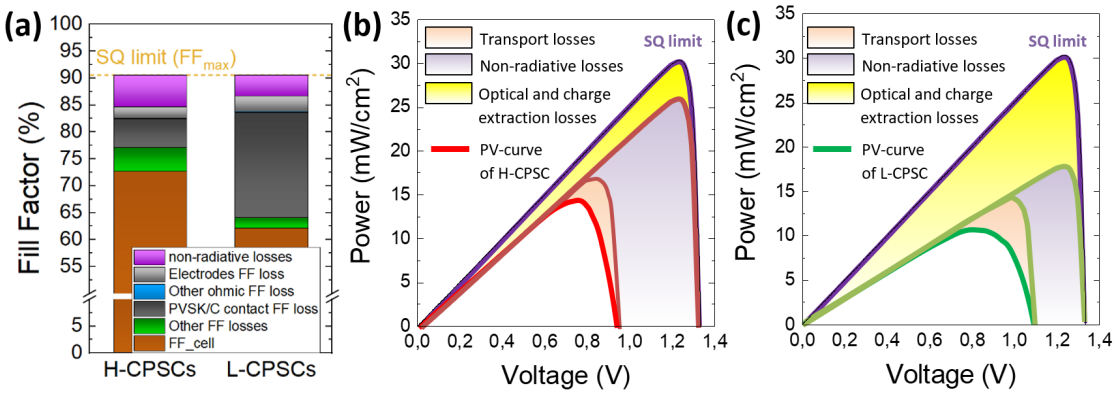


Figure 5.6: Results from the combinatory analysis of PSCs with carbon-based electrodes. (a) Distribution of FF losses in H-CPSCs and L-CPSCs. Visualization of Power density – Voltage (PV) curves of (b) H-CPSCs and (c) L-CPSCs, illustrating the power losses and their origins.

increasing the work-function of carbon-based contact or by reducing the surface recombination velocity of the minority carriers at the back-contact (Fig. S16). However, even if the band-alignment would be close to ideal in H-CPSCs, the V_{OC} would always be limited by the QFLS in perovskite, implying that the non-radiative losses of the photoabsorber itself or at its interfaces need to be reduced in order to obtain V_{OC} beyond 1.1 V.

2. In the studied L-CPSCs, the largest losses were due to a non-ideal FF and J_{SC}. Based on the results from EIS, only reducing the interfacial resistance at perovskite/carbon contact to the same value as it is in H-CPSCs would result in a 15 % increase in FF, leading to the total FF value of >77 %. We have recently demonstrated that the perovskite/carbon contact can be improved by alteration of the graphite powder type. [414] In addition, several reports have shown that the interfacial resistance can be strongly reduced by a press-transfer technique, which resulted in cell efficiencies above 17 % (although the reported PV devices had a HTL). [205, 268, 417] Moreover, Liu *et al.* have shown how interfacial post-treatment with cesium acetate (CsAc) effectively reduces the interfacial resistance at the back-contact and suppresses non-radiative recombination. [308] In addition, increasing the work-function at the perovskite/carbon interface (Fig. S13) could further improve the performance of such cells.

Both cell types also suffer from optical losses, which in case of L-CPSCs could be alleviated for example by the use of indium-doped tin oxide (ITO) as a front electrode, which has less parasitic absorption. However, it was shown before that ITO tends to significantly increase its sheet resistivity when processed at high temperatures, [418] making it unfavorable for H-CPSCs. Naturally photon-management

options (*e.g.* anti-reflective coating), inducing light-trapping is expected to boost the J_{SC} of the PSCs, regardless of the cell stack. Another promising strategy, which is possible in L-CPSCs, but not in H-CPSCs, is to integrate a reflective electron-blocking layer at the perovskite/contact, thereby allowing for transmitted photons in the long-wavelength region to be reflected back into the absorber (which often happens in conventional PSCs with metallic back-contact). Since in H-CPSCs, the porous stack must be infiltrated with a perovskite solution only after all the porous layers are deposited, the integration of a compact reflective layer becomes problematic for solution infiltration. However, this problem does not occur in L-CPSCs, which are deposited layer by layer.

5.6 Conclusion

Although numerous works on perovskite solar cells with high- and low-temperature treated carbon electrodes have been demonstrated, their quantitative comparison, comprehensive understanding of energy losses and identification of promising improvement strategies were not shown up to now. In this work, for the first time we presented a detailed analysis of the fundamental losses in the two basic types of perovskite solar cells with carbon-based counter electrodes complemented by providing the necessary knowledge for further efforts on boosting their PCE. The presented study was aimed at resolving the fundamental differences between the H-CPSCs and L-CPSCs, with as few differences in cell stack as possible, in order to attribute the main differences in cell properties to the absorber itself or to its interface with the charge-transport layers. Therefore, the goal of our work was not to produce most efficient devices (as we did not utilize any hole-transport layer for a more objective comparison), but rather to understand where lie the efficiency gaps of both types of cells and what the most effective strategies to improve device in both configurations could be.

PV devices with contacts treated at high-temperatures (H-CPSCs) contain perovskite crystals, which are constrained to <20 nm size due to process limitations, causing numerous grain-boundaries. As a result, the grain-boundaries cause excessive non-radiative recombination (even for the case of reduced trap densities), which brings down the charge carrier lifetime, PL intensity, and hence QFLS of the neat perovskite and complete cell stack, which consequently strongly limits the V_{OC} (<950 mV) of the manufactured solar cells. In addition, it causes higher ideality factor and J_0, negatively affecting the FF. Although the PCE of such cells was higher than that of L-CPSCs due to higher J_{SC} and FF, it contains a great potential for further performance improvement if the issue of non-radiative recombination at the grain-boundaries can be solved. Even if the hole-selectivity at the back-contact would be further improved, the low QFLS of the perovskite crystals embedded in mesoporous layers of such cells would still limit the cell potential. Therefore, the most promising route to boost the efficiency of H-CPSCs in the future would be

to alter the pore size to accommodate larger perovskite crystals and reduce non-radiative recombination at the grain-boundaries.

In devices where the carbon-based back-contacts are treated at low temperatures (L-CPSCs) and deposited afterwards on top of the perovskite, larger perovskite crystals can be formed. Despite the fact that the perovskite elementary composition was identical in both investigated architectures, we found that larger crystals of planar perovskite in L-CPSC strongly improve the carrier lifetime (from 72.9 ns to almost 1.8 µs), enhance the QFLS to 1.192 eV (compared to 1.15 eV for H-CPSC) and allow for V_{OC} above 1.1 V in HTL-free cells. Although the PCE of L-CPSCs was lower due to worse charge carrier extraction and transport, high quality of the perovskite absorber provides strong potential for improvements, especially considering that L-CPSCs offer higher flexibility for cell stack alteration than H-CPSCs (due to high temperature processing of the latter). Adding HTLs with high hole mobilities and improving the contact between the back-electrode and the layers underneath is the key to unleash the whole potential of the L-CPSCs.

The findings presented in this work are aimed to scrutinize the fundamental differences between these two types of CPSCs, demonstrating their losses and showing effective strategies to improve the PCE of such cells, in order to close the efficiency gap with the conventional PSCs with metal-based contacts.

5.7 Critical discussion

At the beginning of this thesis, both types of CPSCs – the ones with low- and high-temperature treated electrodes – had been studied and demonstrated in literature. A number of works had shown effective approaches to improve the properties of either one or the other type, but their comparison and demonstration of fundamental differences between them were never shown before. This motivated the author of this thesis to conduct the presented study, which contains a broad palette of characterization methods, in order to quantify a wide range of cell properties. However, several key points need to be mentioned for clarification of results:

- Although the simulation using one-dimensional drift-diffusion modelling partially aligns with the experimentally-obtained results, as in every simulation, a number of assumptions have to be considered. The modelled nature of defect energy states was taken from literature and can significantly vary for other PSCs, since defect properties can be affected by the perovskite composition, precursor solution, crystallization process, device architecture *etc.* While the general trend is independent of the choice of parameters: higher number of grain-boundaries increases the defect density and, thus, reduces QFLS, the magnitude of this reduction highly depends on the aforementioned parameters and should be kept in mind for similar modelling approaches. Furthermore, this simulation only considers a simplified case of 1D charge carrier transport and hence grain boundaries transversing across perovskite layer thickness.

More realistic scenarios based on multi-dimensional simulations could be utilized in future works, which would also, however, require more computational power.

- In order to compare both cell types, the layer thicknesses were optimized to obtain the highest PCE in both cases. Therefore, photoabsorbing layers without charge carrier extracting layers manufactured in this work (to analyze properties of the perovskite layer itself) had the same thickness to that of the respective cell. However, the difference in thickness between PiPL and PaPL also introduced a certain ambiguity to the interpretation of results, concerning absorption and radiative recombination processes. For an ideal comparison, the same amount of perovskite should be compared where the only difference is effectively the number of grain-boundaries (induced by ZrO_2 scaffold).
- As could be seen from the top-view SEM images the crystal size in PaPL can differ between ≈ 50-300 nm, suggesting that the grain-boundary density is spatially-inhomogeneous in such samples. A more accurate comparison between both types of perovskite photoabsorbers could be performed if the perovskite layer crystallization would be controlled more precisely with a better grain size homogeneity.
- In the author's opinion this work mainly discusses and quantifies the non-radiative and V_{OC} losses, while the optical and charge extraction losses were compared mostly qualitatively. A further in-depth investigation into the light-scattering induced by the thick mesoporous scaffold of H-CPSCs as well as losses of absorption at long wavelengths due to lack of reflective layer (as in the case of PSCs with metallic electrode) would be particularly valuable in understanding the optical losses in these devices. Such additional insights could facilitate development of novel effective strategies of optical management for better incident photon utilization and improved PCE.
- One of the techniques used to estimate the FF losses in CPSCs was electrochemical impedance spectroscopy. While it is a well-established characterization techniques in some research fields, its utilization for analyzing PSCs is still ambiguous (subsection 2.2.14). In this study, the author attributed the high-frequency semicircle in the Nyquist plot obtained from the EIS measurements of CPSCs to the charge transfer process happening at the perovskite/carbon interface. Although a number of reports on CPSCs contain the same designation of the high-frequency response to this interface, it is still under debate why similar processes at the opposite (perovskite/ETL) interface are not considered, and how to disentangle between contributions from both interfaces if they are. Simultaneously, the low-frequency semicircle is often affiliated with the recombination resistance. However in the author's opinion, such designation is even more equivocal, and much more studies have to be carried out before making such claims. In this work, the designation of high- and low-frequency semicircles of the Nyquist plots was important for quantification of series resistance losses, but the author would advise to treat the values ob-

tained from fitting to the equivalent circuit more qualitatively, rather than quantitatively.

The study presented in this chapter shed new light on a number of critical features and properties of L- and H-CPSCs, which is expected to assist perovskite community in creating effective strategies to develop their PCE further. But an in-depth investigation to understand the stability and compare the degradation mechanisms of CPSCs is also needed to realize the full potential of such PV devices for mass-production. Therefore, further work is needed to resolve all the peculiarities of CPSCs, to understand their behavior and to find new methods to improve their PCE as well as stability.

Chapter 6

Nanoarchitectonics in fully printed perovskite solar cells with carbon-based electrodes

6.1 Preamble

In chapter 5 we have seen that L-CPSCs despite having no designated hole-selective material can still have a QFLS of 1.2 eV and a V_{OC} above 1.1 V. One of the conditions to achieve such high V_{OC} is to ensure that the crystal size in the perovskite layer is sufficiently large to minimize non-radiative recombination at grain boundaries (GBs). This suggests that, if one aims to improve the V_{OC} of H-CPSCs to similar values, it is crucial to develop ways to grow large crystals within the mesoporous cell framework. Therefore, it is favorable to create large pores, mainly at the interface between m-TiO_2 and ZrO_2 layers to allow for growth of larger perovskite crystals, similarly to the L-CPSCs. Consequently, the goal of growing perovskite crystals with large grains translates into a goal of engineering the pore size. In general, the field of modifying the architecture of an opto-electronic device via nano-scaled structural units is called *nanoarchitectonics*. The author of this work tried to utilize it to enhance perovskite crystal size and reduce the non-radiative recombination in H-CPSCs.[§]

[§]This chapter (except for the critical discussion in section 6.7) is a preprint of the research paper, which is currently undergoing a peer-review process:

Bogachuk, D., Girard, J., Tilala, S., Martineau, D., Narbey, S., Verma, A., Hinsch, A., Kohlstädt, M., Wagner, L. Nanoarchitectonics in fully printed perovskite solar cells with carbon-based electrodes, *arXiv*, available at: https://doi.org/10.48550/arXiv.2211.09424

The individual contributions were as follows:

- **D.B.**: conceptualization, writing original draft, development of inkjet-printable PS-nanoparticle suspension, optimization of the PS-ink deposition, performed PL mapping, SEM-, TRPL-, JV-measurements, 3D-nanotomography (from SEM+FIB measurements) and pore distribution analysis via image processing, light intensity-dependent measurements, coordinated the work, analyzed all the measurements and prepared the manuscript, as well as figures.
- **J.G.**: optimization of the PS-ink deposition, perovskite solution filling, sample manufacturing
- **S.T.**: preparation of PS-suspension for spin-coating, spin-coating PS-layer, assistance with optimization of the PS-suspension for inkjet-printing
- **D.M.,S.N.**: sample manufacturing
- **A.V.**: optimization of the PS-ink deposition
- **A.H.,M.K.,L.W.**: contributed to the manuscript preparation, discussion of experiments and interpretation of result.

6.2 Abstract

Perovskite solar cells with carbon-based electrodes (CPSCs) have a tremendous potentialto succeed in the PV market due to their up-scalability, cost-effectiveness and stability. However, the power conversion efficiencies (PCEs) of such devices still need to be improved, especially the open-circuit voltage (V_{OC}). Previously we have shown that V_{OC} of these CPSCs is significantly limited by the non-radiative recombination at the GBs, which can be significantly reduced if the perovskite crystals would be larger. Therefore, in this work we propose the use of nanoarchitectonics to modify the scaffold of mesoporous oxide layers to allow the growth of perovskite photoabsorber with bigger grains. Such modification is obtained by an introduction of a sacrificial template using polystyrene (PS) nanoparticles, which, upon heat treatment create a nanocavity (approximately 100 nm in height) between the mesoporous layers. When this nanocavity is filled with perovskite, the non-radiative recombination in CPSCs is suppressed, leading to a boost in V_{OC}, J_{SC} and, consequently, overall PCE.

6.3 Introduction

Halide perovskites enjoyed the attention of numerous researchers over the recent years due to the fascinating nature of these materials. [49, 72, 114] In particular, the high absorption coefficient, direct bandgap and high defect-tolerance make halide perovskite very promising for photovoltaic (PV) applications. [16, 22, 41] In less than 10 years since the first perovskite solar cell (PSC) has been demonstrated, [46] the reported power-conversion efficiencies (PCE) of these devices skyrocketed. Yet besides high performance, PV devices must also be stable in order to be a sustainable power generation system. This is why more attention is given nowadays within the perovskite community to the device stability. [123] One promising approach to reduce PSC degradation is to utilize carbon-based back-electrodes, which are chemically-inert, moisture-resistant and do not decompose under PV operation conditions. [210, 377] PSCs with carbon-based electrodes (CPSCs) are well-known to be highly-stable and therefore contain strong potential for their commercialization, especially considering that the entire device can be fabricated by up-scalable and cost-effective techniques. [125,203,209,216,378]

However the PCE of CPSCs is still lower than in the case of state-of-the-art PSCs with metal-based electrodes. [210] Specifically, in CPSCs where the electrodes are treated at high temperatures (H-CPSCs), perovskite can only be introduced after the back-electrode is deposited. This implies that the entire device structure must be mesoporous, to allow the solution to fill the mesoporous scaffold and to consequently crystallize perovskite within this porous matrix between the front and back electrodes. In H-CPSCs, the perovskite crystal size and density of GBs are determined by the pore size, because they confine perovskite growth. Since the

particles of the mesoporous scaffold and corresponding pores are typically 20 nm in diameter or less, perovskite grown within mesoporous titanium dioxide (m-TiO_2), zirconium dioxide (ZrO_2) and carbon layers is expected to have numerous GBs with surface defect states. As we have shown in our earlier study, [92] this causes substantial non-radiative recombination in H-CPSCs and limits their potential to reach V_{OC} comparable with that of the traditional PSCs.

Consequently, to overcome this limitation, one needs to enlarge the perovskite crystal size, implying that the pores within the H-CPSCs in which the perovskite is formed need to be enlarged in order to grow crystals with less GBs. In an H-CPSC stack there are three porous layers: m-TiO_2, ZrO_2 and carbon. The m-TiO_2 should be thin to minimize parasitic absorption and porous enough to avoid capacitance issues, [419] which arise from the high dielectric constant of TiO_2. [420] As a result, PSCs with TiO_2 having small surface area (*e.g.* having only a planar TiO_2) typically have severe hysteresis of the JV-characteristics. [49, 123] Therefore, enlarging the pores of m-TiO_2 is not considered a promising strategy to boost the overall device performance. And since the dominant function of the carbon electrode is to simply conduct charge carriers to the respective terminal, enlarging its pores would not affect the non-radiative recombination in a cell. In contrast, perovskite in the pores of ZrO_2 layer needs to have higher absorption and lower non-radiative recombination rate to cause a high QFLS. Therefore, enlarging pores in ZrO_2 will likely suppress the non-radiative recombination rate of the perovskite within due to reduced density of GBs and have the most prominent effect on the device performance.

Such nanostructuring approaches can include pore-engineering, [415, 416, 421–423] nanolithography [424–426] electrochemical template growth [406] *etc.* In this work we propose the use of *nanoarchitectonics* – utilization of nano-scaled and well-arranged structural units – to modify the architecture of the opto-electronic device. According to the author's knowledge, nanoarchitectonics is a rather unexplored research field among perovskite researchers and should be given more attention in the future to boost the PSC (and especially H-CPSC) performance.

The aim of this work is develop a reproducible and an up-scalable approach to nanoengineer the pore size in H-CPSCs, targeting the growth of large perovskite grains on top of the m-TiO_2 (Figure 6.1). Therefore, polysterene (PS) nanoparticles are deposited between m-TiO_2 and ZrO_2 layers. The PS-nanoparticle serve as a sacrifical template to facilitate the creation of cavities at this interface, which will be filled with large perovskite crystals after the cell manufacturing is complete. We demonstrate that inkjet-printing allows to deposit highly-ordered layers of hexagonally arranged PS nanoparticles, on which ZrO_2 layer can be flawlessly deposited. After ZrO_2 sintering, the PS-nanoparticles pyrolise, acting as a sacrificial template to nanostructure the ZrO_2 layer. Although the height of the created cavity is smaller than originally anticipated, the nanoarchitectured cavity is visible in the device structure via 3D-nanotomography. Thereby the enlarged cavity

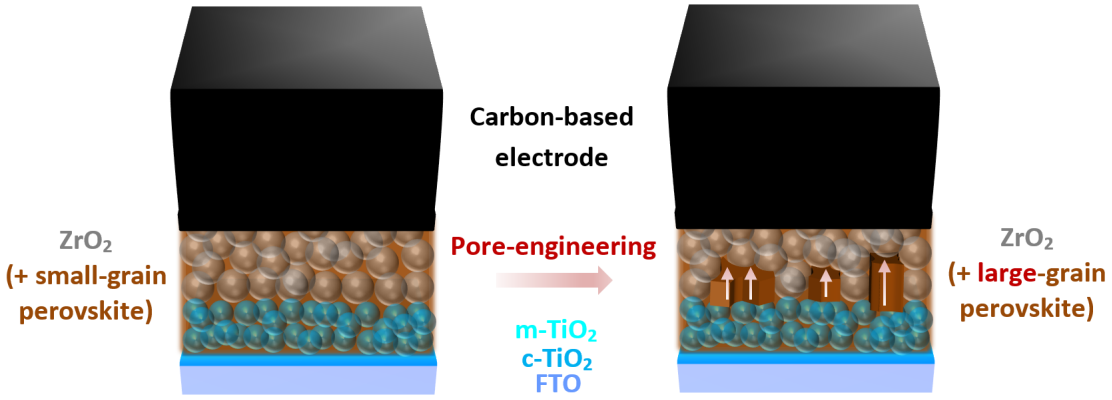


Figure 6.1: The conceptual idea of enlarging the pores of ZrO_2, primarily at the m-TiO_2/ZrO_2 interface in order to grow large perovskite crystals.

reduces the non-radiative recombination, slightly boosting the charge carrier lifetime and device V_{OC}. The nanoarchitectured H-CPSCs also exhibit a small improvement in J_{SC}, suggesting an increase in light absorption due to enhanced perovskite crystal size. Although this study is focused particularly on improving the performance of H-CPSCs, the concept of nanoarchitectonics could be explored in other PSC architectures as well and provides an immense potential for further device enhancement.

6.4 Experimental details

The suspension for spin-coating polysterene (PS) nanoparticles was obtained by combining the dispersion of PS nanoparticles (200 nm diameter purchased from Sigma-Aldrich) with a diluted surfactant solution in a 2:3 volumetric ratio. The latter consisted of methanol and surfactant Triton X-100 with a volume ratio of 400:1. After all the components of the spin-coating PS suspension were added together in a vial, it was vigorously shaken for 1 minute and then sonicated for 10 mins. To produce a homogeneous layer of PS nanoparticles, a volume of 100µL of the synthesized suspension was spin coated on $2.5 \times 2.5\,cm^2$ FTO-substrates. The spinning procedure roughly resembled an approach reported by Hörantner *et al.* [424] and involved 3 steps:

1. 600 rpm for 10 seconds
2. 1000 rpm for 60 seconds
3. 2000 rpm for 60 seconds

After deposition, the PS-layers were left to dry at room temperature for 24 hours. Although spin-coating the PS-suspension led to creation of homogeneous and

well-packed PS-layers, such suspension was not suitable for ink-jet printing. Particularly, the low boiling point of methanol causes fast solvent evaporation from the suspension, leading to particle coagulation and clogging in the inkjet nozzles (since their diameter is in µm-range). Moreover, the concentration of PS-nanoparticles had to be also lower to reduce the rapid clogging of the nozzles. In addition, methanol was replaced with a 1:1 mixture of isopropanol and 1-pentanol and combined with Triton X-100 in the same ratio as in the dilluted surfactant solution needed for the spin-coating PS-suspension. Next, the pristine PS suspension was added in a 1:10 ratio. After that formamide was added to this solution in a 1:5.6 volumetric ratio to limit the ink droplet diameter and to increase the evaporation rate, which was found particularly useful for inkjet-printing silica and PS nanoparticles by Sowade *et al.*. [427] The resulting ink was sonicated for 10 minutes and deposited by an inkjet-printer using a Dimatix printing head with 16 nozzles. The layers were deposited using 800x800 droplets per inch with 10 pL volume each. Then the PS-layers were allowed to dry at room temperature for 24 hours. The deposition of all the other cell components besides PS-layer was performed identically to the procedure described in chapter 5.

The current-density and voltage curves of fabricated devices were measured with a source meter (Keithley 2400) at a scan rate of 40 mV/s using a class A solar simulator providing 100 mW/cm^2, AM1.5G illumination. Scanning Electron Microscopy (SEM) images of the PS-layers were obtained with a Zeiss EVO 10 electron microscope, but for a 3D-nanotomography, Zeiss Auriga 60 equipped with an in-lens secondary electron detector and FIB-gun was utilized. TRPL measurements were conducted using externally triggered CW laser (Coherent Orbis) of 660 nm wavelength with 10 mW power on a spot sized widened to ca 1 cm^2, with a fall and rise time (10 % and 90 %) below 2 ns. The laser was triggered to produce rectangular-shaped signals at 7 Hz frequency. The PL images were obtained by OLYMPUS BX50 stereomicroscope and sCMOS camera ("Zyla 5.5 sCMOS" by Andor) with a long-pass filter while the partial illumination of the sample at an intensity equivalent to approximately 1 sun was provided by a 623 nm LED (Thorlabs, SOLIS-623C). The light intensity-dependent measurements of J_{SC} and V_{OC} were obtained from JV-measurements performed under incident irradiation, varied by polymeric optical density filters to reduce light intensity incident on the cell.

6.5 Results and discussion

For altering the device architecture, in this work we utilize polystyrene nanoparticles with a diameter of approximately 200 nm, which typically have narrow size distribution and suitable glass-transition temperature close to 100°C to be employed as sacrificial template. The PS-suspensions were firstly spin-coated on an FTO and dried at room temperature to produce homogeneous layers of PS-nanoparticles. To

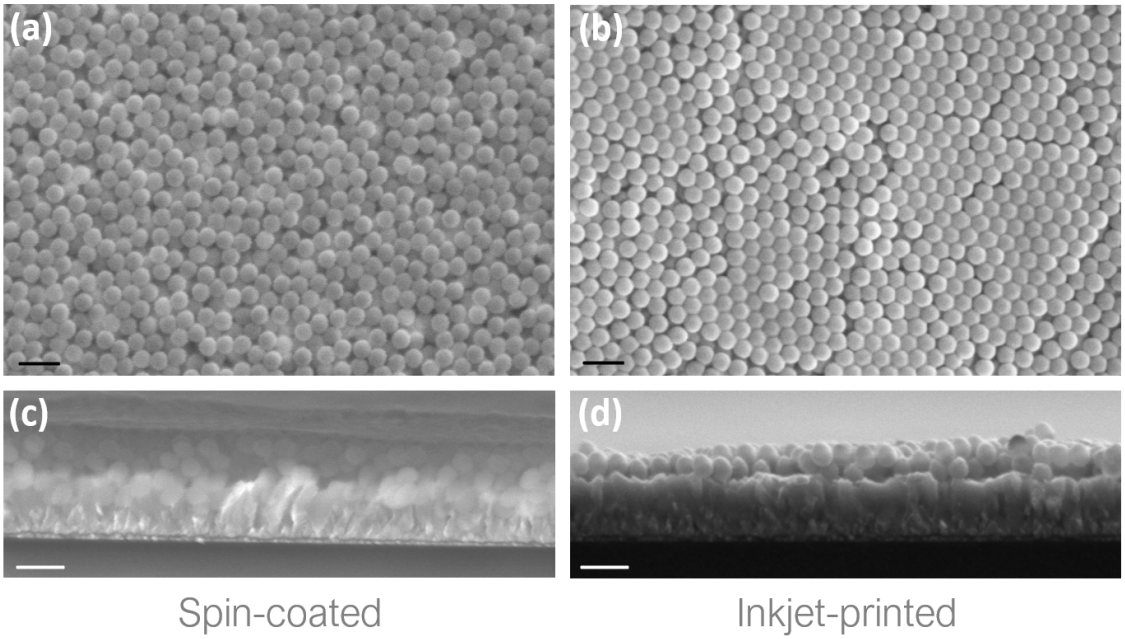


Figure 6.2: Top-view SEM images of (a) spin-coated and (b) inkjet-printed layer of polystyrene (PS) nanoparticles. Cross-section SEM images of (c) spin-coated and (d) inkjet-printed layer of PS nanoparticles. Scale bars – 500 nm.

improve the layer packing density, we added a surfactant (Triton X-100), resulting in a compact spin-coated PS-layer with uniform particle size (Figure 6.2a). However, keeping in mind that spin-coating is not an up-scalable manufacturing technique (*cf.* subsubsection 1.3.5.4), we have altered the PS-suspension composition to be used in inkjet-printing. After rigorous ink optimization, a comparably homogeneous and well-ordered arrangement of PS-nanoparticles was obtained. Surprisingly, the PS particles in the inkjet-printed layers are hexagonally-arranged and appear to be even more ordered than in the case of spin-coated films (Figure 6.2b). However, the spin-coated films had a thickness of ca. 500 nm, while than the printed ones ca. 200-300 nm (Figure 6.2c and d) which is likely to be related to the difference in the ink composition. For further experiments, we only utilize the inkjet-printing technique to coat the substrate with PS-nanoparticles.

ZrO_2 was then screen-printed on top of the deposited PS-layer followed by a slow sintering process (heating up to 500°C), similarly to other nanoarchitectonic approaches to structure the photoabsorber in PSCs. [424] Such method resulted in the creation of localized nano-cavities between the FTO and the ZrO_2, without delamination of the latter layer from the substrate (Figure 6.3a). For more visual comparison, Figure 6.3b shows that the reference sample with Zr_2 deposited on FTO substrate does not have such feature. However, the cavity height is significantly lower than the thickness of a PS layer. Since PS particles in this process undergo the transition

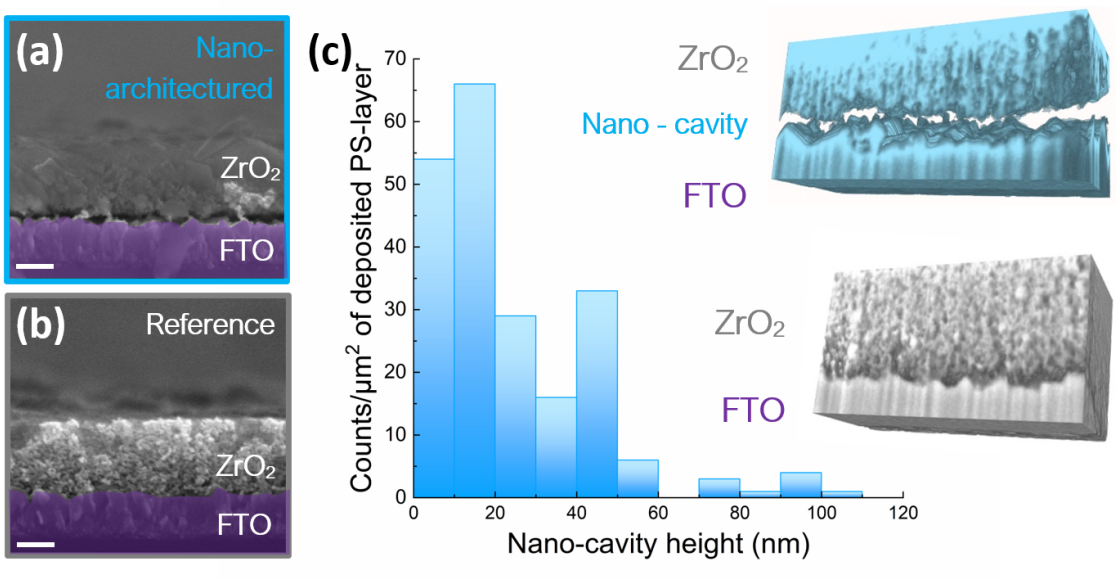


Figure 6.3: Cross-sectional scanning electron microscope (SEM) images of the (a) nanoarchitectured layer of ZrO_2 and (b) reference layer of ZrO_2. Scale bars – 500 nm. (c) Distribution of the cavity height in the nanoarchitectured (blue) and reference (grey) samples, obtained from 3D-nanotomography using focused ion beam (FIB) ablation.

from solid state to rubbery and viscous states, followed by their depolimerization and evaporation, the height of the rubbery or liquid PS layer is expected to be reduced.

To quantify the nano-cavity height distribution in a sample we utilized cross-sectional SEM images coupled with focused ion-beam (FIB) surface polishing. Successively polishing the cross-section and record SEM images of the polished surface allows to obtain information about the sample's appearance along its depth. Combining these 2D SEM images along the axis perpendicular to the plane of taken images allows us to reconstruct a 3D image of our nanoengineered structure. This 3D-nanotomography shown in Figure 6.3 of approximately 2 μm^3 sample volume revealed that additional localized cavities with up to 100 nm in height have been introduced overall across the sample. On the edges of these cavities, ZrO_2 is in direct contact with the FTO, preventing the layer form delamination. In comparison, 3D-nanotomography of a reference sample demonstrates that it does not possess such attribute.

Next we filled the nano-architectured samples with perovskite to study the effect of large perovskite grains grown within on the radiative and non-radiative recombination rates. As can be seen from the TRPL measurement shown in Figure 6.4a, the charge carrier lifetime of PS-samples was found to be 760 ns by

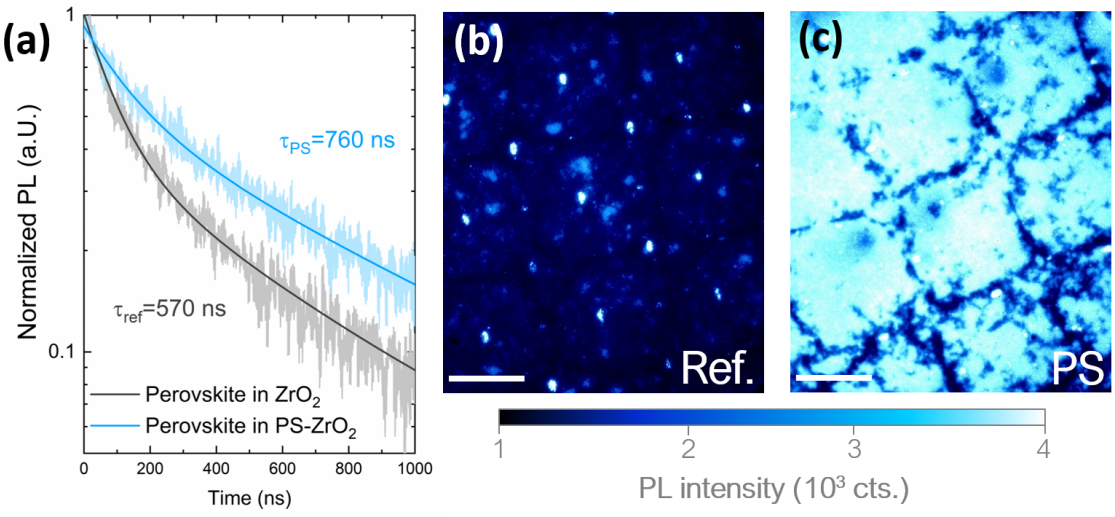


Figure 6.4: (a) Time-resolved photoluminescence measurements of samples having ZrO_2 (reference) and nanoarchitectured ZrO_2 on FTO filled with perovskite. PL maps of (b) reference and (c) nanoarchitectured CPSCs. Scale bar – 150 µm.

fitting the PL behavior to a bi-exponential decay. This is significantly higher than the lifetime of charge carriers in perovskite embedded into the reference ZrO_2 layer, which was found to be 570 ns, suggesting the suppression of non-radiative recombination by reduction of grain boundaries in perovskite.

To test whether this nanoarchitecturing approach also results in the improvement of PV devices, we manufactured H-CPSCs with and without the nano-cavity. Similarly to the prolongation of PL decay and charge carrier lifetime, the PL mapping in Figure 6.4b reveals that the reference H-CPSCs have a much smaller PL intensity than the PS-samples (Figure 6.4c). Therefore high PL intensity and long charge carrier lifetime indicate that the non-radiative recombination in such cells is reduced, which would positively affect the device performance. The JV-statistics and curves of representative cells are presented in Figure 6.5, demonstrating that the nanostructured samples cause a small, but noticeable enhancement in V_{OC} by approximately 30-40 mV and in J_{SC} by 1.5 mA/cm^2. This suggests a 3-5-fold increase in charge carrier densities, agreeing with the PL maps shown in (Figure 6.4b and c). The champion PS-engineered cell had a V_{OC} of 943 mV and a PCE of 15.7 % (non-stabilized).

We also performed light intensity-dependent measurements of V_{OC} to extract the ideality factor n (Figure 6.6a) by applying a linear fit to the semi-log plot of V_{OC} as a function of irradiation intensity. The measured slope corresponds to n, according to Equation 2.4. We find that the n of a reference and PS-cells are 1.37 and 1.29, respectively, which suggests a slightly reduced non-radiative recombination in nanoarchitectured cells.

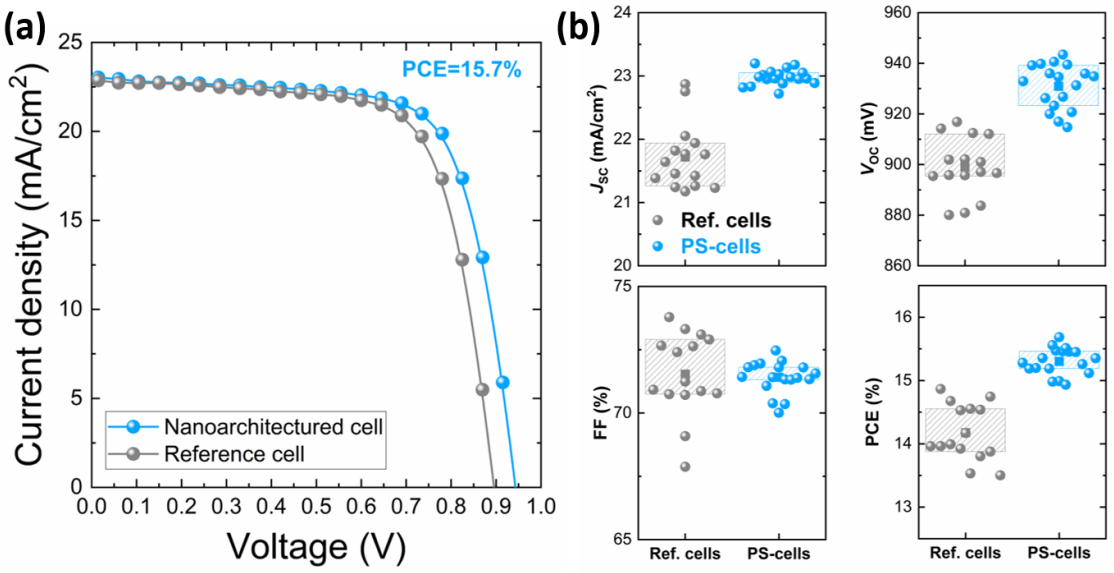


Figure 6.5: (a) *JV*-curves of representative reference and nanorachitectured CPSCs, (b) *JV*-statistics of the manufactured CPSCs with and without nanocavity.

Moreover, measurements of light intensity-dependent J_{SC} and V_{OC} allows to construct a so-called pseudo *JV*-curve (p*JV*-curve) according to the method

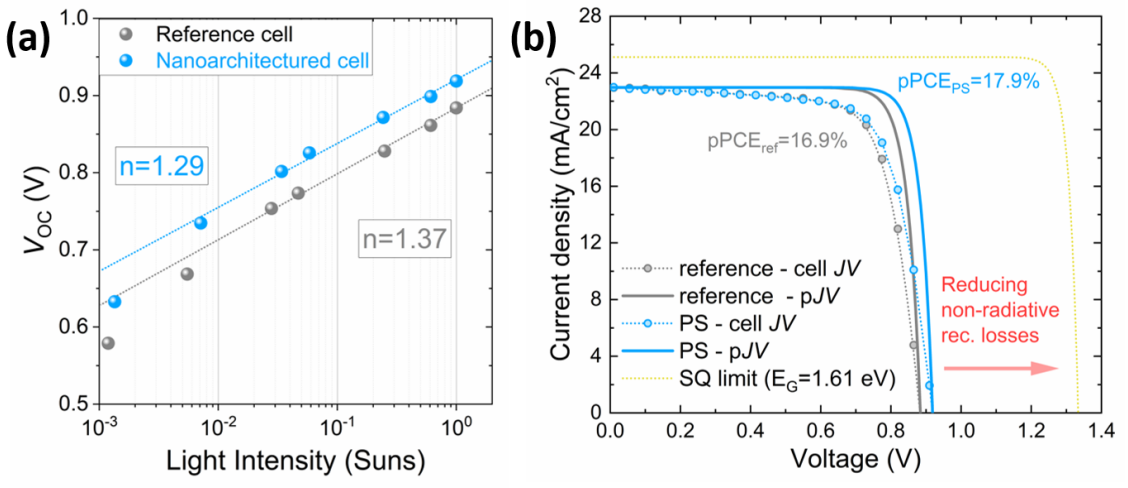


Figure 6.6: (a) Measured V_{OC} as function of light-intensity of reference and nanoarchitectured CPSCs, showing a slight difference in ideality factor n. (b) JV-curves and pseudo-JV curves of the champion reference and nanoarchitectured cells, in comparison with the curve at the Shockley-Queisser limit.

described in subsection 2.2.12. Since V_{OC} is measured under open-circuit, the charge transport outside of the cell is absent and, therefore, the effect of series resistance can be neglected. Thus, the pJV curve in the absence of charge transport losses is obtained, which is then only limited by non-radiative recombination losses.

Figure 6.6b shows the JV- and pJV-curves of the reference and nanoarchitectured CPSCs based on the measurements in Figure 6.6a. It shows that by minimizing the series resistance losses the PCE of the nanoarchitectured CPSC could reach nearly 18 %. In addition, Figure 6.6b shows a JV-curve of an "ideal" solar cell with this perovskite bandgap (1.61 eV), where only radiative recombination is present, according to the Shockley-Queisser limit. By comparing the measured JV-curves with an ideal one, we see that the biggest PCE loss is due to the V_{OC}, which is reduced by as much as 400 mV. This substantial gap implies that although the presented approach can suppress the non-radiative recombination at the GBs to some extent, there is still a lot of room for further improvement.

6.6 Conclusion

In summary, we demonstrated an effective strategy to engineer the architecture of perovskite solar cells with carbon-based electrodes in order to create nanocavities between the m-TiO_2 and the ZrO_2 layers. These nanocavities were formed by depositing ZrO_2 on an inkjet-printed and highly-ordered layer of polystyrene nanoparticles, which acts as a sacrificial template, arranging the ZrO_2 particles around them. The formation of the nanocavity was confirmed by SEM measurements coupled with cross-sectional FIB-polishing to produce a 3D-nanotomogram of the nanoarchitectured sample, from which we quantified the cavity height distribution by image analysis. It is worth noting that the nanocavity height was below 100 nm, which significantly lower than desired, since it would only allow the growth of 100 nm-thick perovskite crystals (at best). Nevertheless, by transient and steady-state PL characterization techniques we demonstrate that the introduction of these nanocavities indeed causes a suppression of non-radiative recombination in perovskite photoabsorber and leads to an improvement in charge carrier lifetime. Consequently, the V_{OC} has been improved by nearly 40 mV accompanied by a small increase in J_{SC}, resulting in a champion PCE of 15.7 %. Furthermore, by performing light intensity dependent-measurements we show that the ideality factor n has been reduced in cells with larger perovskite crystals agreeing with the results from PL analysis. Based on these measurements, we construct a pseudo JV-curve, demonstrating a potential of these nanoarchitectured cells to reach PCE of 17.9 %, if the charge-transport losses would be minimized. The findings of this work revolve around a conceptually new idea of nanoarchitectonics in PSCs as a new method to boost their PV performance (particularly in the case of devices with mesoporous structures) and potentially bring it closer to the radiative limit.

6.7 Critical discussion

The presented study demonstrates how the architecture of a CPSC can be modified to accommodate the growth of larger perovskite crystals with more favorable opto-electronic properties. In the author's opinion, the strategy of nanoarchitectonics for PCE enhancement is not only applicable for CPSCs, but also for other PSC architectures and even other types of perovskite-based opto-electronic devices (*e.g.* LEDs, photodetectors, transistors). But despite the novelty of this approach, several crucial remarks need to be made:

- The process of PS-nanoparticle state transition and decomposition is an important step in the formation of these nanocavities but it has not been studied in detail. Further work needs to elaborate on this issue, in order to gain a better understanding of the PS-nanoparticle state transitioning during ZrO_2 sintering. Such information would help to develop methods to control the cavity height and shape, and, thus, template the growth of perovskite within.
- Unfortunately, the cavity height shown in this work is rather small, translating into a performance boost that is only slightly outside of the margin of error of $1\,\%_{abs.}$. To demonstrate the full potential of this approach, the deposited PS-layer must be thicker, in order to grow larger nanocavity. However, if the cavity would be too large it might cause ZrO_2 delamination, so the device architecturing must be carefully optimized.
- It would be beneficial to show the difference in perovskite structural properties between the crystals grown inside the cavity with the ones grown within ZrO_2 pores. For example by FIB-polishing the cross-section, a transmission-electron microscope (TEM) or scanning electron-diffraction (SED) measurements at different locations of the sample cross-section could be a direct way to gain a deep understanding of the crystallographic characteristics and how the perovskite growth inside such cavities differ from the growth inside ZrO_2 pores.
- From cross-sectional SEM images (even if the perovskite crystals would be large) it is fairly difficult to recognize the individual perovskite grains, since such assessment must be done via diffraction-based techniques. If an electron back-scattered diffraction (EBSD) measurement would have a high enough resolution to be utilized on such cross-sections, it would provide a deep insight into the grain size, orientation distribution, spread *etc.* to gain a better quantification of the perovskite crystal size and their properties.
- To illustrate the effect of the nanocavity, it would be particularly interesting to compare nanoarchitectured samples with different thicknesses of PS-layers or different PS particle sizes. Similar PS-inks can be developed to produce nanocavities with different heights and shapes, resulting in different extent of SRH surface recombination suppression.

The nanoarchitectonics approach presented here only demonstrates an implementation of self-arranged PS-nanoparticles as structural units to alter the device architecture. But other types of sacrificial nanoparticles, surfactants, solvents, deposition techniques *etc.* can be also employed to tailor this approach to specific applications.

The points mentioned above could be implemented before the draft is submitted for publication to improve the quality of research. One of the major conclusions of this study is the experimental evidence that the larger perovskite growth in H-CPSCs can results in the reduction of non-radiative recombination and performance improvement. Importantly, this study was proposed in an earlier publication in chapter 5 as a result of gaining a deep understanding of the charge carrier dynamics and recombination processes. This chapter presents an experimental proof that this hypothesis is correct, paving way for further improvement in the future work.

Chapter 7

Natural and synthetic graphites for electrodes in perovskite solar cells

7.1 Preamble

Besides enhancing the performance by reduction of non-radiative recombination at the grain boundaries (*cf.* chapter 6), the device performance could be further improved if one would find a way to minimize the series resistance losses. As discussed in the chapter 3, the modification of the graphite crystals can lead to a significant reduction of sheet and/or interfacial resistance in a photovoltaic device. While an alternation of the graphite crystal size has already been demonstrated in literature, a detailed investigation and comparison of different types of graphite crystals was not reported (particularly, in the context of PSCs). Therefore, the author of this work chose to compare different artificial and natural graphite types, which could be embedded into the carbon-based electrode. This chapter describes a comparison study of these graphites, in terms of their structural, morphological as well as electrical properties, and how their incorporation into the carbon-based electrode influences the performance of CPSCs.*

*This chapter (except for the critical discussion in section 7.7) has been published as peer-reviewed research paper in the scientific journal "Carbon" (impact factor 2022: 9.6):

Bogachuk, D., Tsuji, R., Martineau, D., Narbey, S., Herterich, J.P., Wagner, L., Suginuma, K., Ito, S. and Hinsch, A., (2021) Comparison of highly conductive natural and synthetic graphites for electrodes in perovskite solar cells. *Carbon*, 178, pp.10-18.

The individual contributions were as follows:

- **D.B.**: Writing - original draft, conceptualization, formal analysis, carried out the EIS, SEM, optical microscopy, TRPL, V_{OC} decay and stability measurements, generated the concept of this publication, coordinated the work, analyzed all the measurements and prepared the manuscript, as well as figures, has performed Raman shift spectroscopy.
- **R.T.**: contributed to writing the manuscript, XRD measurements, providing the graphite powders, which were used to manufacture respective carbon-based pastes.
- **D.M.**: contributed to writing the manuscript, measured the sheet resistance of the carbon-based contacts by 4-point probe measurement and the JV-parameters of the manufactured solar cells, manufactured the carbon-based pastes, perovskite solution and complete PV-devices.
- **S.N.**: contributed to writing the manuscript, manufactured the carbon-based pastes, perovskite solution and complete PV-devices.
- **J.P.H.**: contributed to writing the manuscript, performed a steady-state PL spectroscopy.
- **L.W.**: Conceptualization, provided important conceptual ideas, contributed to the manuscript preparation and results interpretation.
- **K.S.**: provided the graphite powders, which were used to manufacture respective carbon-based pastes.
- **S.I.**: provided essential ideas regarding the nature of graphite particles and differences in their properties.
- **A.H.**: Conceptualization, provided important conceptual ideas, contributed to the manuscript preparation and results interpretation.
- **All authors**: reviewed the manuscript.

7.2 Abstract

In this work we compare seven different types of natural and synthetic graphite particles and examine how their integration into the cathode of carbon-based perovskite solar cells (CPSCs) is influencing their opto-electronic properties. By combining X-ray diffraction, Raman spectroscopy and 4-point probe measurements we show that the differences in graphite crystallinity significantly affect the sheet resistance of the carbon-based cathode. The most conductive carbon-based film with an exceptional sheet resistance of 4 Ω/sq. have been produced from scaly graphite with the crystallite dimensions of L_a=60.6 nm and L_c=28.6 nm. Electrochemical Impedance Spectroscopy further revealed that charge transfer resistance at the perovskite/carbon contact differ for each graphite type. Overall, the pyrolytic graphite was found to be the best compromise between high conductivity and low charge transfer resistance leading to least series resistance losses and a fill factor (FF) above 74 % (in perovskite solar cells with area of 0.64 cm^2). However, an overall efficient hole extraction and less non-radiative charge recombination in CPSCs with scaly graphite resulted in the highest average power conversion efficiency and a champion device reaching 14.63 %. All the CPSCs display exceptional moisture stability for 5,000 h under ambient condition, with a PCE decrease of less than 3 %.

7.3 Introduction

In recent years, the field of perovskite opto-electronic devices has attracted researchers across the globe due to the unique properties of perovskite materials, providing a broad spectrum of applications to explore. [12, 428] One of the most rapidly developing fields is perovskite photovoltaics (PV), where the state-of-the-art laboratory-scale solar cells can already compete with the traditional silicon solar cells in terms of power conversion efficiency (PCE). [50] Despite tremendous progress in the development of strategies to boost PCEs of such solar cells, the up-scaling to perovskite solar modules is still challenging, partially due to the fact that most of the high-efficient devices have been manufactured by spin-coating method. [71, 114] Additionally, the use of organic doped hole-selective layers (HSL) and costly counter electrodes, which consist of noble metals, not only strongly elevates the cost [122, 209] and CO_2-footprint [217] of such PV devices, but also reduces their stability. [123, 161, 179, 184] A solution to these issues can be realized by the implementation of the HSL-free perovskite solar cells with carbon-based electrodes (CPSCs), [216] which primarily consist of graphite and carbon black particles. [124] These low-cost electrodes can provide a comparably high conductivity, while simultaneously hindering the moisture and air ingress into the PSC, owing to the hydrophobic nature of thick carbon-based back-contact. [126,127,197,198]

In 2014 Mei *et al.* have proposed to use a triple-layer CPSC architecture consisting of mesoporous titanium dioxide (m-TiO_2) as electron-selective material,

zirconium dioxide (ZrO_2), acting as a spacer layer and a carbon-based electrode, consisting primarily of graphite flakes and carbon black nanoparticles. [125] After the triple-layer m-TiO_2/ZrO_2/C cell stack is deposited, it is infiltrated with a perovskite precursor solution, which penetrates through the pores and crystallizes into perovskite photoabsorber upon the removal of the solvent (*e.g.* by annealing). [125, 197, 225, 429] Although CPSCs represent a promising route towards low-cost, stable and sustainable option for perovskite photovoltaics, the PCEs of those devices still lag behind the conventional ones with metallic electrodes and organic hole-selective layers. [210]

In CPSCs, the graphite acts as both a hole extraction layer and a back-electrode. For the latter, it is important to achieve low series resistance losses to maximize the fill factor (FF), in order to reach high power conversion efficiencies in solar cells and modules. The total electrode resistance is defined by two parameters: material resistivity and electrode dimensions (*i.e.* width, length and thickness). As the width and length are determined by the layout, thickness can be increased in order to reduce the series resistance. However, since in CPSCs, the perovskite solution needs to penetrate through the entire porous cell stack, very thick electrodes result in incomplete pore filling and reduced photovoltaic performance. In addition to the lateral conductivity, the series resistance is also affected by the interfacial resistance that depends on the quality of the carbon/perovskite contact. Therefore, addressing the issue of electrode conductivity and interfacial resistance in CPSCs becomes crucial for boosting the power conversion efficiencies (PCEs) of such cells.

Graphite is a crystalline material, consisting of hexagonally arranged 2D carbon sheets which are stacked onto each other via weak van der Waals interaction. [276] Over the years, the properties of different natural artificial graphite types have been studied by researchers in detail. However, a quantitative comparison of these graphite types in the context of applications for electrodes in perovskite solar cells has not yet been carried out and is therefore addressed here.

In this work, we demonstrate how the graphite crystal type which originates from the graphitization route influences the structural and electronic properties of the graphite particles and the carbon-based electrodes containing them, which consequently affect the performance of the final CPSCs. The characteristics of six different types of graphite crystals have been investigated which will be referred to as artificial, scaly, pyrolytic, flaky, needle, amorphous graphites. These are compared with a reference graphite obtained from a commercially available carbon-graphite paste (Elcocarb B/SP produced by Solaronix SA). Scaly (sometimes also referred to as lump or vein graphite), flaky and amorphous graphites belong to the naturally occurring types of graphite, which can be extracted from ore deposits. The high-quality artificial, needle and pyrolytic graphites are the so-called synthetic graphites, which can be produced from petroleum- or coal-based coke heated up to high temperatures (2500-3000°C) for graphitization – a process when carbon atoms

re-arrange to form graphite particles. [430]

We have coupled the results from X-ray diffraction (XRD) with Raman spectroscopy to evaluate the crystallite dimensions and defect density of each graphite type. Each graphite type was furthermore used to produce separate carbon pastes, which were implemented to prepare carbon-based electrodes for the CPSCs. We quantitatively compare the resistive losses due to different sheet resistance of these carbon-based electrodes. Moreover, the effect of the electrode on charge extraction and recombination at the carbon/perovskite interface were assessed to identify the most optimal graphite type. The highest efficiency was achieved with a scaly graphite type electrode that yielded remarkably low sheet resistance of 4 Ω/sq. and a PCE of 14.63 % with a FF of 71.1 % (on 0.64 cm^2) These new findings highlight the significance of the choice of graphite for the development of efficient perovskite PV devices with carbon-based electrodes.

7.4 Experimental details

Materials

Fluorine-doped tin oxide glass substrates TCO22-7/LI (sheet resistance 7 Ω/sq.), silver paste Elcosil SG/SP, titania paste Ti-nanoxide T165/SP, zirconia paste Zr-nanoxide ZT/SP, carbon-graphite paste Elcocarb B/SP and methylammonium lead iodide perovskite solution with 5-ammonium valeric acid additive (5-AVAI) were provided by Solaronix SA. Acetone was purchased from Carl-Roth, ethanol was purchased from Alcosuisse. Titanium diisopropoxide bis (acetylacetonate) (75 % in isopropanol), Hellmanex and isopropanol were purchased from Sigma-Aldrich. Flaky (V14), scaly (SPR150) and pyrolytic (PC30) graphite powders were obtained from Ito graphite Co. Amorphous and needle graphite powders were purchased from Oriental Industry Co. Ltd., whereas artificial graphite fine powders (UFG30) were purchased from Showa Denko K.K. Experimental graphite pastes were prepared as analogues of Elcocarb B/SP manufactured by Solaronix SA, substituting the reference graphite for another graphite types.

Fabrication of perovskite solar cells with carbon-based electrodes

Devices were fabricated on 10x10 cm^2 plates of FTO-coated glass. First, a laser pattern defined cathode and anode areas with an automated fiber laser. After that, the substrate was subjected to sequential cleaning steps in 1 % aqueous solution of Hellmanex, acetone, and isopropanol respectively (15 min each) in an ultrasonic bath and subsequently dried in air. The thin compact titania layer (c-TiO_2) was grown by spray-pyrolysis on a hot-plate set to 450°C, using a glass mask to protect the contact areas. A volume of 20 mL of titanium diisopropoxide bis

(acetylacetonate) diluted in absolute ethanol (1:160) was sprayed with oxygen as a carrier gas, and warming was prolonged for 30 min before allowing the sample to cool down. An array of 18 electrodes was subsequently defined by screen-printing silver contacts, m-TiO_2, ZrO_2 and carbon paste using a 100-40, 165–30, 90–48, and 43–80 mesh stencil, respectively (the number of strands is per cm). After printing the wet film, each screen-printed layer was allowed to dwell for 10 min before drying at 120°C for 10 min, followed by a firing step at 500°C (or 400°C for carbon) for 30 min, after a 30 min ramp.

The freshly fired electrodes were masked with an adhesive polyimide gasket (provided by Solaronix) to delimit the wet area. The perovskite precursor was re-dissolved at 70°C right prior to use. An empirically determined volume of 5.76 µl of the perovskite precursor solution was dropped in the center of each electrode using a micropipette. The infiltration of the perovskite ink was done using a home-made semi-automated dispensing system. The wet samples were then moved to an oven set to 50°C where they were dried for 60 min, thus forming the perovskite crystals in the porous electrode structure. The polyimide adhesive gasket was carefully peeled off, and the solar cells were individualized by cutting the glass substrate into the corresponding solar cells. The resulting devices were submitted to heat and damp treatment at 40°C and 75 % R.H. for 150 h. according to the previously reported method by Hashmi *et al.* [381]

Characterization

The crystal structure of the graphite was characterized by X-ray diffractometer MiniFlex II, Rigaku using CuKα radiation at a scan rate of 2 °/min (for patterns between 3 and 0.4 °/min (for more highly resolved patterns along specific planes). Raman spectra were measured on aWITec alpha500 Spectrometer with a Nd:YAG laser (λ=532 nm) using a thermoelectrically cooled CCD detector in a range of 70-3700 cm^{-1}. The optical microscopy images were obtained by an OLYMPUS BX50 stereomicroscope and a sCMOS camera ("Zyla 5.5 sCMOS" by Andor) while the partial illumination of the sample was provided by a halogen lamp. To measure sheet resistance, a portion of the carbon paste was casted into a film on bare glass, which was covered on two ends with parallel strips of adhesive tape. Those acted as spacer for the subsequent blade-coating of the carbon paste. The freshly casted layer was fired at 400°C for 30 min. After cooling down to room-temperature, the sheet resistance of resulting carbon layer was measured in several places with a 4-pin probe sheet resistance meter Guardian Manufacturing SRM-232-100. Scanning Electron Microscopy (SEM) images were obtained with a Zeiss Auriga 60 electron microscope. The current-density and voltage curves of as-prepared solar cells were measured under simulated AM1.5G illumination at a scan rate of 4.17 mV/s.

Time-resolved PL decay measurement were conducted using an externally

triggered, optically widened CW laser (Coherent Orbis) of 660 nm wavelength with 100 mW power, with a fall and rise time (10 % and 90 %) below 2 ns. The laser was triggered to produce rectangular-shaped signals at 7Hz frequency. For the transient photovoltage measurement (V_{OC} decay), cells were illuminated using a red LED (635 nm) from Thorlabs. All the cells were light soaked for 15ms followed by switching off the light, after which the resulting voltage decay curve was captured using a PicoScope 5000 series. The measurement was carried out in a dark room to prevent the influence of stray light. The Electrochemical Impedance Spectroscopy (EIS) was carried out using a Ivium CompactStat in the frequency range of 100 mHz to 1 MHz at negative voltage bias and under illumination of 100 kLUX. Steady state Photoluminescence measurements were performed with an Andor Shamrock 193i Czerny-Turner type spectrometer. The illumination source is a frequency doubled Nd-YAG laser from Pegasus laser systems (Pluto, P532.400, λ=532 nm). Its intensity is adjusted to a value such that I_{SC} of the measured cell matches I_{SC} measured on the mismatch corrected solar simulator ensuring the PL measurement to be conducted in an excitation regime close to one sun illumination. The current-density and voltage curves of aged devices were measured with a source meter (Keithley 2400) at a scan rate of 50 mV/s using a class A solar simulator providing 100 mW/cm^2, AM1.5G illumination.

7.5 Results and discussion

The difference between various types of graphite crystals originates from the graphite formation process at the source (*i.e.* ore deposits) and/or preparation methods. These differences result in fundamentally different crystal structures and morphology, which have a direct impact on the electronic properties. [274] In this study, we compared six different types of graphite: artificial, scaly, pyrolytic, flaky, needle and amorphous. Additionally, the graphite used in the Elcocarb B/SP carbon paste produced by Solaronix SA was considered as a reference, as it is often used for the preparation of CPSCs. [203, 381, 429, 431, 432]

We firstly perform X-ray diffraction measurement on graphite powders, in order to gain insights into the graphite crystal structure. Since graphite is a poly-crystalline material, one needs to differentiate between the flake/particle (which is normally in the µm range) and the crystallite size, which consists (with exceptions of impurities) of periodically repeated and hexagonally arranged carbon atoms. Figure 7.1a, displays a visual representation of a small graphite particle/flake consisting of four crystallites as an example. From the XRD patterns of each graphite type (Figure 7.1b) the most pronounced peak appears at approximately 2θ = 26.4°, corresponding to the (002) plane (Figure 7.1b). Additionally, peaks at 2θ = 44.1-44.5°, 42.1-42.3°, 54.4-54.5°, 59,5° and 77.1-77.4° corresponding to (100), (101), (004), (103) and (110) planes, respectively, can be observed.

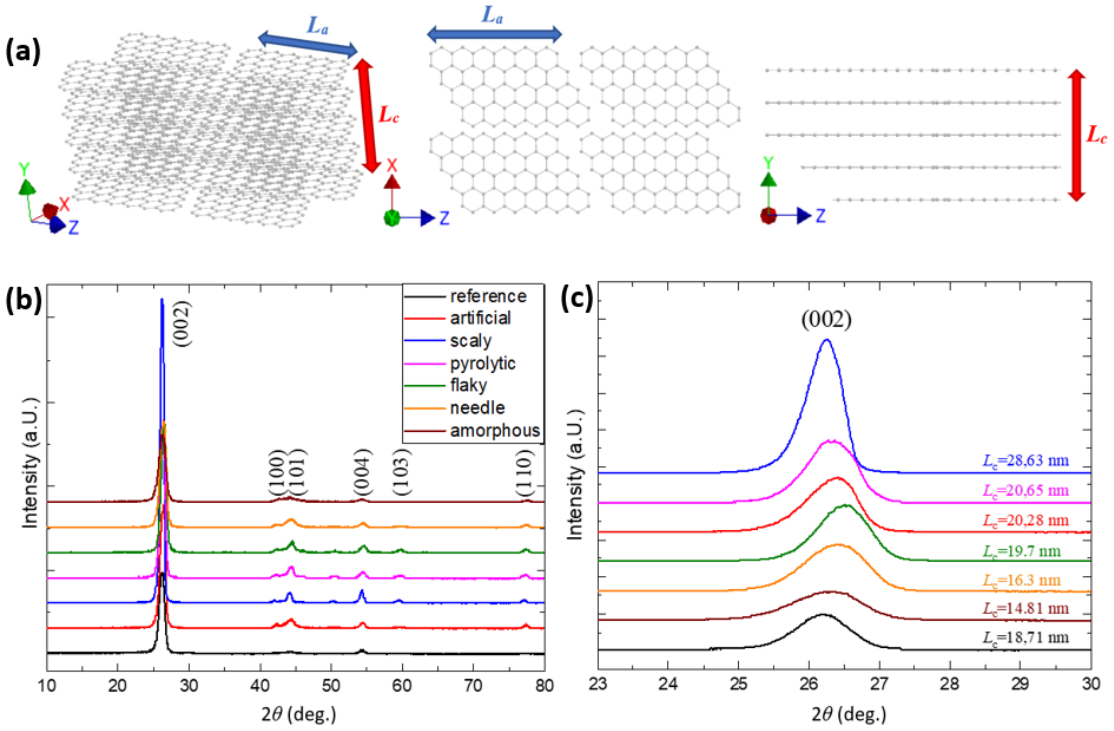


Figure 7.1: (a) Illustration of a graphite particle consisting of crystallites, represented by stacked uninterrupted 2D carbon layers, depicting crystallite height (L_c) and lateral dimensions (L_a) (b) XRD patterns of different types of graphites, showing reflections affiliated with corresponding planes. (c) close-up of image a), showing diffraction intensities of different types of graphite along (002) plane.

The diffraction intensity along such $(00l)$ planes can be related to the crystallite height (L_c), [433–435] whereas intensities from $(hk0)$ planes yield information about the size of a 2D carbon layer (L_a), [433, 436, 437] illustration of which can be seen in Fig. 1c. We use Scherrer equation with a shape factor $K = 0.94$ for polycrystalline graphite to find the crystallite height from the diffraction along (002) plane, revealing that the scaly graphite has the highest L_c of 60.6 nm, followed by artificial (51.5 nm), pyrolytic (50.3 nm) and flaky (48.3 nm) graphites, while amorphous, needle and our reference graphite exhibit lower crystallite height. The two-dimensional carbon layer dimensions L_a, determined from the (110) reflection, can be derived, according to Warren, [436] by:

$$L_a = \frac{1.84 \cdot \lambda}{FWHM \cdot \cos\theta} \tag{7.1}$$

The calculated L_a for different types of graphites are displayed in Table 7.1, where the scaly graphite has the largest crystallite lateral size of 28.6 nm. These results

Table 7.1: Crystallite height (L_c), crystallite lateral dimensions (L_a) and I_D/I_G band ratio describing the lattice disorder in different types of graphites.

Graphite type	L_c (nm)	L_a (nm)	I_D/I_G
Reference	18.7	43.7	0.08
Artificial	20.3	51.5	0.069
Scaly	28.6	60.6	0.064
Pyrolytic	20.7	50.3	0.033
Flaky	19.7	48.3	0.041
Needle	16.3	42	0.113
Amorphous	14.8	37.8	0.109

show that after the graphitization process, scaly graphite provides the largest crystallites (regarding height and lateral size). We hypothesize that graphites with a larger uninterrupted periodic crystal structure would result in less grain boundaries and provide better charge carrier mobility as well as faster charge transport along graphite, resulting in better conductivity.

To gain more insight into the density of crystal defects, Raman spectra of each graphite type were measured (Figure 7.2). The bands at 1355 cm^{-1} and 1580 cm^{-1}

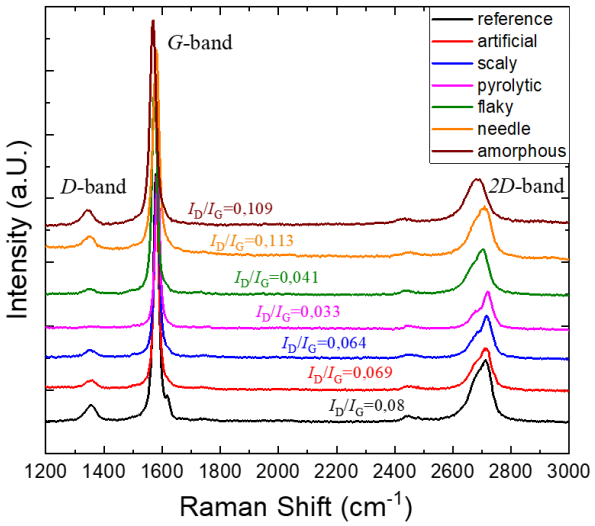


Figure 7.2: (a) Raman shift spectra of different graphite types, highlighting the D-, G- and 2D-bands, as well as the ratio of intensities of D- and G-bands for each type.

are commonly attributed to D and G bands respectively, while the 2D band appears at around 2670 cm^{-1}. The D band is normally defect-induced and occurs only when the translational symmetry of two-dimensional carbon periodic structure is broken, resulting in A_{1g} vibrational mode, while the G band is strongly related to the E_{2g} vibrational mode of the sp^2-hybridized carbon lattice. [433, 437] Therefore, the intensity ratio of D and G bands (I_D/I_G) is often used as a measure of lattice disorder, [437, 438] which is low for highly crystalline graphene/graphite and high for turbostratic or disordered structure of non-graphitic carbon. As seen from the obtained Raman shift spectra in Figure 7.2, the I_D/I_G is increasing in the order pyrolytic < flaky < scaly < artificial < reference < amorphous < needle. This result suggests that pyrolytic type of graphite possesses the lowest number of structural defects and provides potential for reaching higher charge carrier mobility and layer conductivity, consistent with the demonstrated reports displaying well-aligned individual crystallites with a low mosaic spread angle in pyrolytic graphite. [439]

Coming from the sub-nanometer crystallites to the larger graphite flakes, we recorded SEM images, of powders of each graphite type, as presented in Figs. S1 and S2. The flakes of artificial, scaly, pyrolytic and flaky tend to be larger and more parallel-stacked, whereas the amorphous one tends to form separate small-sized clusters. Our reference graphite does not exhibit large crystals, although tightly interconnected in between and seems to be more truncated than most of other graphite types.

Next, these graphite powders were used for the preparation of respective carbon-based pastes, in order to screen-print them on the cell stack shown in Figure 7.3. The pastes were prepared in exactly same manner as it was done for the reference Elcocarb B/SP paste, except for the replacement of reference graphite with the natural and synthetic graphite powders described above. Regarding the optical appearance, the pastes with needle and amorphous types proved to result in layers of comparable high quality and homogeneity with the reference one. In contrast, those containing artificial and flaky graphites seemed to be printed less homogeneously, as seen from the optical microscopy images in Fig. S3 where an obvious pattern resulting from the screen mesh is visible. Moreover, in all the deposited layers, except for the reference and the one containing pyrolytic graphite, several small voids could be observed in the microscope, possibly arising from the inhomogeneous spreading of the paste. The pastes containing scaly graphite was the most challenging to print evenly across the whole printing pattern, suggesting a correlation between the graphite flake size and paste rheology.

The fabricated CPSCs have a standard structure , constituting fluorine-doped tin oxide (FTO) as a front electrode, compact titanium dioxide (c-TiO_2) as a hole blocking layer, mesoporous titanium dioxide (m-TiO_2) acting as an electron selective layer, a spacer layer of zirconium dioxide (ZrO_2) covered by a carbon-based back-electrode (Figure 7.3). After the cathode deposition, the cells were filled

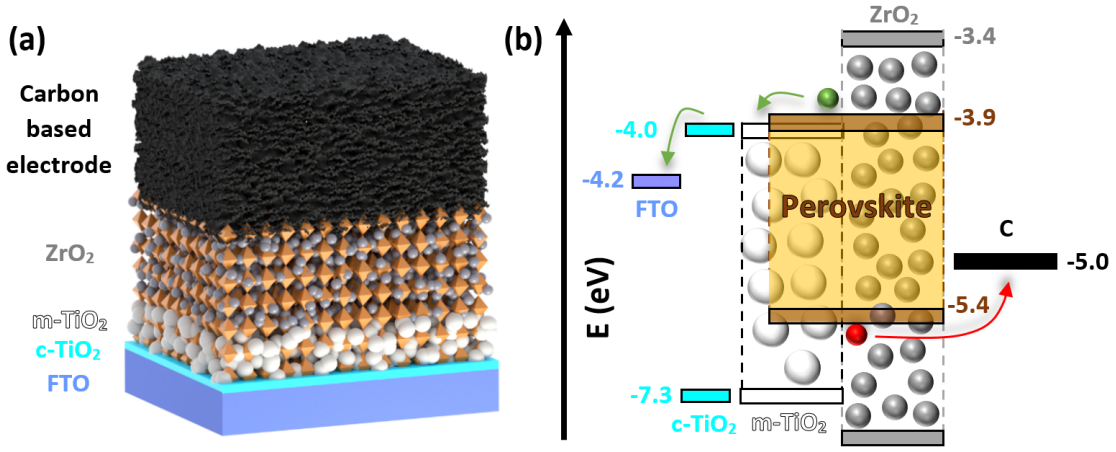


Figure 7.3: (a) Architecture of the fabricated carbon-based perovskite solar cells. (b) Energy band diagram of the CPSCs depicting the extraction of photogenerated electrons (green) and holes (red) by the m-TiO_2 and carbon-based electrode, respectively.

with the mixed dimensional (2D/3D) $5AVA_{1-x}(CH_3NH_3)_xPbI_3$ perovskite absorber, employing an automatic CNC-controlled pipetting device with precisely controlled drop-casting. The measured photoluminescence (PL) spectra of each cell type (Fig. S4) confirmed the peak position at 764 nm and a bandgap of 1.62 eV, consistent with the previous reports on CPSCs with such absorber. [203] Since the perovskite properties are not influenced by the graphite type in the electrode, it is not surprising that the PL peak for all cell types is the same. Nine cells with carbon-based electrodes of each graphite type were fabricated and JV-scans were measured under a solar simulator. The short-circuit current density (J_{SC}), open-circuit voltage (V_{OC}), fill factor (FF) and power-conversion efficiency (PCE) are presented in Figure 7.4.

Cells with reference, artificial and scaly graphites display slightly higher J_{SC} and V_{OC} than the pyrolytic, flaky and needle graphites. The most pronounced difference between the cells is seen in the FF. This is not surprising, considering that one of the main roles of carbon-based layer is being a back-contact of the cell and the resistance losses in the cell are strongly affected by it. Remarkably, some CPSCs with electrodes constituting pyrolytic graphite flakes have FFs even above 74 %, although the devices with scaly and artificial graphites that yielded the highest PCE did not have the highest FFs. The scaly graphite in the carbon-based electrode was found to be the most optimal type, leading to a champion efficiency of 14.63 %. Notably, as seen from the cross-sectional SEM (Fig. S5) images although the carbon-based electrodes with scaly graphite were found to be the thinnest (probably attributed to inhomogeneous layer printing), their sheet resistance is the lowest,

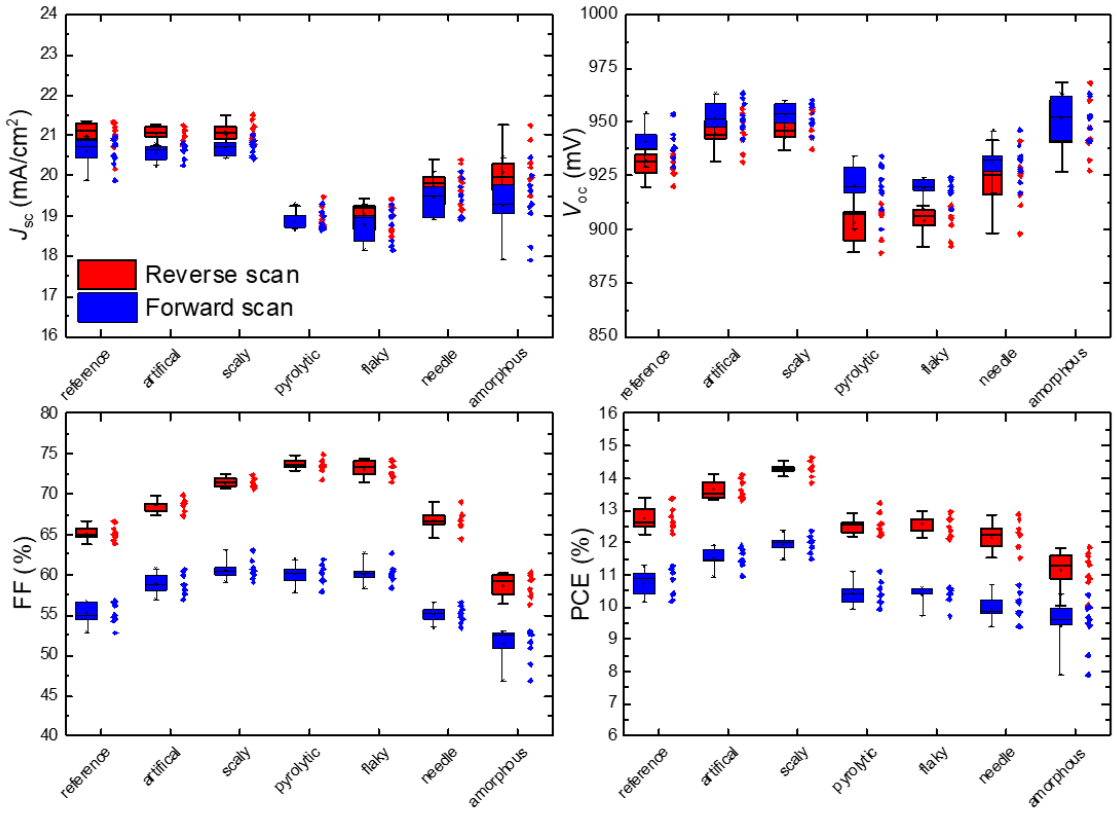


Figure 7.4: JV-parameters obtained from reverse (red) and forward (blue) voltage sweeps of CPSCs with electrodes made of different graphite types.

suggesting that the FF can be further improved by increasing the electrode thickness.

To elucidate the influence of graphite type on the cell's series resistance losses we performed sheet-resistance measurement and electrochemical impedance spectroscopy (EIS) on the cells. From the sheet resistance measurement shown in Figure 7.5, the scaly and pyrolytic graphites display exceptionally low sheet resistance close to 4 Ω/sq. lower than the sheet resistance of conducting oxides such as fluorine- or indium-doped tin oxides with comparable sheet resistances of 7-10 Ω/sq. and 13-20 Ω/sq. respectively, [440–442] which are widely used in PSCs. Moreover, all the other types of carbon-layers except for needle, reference and amorphous ones, exhibit sheet resistance below 10 Ω/sq. highlighting great potential to be an efficient alternative to costly metal-based contacts. From Figure 7.5 it can be seen that the trends between the sheet resistance and the series resistance (R_s) extracted from the EIS measurements are in good accordance. The results indicate that the high crystallite height L_c, low number of structural defects, high graphite crystallinity and flake stacking (as in the case of scaly, artificial, pyrolytic and flaky graphites) seem to strongly reduce the series resistance losses of the solar cell,

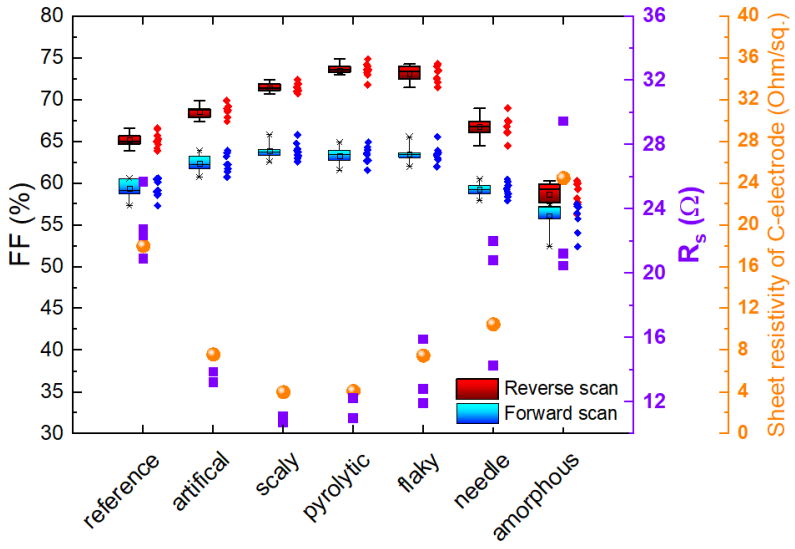


Figure 7.5: Fill factor of CPSCs fabricated using different graphite sources from applied reverse and forward voltage scans, which correlates with the sheet resistance of the respective carbon-based electrode and series resistance (R_s) obtained from the Nyquist plot (3 cells per group are shown, measured at 0.6 V)

positively influencing the PCE.

Looking at the SEM cross-section of the cells, presented in Fig. S5, we note that the cells with artificial, scaly, pyrolytic and flaky graphites are well-aligned along the longitudinal plane (*i.e.* in-plane with the substrate) providing an efficient lateral charge transport through the highly conductive carbon-based contact. On the contrary, in needle graphite vertically arranged flakes are frequently occurring, hindering efficient charge transport along the longitudinal plane. In amorphous layers, the graphite flakes are much smaller than in other cells. This indicates that the exceptionally low series resistance of the cells with scaly, pyrolytic and flaky graphites could also partially originate from the large and well-aligned flakes of the respective carbon layers.

Although the correlation between the R_s of the cell and FF are clear, there are some deviations from this trend (*e.g.* the most conductive scaly graphite does not have the highest FF). At the Nyquist plot in Fig. S6, two semicircles can be observed: the high-frequency one, which was attributed to the perovskite/carbon interface and the low-frequency one, which corresponds to charge recombination resistance at perovskite/TiO_2 interface. The latter one is similar in all cells regardless of the respective graphite type due to unaltered properties of the perovskite/TiO_2 contact. The perovskite/carbon interface changes depending on the graphite type in the carbon-based electrode. As shown in Figure 7.6b, the lowest interfacial resistance (R_{CE}) at the counter-electrode was seen in the flaky

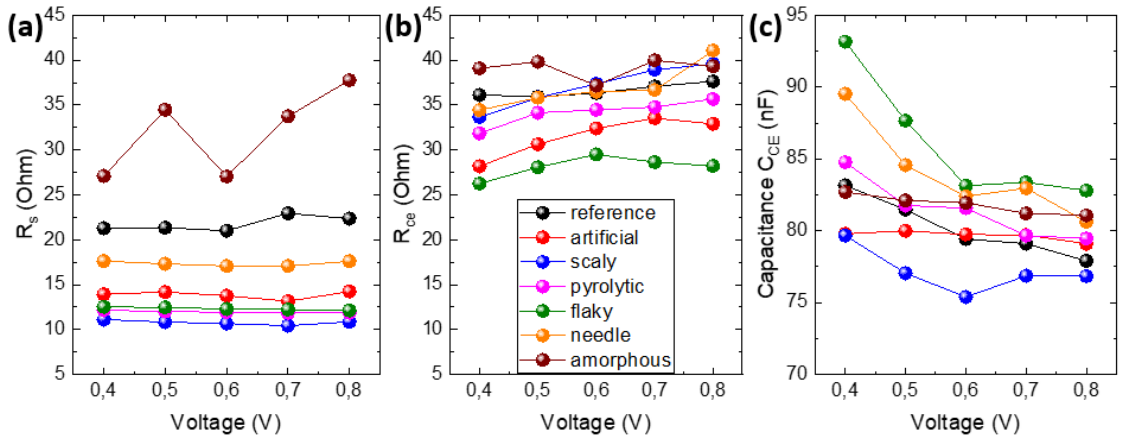


Figure 7.6: R_s and R_{CE} extracted from the Nyquist plots at different applied voltage bias for CPSCs with various graphite types

graphite, followed by the artificial one. Therefore, we postulate that the FF is influenced by the final interplay between the R_s and the interfacial resistance R_{CE} at the perovskite/carbon contact.

Looking closer at the semi-circle corresponding to carbon/perovskite interface, it can be noticed that cells with reference, artificial and scaly graphites display the smallest capacitance at the interface with values below 80 nF (Figure 7.6c). This means that less charge accumulation happens on each side of the interface, providing an easier hole injection from perovskite to carbon and resulting in higher J_{SC} values. To confirm this, we additionally perform time-resolved photoluminescence (TRPL) measurements, evaluating charge carrier extraction by the selective layers. The only difference between the samples is the graphite source, which makes it reasonable to assume that perovskite/m-TiO_2 interface is similar in all cases, as also suggested by the EIS results. Thus, it is reasonable to assume that the variations between the PL decays after excitation arises from the different graphite types and carbon/perovskite contact. The carrier extraction time was estimated by fitting the TRPL measurement to a bi-exponential decay function (Fig. S7). Scaly, artificial and reference graphites have a short extraction time of 6.92 ns, 9.79 ns and 10.54 ns respectively, whereas in cells with pyrolytic, flaky, needle and amorphous graphite types, charge extraction time is longer – 14.91 ns, 22.63 ns, 12.37 ns and 11.53 ns respectively. The shorter charge carrier extraction time suggests that the hole extraction by graphite are enhanced, leading to higher photo-currents, which have been demonstrated earlier in Figure 7.4.

The difference in V_{OC} between cells with different graphites, suggests that the non-radiative recombination at the back-contact can also be influenced by the graphite type. The transient V_{OC} measurement conducted in high-perturbation

mode (details in Experimental Section) are shown in Fig. S8 which indicates that the charge carrier recombination at the back-contact is slower in cells with scaly graphite, followed by reference, artificial and amorphous types. The fastest recombination seen in the V_{OC} decay occurs in cells with needle graphite, suggesting that the recombination at the perovskite/carbon interface in such type of cells is the highest. Interestingly, amorphous flakes, which have the highest portion of non-graphitic carbon (as was demonstrated from Raman Shift spectra) does not have a negative effect on the recombination at the back contact and V_{OC}. The trend between the recombination at the back-contact aligns with the measured V_{OC} obtained from the JV-scan of respective graphite types, where the scaly and amorphous graphites which have the highest V_{OC} exhibit longer charge carrier lifetime, whereas in flaky and needle types it is shorter resulting in a lower V_{OC}.

As was shown earlier, the graphite type can also affect the carbon-layer morphology. HSL-free CPSCs typically exhibit higher stability than cells with HSLs and metal-based contacts. Besides the fact that graphite itself does not degrade or react with the perovskite, this could be due to the presence thick hydrophobic carbon-based back-contact filled with perovskite that prevents moisture ingress. The latter implies that, thinner and less homogeneous carbon layers could facilitate easier moisture and air ingress into the sensitive perovskite photoabsorber, leading to faster degradation. In order to evaluate the effect of graphite type on cell's stability, cells with different graphite types were stored under ambient conditions (40-50 % R.H.) in the dark for 5,000 hours. As seen from the Figure 7.7, the scaly

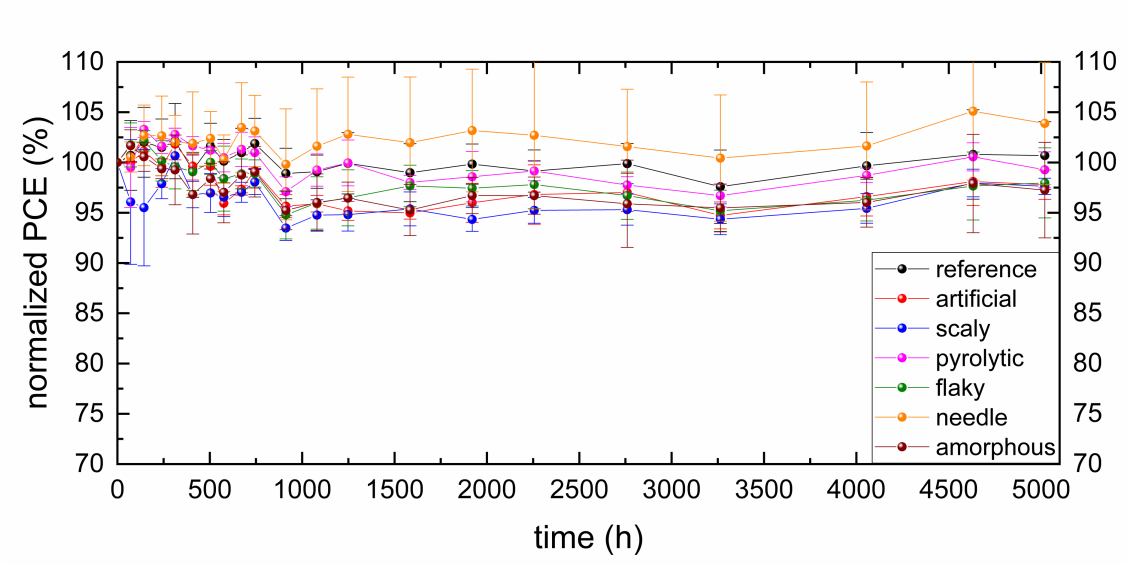


Figure 7.7: PCE evolution during the storage of non-encapsulated CPSCs under ambient environment (R.H. = 40-50 %) in the dark. Each data point represents an average between the measured samples of each point with a std. deviation.

and amorphous graphites show the fastest degradation, losing less than 3 % of the initial efficiency, whereas the cells with needle and reference graphites demonstrate high shelf-stability by retaining nearly same PCE or even higher during the whole ageing period. Notably, the cells with pyrolytic graphite also appear to be more stable, which we attribute to the absence of voids in the carbon-based cathode, which appeared during the layer deposition. In contrast, CPSCs with other graphite types have a slightly reduced performance that we attribute to an easier ingress of moisture and air into the sensitive perovskite photoabsrober, leading to degradation. Although the electrodes based on amorphous graphite were deposited homogeneously, the observed degradation is likely to be related to a small particle graphite size (as was seen from SEM images earlier), which cannot provide a sufficient protection against ambient environment. These results point out that in order to ensure the long-term stability of cells with carbon-based electrodes, the paste rheology, particle size and homogeneity of the deposition have to be carefully optimized.

7.6 Conclusion

In this work, we have analyzed the differences between three types of naturally-occurring graphites, namely, scaly, flaky and amorphous, as well as three types of synthetic graphites: artificial fine powder graphite, highly ordered pyrolytic one and needle graphite in the context of applications for carbon-based electrodes for perovskite solar cells. We compared their properties with our reference graphite – Elcocarb B/SP, obtained from Solaronix S.A. The scaly type, having a unique graphitization route, yielded graphite particles with the largest crystallite dimensions, whereas pyrolytic graphite had the lowest number of structural defects. The FF of the fabricated cells was found to be most affected by different graphite types and is influenced not only by sheet resistance of the electrodes, but also by its interfacial resistance to perovskite. The electrodes produced from the pyrolytic, flaky and scaly graphite had the least series resistance losses, leading to FFs above 70 % in cells with a 0.64 cm^2 active area. Although the cells with pyrolytic graphite exhibited the least series resistance loss, the J_{SC} of these cells were reduced due to the build-up of a higher capacitance and reduced charge extraction at perovskite/carbon interface. Interestingly, under continuous sun illumination, the overall difference in V_{OC} for cells with all graphite types is rather low – approximately 50 mV. CPSCs with electrodes made from scaly and artificial graphites has proven to have better charge transport properties, resulting in enhanced photovoltaic performance, where the champion cell with a scaly graphite reached a PCE of 14.6 %. The printability and adhesion to the layer underneath was found to affect the homogeneity of the electrode deposition, which was found to affect the cell moisture-stability. All the CPSCs were found to be quite stable, where the least stable cells with scaly and amorphous graphite lost less than 3 % of initial PCE after 5,000 h of storage in the ambient environment. The reference cells with electrodes based on Elcocarb

B/SP paste remained the initial PCE, while the cells with needle-based graphite had slightly improved performance after ageing. This work paves a way towards optimizing the low-cost and up-scalable carbon-based electrodes for efficient perovskite PV devices with low series resistance losses, which is essential for its successful commercialization.

7.7 Critical discussion

Understanding the structure of graphite is paramount to reduce losses in CPSCs caused by the carbon-based electrodes. The presented investigation discusses several types of graphite crystals with different crystallographic and electronic properties, which naturally influence the performance of a perovskite PV device with carbon-based electrodes. Despite the very detailed and systematic analysis of different graphites in CPSCs, a couple of questions in this study remained unanswered:

- In this study the XRD measurement in Bragg-Brentano mode was utilized to investigate crystallographic properties of different graphites. However, a more accurate technique, such as single-crystal XRD (subsection 2.2.1) would yield a more precise result regarding the crystallite dimensions (L_a and L_c), especially considering that in all the graphite types they are rather similar in value.
- Most of the attention in this research was given to the influence of graphite type on series resistance losses, and thus FF. However, a significant difference in J_{SC} and V_{OC} were also found in for samples comprising different graphites, which were however discussed only briefly. A further investigation of the influence of graphite type in the carbon-based electrode on the J_{SC} and V_{OC} would provide a more complete picture of the interplay between the graphite flakes and the final device properties.
- It is interesting to note that the here analyzed cells could withstand 5,000 hours of storage in the dark under ambient environment conditions, but harsher accelerated ageing tests would have been more informative. For example, placing cells under humid (R.H.>80 %) and/or hot environment (*e.g.* >80°C) and measuring their performance over time or thermal cycling tests would provide a definitive information whether carbon electrodes with different graphite types can retard/accelerate degradation mechanisms.
- Due to a newly-developed protocol for these previously "untested" graphites, the paste preparation and its deposition procedure were not optimized. Therefore, the layers were typically thinner (Figure 7.8) as compared to the well-optimized reference one and occasionally had spots without carbon in the active area (*i.e.* locations where perovskite in ZrO_2 was directly exposed to ambient). Although producing electrodes with the same thickness would have provided a more direct comparison, it is remarkable that despite having lower

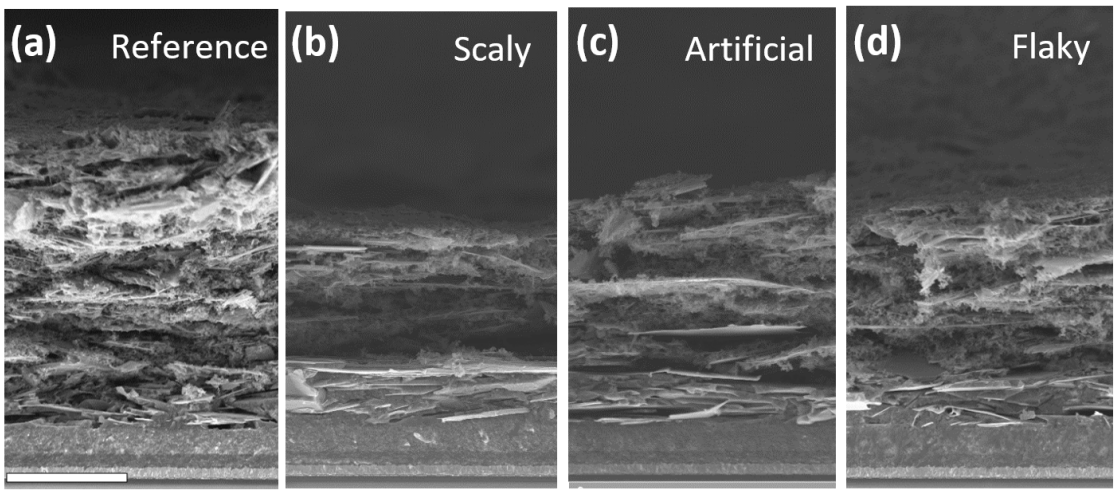


Figure 7.8: SEM images of the cross-section of H-CPSCs with electrodes manufactured from different graphites: (a) reference, (b) scaly, (c) artificial and (d) flaky types

thickness, electrodes with certain highly-conductive graphites could still have lower sheet resistance.

The results presented in this study suggest that scaly or pyrolytic graphites are particularly beneficial for lateral charge transport within carbon electrode, while flaky and artificial graphites have a slightly better electrical coupling to the photoabsorber, providing low interfacial resistance at the perovskite/carbon contact. This inspired the author of this study to develop a composite graphite electrode, which combines the advantages of both: (1) highly conductive graphite for good lateral charge conductivity and (2) graphite forming a favorable perovskite/carbon interface. Two approaches were tried:

1. Double-layer: depositing carbon-based electrode with scaly graphite on top of a layer of flaky electrode
2. Composite blend: embedding both types of graphite (for high lateral conductivity and low interfacial resistance) together into a paste and depositing it as single carbon layer.

Despite the initial improvement in PCE of utilizing these graphites in H-CPSCs, the devices with composite structure, unfortunately, only had lower PCE. One possible explanation why the double-layer approach didn't perform as expected would be the increased layer thickness, which might have hindered effective impregnation of the cell stack with perovskite solution. The question as to why the blending approach did not provide high-efficient devices (or at least the devices with comparable PCE to reference cells) remains unanswered and may require further process optimization. Notably, if both approaches would not lead to an improved performance it would have been interesting to investigate why.

Chapter 8

Perovskite photovoltaic devices with carbon-based electrodes under reverse bias

8.1 Preamble

After the identification of the main energy loss mechanisms (*cf.* chapter 5) and addressing them via nanoarchitectonics (*cf.* chapter 6), as well as optimization of the carbon electrode (*cf.* chapter 7), the focus of this work moved forward from CPSC performance towards its stability. While most reports discuss degradation caused by heating in dry or wet environment, continuous 1-Sun illumination or thermal cycling, few attention has been given to degradation under reverse bias. Hence, the author of this work decided to focus on this challenging issue of reverse bias-induced degradation of CPSCs and how perovskite PV devices with carbon-based electrodes behave under such conditions.[♮]

[♮]This chapter (except for the critical discussion in section 8.7) has been published as peer-reviewed research paper in the scientific journal "Solar RRL" (impact factor 2022: 8.6):

Bogachuk, D., Saddedine, K., Martineau, D., Narbey, S., Verma, A., Gebhardt, P., Herterich, J.P., Glissmann, N., Zouhair, S., Markert, J., Gould, I.E., McGehee, M., Würfel, U., Hinsch, A. and Wagner, L. (2021) Perovskite Photovoltaic Devices with Carbon-Based Electrodes Withstanding Reverse-Bias Voltages up to -9 V and Surpassing IEC 61215:2016 International Standard. *Sol. RRL*, p.2100527.

The individual contributions were as follows:

- **D.B.**: conceptualization and idea of publication, simulation of series-interconnected CPSCs, explanation of device behavior under reverse bias, performing JV-measurements, UV–vis measurements, coordinated the work, analyzed all the measurements and prepared the manuscript, as well as figures
- **K.S.**: performing JV-measurements
- **D.M.**: manufacturing perovskite solar modules with carbon-based contacts, contributed to writing the manuscript
- **S.N., A.V.**: manufacturing perovskite solar cells with carbon-based contacts
- **P.G.**: analyzed and prepared report of the hotspot test, as well as part of the manuscript corresponding to the IEC 61215-2:2016 test description
- **J.P.H.**: performing IR thermographic measurement
- **N.G.**: performing XRD measurements
- **S.Z.**: simulation of series-interconnected CPSCs
- **J.M.**: performing the official “hotspot” test at the accredited laboratory “TestLab PV Modules” at Fraunhofer ISE
- **I.E.G.**: contributed to the manuscript preparation and results interpretation
- **M.M.**: provided valuable ideas and contributed to the manuscript preparation and results interpretation
- **U.W., A.H.**: contributed to the manuscript preparation and results interpretation
- **L.W.**: conceptualization, explanation of device behavior under reverse bias, contributed to the manuscript preparation and results interpretation
- **All authors**: reviewed the manuscript and made valuable comments to it

8.2 Abstract

One of the key challenges of perovskite photovoltaics (PV) is the long-term stability. Although efforts have been made to improve the lifetime of perovskite PV devices, their degradation under reverse-bias conditions has been barely addressed. In this work, perovskite solar cells with carbon-based electrodes are presented which demonstrate superior resilience against reverse-bias-induced degradation. Although their breakdown voltage was identified to be at approximately -3.6 V, cells do not degrade until the applied reverse-bias exceeds -9 V. Two main degradation mechanisms have been identified: (i) iodine loss due to hole tunneling into perovskite, which takes place even at low reverse-bias but decomposes the perovskite only after long time durations and (ii) rapid heating at large reverse-bias leading to formation of PbI_2, which starts at shunts and then follows the path of the least resistance for the cell current, which is primarily influenced by the electrode sheet resistances. Finally, perovskite solar modules with carbon-based electrodes have been demonstrated, which were subjected to a "hot-spot" test described in the IEC 61215:2016 international standard at an accredited module testing laboratory. Passing this accelerated test for the first time confirms the superior stability of perovskite PV devices with carbon-based electrodes and highlights their large industrialization potential.

8.3 Introduction

Countless researchers across the scientific world have been attracted by perovskite materials, which exhibit favorable properties for their applications in semiconductor devices, [52, 54, 58] particularly, in photovoltaics (PV). [49, 69, 70, 72, 114, 443, 444] Although the power conversion efficiency (PCE) of perovskite solar cells (PSCs) already reached comparable values of those in conventional silicon-based PV cells, [50, 445] the device stability (intrinsic and extrinsic) is still a challenge on which tremendous efforts in the perovskite community are currently focused. [87, 123, 137, 138, 179, 210]

Numerous different strategies have been demonstrated in order to improve the stability of PSCs under conditions described in the IEC 61215:2016 international standard, [446] which represents a benchmark for commercializing any emerging PV technology and is comprised of several accelerated aging tests to determine the operational stability of a PV module. [447] Most of the reports have primarily focused on passing the damp-heat test (85°C, 85 % R.H., 1000 h) [194, 378, 448, 449] and continuous 1-Sun illumination test (AM1.5G, 1000 h). [125, 189, 209, 378, 450–452] There are also few works demonstrating the humidity-freeze test (10 cycles of temperature variation from -40°C to 80°C at 85 % R.H.), [448] thermal cycling tests (50 cycles of temperature variation from -40°C to 85°C) [378, 449, 453] and UV-pre-exposure tests (15 kWh/m^2 dose of UV-light) [378, 449, 454] which are also required by the IEC 61215:2016 standard.

However, up to now only few works have focused on the reverse-bias-induced degradation, understanding its nature [455, 456] and developing strategies to suppress it, [457] while the issue of hotspot creation and bypass diode thermal tests for perovskite solar modules (PSMs) have still not been investigated, according to our knowledge. In fact, the authors of these works [455–457] demonstrated that perovskite solar cells rapidly degrade even under mild reverse-bias conditions, highlighting that this issue is critical for bringing perovskite PV to the market. It is surprising to see that the reverse-bias behavior of perovskite PV has been so greatly overlooked, considering that the creation of hotspots (which occur when PV device operates under reverse-bias) is one of the key challenges for the well-established PV technologies, such as silicon PV. [447] Defective or current mismatched PV cells can be considered as the intrinsic origins of the creation of hotspots in modules, while partial shading of a PV module during its operation is considered an extrinsic and often occurring cause of reverse-bias induced degradation. [447] Therefore, if perovskite PV module manufacturers plan to contribute to sustainable electrical energy infrastructure, they need to find solutions to pass the reverse bias test.

In this work, we systematically investigate the reverse-bias behavior of the perovskite solar cells with carbon-based back-electrode (CPSCs), which exhibit exceptional resilience to the reverse-bias-induced degradation. Although the breakdown voltage of the single cell was identified to be at around -3.6 V, these cells were proven to successfully withstand higher reverse-bias voltages and even current densities close to 70 mA/cm^2 when fully shaded. The impressive stability under reverse-bias is attributed to lack of metal-induced degradation mechanisms (electrode melting and metal ion diffusion at elevated temperatures), phase-segregation and degradation of organic charge extraction layers. Furthermore, we manufacture 10x10 cm^2 perovskite solar module with carbon-based back-contacts, which we subjected to the hotspot tests (according to norms for silicon-based PV and thin-film-based PV modules) described in IEC 61215-2:2016 standard. To the best of our knowledge, these are the first published certified tests addressing the reverse-bias induced degradation in perovskite PV modules. As our modules have successfully passed these accelerated ageing tests, this study represents a breakthrough in tackling the challenge of reverse-bias induced degradation, thus, bringing the perovskite solar cells closer to commercialization.

8.4 Experimental details

Materials

Fluorine-doped tin oxide glass substrates TCO22-7/LI (sheet resistance 7 Ω/sq.), silver paste Elcosil SG/SP, titania paste Ti-nanoxide T165/SP, zirconia paste Zr-nanoxide ZT/SP, carbon-graphite paste Elcocarb B/SP and methylammonium

lead iodide perovskite solution with 5-ammonium valeric acid additive (5-AVAI) were provided by Solaronix SA. Acetone was purchased from Carl-Roth, ethanol was purchased from Alcosuisse. Titanium diisopropoxide bis (acetylacetonate) (75 % in isopropanol), Hellmanex and isopropanol were purchased from Sigma-Aldrich.

Fabrication of perovskite solar cells with carbon-based electrodes

Devices were fabricated on 10x10 cm^2 plates of FTO-coated glass. First, a laser pattern defined cathode and anode areas with an automated fiber laser. After that, the substrate was subjected to sequential cleaning steps in 1 % aqueous solution of Hellmanex, acetone, and isopropanol respectively (15 min each) in an ultrasonic bath and subsequently dried in air. The thin compact titania layer (c-TiO_2) was grown by spray-pyrolysis on a hot-plate set to 450°C, using a glass mask to protect the contact areas. A volume of 20 mL of titanium diisopropoxide bis (acetylacetonate) diluted in absolute ethanol (1:160) was sprayed with oxygen as a carrier gas, and warming was prolonged for 30 min before allowing the sample to cool down. For the manufacturing of CPSCs, an array of 18 electrodes was subsequently defined by screen-printing silver contacts, m-TiO_2, ZrO_2 and carbon paste using a 100-40, 165–30, 90–48, and 43–80 mesh stencil, respectively (the number of strands is per cm). After printing the wet film, each screen-printed layer was allowed to dwell for 10 min before drying at 120°C for 10 min, followed by a firing step at 500°C (or 400°C for carbon) for 30 min, after a 30 min ramp.

The freshly fired electrodes were masked with an adhesive polyimide gasket (provided by Solaronix) to delimit the wet area. The perovskite precursor was re-dissolved at 70°C right prior to use. An empirically determined volume of 5.76 µl of the perovskite precursor solution was dropped in the center of each electrode using a micropipette. The infiltration of the perovskite ink was done using a home-made semi-automated dispensing system.

Same processes were used to manufacture CPSMs with 12 series-interconnected cells except for the aperture area of the screen-printing mesh and perovskite filling procedure. The infiltration of the modules with perovskite solution was conducted via inkjet-filling process with a 10pL droplet volume and 1200x1200 dpi resolution.

The wet samples (cells and modules) were then moved to an oven set to 50°C where they were dried for 60 min, thus forming the perovskite crystals in the porous electrode structure. The polyimide adhesive gasket was carefully peeled off, and the solar cells were individualized by cutting the glass substrate into the corresponding solar cells. The resulting devices were submitted to heat and damp treatment at 40°C and 75 % R.H. for 150 h. according to the previously reported method by Hashmi *et al.* [381]

Characterization

The current-density and voltage curves of solar cells were measured with a source meter (Keithley 2400) at a scan rate of 20 mV/s using a class A solar simulator providing 100 mW/cm^2, AM1.5G illumination. Same equipment was used for obtaining IV-curves of the modules, but the scan rate was set to 100 mV/s in this case. The current measurement of a cell without illumination at a fixed voltage for specific time durations have been measured with the same source meter. After this measurement, slow V_{OC} recovery process is observed (as mentioned in the main text), which depends on the magnitude of applied reverse-bias. For the reason of objective comparison, the cells were measured the next day, in order to determine the performance change after the applied bias for specific time duration. Sheet resistance of front and back-electrodes was measured in several places with a 4-pin probe sheet resistance meter Guardian Manufacturing SRM-232-100.

The light reflection, transmission and absorption were measured with Perkin Elmer Lambda 950 UV-VIS/NIR spectrophotometer with an integrating sphere. XRD diffraction patterns were recorded at room temperature with an XPERT-3 MRD system using a Xe point detector, Bragg-Brentano beam optics and a Cu-Kα radiation source. Diffraction spectra were recorded between $2\theta = 5°$ to $2\theta = 65°$ at a scan rate of 1.5° per minute with a step size of 0.015°. The setup used for DLIT characterization was a custom-made tool by the company IRCAM GmbH. The camera contained an InSb-based mid-wave infrared focal plane array (MWIR FPA) detector, sensitive to IR radiation in the range of 1.5–5 µm, and was actively cooled. The solar cell was subjected to bias voltage of a Toellner four-quadrant power supply and the IR camera signal was analyzed as a real-time video. For the measurements of cell temperature over the whole active area, a thermometer-set Qtemp 200 (manufactured by VWR International GmbH) was utilized.

Details on the characterization of modules during the IEC IEC 61215-2 MQT 09.1 and MQT 09.2 can be found in the hot-spot test report in the Supplementary Information.

8.5 Results and discussion

Dark *JV*-curves of perovskite solar cells with carbon-based contacts

The standard device characterization of solar cells is the measurement of the IV-curve under illumination in a forward bias regime between applied positive voltages V_a=0 (*i.e.* short-circuit) and V_a= V_{OC} (*i.e.* open-circuit). In the reverse bias regime, however, the V_a is negative and the larger V_a leads to a higher

potential difference between electron and hole quasi Fermi-levels (although in PSCs it is also influenced by an additional ion-induced electric field at interfaces [458]. Throughout the manuscript we will always refer to the absolute voltage value in the context of applied reverse bias *i.e.* high reverse-bias means more negative voltage values. If the reverse-bias voltage is high enough, the conduction and valence bands of perovskite are bent stronger and at a certain point the peak electric field will exceeding breakdown threshold causing large currents to flow under negative voltages [7]. The voltage at which breakdown occurs is referred to as breakdown voltage (V_{br}) and it is a critical parameter for the design of photovoltaic modules. [9]

The CPSCs utilized in this work are comprised of compact titanium dioxide (c-TiO_2) coated on FTO, with a mesoporous titanium dioxide (m-TiO_2) as electron selective layer (ESL), zirconium dioxide (ZrO_2) insulating spacer layer and a carbon-based electrode (Figure 8.1a). We note that this architecture does not include a hole-selective-layer (HSL). After the back-electrode is deposited, the entire mesoporous stack is infiltrated with perovskite solution, which crystallizes into $5AVA_{1-x}(CH_3NH_3)_xPbI_3$ perovskite (where $0<x<1$ and 5AVA denotes 5-aminovaleric acid) after annealing. Although, it has been demonstrated that the CH_3NH_3-based perovskite films in solar cells with standard n-i-p or p-i-n architectures are prone to degradation (*e.g.* thermal, under illumination [121, 123, 459]), when such perovskites are integrated into a CPSC structure, the cells exhibit 9,000-10,000 hours of operational stability under full sun (AM1.5G spectrum) illumination at 55°C, which are the longest stability measurements to date. [203, 378] This highlights that even with CH_3NH_3-based photoabsorber, CPSCs display

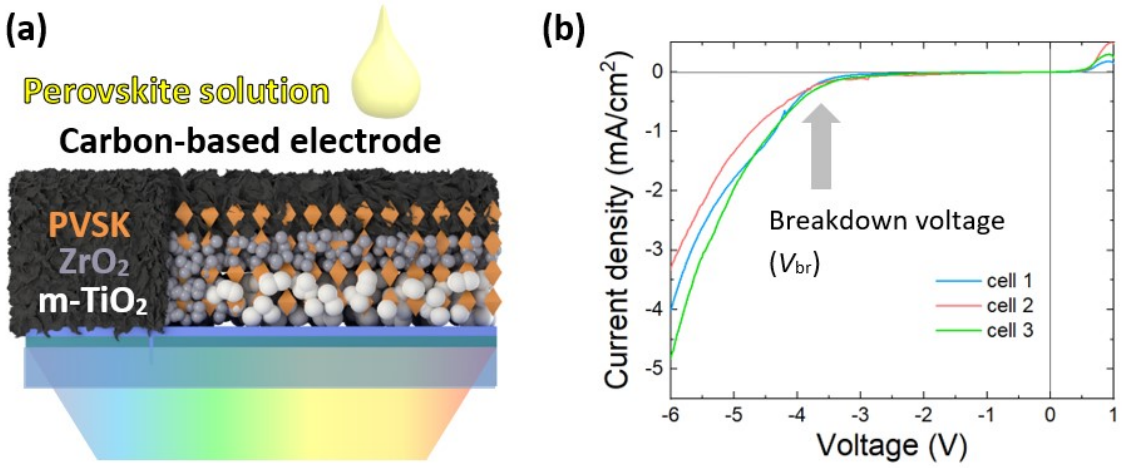


Figure 8.1: (a) Architecture of perovskite solar cell with carbon-based electrode. (b) Dark IV-measurements of CPSCs, displaying a breakdown voltage at around -3.6 V.

superior stability and resilience to degradation under various ambient conditions.

We start investigating the reverse-bias behavior of CPSCs by measuring the dark *IV*-curves, primarily in the reverse-bias regime. The *IV*-curves (from 1 V to -6 V) of the manufactured cells are presented in Figure 8.1b. We note, that according to our knowledge, there have not been reports of reverse-bias testing of PSCs up to such large reverse-bias voltages.

From the dark *IV*-measurement we identify the breakdown voltage to be at around -3.5 V to -3.7 V which is higher than the values demonstrated in literature, regarding reverse-bias behavior of perovskite solar cells (which are typically between -1 V to -3 V). [455, 456] Remarkably, the *IV*-measurements of illuminated cells before and after the dark *IV*-sweeps show no signs of degradation as can be inferred from invariable device performance (Figure S1). Moreover, conducting an *IV*-sweep of an illuminated cell until various negative voltages also does not cause degradation (Figure S2). However, we observed that the larger applied negative bias during *IV*-scan was, the longer it took for the V_{OC} to recover (Figure S3).

Mimicking the behavior of a module with partially shaded sub-cell

Next, we study the behavior of modules by series-connection of individual solar cells. Therefore, we first investigate shading effects of single cells. The *IV*-curves of solar cells illuminated on the entire active cell area (1.44 cm^2) and on a masked area (0.096 cm^2) are presented in Figure S4. We attribute the strong difference in FF to an increased series resistance loss for fully illuminated devices, which is a typical challenge in up-scaling solar cells. In turn, the lower V_{OC} of the masked cell can be explained by the non-illuminated area of the cell which is a passive volume that does not contribute to charge carrier generation but still causes non-radiative recombination. [460]

Since photovoltaic modules are typically comprised of sub-cells (cells connected in series forming a string of a module), we investigate the behavior of series-interconnected CPSCs (Figure 8.2a), thus mimicking a perovskite PV module with carbon-based counter electrodes. The *IV*-curves of CPSCs connected in series, forming a string of up to six sub-cells is shown in Figure 8.2b, where we subsequently added one sub-cell after another. In this case, the total V_{OC} is equal to the sum of V_{OC}s of each individual sub-cell. The apparent decrease in FF is a main challenge for series connected modules and can be attributed to additional series resistance losses from the sub-cells and the external interconnection (Figure S5). Although the I_{SC} in series-interconnected sub-cells should be limited by the lowest I_{SC} in the circuit, here the I_{SC} slightly increases with the number of connected sub-cells. This peculiar effect might be due to a relatively low shunt

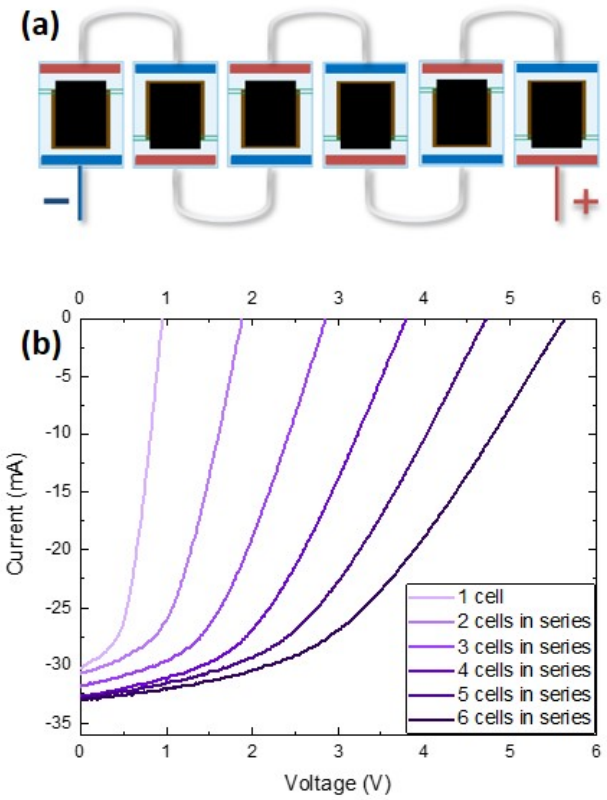


Figure 8.2: a) Illustration of the series-interconnected CPSCs, mimicking behavior of a string in a module with six subcells. b) The IV-curves of the series-interconnected cells under illumination.

resistance (as can be seen from the IV-slope at V=0), which causes an increase in I_{SC}, even though it should normally not increase with high-performing sub-cells.

If one of the series-connected sub-cells is shaded, it is reverse-biased with photo-voltage from the other, unshaded sub-cells. In the IV-plot, this is equivalent with mirroring the IV-curve at the I axis. The operating point of the shaded sub-cell is represented by the intersection between the IV-curves of the (transposed) shaded and the unshaded sub-cells. [9, 461, 462] In Figure 8.3a, we illustrate a situation when one of the interconnected sub-cells is fully shaded (thus producing a dark IV-curve, which was shown in Figure 8.1b) and the other 5 unshaded sub-cells act as a reverse bias voltage source on the shaded one. It can be clearly seen that the operating point shifts to higher voltages with higher number of unshaded sub-cells in the string.

The behavior of complete shading of one sub-cell in a string has been studied in Figure S6. When 5 out of 6 sub-cells in a string are fully shaded, the string produces no net current, as it is normally dominated by the smallest current in the string. However, as the number of shaded sub-cells decreases, the current becomes

higher than zero, where in the case of 1 non-shaded sub-cell and 5 shaded ones, the I_{SC} becomes around 11.3 mA. This peculiar phenomenon implies that even when one of the sub-cells in the module is fully shaded, the string can still produce some output power even without a bypass diode (although output power would be rather small). When 5 sub-cells in a string are illuminated, they induce around -4.63 V (Figure S6) voltage bias on the shaded sub-cell. As shown above (Figure 8.1b), this reverse-bias is already beyond the breakdown voltage, which explains the observed reverse current in the string, which is not close to zero anymore. Remarkably, none of the sub-cells displayed any signs of degradation after this experiment (Figure S7).

Partial shading of a sub-cell in a string (as opposed to complete shading shown in Figure 8.3a) is even more critical for device degradation (due to amount of dissipated heat) as it shifts the operating point closer to the maximum power point of the unshaded sub-cells. Figure 8.3b illustrates how much heat would be dissipated in a shaded sub-cell, with various shaded portions of the sub-cell. In our CPSCs, the FF is significantly limited by the long transport distance for holes through the carbon-based electrode, which would not be the case in the complete

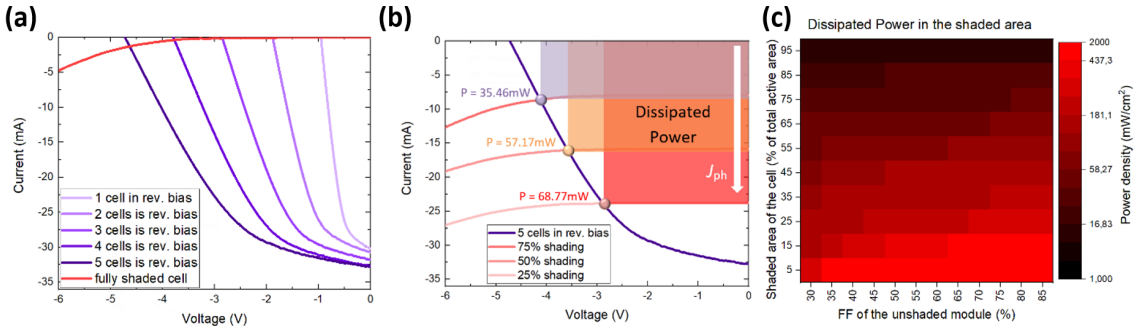


Figure 8.3: a) Illustration of IV-curve produced by six series-interconnected CPSCs, where one cell is fully shaded (producing an IV-curve shown in Figure 8.1b), forcing the other (1-5) unshaded cell(s) to act as a reverse-bias voltage source. This representation is based on the measured IV-curves in Figure 2b, which were mirrored across the I axis to mimic a reverse-bias voltage source. The operating point of the string in this case would be at the intersection between the shaded and unshaded cells. b) Illustration of the operating point dependency (and this dissipated power) on the shaded area, which influences the photocurrent J_{ph}. c) Simulated heatmap, visualizing the influence of the shaded area and FF of unshaded module (in this example only six subcells were considered) on the dissipated power in the shaded area. The heatmap was constructed based on the operating points of simulated unshaded interconnected five subcells and one partially shaded cell, presented in Figure S8, Supporting Information. Note that the scale is logarithmic.

perovskite modules with carbon-based back-contacts (CPSMs) due to optimized cell geometry. The simulated heatmap in Figure 8.3c (based on the simulated module with 6 cells in Figure S8) gives an example of the power dissipated as heat as a function of the FF of the non-shaded areas of a module (consisting of only 1 string with 6 sub-cells) and the shading area of the sub-cell. Both parameters play a significant role in the creation of the so-called "hot-spots" – locations with high energy dissipation (as shown in Figure 8.3c, the power density value varies even over an order of magnitude). In case of CPSMs with high FFs (>70 %) the power dissipated as heat in a 5 % shaded sub-cell can reach values above 1 W/cm^2 of the shaded area, meaning that if a sub-cell, for example, has a size of 100 cm^2 there will be 5 W of power dissipated as heat in the shaded 5 cm^2 area, *i.e.* 1 W/cm^2, which is the power equivalent to 10 suns (referring to the standard AM1.5G spectrum).

Identifying the critical reverse-bias voltage in CPSCs

Up to now, despite the applied high reverse-bias voltages, we do not observe any signs of degradation in CPSCs. However, as it is reasonable to assume that strings in large scale PSMs would have more than 10 sub-cells, the reverse-bias voltage can easily go beyond 10 V (assuming the V_{OC} of each sub-cell is at least 1 V). Even in silicon-based PV modules, where the breakdown voltage is typically at around -13 V, [463–465] bypass diodes are included for every series-interconnected string of 20-24 cells, to prevent the reverse bias voltages during shading of reaching values close to junction breakdown value.

We expect that reverse-bias induced device failure is a function of both applied bias and dwell time at this bias point. Hence, we measured the current of single cells at fixed negative voltage values for different dwell times (Figure 8.4a). Instantly after applying the reverse-bias, the current sharply increases, followed by the slower decrease and stabilization, which will be discussed in the following section.

Figure 8.4b shows the PCE change in the CPSCs depending on the value and duration of the applied reverse-bias. Surprisingly, the cells exhibit outstanding resilience to reverse-bias degradation, showing no significant losses even after biasing with -9 V for as long as 30 minutes. When a voltage of -10 V is applied, PCE starts to rapidly decrease and after a bias of -11 V, (Figure S9 for -11 V) the cells show drastic degradation. As can be seen from the photographs in Figure S10, higher applied negative bias leads to a decrease in absorption in the visible light spectrum and the emergence of yellow regions which, as confirmed by the XRD-measurement (Figure S11) can be attributed to the (partial) decomposition from perovskite to PbI_2. This in turn reduces the device active area, which leads to a decrease of the I_{SC} and hence overall device PCE.

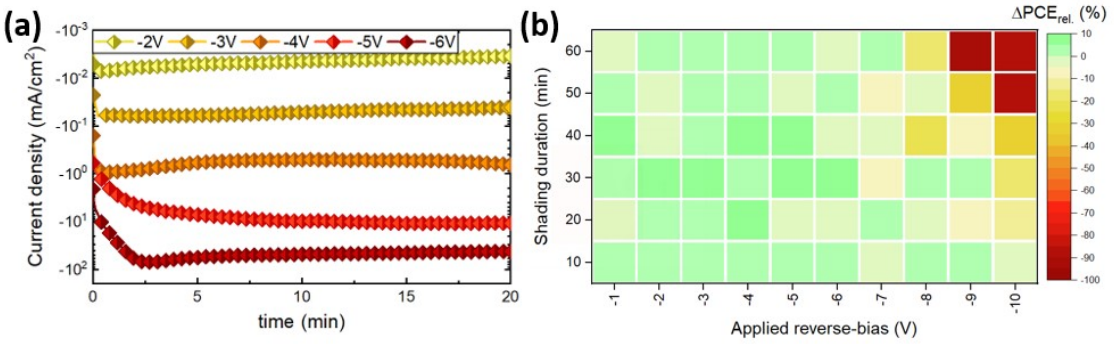


Figure 8.4: (a) Current of the cell in the dark as a function of time under reverse-bias (-1 to -6 V), thus mimicking the shading of sub-cell in a module. Note that the scale is logarithmic since the current increases exponentially under reverse-bias. (b) the change in PCE of CPSCs before and after applying reverse-bias (-1 to -10 V) for a specific time duration (10-60 mins) in the dark.

Reverse-bias behavior of perovskite solar cells and origins of degradation

In semiconductor devices, the junction breakdown typically occurs via one of the following three mechanisms: (i) thermal runaway (also known as thermal instability), (ii) tunneling or (iii) avalanche multiplication. Normally, for junctions with breakdown voltages $V_{br} > 6\,E_g/q$, the breakdown can be attributed to impact ionization leading to avalanche multiplication, whereas for $4\,E_g/q < V_{br}$ the breakdown happens due to tunneling effect. For $4\,E_g/q < V_{br} < 6\,E_g/q$ the breakdown is assumed to happen by the interplay of both mechanisms.[37]

Since the bandgap of the $CH_3NH_3PbI_3$-based perovskite utilized in this study is approximately 1.6 eV [414] and $V_{br} < 4$ V, the junction breakdown probably occurs first via tunneling, followed by the thermal runaway. It was previously observed that in PSCs thermal runaway causes localized heating of the metal back-contact, causing electrode melting (*e.g.* silver). [455] In addition, Razera *et al.* also mentioned that the localized shunting induced by reverse-bias may originate from the metal ion migration towards the perovskite layer. [456] Moreover, phase-segregation in the mixed perovskite compositions (multi-cation, and multi-halide) was suggested to play a role in the reverse-bias degradation. [456] It is clear, that the metallic contact-induced degradation (electrode melting and metal ion-migration) do not happen in CPSCs and since the perovskite composition utilized in this work consists of only one A-site cation and one type of halide, phase-segregation can also be excluded. We also note that larger thickness of intrinsic (i) region of the CPSCs, where perovskite is embedded in ZrO_2 is likely to reduce the electric field and electric potential gradients in comparison to the standard PSCs thinner perovskite films. This in turn could result in lower local charge densities, decrease tunneling probability

and increase breakdown voltage (more details can be found in the Supplementary Note 1). However, we note that a more detailed investigation is needed to accurately determine whether the main improvements against reverse-bias induced degradation come from the presence of carbon electrode or the mesoscopic structure.

Degradation due to iodine loss

An increase in the applied negative voltage, results in stronger band bending and thus electric field, which leads to redistribution of mobile ions from perovskite bulk towards its interfaces to charge-extracting layers. [458] Bowring *et al.* have earlier suggested that the initial sharp current increase under fixed reverse-bias, similarly to what we demonstrated in Figure 8.4a, is due to rapid cation (most likely iodine vacancies in $CH_3NH_3PbI_3$-based perovskites [466–470] movement towards the interface between the HSL and perovskite. [455] In the case of our HSL-free CPSCs, these iodine vacancies will accumulate at the perovskite/carbon contact, which in turn produces a region with an excess of anions close to the ESL/perovskite interface. [458] Increase of the band bending at this interface reduces potential barrier width between the conduction band of ESL and valence band of perovskite, allowing holes to tunnel to perovskite. [455] Higher hole densities, in relation to electron densities, could result in oxidation of iodide and creation of iodine vacancies and interstitials. [466, 471, 472] Furthermore, created iodine interstitials will undergo structural relaxations towards more thermodynamically favorable iodine compounds such as I_2 and I_3^{2-}. [466] Their formation in perovskites under illumination was already demonstrated experimentally [466, 473] and was found to negatively affect the device performance. [474]

To probe whether molecular iodine is created in our CPSCs under reverse-bias we submerge a solar cell in toluene (2 ml), while applying -3 V bias to it (Figure S12) in the dark. After 24 hours, the toluene was extracted to measure its UV-Vis absorption spectrum. As can be seen in Figure S13a, in comparison to a cell which underwent the same treatment but without an applied bias, the absorption is strongly increased in 300-400 nm wavelength region and a characteristic peak of I_2 at ~500 nm appeared. Similar behavior was observed for iodine dissolved in toluene [475] and iodine compounds formed in perovskites under illumination. [466, 473] The absorption of iodine dissolved in toluene (Figure S13b) shows strong absorption in those wavelength regions, confirming our hypothesis. Moreover, the photograph in Figure S12 shows strong change in light-absorbing properties inside the perovskite active area of cells which were under reverse-bias in toluene. For comparison, a cell also kept in toluene for 24 hours but under open-circuit condition didn't show any visible changes in the active area. Moreover, the cell subjected to reverse-bias does not show visible degradation in the "dead area" between the laser lines, confirming further that the degradation is bias-induced. Thus, we can clearly see that even though CPSCs can withstand low reverse-bias

for a short time (< 1 hour) without a drop in performance, prolonged applied negative voltages cause significant iodine loss from perovskite crystal structure, which will be detrimental for the device lifetime.

Degradation due to excessive heating

In order to elucidate the causes of degradation mechanisms in CPSCs happening at large negative voltages we perform real-time infra-red imaging. Thermal radiation is detected with an infra-red camera, while a bias voltage is applied to the device in the dark. At low reverse-bias (for the shown device >-7 V) we do not observe a significant inhomogeneity in cell temperature except for a local shunt (Figure 8.5a). Here we define shunts as regions with reduced shunt resistance due to printing defects / pinholes or artefacts, causing excessive localized heating of the device

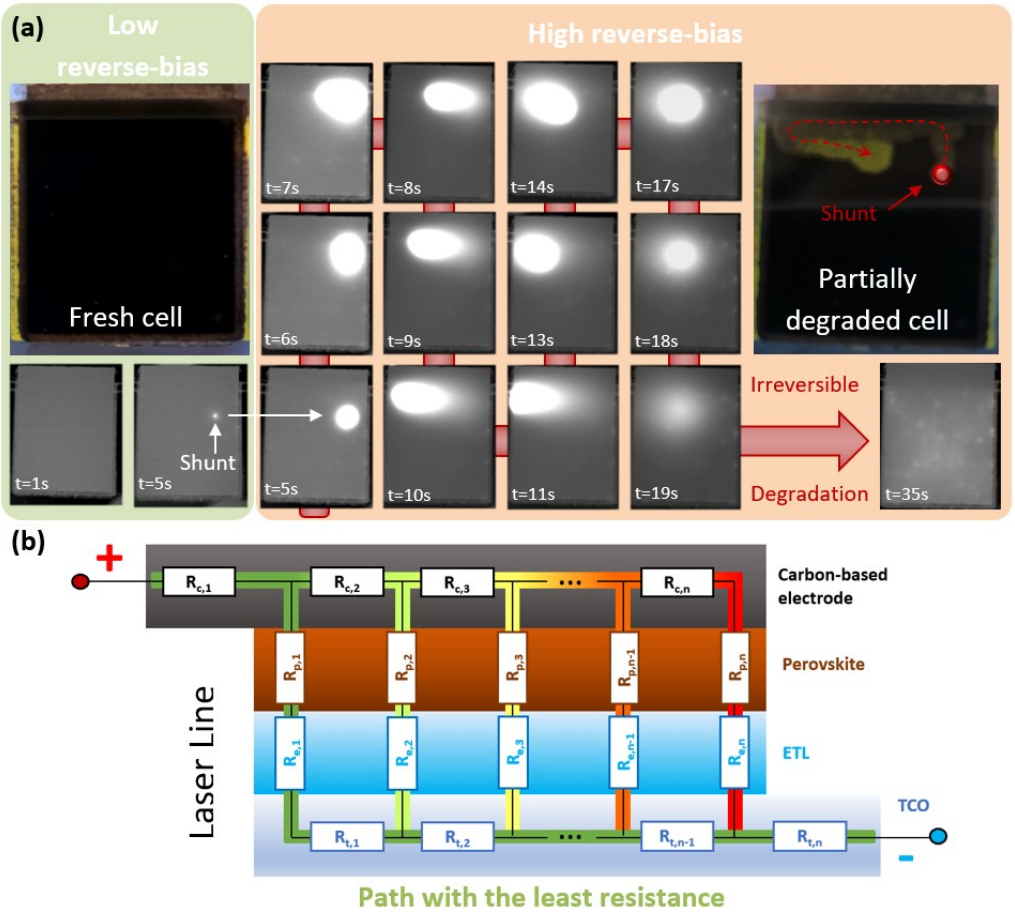


Figure 8.5: (a) Infra-red thermography measurements at low and high applied negative biases, showing that in shunted cells, the degradation starts at the location of a shunt, leading to overheating and decomposition of perovskite. (b) Proposed electrical circuit model to explain the hot-spot movement resulting in partial degradation of CPSCs.

under reverse bias. However, once a high reverse-bias is applied (*e.g.* <=-7 V) the temperature at the shunt and neighboring region increases dramatically, which leads to perovskite degradation. This strong increase in temperature is caused by a strong increase in reverse current. Notably, we notice a peculiar feature, where after the local degradation at the shunt location, the "hot-spot" moves towards the region close to the P1 laser line (located at the upper part of the cell), followed by moving further along the laser line and regions close to it. After about 19 seconds, the hot-spot vanishes and the power is again dissipated almost evenly throughout the area of the cell (although some spots still appear hotter than others). The vanishing of the hot-spot is accompanied by a decrease in reverse current. The entire real-time infra-red measurement showing the degradation process can also be found in Video S1 of the Supplementary Information.

Looking at the active area we can see a strong correlation between the hot-spot "path" and the degraded regions of the cell, from which we could also reconstruct the degradation path. Here, the degradation might have been caused by two mechanisms: (1) the rate of iodide oxidation is increased leading to higher iodine loss and/or (2) heat up of perovskite beyond its decomposition temperature. [357] Further investigation is needed to specifically resolve this ambiguity and pin-point the main origin of the degradation under reverse-bias in such solar cells. We note however, that under a bias of -9 V overall cell temperature (not localized) can reach temperatures close to 100°C (Fig. S14), suggesting that degradation of the $CH_3NH_3PbI_3$-based perovskite is likely to occur at such voltage levels. For the local hot-spots as shown in Figure 8.5a, the DLIT-signal exceeded the detector range and it is reasonable that the power dissipated at the small spots induces a much higher local heating. Nevertheless, as can be seen from Figure S15, after the reverse-bias is applied to the shunted cell, the degradation does not progress unless the applied bias is above -9 V. Once, it happens, most of the active area rapidly heats up (Figure S15 and Video S2), turning yellow, suggesting the formation of PbI_2 across most of the active area. We note, however, that some XRD peaks corresponding to perovskite reflection planes (*e.g.* (220), (211)) can still be observed in the degraded samples.

To explain why the hot-spots occur primarily close to the laser line, we propose the electrical circuit model shown in Figure 8.5b. Assuming that the resistance of the perovskite and m-TiO_2 layer are nearly constant across the active area, the path of the least resistance for current is dictated by the resistance of the front- and back-electrodes. According to our 4-point probe measurements, the sheet resistance of the carbon-based electrode and FTO are around 18±2 Ω/sq. and 8.5 ±1.5 Ω/sq., respectively, demonstrating that there are more resistive losses in the back-contact rather than in the front-electrode. [414] This suggests that the current path with the least resistance (marked with green color in Figure 8.5b) contains minimal distance through the back-electrode (carbon) and maximal distance through the front-electrode (FTO). Clearly, such path goes through regions close to

the laser line, which is why the DLIT-signal increases at this location first (as seen from Video S1). The high current at these spots leads to local heating, causing thermal decomposition of the perovskite into PbI_2, most likely due to evaporation of the more volatile methylammonium iodide. [357] As the residual PbI_2 is less conductive than the pristine perovskite at the surrounding areas, another location becomes the path of least resistance. The local heating makes it likely that this location is neighboring the "just-degraded" spot. However, we highlight that if shunts are present, degradation will firstly happen at the shunt since it is the path of least resistance. After the perovskite near the shunt degrades, the hot-spot will appear close to the laser line. However, these regions will not degrade because they are shunted, but because these locations represent the past of least resistance for the current.

As we pointed out, the location of the initial degradation (in the absence of shunts) depends on the electrode sheet resistivities and their relation to each other. That means if the electrode sheet resistances were equal, the degradation would occur more homogeneously across the active area, since the current flow would be distributed more homogeneously across the cell area, and so would the heat.

Hot-spot test of perovskite solar modules with carbon-based electrodes

Inspired by the outstanding stability of the individual cells to negative voltage bias, we manufactured perovskite minimodules with carbon-based back-contacts on a 10x10 cm^2 FTO substrate. Figure 8.6a shows a photograph of the encapsulated CPSM with a 56.8 cm^2 aperture area and a geometrical fill factor of 93.4 %. From the IV-measurement the power conversion efficiency of the module was determined to be 11.1 % (reverse sweep).

To pass the "Hot-Spot Test" described in the IEC 61215-2:2016 standard, a PV module needs to be subjected to a partial shading representing the "worst case" shading and operation conditions. [446] In general, there are two different types of hot-spot tests that are applied to PV modules: 1) test for silicon wafer-based (IEC 61215-2, MQT 09.1) modules and 2) test for thin-film technologies (IEC 61215-2, MQT 09.2). The key difference between both tests is the presence of the partial shading condition: MQT 09.2 test only requires full shading of one or more sub-cells, whereas for MQT 09.1 the full sub-cell area shading is followed by an additional partial shading of a sub-cell (as will be shown below). As discussed above (and shown in Figure 8.3b,c), partial shading of a sub-cell can be more detrimental, and the closer the operating point of the module to the MPP, the more power will be dissipated as heat. As for the tested module, the partial shading conditions lead to operation close to the MPP, highlighting that the MQT 09.1 is a harsher test and is more likely to result in module deterioration. Nevertheless, due to the lack

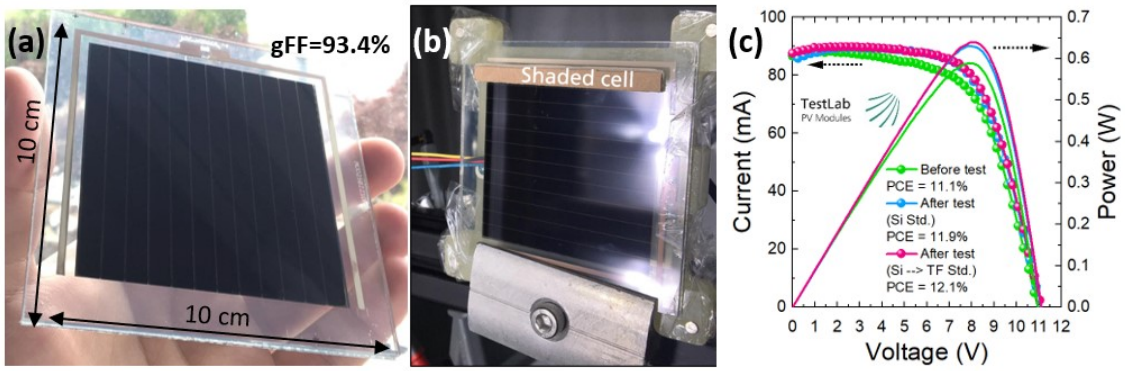


Figure 8.6: (a) Photograph of an encapsulated perovskite solar module with carbon-based contact (CPSM). (b) Photograph of the module with one fully shaded cell during the hot-spot test. shading conditions (c) *IV*- and *PV*-curves of the module before (green) and after conducting test according to Silicon ageing test (blue), followed by conducting an additional thin-film ageing test (cerise) on the same module, showing no loss of performance after both IEC-compliant tests.

of a standard specifically for the perovskite PV modules, both tests (MQT 09.1 and MQT 09.2) were applied sequentially on the same module at an accredited laboratory "TestLab PV Modules" at Fraunhofer ISE. [446]

According to the standardized procedure MQT 09.1, after measuring the *IV*-curve of our CPSM (without shading) we fully shade each individual sub-cell (Figure 8.6b) and obtain the module *IV*-curve when each cell is fully shaded (Figure S16). From these curves, a cell with the lowest shunt resistance is identified, suggesting that this cell might have the highest chance to rapidly heat up at the shunt location under shading conditions. The shaded area of the cell with the least shunt resistance was reduced from 100 % to 25 %, and the condition resulting in the highest temperature was held for 1 h. Subsequently, the procedure for thin-film modules (MQT 09.2) was carried out in which the shading of one or more cells was adjusted so that the I_{SC} of the shaded module is equal to the I_{MPP} of the non-shaded module. This condition was again sustained for 1 h. More details on the testing procedures, *JV*-curves of CPSM under different shading conditions and infra-red temperature measurements can be found in the hot-spot test report in the Supplementary Information.

The maximum temperature observed was below 50°C in both tests. The module passed the criteria of visual inspection and *IV*-curve characteristics after both shading conditions. As can be clearly seen from the Figure 8.6c, the module does not exhibit significant signs of degradation after the test, and the PCE has in fact, slightly enhanced. To confirm this performance improvement, we track the PCE of the module for 1 hour under full sun illumination (Figure S17), which also shows that the aged device has a higher stabilized PCE. This agrees with our previ-

ously shown results of individual CPSCs subjected to constant negative voltages in Figure 8.4b, where the cell PCE often slightly increases if the reverse-bias is below -8 V. Although, the results suggest that these CPSMs have a sufficient stability to withstand the reverse operating conditions during the hot-spot test, *e.g.* in the context of module certification, the module size and encapsulation could change during the still ongoing module development, which is why the insulation criteria, specified in the IEC 61215-2 were not applied during the test. The relatively low temperatures measured (< 50°C) can be attributed in part to the small cell sizes and the resulting low power that is dissipated under shading conditions. Therefore, the test could yield different results for modules with larger cells or longer cell strings and should be reassessed in these cases.

8.6 Conclusion

Although preventing degradation of perovskite photovoltaic devices is commonly considered a cornerstone of commercialization of PV modules of this technology, there are only few studies on the degradation under reverse-bias conditions, indicating that this could be an Achilles heel for PSCs. In this work, we address this fundamental problem and demonstrate that perovskite solar cells with carbon-based electrodes are remarkably resilient against reverse-bias stress. These cells have a breakdown voltage at approximately -3.6 V, suggesting that the junction breakdown occurs via tunneling. Since carbon-based electrodes are not prone to melting at high temperature, neither to migration of (metal) ions from the electrode into perovskite absorber, nor to electrode oxidation, they represent an ideal candidate for improving the stability of PSCs under reverse-bias conditions. Moreover, the stability of cells demonstrated here is further improved by the utilization of single-cation and single-halide perovskite, avoiding phase segregation. These advantages allow PSCs with carbon-based electrodes to withstand at least 60 minutes under -8 V and 30 minutes at -9 V.

We demonstrate, however, that the CPSCs undergo iodine loss under even mild negative voltages, due to tunneling of holes, which oxidize iodide incorporated into perovskite lattice and form iodine compounds. Although we note that this reaction might be reversible, unlike degradation which happens under high reverse-bias. By real-time infra-red thermography measurement, we show that the degradation at high negative voltages starts in shunts, where heat is dissipated. After that (or in the absence of shunts), the degradation follows the current path of least resistance, which depends on the sheet resistances of front- and back-electrodes. Combining these findings with the XRD measurements we demonstrate that the main mechanism leading to degradation of CPSCs under high reverse-bias is conversion of perovskite to PbI_2 at high temperatures.

Finally, we manufactured perovskite modules with 56.8 cm^2 aperture area

and subjected them to the "hot-spot" stability test at an accredited laboratory, "TestLab PV Modules" at Fraunhofer ISE. For the first time, we show perovskite modules which endure the IEC 61215-2:2016 standard test procedures, underlining excellent potential of such modules for commercialization. Finally, we highlight that further improvement of the standardization of the hot-spot tests for perovskite (single- and multi-junction) modules is needed in order to accurately assess the long-term stability of such PV devices.

8.7 Critical discussion

The study presented in this chapter discusses how and why perovskite PV devices with carbon-based electrodes can be particularly stable to reverse-bias conditions in comparison to the traditional analogues with metal-based electrodes. However, addressing the following points could have provided a deeper insight into the behavior of such devices under reverse-bias:

- Clearly, replacing metallic electrodes with carbon-based ones helps to avoid electrode melting and diffusion of metal ions towards perovskite. However, as briefly mentioned in the article, the mesoporous scaffold and perovskite within carbon electrode can have a significant effect on the degradation, which, unfortunately, has not been investigated. Further research is needed to gain a deeper understanding of how the thick mesoscopic layers and perovskite with numerous grain boundaries (*cf.* chapter 5) impact the electric field in perovskite, or, more specifically, its gradient along the cell cross-section. In the author's opinion such study would be crucial for understanding reverse bias-induced degradation in PSCs and could facilitate the development of useful methods to overcome this complex issue. Furthermore, a similar study on L-CPSCs could also be helpful in understanding the role of carbon-electrode itself (excluding the impact of the mesoporous structure) in retarding the reverse bias degradation.
- The explanation of reverse bias-induced degradation in this work strongly relies on the reports from literature attributing it to iodide oxidation and the formation of iodine gas. However, more characterization of the chemical reaction occurring within cells placed under reverse-bias would be beneficial to more specifically pin-point the degradation mechanisms. Moreover, perovskites with different compositions are likely to exhibit different reactions, especially the ones with high Br^- or Cl^- content. Therefore, much of the reverse bias-induced degradation of PSCs still remains unexplored.
- It is, of course, encouraging to see that the PV modules with carbon-based electrodes could withstand the conditions of the IEC hot-spot test, but it still doesn't explicitly prove that commercial-sized modules based on the same structure could withstand them as well. The module size and the area of each

sub-cell determines the power that will be dissipated as heat through a hot-spot and unlike the modules demonstrated in this study, the sub-cell of a large module, which produces significantly less current can become reverse-biased at much more negative voltage levels than -9 V. Therefore, in the author's opinion, reverse bias-induced degradation in perovskite solar modules is highly critical and often overlooked challenge, that the companies, which plan to commercialize perovskite PV need to tackle.

It is important to note that HTL-free CPSCs, in the author's opinion, represent a more "reliable" system to study the degradation mechanisms of perovskite photoabsorber itself due to an absence of additional effects, which could be caused by hole-transport layers and metal-based electrodes. Moreover, carbon-electrodes provide a unique opportunity to study the reverse-bias degradation of perovskite layer without considering device shunting or electrode melting, which makes them highly attractive for researchers investigating this issue.

One of the highlights of this work is the first demonstration of a perovskite PV module withstanding conditions of the IEC 61215 hot-spot test. However, as mentioned in the publication, currently the infrastructure for ageing tests of perovskite PV, even at the accredited laboratories, is at its infancy due to the scarcity of modules to test. Furthermore, it is currently not clear whether the accelerated ageing tests performed on perovskite PV modules must be the same as for the case of thin-film modules, c-Si modules or neither, meaning that a new ageing test needs to be developed. Therefore, the standardization of stability measurements of perovskite PV modules needs to be addressed soon in order to provide module manufacturers (and potential investors) with an objective figure of merit to determine whether such devices can function for a desired period of time.

Chapter 9

Remanufacturing perovskite solar cells and modules – a holistic case study

9.1 Preamble

It is only natural for researchers in the field of emerging cost-effective PV to focus most of their initial efforts on boosting PCE and finding new strategies to prolong their operational lifetime. However, returning back to the chapter 3, one can recall that besides improving performance and device stability, its sustainability must also be kept in mind for developing a truly environmentally-conscious energy system. Therefore after investigating methods to enhance power conversion efficiency of CPSCs (*cf.* chapters 6 and 7) and studying the degradation of such devices (*cf.* chapter 8), the author sought new ways to reduce the negative environmental impact of perovskite PV modules with carbon-based electrodes. One way to do that is to consider recycling or remanufacturing perovskite PV devices with carbon-based electrodes,[◊] how such processes could be performed in the most sustainable way and how significant would be the impact of this strategy.

[◊]This chapter (except for the critical discussion in section 9.8) is a preprint of the research paper, which is currently undergoing a peer-review process:

Bogachuk, D., van der Windt, P.„ Wagner, L., Martineau, D., Narbey, S., Verma, A., Lim, J., Zouhair, S., Kohlstädt, M., Hinsch, A., M., Stranks S.D., Würfel, U., Glunz, S.. (2022) Remanufacturing Perovskite Solar Cells and Modules – a Holistic Case Study, *Research Square*, available at: https://doi.org/10.21203/rs.3.rs-1767937/v1

The individual contributions were as follows:

- **D.B.**: conceptualization and idea of publication, development of the remanufacturing process, SEM/EDX measurements, coordinated the work, analyzed all the measurements and prepared the manuscript as well as figures (**equal contribution**)
- **P.v.d.W.**: conceptualization and idea of publication, performing LCA of perovskite PV devices with carbon-based electrodes, analysing environmental impact of recycling, remanufacturing development of the remanufacturing process, partially prepared the manuscript (**equal contribution**)
- **L.W.**: provided valuable ideas and contributed to the manuscript preparation
- **D.M.,A.V.**: manufacturing perovskite solar cells with carbon-based contacts
- **S.N.**: performing *JV*-measurements
- **J.L.**: development of the remanufacturing process
- **S.Z.,M.K.,S.D.S.**: provided valuable ideas and contributed to the manuscript preparation
- **A.H.,U.W.**: contributed to the manuscript preparation and results interpretation
- **S.G.**: contributed to the manuscript preparation, and results interpretation, coordinated the work
- **All authors**: reviewed the manuscript and made valuable comments to it

9.2 Abstract

While perovskite photovoltaic (PV) devices are on the verge of their commercialization, promising methods to recycle or remanufacture fully-encapsulated perovskite solar cells (PSCs) and modules are still missing. Through detailed life-cycle assessment shown in this work, we identify that the majority of the greenhouse gas emissions can be reduced by re-using the glass substrate and parts of the PV cells. Based on these analytical findings, we develop a novel thermally-assisted mechanochemical approach to remove the encapsulants, the electrode and the perovskite absorber, allowing to re-use most of the device constituents for remanufacturing PSCs, which recovered nearly 90 % of their initial performance. This remanufacturing strategy allows to save up to 33 % of the module's global warming potential. Finally, we demonstrate that the CO_2-footprint of these remanufactured devices can become less than 30 g/kWh, which is the value for state-of-the-art c-Si PV modules and can even reach 15 g/kWh assuming a similar lifetime.

9.3 Introduction

To comply with the climate goals of the Paris Agreement, the global installed photovoltaic (PV) capacity is projected to enter the multi-terawatts scale in the forthcoming years. [476–479] Despite PV's potential to be an environmentally friendly alternative to fossil fuel energy sources, emissions associated with PV are non-negligible [216, 479] and the projected increase in PV installations is estimated to lead to 78 million tons of waste cumulatively by 2050. [480] Recycling could mitigate the amount of PV related waste and has become one of the central discussions in the PV sector. [481–483]

However, recent studies have shown that bulk recycling is not necessarily more environmentally friendly than technologically simpler End-of-life (EoL) treatments such as landfill disposal or incineration [484] due to the energy intensive separation of PV module materials at their EoL and processing of recycled materials. The re-use of entire modules or parts thereof could offer an environmentally friendly alternative to such methods. This could be particularly viable for PV modules compatible with solution-based processing techniques, such as perovskites. Here, the active components of the solar cell can potentially be washed off to directly re-use bulk materials with high environmental impact such as glass. In such case when a combination of re-used, recycled, repaired or replaced parts serves to manufacture a new product, the term remanufacturing is normally employed.

Perovskite photoabsorbers have a high absorption coefficient, requiring significantly less material for building a PV module, in comparison to silicon devices and, therefore, have the potential to reduce the mass in PV-associated waste streams. [41] In addition, their solution-based processing – a unique feature for

such well-performing semiconductors – allows for tremendous reduction in the energy demand not only during fabrication but also for recycling or remanufacturing. [485] Methods for perovskite recycling or remanufacturing should be considered and evaluated before such devices are introduced to the market, so that their widespread adoption could already substantially reduce PV related waste streams and greenhouse gas emissions.

Several works have demonstrated recycling approaches of perovskite solar cells (PSCs), showing almost no performance loss, even after multiple recycling cycles. [318, 486] To our knowledge, however, previously published reports only developed processes for recycling PV cells and no real case studies on encapsulated devices have been performed. Yet, to produce modules with lifetimes suitable for actual commercial deployment (>25 years), perovskite solar modules (PSMs) need to be equipped with additional barriers to limit environmental degradation (*e.g.* from moisture and air), such as encapsulation materials and a back sheet glass. [216, 487] which could also ideally be complemented by lead-sequestrating materials embedded into the modules. [488–490] Thus, the practical applications for recycling unencapsulated PSCs are limited without suitable methods to cleanly get rid of the encapsulant material.

In this work, we demonstrate for the first time a remanufacturing strategy for glass-glass encapsulated perovskite solar cells. [114, 125, 203, 210, 377] Our study presents a facile experimental method to remove the edge-sealant, encapsulant, back electrode and degraded perovskite, allowing to re-use the device constituents with the highest global warming potential – glass substrate and back-sheet. By performing a life cycle assessment, we show that directly re-using the glass substrate, is a more environmentally favorable option than recycling, which can lead to a strong reduction of the PV module's global warming potential. By definition, recycling implies the disintegration of the waste material into a recyclate (*i.e.* small constituents of the waste material), which is then re-processed for the production of a new object. In contrast, remanufacturing implies that parts of the waste product can be reused – utilized in a new product directly without additional energy spent on creation of recyclate and its re-processing. Although in this study we utilize PSCs with carbon-based electrodes (CPSCs) due to their promising commercialization potential and device stability, the herein developed remanufacturing approach is also applicable to other PSC architectures, especially n-i-p based ones. This remarkable strategy paves a new way to strongly reduce the global warming potential of PV modules and tremendously reduce their waste streams, which is essential for the terawatt-scale PV installations of the future.

9.4 Experimental details

Materials

Fluorine-doped tin oxide glass substrates TCO22-7/LI (sheet resistance 7 Ω/sq.), silver paste Elcosil SG/SP, titania paste Ti-Nanoxide T165/SP, zirconia paste Zr-Nanoxide ZT/SP, carbon-graphite paste Elcocarb B/SP and methylammonium lead iodide perovskite solution with 5-ammonium valeric acid additive (5-AVAI) were provided by Solaronix SA. Acetone was purchased from Carl-Roth, ethanol was purchased from Alcosuisse. Titanium diisopropoxide bis (acetylacetonate) (75 % in isopropanol), Hellmanex and isopropanol were purchased from Sigma-Aldrich. Thermoplastic polyolefin (TPO) ENLIGHT XUS62250 was obtained from FirstPVM and polyisobutylene (PIB)-based edge seal Solargain Edge Tape was obtained from Quanex.

Fabrication of perovskite solar cells with carbon-based electrodes

Devices were fabricated on 10x10 cm^2 plates of FTO-coated glass. First, a laser pattern defined cathode and anode areas with an automated fiber laser. After that, the substrate was subjected to sequential cleaning steps in 1 % aqueous solution of Hellmanex, acetone, and isopropanol respectively (15 min each) in an ultrasonic bath and subsequently dried in air. The thin compact titania layer (c-TiO_2) was grown by spray-pyrolysis on a hot-plate set to 450°C, using a glass mask to protect the contact areas. A volume of 20 mL of titanium diisopropoxide bis (acetylacetonate) diluted in absolute ethanol (1:160) was sprayed with oxygen as a carrier gas, and warming was prolonged for 30 min before allowing the sample to cool down. For the manufacturing of CPSCs, an array of 4 electrodes was subsequently defined by screen-printing silver contacts, m-TiO_2, ZrO_2 and carbon paste using a 100-40, 165–30, 90–48, and 43–80 mesh stencil, respectively (the number of strands is per cm). After printing the wet film, each screen-printed layer was allowed to dwell for 10 min before drying at 120°C for 10 min, followed by a firing step at 500°C (or 400°C for carbon) for 30 min, after a 30 min ramp.

Then, perovskite precursor solution was deposited selectively on the area of interest by inkjet with a 10 pL droplet volume and a spatial resolution tuned to match the desired quantity. The optimal resolution was determined to be 1200x1200 dpi. Same processes were used to manufacture perovskite solar modules with carbon-based electrodes with 12 series-interconnected cells except for the aperture area of the screen-printing mesh and perovskite filling procedure.

The wet samples (cells and modules) were then moved to an oven set to 50°C where they were dried for 10 min, thus forming the perovskite crystals in the porous electrode structure. The resulting devices were submitted to heat and

damp treatment at 40°C and 75 % R.H. for 150 hours according to the previously reported method by Hashmi et al. [381] After the damp treatment the devices were encapsulated with TPO and PIB by a home-built vacuum laminator for 10 minutes at 110°C.

Characterization

The current-density and voltage curves of solar cells were measured with a source meter at a scan rate of 5 mV/s using a class A solar simulator providing 100 mW/cm^2, simulated AM1.5G illumination, corrected for spectral mismatch. The same equipment was used for obtaining *IV*-curves of the modules, but the scan rate was set to 100 mV/s in this case. SEM/EDX images were obtained using Zeiss EVO 10 scanning electron microscope.

Life-cycle assessment

The details of the life-cycle-assessment (*e.g.* scope definition, indicators, assumptions) can be found in the Supporting information.

9.5 Results

Environmental potential of recycling and remanufacturing encapsulated perovskite PV devices

The solar cell stack includes a fluorine-doped tin oxide (FTO) front electrode, compact and mesoporous titanium dioxide (c-TiO_2 and m-TiO_2, respectively), zirconium dioxide (ZrO_2) and a carbon-based back electrode (Figure 9.1a). After infiltration and crystallization of the perovskite inside the mesoscopic scaffold, the cells were encapsulated with thermoplastic olefins (TPO) and polyisobutylene (PIB)-based edge seal (photographs in Figure 9.1a). The justification of the encapsulation method selection can be found in the Supplementary Note 1. Statistics of the device power conversion efficiency (PCE) in Figure 9.1b demonstrates high reproducibility of this encapsulation approach with an average PCE in reverse-scan of 14.5 % and 13.7 % before and after encapsulation, respectively. However, we also note an increase in hysteresis upon encapsulation. The complementary performance statistics can be found in Fig. S1.

From an environmental perspective, the focus of any waste reduction route should be to recover and re-use those materials with high associated environmental impacts. To identify these environmental hotspots, a life cycle analysis (LCA) was conducted on the PSMs with carbon-based electrodes (CPSMs) reviewed in

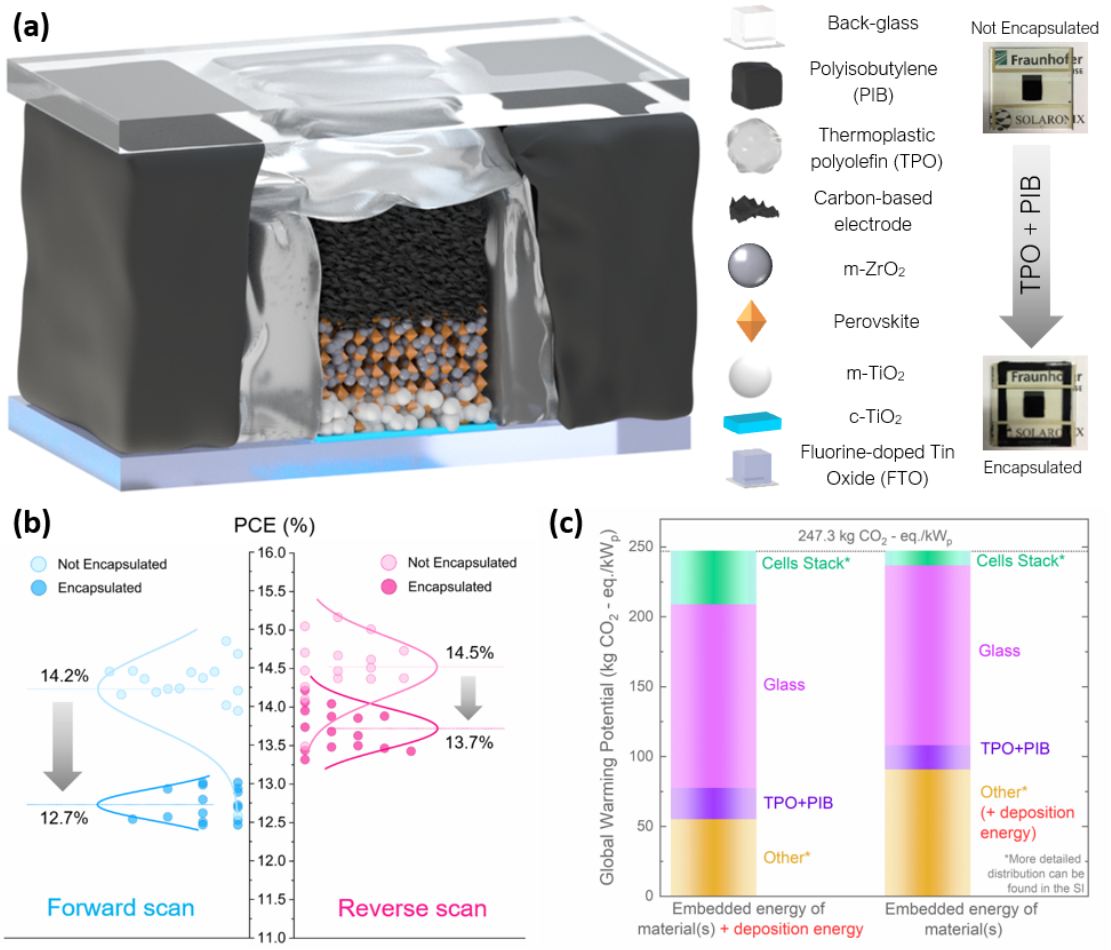


Figure 9.1: (a) Illustration of device stack of the encapsulated photovoltaic perovskite solar cells and modules with carbon-based electrodes employed in this study, with photographs (right) of the cells prior and after the encapsulation with TPO and PIB. (b) Power conversion efficiency of the cells before and after their encapsulation. (c) Global warming potential obtained from an LCA of a module based on the device structure shown in (a).

this study (details of which can be found in the Supporting Information and Fig. S2). For the assessment we consider a CPSM with a PCE of 13.2 %, based on the current-voltage (IV) measurement of a module we manufactured (Fig. S3). In this work we focused primarily on the global warming potential (GWP), expressed in kg of CO_2-equivalent per kWp of generated power, as this quality is the most direct link between the energy generation system and its greenhouse gas emissions. Figure 9.1c presents two distribution charts of individual contributions of device constituents to the total GWP.

The chart on the left side shows the amount of kg CO_2-eq. emitted during the full

processing of each module component (including the energy needed to deposit the layers, *e.g.* for screen-printing and sintering). Thus, this graph shows the potential GWP reduction per layer that can be achieved if layers are re-used without re-processing after EoL. The chart on the right side visualizes the embedded GWP per deployed material itself and has a separate part included in the "Other" contribution to account for all the energy and solvents used to fully process the layers (and overhead energy). More detailed distribution of individual contributions (*e.g.* cell layers, junction box, bus bars) to the total GWP (and other environmental impact categories) can be found in the Figs. S4 and S5. We highlight that during this LCA, we deliberately made conservative assumptions (such as a total glass thickness of 5.2 mm, which can be further reduced, and conservative estimates of overhead electricity), to avoid portraying an ideal case and showcase a more realistic scenario of the potential GWP upon commercial production.

Nevertheless, we note that the total GWP of encapsulated CPSMs was estimated to be 247.3 kg CO_2-eq./kW_p, which is one of the lowest GWPs reported for perovskite PV modules (Fig. S6), according to our knowledge. However, the LCAs of perovskite PV devices in literature often linearly extrapolate the known values of energy consumption of lab-scale production to manufacturing processes of m^2 modules, resulting in an assumption of an energy inefficient production and overestimation of the required resources. More importantly, the evaporation techniques required for metal electrode deposition, which are typically used as back-contacts in conventional PSCs are highly energy-intensive steps (not to mention the very negative environmental impact of gold), limiting the potential of perovskite PV to reach low GWPs. [217]

The second chart depicts that only a small part of the GWP contribution of the cell stack comes from the materials itself (5 %), while the majority originates from the energy and solvents used to deposit these layers. Thus, for the cell stack, possible GWP reduction can primarily be achieved by re-using the components in layer form (as they were originally deposited), which should be the initial aim of PSM remanufacturing schemes. Contrarily, the GWP mitigation potential for the recovery and subsequent reprocessing of the cell stack materials is limited.

In this study we do not consider module components such as the junction box, as these are typically separated before PV module recycling/remanufacturing and sent to designated electronic waste recycling plants. [491] Besides the materials and energy used directly for the fabrication of PSMs, GWP impact comes from indirect processes such as overhead electricity, infrastructure and packaging (included in "other" in Figure 9.1c), which are not module components that can be recycled. Recycling the TPO and the PIB-based edge seal is relatively complicated because they both contain additives (necessary to obtain desirable encapsulation traits). The presence of such additives may lead to degradation during melting and re-extrusion or cause catalyst deactivation in thermal recycling processes, thereby

reducing the quality of the material. [492] High-quality recycling of the encapsulant and edge seal would require processes and installations outside the scope of this project and is thus not considered here.

Both charts clearly demonstrate that the main GWP reduction can be achieved by re-using or recycling the glass (front and back), which can potentially reduce the GWP of PSMs by up to 53 % and 52 %, respectively. However, glass recycling comes with additional transport and energy to produce glass cullet and subsequently melt this into recycled glass. Due to these added efforts, glass recycling would likely bring little to no environmental impact reduction in respect to GWP (Figs. S7 and S8). Correspondingly, our main aim was to design a remanufacturing process that allows the direct re-use of glass and as many PSC layers as possible, since this can potentially provide a substantial decrease in GWP impact.

Development of the resource separation process

Among all the cell components presented in Figure 9.1a, perovskite is the one most likely to deteriorate in the shortest time, meaning that in order to replace it at least the PIB, TPO and back-glass have to be removed. Given that PIB is a rubber elastomer with glass transition temperature below room temperature, additional heating induces softening, allowing an easier mechanical separation of the back-sheet glass from the FTO (with cell stack). However, we note that heating the encapsulated cell above 160°C would melt the TPO due to presence of polypropylene (with melting point at 160°C), which then strongly adheres to the FTO surface. Therefore, we identified the ideal processing window for glass substrate separation (FTO and back-glass) to be between 120-140°C. The separation was assisted by making incision through the PIB rubber with a blade, which can also be done with a thin metallic wire on larger scale, since the gap between the glass substrates is around 400-500 µm, as can be seen from the SEM image in Fig. S9. After separation (Fig. S10) the glass substrates were left to cool down to room temperature before the encapsulant removal step.

Among the screened solvents, which could potentially dissolve PIB and TPO, none of them allowed a complete removal without an intensive additional manual effort (Fig. S11). Therefore, a "one-step" recycling process using a chemical bath with solvent that can dissolve edge-seal, encapsulant and perovskite was not possible for devices encapsulated with TPO and PIB. However, after keeping the substrates with PIB and TPO in acetone for 1 h, both the edge sealant and the encapsulant could be easily peeled off (Figure 9.2). Although acetone itself does not dissolve any of the cell layers except perovskite, keeping the cell stack with TPO in acetone for longer times results in partial decomposition of the carbon with perovskite (Fig. S12). The exact composition of the TPO materials can vary, depending on the manufacturer, but typically their main components are various

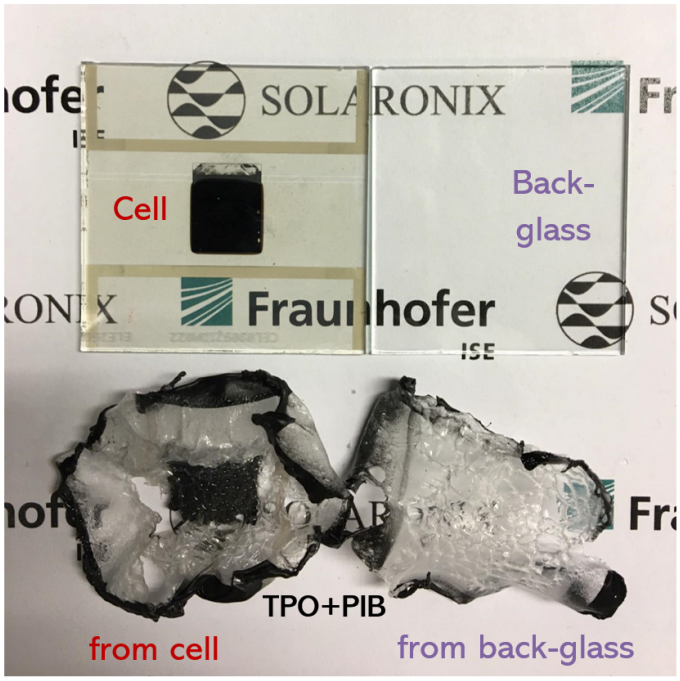


Figure 9.2: Photographs demonstrating a neat removal of encapsulants (TPO+PIB) and back-glass from the solar cell using the proposed thermally-assisted mechanochemical process, allowing to recycle them to potentially reduce the device GWP.

types of polyethylene (PE). [493] Since PE can be dissolved in acetone, the loss of TPO adhesion to the FTO is attributed to the partial dissolution of PE in TPO.

After the TPO and PIB are peeled off, the devices were dipped into a bath of methylamine (MA^0) and ethanol to liquefy and wash out the perovskite. Among the commonly used solvents such as DMF, DMSO, NMP and GBL, MA^0/EtOH has the lowest boiling point, allowing for its rapid evaporation from the cell stack, after perovskite has been removed. [367] Further annealing at 400°C allows to remove perovskite and carbon remnants from the stack, leaving m-TiO_2 and ZrO_2 intact. Cross-sectional SEM images in Fig. S13 demonstrate a comparison between these layers which were "as-deposited" (before the device manufacturing is complete) and the same layers after TPO, PIB, carbon and perovskite have been removed, clearly showing that the layer morphology and thickness are preserved. Therefore, carbon deposition and perovskite solution infiltration, followed by the encapsulation with TPO and PIB can be performed again to complete the remanufacturing loop, depicted in Figure 9.3. This remanufacturing route is appealing in terms of solar module EoL due to its simplicity, effective re-use of most of the layers in the cell stack and lack of energy-intensive process steps, such as glass melting.

The recovery of carbon or perovskite was not considered, since their recy-

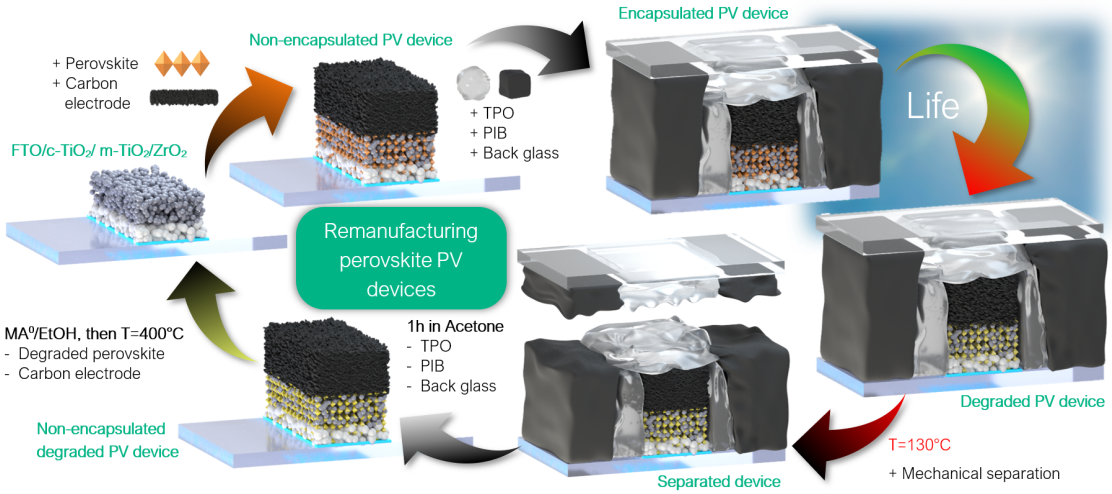


Figure 9.3: Proposed remanufacturing route for carbon-based perovskite PV modules based on a thermally-assisted mechanochemical method to separate the back-glass, encapsulants, degraded perovskite and carbon layer. This allows to re-use the rest of the layers and to lower the GWP of a perovskite PV module significantly.

cling might be more challenging in terms of processing, translating into additional GWP and reducing the environmental benefit. Especially removal of perovskite and its recovery at high purity to allow for recrystallization in a solar cell might become particularly challenging, since its opto-electronic quality must be high to ensure decent device performance and thus lower GWP. Although methylamine liquefaction and recrystallization has been demonstrated for PSC recycling before, this process requires high content of methylamine to remove perovskite to a reasonable extent, which typically results in creation of pin-holes and defects. [257, 316] Considering that TPO and PIB are nearly intact after their removal from the module, these could possibly be recycled to further reduce PV material waste. However, as mentioned earlier, quality decrease upon recycling limits the utilization of these materials for PV applications, meaning they would be more suitable to produce materials (of lower quality) for other purposes.

Solar cell remanufacturing

The encapsulated CPSCs shown in Figure 9.1 were remanufactured according to the developed thermally-assisted mechanochemical approach. The removal of perovskite and carbon, according to the procedure in Figure 9.3 allows to re-use the metal oxide layers (TiO_2, ZrO_2) deposited on the FTO (Figure 9.4a) in order to remanufacture encapsulated CPSCs. After remanufacturing, the devices look pristine, without obvious damage to the cell active area (Figure 9.4b). To evaluate the effi-

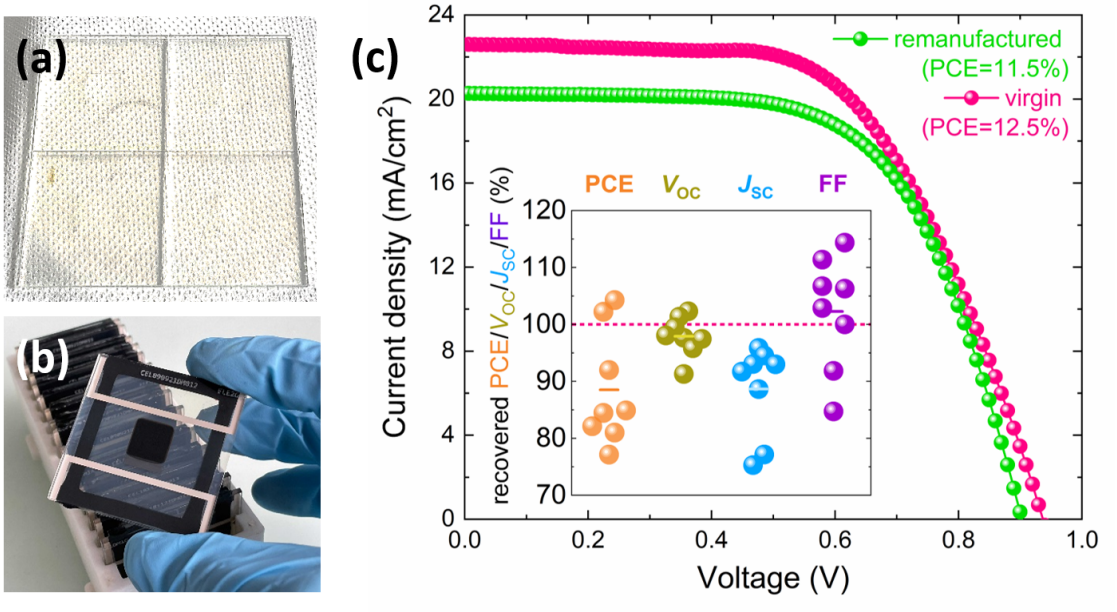


Figure 9.4: Photographs of recovered (a) FTO/c-TiO_2/m-TiO_2/ZrO_2 and (b) complete encapsulated CPSCs. (c) *JV*-curves of a representative CPSC before and after remanufacturing with 92 % recovered PCE. Device statistics are shown in the inset, demonstrating a change in each individual *JV*-parameter: PCE, V_{OC}, J_{SC} and FF after recycling relative to the initial (virgin) characteristics.

cacy of our proposed remanufacturing route, we have compared the *JV*-parameters of cells before and after remanufacturing. Figure 9.4c demonstrates that while some remanufactured cells have a slightly better PCE than before, the average recovered PCE after remanufacturing is 88 % of their initial value. We note that all the cells (virgin and recycled) were always measured 4 days after encapsulation (stored in the dark under 30-40 % R.H., room temperature).

The PCE loss occurs primarily due to a significant decrease in J_{SC}, suggesting a presence of additional optical or charge extraction losses. We speculate that the surface of the oxide layers could have been modified after the remanufacturing procedure, causing additional optical or charge-extraction losses, or a combination of both. The *JV*-parameters obtained from forward scans can be found in Fig. S14.

9.6 Discussion

The proposed remanufacturing method separates itself from traditional PV (bulk) recycling methods, as most of the device constituents are simply re-used and only perovskite, electrode, encapsulant and edge-seal need to be replaced. As can be seen from Table 1, these constituents account for only around 15 % of the device

Table 9.1: List of the device constituents, their EoL and corresponding GWP.

	Re-used?	GWP (kg CO_2-eq./ kW_p)	% of total GWP
Glass	yes	131.3	53.1
FTO	yes	9.4	3.8
c-TiO_2	yes	3.6	1.5
m-TiO_2	yes	5.6	2.2
ZrO_2	yes	4.5	1.8
Perovskite	no	8.2	3.3
Carbon	no	7	2.8
TPO+PIB	no	22.4	9

GWP, while the re-used components represent over 62 % of the module GWP (note that some of the GWP, such as from overhead electricity or packaging, is not directly embedded in the module).

Next, we evaluate the environmental benefit of remanufacturing modules ($1m^2$) using our newly-developed thermally-assisted mechanochemical approach. A comparison in GWP for virgin, remanufactured with 88 % of recovered PCE (based on the mean performance loss of cells shown in Figure 9.4c) and "ideal remanufactured" (without any loss of PCE after remanufacturing) are presented in Figure 9.5a. A complete environmental profile of the remanufactured modules is shown in Fig. S15. Our findings illustrate how this remanufacturing route could reduce the GWP of CPSMs by 24 % or even by 33 % if the remanufacturing process is optimized. This could result in 82 kg CO_2-eq./kW_p savings as well as an impact reduction in most other categories. Note that, despite fully re-using parts constituting 62.4 % of the GWP, the reduction in GWP (compared to virgin modules) due to remanufacturing is substantially lower. This difference in GWP results from the additional processes required for remanufacturing. Predominantly the chemical treatment in MA^0/EtOH baths, but also the temperature-assisted mechanical separation of glass substrates and annealing at 400°C result in non-negligible CO_2-eq. emissions.

In Fig. S16 we observe that, with our assumptions, such as linear degradation over lifetime, location of Freiburg, Germany, annual generation of 1429.2 kWh/m^2/y *etc.* (more details are discussed in the SI) a lifetime of over 16 years is required for virgin PSMs to have lower CO_2 emissions per kWh than c-Si modules – 30.8 g CO_2-eq./kWh. [494] (background parameters adjusted to match this study, see SI). However, this lifetime requirement can be lowered down to 10.7 years when the

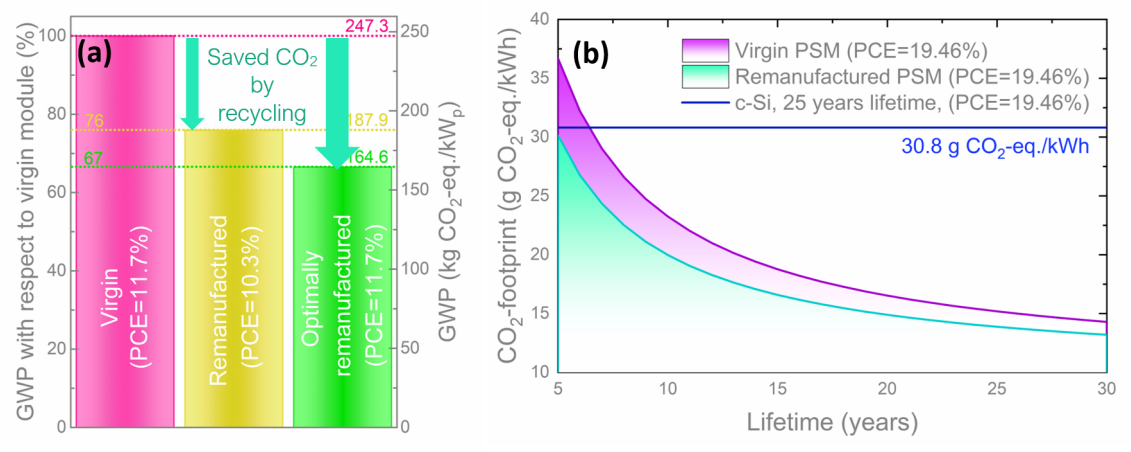


Figure 9.5: (a) GWP comparison of the virgin CPSMs in comparison to the recycled device with a loss in PCE equivalent to the mean experimentally-obtained value of 12 % relative PCE loss in Figure 9.4a, as well as hypothetical case of no performance loss. (b) CO_2-footprint of virgin and remanufactured PSMs as a function of device lifetime in comparison to c-Si modules [494] currently available on the market (as baseline). Note that in both graphs the PCE over the total area is considered (*i.e.* a product of PCE on the active are and geometrical FF)

modules are remanufactured. We also notice that the beneficial effects of recycling diminish with an increase in lifetime. This is due to the relatively higher impact of Balance of System (BoS) components at higher lifespans because the lifetime of these parts is independent of that of PSMs. Correspondingly, we recommend further research into the efficient reuse and remanufacture of BoS components to decrease the carbon footprints of not only perovskite, but PV power generation as a whole.

Despite the diminishing results of remanufacturing at increased lifetimes, Figure 9.5 shows that module-related emissions of perovskite PV can be substantially reduced by remanufacturing, especially when the PCE loss is kept to a minimum. Additionally, the remanufacturing process described here does not rest on overly optimistic assumptions and can likely still be optimized to further reduce the GWP. For example, we did not consider solvent recycling or re-use (either directly or through distillation) during the remanufacturing process. This could further reduce the GWP of remanufactured PSMs, given that the demand for solvent purity in the described process is rather low and solvents comprise the bulk of the GWP of remanufacturing efforts (Fig. S17). More importantly, this remanufacturing strategy utilizes solvents and treatments that do not decompose inorganic device constituents such as metal oxide layers. Therefore, it can also be applied to more traditional n-i-p architectured devices (which currently still hold the last certified PCE world-records among PSCs [49]) and some inorganic p-i-n based ones.

It is highly likely that upon eventual market introduction, PSMs should have comparable PCEs with c-Si devices. Figure 9.5b presents the CO_2-footprint of high-efficient virgin and remanufactured PSMs having the same PCE as the state-of-the-art c-Si modules, clearly showing that a further decrease in carbon emissions per kWh could be attained with the proposed production and remanufacturing schemes. If such high performing PSMs were to be produced similarly and remanufactured according to the procedure we describe, their CO_2-footprint would already be lower than that of c-Si modules even after a lifetime of 5 years. With similar lifetimes (25 years), these modules would have a footprint of only 14.4 g CO_2-eq./kWh – less than half of c-Si.

9.7 Conclusion

In summary, this holistic study presents a life-cycle assessment of perovskite solar modules and how their remanufacturing may affect their carbon footprint. After identifying the glass substrate as the main contributing factor to the global warming potential of PSMs, we developed an effective approach to re-use the substrate together with most of the cell layers and replace the missing components, thus leading to a development of a perovskite PV device remanufacturing process, for the first time. This thermally-assisted mechanochemical remanufacturing method consists of only a few process steps, does not use toxic solvents like DMF, and produces remanufactured encapsulated devices with a PCE close to 90 % of virgin devices. Moreover, this procedure is universally applicable to other perovskite-based devices as well, especially nip-based ones, which utilize inorganic metal oxide layers deposited on glass substrates. Despite the obvious need for perovskite PV devices to be encapsulated, this is, according to our knowledge, the first study that experimentally showcases the remanufacturing of PSCs with a module-like architecture (*i.e.* including back glass, encapsulant and an edge-seal). We estimate that the GWP of PSM production can be reduced by 24 %, or even 33 % when the remanufactured modules show no PCE reduction compared to virgin modules through the described remanufacturing method, while also reducing its overall environmental impact. Further, we show that the CO_2-footprint of electricity generated by (remanufactured) PSM systems can become lower than that of c-Si, even at comparatively low lifetime and PCE. Correspondingly, we highlight that a substantial reduction in environmental impact can still be achieved by enhancing device PCE and stability. Overall, this work uniquely combines analytical and experimental methods to assess the sustainability of an emerging perovskite PV technology and to develop efficacious methods to improve it further towards a more environmentally-conscious energy generation system.

9.8 Critical discussion

The presented study contains a unique combination of analytical (LCA) and experimental (*e.g.* manufactured samples, measurements) research, underlining its strong advantage in comparison to works on similar topics in literature. Often, reports in the experimental field propose new methods to recycle PSCs (always without encapsulation), but without demonstrating the potential environmental impact of this recycling strategy. On the other hand there are researchers who conduct more analytical studies on sustainability and LCAs of PSCs, based on assumptions, which are sometimes distant from the current state-of-the-art (module efficiency, stability *etc.*). Therefore, this study was aimed to combine both types of research and to draw a direct link between new findings obtained from the applied science and the impact it could have on the environmental profile of such PV generation system. Nevertheless, several points could have been developed further to improve this work:

- As mentioned in the study the encapsulation route plays key role for the device stability. Despite the fact that a combination of TPO and PIB was used previously in other reports to demonstrate impressive resilience to moisture-induced degradation, [194] further justification of such encapsulation would be beneficial. An additional complementary experimental evidence how TPO and PIB prevents degradation under damp-heat conditions for at least 1,000 hours (according to the IEC standard requirement) would be particularly useful.
- The remanufacturing route proposed in this work can be utilized to remove the TPO and PIB from a perovskite PV device. But if other encapsulation strategies will be developed in the future, which might be deemed better in protecting PV device from the ambient, a new remanufacturing strategy would need to be developed. Consequently, its environmental impact might also significantly differ and therefore, the benefit of remanufacturing such solar modules might change.
- For the calculation of remanufacturing impact, an assumption is taken that the performance loss during remanufacturing would be equivalent for cells and modules. However, this assumption is rather optimistic, since the complete removal of TPO, PIB, carbon and perovskite from a large (*e.g.* 10x10 cm^2) module is likely to be more difficult to achieve (in comparison to removal from a cell) due to higher chance of damaging active area, inhomogeneous removal of perovskite and carbon *etc.*. Proving the opposite by remanufacturing not only small CPSCs, but also large modules (like the ones demonstrated in chapter 8) with a similar (or less) performance loss would eliminate these doubts and prove that such recycling approach is applicable even to large PV devices.

Overall, the sustainability study presented in this work highlighted not only that perovskite PV modules with carbon-based electrodes can have a lower global warming potential than the traditional c-Si PV, but also that it can be reduced further by the newly-developed universally-applicable remanufacturing process.

Chapter 10

Conclusion

10.1 Summary

In this work, perovskite photovoltaic devices with carbon-based electrodes were investigated in depth, with the aim to improve their characteristics and bring such energy generation technology closer to its commercialization. It starts with **understanding** the main properties of these carbon electrodes, the perovskite crystallization process and the device physics of such photovoltaic devices. Based on this knowledge new effective methods were demonstrated to **improve** the solar cell performance. Then, the **stability** and degradation mechanisms of cells and modules with carbon-based electrodes were investigated, revealing why such devices are particularly stable under reverse bias conditions. Finally, the **environmental impact** of these modules was evaluated and a novel method for recycling these devices was developed, which helped to decrease its CO_2-footprint.

- **Properties of carbon-based electrodes and their application in perovskite PV devices**

  Firstly, the main properties of carbon-based electrodes have been investigated, how can they be applied and how do they affect the performance and stability of a perovskite PV device. The strong advantages of the carbon-based electrodes in comparison to their metallic equivalents (which are normally used for traditional perovskite solar cells) are mainly their stability and low cost. These carbon-based materials are chemically-inert, do not decompose under high temperature and retain their structure even in the aged devices. Simultaneously, the carbon materials cost less and can be deposited with fast-throughput equipment without the need for high vacuum conditions. However, the power conversion efficiency of perovskite PV devices with such carbon electrodes needs to be improved further, necessitating a deep understanding of perovskite crystallization control and charge carrier dynamics in such devices. A timely review shown in this work provides a comprehensive overview on the benefits of carbon-based electrodes, current challenges and potential improvements.

- **Perovskite liquefaction and crystalllization mechanisms**

  In this work, the perovskite liquefaction and crystallization using a novel methylamine (MA^0)-based approach were studied in detail using advanced crystallographic, chemical and opto-electronic characterization methods. The obtained results allowed to resolve the reaction mechanisms, formation of molecular bonds and crystallization kinetics when MA^+-based perovskite are exposed to MA^0. For the first time, it was experimentally proven that perovskite interacts with methylamine by forming a complex via Pb-N bonds and MA^+-MA^0 dimers via hydrogen bonds. When the perovskite

photoabsorber is crystallized from a liquid methylamine-perovskite complex, the concentration of methylamine and moisture play an important role in determining perovskite opto-electronic quality, composition homogeneity and phase purity.

- **The effect of grain size in perovskite solar cells with carbon-based electrodes**

  One of the most important technological aspects that essentially defines the solar cell architecture, its possible constituents and its potential performance is the curing temperature of the carbon-based electrode. It determines whether the photoabsorbing material will be added before or after the deposition of the carbon layer. This deposition sequence introduces a crucial difference between the perovskite photoabsorber layer and its crystallization, consequently affecting the device opto-electronic properties. A thorough investigation of perovskite solar cells with carbon electrodes with different perovskite grain sizes allowed to unequivocally assign the differences in opto-electronic properties to this salient characteristic and determine its effect on the device performance. The presented quantitative analysis of generation, charge transport and recombination losses revealed that the cells with high-temperature electrodes (which are predominantly discussed in this work) mostly suffer from the non-radiative recombination at the perovskite grain-boundaries. If the perovskite grain size can be similar as in the case of conventionally-processed poly-crystalline perovskite films, non-radiative recombination can be significantly suppressed, providing potential to boost the open-circuit voltage of a device from 0.9 V to over 1.1 V. Further efficiency gains could be obtained by decreasing the sheet resistivity of the carbon electrode, optimizing the perovskite/carbon contact and reducing the optical losses.

- **Nanoarchitectonic approach to control the perovskite crystal size in mesoscopic structures**

  Based on the in-depth analysis of devices with carbon-based electrodes, a novel nanorachitectonics approach was developed to obtain a more favorable porous layer structure, which promoted the growth of larger perovskite crystals. Such strategy allowed to reduce the density of grain boundaries, and thus, number of non-radiative recombination centers, enhancing the charge carrier lifetime and open-circuit voltage. However, the performance enhancement was only 30 mV, due to the non-optimized size of the nanoarchitectured cavity and, therefore, perovskite crystals. Nevertheless, this work serves as a proof-of-concept study with a number of possible further optimization methods.

- **Reducing series resistance losses of carbon-based electrodes via natural and synthetic graphites**

  Since graphite crystals are the main conductive component of the carbon-based electrode, their crystallographic and morphological properties directly affect the charge carrier transport in the solar cell. A comparison of different types of graphite crystals demonstrated that some of them feature a higher order of structural symmetry and a lower number of crystallographic defects, which has a positive influence on the charge carrier transport and sheet resistivity. In addition, the graphite crystal size and contact with perovskite determine the interfacial resistance and charge extraction losses. Therefore, the cumulative impact of the graphite crystals on the cell fill factor is a complex interplay between the sheet resistivity and the interfacial resistance, with scaly graphite being the most optimal graphite type in carbon-based electrode, enabling fill factors close to 75 %.

- **Testing reverse bias-induced degradation of perovskite PV devices with carbon-based electrodes**

  Considering that metallic electrodes are often (at least partially) responsible for the degradation of the perovskite PV devices under reverse bias, carbon-based analogues provide a unique potential to overcome this issue to a significant extent. The work within this thesis has proven experimentally that perovskite solar cells and modules with these carbon electrodes can withstand voltages up to -9 V and can meet the harsh "hot-spot" conditions according to the internationally acknowledged IEC 61215:2016 standard for industrial PV. This was the first demonstration of a perovskite PV device stable under such conditions, highlighting the distinctive feature of enhanced stability.

- **Reduction of environmental impact of perovskite PV modules with carbon-based electrodes via remanufacturing**

  To evaluate methods of decreasing the negative environmental impact of the perovksite PV modules with carbon electrodes a life-cycle assessment of these devices was conducted. This analysis showed that in contrast to recycling techniques, directly re-using the glass substrates and (optionally) parts of the cell stack can result in the significant reduction of the module's global warming potential. Therefore, a novel thermally-assisted mechanochemical separation approach was developed to disassemble the device, enabling the re-use of the glass substrates (front- and back-glass) and most of the cell stack. Remarkably, this remanufacturing method resulted in a relatively high-quality recovery of the material with remanufactured cells having 88 % (mean) of the

initial PCE. Such strategy would allow to save almost 24 % of the module's global warming potential or even by 33 % if the loss in power output after remanufacturing would be minimized. Furthermore, if a remanufactured module would have a lifetime of 11 years, its CO_2-footprint would already be lower than that of the state-of-the-art Si-PV modules, whereas the virgin modules would need to have a lifetime of >16 years. Notably, the notion that perovskite PV devices (especially encapsulated ones) can be designed for remanufacturing is a conceptually new idea in the PV research field and it will likely gain a significant attention in the perovskite community.

Overall, this dissertation covers a wide range of questions starting from understanding the chemical and material properties, as well as charge carrier dynamics, extending to advanced characterization of manufactured solar cells and modules, which is then wrapped up with a sustainability analysis, viewed from a broader perspective. All of the presented work provided new significant insights and deep understanding of the various phenomena in perovskite PV devices with carbon-based electrodes occurring on different scales: from sub-nanometer dimension to discussions of (hypothetical) $\approx m^2$-modules. These results are expected to be particularly useful to the perovskite PV community and the author believes that these findings will facilitate a faster development of perovskite PV devices with carbon-based electrodes and help to bring them closer to the commercialization.

10.2 Perspective

The findings of this thesis significantly contributed to reaching the milestones in the research projects funded by the European Commission and German Ministry of the Education and Research, aimed at bringing perovskite PV with carbon-based electrodes closer to commercialization. The effective methods to boost the performance of these devices as well as their exceptional stability under reverse bias conditions gained significant attention from the industry partners. During this work, these collaborative activities have facilitated a faster learning curve, development of new performance-enhancing strategies and potential for future projects. Due to a strong commercial potential of perovskite PV devices with carbon-based electrodes, several companies plan to implement this technology in the fields outside of PV-power plant applications, such as internet-of-things (IoT), wearable electronics and even space applications.

Just recently a new project PEROGAIN was granted by the Deutsche Forschungsgemeinschaft (DFG) to investigate the properties of perovskite solar cells with low-temperature carbon electrodes, understand the charge carrier dynamics at the interfaces and degradation mechanisms. In addition, a project DIAMOND funded by the EU-2020 Horizon program will also start in 2022 and will be dedicated to

bringing the perovskite PV devices with low-temperature carbon electrodes closer to commercialization. Such immense interest and support from the national and european agencies underline further the strong potential of this technology to penetrate the PV market within the next years.

In the last couple of years, numerous researchers demonstrated various stabilization strategies to produce a mixed tin-lead perovskites with low energy bandgap. This lead a significant progress in multi-junction perovskite solar cells, where carbon-based electrodes can also be applied to improve the device stability. Although such devices have not been demonstrated in literature yet, this could potentially be a breakthrough towards devices with these electrodes having >25 % PCE.

Finally, the perovskite PV technology with carbon-based electrodes can facilitate a faster growth of the PV industry and decarbonization of our energy sector, which is essential for reaching global sustainability goals.

Chapter 11

Scientific contributions

11.1 Publications

2022

1. **Bogachuk, D.**, Girard, J. Tilala, S., Martineau, D., Narbey, S., Verma, A., Hinsch, A., Kohlstädt, M., Wagner, L. (2022) Nanoarchitectonics in fully printed perovskite solar cells with carbon-based electrodes, *arXiv*, available at: https://doi.org/10.48550/arXiv.2211.09424
2. Yang, B., **Bogachuk, D.**, Suo, J., Wagner, L., Kim, H., Lim, J., Hinsch, A., Boschloo, G., Nazeeruddin, M.K., Hagfeldt A. (2022) Strain effects on halide perovskite solar cells, *Chem. Soc. Rev.*, 51, 7509-7530
3. **Bogachuk, D.**, van der Windt, P., Wagner, L., Martineau, D., Narbey, S., Verma, A., Lim, J., Zouhair, S., Kohlstädt, M., Hinsch, A., M., Stranks S.D., Würfel, U., Glunz, S.. (2022) Remanufacturing Perovskite Solar Cells and Modules – a Holistic Case Study, *Research Square*, available at: https://doi.org/10.21203/rs.3.rs-1767937/v1
4. Wagner, L., Schygulla, P., Herterich, J.P., Elshamy, M., **Bogachuk, D.**, Zouhair, S., Mastroianni, S., Würfel, U., Liu, Y., Zakeeruddin, S.M., Grätzel, M., Hinsch, A., Glunz, S. (2022) Revealing fundamentals of charge extraction in photovoltaic devices through potentiostatic photoluminescence imaging. *Matter*, 5(7), 2352-2364
5. Zouhair, S., Yoo, S.M., **Bogachuk, D.**, Herterich, J.P., Lim, J., Kanda, H., Son, B., Yun, H.J., Würfel, U., Chahboun, A., Nazeeruddin, M.K., Hinsch, A., Wagner, L., Kim, H. (2022) Employing 2D-Perovskite as an Electron Blocking Layer in Highly Efficient (18.5%) Perovskite Solar Cells with Printable Low Temperature Carbon Electrode. *Adv. Energy Mater.*, p.2200837.
6. **Bogachuk, D.**, Yang, B., Suo, J., Martineau, D., Verma, A., Narbey, S., Anaya, M., Frohna, K., Doherty, T., Müller, D., Herterich, J.P., Zouhair, S., Hagfeldt, A., Stranks, S.D., Würfel, U., Hinsch, A., Wagner, L. (2022) Perovskite Solar Cells with Carbon-Based Electrodes-Quantification of Losses and Strategies to Overcome Them. *Adv. Energy Mater.*, 12(10), p.2103128

2021

7. Zouhair, S., Luo, B., **Bogachuk, D.**, Martineau, D., Wagner, L., Chahboun, A., Glunz, S.W. and Hinsch, A., (2021) Fill Factor Assessment in Hole Selective Layer Free Carbon Electrode-Based Perovskite Solar Cells with 15.5% Certified Power Conversion Efficiency. *Sol RRL*, 6(2), p.2100745.
8. Wagner, L., Qiu, C., Unmüssig, M., **Bogachuk, D.**, Mastroianni, S., Würfel, U., Hu, Y., Han, H. and Hinsch, A., (2021) A 2D Model for Interfacial Recombination in Mesoscopic Perovskite Solar Cells with Printed Back Contact. *Sol. RRL*, 5(1), p.2000595.
9. Yang, B., Suo, J., Di Giacomo, F., Olthof, S., **Bogachuk, D.**, Kim, Y., Sun, X., Wagner, L., Fu, F., Zakeeruddin, S.M., Hinsch, A., Grätzel, M., Di Carlo, A., Hagfeldt, A., (2021) Interfacial Passivation Engineering of Perovskite Solar Cells with Fill Factor over 82% and Outstanding Operational Stability on nip Architecture. *ACS Energy Lett.*, 6(11), pp.3916-3923.
10. **Bogachuk, D.**, Saddedine, K., Martineau, D., Narbey, S., Verma, A., Gebhardt, P., Herterich, J.P., Glissmann, N., Zouhair, S., Markert, J., Gould, I.E., McGehee, M.D., Würfel, U., Hinsch, A., Wagner, L. (2022) Perovskite Photovoltaic Devices with Carbon-Based Electrodes Withstanding Reverse-Bias Voltages up to -9 V and Surpassing IEC 61215: 2016 International Standard. *Sol. RRL*, 6(3), p.2100527.
11. **Bogachuk, D.**, Tsuji, R., Martineau, D., Narbey, S., Herterich, J.P., Wagner, L., Suginuma, K., Ito, S. and Hinsch, A., (2021) Comparison of highly conductive natural and synthetic graphites for electrodes in perovskite solar cells. *Carbon*, 178, pp.10-18.

2020

12. Tsuji, R., **Bogachuk, D.**, Martineau, D., Wagner, L., Kobayashi, E., Funayama, R., Matsuo, Y., Mastroianni, S., Hinsch, A. and Ito, S., 2020, December. Function of Porous Carbon Electrode during the Fabrication of Multiporous-Layered-Electrode Perovskite Solar Cells. *MDPI Photonics*, 7(4), p. 133
13. **Bogachuk, D.**, Zouhair, S., Wojciechowski, K., Yang, B., Babu, V., Wagner, L., Xu, B., Lim, J. Mastroianni, S., Pettersson, H., Hagfeldt, A. Hinsch, A. (2020). Low-temperature carbon-based electrodes in perovskite solar cells. *Energy Environ. Sci.*, 13(11), 3880-3916.
14. Tsuji, R., **Bogachuk, D.**, Luo, B., Martineau, D., Kobayashi, E., Funayama, R., Mastroianni, S., Hinsch, A. and Ito, S., (2020) Activation of Weak Monochromic Photocurrents by White Light Irradiation for Accurate IPCE Measurements of Carbon-Based Multi-Porous-Layered-Electrode Perovskite Solar Cells, *Electrochemistry*, 88(5) pp.20-64074.
15. **Bogachuk, D.**, Wagner, L., Mastroianni, S., Daub, M., H., Hillebrecht, A. Hinsch, A. (2020). The nature of the methylamine- $MAPbI_3$ complex: fundamentals of gas-induced perovskite liquefaction and crystallization. *J. Mater. Chem. A*, 8(19), 9788-9796.
16. Mathiazhagan, G., Wagner, L., Bogati, S., Unal, K.Y., **Bogachuk, D.**, Kroyer, T., Mastroianni, S. and Hinsch, A., (2020) Double-mesoscopic hole-transport-material-free perovskite solar cells: overcoming charge-transport limitation by sputtered ultrathin Al_2O_3 isolating layer. *ACS Appl. Nano Mater.*, 3(3), pp.2463-2471

11.2 Oral contributions at international conferences

2022

1. Wagner, L., Pietzcker, R., Friedrich, L., **Bogachuk D.**, Goldschmidt, J.C. The Resource Footprint of Tomorrow's PV Industry. *European Materials Research Society Conference - Fall Meeting* (E-MRS 2022 Fall Meeting), 19-22.09.2022, Warsaw, Poland
2. Wagner, L., Schygulla, P., Herterich, J.P., Elshamy, M., **Bogachuk D.**, Zouhair, S., Mastroianni, S., Würfel, U., Liu, Y., Zakeeruddin, S.M., Grätzel, M., Hinsch, A., Glunz, S.W. Potentiostatic Photoluminescence Imaging of Charge Extraction in Perovskite Solar Cells. *49th IEEE Photovoltaic Specialists Conference* (IEEE PVSC 49), 05.06.-10.06.2022, Philadelphia, PA, USA
3. **Bogachuk, D.**, van der Windt, P., Martineau, D., Verma, A., Narbey, S., Zouhair, S., Hinsch, A., Kohlstädt, M., Wagner, L. A novel recycling method for encapsulated perovskite mesoscopic photovoltaic devices with minimal performance loss. *15th International Conference on Hybrid and Organic Photovoltaics* (HOPV22), 19.05.-25.05.2022, Valencia, Spain
4. **Bogachuk, D.**, Wagner, L., Martineau, M., van der Windt, P., Zouhair, S., Hinsch, A. Stable, cost-effective, sustainable and recyclable perovskite photovoltaics using carbon-based electrodes. *nanoGe Spring Meeting* (NSM22), 07.03.-11.03.2022, Online
5. Zouhair, S., Yoo, S.M., **Bogachuk, D.**, Herterich, J.P., Lim, J., Würfel, U., Chahboun, A., Nazeeruddin, M.K., Hinsch, A., Wagner, L., Kim, H. Low Dimensional 2D Perovskite As An Effective Electron Blocking Layer In Efficient (18.5%) And Stable Hole-Selective Layer-Free Carbon Electrode Based Perovskite Solar Cells. *nanoGe Spring Meeting* (NSM22), 07.03.-11.03.2022, Online
6. **Bogachuk, D.**, Wagner, L., Martineau, M., Narbey, S., Verma, A., Zouhair, S., Hinsch A. How to make perovskite photovoltaic devices stable under reverse bias. *International Online Conference on Perovskite Thin Film Photovoltaics and Perovskite Photonics and Optoelectronics* (NIPHO22). 14.02.-15.02.2022, Online
7. Zouhair, S., Yoo, S.M., **Bogachuk, D.**, Herterich, J.P., Lim, J., Würfel, U., Chahboun, A., Nazeeruddin, M.K., Hinsch, A., Wagner, L., Kim, H. Electron Blocking 2D Perovskite In Highly Efficient (18.5%) Hole-Selective Layer-Free Perovskite Solar Cells Using Low-Temperature Processed Carbon Electrode. *International Online Conference on Perovskite Thin Film Photovoltaics and Perovskite Photonics and Optoelectronics* (NIPHO22). 14.02.-15.02.2022, Online

2021

8. **Bogachuk, D.**, Saddedine, K., Martineau, D., Narbey, S., Verma, A., Gebhardt, P., Herterich, J.P., Glissmann, N., Zouhair, S., Markert, J., Gould, I.E., McGehee, M.D., Würfel, U., Hinsch, A., Wagner, L. Outstanding Stability of Perovskite Photovoltaic Devices with Carbon-Based Contacts Under Reverse-bias Conditions. *Solar-Power-Tech Conference* (SPT2021), 05.07.-08.07.2021, Online
9. Wagner, L., Qiu, C., Unmüssig, M., **Bogachuk, D.**, Mastroianni, S., Würfel, U., Hu, Y., Han, H., Hinsch, A. Unraveling the decoupled 2D charge transport and extraction in mesoscopic perovskite solar cells. *European Materials Research Society Sprint Meeting* (E-MRS), 31.05.-03.06.2021, Online
10. **Bogachuk, D.**, Yang, B., Suo, J., Martineau, D., Verma, A., Narbey, S., Anaya, M., Frohna, K., Doherty, T., Müller, D., Herterich, J.P., Zouhair, S., Wagner, L., Würfel, U., Hagfeldt, A., Stranks, S.D., Hinsch, A. Quantifying Losses of Perovskite Solar Cells with Carbon-based Back-contacts and Outlining a Roadmap on Boosting Their Power Conversion Efficiencies. *13th International Conference on Hybrid and Organic Photovoltaics* (HOPV21), 25.05.-28.05.2021, Online

2020

11. **Bogachuk, D.**, Wagner, L., Hinsch, A. How to Boost the Power Conversion Efficiency of Carbon-based Perovskite Solar Cells. *International online conference on hybrid materials and optoelectronic devices* (HYBRIDOE) 15.12.-17.12.2020, Online
12. Mastroianni, S., Wagner, L., Mathiazhagan, G., **Bogachuk, D.**, Yasaroglu, K., Bogati, S., Kroyer, T., Daub, M., Hillebrecht, H., Rehspringer, J.-L., Dinia, A., Hinsch, A. Towards a sustainable energy future: fully printable carbon-based Perovskite Solar Cells with overcome Charge Transport Limitation and improved light-harvesting efficiency. *Asia-Pacific International Conference on Perovskite, Organic Photovoltaics and Optoelectronics* (IPEROP20), 20.01.-22.01.2020, Tsukuba, Japan

Chapter 12

Acknowledgements

I would like to express my gratitude to a number of people who have continuously supported me during this work.

Firstly, I would like to thank the Deutsche Bundesstiftung Umwelt (DBU) for providing me with a scholarship to conduct my research freely and making my PhD possible. I am also exceptionally grateful to **Prof. Dr. Stefan Glunz**, who not only sparked my interest for photovoltaics with his fascinating lectures in the first place, but also always supported me in my research activities. Thank you, Prof. Glunz, for always being responsive, helpful, for finding time for our discussions and for being a fantastic supervisor of my thesis! I also would like to thank **Dr. Severin Vierrath** for being my second supervisor, **Prof. Dr. Seigo Ito** for our great collaboration in the past and for agreeing to be an external examiner, as well as **Prof. Dr. Oliver Ambacher** for being the chairman at my PhD defense and for captivating lectures in solid-state physics.

Next, I would like to thank **Dr. Lukas Wagner**, who inspired me to become a researcher in the field of perovskites and always supported my endeavors. Thank you, Lukas, for always being there and for being my mentor. I have learnt a lot from you (or at least I like to think so) and I will always be grateful for your help, advices, scientific and philosophical discussions we had and overall support, throughout our time at Fraunhofer ISE. Also, I would like to thank **Dr. Andreas Hinsch** for always being open to very interesting discussions, for giving academic advices, sharing deep scientific insights, planning the most peculiar experiments and making science fun! In addition, I am thankful to **Dr. Uli Würfel**, who always took time to listen and provide such valuable advices, suggestions and insights in physics and beyond. Moreover, I would like to thank **Dr. Simone Mastroianni**, who also has taught me so much and to whom I am indebted for becoming the researcher I am today. *Grazie, Simone!*

I also would like to thank the colleagues in my group, particularly, **Salma Zouhair**, who has been together with me in the "trenches" of the intense PhD life. Thank you for having my back and always helping me! In addition, I would like to thank **Dr. Gayathri Mathiazhagan**, who could always lift up the spirits in our team and create such a warm and positive atmosphere in the group. Special thanks goes to **Jaekeun Lim**, who is not only an excellent researcher and a team member, but also a fantastic cook and a great friend! Moreover, I would like to express my gratitude to **Siddharth Tilala**, who has always been very helpful, responsive and kind throughout my PhD.

It has been a great pleasure to work in this group and I would like to thank all the other team members, all of whom have contributed to making our team really special over the years: **Mohamed El Shamy, Benedict Szabo, Kevin Eble, Jutta Zielonka, Sijo Chacko, Kübra Yasaroglu, Konrad Fischer, Bin Luo, Karima Saddedine, Nico Glissmann, Soyul Kang, Eric Seger,**

Burcu Gulsen, Hadi Mohammadzadeh, Lennart Wolf, Daniel Sänger, Jessie Lin and Peter van der Windt. Without you guys, the team would not have had the same spirit or freedom, openness and positivity! I also would like to thank members of our group at FMF: **Markus Kohlstädt, Jan Herterich, Max Ernst, Georgios Loukeris, David Müller, Clemens Baretzky, Sergei Vedernikov and Andrea Martinez**, who always found time to help with experiments and my work. Furthermore, I am grateful to the members of the perovskite/Si tandem group at Fraunhofer ISE, particularly to **Dr. Patricia Schulze**, who has always been very kind, open and helpful. Special thanks goes to **Oussama Er-Raji** for being an incredibly nice person and a great researcher to work with! Also I would like to thank **Özde Kabakli, Jacob Myers, Zak Newcomb-Hall, Maryam and Mina Heydarian, as well as Dr. Alexander Bett** for pleasant discussions and help with experiments! Furthermore, I would like to express my gratitude to the head of the CalLab PV Cells group – **Dr. Jochen Hohl-Ebinger**, who could always find time and energy for measurements and interesting discussions. And I am also thankful to **Dr. Paul Gerbhardt** for being responsive, curious and helpful at all times, during our work together.

I am also extremely grateful to a number of collaborators, with whom it was a pleasure and a privilege of working. Particular thanks goes to **Dr. Bowen Yang** and **Dr. Jiajia Suo**, who have always been so exceptionally friendly, kind, supportive and open. I am extremely glad I had the chance to meet you, guys! Also, I would like to thank **Dr. David Martineau** for continuous support throughout my PhD and for being such an *incroyable* collaborator! Furthermore, I would like to thank **Stephanie Narbey, Anand Verma** and the whole Solaronix and Perovskia teams for helping with my research and for your hospitality during my visits to Switzerland. In addition, I am grateful to **Dr. Tiarnan Doherty**, with whom I had the chance of working on several interesting projects, sharing sandy beers on Valencian beach and who was always a supportive, helpful and, simply, great collaborator. Moreover, I am very thankful to **Kyle Frohna, Dr. Miguel Anaya and Dr. Sam Stranks** for our past and ongoing collaborations. I would also like to thank **Ryuki Tsuji** for being responsive, supportive and friendly, as well as for our excellent work together. Thank you very much, **Prof. Michael McGehee** and **Isaac Gould** for our fascinating discussions, sharing your ideas and openness to collaborate. I am also grateful to **Dr. Michael Daub and Prof. Harald Hillebrecht**, who have provided so much help and expertise during our work together.

Most importantly, I would like to especially thank people closest to me, who have been supporting me on this fantastic journey. First of all, my wife – **Fan Guo**, who was always there for me, who continuously supported my endeavors, encouraged and motivated me, who helped me so much in so many different ways. *Schatzi,* my everlasting companion, my "partner in crime", without your endless love and care I would not be able to do it. And of course, I am eternally grateful to **my**

amazing family, who always loved me, who supported my education, my choices and decisions in life. I consider myself remarkably lucky for being surrounded by so many loving people, because as one of the most prominent physicists of all time – Richard Feynman – once said: "Physics isn't the most important thing. *Love* is."

Bibliography

[1] J. Powell, "Scientists reach 100% consensus on anthropogenic global warming," *Bulletin of Science, Technology & Society*, vol. 37, no. 4, pp. 183–184, 2017.

[2] M. Lynas, B. Z. Houlton, and S. Perry, "Greater than 99% consensus on human caused climate change in the peer-reviewed scientific literature," *Environmental Research Letters*, vol. 16, no. 11, p. 114005, oct 2021. [Online]. Available: https://doi.org/10.1088/1748-9326/ac2966

[3] IRENA, "Global energy transformation: a roadmap to 2050 (2019 edition)," 2019.

[4] W. W. S., Philips, "Photovoltaics report," *Fraunhofer ISE*, 2021.

[5] L. Argote and D. Epple, "Learning curves in manufacturing," *Science*, vol. 247, no. 4945, pp. 920–924, 1990. [Online]. Available: https://www.science.org/doi/abs/10.1126/science.247.4945.920

[6] VDMA, "International technology roadmap for photovoltaic (itrpv)," 2020.

[7] M. Sze Simon and K. Ng Kwok, "Physics of semiconductor devices," *Wiley-Interscience*, vol. 7, pp. 237–244, 2006.

[8] P. Würfel and U. Würfel, *Physics of solar cells: from basic principles to advanced concepts*. John Wiley & Sons, 2016.

[9] J. K. Isabella Olindo, Smets Arno, M. Zeman, and R. van Swaaij, "Solar energy: The physics and engineering of photovoltaic conversion, technologies and systems," *UIT Cambridge Limited*, 2016.

[10] A. G. Aberle, S. Glunz, and W. Warta, "Impact of illumination level and oxide parameters on shockley–read–hall recombination at the si-sio2 interface," *Journal of Applied Physics*, vol. 71, no. 9, pp. 4422–4431, 1992.

[11] L. Krückemeier, B. Krogmeier, Z. Liu, U. Rau, and T. Kirchartz, "Understanding transient photoluminescence in halide perovskite layer stacks

and solar cells," *Advanced Energy Materials*, vol. 11, no. 19, p. 2003489, 2021. [Online]. Available: https://onlinelibrary.wiley.com/doi/abs/10.1002/aenm.202003489

[12] W. A. Dunlap-Shohl, Y. Zhou, N. P. Padture, and D. B. Mitzi, "Synthetic approaches for halide perovskite thin films," *Chemical reviews*, vol. 119, no. 5, pp. 3193–3295, 2018.

[13] Q. Chen, N. De Marco, Y. M. Yang, T.-B. Song, C.-C. Chen, H. Zhao, Z. Hong, H. Zhou, and Y. Yang, "Under the spotlight: The organic–inorganic hybrid halide perovskite for optoelectronic applications," *Nano Today*, vol. 10, no. 3, pp. 355–396, 2015.

[14] J. Wu, S.-C. Liu, Z. Li, S. Wang, D.-J. Xue, Y. Lin, and J.-S. Hu, "Strain in perovskite solar cells: origins, impacts and regulation," *National science review*, vol. 8, no. 8, p. nwab047, 2021.

[15] D. Weber, "Ch3nh3pbx3, ein pb (ii)-system mit kubischer perowskitstruktur/ch3nh3pbx3, a pb (ii)-system with cubic perovskite structure," *Zeitschrift für Naturforschung B*, vol. 33, no. 12, pp. 1443–1445, 1978.

[16] R. E. Brandt, V. Stevanović, D. S. Ginley, and T. Buonassisi, "Identifying defect-tolerant semiconductors with high minority-carrier lifetimes: beyond hybrid lead halide perovskites," *MRS Communications*, vol. 5, no. 2, pp. 265–275, 2015.

[17] J. Even, L. Pedesseau, C. Katan, M. Kepenekian, J.-S. Lauret, D. Sapori, and E. Deleporte, "Solid-state physics perspective on hybrid perovskite semiconductors," *The Journal of Physical Chemistry C*, vol. 119, no. 19, pp. 10 161–10 177, 2015.

[18] T. Umebayashi, K. Asai, T. Kondo, and A. Nakao, "Electronic structures of lead iodide based low-dimensional crystals," *Phys. Rev. B*, vol. 67, p. 155405, Apr 2003. [Online]. Available: https://link.aps.org/doi/10.1103/PhysRevB.67.155405

[19] B. J. Foley, D. L. Marlowe, K. Sun, W. A. Saidi, L. Scudiero, M. C. Gupta, and J. J. Choi, "Temperature dependent energy levels of methylammonium lead iodide perovskite," *Applied physics letters*, vol. 106, no. 24, p. 243904, 2015.

[20] A. M. Leguy, P. Azarhoosh, M. I. Alonso, M. Campoy-Quiles, O. J. Weber, J. Yao, D. Bryant, M. T. Weller, J. Nelson, A. Walsh *et al.*, "Experimental and theoretical optical properties of methylammonium lead halide perovskites," *Nanoscale*, vol. 8, no. 12, pp. 6317–6327, 2016.

[21] G. Landi, H. C. Neitzert, C. Barone, C. Mauro, F. Lang, S. Albrecht, B. Rech, and S. Pagano, "Correlation between electronic defect states distribution and device performance of perovskite solar cells," *Advanced Science*, vol. 4, no. 10, p. 1700183, 2017. [Online]. Available: https://onlinelibrary.wiley.com/doi/abs/10.1002/advs.201700183

[22] W. Tress, "Perovskite solar cells on the way to their radiative efficiency limit–insights into a success story of high open-circuit voltage and low recombination," *Advanced Energy Materials*, vol. 7, no. 14, p. 1602358, 2017.

[23] T. Leijtens, G. E. Eperon, A. J. Barker, G. Grancini, W. Zhang, J. M. Ball, A. R. S. Kandada, H. J. Snaith, and A. Petrozza, "Carrier trapping and recombination: the role of defect physics in enhancing the open circuit voltage of metal halide perovskite solar cells," *Energy & Environmental Science*, vol. 9, no. 11, pp. 3472–3481, 2016.

[24] M. Samiee, S. Konduri, B. Ganapathy, R. Kottokkaran, H. A. Abbas, A. Kitahara, P. Joshi, L. Zhang, M. Noack, and V. Dalal, "Defect density and dielectric constant in perovskite solar cells," *Applied Physics Letters*, vol. 105, no. 15, p. 153502, 2014.

[25] H.-S. Duan, H. Zhou, Q. Chen, P. Sun, S. Luo, T.-B. Song, B. Bob, and Y. Yang, "The identification and characterization of defect states in hybrid organic–inorganic perovskite photovoltaics," *Physical chemistry chemical physics*, vol. 17, no. 1, pp. 112–116, 2015.

[26] Y. Tian, A. Merdasa, M. Peter, M. Abdellah, K. Zheng, C. S. Ponseca Jr, T. Pullerits, A. Yartsev, V. Sundstrom, and I. G. Scheblykin, "Giant photoluminescence blinking of perovskite nanocrystals reveals single-trap control of luminescence," *Nano Letters*, vol. 15, no. 3, pp. 1603–1608, 2015.

[27] A. Guerrero, E. J. Juarez-Perez, J. Bisquert, I. Mora-Sero, and G. Garcia-Belmonte, "Electrical field profile and doping in planar lead halide perovskite solar cells," *Applied Physics Letters*, vol. 105, no. 13, p. 133902, 2014.

[28] B. Wang, K. Y. Wong, S. Yang, and T. Chen, "Crystallinity and defect state engineering in organo-lead halide perovskite for high-efficiency solar cells," *Journal of Materials Chemistry A*, vol. 4, no. 10, pp. 3806–3812, 2016.

[29] H. Jin, E. Debroye, M. Keshavarz, I. G. Scheblykin, M. B. Roeffaers, J. Hofkens, and J. A. Steele, "It's a trap! on the nature of localised states and charge trapping in lead halide perovskites," *Materials Horizons*, vol. 7, no. 2, pp. 397–410, 2020.

[30] J. Chang, H. Zhu, B. Li, F. H. Isikgor, Y. Hao, Q. Xu, and J. Ouyang, "Boosting the performance of planar heterojunction perovskite solar cell by controlling the precursor purity of perovskite materials," *Journal of Materials Chemistry A*, vol. 4, no. 3, pp. 887–893, 2016.

[31] J. Kim, S.-H. Lee, J. H. Lee, and K.-H. Hong, "The role of intrinsic defects in methylammonium lead iodide perovskite," *The journal of physical chemistry letters*, vol. 5, no. 8, pp. 1312–1317, 2014.

[32] A. Buin, P. Pietsch, J. Xu, O. Voznyy, A. H. Ip, R. Comin, and E. H. Sargent, "Materials processing routes to trap-free halide perovskites," pp. 6281–6286, 2014.

[33] W.-J. Yin, T. Shi, and Y. Yan, "Unusual defect physics in ch3nh3pbi3 perovskite solar cell absorber," *Applied Physics Letters*, vol. 104, no. 6, p. 063903, 2014.

[34] E. Gutierrez-Partida, H. Hempel, S. Caicedo-Dávila, M. Raoufi, F. Peña-Camargo, M. Grischek, R. Gunder, J. Diekmann, P. Caprioglio, K. O. Brinkmann *et al.*, "Large-grain double cation perovskites with 18 μs lifetime and high luminescence yield for efficient inverted perovskite solar cells," *ACS Energy Letters*, vol. 6, no. 3, pp. 1045–1054, 2021.

[35] A. Al-Ashouri, E. Köhnen, B. Li, A. Magomedov, H. Hempel, P. Caprioglio, J. A. Márquez, A. B. M. Vilches, E. Kasparavicius, J. A. Smith, N. Phung, D. Menzel, M. Grischek, L. Kegelmann, D. Skroblin, C. Gollwitzer, T. Malinauskas, M. Jošt, G. Matič, B. Rech, R. Schlatmann, M. Topič, L. Korte, A. Abate, B. Stannowski, D. Neher, M. Stolterfoht, T. Unold, V. Getautis, and S. Albrecht, "Monolithic perovskite/silicon tandem solar cell with >29% efficiency by enhanced hole extraction," *Science*, vol. 370, no. 6522, pp. 1300–1309, 2020. [Online]. Available: https://www.science.org/doi/abs/10.1126/science.abd4016

[36] D. W. DeQuilettes, S. Koch, S. Burke, R. K. Paranji, A. J. Shropshire, M. E. Ziffer, and D. S. Ginger, "Photoluminescence lifetimes exceeding 8 μs and quantum yields exceeding 30% in hybrid perovskite thin films by ligand passivation," *ACS Energy Letters*, vol. 1, no. 2, pp. 438–444, 2016.

[37] Q. Jiang, Y. Zhao, X. Zhang, X. Yang, Y. Chen, Z. Chu, Q. Ye, X. Li, Z. Yin, and J. You, "Surface passivation of perovskite film for efficient solar cells," *Nature Photonics*, vol. 13, no. 7, pp. 460–466, 2019.

[38] I. L. Braly, D. W. DeQuilettes, L. M. Pazos-Outón, S. Burke, M. E. Ziffer, D. S. Ginger, and H. W. Hillhouse, "Hybrid perovskite films approaching the radiative limit with over 90% photoluminescence quantum efficiency," *Nature Photonics*, vol. 12, no. 6, pp. 355–361, 2018.

[39] Z. Liu, L. Kruckemeier, B. Krogmeier, B. Klingebiel, J. A. Márquez, S. Levcenko, S. Oz, S. Mathur, U. Rau, T. Unold, and T. Kirchartz, "Open-circuit voltages exceeding 1.26 v in planar methylammonium lead iodide perovskite solar cells," *ACS energy letters*, vol. 4, no. 1, pp. 110–117, 2018.

[40] R. E. Brandt, J. R. Poindexter, P. Gorai, R. C. Kurchin, R. L. Hoye, L. Nienhaus, M. W. Wilson, J. A. Polizzotti, R. Sereika, R. Zaltauskas *et al.*, "Searching for "defect-tolerant" photovoltaic materials: combined theoretical and experimental screening," *Chemistry of Materials*, vol. 29, no. 11, pp. 4667–4674, 2017.

[41] S. De Wolf, J. Holovsky, S.-J. Moon, P. Loper, B. Niesen, M. Ledinsky, F.-J. Haug, J.-H. Yum, and C. Ballif, "Organometallic halide perovskites: sharp optical absorption edge and its relation to photovoltaic performance," *The journal of physical chemistry letters*, vol. 5, no. 6, pp. 1035–1039, 2014.

[42] J. H. Noh, S. H. Im, J. H. Heo, T. N. Mandal, and S. I. Seok, "Chemical management for colorful, efficient, and stable inorganic–organic hybrid nanostructured solar cells," *Nano letters*, vol. 13, no. 4, pp. 1764–1769, 2013.

[43] G. E. Eperon, S. D. Stranks, C. Menelaou, M. B. Johnston, L. M. Herz, and H. J. Snaith, "Formamidinium lead trihalide: a broadly tunable perovskite for efficient planar heterojunction solar cells," *Energy Environ. Sci.*, vol. 7, pp. 982–988, 2014. [Online]. Available: http://dx.doi.org/10.1039/C3EE43822H

[44] Y. Chang, C. H. Park, and K. Matsuishi, "First-principles study of the structural and the electronic properties of the lead-halide-based inorganic-organic perovskites (ch˜ 3nh˜ 3) pbx˜ 3 and cspbx˜ 3 (x= cl, br, i)," *Journal-Korean Physical Society*, vol. 44, pp. 889–893, 2004.

[45] I. Borriello, G. Cantele, and D. Ninno, "Ab initio investigation of hybrid organic-inorganic perovskites based on tin halides," *Physical Review B*, vol. 77, no. 23, p. 235214, 2008.

[46] A. Kojima, K. Teshima, Y. Shirai, and T. Miyasaka, "Organometal halide perovskites as visible-light sensitizers for photovoltaic cells," *Journal of the American Chemical Society*, vol. 131, no. 17, pp. 6050–6051, 2009, pMID: 19366264. [Online]. Available: https://doi.org/10.1021/ja809598r

[47] B. O'regan and M. Grätzel, "A low-cost, high-efficiency solar cell based on dye-sensitized colloidal tio2 films," *nature*, vol. 353, no. 6346, pp. 737–740, 1991.

[48] H.-S. Kim, C.-R. Lee, J.-H. Im, K.-B. Lee, T. Moehl, A. Marchioro, S.-J. Moon, R. Humphry-Baker, J.-H. Yum, J. E. Moser, M. Grätzel, and N.-G. Park, "Lead iodide perovskite sensitized all-solid-state submicron thin film mesoscopic solar cell with efficiency exceeding 9%," *Scientific Reports*, vol. 2, Aug 2012, article. [Online]. Available: https://doi.org/10.1038/srep00591

[49] J. Y. Kim, J.-W. Lee, H. S. Jung, H. Shin, and N.-G. Park, "High-efficiency perovskite solar cells," *Chemical Reviews*, vol. 120, no. 15, pp. 7867–7918, 2020.

[50] NREL, "Best research research cell efficiencies," 2022.

[51] Z. Li, T. R. Klein, D. H. Kim, M. Yang, J. J. Berry, M. F. Van Hest, and K. Zhu, "Scalable fabrication of perovskite solar cells," *Nature Reviews Materials*, vol. 3, no. 4, pp. 1–20, 2018.

[52] Y.-H. Kim, J. S. Kim, and T.-W. Lee, "Strategies to improve luminescence efficiency of metal-halide perovskites and light-emitting diodes," *Advanced Materials*, vol. 31, no. 47, p. 1804595, 2019. [Online]. Available: https://onlinelibrary.wiley.com/doi/abs/10.1002/adma.201804595

[53] K. Ji, M. Anaya, A. Abfalterer, and S. D. Stranks, "Halide perovskite light-emitting diode technologies," *Advanced Optical Materials*, vol. 9, no. 18, p. 2002128, 2021. [Online]. Available: https://onlinelibrary.wiley.com/doi/abs/10.1002/adom.202002128

[54] S. P. Senanayak, M. Abdi-Jalebi, V. S. Kamboj, R. Carey, R. Shivanna, T. Tian, G. Schweicher, J. Wang, N. Giesbrecht, D. D. Nuzzo, H. E. Beere, P. Docampo, D. A. Ritchie, D. Fairen-Jimenez, R. H. Friend, and H. Sirringhaus, "A general approach for hysteresis-free, operationally stable metal halide perovskite field-effect transistors," *Science Advances*, vol. 6, no. 15, p. eaaz4948, 2020. [Online]. Available: https://www.science.org/doi/abs/10.1126/sciadv.aaz4948

[55] F. Paulus, C. Tyznik, O. D. Jurchescu, and Y. Vaynzof, "Switched-on: Progress, challenges, and opportunities in metal halide perovskite transistors," *Advanced Functional Materials*, vol. 31, no. 29, p. 2101029, 2021. [Online]. Available: https://onlinelibrary.wiley.com/doi/abs/10.1002/adfm.202101029

[56] V. Venugopalan, R. Sorrentino, P. Topolovsek, D. Nava, S. Neutzner, G. Ferrari, A. Petrozza, and M. Caironi, "High-detectivity perovskite light detectors printed in air from benign solvents," *Chem*, vol. 5, no. 4, pp. 868–880, 2019. [Online]. Available: https://www.sciencedirect.com/science/article/pii/S2451929419300312

[57] L. Sun, W. Li, W. Zhu, and Z. Chen, "Single-crystal perovskite detectors: development and perspectives," *J. Mater. Chem. C*, vol. 8, pp. 11 664–11 674, 2020. [Online]. Available: http://dx.doi.org/10.1039/D0TC02944K

[58] K. Liao, X. Hu, Y. Cheng, Z. Yu, Y. Xue, Y. Chen, and Q. Gong, "Spintronics of hybrid organic–inorganic perovskites: Miraculous basis of integrated optoelectronic devices," *Advanced Optical Materials*, vol. 7, no. 15, p. 1900350, 2019. [Online]. Available: https://onlinelibrary.wiley.com/doi/abs/10.1002/adom.201900350

[59] J. Wang, C. Zhang, H. Liu, R. McLaughlin, Y. Zhai, S. R. Vardeny, X. Liu, S. McGill, D. Semenov, H. Guo *et al.*, "Spin-optoelectronic devices based on hybrid organic-inorganic trihalide perovskites," *Nature communications*, vol. 10, no. 1, pp. 1–6, 2019.

[60] T. Lemercier, L. Perrin, E. Planès, S. Berson, and L. Flandin, "A comparison of the structure and properties of opaque and semi-transparent nip/pin-type scalable perovskite solar cells," *Energies*, vol. 13, no. 15, p. 3794, 2020.

[61] A. Al-Ashouri, A. Magomedov, M. Roß, M. Jošt, M. Talaikis, G. Chistiakova, T. Bertram, J. A. Márquez, E. Köhnen, E. Kasparavičius *et al.*, "Conformal monolayer contacts with lossless interfaces for perovskite single junction and monolithic tandem solar cells," *Energy & Environmental Science*, vol. 12, no. 11, pp. 3356–3369, 2019.

[62] M. Stolterfoht, P. Caprioglio, C. M. Wolff, J. A. Márquez, J. Nordmann, S. Zhang, D. Rothhardt, U. Hörmann, Y. Amir, A. Redinger *et al.*, "The impact of energy alignment and interfacial recombination on the internal and external open-circuit voltage of perovskite solar cells," *Energy & environmental science*, vol. 12, no. 9, pp. 2778–2788, 2019.

[63] P. Tiwana, P. Docampo, M. B. Johnston, H. J. Snaith, and L. M. Herz, "Electron mobility and injection dynamics in mesoporous zno, sno2, and tio2 films used in dye-sensitized solar cells," *ACS nano*, vol. 5, no. 6, pp. 5158–5166, 2011.

[64] S. Sun, T. Buonassisi, and J.-P. Correa-Baena, "State-of-the-art electron-selective contacts in perovskite solar cells," *Advanced Materials Interfaces*, vol. 5, no. 22, p. 1800408, 2018.

[65] Y. Wu, X. Yang, H. Chen, K. Zhang, C. Qin, J. Liu, W. Peng, A. Islam, E. Bi, F. Ye *et al.*, "Highly compact tio2 layer for efficient hole-blocking in perovskite solar cells," *Applied physics express*, vol. 7, no. 5, p. 052301, 2014.

[66] M. Stolterfoht, C. M. Wolff, J. A. Márquez, S. Zhang, C. J. Hages, D. Rothhardt, S. Albrecht, P. L. Burn, P. Meredith, T. Unold *et al.*, "Visualization and suppression of interfacial recombination for high-efficiency large-area pin perovskite solar cells," *Nature Energy*, vol. 3, no. 10, pp. 847–854, 2018.

[67] R. Swartwout, M. T. Hoerantner, and V. Bulović, "Scalable deposition methods for large-area production of perovskite thin films," *ENERGY & ENVIRONMENTAL MATERIALS*, vol. 2, no. 2, pp. 119–145, 2019. [Online]. Available: https://onlinelibrary.wiley.com/doi/abs/10.1002/eem2.12043

[68] M. Jung, S.-G. Ji, G. Kim, and S. I. Seok, "Perovskite precursor solution chemistry: from fundamentals to photovoltaic applications," *Chemical Society Reviews*, vol. 48, no. 7, pp. 2011–2038, 2019.

[69] M. Saliba, J.-P. Correa-Baena, M. Grätzel, A. Hagfeldt, and A. Abate, "Perovskite solar cells: from the atomic level to film quality and device performance," *Angewandte Chemie International Edition*, vol. 57, no. 10, pp. 2554–2569, 2018.

[70] N.-G. Park and K. Zhu, "Scalable fabrication and coating methods for perovskite solar cells and solar modules," *Nature Reviews Materials*, vol. 5, no. 5, pp. 333–350, 2020.

[71] Z. Li, T. R. Klein, D. H. Kim, M. Yang, J. J. Berry, M. F. Van Hest, and K. Zhu, "Scalable fabrication of perovskite solar cells," *Nature Reviews Materials*, vol. 3, no. 4, pp. 1–20, 2018.

[72] J.-P. Correa-Baena, M. Saliba, T. Buonassisi, M. Grätzel, A. Abate, W. Tress, and A. Hagfeldt, "Promises and challenges of perovskite solar cells," *Science*, vol. 358, no. 6364, pp. 739–744, 2017.

[73] X. Dai, Y. Deng, C. H. Van Brackle, and J. Huang, "Meniscus fabrication of halide perovskite thin films at high throughput for large area and low-cost solar panels," *International Journal of Extreme Manufacturing*, vol. 1, no. 2, p. 022004, 2019.

[74] H. Chen, F. Ye, W. Tang, J. He, M. Yin, Y. Wang, F. Xie, E. Bi, X. Yang, M. Grätzel *et al.*, "A solvent-and vacuum-free route to large-area perovskite films for efficient solar modules," *Nature*, vol. 550, no. 7674, pp. 92–95, 2017.

[75] J. Luo, J. Xia, H. Yang, C. Sun, N. Li, H. A. Malik, H. Shu, Z. Wan, H. Zhang, C. J. Brabec *et al.*, "A pressure process for efficient and stable perovskite solar cells," *Nano Energy*, vol. 77, p. 105063, 2020.

[76] S. Das, B. Yang, G. Gu, P. C. Joshi, I. N. Ivanov, C. M. Rouleau, T. Aytug, D. B. Geohegan, and K. Xiao, "High-performance flexible perovskite solar cells by using a combination of ultrasonic spray-coating and low thermal budget photonic curing," *Acs Photonics*, vol. 2, no. 6, pp. 680–686, 2015.

[77] A. T. Barrows, A. J. Pearson, C. K. Kwak, A. D. F. Dunbar, A. R. Buckley, and D. G. Lidzey, "Efficient planar heterojunction mixed-halide perovskite solar cells deposited via spray-deposition," *Energy Environ. Sci.*, vol. 7, pp. 2944–2950, 2014. [Online]. Available: http://dx.doi.org/10.1039/C4EE01546K

[78] J. Tait, S. Manghooli, W. Qiu, L. Rakocevic, L. Kootstra, M. Jaysankar, C. M. De La Huerta, U. W. Paetzold, R. Gehlhaar, D. Cheyns *et al.*, "Rapid composition screening for perovskite photovoltaics via concurrently pumped ultrasonic spray coating," *Journal of Materials Chemistry A*, vol. 4, no. 10, pp. 3792–3797, 2016.

[79] A. A. Petrov, N. A. Belich, A. Y. Grishko, N. M. Stepanov, S. G. Dorofeev, E. G. Maksimov, A. V. Shevelkov, S. M. Zakeeruddin, M. Graetzel, A. B. Tarasov, and E. A. Goodilin, "A new formation strategy of hybrid perovskites via room temperature reactive polyiodide melts," *Mater. Horiz.*, vol. 4, pp. 625–632, 2017. [Online]. Available: http://dx.doi.org/10.1039/C7MH00201G

[80] I. Turkevych, S. Kazaoui, N. A. Belich, A. Y. Grishko, S. A. Fateev, A. A. Petrov, T. Urano, S. Aramaki, S. Kosar, M. Kondo *et al.*, "Strategic advantages of reactive polyiodide melts for scalable perovskite photovoltaics," *Nature nanotechnology*, vol. 14, no. 1, pp. 57–63, 2019.

[81] V. K. LaMer and R. H. Dinegar, "Theory, production and mechanism of formation of monodispersed hydrosols," *Journal of the american chemical society*, vol. 72, no. 11, pp. 4847–4854, 1950.

[82] N. J. Jeon, J. H. Noh, Y. C. Kim, W. S. Yang, S. Ryu, and S. I. Seok, "Solvent engineering for high-performance inorganic–organic hybrid perovskite solar cells," *Nature materials*, vol. 13, no. 9, pp. 897–903, 2014.

[83] M. Saliba, J.-P. Correa-Baena, C. M. Wolff, M. Stolterfoht, N. Phung, S. Albrecht, D. Neher, and A. Abate, "How to make over 20% efficient perovskite solar cells in regular (n–i–p) and inverted (p–i–n) architectures," *Chemistry of Materials*, vol. 30, no. 13, pp. 4193–4201, 2018.

[84] S. Chen, X. Xiao, B. Chen, L. L. Kelly, J. Zhao, Y. Lin, M. F. Toney, and J. Huang, "Crystallization in one-step solution deposition of perovskite films: Upward or downward?" *Science Advances*, vol. 7, no. 4, p. eabb2412, 2021.

[85] J. M. Azpiroz, E. Mosconi, J. Bisquert, and F. De Angelis, "Defect migration in methylammonium lead iodide and its role in perovskite solar cell operation," *Energy & Environmental Science*, vol. 8, no. 7, pp. 2118–2127, 2015.

[86] T. Chen, B. J. Foley, C. Park, C. M. Brown, L. W. Harriger, J. Lee, J. Ruff, M. Yoon, J. J. Choi, and S.-H. Lee, "Entropy-driven structural transition and kinetic trapping in formamidinium lead iodide perovskite," *Science advances*, vol. 2, no. 10, p. e1601650, 2016.

[87] J. M. Frost, K. T. Butler, F. Brivio, C. H. Hendon, M. Van Schilfgaarde, and A. Walsh, "Atomistic origins of high-performance in hybrid halide perovskite solar cells," *Nano letters*, vol. 14, no. 5, pp. 2584–2590, 2014.

[88] C. Eames, J. M. Frost, P. R. Barnes, B. C. O'regan, A. Walsh, and M. S. Islam, "Ionic transport in hybrid lead iodide perovskite solar cells," *Nature communications*, vol. 6, no. 1, pp. 1–8, 2015.

[89] W. Tress, "Metal halide perovskites as mixed electronic–ionic conductors: Challenges and opportunities from hysteresis to memristivity," *The journal of physical chemistry letters*, vol. 8, no. 13, pp. 3106–3114, 2017.

[90] L. Rakocevic, L. E. Mundt, R. Gehlhaar, T. Merckx, T. Aernouts, M. C. Schubert, S. W. Glunz, and J. Poortmans, "Loss analysis in perovskite photovoltaic modules," *Solar RRL*, vol. 3, no. 12, p. 1900338, 2019. [Online]. Available: https://onlinelibrary.wiley.com/doi/abs/10.1002/solr.201900338

[91] NREL, "Champion photovoltaic module efficiency chart," 2022.

[92] D. Bogachuk, B. Yang, J. Suo, D. Martineau, A. Verma, S. Narbey, M. Anaya, K. Frohna, T. Doherty, D. Müller, J. P. Herterich, S. Zouhair, A. Hagfeldt, S. D. Stranks, U. Würfel, A. Hinsch, and L. Wagner, "Perovskite solar cells with carbon-based electrodes – quantification of losses and strategies to overcome them," *Advanced Energy Materials*, vol. 12, no. 10, p. 2103128, 2022. [Online]. Available: https://onlinelibrary.wiley.com/doi/abs/10.1002/aenm.202103128

[93] D. Abou-Ras, T. Kirchartz, and U. Rau, *Advanced characterization techniques for thin film solar cells*. John Wiley & Sons, 2016.

[94] G. El-Hajje, C. Momblona, L. Gil-Escrig, J. Ávila, T. Guillemot, J.-F. Guillemoles, M. Sessolo, H. J. Bolink, and L. Lombez, "Quantification of spatial inhomogeneity in perovskite solar cells by hyperspectral luminescence imaging," *Energy & Environmental Science*, vol. 9, no. 7, pp. 2286–2294, 2016.

[95] E. M. Hutter, T. Kirchartz, B. Ehrler, D. Cahen, and E. Von Hauff, "Pitfalls and prospects of optical spectroscopy to characterize perovskite-transport layer interfaces," *Applied physics letters*, vol. 116, no. 10, p. 100501, 2020.

[96] E. von Hauff and D. Klotz, "Impedance spectroscopy for perovskite solar cells: characterisation, analysis, and diagnosis," *J. Mater. Chem. C*, vol. 10, pp. 742–761, 2022. [Online]. Available: http://dx.doi.org/10.1039/D1TC04727B

[97] M. R. Filip, G. E. Eperon, H. J. Snaith, and F. Giustino, "Steric engineering of metal-halide perovskites with tunable optical band gaps," *Nature communications*, vol. 5, no. 1, pp. 1–9, 2014.

[98] R. J. Sutton, G. E. Eperon, L. Miranda, E. S. Parrott, B. A. Kamino, J. B. Patel, M. T. Hörantner, M. B. Johnston, A. A. Haghighirad, D. T. Moore *et al.*, "Bandgap-tunable cesium lead halide perovskites with high thermal stability for efficient solar cells," *Advanced Energy Materials*, vol. 6, no. 8, p. 1502458, 2016.

[99] J. Sun, J. Wu, X. Tong, F. Lin, Y. Wang, and Z. M. Wang, "Organic/inorganic metal halide perovskite optoelectronic devices beyond solar cells," *Advanced Science*, vol. 5, no. 5, p. 1700780, 2018.

[100] L. Mao, Y. Wu, C. C. Stoumpos, M. R. Wasielewski, and M. G. Kanatzidis, "White-light emission and structural distortion in new corrugated two-dimensional lead bromide perovskites," *Journal of the American Chemical Society*, vol. 139, no. 14, pp. 5210–5215, 2017.

[101] L. Meng, E.-P. Yao, Z. Hong, H. Chen, P. Sun, Z. Yang, G. Li, and Y. Yang, "Pure formamidinium-based perovskite light-emitting diodes with high efficiency and low driving voltage," *Advanced Materials*, vol. 29, no. 4, p. 1603826, 2017.

[102] A. Sadhanala, A. Kumar, S. Pathak, A. Rao, U. Steiner, N. C. Greenham, H. J. Snaith, and R. H. Friend, "Electroluminescence from organometallic lead halide perovskite-conjugated polymer diodes," *Advanced Electronic Materials*, vol. 1, no. 3, p. 1500008, 2015.

[103] T. Gupta, D. Ghoshal, A. Yoshimura, S. Basu, P. K. Chow, A. S. Lakhnot, J. Pandey, J. M. Warrender, H. Efstathiadis, A. Soni *et al.*, "An environmentally stable and lead-free chalcogenide perovskite," *Advanced Functional Materials*, vol. 30, no. 23, p. 2001387, 2020.

[104] L. Dou, Y. M. Yang, J. You, Z. Hong, W.-H. Chang, G. Li, and Y. Yang, "Solution-processed hybrid perovskite photodetectors with high detectivity," *Nature communications*, vol. 5, no. 1, pp. 1–6, 2014.

[105] X. Hu, X. Zhang, L. Liang, J. Bao, S. Li, W. Yang, and Y. Xie, "High-performance flexible broadband photodetector based on organolead halide perovskite," *Advanced Functional Materials*, vol. 24, no. 46, pp. 7373–7380, 2014.

[106] Y. Guo, C. Liu, H. Tanaka, and E. Nakamura, "Air-stable and solution-processable perovskite photodetectors for solar-blind uv and visible light," *The journal of physical chemistry letters*, vol. 6, no. 3, pp. 535–539, 2015.

[107] F. Bella, P. Renzi, C. Cavallo, and C. Gerbaldi, "Caesium for perovskite solar cells: an overview," *Chemistry–A European Journal*, vol. 24, no. 47, pp. 12 183–12 205, 2018.

[108] L. Gu, M. M. Tavakoli, D. Zhang, Q. Zhang, A. Waleed, Y. Xiao, K.-H. Tsui, Y. Lin, L. Liao, J. Wang *et al.*, "3d arrays of 1024-pixel image sensors based on lead halide perovskite nanowires," *Advanced Materials*, vol. 28, no. 44, pp. 9713–9721, 2016.

[109] W. Deng, X. Zhang, L. Huang, X. Xu, L. Wang, J. Wang, Q. Shang, S.-T. Lee, and J. Jie, "Aligned single-crystalline perovskite microwire arrays for high-performance flexible image sensors with long-term stability," *Advanced Materials*, vol. 28, no. 11, pp. 2201–2208, 2016.

[110] Y. Wang, Y. Zhu, J. Huang, J. Cai, J. Zhu, X. Yang, J. Shen, and C. Li, "Perovskite quantum dots encapsulated in electrospun fiber membranes as multifunctional supersensitive sensors for biomolecules, metal ions and ph," *Nanoscale Horizons*, vol. 2, no. 4, pp. 225–232, 2017.

[111] T. N. Huan, D. A. Dalla Corte, S. Lamaison, D. Karapinar, L. Lutz, N. Menguy, M. Foldyna, S.-H. Turren-Cruz, A. Hagfeldt, F. Bella *et al.*, "Low-cost high-efficiency system for solar-driven conversion of co2 to hydrocarbons," *Proceedings of the National Academy of Sciences*, vol. 116, no. 20, pp. 9735–9740, 2019.

[112] M. F. Ayguler, M. D. Weber, B. M. Puscher, D. D. Medina, P. Docampo, and R. D. Costa, "Light-emitting electrochemical cells based on hybrid lead halide perovskite nanoparticles," *The Journal of Physical Chemistry C*, vol. 119, no. 21, pp. 12 047–12 054, 2015.

[113] A. Aguadero, D. Pérez-Coll, J. Alonso, S. Skinner, and J. Kilner, "A new family of mo-doped srcoo3- δ perovskites for application in reversible solid state electrochemical cells," *Chemistry of Materials*, vol. 24, no. 14, pp. 2655–2663, 2012.

[114] Y. Rong, Y. Hu, A. Mei, H. Tan, M. I. Saidaminov, S. I. Seok, M. D. McGehee, E. H. Sargent, and H. Han, "Challenges for commercializing perovskite solar cells," *Science*, vol. 361, no. 6408, p. eaat8235, 2018.

[115] Y. Rong, L. Liu, A. Mei, X. Li, and H. Han, "Beyond efficiency: the challenge of stability in mesoscopic perovskite solar cells," *Advanced Energy Materials*, vol. 5, no. 20, p. 1501066, 2015.

[116] D. Wang, M. Wright, N. K. Elumalai, and A. Uddin, "Stability of perovskite solar cells," *Solar Energy Materials and Solar Cells*, vol. 147, pp. 255–275, 2016.

[117] Q. Wali, F. J. Iftikhar, M. E. Khan, A. Ullah, Y. Iqbal, and R. Jose, "Advances in stability of perovskite solar cells," *Organic Electronics*, vol. 78, p. 105590, 2020.

[118] J. S. Manser, M. I. Saidaminov, J. A. Christians, O. M. Bakr, and P. V. Kamat, "Making and breaking of lead halide perovskites," *Accounts of chemical research*, vol. 49, no. 2, pp. 330–338, 2016.

[119] D. Meggiolaro, E. Mosconi, and F. De Angelis, "Formation of surface defects dominates ion migration in lead-halide perovskites," *ACS Energy Letters*, vol. 4, no. 3, pp. 779–785, 2019.

[120] J. M. Ball and A. Petrozza, "Defects in perovskite-halides and their effects in solar cells," *Nature Energy*, vol. 1, no. 11, pp. 1–13, 2016.

[121] B. Conings, J. Drijkoningen, N. Gauquelin, A. Babayigit, J. D'Haen, L. D'Olieslaeger, A. Ethirajan, J. Verbeeck, J. Manca, E. Mosconi *et al.*, "Intrinsic thermal instability of methylammonium lead trihalide perovskite," *Advanced Energy Materials*, vol. 5, no. 15, p. 1500477, 2015.

[122] Z. Ku, Y. Rong, M. Xu, T. Liu, and H. Han, "Full printable processed mesoscopic ch3nh3pbi3/tio2 heterojunction solar cells with carbon counter electrode," *Scientific Reports*, vol. 3, pp. 3132 EP –, Nov 2013, article. [Online]. Available: https://doi.org/10.1038/srep03132

[123] Q. Wang, N. Phung, D. Di Girolamo, P. Vivo, and A. Abate, "Enhancement in lifespan of halide perovskite solar cells," *Energy & Environmental Science*, vol. 12, no. 3, pp. 865–886, 2019.

[124] F. Meng, A. Liu, L. Gao, J. Cao, Y. Yan, N. Wang, M. Fan, G. Wei, and T. Ma, "Current progress in interfacial engineering of carbon-based perovskite solar cells," *Journal of Materials Chemistry A*, vol. 7, no. 15, pp. 8690–8699, 2019.

[125] A. Mei, X. Li, L. Liu, Z. Ku, T. Liu, Y. Rong, M. Xu, M. Hu, J. Chen, Y. Yang *et al.*, "A hole-conductor–free, fully printable mesoscopic perovskite solar cell with high stability," *Science*, vol. 345, no. 6194, pp. 295–298, 2014.

[126] L. Fagiolari and F. Bella, "Carbon-based materials for stable, cheaper and large-scale processable perovskite solar cells," *Energy & Environmental Science*, vol. 12, no. 12, pp. 3437–3472, 2019.

[127] M. Hadadian, J.-H. Smått, and J.-P. Correa-Baena, "The role of carbon-based materials in enhancing the stability of perovskite solar cells," *Energy Environ. Sci.*, vol. 13, pp. 1377–1407, 2020. [Online]. Available: http://dx.doi.org/10.1039/C9EE04030G

[128] M. V. Khenkin, K. Anoop, E. A. Katz, and I. Visoly-Fisher, "Bias-dependent degradation of various solar cells: lessons for stability of perovskite photovoltaics," *Energy & Environmental Science*, vol. 12, no. 2, pp. 550–558, 2019.

[129] L. Meng, J. You, and Y. Yang, "Addressing the stability issue of perovskite solar cells for commercial applications," *Nature communications*, vol. 9, no. 1, pp. 1–4, 2018.

[130] G. Niu, X. Guo, and L. Wang, "Review of recent progress in chemical stability of perovskite solar cells," *Journal of Materials Chemistry A*, vol. 3, no. 17, pp. 8970–8980, 2015.

[131] N. H. Tiep, Z. Ku, and H. J. Fan, "Recent advances in improving the stability of perovskite solar cells," *Advanced Energy Materials*, vol. 6, no. 3, p. 1501420, 2016.

[132] Q. Fu, X. Tang, B. Huang, T. Hu, L. Tan, L. Chen, and Y. Chen, "Recent progress on the long-term stability of perovskite solar cells," *Advanced Science*, vol. 5, no. 5, p. 1700387, 2018.

[133] K. Domanski, E. A. Alharbi, A. Hagfeldt, M. Grätzel, and W. Tress, "Systematic investigation of the impact of operation conditions on the degradation behaviour of perovskite solar cells," *Nature Energy*, vol. 3, no. 1, pp. 61–67, 2018.

[134] L. K. Ono, Y. Qi, and S. F. Liu, "Progress toward stable lead halide perovskite solar cells," *Joule*, vol. 2, no. 10, pp. 1961–1990, 2018.

[135] M. V. Khenkin, E. A. Katz, A. Abate, G. Bardizza, J. J. Berry, C. Brabec, F. Brunetti, V. Bulović, Q. Burlingame, A. Di Carlo *et al.*, "Consensus statement for stability assessment and reporting for perovskite photovoltaics based on isos procedures," *Nature Energy*, vol. 5, no. 1, pp. 35–49, 2020.

[136] B. Philippe, B.-W. Park, R. Lindblad, J. Oscarsson, S. Ahmadi, E. M. Johansson, and H. Rensmo, "Chemical and electronic structure characterization of lead halide perovskites and stability behavior under different exposures a photoelectron spectroscopy investigation," *Chemistry of Materials*, vol. 27, no. 5, pp. 1720–1731, 2015.

[137] F. Li and M. Liu, "Recent efficient strategies for improving the moisture stability of perovskite solar cells," *Journal of Materials Chemistry A*, vol. 5, no. 30, pp. 15 447–15 459, 2017.

[138] J. Huang, S. Tan, P. D. Lund, and H. Zhou, "Impact of h 2 o on organic–inorganic hybrid perovskite solar cells," *Energy & Environmental Science*, vol. 10, no. 11, pp. 2284–2311, 2017.

[139] R. Wang, M. Mujahid, Y. Duan, Z.-K. Wang, J. Xue, and Y. Yang, "A review of perovskites solar cell stability," *Advanced Functional Materials*, vol. 29, no. 47, p. 1808843, 2019.

[140] J. A. Christians, P. A. Miranda Herrera, and P. V. Kamat, "Transformation of the excited state and photovoltaic efficiency of ch3nh3pbi3 perovskite upon controlled exposure to humidified air," *Journal of the American Chemical Society*, vol. 137, no. 4, pp. 1530–1538, 2015.

[141] J. Yang, B. D. Siempelkamp, D. Liu, and T. L. Kelly, "Investigation of ch3nh3pbi3 degradation rates and mechanisms in controlled humidity environments using in situ techniques," *ACS nano*, vol. 9, no. 2, pp. 1955–1963, 2015.

[142] A. M. Leguy, Y. Hu, M. Campoy-Quiles, M. I. Alonso, O. J. Weber, P. Azarhoosh, M. Van Schilfgaarde, M. T. Weller, T. Bein, J. Nelson *et al.*, "Reversible hydration of ch3nh3pbi3 in films, single crystals, and solar cells," *Chemistry of Materials*, vol. 27, no. 9, pp. 3397–3407, 2015.

[143] C. C. Stoumpos, C. D. Malliakas, and M. G. Kanatzidis, "Semiconducting tin and lead iodide perovskites with organic cations: phase transitions, high mobilities, and near-infrared photoluminescent properties," *Inorganic chemistry*, vol. 52, no. 15, pp. 9019–9038, 2013.

[144] J.-W. Lee, D.-H. Kim, H.-S. Kim, S.-W. Seo, S. M. Cho, and N.-G. Park, "Formamidinium and cesium hybridization for photo-and moisture-stable perovskite solar cell," *Advanced Energy Materials*, vol. 5, no. 20, p. 1501310, 2015.

[145] D. L. Busipalli, K.-Y. Lin, S. Nachimuthu, and J.-C. Jiang, "Enhanced moisture stability of cesium lead iodide perovskite solar cells–a first-principles molecular dynamics study," *Physical Chemistry Chemical Physics*, vol. 22, no. 10, pp. 5693–5701, 2020.

[146] W. Ahmad, J. Khan, G. Niu, and J. Tang, "Inorganic cspbi3 perovskite-based solar cells: A choice for a tandem device," *Solar Rrl*, vol. 1, no. 7, p. 1700048, 2017.

[147] Y. Liu, S. Akin, L. Pan, R. Uchida, N. Arora, J. V. Milić, A. Hinderhofer, F. Schreiber, A. R. Uhl, S. M. Zakeeruddin *et al.*, "Ultrahydrophobic 3d/2d fluoroarene bilayer-based water-resistant perovskite solar cells with efficiencies exceeding 22%," *Science advances*, vol. 5, no. 6, p. eaaw2543, 2019.

[148] S. Zhang, Z. Liu, W. Zhang, Z. Jiang, W. Chen, R. Chen, Y. Huang, Z. Yang, Y. Zhang, L. Han *et al.*, "Barrier designs in perovskite solar cells for long-term stability," *Advanced Energy Materials*, vol. 10, no. 35, p. 2001610, 2020.

[149] H. Zhu, Y. Liu, F. T. Eickemeyer, L. Pan, D. Ren, M. A. Ruiz-Preciado, B. Carlsen, B. Yang, X. Dong, Z. Wang *et al.*, "Tailored amphiphilic molecular mitigators for stable perovskite solar cells with 23.5% efficiency," *Advanced Materials*, vol. 32, no. 12, p. 1907757, 2020.

[150] R. Wang, J. Xue, K.-L. Wang, Z.-K. Wang, Y. Luo, D. Fenning, G. Xu, S. Nuryyeva, T. Huang, Y. Zhao *et al.*, "Constructive molecular configurations for surface-defect passivation of perovskite photovoltaics," *Science*, vol. 366, no. 6472, pp. 1509–1513, 2019.

[151] C. Fei, M. Zhou, J. Ogle, D.-M. Smilgies, L. Whittaker-Brooks, and H. Wang, "Self-assembled propylammonium cations at grain boundaries and the film surface to improve the efficiency and stability of perovskite solar cells," *Journal of Materials Chemistry A*, vol. 7, no. 41, pp. 23 739–23 746, 2019.

[152] Y. Cho, A. M. Soufiani, J. S. Yun, J. Kim, D. S. Lee, J. Seidel, X. Deng, M. A. Green, S. Huang, and A. W. Ho-Baillie, "Mixed 3d–2d passivation treatment for mixed-cation lead mixed-halide perovskite solar cells for higher efficiency and better stability," *Advanced Energy Materials*, vol. 8, no. 20, p. 1703392, 2018.

[153] G.-W. Kim, G. Kang, K. Choi, H. Choi, and T. Park, "Solution processable inorganic–organic double-layered hole transport layer for highly stable planar perovskite solar cells," *Advanced Energy Materials*, vol. 8, no. 26, p. 1801386, 2018.

[154] S. Yang, S. Chen, E. Mosconi, Y. Fang, X. Xiao, C. Wang, Y. Zhou, Z. Yu, J. Zhao, Y. Gao *et al.*, "Stabilizing halide perovskite surfaces for solar cell

operation with wide-bandgap lead oxysalts," *Science*, vol. 365, no. 6452, pp. 473–478, 2019.

[155] J. H. Kim, P.-W. Liang, S. T. Williams, N. Cho, C.-C. Chueh, M. S. Glaz, D. S. Ginger, and A. K.-Y. Jen, "High-performance and environmentally stable planar heterojunction perovskite solar cells based on a solution-processed copper-doped nickel oxide hole-transporting layer," *Advanced materials*, vol. 27, no. 4, pp. 695–701, 2015.

[156] J. You, L. Meng, T.-B. Song, T.-F. Guo, Y. M. Yang, W.-H. Chang, Z. Hong, H. Chen, H. Zhou, Q. Chen *et al.*, "Improved air stability of perovskite solar cells via solution-processed metal oxide transport layers," *Nature nanotechnology*, vol. 11, no. 1, pp. 75–81, 2016.

[157] K. Liu, Y. Yao, J. Wang, L. Zhu, M. Sun, B. Ren, L. Xie, Y. Luo, Q. Meng, and X. Zhan, "Spiro [fluorene-9, 9-xanthene]-based hole transporting materials for efficient perovskite solar cells with enhanced stability," *Materials Chemistry Frontiers*, vol. 1, no. 1, pp. 100–110, 2017.

[158] G.-W. Kim, G. Kang, M. Malekshahi Byranvand, G.-Y. Lee, and T. Park, "Gradated mixed hole transport layer in a perovskite solar cell: improving moisture stability and efficiency," *ACS applied materials & interfaces*, vol. 9, no. 33, pp. 27 720–27 726, 2017.

[159] Y. Yue, N. Salim, Y. Wu, X. Yang, A. Islam, W. Chen, J. Liu, E. Bi, F. Xie, M. Cai *et al.*, "Enhanced stability of perovskite solar cells through corrosion-free pyridine derivatives in hole-transporting materials," *Advanced Materials*, vol. 28, no. 48, pp. 10 738–10 743, 2016.

[160] S. M. Jain, Z. Qiu, L. Häggman, M. Mirmohades, M. B. Johansson, T. Edvinsson, and G. Boschloo, "Frustrated lewis pair-mediated recrystallization of ch 3 nh 3 pbi 3 for improved optoelectronic quality and high voltage planar perovskite solar cells," *Energy & Environmental Science*, vol. 9, no. 12, pp. 3770–3782, 2016.

[161] Z. Hawash, L. K. Ono, S. R. Raga, M. V. Lee, and Y. Qi, "Air-exposure induced dopant redistribution and energy level shifts in spin-coated spiro-meotad films," *Chemistry of Materials*, vol. 27, no. 2, pp. 562–569, 2015.

[162] T. Xu, L. Chen, Z. Guo, and T. Ma, "Strategic improvement of the long-term stability of perovskite materials and perovskite solar cells," *Physical Chemistry Chemical Physics*, vol. 18, no. 39, pp. 27 026–27 050, 2016.

[163] J.-Y. Seo, H.-S. Kim, S. Akin, M. Stojanovic, E. Simon, M. Fleischer, A. Hagfeldt, S. M. Zakeeruddin, and M. Grätzel, "Novel p-dopant toward highly efficient and stable perovskite solar cells," *Energy & Environmental Science*, vol. 11, no. 10, pp. 2985–2992, 2018.

[164] Y. Saygili, H.-S. Kim, B. Yang, J. Suo, A. B. Munoz-Garcia, M. Pavone, and A. Hagfeldt, "Revealing the mechanism of doping of spiro-meotad via zn

complexation in the absence of oxygen and light," *ACS Energy Letters*, vol. 5, no. 4, pp. 1271–1277, 2020.

[165] K. Rakstys, C. Igci, and M. K. Nazeeruddin, "Efficiency vs. stability: dopant-free hole transporting materials towards stabilized perovskite solar cells," *Chemical Science*, vol. 10, no. 28, pp. 6748–6769, 2019.

[166] D. Molina, M. A. Ruiz-Preciado, B. Carlsen, F. T. Eickemeyer, B. Yang, N. Flores-Díaz, M. J. Álvaro-Martins, K. Nonomura, A. Hagfeldt, and Á. Sastre-Santos, "Zinc phthalocyanine conjugated dimers as efficient dopant-free hole transporting materials in perovskite solar cells," *ChemPhotoChem*, vol. 4, no. 4, pp. 307–314, 2020.

[167] L. Zhang, C. Liu, X. Wang, Y. Tian, A. K. Jen, and B. Xu, "Side-chain engineering on dopant-free hole-transporting polymers toward highly efficient perovskite solar cells (20.19%)," *Advanced Functional Materials*, vol. 29, no. 39, p. 1904856, 2019.

[168] R. Chen, T. Bu, J. Li, W. Li, P. Zhou, X. Liu, Z. Ku, J. Zhong, Y. Peng, F. Huang *et al.*, "Efficient and stable inverted planar perovskite solar cells using a triphenylamine hole-transporting material," *ChemSusChem*, vol. 11, no. 9, pp. 1467–1473, 2018.

[169] Y. Li, K. R. Scheel, R. G. Clevenger, W. Shou, H. Pan, K. V. Kilway, and Z. Peng, "Highly efficient and stable perovskite solar cells using a dopant-free inexpensive small molecule as the hole-transporting material," *Advanced Energy Materials*, vol. 8, no. 23, p. 1801248, 2018.

[170] R. Azmi, S. Y. Nam, S. Sinaga, Z. A. Akbar, C.-L. Lee, S. C. Yoon, I. H. Jung, and S.-Y. Jang, "High-performance dopant-free conjugated small molecule-based hole-transport materials for perovskite solar cells," *Nano Energy*, vol. 44, pp. 191–198, 2018.

[171] X. Jiang, D. Wang, Z. Yu, W. Ma, H.-B. Li, X. Yang, F. Liu, A. Hagfeldt, and L. Sun, "Molecular engineering of copper phthalocyanines: a strategy in developing dopant-free hole-transporting materials for efficient and ambient-stable perovskite solar cells," *Advanced Energy Materials*, vol. 9, no. 4, p. 1803287, 2019.

[172] Z. Song, A. Abate, S. C. Watthage, G. K. Liyanage, A. B. Phillips, U. Steiner, M. Graetzel, and M. J. Heben, "In-situ observation of moisture-induced degradation of perovskite solar cells using laser-beam induced current," in *2016 IEEE 43rd Photovoltaic Specialists Conference (PVSC)*. IEEE, 2016, pp. 1202–1206.

[173] S. Kazim, F. J. Ramos, P. Gao, M. K. Nazeeruddin, M. Grätzel, and S. Ahmad, "A dopant free linear acene derivative as a hole transport material for perovskite pigmented solar cells," *Energy & Environmental Science*, vol. 8, no. 6, pp. 1816–1823, 2015.

[174] L. Etgar, P. Gao, Z. Xue, Q. Peng, A. K. Chandiran, B. Liu, M. K. Nazeeruddin, and M. Gratzel, "Mesoscopic ch3nh3pbi3/tio2 heterojunction solar cells," *Journal of the American Chemical Society*, vol. 134, no. 42, pp. 17 396–17 399, 2012.

[175] H. Zhang, H. Wang, W. Chen, and A. K.-Y. Jen, "Cugao2: A promising inorganic hole-transporting material for highly efficient and stable perovskite solar cells," *Advanced materials*, vol. 29, no. 8, p. 1604984, 2017.

[176] X. Yin, Y. Guo, H. Xie, W. Que, and L. B. Kong, "Nickel oxide as efficient hole transport materials for perovskite solar cells," *Solar RRL*, vol. 3, no. 5, p. 1900001, 2019.

[177] Z. Liu, A. Zhu, F. Cai, L. Tao, Y. Zhou, Z. Zhao, Q. Chen, Y.-B. Cheng, and H. Zhou, "Nickel oxide nanoparticles for efficient hole transport in pin and nip perovskite solar cells," *Journal of Materials Chemistry A*, vol. 5, no. 14, pp. 6597–6605, 2017.

[178] J. Cao, H. Yu, S. Zhou, M. Qin, T.-K. Lau, X. Lu, N. Zhao, and C.-P. Wong, "Low-temperature solution-processed nio x films for air-stable perovskite solar cells," *Journal of Materials Chemistry A*, vol. 5, no. 22, pp. 11 071–11 077, 2017.

[179] K. Domanski, J.-P. Correa-Baena, N. Mine, M. K. Nazeeruddin, A. Abate, M. Saliba, W. Tress, A. Hagfeldt, and M. Grätzel, "Not all that glitters is gold: Metal-migration-induced degradation in perovskite solar cells," *ACS Nano*, vol. 10, no. 6, pp. 6306–6314, 2016, pMID: 27187798. [Online]. Available: https://doi.org/10.1021/acsnano.6b02613

[180] S. Seo, S. Jeong, C. Bae, N.-G. Park, and H. Shin, "Perovskite solar cells with inorganic electron-and hole-transport layers exhibiting long-term (≈ 500 h) stability at 85° c under continuous 1 sun illumination in ambient air," *Advanced Materials*, vol. 30, no. 29, p. 1801010, 2018.

[181] C. Besleaga, L. E. Abramiuc, V. Stancu, A. G. Tomulescu, M. Sima, L. Trinca, N. Plugaru, L. Pintilie, G. A. Nemnes, M. Iliescu *et al.*, "Iodine migration and degradation of perovskite solar cells enhanced by metallic electrodes," *The journal of physical chemistry letters*, vol. 7, no. 24, pp. 5168–5175, 2016.

[182] A. Guerrero, J. You, C. Aranda, Y. S. Kang, G. Garcia-Belmonte, H. Zhou, J. Bisquert, and Y. Yang, "Interfacial degradation of planar lead halide perovskite solar cells," *ACS nano*, vol. 10, no. 1, pp. 218–224, 2016.

[183] K. Hooper, H. Lee, M. Newman, S. Meroni, J. Baker, T. Watson, and W. Tsoi, "Probing the degradation and homogeneity of embedded perovskite semiconducting layers in photovoltaic devices by raman spectroscopy," *Physical Chemistry Chemical Physics*, vol. 19, no. 7, pp. 5246–5253, 2017.

[184] S. Svanstrom, T. J. Jacobsson, G. Boschloo, E. M. Johansson, H. Rensmo, and U. B. Cappel, "Degradation mechanism of silver metal deposited on lead

halide perovskites," *ACS Applied Materials & Interfaces*, vol. 12, no. 6, pp. 7212–7221, 2020.

[185] L. Wang, G.-R. Li, Q. Zhao, and X.-P. Gao, "Non-precious transition metals as counter electrode of perovskite solar cells," *Energy Storage Materials*, vol. 7, pp. 40–47, 2017.

[186] C. C. Boyd, R. Cheacharoen, K. A. Bush, R. Prasanna, T. Leijtens, and M. D. McGehee, "Barrier design to prevent metal-induced degradation and improve thermal stability in perovskite solar cells," *ACS Energy Letters*, vol. 3, no. 7, pp. 1772–1778, 2018.

[187] J. Li, Q. Dong, N. Li, and L. Wang, "Direct evidence of ion diffusion for the silver-electrode-induced thermal degradation of inverted perovskite solar cells," *Advanced Energy Materials*, vol. 7, no. 14, p. 1602922, 2017.

[188] J. Zhao, X. Zheng, Y. Deng, T. Li, Y. Shao, A. Gruverman, J. Shield, and J. Huang, "Is cu a stable electrode material in hybrid perovskite solar cells for a 30-year lifetime?" *Energy & Environmental Science*, vol. 9, no. 12, pp. 3650–3656, 2016.

[189] N. Arora, M. I. Dar, A. Hinderhofer, N. Pellet, F. Schreiber, S. M. Zakeeruddin, and M. Grätzel, "Perovskite solar cells with cuscn hole extraction layers yield stabilized efficiencies greater than 20%," *Science*, vol. 358, no. 6364, pp. 768–771, 2017.

[190] S. Wu, R. Chen, S. Zhang, B. H. Babu, Y. Yue, H. Zhu, Z. Yang, C. Chen, W. Chen, Y. Huang *et al.*, "A chemically inert bismuth interlayer enhances long-term stability of inverted perovskite solar cells," *Nature communications*, vol. 10, no. 1, pp. 1–11, 2019.

[191] J.-W. Xiao, C. Shi, C. Zhou, D. Zhang, Y. Li, and Q. Chen, "Contact engineering: electrode materials for highly efficient and stable perovskite solar cells," *Solar RRL*, vol. 1, no. 9, p. 1700082, 2017.

[192] H. Xie and M. Lira-Cantu, "Multi-component engineering to enable long-term operational stability of perovskite solar cells," *Journal of Physics: Energy*, vol. 2, no. 2, p. 024008, 2020.

[193] W. Xiang and W. Tress, "Review on recent progress of all-inorganic metal halide perovskites and solar cells," *Advanced Materials*, vol. 31, no. 44, p. 1902851, 2019.

[194] R. Cheacharoen, C. C. Boyd, G. F. Burkhard, T. Leijtens, J. A. Raiford, K. A. Bush, S. F. Bent, and M. D. McGehee, "Encapsulating perovskite solar cells to withstand damp heat and thermal cycling," *Sustainable Energy & Fuels*, vol. 2, no. 11, pp. 2398–2406, 2018.

[195] L. Shi, M. P. Bucknall, T. L. Young, M. Zhang, L. Hu, J. Bing, D. S. Lee, J. Kim, T. Wu, N. Takamure *et al.*, "Gas chromatography–mass spectrometry analyses of encapsulated stable perovskite solar cells," *Science*, vol. 368, no. 6497, p. eaba2412, 2020.

[196] Z. Liu, L. Qiu, L. K. Ono, S. He, Z. Hu, M. Jiang, G. Tong, Z. Wu, Y. Jiang, D.-Y. Son *et al.*, "A holistic approach to interface stabilization for efficient perovskite solar modules with over 2,000-hour operational stability," *Nature Energy*, vol. 5, no. 8, pp. 596–604, 2020.

[197] J. Chen, Y. Xiong, Y. Rong, A. Mei, Y. Sheng, P. Jiang, Y. Hu, X. Li, and H. Han, "Solvent effect on the hole-conductor-free fully printable perovskite solar cells," *Nano Energy*, vol. 27, pp. 130 – 137, 2016. [Online]. Available: http://www.sciencedirect.com/science/article/pii/S2211285516302294

[198] H. Zhou, Y. Shi, Q. Dong, H. Zhang, Y. Xing, K. Wang, Y. Du, and T. Ma, "Hole-conductor-free, metal-electrode-free tio2/ch3nh3pbi3 heterojunction solar cells based on a low-temperature carbon electrode," *The journal of physical chemistry letters*, vol. 5, no. 18, pp. 3241–3246, 2014.

[199] Z. Yu, B. Chen, P. Liu, C. Wang, C. Bu, N. Cheng, S. Bai, Y. Yan, and X. Zhao, "Stable organic–inorganic perovskite solar cells without hole-conductor layer achieved via cell structure design and contact engineering," *Advanced Functional Materials*, vol. 26, no. 27, pp. 4866–4873, 2016.

[200] X. Li, M. Tschumi, H. Han, S. S. Babkair, R. A. Alzubaydi, A. A. Ansari, S. S. Habib, M. K. Nazeeruddin, S. M. Zakeeruddin, and M. Grätzel, "Outdoor performance and stability under elevated temperatures and long-term light soaking of triple-layer mesoporous perovskite photovoltaics," *Energy Technology*, vol. 3, no. 6, pp. 551–555, 2015.

[201] A. K. Baranwal, S. Kanaya, T. N. Peiris, G. Mizuta, T. Nishina, H. Kanda, T. Miyasaka, H. Segawa, and S. Ito, "100 c thermal stability of printable perovskite solar cells using porous carbon counter electrodes," *ChemSusChem*, vol. 9, no. 18, pp. 2604–2608, 2016.

[202] S. Gholipour, J.-P. Correa-Baena, K. Domanski, T. Matsui, L. Steier, F. Giordano, F. Tajabadi, W. Tress, M. Saliba, A. Abate *et al.*, "Highly efficient and stable perovskite solar cells based on a low-cost carbon cloth," *Advanced Energy Materials*, vol. 6, no. 20, p. 1601116, 2016.

[203] G. Grancini, C. Roldán-Carmona, I. Zimmermann, E. Mosconi, X. Lee, D. Martineau, S. Narbey, F. Oswald, F. De Angelis, M. Graetzel, and M. K. Nazeeruddin, "One-year stable perovskite solar cells by 2d/3d interface engineering," *Nature Communications*, vol. 8, pp. 15 684 EP –, Jun 2017, article. [Online]. Available: https://doi.org/10.1038/ncomms15684

[204] H. Ye, Z. Liu, X. Liu, B. Sun, X. Tan, Y. Tu, T. Shi, Z. Tang, and G. Liao, "17.78% efficient low-temperature carbon-based planar perovskite solar cells using zn-doped sno2 electron transport layer," *Applied Surface Science*, vol. 478, pp. 417–425, 2019.

[205] H. Zhang, J. Xiao, J. Shi, H. Su, Y. Luo, D. Li, H. Wu, Y.-B. Cheng, and Q. Meng, "Self-adhesive macroporous carbon electrodes for efficient and sta-

ble perovskite solar cells," *Advanced Functional Materials*, vol. 28, no. 39, p. 1802985, 2018.

[206] S. Emami, J. Martins, D. Ivanou, and A. Mendes, "Advanced hermetic encapsulation of perovskite solar cells: the route to commercialization," *Journal of Materials Chemistry A*, vol. 8, no. 5, pp. 2654–2662, 2020.

[207] Z. Wu, Z. Liu, Z. Hu, Z. Hawash, L. Qiu, Y. Jiang, L. K. Ono, and Y. Qi, "Highly efficient and stable perovskite solar cells via modification of energy levels at the perovskite/carbon electrode interface," *Advanced Materials*, vol. 31, no. 11, p. 1804284, 2019.

[208] A. Priyadarshi, L. J. Haur, P. Murray, D. Fu, S. Kulkarni, G. Xing, T. C. Sum, N. Mathews, and S. G. Mhaisalkar, "A large area (70 cm^2) monolithic perovskite solar module with a high efficiency and stability," *Energy & Environmental Science*, vol. 9, no. 12, pp. 3687–3692, 2016.

[209] Y. Hu, S. Si, A. Mei, Y. Rong, H. Liu, X. Li, and H. Han, "Stable large-area (10× 10 cm2) printable mesoscopic perovskite module exceeding 10% efficiency," *Solar Rrl*, vol. 1, no. 2, p. 1600019, 2017.

[210] D. Bogachuk, S. Zouhair, K. Wojciechowski, B. Yang, V. Babu, L. Wagner, B. Xu, J. Lim, S. Mastroianni, H. Pettersson, A. Hagfeldt, and A. Hinsch, "Low-temperature carbon-based electrodes in perovskite solar cells," *Energy Environ. Sci.*, vol. 13, pp. 3880–3916, 2020. [Online]. Available: http://dx.doi.org/10.1039/D0EE02175J

[211] N. L. Chang, A. W. Yi Ho-Baillie, P. A. Basore, T. L. Young, R. Evans, and R. J. Egan, "A manufacturing cost estimation method with uncertainty analysis and its application to perovskite on glass photovoltaic modules," *Progress in Photovoltaics: Research and Applications*, vol. 25, no. 5, pp. 390–405, 2017.

[212] N. L. Chang, A. W. Y. Ho-Baillie, D. Vak, M. Gao, M. A. Green, and R. J. Egan, "Manufacturing cost and market potential analysis of demonstrated roll-to-roll perovskite photovoltaic cell processes," *Solar Energy Materials and Solar Cells*, vol. 174, pp. 314–324, 2018.

[213] Z. Song, C. L. McElvany, A. B. Phillips, I. Celik, P. W. Krantz, S. C. Watthage, G. K. Liyanage, D. Apul, and M. J. Heben, "A technoeconomic analysis of perovskite solar module manufacturing with low-cost materials and techniques," *Energy & Environmental Science*, vol. 10, no. 6, pp. 1297–1305, 2017.

[214] M. Xu, W. Ji, Y. Sheng, Y. Wu, H. Cheng, J. Meng, Z. Yan, J. Xu, A. Mei, Y. Hu *et al.*, "Efficient triple-mesoscopic perovskite solar mini-modules fabricated with slot-die coating," *Nano Energy*, vol. 74, p. 104842, 2020.

[215] L. Cai, L. Liang, J. Wu, B. Ding, L. Gao, and B. Fan, "Large area perovskite solar cell module," *Journal of Semiconductors*, vol. 38, no. 1, p. 014006, 2017.

[216] L. Wagner, S. Mastroianni, and A. Hinsch, "Reverse manufacturing enables perovskite photovoltaics to reach the carbon footprint limit of a glass substrate," *Joule*, vol. 4, no. 4, pp. 882–901, 2020.

[217] J. Gong, S. B. Darling, and F. You, "Perovskite photovoltaics: life-cycle assessment of energy and environmental impacts," *Energy & Environmental Science*, vol. 8, no. 7, pp. 1953–1968, 2015.

[218] T. Ibn-Mohammed, S. Koh, I. Reaney, A. Acquaye, G. Schileo, K. Mustapha, and R. Greenough, "Perovskite solar cells: An integrated hybrid lifecycle assessment and review in comparison with other photovoltaic technologies," *Renewable and Sustainable Energy Reviews*, vol. 80, pp. 1321–1344, 2017.

[219] J.-A. Alberola-Borràs, J. A. Baker, F. De Rossi, R. Vidal, D. Beynon, K. E. Hooper, T. M. Watson, and I. Mora-Seró, "Perovskite photovoltaic modules: life cycle assessment of pre-industrial production process," *IScience*, vol. 9, pp. 542–551, 2018.

[220] M. A. Reuter, A. van Schaik, J. Gutzmer, N. Bartie, and A. Abadías-Llamas, "Challenges of the circular economy: a material, metallurgical, and product design perspective," *Annual Review of Materials Research*, vol. 49, pp. 253–274, 2019.

[221] L. Ciacci, E. Harper, N. Nassar, B. K. Reck, and T. Graedel, "Metal dissipation and inefficient recycling intensify climate forcing," *Environmental Science & Technology*, vol. 50, no. 20, pp. 11 394–11 402, 2016.

[222] S. S. Mali, H. Kim, J. V. Patil, and C. K. Hong, "Bio-inspired carbon hole transporting layer derived from aloe vera plant for cost-effective fully printable mesoscopic carbon perovskite solar cells," *ACS applied materials & interfaces*, vol. 10, no. 37, pp. 31 280–31 290, 2018.

[223] Z. Liu and H. He, "Counter electrode materials for organic-inorganic perovskite solar cells," in *Nanostructured Materials for Next-Generation Energy Storage and Conversion*. Springer, 2019, pp. 165–225.

[224] S. Sun, T. Buonassisi, and J.-P. Correa-Baena, "State-of-the-art electron-selective contacts in perovskite solar cells," *Advanced Materials Interfaces*, vol. 5, no. 22, p. 1800408, 2018.

[225] G. Mathiazhagan, L. Wagner, S. Bogati, K. Y. Unal, D. Bogachuk, T. Kroyer, S. Mastroianni, and A. Hinsch, "Double-mesoscopic hole-transport-material-free perovskite solar cells: overcoming charge-transport limitation by sputtered ultrathin al2o3 isolating layer," *ACS applied nano materials*, vol. 3, no. 3, pp. 2463–2471, 2020.

[226] S. Liu, W. Huang, P. Liao, N. Pootrakulchote, H. Li, J. Lu, J. Li, F. Huang, X. Shai, X. Zhao *et al.*, "17% efficient printable mesoscopic pin metal oxide framework perovskite solar cells using cesium-containing triple cation perovskite," *Journal of Materials Chemistry A*, vol. 5, no. 44, pp. 22 952–22 958, 2017.

[227] X. Xu, Z. Liu, Z. Zuo, M. Zhang, Z. Zhao, Y. Shen, H. Zhou, Q. Chen, Y. Yang, and M. Wang, "Hole selective nio contact for efficient perovskite

solar cells with carbon electrode," *Nano letters*, vol. 15, no. 4, pp. 2402–2408, 2015.

[228] S. He, L. Qiu, D.-Y. Son, Z. Liu, E. J. Juarez-Perez, L. K. Ono, C. Stecker, and Y. Qi, "Carbon-based electrode engineering boosts the efficiency of all low-temperature-processed perovskite solar cells," *ACS Energy Letters*, vol. 4, no. 9, pp. 2032–2039, 2019.

[229] J. Ren, J. Qu, J. Chen, Z. Li, Y. Cui, H. Wang, Z. Yu, and Y. Hao, "Fluorinated dopant-free hole-transporting material for efficient and stable perovskite solar cells with carbon cathode," *Journal of Power Sources*, vol. 401, pp. 29–36, 2018.

[230] F. Zhang, X. Yang, M. Cheng, J. Li, W. Wang, H. Wang, and L. Sun, "Engineering of hole-selective contact for low temperature-processed carbon counter electrode-based perovskite solar cells," *Journal of Materials Chemistry A*, vol. 3, no. 48, pp. 24 272–24 280, 2015.

[231] S. Wang, P. Jiang, W. Shen, A. Mei, S. Xiong, X. Jiang, Y. Rong, Y. Tang, Y. Hu, and H. Han, "A low-temperature carbon electrode with good perovskite compatibility and high flexibility in carbon based perovskite solar cells," *Chemical Communications*, vol. 55, no. 19, pp. 2765–2768, 2019.

[232] F. Zhang, X. Yang, M. Cheng, W. Wang, and L. Sun, "Boosting the efficiency and the stability of low cost perovskite solar cells by using cupc nanorods as hole transport material and carbon as counter electrode," *Nano Energy*, vol. 20, pp. 108–116, 2016.

[233] S. Mashhoun, Y. Hou, H. Chen, F. Tajabadi, N. Taghavinia, H.-J. Egelhaaf, and C. J. Brabec, "Resolving a critical instability in perovskite solar cells by designing a scalable and printable carbon based electrode-interface architecture," *Advanced Energy Materials*, vol. 8, no. 31, p. 1802085, 2018.

[234] X. Zheng, H. Chen, Z. Wei, Y. Yang, H. Lin, and S. Yang, "High-performance, stable and low-cost mesoscopic perovskite (ch3nh3pbi3) solar cells based on poly (3-hexylthiophene)-modified carbon nanotube cathodes," *Frontiers of Optoelectronics*, vol. 9, no. 1, pp. 71–80, 2016.

[235] A. T. Kleinschmidt, S. E. Root, and D. J. Lipomi, "Poly (3-hexylthiophene)(p3ht): fruit fly or outlier in organic solar cell research?" *Journal of Materials Chemistry A*, vol. 5, no. 23, pp. 11 396–11 400, 2017.

[236] Q.-Q. Chu, B. Ding, J. Peng, H. Shen, X. Li, Y. Liu, C.-X. Li, C.-J. Li, G.-J. Yang, T. P. White *et al.*, "Highly stable carbon-based perovskite solar cell with a record efficiency of over 18% via hole transport engineering," *Journal of Materials Science & Technology*, vol. 35, no. 6, pp. 987–993, 2019.

[237] K. Cao, Z. Zuo, J. Cui, Y. Shen, T. Moehl, S. M. Zakeeruddin, M. Grätzel, and M. Wang, "Efficient screen printed perovskite solar cells based on mesoscopic tio2/al2o3/nio/carbon architecture," *Nano Energy*, vol. 17, pp. 171–179, 2015.

[238] F. Behrouznejad, C.-M. Tsai, S. Narra, E. W.-G. Diau, and N. Taghavinia, "Interfacial investigation on printable carbon-based mesoscopic perovskite solar cells with nio x/c back electrode," *ACS applied materials & interfaces*, vol. 9, no. 30, pp. 25 204–25 215, 2017.

[239] T. N. Peiris, A. K. Baranwal, H. Kanda, S. Fukumoto, S. Kanaya, L. Cojocaru, T. Bessho, T. Miyasaka, H. Segawa, and S. Ito, "Enhancement of the hole conducting effect of nio by a n 2 blow drying method in printable perovskite solar cells with low-temperature carbon as the counter electrode," *Nanoscale*, vol. 9, no. 17, pp. 5475–5482, 2017.

[240] H. Chen, Z. Wei, H. He, X. Zheng, K. S. Wong, and S. Yang, "Solvent engineering boosts the efficiency of paintable carbon-based perovskite solar cells to beyond 14%," *Advanced Energy Materials*, vol. 6, no. 8, p. 1502087, 2016.

[241] H. Chen, X. Zheng, Q. Li, Y. Yang, S. Xiao, C. Hu, Y. Bai, T. Zhang, K. S. Wong, and S. Yang, "An amorphous precursor route to the conformable oriented crystallization of ch 3 nh 3 pbbr 3 in mesoporous scaffolds: toward efficient and thermally stable carbon-based perovskite solar cells," *Journal of Materials Chemistry A*, vol. 4, no. 33, pp. 12 897–12 912, 2016.

[242] S. Bai, N. Cheng, Z. Yu, P. Liu, C. Wang, and X.-Z. Zhao, "Cubic: column composite structure (nh2ch= nh2) x (ch3nh3) 1-xpbi3 for efficient hole-transport material-free and insulation layer free perovskite solar cells with high stability," *Electrochimica Acta*, vol. 190, pp. 775–779, 2016.

[243] X. Chang, W. Li, H. Chen, L. Zhu, H. Liu, H. Geng, S. Xiang, J. Liu, X. Zheng, Y. Yang *et al.*, "Colloidal precursor-induced growth of ultra-even ch3nh3pbi3 for high-performance paintable carbon-based perovskite solar cells," *ACS Applied Materials & Interfaces*, vol. 8, no. 44, pp. 30 184–30 192, 2016.

[244] C. Zhang, Y. Luo, X. Chen, Y. Chen, Z. Sun, and S. Huang, "Effective improvement of the photovoltaic performance of carbon-based perovskite solar cells by additional solvents," *Nano-micro letters*, vol. 8, no. 4, pp. 347–357, 2016.

[245] X. Zhou, Y. Wang, C. Li, and T. Wu, "Doping amino-functionalized ionic liquid in perovskite crystal for enhancing performances of hole-conductor free solar cells with carbon electrode," *Chemical Engineering Journal*, vol. 372, pp. 46–52, 2019.

[246] X. Liu, Z. Liu, B. Sun, X. Tan, H. Ye, Y. Tu, T. Shi, Z. Tang, and G. Liao, "17.46% efficient and highly stable carbon-based planar perovskite solar cells employing ni-doped rutile tio2 as electron transport layer," *Nano energy*, vol. 50, pp. 201–211, 2018.

[247] J. Liang, C. Wang, Y. Wang, Z. Xu, Z. Lu, Y. Ma, H. Zhu, Y. Hu, C. Xiao, X. Yi *et al.*, "All-inorganic perovskite solar cells," *Journal of the American Chemical Society*, vol. 138, no. 49, pp. 15 829–15 832, 2016.

[248] J. Liang, P. Zhao, C. Wang, Y. Wang, Y. Hu, G. Zhu, L. Ma, J. Liu, and Z. Jin, "Cspb0. 9sn0. 1ibr2 based all-inorganic perovskite solar cells with exceptional efficiency and stability," *Journal of the American Chemical Society*, vol. 139, no. 40, pp. 14 009–14 012, 2017.

[249] J. Liang, Z. Liu, L. Qiu, Z. Hawash, L. Meng, Z. Wu, Y. Jiang, L. K. Ono, and Y. Qi, "Enhancing optical, electronic, crystalline, and morphological properties of cesium lead halide by mn substitution for high-stability all-inorganic perovskite solar cells with carbon electrodes," *Advanced Energy Materials*, vol. 8, no. 20, p. 1800504, 2018.

[250] E. Calabro, F. Matteocci, B. Paci, L. Cina, L. Vesce, J. Barichello, A. Generosi, A. Reale, and A. Di Carlo, "Easy strategy to enhance thermal stability of planar pscs by perovskite defect passivation and low-temperature carbon-based electrode," *ACS Applied Materials & Interfaces*, vol. 12, no. 29, pp. 32 536–32 547, 2020.

[251] A. Clough, D. Peng, Z. Yang, and O. K. Tsui, "Glass transition temperature of polymer films that slip," *Macromolecules*, vol. 44, no. 6, pp. 1649–1653, 2011.

[252] V. Babu, R. Fuentes Pineda, T. Ahmad, A. O. Alvarez, L. A. Castriotta, A. Di Carlo, F. Fabregat-Santiago, and K. Wojciechowski, "Improved stability of inverted and flexible perovskite solar cells with carbon electrode," *ACS Applied Energy Materials*, vol. 3, no. 6, pp. 5126–5134, 2020.

[253] J. Troughton, D. Bryant, K. Wojciechowski, M. J. Carnie, H. Snaith, D. A. Worsley, and T. M. Watson, "Highly efficient, flexible, indium-free perovskite solar cells employing metallic substrates," *Journal of Materials Chemistry A*, vol. 3, no. 17, pp. 9141–9145, 2015.

[254] B. Zimmermann, M. Glatthaar, M. Niggemann, M. Riede, A. Hinsch, and A. Gombert, "Ito-free wrap through organic solar cells—a module concept for cost-efficient reel-to-reel production," *Solar Energy Materials and Solar Cells*, vol. 91, no. 5, pp. 374–378, 2007.

[255] J. Baker, K. Hooper, S. Meroni, A. Pockett, J. McGettrick, Z. Wei, R. Escalante, G. Oskam, M. Carnie, and T. Watson, "High throughput fabrication of mesoporous carbon perovskite solar cells," *Journal of Materials Chemistry A*, vol. 5, no. 35, pp. 18 643–18 650, 2017.

[256] B. Dou, J. B. Whitaker, K. Bruening, D. T. Moore, L. M. Wheeler, J. Ryter, N. J. Breslin, J. J. Berry, S. M. Garner, F. S. Barnes, S. E. Shaheen, C. J. Tassone, K. Zhu, and M. F. A. M. van Hest, "Roll-to-roll printing of perovskite solar cells," *ACS Energy Letters*, vol. 3, no. 10, pp. 2558–2565, 2018. [Online]. Available: https://doi.org/10.1021/acsenergylett.8b01556

[257] D. Bogachuk, L. Wagner, S. Mastroianni, M. Daub, H. Hillebrecht, and A. Hinsch, "The nature of the methylamine–mapbi3 complex: fundamentals of gas-induced perovskite liquefaction and crystallization,"

J. Mater. Chem. A, vol. 8, pp. 9788–9796, 2020. [Online]. Available: http://dx.doi.org/10.1039/D0TA02494E

[258] Y. Galagan, F. Di Giacomo, H. Gorter, G. Kirchner, I. de Vries, R. Andriessen, and P. Groen, "Roll-to-roll slot die coated perovskite for efficient flexible solar cells," *Advanced Energy Materials*, vol. 8, no. 32, p. 1801935, 2018.

[259] L. Wagner, S. Chacko, G. Mathiazhagan, S. Mastroianni, and A. Hinsch, "High photovoltage of 1 v on a steady-state certified hole transport layer-free perovskite solar cell by a molten-salt approach," *ACS Energy Letters*, vol. 3, no. 5, pp. 1122–1127, 2018. [Online]. Available: https://doi.org/10.1021/acsenergylett.8b00293

[260] Q.-Q. Chu, B. Ding, Q. Qiu, Y. Liu, C.-X. Li, C.-J. Li, G.-J. Yang, and B. Fang, "Cost effective perovskite solar cells with a high efficiency and open-circuit voltage based on a perovskite-friendly carbon electrode," *Journal of Materials Chemistry A*, vol. 6, no. 18, pp. 8271–8279, 2018.

[261] Z. Wei, K. Yan, H. Chen, Y. Yi, T. Zhang, X. Long, J. Li, L. Zhang, J. Wang, and S. Yang, "Cost-efficient clamping solar cells using candle soot for hole extraction from ambipolar perovskites," *Energy & Environmental Science*, vol. 7, no. 10, pp. 3326–3333, 2014.

[262] R. Dileep, G. Kesavan, V. Reddy, M. K. Rajbhar, S. Shanmugasundaram, E. Ramasamy, and G. Veerappan, "Room-temperature curable carbon cathode for hole-conductor free perovskite solar cells," *Solar Energy*, vol. 187, pp. 261–268, 2019.

[263] H. Wei, J. Xiao, Y. Yang, S. Lv, J. Shi, X. Xu, J. Dong, Y. Luo, D. Li, and Q. Meng, "Free-standing flexible carbon electrode for highly efficient hole-conductor-free perovskite solar cells," *Carbon*, vol. 93, pp. 861–868, 2015.

[264] Y. Yang, J. Xiao, H. Wei, L. Zhu, D. Li, Y. Luo, H. Wu, and Q. Meng, "An all-carbon counter electrode for highly efficient hole-conductor-free organo-metal perovskite solar cells," *Rsc Advances*, vol. 4, no. 95, pp. 52 825–52 830, 2014.

[265] Z. Liu, T. Shi, Z. Tang, B. Sun, and G. Liao, "Using a low-temperature carbon electrode for preparing hole-conductor-free perovskite heterojunction solar cells under high relative humidity," *Nanoscale*, vol. 8, no. 13, pp. 7017–7023, 2016.

[266] P. Jiang, T. W. Jones, N. W. Duffy, K. F. Anderson, R. Bennett, M. Grigore, P. Marvig, Y. Xiong, T. Liu, Y. Sheng *et al.*, "Fully printable perovskite solar cells with highly-conductive, low-temperature, perovskite-compatible carbon electrode," *Carbon*, vol. 129, pp. 830–836, 2018.

[267] Q.-Q. Chu, B. Ding, Y. Li, L.-L. Gao, Q. Qiu, C.-X. Li, C.-J. Li, G.-J. Yang, and B. Fang, "Fast drying boosted performance improvement of low-temperature paintable carbon-based perovskite solar cell," *ACS Sustainable Chemistry & Engineering*, vol. 5, no. 11, pp. 9758–9765, 2017.

[268] H. Su, J. Xiao, Q. Li, C. Peng, X. Zhang, C. Mao, Q. Yao, Y. Lu, Z. Ku, J. Zhong *et al.*, "Carbon film electrode based square-centimeter scale planar perovskite solar cells exceeding 17% efficiency," *Materials Science in Semiconductor Processing*, vol. 107, p. 104809, 2020.

[269] Y. Yang, M. T. Hoang, D. Yao, N. D. Pham, V. T. Tiong, X. Wang, W. Sun, and H. Wang, "High performance carbon-based planar perovskite solar cells by hot-pressing approach," *Solar Energy Materials and Solar Cells*, vol. 210, p. 110517, 2020.

[270] F. Meng, L. Gao, Y. Yan, J. Cao, N. Wang, T. Wang, and T. Ma, "Ultra-low-cost coal-based carbon electrodes with seamless interfacial contact for effective sandwich-structured perovskite solar cells," *Carbon*, vol. 145, pp. 290–296, 2019.

[271] Z. Wei, H. Chen, K. Yan, and S. Yang, "Inkjet printing and instant chemical transformation of a ch3nh3pbi3/nanocarbon electrode and interface for planar perovskite solar cells," *Angewandte Chemie International Edition*, vol. 53, no. 48, pp. 13 239–13 243, 2014.

[272] C. Zhang, S. Wang, H. Zhang, Y. Feng, W. Tian, Y. Yan, J. Bian, Y. Wang, S. Jin, S. M. Zakeeruddin *et al.*, "Efficient stable graphene-based perovskite solar cells with high flexibility in device assembling via modular architecture design," *Energy & Environmental Science*, vol. 12, no. 12, pp. 3585–3594, 2019.

[273] Y. Wang, H. Zhao, Y. Mei, H. Liu, S. Wang, and X. Li, "Carbon nanotube bridging method for hole transport layer-free paintable carbon-based perovskite solar cells," *ACS applied materials & interfaces*, vol. 11, no. 1, pp. 916–923, 2018.

[274] M. Duan, C. Tian, Y. Hu, A. Mei, Y. Rong, Y. Xiong, M. Xu, Y. Sheng, P. Jiang, X. Hou *et al.*, "Boron-doped graphite for high work function carbon electrode in printable hole-conductor-free mesoscopic perovskite solar cells," *ACS applied materials & interfaces*, vol. 9, no. 37, pp. 31 721–31 727, 2017.

[275] B. Partoens and F. Peeters, "From graphene to graphite: Electronic structure around the k point," *Physical Review B*, vol. 74, no. 7, p. 075404, 2006.

[276] D. Chung, "Review graphite," *Journal of materials science*, vol. 37, no. 8, pp. 1475–1489, 2002.

[277] V. Ferguson, S. R. P. Silva, and W. Zhang, "Carbon materials in perovskite solar cells: Prospects and future challenges," *Energy & Environmental Materials*, vol. 2, no. 2, pp. 107–118, 2019.

[278] M. Chen, R.-H. Zha, Z.-Y. Yuan, Q.-S. Jing, Z.-Y. Huang, X.-K. Yang, S.-M. Yang, X.-H. Zhao, D.-L. Xu, and G.-D. Zou, "Boron and phosphorus co-doped carbon counter electrode for efficient hole-conductor-free perovskite solar cell," *Chemical Engineering Journal*, vol. 313, pp. 791–800, 2017.

[279] K. Liu, P. Avouris, R. Martel, and W. Hsu, "Electrical transport in doped multiwalled carbon nanotubes," *Physical review B*, vol. 63, no. 16, p. 161404, 2001.

[280] X. Zheng, H. Chen, Q. Li, Y. Yang, Z. Wei, Y. Bai, Y. Qiu, D. Zhou, K. S. Wong, and S. Yang, "Boron doping of multiwalled carbon nanotubes significantly enhances hole extraction in carbon-based perovskite solar cells," *Nano letters*, vol. 17, no. 4, pp. 2496–2505, 2017.

[281] J.-W. Lee, I. Jeon, H.-S. Lin, S. Seo, T.-H. Han, A. Anisimov, E. I. Kauppinen, Y. Matsuo, S. Maruyama, and Y. Yang, "Vapor-assisted ex-situ doping of carbon nanotube toward efficient and stable perovskite solar cells," *Nano letters*, vol. 19, no. 4, pp. 2223–2230, 2018.

[282] M. Pimenta, G. Dresselhaus, M. S. Dresselhaus, L. Cancado, A. Jorio, and R. Saito, "Studying disorder in graphite-based systems by raman spectroscopy," *Physical chemistry chemical physics*, vol. 9, no. 11, pp. 1276–1290, 2007.

[283] H. O. Pierson, *Handbook of carbon, graphite, diamonds and fullerenes: processing, properties and applications*. William Andrew, 2012.

[284] L. Zhang, T. Liu, L. Liu, M. Hu, Y. Yang, A. Mei, and H. Han, "The effect of carbon counter electrodes on fully printable mesoscopic perovskite solar cells," *Journal of Materials Chemistry A*, vol. 3, no. 17, pp. 9165–9170, 2015.

[285] T. W. Jones, N. W. Duffy, and G. J. Wilson, "Efficient all-printable solid-state dye-sensitized solar cell based on a low-resistivity carbon composite counter electrode and highly doped hole transport material," *The Journal of Physical Chemistry C*, vol. 119, no. 21, pp. 11 410–11 418, 2015.

[286] C. Phillips, A. Al-Ahmadi, S.-J. Potts, T. Claypole, and D. Deganello, "The effect of graphite and carbon black ratios on conductive ink performance," *Journal of materials science*, vol. 52, no. 16, pp. 9520–9530, 2017.

[287] M. Polovina, B. Babić, B. Kaluderović, and A. Dekanski, "Surface characterization of oxidized activated carbon cloth," *Carbon*, vol. 35, no. 8, pp. 1047–1052, 1997.

[288] G. Song, J. Ryu, S. Ko, B. M. Bang, S. Choi, M. Shin, S.-Y. Lee, and S. Park, "Revisiting surface modification of graphite: Dual-layer coating for high-performance lithium battery anode materials," *Chemistry–An Asian Journal*, vol. 11, no. 11, pp. 1711–1717, 2016.

[289] T. Amaraweera, N. Balasooriya, H. Wijayasinghe, A. Attanayake, B.-E. Mellander, and M. Dissanayake, "Surface modification of natural vein graphite for the anode application in li-ion rechargeable batteries," *Ionics*, vol. 24, no. 11, pp. 3423–3429, 2018.

[290] Y. Zhou, X. Yin, Q. Luo, X. Zhao, D. Zhou, J. Han, F. Hao, M. Tai, J. Li, P. Liu *et al.*, "Efficiently improving the stability of inverted perovskite so-

lar cells by employing polyethylenimine-modified carbon nanotubes as electrodes," *ACS applied materials & interfaces*, vol. 10, no. 37, pp. 31 384–31 393, 2018.

[291] V. D. Punetha, S. Rana, H. J. Yoo, A. Chaurasia, J. T. McLeskey Jr, M. S. Ramasamy, N. G. Sahoo, and J. W. Cho, "Functionalization of carbon nanomaterials for advanced polymer nanocomposites: A comparison study between cnt and graphene," *Progress in Polymer Science*, vol. 67, pp. 1–47, 2017.

[292] T. Minemoto and M. Murata, "Impact of work function of back contact of perovskite solar cells without hole transport material analyzed by device simulation," *Current Applied Physics*, vol. 14, no. 11, pp. 1428–1433, 2014.

[293] Y. Huang, S. Aharon, A. Rolland, L. Pedesseau, O. Durand, L. Etgar, and J. Even, "Influence of schottky contact on the cv and jv characteristics of htm-free perovskite solar cells," *EPJ Photovoltaics*, vol. 8, p. 85501, 2017.

[294] K. M. Kim, S. Ahn, W. Jang, S. Park, O. O. Park, and D. H. Wang, "Work function optimization of vacuum free top-electrode by pedot: Pss/pei interaction for efficient semi-transparent perovskite solar cells," *Solar Energy Materials and Solar Cells*, vol. 176, pp. 435–440, 2018.

[295] J. Kim, G. Lee, K. Lee, H. Yu, J. W. Lee, C.-M. Yoon, S. G. Kim, S. K. Kim, and J. Jang, "Fluorine plasma treatment on carbon-based perovskite solar cells for rapid moisture protection layer formation and performance enhancement," *Chemical Communications*, vol. 56, no. 4, pp. 535–538, 2020.

[296] C. Tian, A. Mei, S. Zhang, H. Tian, S. Liu, F. Qin, Y. Xiong, Y. Rong, Y. Hu, Y. Zhou *et al.*, "Oxygen management in carbon electrode for high-performance printable perovskite solar cells," *Nano Energy*, vol. 53, pp. 160–167, 2018.

[297] S.-S. Li, K.-H. Tu, C.-C. Lin, C.-W. Chen, and M. Chhowalla, "Solution-processable graphene oxide as an efficient hole transport layer in polymer solar cells," *ACS nano*, vol. 4, no. 6, pp. 3169–3174, 2010.

[298] H. Li, K. Cao, J. Cui, S. Liu, X. Qiao, Y. Shen, and M. Wang, "14.7% efficient mesoscopic perovskite solar cells using single walled carbon nanotubes/carbon composite counter electrodes," *Nanoscale*, vol. 8, no. 12, pp. 6379–6385, 2016.

[299] R. Hu, R. Zhang, Y. Ma, W. Liu, L. Chu, W. Mao, J. Zhang, J. Yang, Y. Pu, and X. Li, "Enhanced hole transfer in hole-conductor-free perovskite solar cells via incorporating cus into carbon electrodes," *Applied Surface Science*, vol. 462, pp. 840–846, 2018.

[300] L. Zhou, Y. Zuo, T. K. Mallick, and S. Sundaram, "Enhanced efficiency of carbon-based mesoscopic perovskite solar cells through a tungsten oxide nanoparticle additive in the carbon electrode," *Scientific reports*, vol. 9, no. 1, pp. 1–8, 2019.

[301] P. Jiang, Y. Xiong, M. Xu, A. Mei, Y. Sheng, L. Hong, T. W. Jones, G. J. Wilson, S. Xiong, D. Li *et al.*, "The influence of the work function of hybrid

carbon electrodes on printable mesoscopic perovskite solar cells," *The Journal of Physical Chemistry C*, vol. 122, no. 29, pp. 16 481–16 487, 2018.

[302] J. Liu, Q. Zhou, N. K. Thein, L. Tian, D. Jia, E. M. Johansson, and X. Zhang, "In situ growth of perovskite stacking layers for high-efficiency carbon-based hole conductor free perovskite solar cells," *Journal of Materials Chemistry A*, vol. 7, no. 22, pp. 13 777–13 786, 2019.

[303] H. Tao, Y. Li, C. Zhang, K. Wang, B. Tan, J. Wang, and J. Tao, "Efficiency enhancement of perovskite solar cells by forming a tighter interface contact of c/ch3nh3pbi3," *Journal of Physics and Chemistry of Solids*, vol. 123, pp. 25–31, 2018.

[304] I. Jeon, R. Xiang, A. Shawky, Y. Matsuo, and S. Maruyama, "Single-walled carbon nanotubes in emerging solar cells: synthesis and electrode applications," *Advanced Energy Materials*, vol. 9, no. 23, p. 1801312, 2019.

[305] J. Ryu, K. Lee, J. Yun, H. Yu, J. Lee, and J. Jang, "Paintable carbon-based perovskite solar cells with engineered perovskite/carbon interface using carbon nanotubes dripping method," *Small*, vol. 13, no. 38, p. 1701225, 2017.

[306] X. Hou, Y. Hu, H. Liu, A. Mei, X. Li, M. Duan, G. Zhang, Y. Rong, and H. Han, "Effect of guanidinium on mesoscopic perovskite solar cells," *Journal of Materials Chemistry A*, vol. 5, no. 1, pp. 73–78, 2017.

[307] Y. Rong, X. Hou, Y. Hu, A. Mei, L. Liu, P. Wang, and H. Han, "Synergy of ammonium chloride and moisture on perovskite crystallization for efficient printable mesoscopic solar cells," *Nature communications*, vol. 8, no. 1, pp. 1–8, 2017.

[308] T. Liu, Z. Wang, L. Lou, S. Xiao, S. Zheng, and S. Yang, "Interfacial post-treatment for enhancing the performance of printable carbon-based perovskite solar cells," *Solar RRL*, vol. 4, no. 2, p. 1900278, 2020.

[309] G. Huang, C. Wang, H. Zhang, S. Xu, Q. Xu, and Y. Cui, "Post-healing of defects: an alternative way for passivation of carbon-based mesoscopic perovskite solar cells via hydrophobic ligand coordination," *Journal of Materials Chemistry A*, vol. 6, no. 6, pp. 2449–2455, 2018.

[310] W. Kim, J. B. Park, H. Kim, K. Kim, J. Park, S. Cho, H. Lee, Y. Pak, and G. Y. Jung, "Enhanced long-term stability of perovskite solar cells by passivating grain boundary with polydimethylsiloxane (pdms)," *Journal of Materials Chemistry A*, vol. 7, no. 36, pp. 20 832–20 839, 2019.

[311] Q. Luo, H. Ma, F. Hao, Q. Hou, J. Ren, L. Wu, Z. Yao, Y. Zhou, N. Wang, K. Jiang *et al.*, "Carbon nanotube based inverted flexible perovskite solar cells with all-inorganic charge contacts," *Advanced Functional Materials*, vol. 27, no. 42, p. 1703068, 2017.

[312] S. Zouhair, S.-M. Yoo, D. Bogachuk, J. P. Herterich, J. Lim, H. Kanda, B. Son, H. J. Yun, U. Würfel, A. Chahboun *et al.*, "Employing 2d-perovskite as an elec-

tron blocking layer in highly efficient (18.5%) perovskite solar cells with printable low temperature carbon electrode," *Advanced Energy Materials*, vol. 12, no. 21, p. 2200837, 2022.

[313] H. Zhang, Y. Li, S. Tan, Z. Chen, K. Song, S. Huang, J. Shi, Y. Luo, D. Li, and Q. Meng, "High-efficiency (> 20%) planar carbon-based perovskite solar cells through device configuration engineering," *Journal of Colloid and Interface Science*, vol. 608, pp. 3151–3158, 2022.

[314] K. Ramachandran, C. Jeganathan, and S. Karuppuchamy, "Electrodeposition of nanostructured bilayer cui@ cuscn as hole transport material for highly efficient inverted perovskite solar cells," *Journal of Alloys and Compounds*, vol. 881, p. 160530, 2021.

[315] Z. Zhou, Z. Wang, Y. Zhou, S. Pang, D. Wang, H. Xu, Z. Liu, N. P. Padture, and G. Cui, "Methylamine-gas-induced defect-healing behavior of ch3nh3pbi3 thin films for perovskite solar cells," *Angewandte Chemie International Edition*, vol. 54, no. 33, pp. 9705–9709. [Online]. Available: https://onlinelibrary.wiley.com/doi/abs/10.1002/anie.201504379

[316] L. H. L. S. Y. S.-E. Jiang Yaxiao, Tu Limin and C. Yongsheng, "A feasible and effective post-treatment method for high-quality ch3nh3pbi3 films and high-efficiency perovskite solar cells," *Crystals*, vol. 8, no. 1, 2018. [Online]. Available: http://www.mdpi.com/2073-4352/8/1/44

[317] T. Zhao, S. T. Williams, C.-C. Chueh, D. W. deQuilettes, P.-W. Liang, D. S. Ginger, and A. K.-Y. Jen, "Design rules for the broad application of fast (<1 s) methylamine vapor based, hybrid perovskite post deposition treatments," *RSC Adv.*, vol. 6, pp. 27 475–27 484, 2016. [Online]. Available: http://dx.doi.org/10.1039/C6RA03485C

[318] L. Hong, Y. Hu, A. Mei, Y. Sheng, P. Jiang, C. Tian, Y. Rong, and H. Han, "Improvement and regeneration of perovskite solar cells via methylamine gas post-treatment," *Advanced Functional Materials*, vol. 27, no. 43, p. 1703060, 2017.

[319] Y. Jiang, E. J. Juarez-Perez, Q. Ge, S. Wang, M. R. Leyden, L. K. Ono, S. R. Raga, J. Hu, and Y. Qi, "Post-annealing of mapbi 3 perovskite films with methylamine for efficient perovskite solar cells," *Materials Horizons*, vol. 3, no. 6, pp. 548–555, 2016.

[320] C. Li, S. Pang, H. Xu, and G. Cui, "Methylamine gas based synthesis and healing process toward upscaling of perovskite solar cells: Progress and perspective," *Solar RRL*, vol. 1, no. 9, p. 1700076. [Online]. Available: https://onlinelibrary.wiley.com/doi/abs/10.1002/solr.201700076

[321] M. Long, T. Zhang, H. Zhu, G. Li, F. Wang, W. Guo, Y. Chai, W. Chen, Q. Li, K. S. Wong, J. Xu, and K. Yan, "Textured ch3nh3pbi3 thin film with enhanced stability for high performance perovskite solar

cells," *Nano Energy*, vol. 33, pp. 485 – 496, 2017. [Online]. Available: http://www.sciencedirect.com/science/article/pii/S221128551730071X

[322] A. J. Ramadan, N. K. Noel, S. Fearn, N. Young, M. Walker, L. A. Rochford, and H. J. Snaith, "Unravelling the improved electronic and structural properties of methylammonium lead iodide deposited from acetonitrile," *Chemistry of Materials*, vol. 30, no. 21, pp. 7737–7743, 2018.

[323] B. Conings, S. A. Bretschneider, A. Babayigit, N. Gauquelin, I. Cardinaletti, J. Manca, J. Verbeeck, H. J. Snaith, and H.-G. Boyen, "Structure–property relations of methylamine vapor treated hybrid perovskite ch3nh3pbi3 films and solar cells," *ACS Applied Materials & Interfaces*, vol. 9, no. 9, pp. 8092–8099, 2017.

[324] J.-a. Yang, T. Qin, L. Xie, K. Liao, T. Li, and F. Hao, "Methylamine-induced defect-healing and cationic substitution: a new method for low-defect perovskite thin films and solar cells," *Journal of Materials Chemistry C*, vol. 7, no. 35, pp. 10 724–10 742, 2019.

[325] Y. Zhang, Z. Zhou, F. Ji, Z. Li, G. Cui, P. Gao, E. Oveisi, M. K. Nazeeruddin, and S. Pang, "Trash into treasure: δ-fapbi3 polymorph stabilized mapbi3 perovskite with power conversion efficiency beyond 21%," *Advanced Materials*, vol. 30, no. 22, p. 1707143, 2018.

[326] Y. Zhang, G. Grancini, Z. Fei, E. Shirzadi, X. Liu, E. Oveisi, F. F. Tirani, R. Scopelliti, Y. Feng, M. K. Nazeeruddin *et al.*, "Auto-passivation of crystal defects in hybrid imidazolium/methylammonium lead iodide films by fumigation with methylamine affords high efficiency perovskite solar cells," *Nano Energy*, vol. 58, pp. 105–111, 2019.

[327] N. K. Noel, S. N. Habisreutinger, B. Wenger, M. T. Klug, M. T. Hörantner, M. B. Johnston, R. J. Nicholas, D. T. Moore, and H. J. Snaith, "A low viscosity, low boiling point, clean solvent system for the rapid crystallisation of highly specular perovskite films," *Energy Environ. Sci.*, vol. 10, pp. 145–152, 2017. [Online]. Available: http://dx.doi.org/10.1039/C6EE02373H

[328] M. Wong-Stringer, T. J. Routledge, T. McArdle, C. J. Wood, O. S. Game, J. A. Smith, J. E. Bishop, N. Vaenas, D. M. Coles, A. R. Buckley *et al.*, "A flexible back-contact perovskite solar micro-module," *Energy & Environmental Science*, vol. 12, no. 6, pp. 1928–1937, 2019.

[329] Q. Liu, Y. Zhao, Y. Ma, X. Sun, W. Ge, Z. Fang, H. Bai, Q. Tian, B. Fan, and T. Zhang, "A mixed solvent for rapid fabrication of large-area methylammonium lead iodide layers by one-step coating at room temperature," *J. Mater. Chem. A*, vol. 7, pp. 18 275–18 284, 2019. [Online]. Available: http://dx.doi.org/10.1039/C9TA06084G

[330] D. Burkitt, R. Swartwout, J. McGettrick, P. Greenwood, D. Beynon, R. Brenes, V. Bulović, and T. Watson, "Acetonitrile based single step slot-die

compatible perovskite ink for flexible photovoltaics," *RSC Advances*, vol. 9, no. 64, pp. 37 415–37 423, 2019.

[331] R. Warren and W. Liang, "Raman spectroscopy of new lead iodide intercalation compounds," *Journal of Physics: Condensed Matter*, vol. 5, no. 35, p. 6407, 1993.

[332] R. A. Kerner, T. H. Schloemer, P. Schulz, J. J. Berry, J. Schwartz, A. Sellinger, and B. P. Rand, "Amine additive reactions induced by the soft lewis acidity of pb 2+ in halide perovskites. part i: evidence for pb–alkylamide formation," *Journal of Materials Chemistry C*, vol. 7, no. 18, pp. 5251–5259, 2019.

[333] C. Wu, H. Li, Y. Yan, B. Chi, J. Pu, J. Li, M. Sanghadasa, and S. Priya, "Cost-effective sustainable-engineering of ch3nh3pbi3 perovskite solar cells through slicing and restacking of 2d layers," *Nano Energy*, vol. 36, pp. 295–302, 2017.

[334] S. R. Raga, Y. Jiang, L. K. Ono, and Y. Qi, "Application of methylamine gas in fabricating organic–inorganic hybrid perovskite solar cells," *Energy Technology*, vol. 5, no. 10, pp. 1750–1761, 2017.

[335] R. Eßmann, G. Kreiner, A. Niemann, D. Rechenbach, A. Schmieding, T. Sichla, U. Zachwieja, and H. Jacobs, "Isotype strukturen einiger hexaamminmetall (ii)-halogenide von 3d-metallen:[v (nh3) 6] i2,[cr (nh3) 6] i2,[mn (nh3) 6] cl2,[fe (nh3) 6] cl2,[fe (nh3) 6] br2,[co (nh3) 6] br2 und [ni (nh3) 6] cl2," *Zeitschrift für anorganische und allgemeine Chemie*, vol. 622, no. 7, pp. 1161–1166, 1996.

[336] R. Nasanen, "An x-ray crystallographic study of lead hydroxide iodide," *SUOMEN KEMISTILEHTI*, vol. 39, no. 4, p. 105, 1966.

[337] O. I. Siidra, D. Y. Zenko, A. N. Suknotova, and S. V. Krivovichev, "Crystal structure of a novel synthetic compound, pb2o(oh)i, and structure refinement of 'iodolaurionite', pb(oh)i: hydroxo- and oxocentred units in pb minerals and synthetic compounds," *Mineralogical Magazine*, vol. 77, no. 8, p. 3239–3248, 2013.

[338] S. M. Jain, B. Philippe, E. M. Johansson, B.-w. Park, H. Rensmo, T. Edvinsson, and G. Boschloo, "Vapor phase conversion of pbi 2 to ch 3 nh 3 pbi 3: spectroscopic evidence for formation of an intermediate phase," *Journal of Materials Chemistry A*, vol. 4, no. 7, pp. 2630–2642, 2016.

[339] C. Quarti, G. Grancini, E. Mosconi, P. Bruno, J. M. Ball, M. M. Lee, H. J. Snaith, A. Petrozza, and F. De Angelis, "The raman spectrum of the ch3nh3pbi3 hybrid perovskite: interplay of theory and experiment," *The journal of physical chemistry letters*, vol. 5, no. 2, pp. 279–284, 2013.

[340] D.-N. Jeong, D.-K. Lee, S. Seo, S. Y. Lim, Y. Zhang, H. Shin, H. Cheong, and N.-G. Park, "Perovskite cluster-containing solution for scalable d-bar coating toward high-throughput perovskite solar cells," *ACS Energy Letters*, vol. 4, no. 5, pp. 1189–1195, 2019.

[341] M. Park, N. Kornienko, S. E. Reyes-Lillo, M. Lai, J. B. Neaton, P. Yang, and R. A. Mathies, "Critical role of methylammonium librational motion in methylammonium lead iodide (ch3nh3pbi3) perovskite photochemistry," *Nano letters*, vol. 17, no. 7, pp. 4151–4157, 2017.

[342] T. Glaser, C. Muller, M. Sendner, C. Krekeler, O. E. Semonin, T. D. Hull, O. Yaffe, J. S. Owen, W. Kowalsky, A. Pucci *et al.*, "Infrared spectroscopic study of vibrational modes in methylammonium lead halide perovskites," *The journal of physical chemistry letters*, vol. 6, no. 15, pp. 2913–2918, 2015.

[343] X. Huang, R. Chen, G. Deng, F. Han, P. Ruan, F. Cheng, J. Yin, B. Wu, and N. Zheng, "Methylamine-dimer-induced phase transition toward mapbi3 films and high-efficiency perovskite solar modules," *Journal of the American Chemical Society*, vol. 142, no. 13, pp. 6149–6157, 2020, pMID: 32159948. [Online]. Available: https://doi.org/10.1021/jacs.9b13443

[344] L. Wagner, L. E. Mundt, G. Mathiazhagan, M. Mundus, M. C. Schubert, S. Mastroianni, U. Würfel, A. Hinsch, and S. W. Glunz, "Distinguishing crystallization stages and their influence on quantum efficiency during perovskite solar cell formation in real-time," *Scientific reports*, vol. 7, no. 1, pp. 1–6, 2017.

[345] S. Bonabi Naghadeh, B. Luo, G. Abdelmageed, Y.-C. Pu, C. Zhang, and J. Z. Zhang, "Photophysical properties and improved stability of organic–inorganic perovskite by surface passivation," *The Journal of Physical Chemistry C*, vol. 122, no. 28, pp. 15 799–15 818, 2018.

[346] Y.-F. Li, J. Feng, and H.-B. Sun, "Perovskite quantum dots for light-emitting devices," *Nanoscale*, vol. 11, no. 41, pp. 19 119–19 139, 2019.

[347] X. Li, Y. Wu, S. Zhang, B. Cai, Y. Gu, J. Song, and H. Zeng, "Cspbx3 quantum dots for lighting and displays: room-temperature synthesis, photoluminescence superiorities, underlying origins and white light-emitting diodes," *Advanced Functional Materials*, vol. 26, no. 15, pp. 2435–2445, 2016.

[348] L. Wang, C. McCleese, A. Kovalsky, Y. Zhao, and C. Burda, "Femtosecond time-resolved transient absorption spectroscopy of ch3nh3pbi3 perovskite films: evidence for passivation effect of pbi2," *Journal of the American Chemical Society*, vol. 136, no. 35, pp. 12 205–12 208, 2014.

[349] M. Anaya, J. F. Galisteo-Lopez, M. E. Calvo, C. Lopez, and H. Míguez, "Photophysical analysis of the formation of organic–inorganic trihalide perovskite films: Identification and characterization of crystal nucleation and growth," *The Journal of Physical Chemistry C*, vol. 120, no. 5, pp. 3071–3076, 2016.

[350] V. D'Innocenzo, A. R. Srimath Kandada, M. De Bastiani, M. Gandini, and A. Petrozza, "Tuning the light emission properties by band gap engineering in hybrid lead halide perovskite," *Journal of the American Chemical Society*, vol. 136, no. 51, pp. 17 730–17 733, 2014.

[351] S. I. Seok, M. Grätzel, and N.-G. Park, "Methodologies toward highly

efficient perovskite solar cells," *Small*, vol. 14, no. 20, p. 1704177. [Online]. Available: https://onlinelibrary.wiley.com/doi/abs/10.1002/smll.201704177

[352] J.-H. Im, I.-H. Jang, N. Pellet, M. Grätzel, and N.-G. Park, "Growth of ch3nh3pbi3 cuboids with controlled size for high-efficiency perovskite solar cells," *Nature nanotechnology*, vol. 9, no. 11, pp. 927–932, 2014.

[353] S. Mastroianni, F. D. Heinz, J.-H. Im, W. Veurman, M. Padilla, M. C. Schubert, U. Würfel, M. Grätzel, N.-G. Park, and A. Hinsch, "Analysing the effect of crystal size and structure in highly efficient ch3nh3pbi3 perovskite solar cells by spatially resolved photo- and electroluminescence imaging," *Nanoscale*, vol. 7, pp. 19 653–19 662, 2015. [Online]. Available: http://dx.doi.org/10.1039/C5NR05308K

[354] D. L. Jacobs and L. Zang, "Thermally induced recrystallization of mapbi3 perovskite under methylamine atmosphere: an approach to fabricating large uniform crystalline grains," *Chem. Commun.*, vol. 52, pp. 10 743–10 746, 2016. [Online]. Available: http://dx.doi.org/10.1039/C6CC04521A

[355] A. Ummadisingu and M. Grätzel, "Revealing the detailed path of sequential deposition for metal halide perovskite formation," *Science advances*, vol. 4, no. 2, p. e1701402, 2018.

[356] J. Burschka, N. Pellet, S.-J. Moon, R. Humphry-Baker, P. Gao, M. K. Nazeeruddin, and M. Grätzel, "Sequential deposition as a route to high-performance perovskite-sensitized solar cells," *Nature*, vol. 499, no. 7458, pp. 316–319, 2013.

[357] Z. Song, S. C. Watthage, A. B. Phillips, B. L. Tompkins, R. J. Ellingson, and M. J. Heben, "Impact of processing temperature and composition on the formation of methylammonium lead iodide perovskites," *Chemistry of Materials*, vol. 27, no. 13, pp. 4612–4619, 2015.

[358] Z. Liu, J. Hu, H. Jiao, L. Li, G. Zheng, Y. Chen, Y. Huang, Q. Zhang, C. Shen, Q. Chen *et al.*, "Chemical reduction of intrinsic defects in thicker heterojunction planar perovskite solar cells," *Advanced Materials*, vol. 29, no. 23, p. 1606774, 2017.

[359] S. D. Stranks, G. E. Eperon, G. Grancini, C. Menelaou, M. J. Alcocer, T. Leijtens, L. M. Herz, A. Petrozza, and H. J. Snaith, "Electron-hole diffusion lengths exceeding 1 micrometer in an organometal trihalide perovskite absorber," *Science*, vol. 342, no. 6156, pp. 341–344, 2013.

[360] A. D. Wright, R. L. Milot, G. E. Eperon, H. J. Snaith, M. B. Johnston, and L. M. Herz, "Band-tail recombination in hybrid lead iodide perovskite," *Advanced Functional Materials*, vol. 27, no. 29, p. 1700860, 2017.

[361] Y. Yamada, T. Nakamura, M. Endo, A. Wakamiya, and Y. Kanemitsu, "Photocarrier recombination dynamics in perovskite ch3nh3pbi3 for solar cell applications," *Journal of the American Chemical Society*, vol. 136, no. 33, pp. 11 610–11 613, 2014.

[362] H. Fan, F. Li, P. Wang, Z. Gu, J.-H. Huang, K.-J. Jiang, B. Guan, L.-M. Yang, X. Zhou, and Y. Song, "Methylamine-assisted growth of uniaxial-oriented perovskite thin films with millimeter-sized grains," *Nature communications*, vol. 11, no. 1, pp. 1–10, 2020.

[363] S. Pang, Z. Li, X. Wang, Z. Wang, Z. Shao, L. Hao, X. Du, Y. Rao, C. Chen, D. Liu *et al.*, "Non-aliphatic protic ammonia for post healing of formamidinium-containing perovskite films," 2021.

[364] Z. Shao, Z. Wang, Z. Li, Y. Fan, H. Meng, R. Liu, Y. Wang, A. Hagfeldt, G. Cui, and S. Pang, "A scalable methylamine gas healing strategy for high-efficiency inorganic perovskite solar cells," *Angewandte Chemie International Edition*, vol. 58, no. 17, pp. 5587–5591, 2019.

[365] L. Tian, F. Wen, W. Zhang, H. Zhang, H. Yu, P. Lin, X. Liu, S. Zhou, X. Zhou, Y. Jiang *et al.*, "Rising from the ashes: Gaseous therapy for robust and large-area perovskite solar cells," *ACS Applied Materials & Interfaces*, vol. 12, no. 44, pp. 49 648–49 658, 2020.

[366] R. Swartwout, R. Patidar, E. Belliveau, B. Dou, D. Beynon, P. Greenwood, N. Moody, D. deQuilettes, M. Bawendi, T. Watson, and V. Bulovic, "Predicting low toxicity and scalable solvent systems for high-speed roll-to-roll perovskite manufacturing," *Solar RRL*, vol. 6, no. 3, p. 2100567, 2022. [Online]. Available: https://onlinelibrary.wiley.com/doi/abs/10.1002/solr.202100567

[367] C. Wu, K. Wang, J. Li, Z. Liang, J. Li, W. Li, L. Zhao, B. Chi, and S. Wang, "Volatile solution: the way toward scalable fabrication of perovskite solar cells?" *Matter*, vol. 4, no. 3, pp. 775–793, 2021.

[368] W. Zhou, Z. Zheng, Y. Lu, M. Sui, J. Yin, and H. Yan, "Understanding liquefaction in halide perovskites upon methylamine gas exposure," *RSC Adv.*, vol. 11, pp. 20 423–20 428, 2021. [Online]. Available: http://dx.doi.org/10.1039/D1RA01458G

[369] M. Daub and H. Hillebrecht, "Understanding the "molten salt" synthesis of mapbi3 – characterization of new lead(ii)-ammine complexes as intermediates," *European Journal of Inorganic Chemistry*, vol. 2021, no. 15, pp. 1490–1497, 2021. [Online]. Available: https://chemistry-europe.onlinelibrary.wiley.com/doi/abs/10.1002/ejic.202100077

[370] M. Krummer, M. Daub, and H. Hillebrecht, "New pb(ii)-ammine complexes as intermediates from the interaction of ch3nh2 with pbx2 and ch3nh3pbx3 (x=cl, br)," *Zeitschrift für anorganische und allgemeine Chemie*, vol. n/a, no. n/a, p. e202100176. [Online]. Available: https://onlinelibrary.wiley.com/doi/abs/10.1002/zaac.202100176

[371] C. Li, S. Pang, H. Xu, and G. Cui, "Methylamine gas based synthesis and healing process toward upscaling of perovskite solar cells: Progress and perspective," *Solar RRL*, vol. 1, no. 9, p. 1700076, 2017. [Online]. Available: https://onlinelibrary.wiley.com/doi/abs/10.1002/solr.201700076

[372] B. Chen, P. N. Rudd, S. Yang, Y. Yuan, and J. Huang, "Imperfections and their passivation in halide perovskite solar cells," *Chemical Society Reviews*, vol. 48, no. 14, pp. 3842–3867, 2019.

[373] L. Fu, H. Li, L. Wang, R. Yin, B. Li, and L. Yin, "Defect passivation strategies in perovskites for an enhanced photovoltaic performance," *Energy & Environmental Science*, vol. 13, no. 11, pp. 4017–4056, 2020.

[374] S. Liu, Y. Guan, Y. Sheng, Y. Hu, Y. Rong, A. Mei, and H. Han, "A review on additives for halide perovskite solar cells," *Advanced Energy Materials*, vol. 10, no. 13, p. 1902492, 2020.

[375] T. Li, Y. Pan, Z. Wang, Y. Xia, Y. Chen, and W. Huang, "Additive engineering for highly efficient organic–inorganic halide perovskite solar cells: recent advances and perspectives," *Journal of Materials Chemistry A*, vol. 5, no. 25, pp. 12 602–12 652, 2017.

[376] S. Wu, R. Chen, S. Zhang, B. H. Babu, Y. Yue, H. Zhu, Z. Yang, C. Chen, W. Chen, Y. Huang *et al.*, "A chemically inert bismuth interlayer enhances long-term stability of inverted perovskite solar cells," *Nature communications*, vol. 10, no. 1, pp. 1–11, 2019.

[377] D. Bogachuk, K. Saddedine, D. Martineau, S. Narbey, A. Verma, P. Gebhardt, J. P. Herterich, N. Glissmann, S. Zouhair, J. Markert *et al.*, "Perovskite photovoltaic devices with carbon-based electrodes withstanding reverse-bias voltages up to–9 v and surpassing iec 61215: 2016 international standard," *Solar RRL*, vol. 6, no. 3, p. 2100527, 2022.

[378] A. Mei, Y. Sheng, Y. Ming, Y. Hu, Y. Rong, W. Zhang, S. Luo, G. Na, C. Tian, X. Hou *et al.*, "Stabilizing perovskite solar cells to iec61215: 2016 standards with over 9,000-h operational tracking," *Joule*, vol. 4, no. 12, pp. 2646–2660, 2020.

[379] F. Zhang, X. Yang, H. Wang, M. Cheng, J. Zhao, and L. Sun, "Structure engineering of hole–conductor free perovskite-based solar cells with low-temperature-processed commercial carbon paste as cathode," *ACS applied materials & interfaces*, vol. 6, no. 18, pp. 16 140–16 146, 2014.

[380] X. Xiao, Y. Chu, C. Zhang, Z. Zhang, Z. Qiu, C. Qiu, H. Wang, A. Mei, Y. Rong, G. Xu *et al.*, "Enhanced perovskite electronic properties via a-site cation engineering," *Fundamental Research*, vol. 1, no. 4, pp. 385–392, 2021.

[381] S. G. Hashmi, D. Martineau, X. Li, M. Ozkan, A. Tiihonen, M. I. Dar, T. Sarikka, S. M. Zakeeruddin, J. Paltakari, P. D. Lund, and M. Grätzel, "Air processed inkjet infiltrated carbon based printed perovskite solar cells with high stability and reproducibility," *Advanced Materials Technologies*, vol. 2, no. 1, p. 1600183. [Online]. Available: https://onlinelibrary.wiley.com/doi/abs/10.1002/admt.201600183

[382] K. R. Taretto, "Modeling and characterization of polycrystalline silicon for solar cells and microelectronics," 2003.

[383] T. S. Sherkar, C. Momblona, L. Gil-Escrig, J. Ávila, M. Sessolo, H. J. Bolink, and L. J. A. Koster, "Recombination in perovskite solar cells: significance of grain boundaries, interface traps, and defect ions," *ACS energy letters*, vol. 2, no. 5, pp. 1214–1222, 2017.

[384] A.-F. Castro-Méndez, J. Hidalgo, and J.-P. Correa-Baena, "The role of grain boundaries in perovskite solar cells," *Advanced Energy Materials*, vol. 9, no. 38, p. 1901489, 2019.

[385] J. S. Yun, J. Seidel, J. Kim, A. M. Soufiani, S. Huang, J. Lau, N. J. Jeon, S. I. Seok, M. A. Green, and A. Ho-Baillie, "Critical role of grain boundaries for ion migration in formamidinium and methylammonium lead halide perovskite solar cells," *Advanced Energy Materials*, vol. 6, no. 13, p. 1600330, 2016.

[386] D. W. de Quilettes, S. M. Vorpahl, S. D. Stranks, H. Nagaoka, G. E. Eperon, M. E. Ziffer, H. J. Snaith, and D. S. Ginger, "Impact of microstructure on local carrier lifetime in perovskite solar cells," *Science*, vol. 348, no. 6235, pp. 683–686, 2015.

[387] E. M. Tennyson, T. A. Doherty, and S. D. Stranks, "Heterogeneity at multiple length scales in halide perovskite semiconductors," *Nature Reviews Materials*, vol. 4, no. 9, pp. 573–587, 2019.

[388] G. Landi, H. C. Neitzert, C. Barone, C. Mauro, F. Lang, S. Albrecht, B. Rech, and S. Pagano, "Correlation between electronic defect states distribution and device performance of perovskite solar cells," *Advanced Science*, vol. 4, no. 10, p. 1700183, 2017.

[389] J. S. Yun, A. Ho-Baillie, S. Huang, S. H. Woo, Y. Heo, J. Seidel, F. Huang, Y.-B. Cheng, and M. A. Green, "Benefit of grain boundaries in organic–inorganic halide planar perovskite solar cells," *The journal of physical chemistry letters*, vol. 6, no. 5, pp. 875–880, 2015.

[390] W. Tress, N. Marinova, O. Inganäs, M. K. Nazeeruddin, S. M. Zakeeruddin, and M. Graetzel, "Predicting the open-circuit voltage of ch3nh3pbi3 perovskite solar cells using electroluminescence and photovoltaic quantum efficiency spectra: the role of radiative and non-radiative recombination," *Advanced Energy Materials*, vol. 5, no. 3, p. 1400812, 2015.

[391] K. Tvingstedt, O. Malinkiewicz, A. Baumann, C. Deibel, H. J. Snaith, V. Dyakonov, and H. J. Bolink, "Radiative efficiency of lead iodide based perovskite solar cells," *Scientific reports*, vol. 4, no. 1, pp. 1–7, 2014.

[392] S. D. Stranks and H. J. Snaith, "Metal-halide perovskites for photovoltaic and light-emitting devices," *Nature nanotechnology*, vol. 10, no. 5, pp. 391–402, 2015.

[393] S. D. Stranks, V. M. Burlakov, T. Leijtens, J. M. Ball, A. Goriely, and H. J. Snaith, "Recombination kinetics in organic-inorganic perovskites: excitons, free charge, and subgap states," *Physical Review Applied*, vol. 2, no. 3, p. 034007, 2014.

[394] T. Liu, Y. Rong, Y. Xiong, A. Mei, Y. Hu, Y. Sheng, P. Jiang, X. Hou, M. Duan, Y. Guan *et al.*, "Spacer improvement for efficient and fully printable mesoscopic perovskite solar cells," *RSC advances*, vol. 7, no. 17, pp. 10 118–10 123, 2017.

[395] M. Stolterfoht, M. Grischek, P. Caprioglio, C. M. Wolff, E. Gutierrez-Partida, F. Peña-Camargo, D. Rothhardt, S. Zhang, M. Raoufi, J. Wolansky *et al.*, "How to quantify the efficiency potential of neat perovskite films: Perovskite semiconductors with an implied efficiency exceeding 28%," *Advanced Materials*, vol. 32, no. 17, p. 2000080, 2020.

[396] L. Krückemeier, U. Rau, M. Stolterfoht, and T. Kirchartz, "How to report record open-circuit voltages in lead-halide perovskite solar cells," *Advanced energy materials*, vol. 10, no. 1, p. 1902573, 2020.

[397] T. Liu, L. Liu, M. Hu, Y. Yang, L. Zhang, A. Mei, and H. Han, "Critical parameters in tio2/zro2/carbon-based mesoscopic perovskite solar cell," *Journal of Power Sources*, vol. 293, pp. 533 – 538, 2015. [Online]. Available: http://www.sciencedirect.com/science/article/pii/S0378775315010162

[398] H. Lakhiani, T. Dunlop, F. De Rossi, S. Dimitrov, R. Kerremans, C. Charbonneau, T. Watson, J. Barbe, and W. C. Tsoi, "Variations of infiltration and electronic contact in mesoscopic perovskite solar cells revealed by high-resolution multi-mapping techniques," *Advanced Functional Materials*, vol. 29, no. 25, p. 1900885, 2019.

[399] Y. Zhou and N. P. Padture, "Understanding and engineering grain boundaries for high-performance halide perovskite photovoltaics," in *2020 47th IEEE Photovoltaic Specialists Conference (PVSC)*. IEEE, 2020, pp. 2316–2320.

[400] S. Wieghold, J.-P. Correa-Baena, L. Nienhaus, S. Sun, K. E. Shulenberger, Z. Liu, J. S. Tresback, S. S. Shin, M. G. Bawendi, and T. Buonassisi, "Precursor concentration affects grain size, crystal orientation, and local performance in mixed-ion lead perovskite solar cells," *ACS Applied Energy Materials*, vol. 1, no. 12, pp. 6801–6808, 2018.

[401] X. Ren, Z. Yang, D. Yang, X. Zhang, D. Cui, Y. Liu, Q. Wei, H. Fan, and S. F. Liu, "Modulating crystal grain size and optoelectronic properties of perovskite films for solar cells by reaction temperature," *Nanoscale*, vol. 8, no. 6, pp. 3816–3822, 2016.

[402] S. Jariwala, H. Sun, G. W. Adhyaksa, A. Lof, L. A. Muscarella, B. Ehrler, E. C. Garnett, and D. S. Ginger, "Local crystal misorientation influences nonradiative recombination in halide perovskites," *Joule*, vol. 3, no. 12, pp. 3048–3060, 2019.

[403] I. Mela, C. Poudel, M. Anaya, G. Delport, K. Frohna, S. Macpherson, T. A. Doherty, A. Scheeder, S. D. Stranks, and C. F. Kaminski, "Revealing nanomechanical domains and their transient behavior in mixed-halide perovskite films," *Advanced Functional Materials*, vol. 31, no. 23, p. 2100293, 2021.

[404] G. W. Adhyaksa, S. Brittman, H. Āboliņš, A. Lof, X. Li, J. D. Keelor, Y. Luo, T. Duevski, R. M. Heeren, S. R. Ellis *et al.*, "Understanding detrimental and beneficial grain boundary effects in halide perovskites," *Advanced Materials*, vol. 30, no. 52, p. 1804792, 2018.

[405] H. Sun, G. W. Adhyaksa, and E. C. Garnett, "The application of electron backscatter diffraction on halide perovskite materials," *Advanced Energy Materials*, vol. 10, no. 26, p. 2000364, 2020.

[406] Z. Zhang, M. Wang, L. Ren, and K. Jin, "Tunability of band gap and photoluminescence in ch3nh3pbi3 films by anodized aluminum oxide templates," *Scientific reports*, vol. 7, no. 1, pp. 1–7, 2017.

[407] V. D'Innocenzo, A. R. Srimath Kandada, M. De Bastiani, M. Gandini, and A. Petrozza, "Tuning the light emission properties by band gap engineering in hybrid lead halide perovskite," *Journal of the American Chemical Society*, vol. 136, no. 51, pp. 17 730–17 733, 2014.

[408] G. Grancini, S. Marras, M. Prato, C. Giannini, C. Quarti, F. De Angelis, M. De Bastiani, G. E. Eperon, H. J. Snaith, L. Manna *et al.*, "The impact of the crystallization processes on the structural and optical properties of hybrid perovskite films for photovoltaics," *The journal of physical chemistry letters*, vol. 5, no. 21, pp. 3836–3842, 2014.

[409] L. Wagner, L. E. Mundt, G. Mathiazhagan, M. Mundus, M. C. Schubert, S. Mastroianni, U. Würfel, A. Hinsch, and S. W. Glunz, "Distinguishing crystallization stages and their influence on quantum efficiency during perovskite solar cell formation in real-time," *Scientific reports*, vol. 7, no. 1, pp. 1–6, 2017.

[410] K. Frohna, M. Anaya, S. Macpherson, J. Sung, T. A. Doherty, Y.-H. Chiang, A. J. Winchester, K. W. Orr, J. E. Parker, P. D. Quinn *et al.*, "Nanoscale chemical heterogeneity dominates the optoelectronic response of alloyed perovskite solar cells," *Nature nanotechnology*, vol. 17, no. 2, pp. 190–196, 2022.

[411] J. J. Choi, X. Yang, Z. M. Norman, S. J. Billinge, and J. S. Owen, "Structure of methylammonium lead iodide within mesoporous titanium dioxide: active material in high-performance perovskite solar cells," *Nano letters*, vol. 14, no. 1, pp. 127–133, 2014.

[412] B. Yang, J. Suo, F. Di Giacomo, S. Olthof, D. Bogachuk, Y. Kim, X. Sun, L. Wagner, F. Fu, S. M. Zakeeruddin *et al.*, "Interfacial passivation engineering of perovskite solar cells with fill factor over 82% and outstanding operational stability on nip architecture," *ACS energy letters*, vol. 6, no. 11, pp. 3916–3923, 2021.

[413] L. Wagner, P. Schygulla, J. P. Herterich, M. Elshamy, D. Bogachuk, S. Zouhair, S. Mastroianni, U. Würfel, Y. Liu, S. M. Zakeeruddin *et al.*, "Revealing fundamentals of charge extraction in photovoltaic devices through potentiostatic photoluminescence imaging," *Matter*, 2022.

[414] D. Bogachuk, R. Tsuji, D. Martineau, S. Narbey, J. P. Herterich, L. Wagner, K. Suginuma, S. Ito, and A. Hinsch, "Comparison of highly conductive natural and synthetic graphites for electrodes in perovskite solar cells," *Carbon*, vol. 178, pp. 10–18, 2021.

[415] J. Shao, S. Yang, L. Lei, Q. Cao, Y. Yu, and Y. Liu, "Pore size dependent hysteresis elimination in perovskite solar cells based on highly porous tio2 films with widely tunable pores of 15–34 nm," *Chemistry of Materials*, vol. 28, no. 19, pp. 7134–7144, 2016.

[416] Y. Tanaka, S. L. Lim, W. P. Goh, C. Jiang, S. Y. Tee, T. Ye, X. Li, K. H. Nguyen, C. J. J. Lee, N. Ding *et al.*, "Fabrication of mesoporous titania nanoparticles with controlled porosity and connectivity for studying the photovoltaic properties in perovskite solar cells," *ChemNanoMat*, vol. 4, no. 4, pp. 394–400, 2018.

[417] Y. Yang, M. T. Hoang, D. Yao, N. D. Pham, V. T. Tiong, X. Wang, and H. Wang, "Spiro-ometad or cuscn as a preferable hole transport material for carbon-based planar perovskite solar cells," *Journal of Materials Chemistry A*, vol. 8, no. 25, pp. 12 723–12 734, 2020.

[418] M. Zhang, B. Wilkinson, Y. Liao, J. Zheng, C. F. J. Lau, J. Kim, J. Bing, M. A. Green, S. Huang, and A. W.-Y. Ho-Baillie, "Electrode design to overcome substrate transparency limitations for highly efficient 1 cm2 mesoscopic perovskite solar cells," *Joule*, vol. 2, no. 12, pp. 2694–2705, 2018.

[419] H.-S. Kim, I.-H. Jang, N. Ahn, M. Choi, A. Guerrero, J. Bisquert, and N.-G. Park, "Control of i–v hysteresis in ch3nh3pbi3 perovskite solar cell," *The journal of physical chemistry letters*, vol. 6, no. 22, pp. 4633–4639, 2015.

[420] J. Y. Kim, H. S. Jung, J. H. No, J.-R. Kim, and K. S. Hong, "Influence of anatase-rutile phase transformation on dielectric properties of sol-gel derived tio2 thin films," *Journal of electroceramics*, vol. 16, no. 4, pp. 447–451, 2006.

[421] W. Zhou, F. Sun, K. Pan, G. Tian, B. Jiang, Z. Ren, C. Tian, and H. Fu, "Well-ordered large-pore mesoporous anatase tio2 with remarkably high thermal stability and improved crystallinity: preparation, characterization, and photocatalytic performance," *Advanced Functional Materials*, vol. 21, no. 10, pp. 1922–1930, 2011.

[422] W. Zhou, W. Li, J.-Q. Wang, Y. Qu, Y. Yang, Y. Xie, K. Zhang, L. Wang, H. Fu, and D. Zhao, "Ordered mesoporous black tio2 as highly efficient hydrogen evolution photocatalyst," *Journal of the American Chemical Society*, vol. 136, no. 26, pp. 9280–9283, 2014.

[423] Z.-h. Liu, S. Bi, G.-l. Hou, C.-z. Ying, and X.-j. Su, "Dual-sized tio2 nanoparticles as scaffold layers in carbon-based mesoscopic perovskite solar cells with enhanced performance," *Journal of Power Sources*, vol. 430, pp. 12–19, 2019.

[424] M. Hörantner, W. Zhang, M. Saliba, K. Wojciechowski, and H. Snaith, "Templated microstructural growth of perovskite thin films via colloidal monolayer

lithography," *Energy & environmental science*, vol. 8, no. 7, pp. 2041–2047, 2015.

[425] A. Kessel, C. Frydendahl, S. R. K. C. Indukuri, N. Mazurski, P. Arora, and U. Levy, "Soft lithography for manufacturing scalable perovskite metasurfaces with enhanced emission and absorption," *Advanced Optical Materials*, vol. 8, no. 23, p. 2001627, 2020.

[426] Y. Shen, L.-P. Cheng, Y.-Q. Li, W. Li, J.-D. Chen, S.-T. Lee, and J.-X. Tang, "High-efficiency perovskite light-emitting diodes with synergetic outcoupling enhancement," *Advanced Materials*, vol. 31, no. 24, p. 1901517, 2019.

[427] E. Sowade, T. Blaudeck, and R. R. Baumann, "Inkjet printing of colloidal nanospheres: Engineering the evaporation-driven self-assembly process to form defined layer morphologies," *Nanoscale research letters*, vol. 10, no. 1, pp. 1–9, 2015.

[428] D. A. Egger, A. Bera, D. Cahen, G. Hodes, T. Kirchartz, L. Kronik, R. Lovrincic, A. M. Rappe, D. R. Reichman, and O. Yaffe, "What remains unexplained about the properties of halide perovskites?" *Advanced Materials*, vol. 30, no. 20, p. 1800691, 2018.

[429] S. G. Hashmi, D. Martineau, X. Li, M. Ozkan, A. Tiihonen, M. I. Dar, T. Sarikka, S. M. Zakeeruddin, J. Paltakari, P. D. Lund *et al.*, "Air processed inkjet infiltrated carbon based printed perovskite solar cells with high stability and reproducibility," *Advanced Materials Technologies*, vol. 2, no. 1, p. 1600183, 2017.

[430] M. Wissler, "Graphite and carbon powders for electrochemical applications," *Journal of power sources*, vol. 156, no. 2, pp. 142–150, 2006.

[431] A. Mishra, Z. Ahmad, I. Zimmermann, D. Martineau, R. Shakoor, F. Touati, K. Riaz, S. A. Al-Muhtaseb, and M. K. Nazeeruddin, "Effect of annealing temperature on the performance of printable carbon electrodes for perovskite solar cells," *Organic Electronics*, vol. 65, pp. 375–380, 2019.

[432] A. Verma, D. Martineau, E. Hack, M. Makha, E. Turner, F. Nüesch, and J. Heier, "Towards industrialization of perovskite solar cells using slot die coating," *Journal of Materials Chemistry C*, vol. 8, no. 18, pp. 6124–6135, 2020.

[433] K. Dasgupta and D. Sathiyamoorthy, "Disordered carbon–its preparation, structure, and characterisation," *Materials science and technology*, vol. 19, no. 8, pp. 995–1002, 2003.

[434] J. Meng, S. Li, and J. Niu, "Crystallite structure characteristics and its influence on methane adsorption for different rank coals," *ACS omega*, vol. 4, no. 24, pp. 20 762–20 772, 2019.

[435] E. Crespo, F. Luque, J. Barrenechea, and M. Rodas, "Influence of grinding on graphite crystallinity from experimental and natural data: implications

for graphite thermometry and sample preparation," *Mineralogical magazine*, vol. 70, no. 6, pp. 697–707, 2006.

[436] B. Warren, "X-ray diffraction in random layer lattices," *Physical Review*, vol. 59, no. 9, p. 693, 1941.

[437] D. B. Schuepfer, F. Badaczewski, J. M. Guerra-Castro, D. M. Hofmann, C. Heiliger, B. Smarsly, and P. J. Klar, "Assessing the structural properties of graphitic and non-graphitic carbons by raman spectroscopy," *Carbon*, vol. 161, pp. 359–372, 2020.

[438] W. Peng, H. Li, Y. Hu, Y. Liu, and S. Song, "Characterisation of reduced graphene oxides prepared from natural flaky, lump and amorphous graphites," *Materials Research Bulletin*, vol. 78, pp. 119–127, 2016.

[439] M. Ohler, J. Baruchel, A. Moore, P. Galez, and A. Freund, "Direct observation of mosaic blocks in highly oriented pyrolytic graphite," *Nuclear Instruments and Methods in Physics Research Section B: Beam Interactions with Materials and Atoms*, vol. 129, no. 2, pp. 257–260, 1997.

[440] A. Way, J. Luke, A. D. Evans, Z. Li, J.-S. Kim, J. R. Durrant, H. K. Hin Lee, and W. C. Tsoi, "Fluorine doped tin oxide as an alternative of indium tin oxide for bottom electrode of semi-transparent organic photovoltaic devices," *AIP Advances*, vol. 9, no. 8, p. 085220, 2019.

[441] C. Sima, C. Grigoriu, and S. Antohe, "Comparison of the dye-sensitized solar cells performances based on transparent conductive ito and fto," *Thin Solid Films*, vol. 519, no. 2, pp. 595–597, 2010.

[442] L. Lucera, F. Machui, P. Kubis, H. Schmidt, J. Adams, S. Strohm, T. Ahmad, K. Forberich, H.-J. Egelhaaf, and C. Brabec, "Highly efficient, large area, roll coated flexible and rigid opv modules with geometric fill factors up to 98.5% processed with commercially available materials," *Energy & Environmental Science*, vol. 9, no. 1, pp. 89–94, 2016.

[443] C. M. Wolff, P. Caprioglio, M. Stolterfoht, and D. Neher, "Nonradiative recombination in perovskite solar cells: the role of interfaces," *Advanced Materials*, vol. 31, no. 52, p. 1902762, 2019.

[444] J. Jeong, M. Kim, J. Seo, H. Lu, P. Ahlawat, A. Mishra, Y. Yang, M. A. Hope, F. T. Eickemeyer, M. Kim *et al.*, "Pseudo-halide anion engineering for α-fapbi3 perovskite solar cells," *Nature*, vol. 592, no. 7854, pp. 381–385, 2021.

[445] M. A. Green, E. D. Dunlop, J. Hohl-Ebinger, M. Yoshita, N. Kopidakis, and X. Hao, "Solar cell efficiency tables (version 58)," *Progress in Photovoltaics: Research and Applications*, vol. 29, no. NREL/JA-5900-80028, 2021.

[446] I. IEC, "61215-2: 2016–terrestrial photovoltaic (pv) modules–design qualification and type approval–part 2: Test procedures," *IEC: Geneva, Switzerland*, 2016.

[447] P. Holzhey and M. Saliba, "A full overview of international standards assessing the long-term stability of perovskite solar cells," *Journal of Materials Chemistry A*, vol. 6, no. 44, pp. 21 794–21 808, 2018.

[448] L. Shi, M. P. Bucknall, T. L. Young, M. Zhang, L. Hu, J. Bing, D. S. Lee, J. Kim, T. Wu, N. Takamure *et al.*, "Gas chromatography–mass spectrometry analyses of encapsulated stable perovskite solar cells," *Science*, vol. 368, no. 6497, p. eaba2412, 2020.

[449] R. Cheacharoen, K. A. Bush, N. Rolston, D. Harwood, R. H. Dauskardt, and M. D. McGehee, "Damp heat, temperature cycling and uv stress testing of encapsulated perovskite photovoltaic cells," in *2018 IEEE 7th World Conference on Photovoltaic Energy Conversion (WCPEC)(A Joint Conference of 45th IEEE PVSC, 28th PVSEC & 34th EU PVSEC)*. IEEE, 2018, pp. 3498–3502.

[450] S. Bai, P. Da, C. Li, Z. Wang, Z. Yuan, F. Fu, M. Kawecki, X. Liu, N. Sakai, J. T.-W. Wang *et al.*, "Planar perovskite solar cells with long-term stability using ionic liquid additives," *Nature*, vol. 571, no. 7764, pp. 245–250, 2019.

[451] W. Chen, Y. Wu, Y. Yue, J. Liu, W. Zhang, X. Yang, H. Chen, E. Bi, I. Ashraful, M. Grätzel *et al.*, "Efficient and stable large-area perovskite solar cells with inorganic charge extraction layers," *Science*, vol. 350, no. 6263, pp. 944–948, 2015.

[452] R. Shang, Z. Zhou, H. Nishioka, H. Halim, S. Furukawa, I. Takei, N. Ninomiya, and E. Nakamura, "Disodium benzodipyrrole sulfonate as neutral hole-transporting materials for perovskite solar cells," *Journal of the American Chemical Society*, vol. 140, no. 15, pp. 5018–5022, 2018.

[453] R. Cheacharoen, N. Rolston, D. Harwood, K. A. Bush, R. H. Dauskardt, and M. D. McGehee, "Design and understanding of encapsulated perovskite solar cells to withstand temperature cycling," *Energy & Environmental Science*, vol. 11, no. 1, pp. 144–150, 2018.

[454] F. Bella, G. Griffini, J.-P. Correa-Baena, G. Saracco, M. Grätzel, A. Hagfeldt, S. Turri, and C. Gerbaldi, "Improving efficiency and stability of perovskite solar cells with photocurable fluoropolymers," *Science*, vol. 354, no. 6309, pp. 203–206, 2016.

[455] A. R. Bowring, L. Bertoluzzi, B. C. O'Regan, and M. D. McGehee, "Reverse bias behavior of halide perovskite solar cells," *Advanced Energy Materials*, vol. 8, no. 8, p. 1702365, 2018.

[456] R. A. Razera, D. A. Jacobs, F. Fu, P. Fiala, M. Dussouillez, F. Sahli, T. C. Yang, L. Ding, A. Walter, A. F. Feil *et al.*, "Instability of p–i–n perovskite solar cells under reverse bias," *Journal of Materials Chemistry A*, vol. 8, no. 1, pp. 242–250, 2020.

[457] J. Qian, M. Ernst, D. Walter, M. A. Mahmud, P. Hacke, K. Weber, M. Al-Jassim, and A. Blakers, "Destructive reverse bias pinning in perovskite/silicon

tandem solar modules caused by perovskite hysteresis under dynamic shading," *Sustainable Energy & Fuels*, vol. 4, no. 8, pp. 4067–4075, 2020.

[458] L. Bertoluzzi, C. C. Boyd, N. Rolston, J. Xu, R. Prasanna, B. C. O'Regan, and M. D. McGehee, "Mobile ion concentration measurement and open-access band diagram simulation platform for halide perovskite solar cells," *Joule*, vol. 4, no. 1, pp. 109–127, 2020.

[459] M. Jung, T. J. Shin, J. Seo, G. Kim, and S. I. Seok, "Structural features and their functions in surfactant-armoured methylammonium lead iodide perovskites for highly efficient and stable solar cells," *Energy & Environmental Science*, vol. 11, no. 8, pp. 2188–2197, 2018.

[460] D. Kiermasch, L. Gil-Escrig, H. J. Bolink, and K. Tvingstedt, "Effects of masking on open-circuit voltage and fill factor in solar cells," *Joule*, vol. 3, no. 1, pp. 16–26, 2019.

[461] J. Bishop, "Computer simulation of the effects of electrical mismatches in photovoltaic cell interconnection circuits," *Solar cells*, vol. 25, no. 1, pp. 73–89, 1988.

[462] H. Yang, H. Wang, and M. Wang, "Investigation of the relationship between reverse current of crystalline silicon solar cells and conduction of bypass diode," *International Journal of Photoenergy*, vol. 2012, 2012.

[463] O. Breitenstein, J. Bauer, K. Bothe, W. Kwapil, D. Lausch, U. Rau, J. Schmidt, M. Schneemann, M. C. Schubert, J.-M. Wagner *et al.*, "Understanding junction breakdown in multicrystalline solar cells," *Journal of applied physics*, vol. 109, no. 7, p. 5, 2011.

[464] S. Wendlandt, A. Giese, A. Drobisch, D. Tornow, M. Hanusch, J. Berghold, S. Krauter, and P. Grunow, "The temperature as the real hot spot risk factor at pv-modules," in *27th European Photovoltaic Solar Energy Conference, Frankfurt (Main), Germany*, 2012.

[465] R. G. Vieira, F. M. de Araújo, M. Dhimish, and M. I. Guerra, "A comprehensive review on bypass diode application on photovoltaic modules," *Energies*, vol. 13, no. 10, p. 2472, 2020.

[466] G. Y. Kim, A. Senocrate, T.-Y. Yang, G. Gregori, M. Grätzel, and J. Maier, "Large tunable photoeffect on ion conduction in halide perovskites and implications for photodecomposition," *Nature materials*, vol. 17, no. 5, pp. 445–449, 2018.

[467] A. Senocrate, I. Moudrakovski, G. Y. Kim, T.-Y. Yang, G. Gregori, M. Grätzel, and J. Maier, "The nature of ion conduction in methylammonium lead iodide: a multimethod approach," *Angewandte Chemie International Edition*, vol. 56, no. 27, pp. 7755–7759, 2017.

[468] T.-Y. Yang, G. Gregori, N. Pellet, M. Grätzel, and J. Maier, "The significance of ion conduction in a hybrid organic–inorganic lead-iodide-based perovskite photosensitizer," *Angewandte Chemie International*

Edition, vol. 54, no. 27, pp. 7905–7910, 2015. [Online]. Available: https://onlinelibrary.wiley.com/doi/abs/10.1002/anie.201500014

[469] J. Haruyama, K. Sodeyama, L. Han, and Y. Tateyama, "First-principles study of ion diffusion in perovskite solar cell sensitizers," *Journal of the American Chemical Society*, vol. 137, no. 32, pp. 10 048–10 051, 2015.

[470] E. Mosconi and F. De Angelis, "Mobile ions in organohalide perovskites: interplay of electronic structure and dynamics," *ACS Energy Letters*, vol. 1, no. 1, pp. 182–188, 2016.

[471] G. F. Samu, Á. Balog, F. De Angelis, D. Meggiolaro, P. V. Kamat, and C. Janáky, "Electrochemical hole injection selectively expels iodide from mixed halide perovskite films," *Journal of the American Chemical Society*, vol. 141, no. 27, pp. 10 812–10 820, 2019.

[472] E. J. Wolf, I. E. Gould, L. B. Bliss, J. J. Berry, and M. D. McGehee, "Designing modules to prevent reverse bias degradation in perovskite solar cells when partial shading occurs," *Solar RRL*, vol. 6, no. 3, p. 2100239, 2022.

[473] S. Chen, X. Xiao, H. Gu, and J. Huang, "Iodine reduction for reproducible and high-performance perovskite solar cells and modules," *Science Advances*, vol. 7, no. 10, p. eabe8130, 2021.

[474] S. Wang, Y. Jiang, E. J. Juarez-Perez, L. K. Ono, and Y. Qi, "Accelerated degradation of methylammonium lead iodide perovskites induced by exposure to iodine vapour," *Nature Energy*, vol. 2, no. 1, pp. 1–8, 2016.

[475] Z.-B. Liu, J.-G. Tian, W.-P. Zang, W.-Y. Zhou, F. Song, C.-P. Zhang, J.-Y. Zheng, and H. Xu, "Flexible alteration of optical nonlinearities of iodine charge-transfer complexes in solutions," *Optics letters*, vol. 29, no. 10, pp. 1099–1101, 2004.

[476] "Solar pv tracking report," *International Energy Agency*. [Online]. Available: https://www.iea.org/reports/solar-pv

[477] S. Bouckaert, A. F. Pales, C. McGlade, U. Remme, B. Wanner, L. Varro, D. D'Ambrosio, and T. Spencer, "Net zero by 2050: A roadmap for the global energy sector," 2021.

[478] N. M. Haegel, H. Atwater Jr, T. Barnes, C. Breyer, A. Burrell, Y.-M. Chiang, S. De Wolf, B. Dimmler, D. Feldman, S. Glunz *et al.*, "Terawatt-scale photovoltaics: Transform global energy," *Science*, vol. 364, no. 6443, pp. 836–838, 2019.

[479] J. C. Goldschmidt, L. Wagner, R. Pietzcker, and L. Friedrich, "Technological learning for resource efficient terawatt scale photovoltaics," *Energy & Environmental Science*, vol. 14, no. 10, pp. 5147–5160, 2021.

[480] S. Weckend, A. Wade, and G. A. Heath, "End of life management: solar photovoltaic panels," National Renewable Energy Lab.(NREL), Golden, CO (United States), Tech. Rep., 2016.

[481] F. C. Padoan, P. Altimari, and F. Pagnanelli, "Recycling of end of life photovoltaic panels: A chemical prospective on process development," *Solar Energy*, vol. 177, pp. 746–761, 2019.

[482] R. Deng, N. L. Chang, Z. Ouyang, and C. M. Chong, "A techno-economic review of silicon photovoltaic module recycling," *Renewable and Sustainable Energy Reviews*, vol. 109, pp. 532–550, 2019.

[483] G. A. Heath, T. J. Silverman, M. Kempe, M. Deceglie, D. Ravikumar, T. Remo, H. Cui, P. Sinha, C. Libby, S. Shaw *et al.*, "Research and development priorities for silicon photovoltaic module recycling to support a circular economy," *Nature Energy*, vol. 5, no. 7, pp. 502–510, 2020.

[484] F. Ardente, C. E. Latunussa, and G. A. Blengini, "Resource efficient recovery of critical and precious metals from waste silicon pv panel recycling," *Waste Management*, vol. 91, pp. 156–167, 2019.

[485] X. Tian, S. D. Stranks, and F. You, "Life cycle assessment of recycling strategies for perovskite photovoltaic modules," *Nature Sustainability*, vol. 4, no. 9, pp. 821–829, 2021.

[486] X. Feng, Q. Guo, J. Xiu, Z. Ying, K. W. Ng, L. Huang, S. Wang, H. Pan, Z. Tang, and Z. He, "Close-loop recycling of perovskite solar cells through dissolution-recrystallization of perovskite by butylamine," *Cell Reports Physical Science*, vol. 2, no. 2, p. 100341, 2021.

[487] F. Corsini and G. Griffini, "Recent progress in encapsulation strategies to enhance the stability of organometal halide perovskite solar cells," *Journal of Physics: Energy*, vol. 2, no. 3, p. 031002, 2020.

[488] S. Y. Park, J.-S. Park, B. J. Kim, H. Lee, A. Walsh, K. Zhu, D. H. Kim, and H. S. Jung, "Sustainable lead management in halide perovskite solar cells," *Nature Sustainability*, vol. 3, no. 12, pp. 1044–1051, 2020.

[489] M. Fruchart, Y. Zhou, V. Vitelli *et al.*, "On-device lead sequestration for perovskite solar cells," 2020.

[490] X. Li, F. Zhang, J. Wang, J. Tong, T. Xu, and K. Zhu, "On-device lead-absorbing tapes for sustainable perovskite solar cells," *Nature Sustainability*, vol. 4, no. 12, pp. 1038–1041, 2021.

[491] M. M. Lunardi, S. Moore, J. Alvarez-Gaitan, N. L. Chang, and R. Corkish, "Life cycle assessment on advanced silicon solar modules," in *Asia-Pacific Solar Research Conference. Melbourne*, 2017.

[492] I. Vollmer, M. J. Jenks, M. C. Roelands, R. J. White, T. van Harmelen, P. de Wild, G. P. van Der Laan, F. Meirer, J. T. Keurentjes, and B. M. Weckhuysen, "Beyond mechanical recycling: Giving new life to plastic waste," *Angewandte Chemie International Edition*, vol. 59, no. 36, pp. 15 402–15 423, 2020.

[493] G. Oreski, A. Omazic, G. C. Eder, Y. Voronko, L. Neumaier, W. Mühleisen, C. Hirschl, G. Ujvari, R. Ebner, and M. Edler, "Properties and degradation behaviour of polyolefin encapsulants for photovoltaic modules," *Progress in Photovoltaics: Research and Applications*, vol. 28, no. 12, pp. 1277–1288, 2020.

[494] A. Müller, L. Friedrich, C. Reichel, S. Herceg, M. Mittag, and D. H. Neuhaus, "A comparative life cycle assessment of silicon pv modules: Impact of module design, manufacturing location and inventory," *Solar energy Materials and Solar Cells*, vol. 230, p. 111277, 2021.